



# Carbon Nitride: A Flexible Platform for Net-Oxidative and Net-Neutral Photocatalysis

Dissertation

zur Erlangung des akademischen Grades

"doctor rerum naturalium"

(Dr. rer. nat.)

in der Wissenschaftsdisziplin "Organische Chemie"

eingereicht an der

Mathematisch-Naturwissenschaftlichen Fakultät

der Universität Potsdam

von

Alexey Galushchinskiy

Potsdam 2023

Unless otherwise indicated, this work is licensed under a Creative Commons License Attribution 4.0 International.

This does not apply to quoted content and works based on other permissions.

To view a copy of this licence visit:

<https://creativecommons.org/licenses/by/4.0>

Published online on the

Publication Server of the University of Potsdam:

<https://doi.org/10.25932/publishup-61092>

<https://nbn-resolving.org/urn:nbn:de:kobv:517-opus4-610923>

## Table of Contents

---

Foreword and Goal of this Thesis.....	1
Chapter 1. Solar Photocatalysis: A Review.....	3
1.1. Overview.....	3
1.2. Introduction.....	4
1.3. The Impact of Photocatalysis under Outdoor Solar Light.....	5
1.4. Advantages and Limitations of Photocatalysis under Outdoor Solar Light.....	6
1.5. Operating and Developing Technologies.....	8
1.6. Proof-of-Concept Research on Organic Small Molecules.....	20
1.7. Overview of Reactors. Examples of Using Reactors to Enable Photocatalytic Reactions.....	28
1.8. Challenges and Perspectives.....	31
1.9. Conclusion.....	32
Chapter 2. Deoxygenation Reaction Mediated by Anionic Carbon Nitride.....	33
2.1. Overview.....	33
2.2. Introduction.....	34
2.3. Results and Discussion.....	36
2.4. Conclusion.....	45
Chapter 3. Oxygenation of Oxazolidinones using Carbon Nitride Photobase.....	47
3.1. Overview.....	47
3.2. Introduction.....	48
3.3. Results and Discussion.....	51
3.4. Conclusion.....	66
Chapter 4. Mixed Phase Carbon Nitrides for Multiple Photocatalytic Applications.....	67
4.1. Overview.....	67

4.2. Introduction .....	68
4.3. Results and Discussion.....	69
4.4. Conclusion.....	91
5. Overall Conclusions and Outlook.....	93
6. Acknowledgements.....	96
7. Appendix — Supplementary Information.....	98
7.1. SI for Chapter 1 .....	98
7.2. SI for Chapter 2.....	99
7.3. SI for Chapter 3.....	212
7.4. SI for Chapter 4.....	297
8. Abbreviations .....	326
9. References.....	332
Afterword.....	351

## Foreword and Goal of this Thesis

---

Catalytic processes are a backbone of modern chemical research and technology, starting from test laboratory scales and ending up with bulk industrial products. Implementation of catalysts lowers thermodynamic barriers by introducing additional intermediate steps into the process via its temporary interaction with the substrates, decreasing the energy necessary for the transformation. As a result, the reaction is sped up significantly, and sometimes even previously kinetically forbidden transformations become possible. However, the catalyst typically still needs energy for activation, albeit in smaller amounts than for regular non-catalyzed process.

One of many pathways to provide energy to the catalyst is to use light as a driving force of the reaction, in this case, the process is referred to as photocatalysis. There is a plethora of photosensitive substances reported in literature for the past two decades capable of catalyzing chemical transformations, including organic molecules, transition metal complexes, and semiconductors. However, the main issues with the first two categories are that these substances are difficult to separate and recycle, and sometimes they are degraded during the reaction; additionally, the most employed ruthenium- and iridium-based photocatalysts are quite expensive and not sustainable.

Considering the reasons mentioned above, a possible solution to make photocatalysis widely applicable and ready for industrial application is to utilize heterogeneous semiconductor sensitizers (e.g., titania or cadmium sulfide), which can easily be separated and recycled from the reaction medium. Carbon nitrides are a class of such organic semiconductors. These materials are quite cheap, can be finely tuned for a specific task both during their synthesis and post-treatment, and has reasonably high absorption in the visible range of electromagnetic spectrum, making them attractive candidate platforms for sustainable photocatalysis.



The aim of this work is to explore the new net-neutral and net-oxidative organic reactions mediated by carbon nitride photocatalysts. The latter processes are of particular interest as they provide an opportunity to avoid costly and atomically ineffective oxidants by instead generating active oxygen species during the photocatalytic cycle, providing ultimate oxidizing agents literally 'out of thin air'. Then, the knowledge gained from studying these processes would be applied to make new versatile species of carbon nitride photocatalyst which would then be tested in different organic reactions and as a platform for solar photocatalytic cell to demonstrate their readiness for further implementation in actual scaled up processes, the importance of which is covered in the review preceding the experimental work.

The thesis begins with the introduction (Chapter 1), a review that extensively covers solar photocatalysis and outlines its perspectives and industrial application. Following, experimental projects are presented showing the implementation of graphitic carbon nitride and poly(heptazine imide) photocatalysts in oxygenation reactions, and finally, development of a novel family of carbon nitride materials suitable for net-oxidative and redox-neutral photocatalysis (Chapters 2 to 4). Figures, tables and schemes are numbered restarting each chapter and corresponding subsection of supplementary data, including the chapter number in the numeration; for instance, Chapter 2 contains illustrative materials numbered 2.X and its SI data has numeration S.2.Y. Compound names are numbered restarting for every chapter omitting chapter number for clarity. The chapters are accompanied by extensive Supplementary Information, which can be found in the Appendix (Section 7).

Finally, overall conclusions and outlooks (Section 5) are given, outlining the accomplished work.

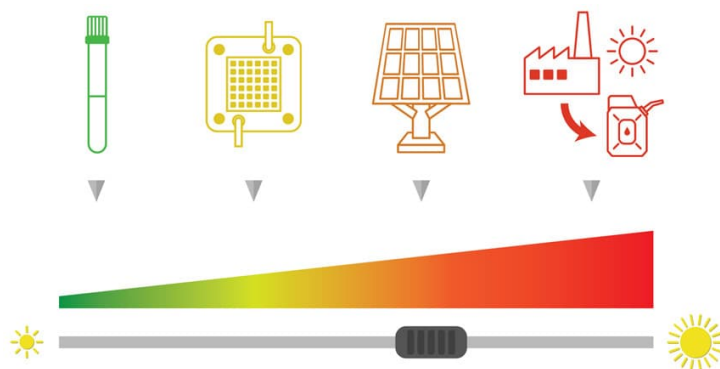


# Chapter 1. Solar Photocatalysis: A Review

---

## 1.1. Overview

With photovoltaics becoming a mature, commercially feasible technology, society is willing to allocate resources for developing and deploying new technologies based on using solar light. Analysis of projects supported by the European Commission in the last decade indicates exponential growth of funding to photocatalytic (PC) and photoelectrocatalytic (PEC) technologies that aim either at TRL 1-3 or TRL > 3, with more than 75M€ allocated from the year 2019 onwards. This review provides a summary of PC and PEC processes for the synthesis of bulk commodities such as solvents and fuels, as well as chemicals for niche applications. An overview of photoreactors for photocatalysis on a larger scale is provided. The review rounds off with the summary of reactions performed at lab scale under natural outdoor solar light to illustrate conceptual opportunities offered by solar-driven chemistry beyond the reduction of CO<sub>2</sub> and water splitting. Authors offer their vision of the impact of this area of research on society and the economy.



This chapter is an adapted version of the article:

A. Galushchinskiy, R. González-Gómez, K. McCarthy, P. Farràs, A. Savateev, *Energy Fuels* 2022, 36, 9, 4625–4639



## 1.2. Introduction

The depletion of fossil fuel reserves<sup>1, 2</sup> has led to the search for alternative sources of energy and raw materials for the chemical industry. Solar irradiation has emerged as an important alternative due to its abundance and cost-effectiveness. Photocatalytic reactions under sunlight irradiation can lead to the production of a variety of bulk and non-bulk chemicals. Bulk products such as hydrogen, syngas, methanol, formaldehyde, and formic acid can be generated through photocatalytic reactions under sunlight irradiation.<sup>3, 4</sup> Solar energy is utilized as a power source to drive these chemical transformations, leading to a cost-effective and sustainable production process. These bulk chemicals have numerous industrial applications and can serve as feedstock for the production of various other products. Non-bulk chemicals such as pharmaceuticals, additives, and reagents can also be obtained through sunlight irradiation. However, the demand and economic impact of solar chemistry for non-bulk chemicals is much lower, because their production requires a high level of precision and control, making the process more challenging and expensive.

The development of solar photocatalysis is influenced by the accumulation of carbon dioxide, which contributes significantly to the overall carbon mass in the Earth's atmosphere. Currently, the average concentration of carbon dioxide in the air is between 400 and 500 ppm, with an overall atmospheric mass of around 3200 gigatons.<sup>5</sup> While CO<sub>2</sub> is a growing threat to the biosphere, it also represents an attractive carbon reservoir. Photocatalytic fixation of carbon dioxide into bulk materials and solvents can decrease the rate of production for corresponding petrochemical products and simultaneously lower atmospheric CO<sub>2</sub> concentration, provided an efficient direct air capture (DAC) technology is developed.



Biomass is an alternative carbon source that is widely available and lower in price than fossil fuels and commercial carbon dioxide. Plants produce approximately 146 billion metric tons of biomass each year,<sup>6</sup> making it a highly abundant feedstock. Biomass can be stored for a prolonged amount of time and provide a broad scope of chemical products, similar to those derived from the oil industry.<sup>7</sup> Additionally, fractionation of non-processable biomass, such as agricultural and wood wastes, can produce several products from cellulose and lignin decay. These products can be utilized as ready-to-use chemicals or converted into biocompatible and biodegradable polymers. Further discussion on the matter is provided in Section 1.5.2.

This chapter aims to focus on the chemical, engineering, and economic aspects of bulk solar photocatalysis, specifically for the processing of CO<sub>2</sub> and biomass. The chapter provides an overview of novel experimental and pilot-scale reactors that have been reported in recent years. It also covers proof-of-concept reports, including complex organic transformations under sunlight and experimental photocatalytic setups, with an emphasis on recent results and precious metal-free catalysts. The chapter *exclusively covers natural sunlight-driven photocatalytic processes* as a demonstration of researchers' intent for potential industrial applications. Therefore, examples that use simulated or artificial light are omitted.

### 1.3. The Impact of Photocatalysis under Outdoor Solar Light on Economy

The main justification for utilizing solar energy technologies is the abundance of solar energy that Earth's surface receives from the sun, which greatly surpasses the yearly energy requirements of the global population.<sup>8</sup> Nevertheless, the commercial feasibility of a solar-powered technology is largely determined by the location and spectrum of chemical products that are generated. Solar irradiance is at its maximum in tropical areas but declines as one moves away from the equator towards the north or south



poles.<sup>9</sup> As a result, the social and economic advantages of solar-driven technologies are greatest in regions where solar irradiation is the most intense and sustained throughout the year.

The productivity of photo(electro)chemical reactors is limited by the penetration depth of electromagnetic radiation into the reactor, as predicted by the Beer-Lambert law. Therefore, the productivity of these reactors is dependent on the surface area rather than the volume. The economic potential of different geographic locations is determined by their level of development, with urban centers requiring higher value goods and services per unit area to remain competitive. Consequently, the success of bulk commodities and solar fuels, which are intermediate products in the value chain, is dependent on the availability of land ready for construction of solar facilities and high solar irradiance. In contrast, regions with a higher cost of land and lower solar radiation are more suited for the production of fine chemicals, which have a higher market value. Deploying solar harvesting devices may have environmental impacts on the local ecosystem, highlighting the importance of considering economic viability alongside scientific optimization of photocatalysts and reactors to ensure the development and deployment of appropriate technologies.<sup>10</sup>

#### 1.4. Advantages and Limitations of Photocatalysis under Outdoor Solar Light

Solar photocatalysis offers a significant advantage in terms of an abundant and free energy source to drive reactions, making it a feasible ambient temperature reaction. It also offers the potential for achieving desired internal temperatures without external heating. However, there are limitations associated with the use of solar irradiation, such as the significant impact of atmospheric gases ( $\text{N}_2$ ,  $\text{O}_2$ ,  $\text{CO}_2$ , Ar,  $\text{O}_3$ ,  $\text{NO}_x$ ,  $\text{SO}_2$ ,  $\text{CH}_4$ ) and air humidity on light absorption, as well as the uneven distribution of irradiation intensity



across the spectral range.<sup>11</sup> These limitations can affect the design of photocatalytic reactions, particularly those that require UV irradiation. Such reactions require transparent materials that are both stable under outdoor conditions and absorb UV radiation below 300 nm. While highly-fluorinated polymers are good for this purpose, providing access to photoreactors of complex shapes, they have poor mechanical properties.<sup>12</sup> Low-iron silica-doped borosilicate glasses offer excellent resistance to outdoor weather conditions and transparency until 280-285 nm, but suffer from so-called 'UV solarization', leading to changes in the material structure under high-energy irradiation, particularly the oxidation of  $\text{Fe}^{2+}$  to  $\text{Fe}^{3+}$ , which is a much stronger absorber at both UV and visible range.<sup>13</sup> The increasing use of photoredox catalysts in recent years has shifted the operational range to visible light, allowing a broader selection of transparent materials to be used, reducing the strict requirements for transparent materials. Additionally, there is a couple of more obvious parameters related to irradiation, namely diurnal light cycle in operating area and weather conditions. Effectively, these make subtropical and tropical countries seem to be the most suitable areas for solar chemical plants due to optimal insolation, day-night time ratio and lack of cloudy days, as cloudiness can obscure up to 50% of solar irradiance.<sup>14</sup>

In the realm of photochemistry and photocatalysis, chemical kinetics, thermodynamics, flow dynamics, and mass transfer are important factors to consider when scaling up reactions. Unlike conventional reactions, photochemical reactions are surface-dependent and may not effectively penetrate the bulk of the medium, particularly when the reaction medium is highly concentrated. As the linear size increases, the surface-to-volume ratio changes in reverse proportion, making batch reactors unsuitable for large-scale applications. The use of heterogeneous photocatalysts introduces additional catalyst-reagent phase interactions that must also be considered, along with specific challenges such as fouling, which occurs due to photocorrosion, surface potential



redistribution, or the accumulation of tarry by-products on reactor window.<sup>15</sup> Therefore, reactor design must take into account those new parameters.

Photocatalytic activity is evaluated using several metrics, including the apparent quantum efficiency (AQE) or apparent quantum yield (AQY) of the catalyst and the external quantum efficiency (EQE). AQE is determined by the ratio of the number of reacted molecules to the amount of incident photons under monochromatic irradiation. In contrast, EQE reflects spectral irradiation and is a more representative value for solar photocatalysis. However, AQE and EQE are sometimes used interchangeably.<sup>16</sup> Current photocatalysts typically exhibit EQE values of no more than 30% (using visible light wavelengths  $\leq 500$  nm as a reference),<sup>17-23</sup> although some recent studies report promisingly high (>60%) efficiencies for hydrogen evolution.<sup>24-26</sup>

## 1.5. Operating and Developing Technologies

### 1.5.1. Funding statistics, from basic research to applied technology

The European Commission (EC), being a leading research funding organization in Europe, supports the development of innovative and environmentally friendly projects to decarbonize the European economy. The projects are initiated at various stages, starting from basic principles to technology validation, and then advancing them towards industrial-scale processes, followed by commercialization. The EC is committed to promoting solar-driven technologies, particularly photoelectrocatalysis (PEC) and photocatalysis (PC), due to their demonstrated ability to generate value-added chemicals using sunlight (i.e., solar fuels and solar raw chemicals). These technologies have become increasingly important as they align with the EC's objectives to develop sustainable and renewable energy sources.

The European Commission has been promoting the development of solar-driven technologies such as photoelectrocatalysis (PEC) and photocatalysis (PC) for the



production of value-added chemicals using sunlight. The relevance of these technologies can be measured by the budget allocated to PEC- and PC-based projects by the EC. In the last decade, there has been a significant increase in the number of projects awarded and the budget allocated for solar-driven technologies. Less than €10M was assigned to PEC and PC-based projects in 2009-2010, compared to more than €75M designated from 2019 onwards (see [Figure 1.1](#)). This exponential growth is expected to continue with the launch of the EU Green Deal, as more projects aimed at innovating green technologies will need to be financed by European agencies.

In the early 2010s, the awarded solar-driven projects mainly investigated the basic principles of PEC and PC technologies at low technology readiness levels (TRLs). At that time, there were few proven systems to be validated, and funding calls focused on alternative green technologies such as electrolysis. In later years, PEC- and PC-based projects with higher TRLs have been prioritized and have seen a sharp increase in funding. However, projects with TRLs of 1-3 have suffered lesser growth recently.



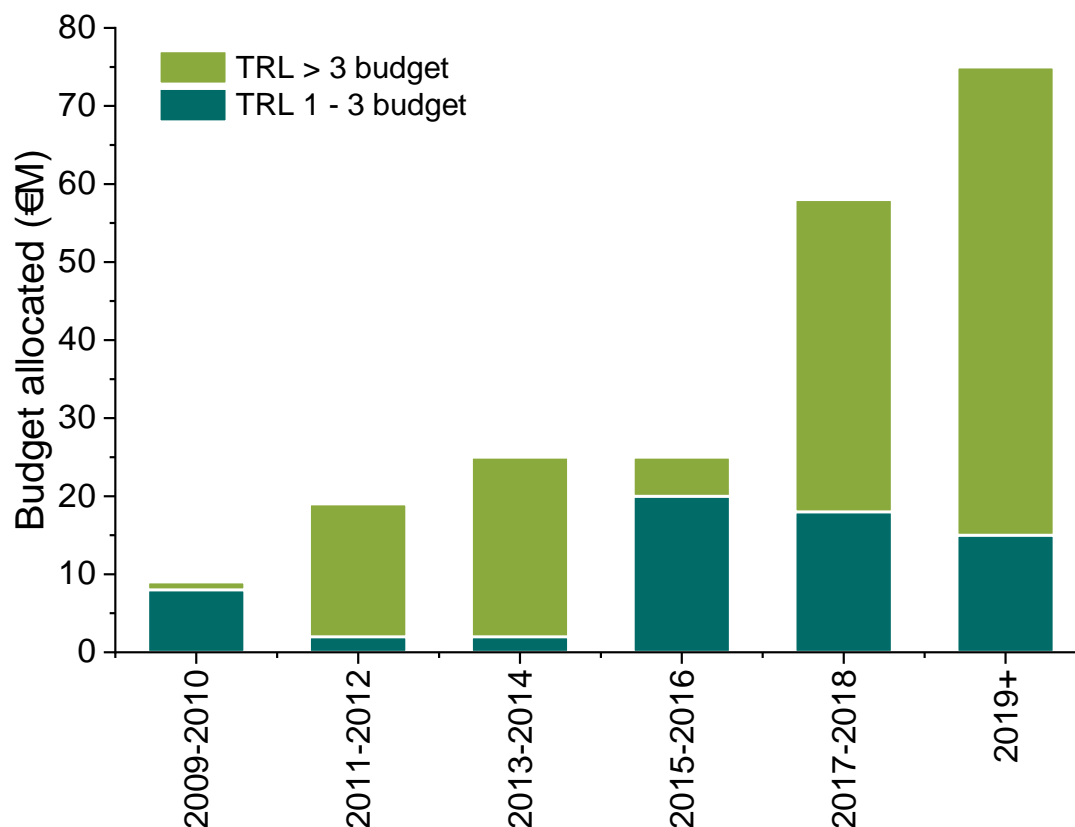


Figure 1.1. Total budget allocated biannually for PEC and PC-based projects in Europe bundled according to the TRL scale. Exponential line was fitted to the total budget awarded. Data on funded projects has been taken from CORDIS.

In the early 2010s, the European Commission (EC) funded PEC- and PC-based projects that focused on generating hydrogen fuel through water splitting, which was a relatively simple application of these technologies compared to producing solar fuels from CO<sub>2</sub>. However, the focus has shifted towards using CO<sub>2</sub> as a starting molecule to produce carbon-based materials for the chemical industry. Solar-driven projects awarded by the EC have shifted towards the production of solar chemicals, such as short-chain alcohols and carbon-based precursors, for manufacturing value-added chemicals. In terms of solar-driven technologies, early in the last decade, PEC and PC-based projects were comparably funded. Although the number of funded projects has increased over the decade, PEC-based projects have seen a slight decline over the last five years, while PC-



based projects have tripled. [Table S1.1](#) in the Supplementary Information provides a compilation of the PEC- and PC-based projects funded by the EC since 2009 and highlights the discussed trends.

Over the last decade, research efforts initially focused on investigating the fundamental principles of PEC and PC-based technologies. However, there was limited scope for validating the concepts. One of the first TRL > 3 projects in PEC-based technology for hydrogen fuel production was *PECDEMO*, which began in 2014. Its goal was to build a hybrid PEC-photovoltaic device that could split water to oxygen and hydrogen in a solar-driven process. *PECDEMO* worked with industry collaborators to scale up these devices. However, the solar-to-hydrogen (STH) conversion efficiencies at large-scale were inadequate for the devices to be commercially viable. Subsequently, more projects have been awarded to scale up solar-driven processes and validate them. In 2019, *Bac-to-Fuel* commenced work on the conversion of CO<sub>2</sub> and H<sub>2</sub> into biofuels. Their objective is to produce renewable hydrogen from the photocatalytic splitting of water. The produced green hydrogen is then combined with CO<sub>2</sub> to produce cost-effective biofuels using modified bacterial media in an electro-biocatalytic reactor. The prototype of such system is to be validated to TRL 5.

In recent years, PEC and PC-based projects have been focused on producing elaborated carbon-based molecules for the chemical industry. One such molecule is ethylene, which has been the subject of two TRL > 3 EU funded projects. *FlowPhotoChem*, initiated in June 2020, aims to construct an integrated modular system consisting of PEC, PC, and electrochemical reactors to produce ethylene and other value-added chemicals, such as ethanol, ethyl acetate, and *n*-propanol, through CO<sub>2</sub> reduction. *Sun2Chem*, launched in October 2020, intends to use a tandem PEC device and a PC reactor to produce ethylene from CO<sub>2</sub>. Additionally, other carbon-based chemicals have been the focus of TRL > 3 projects aimed at scaling up the production of green chemicals by using PEC and PC-



based technologies. The *DECADE* project, initiated in May 2020, strives to use a novel PEC system to produce green solvents and bulk chemicals, including ethyl acetate and ethyl formate, from waste CO<sub>2</sub> and bioethanol. This system would be scaled-up, and a prototype would be designed, manufactured, and validated to TRL 5. Finally, *SunCoChem*, launched in May 2020, aims to produce valuable oxygen-containing green chemicals in a PEC tandem reactor by reacting CO<sub>2</sub> and water with alkenes and polyunsaturated hydrocarbons, such as butene and limonene.

As Europe transitions towards a decarbonized economy, there is an increasing demand for funding towards the development and application of green technologies such as PEC and PC. In the short term, solar-driven technologies are expected to be scaled up and validated for industrialization and commercialization aiming to achieve commercial competitiveness. Following the examples of the US and Japan, *SUNERGY*<sup>27</sup> is a public-private initiative created by the coordination support actions *ENERGY-X* and *SUNRISE*, together with the EC. They are currently working on finalizing a European roadmap that will guide future funding calls. Globally, Mission Innovation 5 on Converting Sunlight published a roadmap in February 2021 with the aim of linking these innovative technologies with a Green Circular Economy.<sup>28</sup>

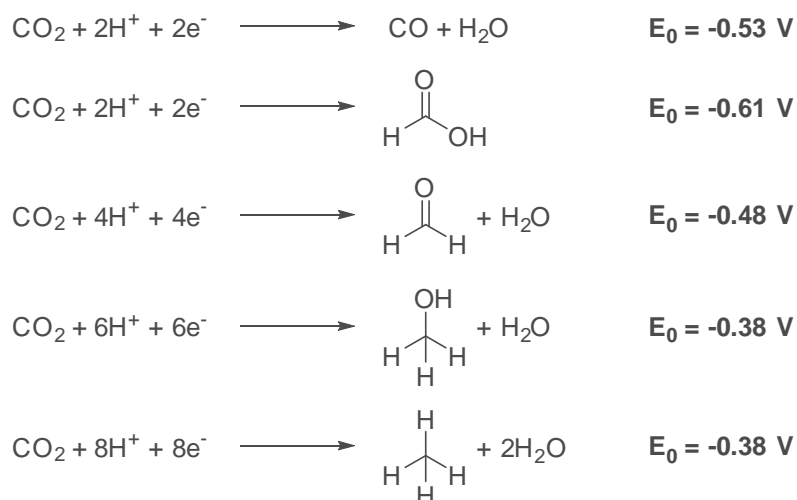
### 1.5.2. Main Chemical Targets

#### *CO<sub>2</sub> reduction products*

Carbon dioxide (CO<sub>2</sub>) is a widely available carbon-based compound and a major contributor to the increasing levels of greenhouse gases in the Earth's atmosphere.<sup>29</sup> Consequently, it has become a primary target for organic solar fuel research, as the solar economy aims to decarbonize industrial processes. Various electrochemical reactions have been investigated as potential methods for the chemical utilization of atmospheric CO<sub>2</sub>, as illustrated in [Scheme 1.1](#).<sup>30</sup>



Scheme 1.1. Reactions of CO<sub>2</sub> reductions and their electrochemical potentials. Adapted with permission from ref. (30). Copyright 2009 Royal Society of Chemistry



The scheme depicts several potential electrochemical reactions for the utilization of carbon dioxide, a readily available carbon-based compound that accumulates in the Earth's atmosphere and is a primary source material for organic solar fuel research. These reactions involve proton-coupled electron transfer (PCET) processes that can lead to the production of methane (through full reduction), methanol, formaldehyde, and acetic acid (through partial reductions). However, these reactions require multiple electron transfer steps and necessitate efficient and selective catalyst design to produce a specific product. Alternatively, CO<sub>2</sub> reduction without the formation of carbon-hydrogen (C-H) bonds results in the production of carbon monoxide, which can be mixed with hydrogen on-site to produce syngas, a valuable precursor for bulk chemicals<sup>31</sup> typically obtained through coal gasification or methane steam reforming.<sup>32</sup> A competing hydrogen evolution process typically accompanies CO<sub>2</sub> reduction at lower pH values, reducing catalyst efficiency.<sup>33, 34</sup> The structure and morphology of the catalyst are also crucial in determining selectivity, as the surface of the catalyst must first adsorb CO<sub>2</sub> and water before becoming photoactivated, and the distribution of local charges and vacancies plays an essential role.<sup>35</sup> Various heterogeneous catalysts, including metal



(primarily copper) oxides and chalcogenides systems,<sup>36, 37</sup> carbon nitrides,<sup>38</sup> graphene materials,<sup>39</sup> metal-organic frameworks (MOFs),<sup>40</sup> and MXene-based co-catalytic tandems,<sup>41</sup> are currently being studied for CO<sub>2</sub> photoreduction.

Recent scientific studies<sup>42</sup> propose that solar energetics could play a crucial role in solving the problem of CO<sub>2</sub>-fixation by converting it into methanol or longer atom chain carbohydrates, such as Fischer-Tropsch fuels and polymers. However, there is currently a lack of efficient commercial photocatalysts and reactor designs that can handle this process at an economically feasible rate in comparison to the established process of photothermal reduction. Several research initiatives are currently working on resolving this issue. Pilot plant projects relying on direct air capture (DAC) technology demonstrate that there is a significant demand for solar fuels in the market, but they do not employ photo(electro)chemical processes. The future Synhelion plant in Jülich, Germany, will utilize a solar concentrating thermal setup designed in ETH Zürich with a solar-to-work efficiency of 67.3% (the setup is shown on [Figure 1.2](#)).<sup>43, 44</sup> Similarly, the pilot SOLETAIR setup in Lappeenranta University of Technology can simultaneously reduce CO<sub>2</sub> and electrolyze water driven by photovoltaic power with syngas co-feeding (see [Figure 1.3](#)).<sup>45</sup> However, the main bottleneck of the industrial photo(electro)chemical approach remains the absence of efficient commercial photocatalysts and reactor designs that can handle the process at an economically feasible rate.<sup>46</sup> There are currently a few initiatives working on resolving this issue.<sup>47, 48</sup> Additionally, CO<sub>2</sub> reduction products, mainly methanol and syngas, possess significant market value and require selective transformations with differently designed catalysts for each setup, depending on the desired process.<sup>49, 50</sup> An alternative approach to industrial CO<sub>2</sub>-harvesting is the exploitation of the natural mechanism of photosynthesis in microalgae, although current technologies yield biodiesels that are too costly to be competitive on the market at the present moment.<sup>51</sup>



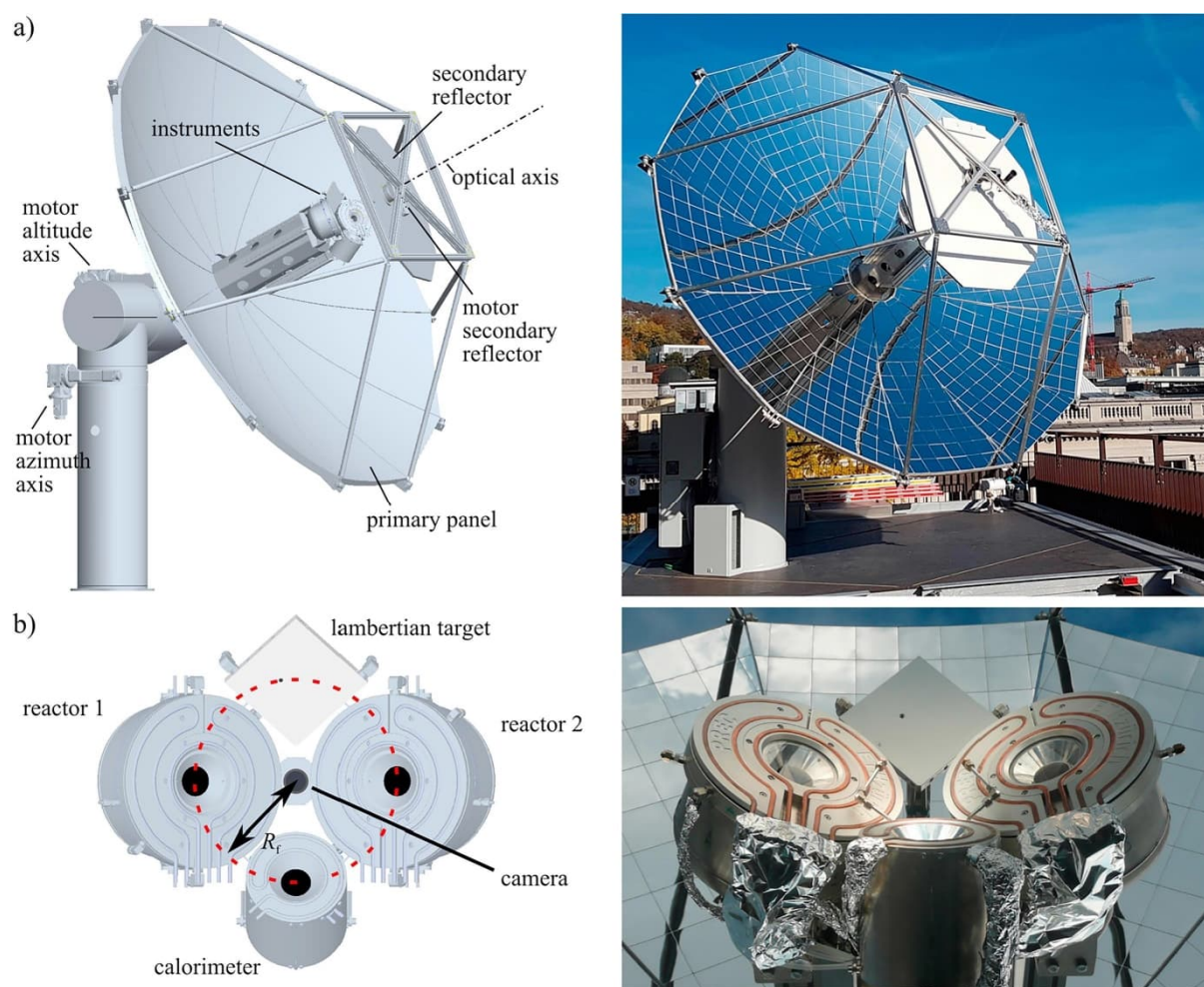


Figure 1.2. Rendered schematics and photos of a) solar tracking parabolic concentrator and b) mounted solar reactors for photothermal  $\text{CO}_2$  reduction in ETHZ. Reprinted with permission from ref (44). Copyright 2018 Elsevier.



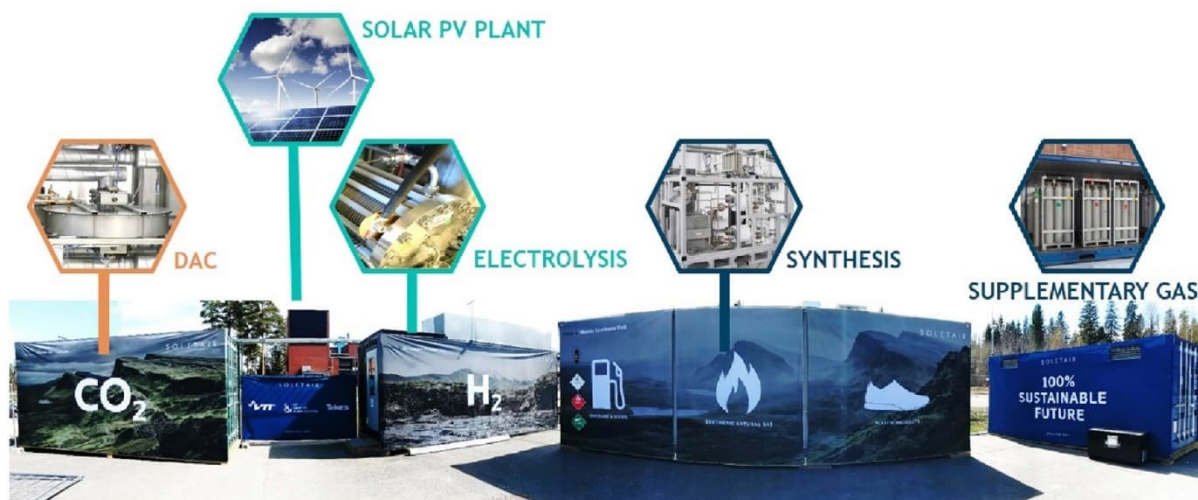


Figure 1.3. Outer view of SOLETAIR CO<sub>2</sub> processing setup modules. Reprinted with permission from ref (45). Copyright 2018 Elsevier.

The use of natural sunlight for carbon dioxide reduction is not common in scientific literature. Typically, researchers use standardized AM1.5 solar simulators for accurate and reproducible results. However, actual sunlight testing is crucial for designing genuine pilot setups and obtaining productivity information under working conditions. [Table 1.1](#) summarizes selected reports on CO<sub>2</sub> reduction under sunlight, where various types of heterogeneous catalysts, such as titania,<sup>52, 53</sup> graphitic carbon nitride (g-CN),<sup>54</sup> MOFs,<sup>55, 56</sup> and metal phosphides,<sup>57</sup> are used to selectively yield either syngas or methanol. One pilot solar concentrator setup ([Figure 1.4](#))<sup>52</sup> is notable for producing a mixed C<sub>2</sub> gas fraction from carbon dioxide and water, with acetylene and ethylene as major products and small methane impurity. The setup uses a batch reactor chamber with a transparent window mounted in the focus of a round parabolic mirror, allowing for concentration rates up to 800. Although the conversion rates are currently low and the rates for individual molecular products are lower than 1 mmol·g<sup>-1</sup>·h<sup>-1</sup>, this approach may have potential for emerging C<sub>2+</sub> solar fuel technology.



Table 1.1. Examples of sunlight-driven photocatalytic CO<sub>2</sub> reduction in literature.

Entry	Catalyst	Catalyst efficiency, %	Solvent	Conditions	Products	Conv. (%)	Yield	Ref
1	TiO <sub>2</sub> nanotube arrays	STC 0.0025-0.012 (AM1.5)	H <sub>2</sub> O	Solar concentrator reactor with CR = 200-800, 0.05 MPa CO <sub>2</sub> partial pressure, 3.5 h	CH <sub>4</sub> , C <sub>2</sub> H <sub>2</sub> , C <sub>2</sub> H <sub>4</sub> , C <sub>2</sub> H <sub>6</sub>	0.27	258, 3077, 1736, 929 μmol·g <sup>-1</sup> , respectively (after 3.5 h)	(52)
2	Cu/C-co-doped TiO <sub>2</sub> nanoparticles	N/R	Seawater	3 wt.% catalyst, constant saturation of solution with CO <sub>2</sub>	Methanol	N/R	188 μmol·g <sup>-1</sup> ·h <sup>-1</sup>	(53)
3	g-CN	AQE 2.4 (355 nm)	H <sub>2</sub> O	1 g·L <sup>-1</sup> catalyst, 3.4 atm CO <sub>2</sub>	Methanol	N/R	130 μmol·g <sup>-1</sup> ·h <sup>-1</sup>	(54)
4	Hf <sub>12</sub> -Ru-Re (2D-MOF)	N/R	CH <sub>3</sub> CN	0.1 μM cat. (Re-based), 1 atm CO <sub>2</sub> , 24 h, 0.05 v/v TEOA, 0.1M sacrificial agent	CO (HCO <sub>2</sub> H as a side product)	N/R (TON = 359, 6, 24 h)	N/R (selectivity for CO >99%)	(55)
5	Ru@Cu-HHTP (Ru-sensitized MOF)	N/R	CH <sub>3</sub> CN/H <sub>2</sub> O 4:1	0.043 g·L <sup>-1</sup> catalyst, 1 atm CO <sub>2</sub> , 24 h, 0.3M TEOA	CO	N/R	69.5 mmol·g <sup>-1</sup> ·h <sup>-1</sup> , selectivity 91.3%	(56)
6	Cd <sub>4</sub> P <sub>2</sub> Br <sub>3</sub> /Ni <sub>x</sub> P <sub>y</sub>	AQE 4.11 (artificial light), 9.83 (sunlight)	H <sub>2</sub> O	0.18 M Na <sub>2</sub> S, 0.24 M Na <sub>2</sub> SO <sub>3</sub>	CO, CH <sub>4</sub> , H <sub>2</sub>	N/R	9258 μmol·h <sup>-1</sup> ·g <sup>-1</sup> (measured for H <sub>2</sub> )	(57)





Figure 1.4. Solar concentrator setup for batch photocatalytic CO<sub>2</sub> reduction (left) and close-up of its reaction chamber (right). Reprinted with permission from ref <sup>(52)</sup>. Copyright 2021 AIP Publishing.

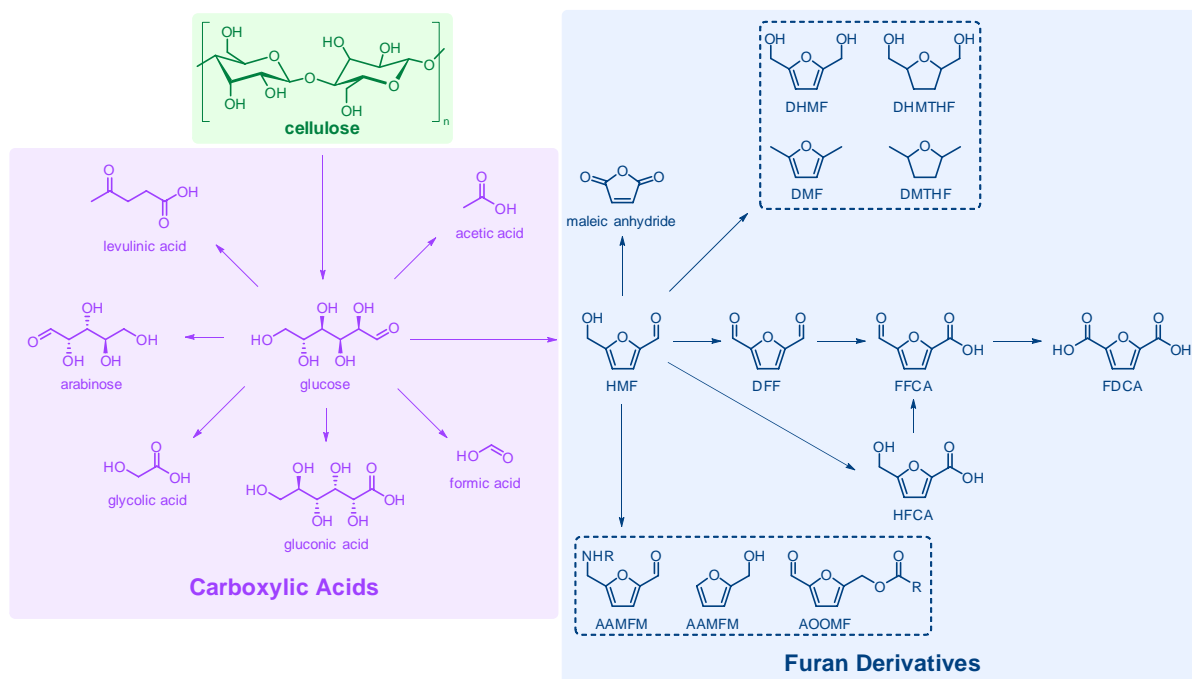
### *Biomass valorization products*

Biomass and its wastes, which are mainly composed of various types of biopolymers, present a challenging target for selective reforming through chemical pathways due to their complex and heterogeneous nature. As such, biotechnology is considered a more promising and efficient solution for their conversion. While numerous photocatalytic approaches have been proposed for biomass transformation, their technology readiness levels (TRL) are still low, and pyrolysis and bioprocessing reactors remain the predominant means of biomass conversion.<sup>58-60</sup> The key transformations involved in the conversion of cellulose biomass are depicted in [Scheme 1.2](#). Hydrolytic pre-treatment is used to break down the polymer chain into glucose monomers, which can then be oxidized to shorter chain acids such as acetic, formic or glycolic acid. Alternatively, chain breaking, terminal carbon oxidations, or rearrangement products may occur, including



5-hydroxymethylfurfural (HMF), a valuable precursor to numerous furan-based building blocks, as shown in Scheme 1.2.<sup>61</sup>

Scheme 1.2. Pathways of cellulose biomass processing. Adapted with permission from ref (61). Copyright 2021 Frontiers.



Currently, there is limited literature reports regarding the utilization of actual solar irradiation for photocatalytic processing of biomass and its derivatives. The majority of research in this area has focused on the conversion of biomass to hydrogen, as well as the transformation of feedstock into small furan-based molecules.

In one report, researchers examined the use of rice husk, a form of cellulose biomass, as a source of electrons in the process of hydrogen evolution while humins were simultaneously formed in the presence of a Pt/TiO<sub>2</sub> photocatalyst. The hydrogen yield obtained varied between 4 and 8 μmol·h<sup>-1</sup>, with the catalyst loading being 2 g·L<sup>-1</sup>, while the yield of humins was not mentioned in the study.<sup>62</sup>



Marcì *et al.* synthesized diformylfuran (DFF) by using thermally etched polymeric carbon nitride (CN) as a photocatalyst to convert HMF as a starting material. The reaction was performed in the presence of hydrogen peroxide adduct with the catalyst, and the product was obtained with a 20% yield and 88% selectivity after 4 hours. However, when carbon nitride was used alone as the photocatalyst, the yield and selectivity were as low as 47% and 38%, respectively.<sup>63</sup> Another study by Marcì *et al.* showed that porphyrin-impregnated CN improved the conversion rate of HMF to DFF up to 73%, but the selectivity for DFF decreased to 37%.<sup>64</sup>

Lignin degradation is a promising process for researchers due to its ability to provide access to products containing multiple aromatic rings. One example of this is the use of soft-template  $Zn_{0.95}Bi_{0.05}O$  nanocomposites to achieve 95% depolymerization of lignin in dioxane in 60-90 minutes. This process resulted in the formation of a range of diverse products, including phenol (21%), 2-methoxy-4-methylphenol (16%), syringaldehyde, sinapyl alcohol, phthalate esters and salts, and 4-hydroxy-benzoic acid.<sup>65</sup>

New findings have shown that a cobalt(II) terpyridine catalyst supported on titanium dioxide can be used for simultaneous  $CO_2$  reduction and biomass processing. The process involves the reduction of carbon dioxide to CO, and the conversion of pre-treated cellulose into formate accompanied by syngas production with a  $HCO_2H$  ratio of approximately 1. The yield of formate was up to 39% based on cellulose. It is important to note, however, that the experiment was carried out exclusively under AM1.5G conditions.<sup>66</sup>

## 1.6. Proof-of-Concept Research on Organic Small Molecules

Since the 1990s, researchers have been investigating the photocatalytic or photochemical synthesis of valuable organic compounds, including pharmaceutical building blocks and final target molecules, under direct solar irradiation.<sup>67</sup> However, this



approach is less economically feasible than bulk small molecules or hydrogen production due to several factors. The demand for these products is not as high as for CO<sub>2</sub> reduction or water splitting, and the insufficient TRL of pilot setups delays their implementation into industrial production pipelines.<sup>68</sup> There is also a problem of reactor versatility for processes that require different parameters, such as sunlight concentration factor, functional wavelength range, and multiple phase interaction in a concerted process.<sup>69</sup> This section covers a few selected reactions of potential value that have been tested under actual solar irradiation on a mmol scale in common lab glassware and equipment, and cannot be considered a technology ready for industrial application. The purpose here is to demonstrate the potential of the solar-to-chemical photocatalysis concept for possible scale-up and implementation. The emphasis is on net-oxidative and redox-neutral photocatalytic reactions, which align with the principles of green chemistry and do not require costly and atom-inefficient sacrificial electron donors or acceptors.

#### 1.6.1. Net-Oxidative Reactions

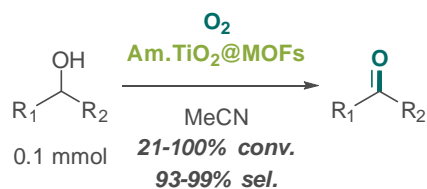
Net-oxidative photocatalytic reactions involve redox cycles, which can introduce oxygen atoms into a molecule ("oxygenase"-like transformations) or abstract protons ("oxidaze"-like processes),<sup>70</sup> forming new bonds. Photocatalytic oxidation is a promising area of research because it can utilize atmospheric oxygen as a terminal oxidant, making the process more cost-effective and environmentally friendly. The use of this approach is attractive from green chemistry principles, which do not require additional oxidizing agents to be introduced, reducing waste and resource consumption. Researchers are interested in exploring these reactions to synthesize valuable organic compounds, such as pharmaceutical building blocks, through direct solar irradiation (Scheme 1.3).



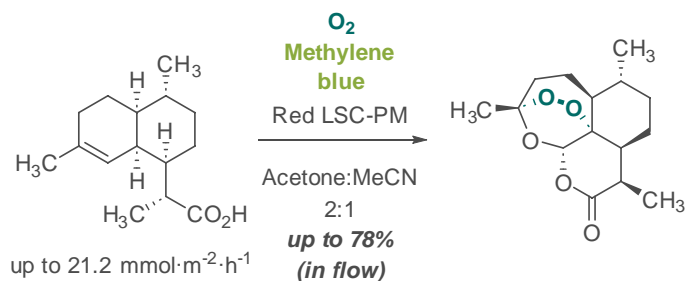
Scheme 1.3. Proof-of-concept sunlight-driven net-oxidative photocatalytic reactions used in organic synthesis.

## Net-oxidative reactions

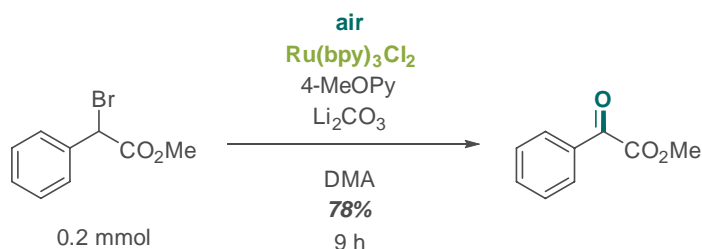
*Abedi et al., 2014*



*Cambié et al., 2019*



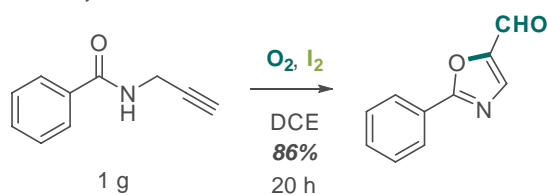
*Su et al., 2011*



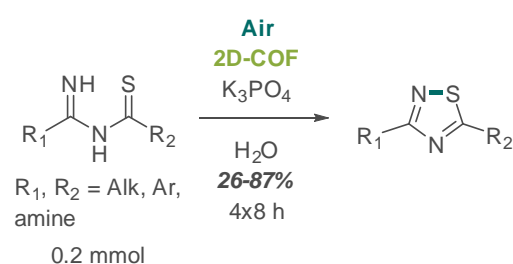
*Markushyna et al., 2021*



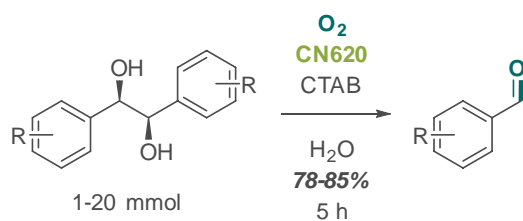
*Liu et al., 2017*



*Yuan et al., 2020*



*Niu et al., 2020*



The oxidation of alcohols is a highly desirable application of organic photoredox catalysis, particularly in case of primary alcohols. The conventional method of oxidation of alcohols involves the use of toxic, expensive high molecular mass reagents like pyridinium chlorochromate (PCC),<sup>71</sup> Dess-Martin periodinane (DMP),<sup>72</sup> or multistep procedures like DMSO-mediated oxidation (Swern reaction and similar protocols)<sup>73</sup> to achieve selectivity towards carbonyl products like aldehydes and ketones, while preventing over-oxidation products (carboxylic acids, chain breaking products, etc.). Therefore, the use of aerobic oxidation to obtain aldehydes and ketones has gained attention due to cost-efficiency and, essentially, ultimate atom economy. The synthesis of benzaldehydes from corresponding benzyl alcohols has become a widespread "benchmark reaction" for testing new photocatalysts. For instance, the sunlight-driven oxidation of a number of benzyl alcohols was conducted using MOFs as catalysts.<sup>74</sup>

The production of endoperoxides through photochemical reactions is a process of significant interest in solar organic synthesis. Artemisinins, which are polycyclic endoperoxides, have been widely used as antimalarial drugs for many years.<sup>75</sup> Despite the emergence of resistance to this type of therapy, artemisinin and its derivatives are still in high demand. Biosynthetic methods, such as using plant producers like *Artemisia annua* or engineered microorganisms, are widely used to manufacture artemisinin. However, a few alternative chemical pathways also exist, including the photochemical formation of a key 1,2,4-trioxane ring from artemisinic acid, which is a precursor derived from natural sources or via biotechnological processes. Sanofi had previously developed a process that involves the use of tetraphenylporphyrin (TPP) to generate singlet oxygen under irradiation by mercury vapor lamps in a semi-batch fashion, which produces up to 370 kg at a time.<sup>76</sup> However, the production cost of the final product is still too high to compete with natural sources. An attempt was made to improve the reaction on a lab-scale using a flow luminescent solar concentrator photomicroreactor



and methylene blue as a catalyst under outdoor sunlight. This process produced artemisinin with up to 78% yield.<sup>77</sup>

Atmospheric photocatalytic oxidation under sunlight has been utilized for the synthesis of small molecules. In one example, a series of 5-formyl-1,3-oxadiazoles were prepared by oxidative cyclization of *N*-propargyl amides under sunlight and air atmosphere using elemental iodine as both a photosensitizer and a catalyst to facilitate formation of reactive species. The aldehyde moieties were produced with only slightly lower yields than under monochromatic LED irradiation (80% under sunlight after 16 h, 83% and 86% under 450 and 395 nm LEDs, respectively, in screening conditions).<sup>78</sup> Another example demonstrated the preparation of 1-oxoesters, multifunctional precursors, from common 1-bromoesters, using a Ru(II) photocatalyst. The reaction time under sunlight was shortened from 24 h to 9 h to achieve the same yield as with a common 24W PL household lightbulb.<sup>79</sup> In addition, oxidation of heteroatoms was demonstrated in a recent publication, where protected thiophenols were converted to other valuable sulfur-containing molecules, such as sulfonyl chlorides, by a poly(heptazine imide) carbon nitride catalyst under solar irradiation, resulting in a four-fold reduction in reaction time compared to 50W 465 nm LED.<sup>80</sup>

Solar photocatalytic reactions for dehydrogenation are not limited to oxygenation reactions and can be used for other transformations. An example of this is the use of 2D-COFs as photocatalysts in the synthesis of 1,2,4-thiadiazoles through cyclization of *N*-guanyl thioureas, *N*-imidoyl thioureas, and *N*-imidoyl thioamides, using O<sub>2</sub> as a terminal oxidation agent.<sup>81</sup> In this process, oxygen abstracts two protons, leading to the formation of a new N-S bond. Another interesting reaction is the cleavage of vicinal bis-aryldiols into two respective benzaldehydes using carbon nitrides. This reaction can be performed in up to 20 mmol scale runs and may be considered as a test reaction for photocatalytic lignin processing.<sup>82</sup>

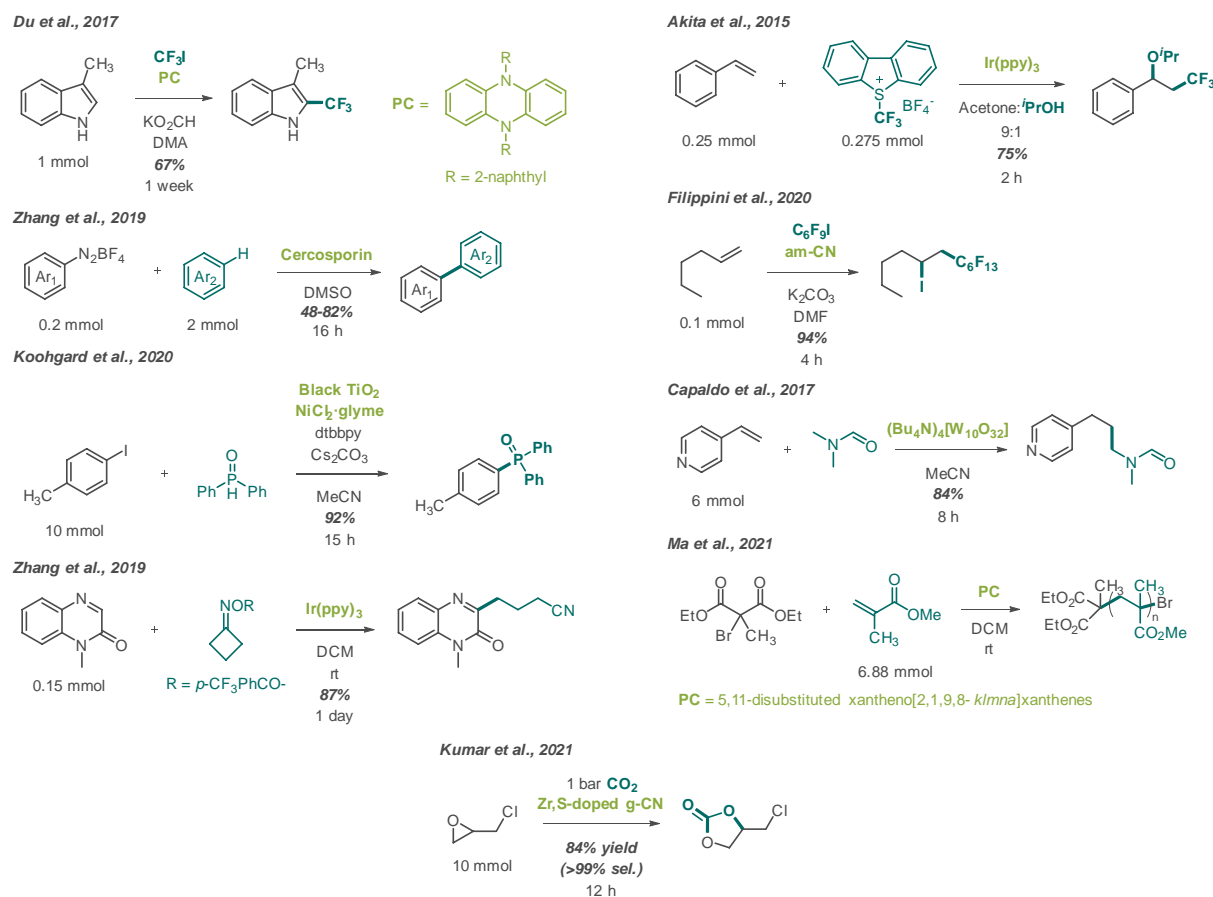


## 1.6.2. Redox-Neutral Reactions

In the field of organic chemistry, redox-neutral reactions refer to reactions where there is no net transfer of electrons from starting material(s) to other reactants, such as cross-coupling reactions (both C-H and C-X functionalizations), multiple bond additions and insertions, and recyclizations. These reactions can lead to the synthesis of complex and valuable chemicals with high efficiency, comparable to traditional methods using transition metal catalysts, as shown in Scheme 1.4.

Scheme 1.4. Proof-of-concept sunlight-driven redox-neutral photocatalytic reactions and cross-coupling used in organic synthesis.

## Redox-neutral reactions &amp; Cross-coupling



Sunlight has been used to drive a variety of cross-coupling reactions such as trifluoromethylation of indoles,<sup>83</sup> C-C-coupling of diazonium salts with non-halogenated arenes,<sup>84</sup> and dual Ni-photoredox reaction to connect aryl iodides and P(=O)-H bonds<sup>85</sup>. These protocols have the distinct feature of allowing for C-H functionalization with only one of the blocks containing leaving groups or replacing palladium(0) complexes with nickel precatalysts, making the chemistry more sustainable. Furthermore, a regioselective introduction of a primary alkyl chain to quinoxalinones by ring-opening of active cyclic *O*-substituted oximes was demonstrated with yields comparable to those achieved with LED light sources.<sup>86</sup>

Sunlight photocatalysis has been used for ene addition reactions to generate functionalized blocks. Fluoroalkylated ethers<sup>87</sup> and alkyl iodides<sup>88</sup> have been synthesized using solar photocatalysis, which involves the integration of perfluoroalkanes into aliphatic chains. Tetrabutylammonium decatungstate has been used as a photocatalyst to generate N-formyl aminoalkylpyridines from C-H insertion of vinyl pyridines, including artificial flavoring agents. The use of natural sunlight resulted in a yield of 84%, which was higher than that obtained with a solar simulator (77%), but the yield was still lower than that obtained with a setup of 10x15W fluorescent lamps (94%).<sup>89</sup> Furthermore, the co-polymerization of brominated malonic ester and acryl monomers using xantheno[2,1,9,8-*klmna*]xanthene photocatalysts to maintain chain propagation has been reported. The resulting product polymers had a mass of several kDa and were obtained without the use of harmful radical initiators, although the performance under blue LED irradiation was superior.<sup>90</sup>

In the industrial production of synthetic blocks and bulk solvents, the synthesis of ethylene carbonates from oxiranes and carbon dioxide is a critical process.<sup>91</sup> A new study reported the photocatalytic insertion of carbon dioxide into an epichlorohydrin cycle with the help of zirconium-thiamine doped graphitic carbon nitride. This process



results in the production of chloropropylene carbonate with excellent yield and selectivity. Furthermore, this photocatalytic reaction requires only half the reaction time compared to a 250W Hg lamp.<sup>92</sup>

### 1.6.3. Outline of Catalytic Systems Used for Photoredox Transformations

Based on the examples presented, it is evident that organic photocatalysis research is gradually shifting from using expensive and less abundant ruthenium- and iridium-based photocatalysts to cheaper and more sustainable alternatives. Photoredox-active compounds are becoming increasingly popular and are used extensively, ranging from well-known molecules like methylene blue and iodine to natural dyes, synthetic polyaromatic systems, and polytungstate anionic clusters. The use of these compounds can lead to comparable photocatalytic performance without the need for precious metals.

In current photoredox studies, the use of heterogeneous semiconductors as recyclable photocatalysts is a prominent feature. Among these, titanium dioxide is a widely known example with a long history of photocatalytic applications.<sup>93</sup> It is attractive due to its abundance, and its band structure and light absorption can be easily modified by sensitization or doping with different elements.<sup>94-96</sup> Other materials, such as carbon-based catalysts and 2D nanomaterials, have also emerged as promising alternatives in the past two decades. These materials have the potential to enhance photocatalytic properties and achieve better fine-tuning of the material properties.

Carbon-based catalysts and composites are considered as promising materials in the field of organic photocatalysis. These materials can be synthesized from various organic precursors in an eco-friendly manner, exhibiting high surface area and favorable photophysical properties. Although these materials have not been fully explored for



organic photocatalysis, current research is actively studying their potential application in other fields such as water splitting<sup>97</sup> and oxidative waste processing<sup>98</sup>.

In the field of organic photocatalysis, two-dimensional nanomaterials are being explored as semiconductors with a layered sheet structure that offers a variety of possibilities for doping and modification.<sup>99</sup> This class of semiconductors includes 2D covalent and metal organic frameworks (2D-COFs, 2D-MOFs) as well as carbon nitrides. These materials have shown to be versatile in conducting different types of photoredox transformations, such as net-oxidative, net-neutral, net-reductive, and dual metal-photoredox processes.<sup>100-102</sup>

## 1.7. Overview of Reactors. Examples of Using Reactors to Enable Photocatalytic Reactions

Currently, only a limited number of gram-scale solar photoreactors have been utilized for various reactions, with some of them still in operation. These photoreactors, including SOLFIN, SOLARIS/PROPHIS, and Sunflow, among others, and their respective applications, have been extensively reviewed in previous reports on solar photocatalysis.<sup>67, 103, 104</sup> Therefore, this section will highlight recent prototypes and new technologies that are emerging in the field.

Integrated photoelectrochemical (IPEC) devices are commonly used in low-TRL setups for hydrogen evolution, where photoactive material is separated from an electrolyte by conductive layers in a packed cell. IPEC systems allow for efficient external cooling and limiting energy losses in comparison to divided cells. The compact size of the reactor cells simplifies solar device construction. In EPFL, such IPEC device has been operational since 2019 coupled with a so-called 'solar dish', which concentrates light in a focal spot where IPEC is installed (Figure 1.5).<sup>105</sup> This design enables the system to track the Sun during the day and provides higher concentration rates per reactor area than linear



concentrator setups. The scalability of this design, however, poses challenges due to the chip to dish surface ratio, occupied space, and limited productivity of a compact reactor design. It is also important to note that these setups are usually employed for hydrogen evolution and water splitting, and the potential of utilizing IPEC devices for organic transformations or CO<sub>2</sub> reduction is still uncertain and demands further research.

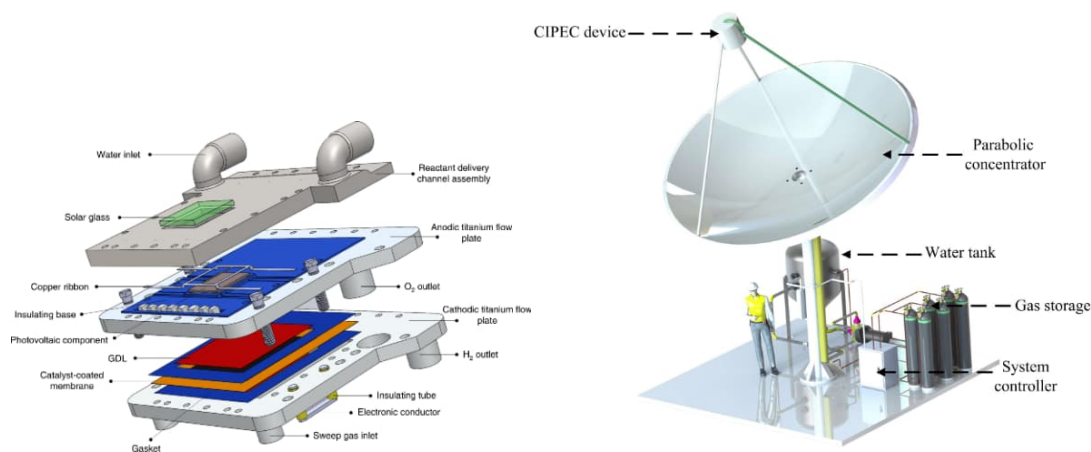


Figure 1.5. Schematic of integrated PEC unit (left) and illustration of 'solar dish' light concentrator device at EPFL (right). Reprinted with permission from ref (105). Copyright 2019 Springer Nature.

Solar concentrators are highly efficient at providing a high photon flux per unit of surface area, but their implementation leads to complex device construction and maintenance. To increase the productivity of solar chemistry products at a lower cost, it is preferable to use more efficient and stable photocatalysts. Recently, a battery of inclined plate collectors (IPCs) for water splitting tests was set up at the University of Tokyo to support this hypothesis (Figure 1.6).<sup>106</sup> The setup uses the same principles as various water treatment panels, where each reactor consists of a 625 cm<sup>2</sup> glass sheet coated with SrTiO<sub>3</sub>:Al particles with a diameter of <1 μm. The panel field consists of 1600 reactor units, which is 100 m<sup>2</sup> in total and can reach STH efficiency of 0.76%. Water is fed into the lower part of the panels through a 0.1 mm gap between the window and the active layer, and during water splitting, it forms a moist hydrogen-oxygen mixture that leaves through an exhaust tube on top. The output from multiple cells is



combined, dehumidified and further separated in a central unit, producing hydrogen with >95% purity at a flow rate of up to  $3.7 \text{ L}\cdot\text{min}^{-1}$ . The productivity of this setup can be further increased by improving the catalyst properties.

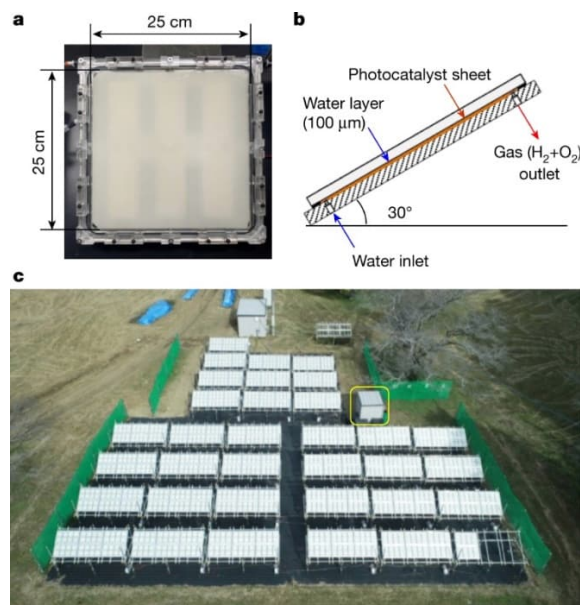


Figure 1.6. Experimental photocatalytic hydrogen evolution setup at the University of Tokyo. a) Individual reactor unit ( $625 \text{ cm}^2$ ). b) Schematic of reactor unit positioning from the side. c) Overhead view of the entire  $100 \text{ m}^2$  hydrogen production system. Reprinted with permission from ref (<sup>106</sup>). Copyright 2021 Springer Nature.

There have been previous attempts to use ICP/flatbed reactors for organic synthesis, but the use of concentrators remains dominant in the field.<sup>107</sup> A comparable reactor is operational in JCU in Townsville, Australia, which uses a reflecting back surface and homogeneous catalysts.<sup>108</sup> Despite these developments, there is a considerable disparity between the current state-of-the-art flatbed photoreactors for organic syntheses and their industrial implementation. The primary concern is poor mass transfer, both in general with laminar flow, and in the contact between the liquid phase and a catalyst, specifically for reactors with a heterogeneous catalyst bed. Further research is needed to address these limitations and develop efficient and cost-effective industrial-scale photoreactors for organic synthesis.



## 1.8. Challenges and Perspectives

The major hurdle to widespread adoption of solar photocatalysis is the scarcity of catalysts that can generate target compounds with commercially viable yields and production rates. While the hydrogen evolution reaction has been transferred to pilot photocatalytic setups, CO<sub>2</sub> reduction is still an emerging technology that is outperformed by the simpler photothermal reduction. The commercial viability of CO<sub>2</sub> reduction photocatalysts requires high selectivity towards specific products, such as syngas or methanol, along with structural stability and consistent efficiency when implemented with direct air capture technology. However, currently available materials do not meet all of these criteria.

An important issue that needs to be addressed for wider implementation is the reactor design. Currently, there are two main paradigms for reactor design, which depend on the use of solar concentrators. The choice of design has an impact on the catalyst properties and the technical aspects of the process. Solar photocatalytic panels can use a significant amount of irradiation per catalyst mass, but require higher catalyst efficiency. On the other hand, tubular, chamber, and chip devices with solar concentrators are less demanding on the catalyst, but require careful phase flow design. Achieving an optimal technological balance between these competing paradigms would be necessary for commercial-scale implementation of solar photocatalysis.

Currently, solar photocatalysis is limited to lab-scale, proof-of-concept studies when it comes to complex organic transformations. Although multiple gram-scale experiments have been reported in the past, they were not successful in achieving a commercial process. The lack of flexibility and versatility to carry out multiple processes without significant reconfiguration is the primary obstacle hindering the widespread adoption of universal reactors for organic synthesis under sunlight, at least on a pilot scale. In the



case of industrial processes, such as pharmaceuticals, sunlight photocatalysis would be particularly advantageous for high-demand, best-selling drugs, as it would significantly reduce irradiation costs. However, this still requires very high efficiency and low capital costs of the photochemical or photoredox process. An example is the Sanofi artemisinin process discussed earlier, where the photochemical process could not compete with the cost of plant-derived product, and the whole plant was eventually sold after a few years of operation.<sup>109</sup> One solution to address this problem is to shift from ruthenium and iridium complexes to organic dye photocatalysts and semiconductors for sustainability and recyclability.

Notwithstanding, coming to a stable solar economy is a challenging yet achievable goal. The idea of using low-cost energy for the chemical industry has drawn significant investment for research and development, which is increasing steadily every year. Although current state-of-the-art technology may not meet all the requirements, the rapid progress in this field suggests that we may be able to establish the first solar plants in the near future, possibly by the end of the decade.

## 1.9. Conclusion

Despite significant efforts in solar fuel research, the industry of sunlight photocatalysis is still emerging and not mature enough for proper commercialization, and examples of high TRL prototypes and pilot setups are scarce. Recent successes in solar hydrogen evolution and CO<sub>2</sub> reduction are inspiring, and solar fuel projects tend to receive increased funding; however, demand for catalysts with sufficient efficiency and stability is still not satisfied, and uncertainty in the setup design hinders further progress in these fields. If these challenges are overcome, the future of solar fuels, at least for hydrogen and bulk chemicals, appears promising.

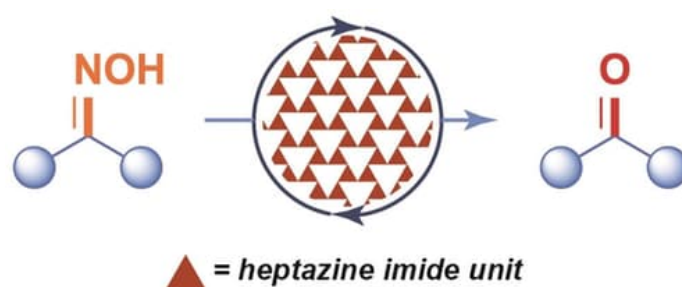


## Chapter 2. Deoxygenation Reaction Mediated by Anionic Carbon Nitride

---

### 2.1. Overview

Following our previous studies on potassium poly(heptazine imide) (K-PHI) – catalyzed photooxidative [3+2] aldoxime-to-nitrile addition to form 1,2,4-oxadiazoles, we discovered that electron-rich oximes yield the parent aldehydes instead of target products. In this work, the mechanism of this singlet oxygen-mediated deoxygenation process was established using a series of control reactions and spectroscopic measurements such as steady-state and time-resolved fluorescence quenching experiments. Additionally, singlet-triplet energy gap value was obtained for K-PHI in suspension, and the reaction scope was broadened to include ketoximes.



This chapter is an adapted version of the article:

A. Galushchinskiy, K. ten Brummelhuis, M. Antonietti, A. Savateev. Insights into the Mechanism of Energy Transfer with Poly(Heptazine Imide)s in Deoxygenation Reaction. *ChemPhotoChem* 2021, 5, 1020.



## 2.2. Introduction

In recent years, photoredox catalysis has emerged as a versatile and powerful technique for synthetic chemists, due to its ability to facilitate a broad range of single-electron transfer reactions.<sup>110</sup> These reactions can be used for various purposes, including the introduction of isotopes into organic compounds<sup>111</sup> and the transformation of complex molecules<sup>112-114</sup>. The approach relies on the transfer of electrons between the reactants and a photocatalyst, eliminating the need for toxic organometallic reagents and unstable initiators. Instead, the process utilizes readily available sacrificial electron acceptors, such as oxygen from the air, and electron donors, such as ethanol derived from biomass.<sup>115</sup>

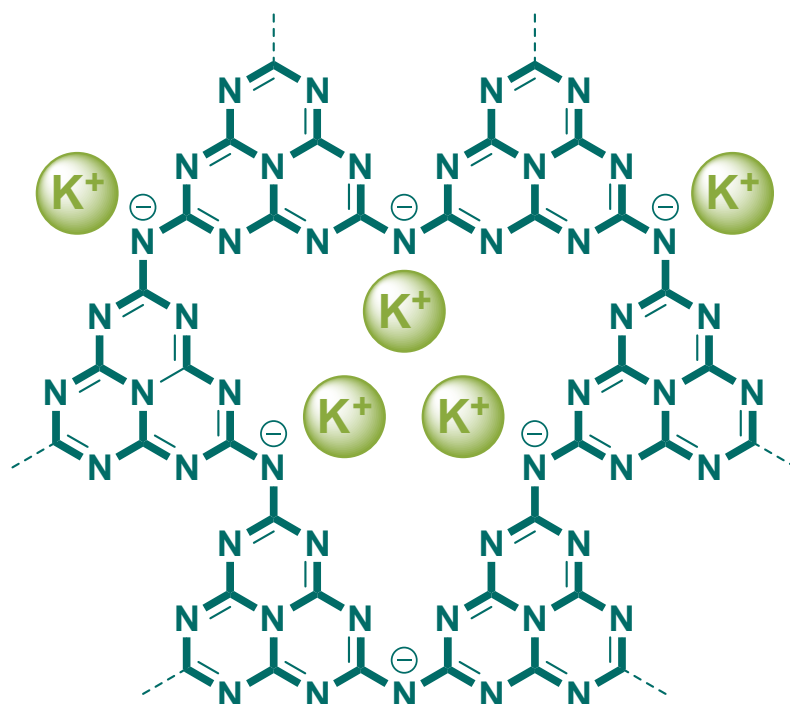
Carbon nitrides are a type of heterogeneous photocatalysts that are semiconductors, and are commonly used for photoelectrochemical water splitting and artificial photosynthesis.<sup>116, 117</sup> However, recent studies show that they are also being used more extensively for organic photocatalysis.<sup>118-120</sup> While their current range of reactions is not as extensive as homogeneous catalysts such as  $\text{Ru}(\text{bpy})_3\text{Cl}_2$  and  $\text{Ir}(\text{ppy})_3$ , carbon nitrides exhibit similar activity<sup>121</sup> and even enable unique transformations<sup>122</sup>. Furthermore, carbon nitrides offer several advantages, such as being cost-effective, easy to handle, and can be easily separated from the reaction mixture and reused multiple times.

In both molecular and semiconductor photocatalysis, electron transfer is the main mechanism of the reactions. However, there are few known reactions that proceed via energy transfer, mostly limited to cyclizations and singlet oxygen generation.<sup>123</sup> Our group has previously developed an example of an energy transfer reaction using carbon nitride as a catalyst:<sup>124</sup> the synthesis of 1,2,4-oxadiazoles. In this reaction, potassium poly(heptazine imide) (K-PHI, [Figure 2.1a](#)) was used as a solid-state sensitizer for



singlet oxygen, which then converted aldoximes to corresponding nitrile oxides that underwent a subsequent click reaction with nitriles.

a)



b)

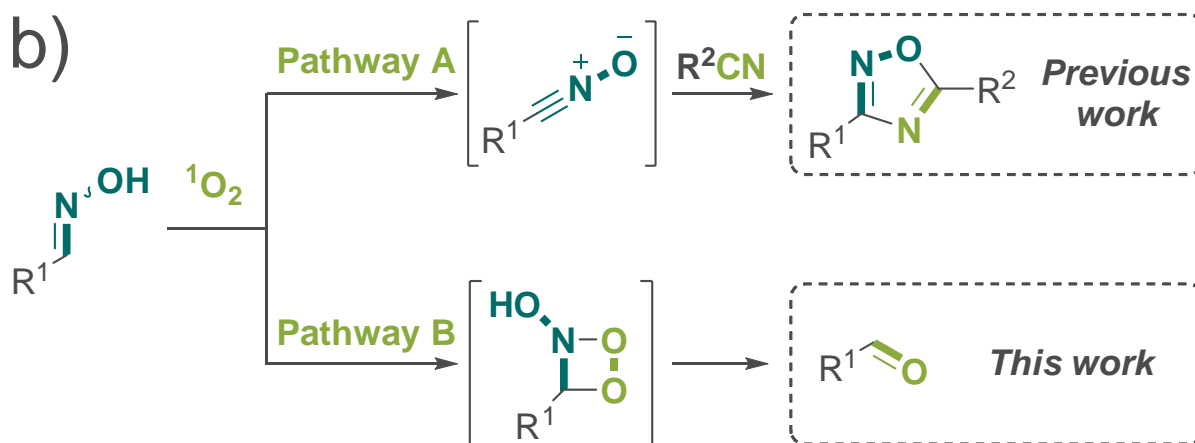


Figure 2.1. a) Idealized structure of potassium poly(heptazine imide) (K-PHI) layer b) Different pathways of singlet oxygen quenching by oximes



However, when more electron-rich oximes were used, the expected [3+2]-cyclization products were not obtained, and instead, aldehydes were formed (Figure 2.1b). In this chapter, we explore the mechanism behind this phenomenon in greater detail as it may have practical applications, such as the use of oxime as a carbonyl protecting group<sup>125</sup> or the production of aldehydes and ketones from non-aromatic nitrosation products (Figure S2.46),<sup>126, 127</sup> particularly for unstable substrates that are prone to degradation under standard oxime hydrolysis conditions.

## 2.3. Results and Discussion

For our investigation, we selected a set of aldoximes 1a-e from our prior research that were not prone to oxidative dehydrogenation (Figure S2.45, Table 2.1), as well as some commonly used ketoximes 1f-h and 1j-l. The aim was to study how the absence of the aldoxime C-H proton affects the reaction pathway and the final product's structure. We also chose oxime 1i as a substrate for mechanistic studies due to its ease of differentiation from the parent coumarin 2i in the NMR spectrum of the crude reaction mixture. Additionally, coumarin 2i fluoresces significantly more strongly than oxime 1i, and the conversion of oxime 1i to the corresponding lactone may be an example of a switch-ON fluorescence reaction activated by photochemistry or photocatalysis. Previously, this reaction was enabled by a chemical oxidant, trichloroisocyanuric acid.<sup>128</sup> Finally, we synthesized the oxygen-18 isotopomer 1g-<sup>18</sup>O to verify our initial hypothesis that the reaction proceeds through [2+2]-cycloaddition of <sup>1</sup>O<sub>2</sub> to the oxime C=N bond.

The research was initiated via investigating the conditions for the conversion of 1i into 2i by varying the parameters (Figure 2.2). As photochemical cleavage of C=X bonds has been studied under visible light irradiation,<sup>129, 130</sup> the experiments were carried out under four different LED irradiation wavelengths: blue (461 nm), green (525 nm), and red (625 nm), along with a control set kept in the dark.



Based on the results obtained, it can be concluded that the conversion of **1i** to **2i** occurs solely via photochemical means under blue and green light irradiation. The yields obtained in experiments with K-PHI are considerably reduced, possibly due to the subsequent oxidation of coumarin **2i** by  $^1\text{O}_2$ . However, under red light irradiation, a photocatalytic process is observed, and the absence of K-PHI results in only trace amounts of the ketone **2i**. As anticipated, the reaction becomes slow in the absence of light or under an inert atmosphere, indicating the significant role of oxygen in the reaction. The fluorescence quantum efficiency of **1i** is 0.07%, while that of **2i** is 2.2%, which can be observed with the naked eye (Figure S2.8).

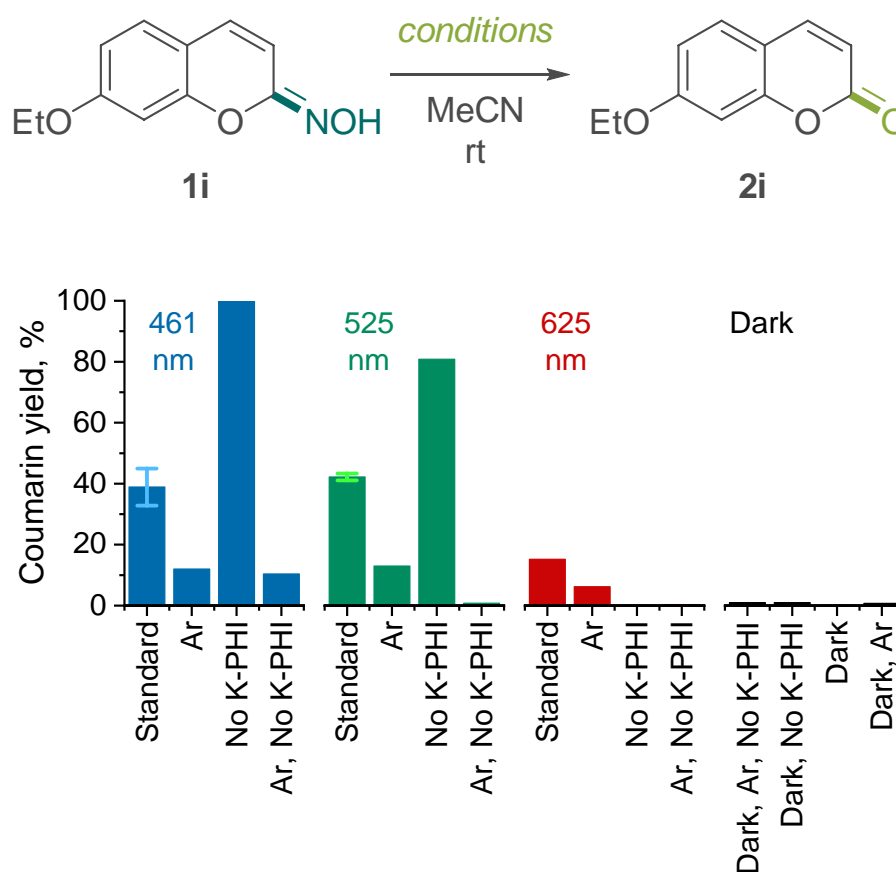


Figure 2.2. Set of reaction conditions for oxime **1i** conversion into ketone **2i** (standard conditions: substrate (50  $\mu\text{mol}$ ); K-PHI (5 mg), MeCN (2 mL),  $\text{O}_2$  (1 bar), light irradiation, 24 h; yield values are based on quantitative NMR (qNMR) data). Error bars represent average  $\pm$  std ( $n = 2$ ).



In order to investigate the feasibility of using *O*-substituted oximes in the reaction, we synthesized *O*-benzyl (1i-Bn) and *O*-methyl (1i-Me) derivatives of oxime 1i and conducted the reactions under blue and green light irradiation. The yields of the ketone product were determined and compared to those obtained from the non-substituted oxime 1i (Figure 2.3).

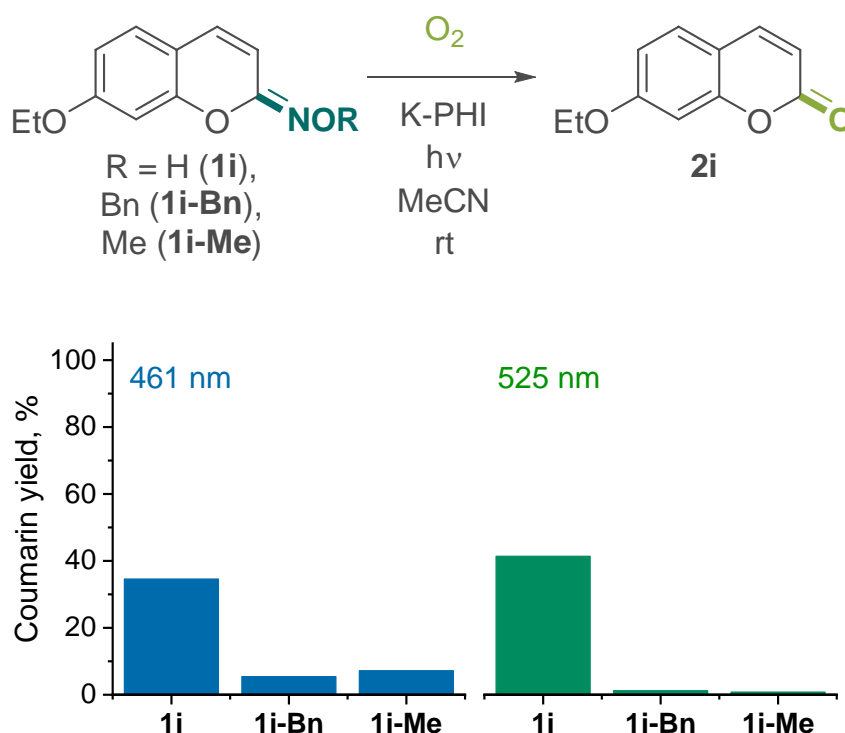


Figure 2.3. Comparison of *O*-unsubstituted (1i) and *O*-alkyl (2a,b) oximes reactivity (conditions: substrate (50  $\mu$ mol), K-PHI (5 mg), MeCN (2 mL), O<sub>2</sub> (1 bar), light irradiation, 24 h; yield values are based on qNMR data).

The conversion of *O*-alkyl oximes 1i-Bn and 1i-Me into the corresponding ketones showed very low reactivity, indicating that the presence of the O–H proton is necessary for C=N bond cleavage. The reaction was performed with and without the photocatalyst, K-PHI, under an inert atmosphere, and also under irradiation with blue and green light. In contrast to 1i, which produced 2i with a 40% yield, the *O*-alkyl oximes either did not react or provided insignificant yields <10%. This suggests that the presence of the O–H



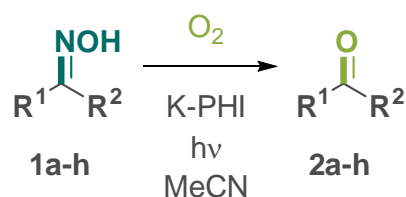
proton is essential for the reaction to occur. To determine whether the reaction is a photochemical or photocatalytic process, we studied the oxidation of oximes 1a-h under a range of conditions outlined in [Table 2.1](#).

The outcome of the oxime conversion reaction is not uniform and varies depending on the structure of the initial oxime. The presence of K-PHI catalyst allows the reaction to proceed more selectively towards a parent carbonyl compound under blue light irradiation in most cases except for the aromatic acetophenone 1h. Aromatic character of the starting oxime switches the process to mostly photochemical pathway. The nature of the oxime group, whether it is derived from an aldehyde or a ketone, also has a significant influence on the course of the reaction. Ketoximes 1f-h show good selectivity and moderate yields of the corresponding ketones 2f-h under K-PHI catalysis under red light, while aliphatic aldoxime 1d demonstrates poor conversion to the target aldehyde 2d in case of K-PHI catalysis or purely photochemical process both under blue and red light irradiation. The highly positive potential of the valence band (+2.2 V vs NHE)<sup>122</sup> may be responsible for the follow-up oxidation of ketones or the competitive side oxidation reaction of the oximes. Additionally, the hydrolysis of oxime occurs easily, even water is present only in trace quantities. For 1g, a virtually higher selectivity was observed when the reaction was performed under red light for 120 h compared to 24 h, which can be explained by the imprecision of qNMR analysis of approximately 5%.

In the following experiments, we examined the potential of using acyclic substrates 1j-l with branched alkyl groups in the conversion of aliphatic ketoximes to explore the synthetic feasibility of the reaction. Our results revealed that the presence of bulky substituents in the proximity of the oxime group significantly reduced both the conversion and yield, thus limiting the synthetic scope of the reaction. However, the findings also suggested that direct interaction between the C=N bond of the oxime group and oxygen may play a crucial role in facilitating the reaction.



The absorption spectra of oxime 1i and its *O*-alkyl derivatives demonstrate no significant overlap with the emission range of LEDs, suggesting that the sensitization of the oxime is not the crucial step in the reaction. The process is more likely to proceed via photoactivation of oxygen. This is demonstrated by UV-Vis absorption spectra of the oximes and the emission spectra of the LEDs, as shown in Figure 2.4a.

Table 2.1. Scope of oximes 1a-h.<sup>[a]</sup>

Entry	Substrate	Yield (Conversion), %			
		Blue LED, 461 nm		Red LED, 625 nm	
		K-PHI, 24 h	No K-PHI, 24 h	K-PHI, 24 h	K-PHI, 120 h
1	1a	17 (>99)	12 (>99)	2 (23)	6 (55)
2	1b	10 (>99)	2 (56)	7 (62)	14 (91)
3	1c	11 (94)	<1 (5)	3 (45)	5 (46)
4	1d	7 (90)	0 (70)	3 (56)	3 (96)
5	1e	<1 (37)	0 (0)	1 (31)	2 (65)
6	1f	45 (80)	<1 (16)	10 (22)	84 (84)
7	1g	38 (40)	0 (0)	6 (11)	25 (26)
8	1h	58 (>99)	>99 (>99)	4 (17)	16 (35)
9	1j	47 (88)	0 (0)	0 (0)	0 (5)
10	1k	40 (83)	0 (0)	0 (8)	14 (35)
11	1l	20 (47)	1 (17)	1 (20)	7 (41)

[a] – Conditions: oxime (50  $\mu\text{mol}$ ), K-PHI (5 mg), MeCN (2 mL), O<sub>2</sub> (1 bar). Conversion and yield values were obtained using qNMR data.



In order to determine the mechanism of the reaction, we performed both static and time-resolved fluorescence quenching experiments using K-PHI. A steady-state Stern-Volmer experiment was carried out using varying concentrations of **1 i**, and the slope constant  $K_{SV}$  was calculated to be  $155.353 \pm 2.098 \text{ M}^{-1}$ .

The available data for *O*-substituted oximes with iridium bipyridyl catalysts<sup>131-133</sup> suggests that the steady-state quenching is typically 1 to 3 orders of magnitude less intense for oximes that do not have any additional redox-active functionalities such as unsaturated C-C bonds or aromatic rings. These findings suggest that the activity of the C=N bond alone is not sufficient for the reaction to take place. This, in combination with our own reactivity data (as presented in [Table 2.1](#)), supports the hypothesis that singlet oxygen is required to initiate the reaction. The presence of conjugated  $\pi$ -system, on the other hand, likely promotes other possible photoredox reactions, both main and side pathways at the same time, presumably by involving the aromatic ring in redox processes via direct sensitization or formation of charge transfer complexes.

In order to determine the fluorescence quenching rate constant, we employed **1 i** as a quencher in time-resolved fluorescence measurements. The resulting rate constant  $k_Q$  was found to be  $(4.656 \pm 0.648) \cdot 10^9 \text{ M}^{-1}\text{s}^{-1}$  ([Figure 2.4c](#)), which is comparable to the rate of diffusion-limited reactions in dilute solvent media.<sup>134, 135</sup> This indicates that quenching is only possible with a tight contact by orbital overlapping, definitively establishing the Dexter mechanism as the means by which the reaction proceeds. Notably, it has been reported that the quenching of singlet oxygen by ruthenium catalysts also proceeds via Dexter energy transfer.<sup>136, 137</sup>

The singlet-triplet energy gap  $\Delta E_{ST}$  of K-PHI suspension was analyzed using emission decay curves with a delay time ranging from 0.1 to 950 ns. The emission maximum was found to shift from around 530 nm for short time delays (<20 ns), which could be



identified as fluorescence (radiative relaxation of K-PHI singlet excited state), to over 600 nm for longer time delays (>20 ns), which could be attributed to phosphorescence (radiative relaxation of K-PHI triplet excited state with a longer lifetime). The spectral maxima were then used to calculate the singlet-triplet energy gap, which was determined to be  $0.24 \pm 0.12$  eV. This value is in line with our previous findings of 0.2 eV for solid K-PHI<sup>124</sup> and is at the upper range for reported carbon nitrides.<sup>138, 139</sup> Further details are available in the Supporting Information, Figure S2.6-7.

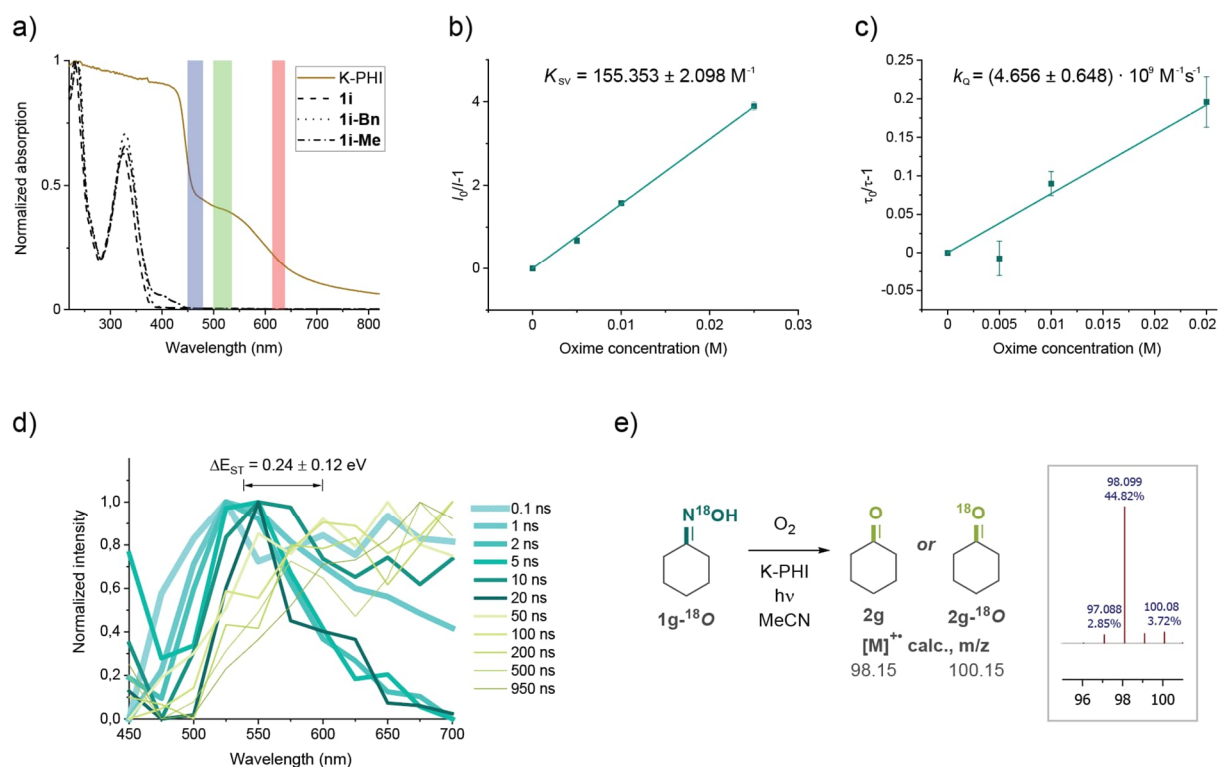


Figure 2.4. Mechanism study. a) Normalized UV-Vis-NIR absorption spectra of 1i, 1i-Bn, 1i-Me and K-PHI with the emission bands of the used LEDs (band width is shown approximately as the emission half-peak width) b) Stern-Volmer plot derived from steady-state emission spectra of 1i.  $\lambda_{exc} = 375$  nm. Error bars represent average $\pm$ std (n=3). c) Stern-Volmer plot derived from TCSPC TRES of 1i.  $\lambda_{exc} = 375$  nm. Error bars represent average $\pm$ std (n=3). d) Determination of K-PHI singlet-triplet energy gap. e) Labeled oxygen-18 experiment and spectrum fragment of ketone product GC-MS fraction.



The rate constant of intersystem crossing is inversely proportional to the singlet-triplet energy gap ( $\Delta E_{ST}$ ), indicating that a lower value of  $\Delta E_{ST}$  facilitates the formation of singlet oxygen.<sup>140</sup> The reported  $\Delta E_{ST}$  values for efficient oxygen sensitizers are in the range of 0.75 to 0.2 eV.<sup>141-143</sup> Thus, K-PHI shows a comparable or better sensitizing capacity in terms of energy conversion, which is corroborated by its low PL internal quantum efficiency of 0.072%.<sup>124</sup> However, the relatively low absorption of light with wavelengths above 550 nm suggests that there is room for modification of the catalyst. The overall Jablonski diagram for K-PHI suspension is depicted in [Figure 2.5a](#).

The experiment with 1g-<sup>18</sup>O isotope label ([Figure 2.4e](#)) provides evidence that the primary product of deoxygenation is non-labeled cyclohexanone 2g, indicating that the singlet oxygen undergoes [2+2]-addition with subsequent elimination of nitrous acid. In the previous work of our group, it was directly observed that there is phosphorescence of <sup>1</sup>O<sub>2</sub> at 1271 nm under similar conditions as those used in the current study.<sup>124</sup> However, the GC-MS fraction also contains 7.7% of the labeled ketone 2g-<sup>18</sup>O, which corresponds to a 12% <sup>18</sup>O isotope yield from 64%-enriched ketone, indicating that some of the oxygen atoms in the product originate from the starting materials. We propose a mechanism for this transformation, as shown in [Figure 2.5b](#).



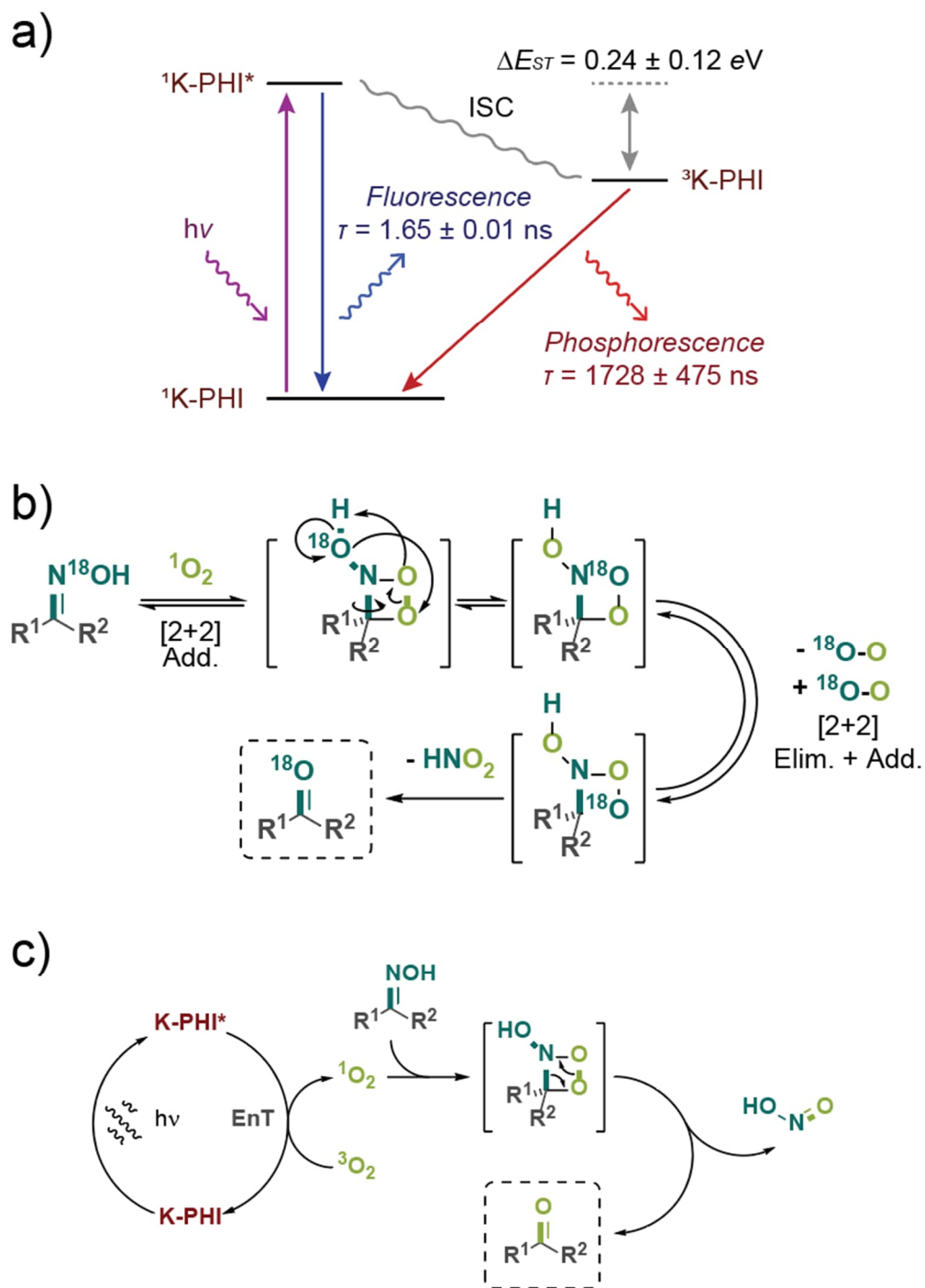


Figure 2.5. Energy transfer and overall reaction mechanism. a) Jablonski diagram for K-PHI in MeCN ( $2.5 \text{ mg mL}^{-1}$ ). b) Proposed mechanism for transformations of four-membered cyclic intermediate. c) Proposed deoxygenation mechanism.



The proposed mechanism for the transformation of the oxime to the ketone involves the initial [2+2]-cycloaddition of singlet oxygen to the C=N bond. Subsequently, the cyclic intermediate is formed, and the O-O bond in the cyclic intermediate is cleaved assisted by O-H bond dissociation. The cycle is then restored by C-N bond rotation and incorporation of  $^{18}\text{O}$ , followed by the elimination and addition of labeled oxygen in a different position to form C- $^{18}\text{O}$  bond. Finally, elimination of  $\text{HNO}_2$  yields  $^{18}\text{O}$ -ketone. The overall reaction can be summarized by the key steps of [2+2]-cycloaddition of  $^1\text{O}_2$  to C=N bond followed by extrusion of  $\text{HNO}_2$ . According to isotope distribution in the final product, this process has no significant impact on the overall reaction. The mechanism is depicted in [Figure 2.5c](#).

## 2.4. Conclusion

The investigation of photoredox deoximation catalyzed by potassium poly(heptazine imide) (K-PHI) began with control experiments on coumarin oxime proto-fluorescent probes. The reaction was found to be photocatalytic under red light, while green and blue irradiation mainly produced photochemical reactions. Aliphatic and aromatic ketoximes, as well as electron-rich aldoximes, were subsequently included in the reaction scope. qNMR experiments demonstrated that the oxime photoreactivity was induced by a neighboring aromatic ring but also promoted undesired side reactions. In contrast, aliphatic ketoximes exhibited moderate to good yields in the presence of K-PHI catalyst with enhanced selectivity under 625 nm. Therefore, this method may serve as a starting point for chromoselective preparation of ketones from non-aromatic nitrosation products, but the catalyst needs further improvements to effectively operate under the longer wavelength part of the visible spectrum. Additionally, further studies on functional group tolerance in substrates are required.



During our fluorescence quenching experiments, we observed a surprisingly high rate of Stern-Volmer quenching for our substrate, which is unusual for simple oxime derivatives. Additionally, the rate of time-resolved quenching indicated that the reaction is limited by diffusion. These results support our initial hypothesis that the reaction proceeds via a [2+2] addition of singlet oxygen to the C=N double bond with HNO<sub>2</sub> elimination, and confirmed the Dexter mechanism for the process. To conclude our emission spectroscopy studies, we measured the singlet-triplet energy gap for K-PHI suspension in acetonitrile and compared it to reported values for carbon nitride and molecular photocatalysts used for singlet oxygen generation.

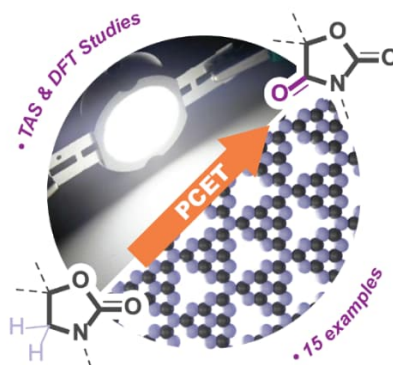
To provide further evidence for the proposed mechanism, we conducted experiments using an oxygen-18 labeled oxime as a substrate. The results showed that while the majority of the reaction product was the <sup>16</sup>O (unlabeled) ketone, a small fraction of <sup>18</sup>O was incorporated into the final product. We put forth a proposed explanation for this minor transformation process.



## Chapter 3. Oxygenation of Oxazolidinones using Carbon Nitride Photobase

### 3.1. Overview

Graphitic carbon nitride (g-CN) is a transition metal free semiconductor that mediates a variety of photocatalytic reactions. Although photoinduced electron transfer is often postulated in the mechanism, proton-coupled electron transfer (PCET) is a more favorable pathway for substrates possessing X–H bonds. Upon excitation of an (sp<sup>2</sup>)N-rich structure of g-CN with visible light, it behaves as a photobase – it undergoes reductive quenching accompanied by abstraction of a proton from a substrate. The results of modelling allowed us to identify active sites for PCET – the ‘triangular pockets’ on the edge facets of g-CN. We then employ excited state PCET from the substrate to g-CN to cleave selectively *endo*-(sp<sup>3</sup>)C–H bond in oxazolidine-2-ones followed by trapping the radical with O<sub>2</sub>. This reaction affords 1,3-oxazolidine-2,4-diones. Measurement of apparent pK<sub>a</sub> value and modeling suggest that g-CN excited state can cleave X–H bonds that are characterized by bond dissociation free energy (BDFE) of about 100 kcal mol<sup>-1</sup>.



This chapter is an adapted version of the article:

A. Galushchinskiy, Y. Zou, J. Odutola, J. Nikačević, J.-W. Shi, N. Tkachenko, N. López, P. Farràs, O. Savateev. Insights into the Role of Graphitic Carbon Nitride as a Photobase in Proton-Coupled Electron Transfer in (sp<sup>3</sup>)C–H Oxygenation of Oxazolidinones. *Angew. Chem. Int. Ed.* 2023, e202301815; *Angew. Chem.* 2023, e202301815.



## 3.2. Introduction

Photocatalysts, such as excited states of organic molecules,<sup>115</sup> transition metal complexes,<sup>144</sup> and semiconductors,<sup>145</sup> can facilitate the oxidation and reduction of organic molecules through single electron transfer (SET) reactions. These reactions produce charged radical intermediates, cations and anions,<sup>115</sup> and require the excited state of the photocatalyst to have sufficient oxidative and/or reductive properties. Proton-coupled electron transfer (PCET, [Figure 3.1a](#))<sup>146</sup> can make redox reactions easier by coupling them with the transfer of a proton. Unlike radical ions formed by SET, PCET reactions produce electrically neutral radicals. The PCET process is more reliant on thermodynamic and kinetic factors of the proton, such as acid-base interaction between the substrate and the catalyst and tunneling effects, rather than on electrochemistry alone, to lower the energy barriers for transition states.<sup>147, 148</sup> The activation energy for these reactions is low enough to drive efficient enzyme-catalyzed biochemical redox processes at low temperatures.<sup>149, 150</sup>

In recent years, there has been a growing interest in the selective and facile modification of X-H sites in organic molecules through photoredox catalysis-driven PCET.<sup>151-153</sup> This involves combining an oxidative excited state of a molecular sensitizer, such as an Ir-polypyridine complex, with a Brønsted base to break relatively strong N-H and O-H bonds in amides and phenols and generate alkoxy and amidyl radicals, respectively, via *oxidative* multisite PCET.<sup>154, 155</sup> In aqueous environments, a base/oxidant couple delivers the required energy for homolytic X-H bond cleavage in a substrate, formal bond dissociation free energy (BDFE, kcal mol<sup>-1</sup>), which is determined by the pKa of the acid conjugated to the Brønsted base and reduction potential of the sensitizer excited state ( $E_{red}^*$ , V vs. NHE):<sup>146</sup>

$$BDFE = 1.37pKa + 23.06E_{red}^* + 57.6 \quad (3.1)$$



Nonetheless, organic dyes such as Eosin Y<sup>156</sup> can also act as HAT agents themselves without the need for an auxiliary base due to the presence of hydrogen bond donors and acceptors providing interaction with a substrate.<sup>157, 158</sup> g-CN materials have been found to mediate a number of reactions via PCET either explicitly or implicitly,<sup>159, 160</sup> in combination with organic bases and alone, due to presence of basic pyridine-type nitrogen centers<sup>121</sup> providing interaction with proton donors.<sup>161-163</sup> For example, cyanamide-modified carbon nitride with tributylmethylammonium dibutylphosphate as a base generates an *N*-centered radical from carbamate, which undergoes intramolecular Giese addition to an allylic moiety.<sup>164</sup> Mesoporous g-CN (mpg-CN) in combination with Br• produces an alkyl radical from *N,N*-dialkylformamide and enables the subsequent C–C cross coupling with arylhalides.<sup>165</sup> K-PHI, an ionic carbon nitride, is capable of abstracting electrons and protons from amines and storing them as separately within the bulk, as indicated by our group's previous research.<sup>166, 167</sup> The photocharged K-PHI can then be used in *reductive* PCET to produce Ar–H compounds by overcoming the high stability of otherwise non-reducible aryl halides.<sup>167</sup>

The ability of mpg-CN, albeit with an unknown  $pK_a$  value when protonated, to cleave C–H bonds of *N*-alkyl amides with BDFE values ranging from 89-94 kcal·mol<sup>-1</sup> is expected,<sup>165</sup> given its nitrogen-rich structure and its  $E_{VB}$  potential of +1.45 V vs. NHE, as well as the results from equation (3.1). This oxidation leads to the formation of imides, such as 1,3-oxazolidine-2,4-diones (Figure 3.1b, see SI for discussion), which are highly sought-after despite being difficult to synthesize. While the synthesis of 5-ylidene-substituted derivatives can be achieved via base-catalyzed ring formation of propargylic amides with carbon dioxide,<sup>168</sup> regular oxazolidinediones require cyclization of carbonate synthons, which are not as readily available, such as iso(thio)cyanates and  $\alpha$ -hydroxycarboxylates (Figure 3.1c).<sup>169, 170</sup>



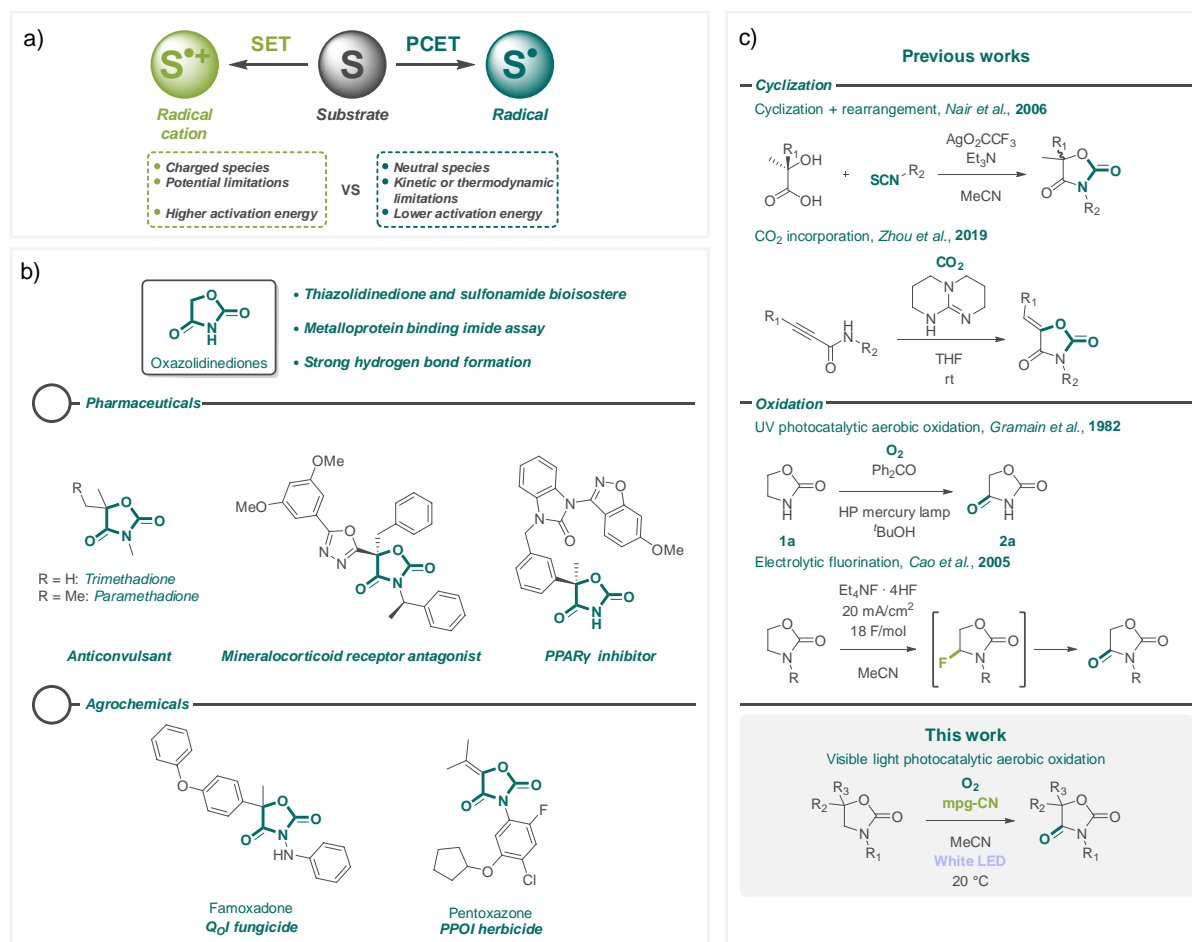


Figure 2.1. Concept of the project. a) Intermediates and features of oxidative SET and PCET catalytic pathways. b) Examples of biological activity of oxazolidinedione containing molecules. c) Formation of 1,3-oxazolidine-2,4-diones reported in literature and in this work.

An alternative approach to the challenging synthesis of 1,3-oxazolidine-2,4-diones could be achieved by the oxidation of 1,3-oxazolidine-2-ones, which can be obtained commercially or prepared from the corresponding  $\alpha$ -aminoalcohols, or through the reaction between oxiranes and isocyanates.<sup>171</sup> However, this pathway is difficult since oxazolidinones are relatively stable against oxidation. The high peak potential  $E_p > 1.67$ – $2.72$  V vs. SCE<sup>172</sup> requires strong oxidizing agents, making it challenging to achieve direct electron extraction. There have been only two successful oxidation publications of oxazolidinones at the 4<sup>th</sup> position of the ring. The first was reported in 1982 by Gramain *et al.* through photocatalytic reaction of oxazolidin-2-one 1a with oxygen under



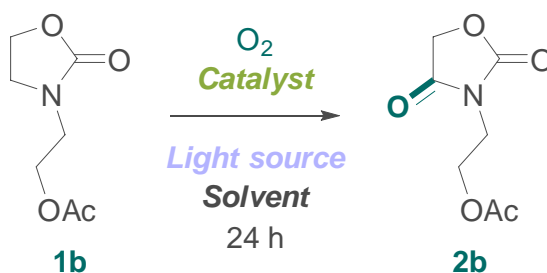
irradiation using a benzophenone catalyst for 68 hours at room temperature.<sup>173</sup> The second was achieved in 2005 by Gao *et al.* through electrolytic partial fluorination of *N*-substituted oxazolidinones, where non-acyl substituents yielded unstable 4-fluoro derivatives that were hydrolyzed and further oxidized to diones.<sup>172</sup> These methods require harsh conditions such as strong UV irradiation or corrosive acidic fluoride solutions.

In this chapter, the focus is on investigating the PCET process with mpg-CN upon band gap excitation for the synthesis of 1,3-oxazolidine-2,4-diones from the corresponding oxazolidinones. The mpg-CN excited state acts as both an organobase and a sensitizer, which enables it to selectively cleave an endocyclic C-H bond in a  $\beta$ -position to the amide nitrogen, followed by trapping the resulting C-centered radical with O<sub>2</sub>. Experimental data and DFT simulations suggest that the combination of mpg-CN's surface basic character and the potential of the valence band allows it to cleave X-H bonds with a BDFE of around 100 kcal·mol<sup>-1</sup>.

### 3.3. Results and Discussion

Compound 1b is an appropriate system to investigate selectivity of oxygenation due to its *endo*- and *exo*-CH<sub>2</sub> groups. The oxidation of secondary amides is generally easier than that of tertiary amides since proton abstraction or its migration to oxygen is possible.<sup>174-176</sup> In fact, some synthetic procedures are based on the pathway of *N*-acylimine formation during oxidation.<sup>177, 178</sup> Consequently, the oxygenation of tertiary amides poses a synthetic challenge, while the research aims to develop a synthetic protocol that is applicable to both *N*-substituted and unsubstituted substrates.



Table 3.1. Screening for optimal reaction conditions of oxazolidinone oxidation<sup>[a]</sup>

Yield, %

Catalyst <sup>[b]</sup>		Light source <sup>[c]</sup>		Solvent <sup>[d]</sup>	
mpg-CN	25.5	UV LED (365 nm)	70.0	CH <sub>3</sub> CN	55.5
K-PHI	21.0	Purple LED (410 nm)	14.5	MeOH	2.0
Na-PHI	7.5	Blue LED (465 nm)	25.5	EtOH	1.5
RFTA	1.0	Green LED (535 nm)	5.0	<i>n</i> BuOH	5.0
Ir(ppy) <sub>3</sub>	0.2	Red LED (625 nm)	0.5	<i>t</i> BuOH	37.5
Ru(bpy) <sub>3</sub> Cl <sub>2</sub> · 6H <sub>2</sub> O	0.4	White LED	55.5	1,4-dioxane	1.5
Benzophenone	0.2	<i>No light</i>	0	Hexane	5.5
Methylene blue	0.2			Toluene	26.5
Rhodamine B	2.4			CHCl <sub>3</sub>	13.5
Eosin Y	2.2			CH <sub>2</sub> Cl <sub>2</sub>	37.0
CdS	0.4			H <sub>2</sub> O	22.5
WO <sub>3</sub>	0.1			MeNO <sub>2</sub>	45.0
mpg-CN (Ar, control)	2.8			DMSO	0
<i>No catalyst</i>	0 <sup>[e]</sup>			DMF	0
<i>No catalyst</i>	10 <sup>[f]</sup>				

[a] – Reaction conditions: 0.05 mmol of 1b, O<sub>2</sub> (1 bar), 2 mL of solvent (0.025M), LED irradiation, catalyst: 5 mg (for heterogeneous, 100 g mol<sup>-1</sup>), 5 mol.% (for homogeneous); yield values were obtained by quantitative <sup>1</sup>H NMR using 1,3,5-trimethoxybenzene as an internal standard. [b] – the catalysts were screened using an optimal light source with respect to their absorption maxima, see Supplementary Information for details; acetonitrile was used as a solvent. RFTA – riboflavin tetraacetate. [c] – mpg-CN was used as a catalyst with acetonitrile as a solvent. [d] - mpg-CN was used as a catalyst under white LED irradiation. [e] – blue LED (465 nm). [f] – UV LED (365 nm). Photon fluxes of LED sources: UV LED (365 nm) 0.2 μmol cm<sup>-2</sup> s<sup>-1</sup>; purple LED (410 nm) 0.4 μmol cm<sup>-2</sup> s<sup>-1</sup>; blue LED (465 nm) 0.8 μmol cm<sup>-2</sup> s<sup>-1</sup>; green LED (535 nm) 0.4 μmol cm<sup>-2</sup> s<sup>-1</sup>; red LED (625 nm) 1.6 μmol cm<sup>-2</sup> s<sup>-1</sup>.



In the initial screening, a range of heterogeneous carbon nitride photocatalysts including mpg-CN,<sup>179</sup> potassium poly(heptazine imide) (K-PHI),<sup>180</sup> and sodium poly(heptazine imide) (Na-PHI)<sup>181</sup> were prepared in-house and tested. The photocatalytic reaction was carried out in acetonitrile under blue light irradiation ( $465 \pm 10$  nm) in the presence of an oxygen atmosphere. Among the tested photocatalysts, the highest yield of oxazolidinedione 2b (25.5% by qNMR with incomplete conversion of 1b) was obtained with mpg-CN (Table 3.1). Further investigation showed that mpg-CN could also produce 2b after being used in three consecutive rounds of the reaction (see SI for more information).

K-PHI and Na-PHI gave 2b with diminished yields likely due to decreased surface area of couple dozens of  $\text{m}^2 \text{g}^{-1}$ .<sup>181, 182</sup> Molecular sensitizers such as Riboflavin tetraacetate, Rhodamine B, and Eosin Y also produced 2b, but with lower yields, likely due to the presence of carbonyl and/or carboxyl functionalities in their structure.<sup>156</sup> Although benzophenone was reported earlier to oxidize 1a, likely due to interaction of amide NH with the photocatalyst C=O group, it failed to convert 1b.<sup>173</sup> CdS and  $\text{WO}_3$  did not produce any significant quantities of 2b, presumably due to a lack of sufficient basicity on their terminal sites to participate in PCET. Excited state of Ir- and Ru-complexes are powerful SET agents, but in the absence of an additional base capable of engaging in multisite PCET, they failed to produce 2b.<sup>147</sup> Where the yield of 2b was low in Table 3.1, conversion of 1b was also close to zero. Control experiments under inert atmosphere confirmed that oxygen is incorporated from the gas phase, and the reaction did not proceed in the absence of mpg-CN and blue light irradiation. Excitation at 365 nm in the absence of mpg-CN, however, resulted in a photochemical process that produced 2b with a 10% yield.



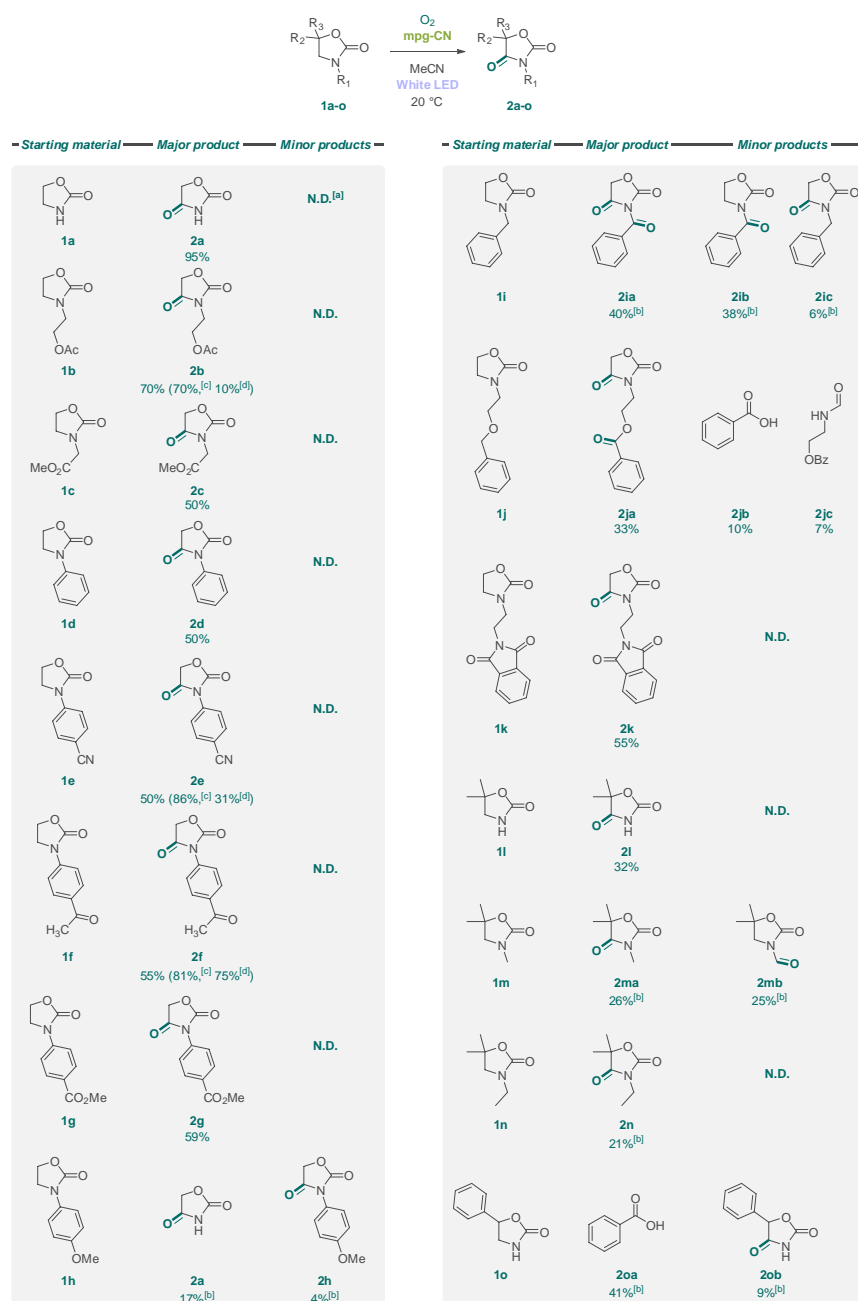


Figure 3.2. Scope of oxazolidinones 1a-o used for scaled-up oxidation. Reaction conditions: 1 (1.25 mmol), O<sub>2</sub> (1 bar), acetonitrile (50 mL), mpg-CN (125 mg), white LED (4x50W modules), 20 °C. The reaction was carried out until complete consumption of a starting material is achieved (24-72 h, monitored by <sup>1</sup>H NMR). Percent values indicate isolated yields unless stated otherwise. [a] – “N.D.” indicates absence of data for side products (either their formation was not observed by <sup>1</sup>H NMR or reaction mixture was too complex to distinguish minor components). [b] – quantitative <sup>1</sup>H NMR yields using 1,3,5-trimethoxybenzene as an internal standard. [c] – 1 (0.05 mmol), UV LED (365 nm). [d] – 1 (0.05 mmol), UV LED (365 nm) without mpg-CN.



Illumination with white LED increased the yield of 2b to 55.5% after 24 hours, which is due to predominance of 450 nm photons in the LED emission spectrum (Figure S3.28), and mpg-CN produced 2b with a 70% yield when excited at 365 nm. Assuming that 10% of the yield is due to purely photochemical process, the remaining 60% are photocatalytic component of the yield, which is similar to 56% obtained upon mpg-CN excitation with white LED. Using acetonitrile as a solvent provided the most suitable environment for the oxygenation of oxazolidinone 1b under white LED illumination due to its polarity, chemical stability, and lack of reactive C-H bonds (see SI). Under the reaction conditions using mpg-CN as the catalyst and acetonitrile as the solvent, a batch experiment was conducted to scale up the reaction to 1.25 mmol of substrate. A series of oxazolidinones 1a–o were tested under these conditions (Figure 3.2).

The use of low-cost UV photons may enable the oxygenation of *N*-aryl substituted oxazolidinones (e.g. 1e, 1f) without the need for mpg-CN.<sup>183</sup> However, the aim of this study was to establish a general protocol for a broad range of substrates with and without chromophores and investigate the role of mpg-CN as the photobase. Therefore, a white LED without UV-contribution was used to avoid direct excitation of the substrates. The study demonstrated almost quantitative yield for unsubstituted oxazolidinone 1a and moderate to good yields for *N*-substituted derivatives 1b–k, with a few exceptions. The behavior of substrates with electron-rich groups, such as the 4-methoxyphenyl (PMP) protecting group in 1h, was observed to be typical, wherein it is readily cleaved under photocatalytic oxidative conditions;<sup>125</sup> the main product of 1h oxygenation was a parent oxazolidinedione 2a, while only a small amount of the target product 2h was observed. Substrates 1i and 1j bearing *O*- and *N*-benzyl fragments gave the corresponding benzoyl-substituted oxazolidinediones (2ia and 2ja, respectively) as major products with minimal to no yield of the target product of ring oxygenation only, such as 2ic. Further oxidation product 2jc was observed, and benzoic acid, the product



of benzoyl cleavage, was isolated. The yields of 5,5-dimethylated substrates 1l–n decreased significantly compared to the derivatives free of the substituent in the 5<sup>th</sup> position, with lower selectivity due to competitive oxygenation of *endo*- and *exo*-CH<sub>2</sub> groups in 1m. Earlier, it was reported that Br• radical abstracts hydrogen atoms in lactams both from *endo*- and *exo*-CH<sub>2</sub>-group with a higher preference for the former.<sup>165</sup> In this study, mpg-CN was observed to abstract selectively hydrogen atom from *exo*-CH<sub>2</sub>-group in all cases except for 1m. Nonetheless, in cases where the substrate possesses benzylic CH<sub>2</sub>, PCET at this site becomes facile, as illustrated by oxygenation of 1i and 1j. The introduction of a bulky and electron donating phenyl group into the 5<sup>th</sup> position, as in compound 1o, reduced yield by promoting ring opening side reactions, and benzoic acid was obtained as the main product.

Various non-photocatalytic oxidation procedures for the synthesis of 2k were evaluated, as shown in Figure 3.3 (see SI for protocols and references). Among them, only the RuO<sub>4</sub>/NaIO<sub>4</sub> process provided a comparable yield to the photocatalytic reaction. However, this method was inferior to mpg-CN photocatalytic one in terms of both yield and synthetic utility, as the use of ruthenium tetroxide as a reagent for such processes is complicated by its severe toxicity and incompatibility with many functional groups.<sup>184</sup>

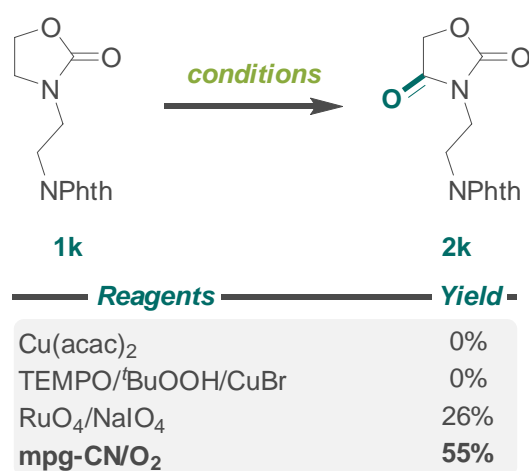


Figure 3.3. Comparison of the isolated yield of 2k using different oxidation procedures.



The results from the conditions screening and scope studies provided initial insights into the reaction mechanism. Three potential pathways were identified (Figure 3.4), including 1) the reaction of the substrate with singlet oxygen, 2) direct oxidation of the substrate via photoinduced electron transfer (PET), or 3) the generation of a C-radical via proton-coupled electron transfer (PCET). As our catalytic system does not include a sacrificial electron donor, which could quench the photogenerated hole and promote oxygen reduction to superoxide radical, the only possibility for oxygen activation is via the formation of singlet oxygen by the energy transfer (EnT) pathway from the catalyst. It was previously reported that K-PHI and mpg-CN can sensitize  $^1\text{O}_2$ , which indicates the possibility of such pathway occurring in this case.<sup>124</sup>

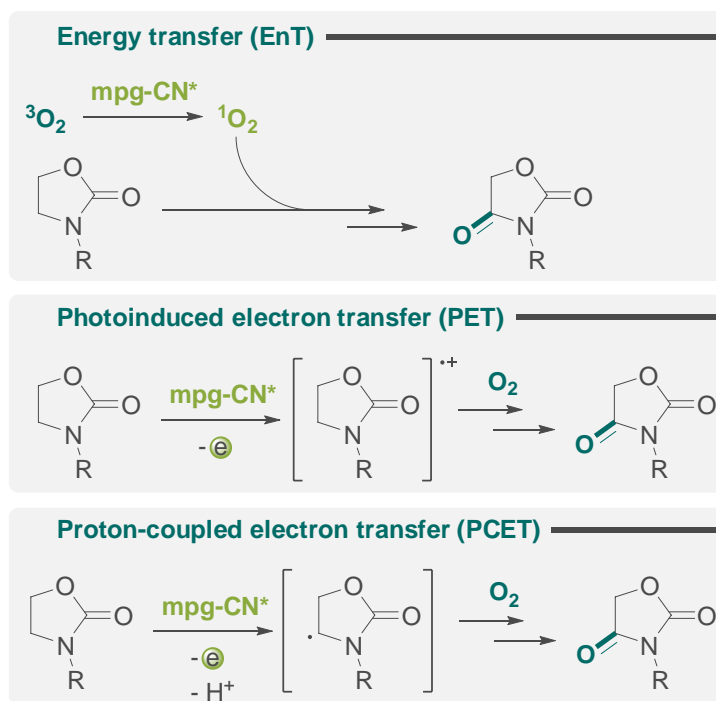


Figure 3.4. Simplified pathways of possible oxazolidinone oxidation mechanisms. Further steps regarding interaction with oxygen are omitted for clarity.

As a support for EnT pathway, the results on other well-known singlet oxygen generating catalysts, including methylene blue, Eosin Y, and Rhodamine B,<sup>185</sup> could be compared to the established protocol. However, the yields were minimal (see Table



3.1), providing evidence to exclude this pathway from further investigation.

Additionally, the reaction was conducted under varying oxygen pressures (1 to 4 bars) to investigate the influence of oxygen concentration on product yield. The results showed negligible effect on the product yield, indicating that active oxygen species did not participate in the reaction mechanism. Nevertheless,  $^1\text{O}_2$  may still be involved in side reactions at higher oxygen pressures due to increase in conversion (Figure 3.5a). Furthermore, the behavior of 5-substituted oxazolidinones, such as 1l-m, in the reaction suggests the existence of some sort of steric hindrance factor that decreases reaction selectivity, which would be negligible if a small molecule like  $^1\text{O}_2$  were to interact with the substrate.

In order to investigate the mechanism of the reaction from the perspective of PET, cyclic voltammetry experiments were carried out on substrates 1b, 1d, 1e, and 1h to assess their oxidation potentials (Figure 3.5b, S3.5). Data for oxidation potential of 1d, +1.58 V vs. SCE (at half peak) matches that reported earlier, +1.67 V vs. SCE (peak).<sup>172</sup> The results showed that all four compounds had higher oxidation potentials ( $\geq +1.26\text{V}$  vs. SCE) than the potential of the photogenerated hole in mpg-CN (+1.20 V vs. SCE),<sup>179</sup> indicating that PET from oxazolidinones to mpg-CN is thermodynamically prohibited. This finding refutes the involvement of direct oxidation of the substrate via photoinduced electron transfer. Instead, it leaves the only option that the most likely mechanism of the reaction is proton-coupled electron transfer. In addition, the steric hindrance factor observed for 5-substituted oxazolidinones in the reaction suggests the existence of direct interaction between the substrate and the catalyst. The reported results also indicate that the photocatalytic oxidation of oxazolidinone 1a using benzophenone under UV proceeds via transfer of both proton and electron (Figure 3.1c).<sup>173, 186, 187</sup>



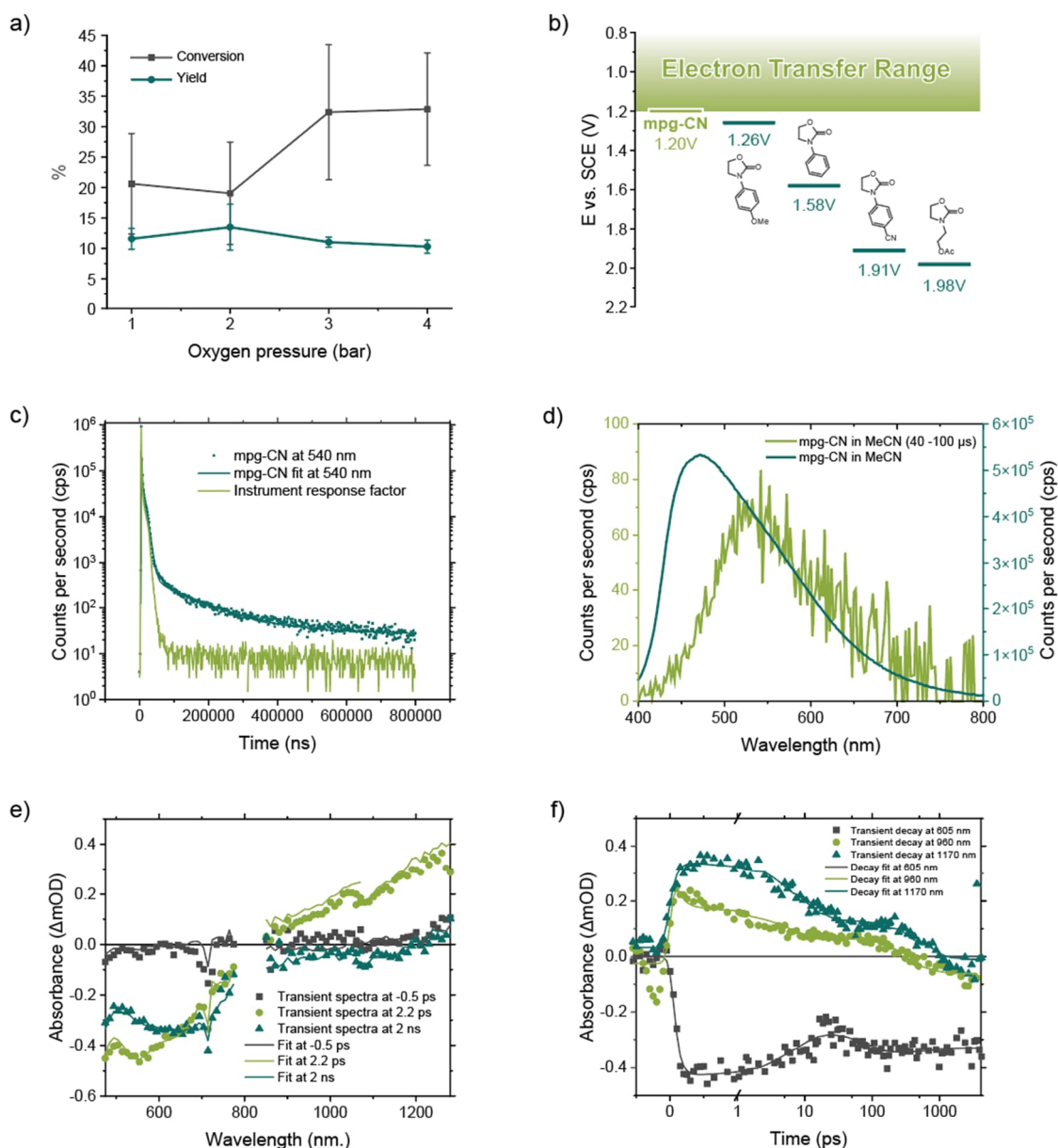


Figure 3.5. Investigation of oxazolidinones photocatalytic oxidation mechanism. a) Yield of 2b and conversion of 1b in the photocatalytic reaction performed under different oxygen pressure. Error bars represent average $\pm$ std (n=3). b) mpg-CN valence band potential and half-peak oxidation potentials of 1b, 1d, 1e and 1h with respect to SCE. Orange gradient band indicates the upper limit of potentials range, where SET from a substrate to mpg-CN excited state is thermodynamically feasible. c) Tr-PL decay of mpg-CN and the IRF. d) Steady-state fluorescence (magenta) and tr-PL (orange) spectra of mpg-CN, the latter was measured by gating the emission from 40–100  $\mu$ s with the pulsed xenon lamp. e) Transient absorption spectra of mpg-CN in MeCN under N<sub>2</sub>. Spectra around 800 nm is cut off due to fundamental of the laser. f) Transient decay of mpg-CN in MeCN under N<sub>2</sub>. The first picosecond is in linear scale while the rest has a logarithmic scale.



The apparent quantum yield (AQY) for oxidation of 1b was determined to be 0.026% at 465 nm and 0.065% at 365 nm, and the higher AQY obtained upon reaction mixture irradiation with UV light is attributed to the higher extinction coefficient of mpg-CN, excluding chain propagation in both cases.

Based on time resolved photoluminescence (tr-PL) spectroscopic measurements, it was found that most of the excited states of mpg-CN decay rapidly, but a small fraction survives for more than 400  $\mu\text{s}$  after excitation (Figure 3.5c). A fluorescence peak at  $\sim 472$  nm was observed in tr-PL spectra (Figure 3.5d), along with a lower intensity phosphorescence peak at  $\sim 540$  nm measured by gating the emission from 40–100  $\mu\text{s}$  with a pulsed xenon lamp. The singlet-triplet energy gap ( $\Delta E_{\text{ST}}$ ) determined as a difference between steady-state fluorescence and tr-PL maxima is 0.33 eV, consistent with the one reported earlier for K-PHI (see Chapter 2).<sup>124, 188</sup> The low  $\Delta E_{\text{ST}}$  indicates that triplet excited state has an energy comparable to the singlet, and should be beneficial for the cleavage of C–H bond in oxazolidinones alongside with the lifetime above  $\mu\text{s}$  range. The presence of the substrate 1b and/or oxygen does not quench neither singlet nor triplet excited state of the mpg-CN (Supplementary Discussion 1). Transient absorption spectra of mpg-CN in MeCN recorded under deoxygenated conditions (Figure 3.5e) showed a strong negative signal between 500–750 nm and a positive signal between 850–1280 nm, attributed to ground state bleaching and the photogenerated excited state of mpg-CN, respectively. The crossing point was  $\sim 800$  nm. At delay above 2 ns, the intensity of the positive signal reduced at a faster rate than the negative signal and the crossing point is red-shifted to  $\sim 1200$  nm. The behavior of mpg-CN excited state on the nanosecond time scale is similar to that of K-PHI (Figure 3.5f, traces at 605, 960 and 1170 nm).<sup>124</sup> The TAS study did not reveal differences in mpg-CN excited state electronic signatures and dynamics, both singlet and triplet, in the presence or absence of  $\text{O}_2$  and 1b. These observations can be explained by the low,



0.065%, apparent quantum yield (AQY) of the studied reaction and the sensitivity of the instruments to be not high enough to detect this small quenching of mpg-CN excited states.

The 1b oxidation pathway by mpg-CN was computed using Density Functional Theory (DFT) implemented in the Vienna Ab initio Simulation Package (VASP).<sup>189, 190</sup> Our model of carbon nitride involved a six-heptazine-layer wide 2D surface with NH, NH<sub>2</sub>, and OH groups at the termination sites.<sup>165</sup> We obtained the reaction energy profile at the PBE level, as shown in [Figure 3.6](#).<sup>191</sup>

The modeled structures used in the study were deposited in the ioChem-BD database.<sup>192</sup> Upon excitation of mpg-CN by light, the electrons from the valence band move across the band gap and occupy the conduction band, leading to the separation of the hole and electron by four heptazine units.<sup>193</sup> The computed band gap value of 2.6 eV, determined using the HSE06 hybrid functional,<sup>194, 195</sup> is consistent with the experimental value of 2.7 eV. This explains why the reaction proceeds most efficiently under quasi-monochromatic light sources in the UV and blue LED regions, as indicated in [Table 3.1](#).



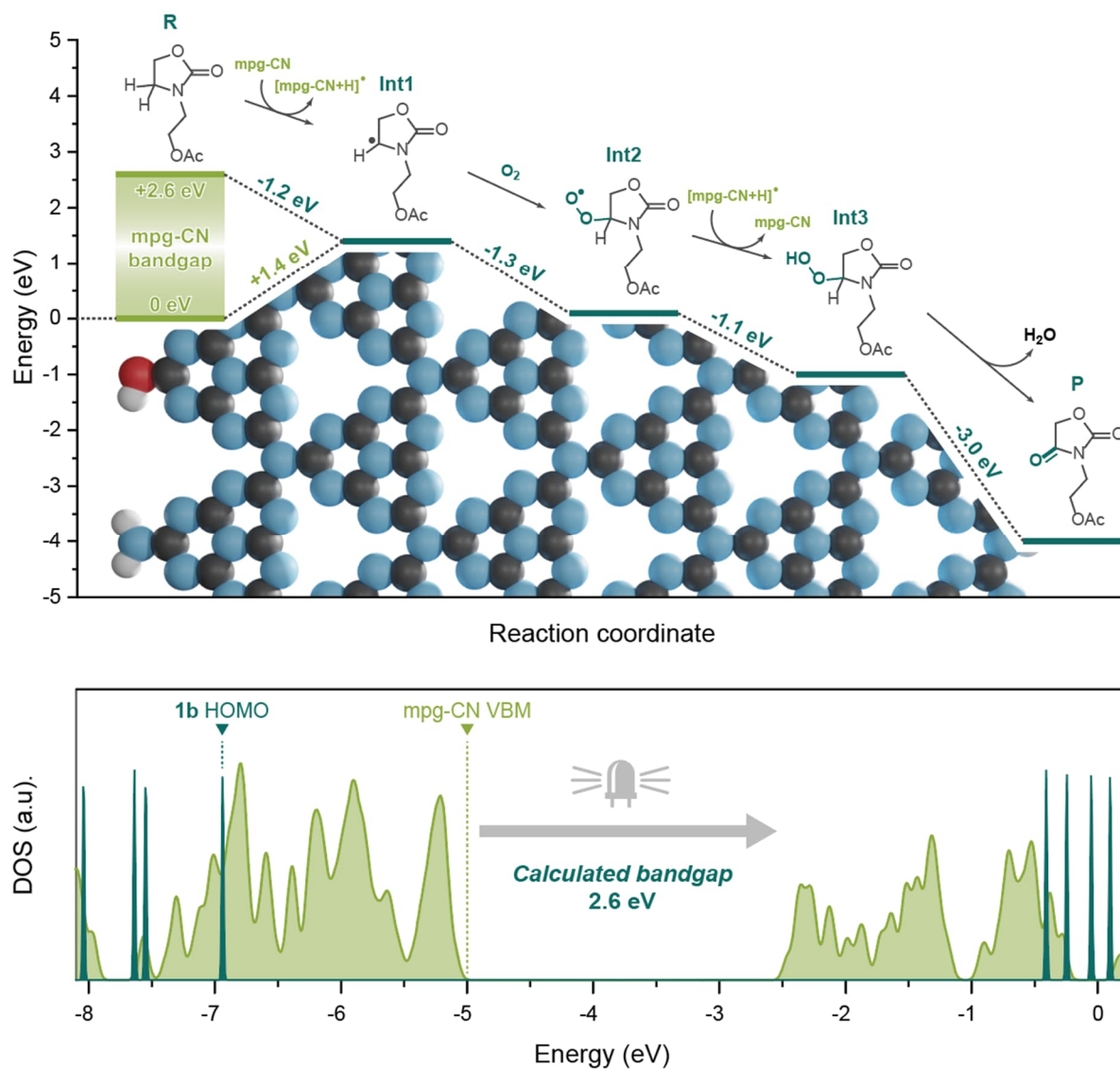


Figure 3.6. DFT results. a) Proposed mechanism for oxazolidinone 1b oxidation at mpg-CN with potential energy differences of the respective intermediates. The mpg-CN+H model used in DFT calculations is shown in the lower part of the figure. The model contains NH, NH<sub>2</sub>, and OH groups at the surface terminations, which is consistent with the experimental data.<sup>165</sup> b) DOS for mpg-CN (orange) and oxazolidinone 1b (purple). The DFT energy scale corresponds to the energies obtained directly from the VASP output files. The correspondence between the two systems was confirmed by aligning the energies of oxygen 2s electrons between these systems (not shown in the figure).



The density of states (DOS) plot supports our cyclic voltammetry (CV) results and indicates that the highest occupied molecular orbital (HOMO) of oxazolidinone 1b is lower than the valence band of mpg-CN, indicating that photoinduced electron transfer (PET) is unlikely to occur without proton transfer. When oxazolidinone 1b is oxidized, a proton and an electron are transferred to the carbon nitride scaffold, resulting in the formation of the oxazolidinone 1b radical, Int1, and the hydrogenated carbon nitride radical [mpg-CN+H]•. The Fermi level of the [mpg-CN+H]• radical is close to the conduction band due to the additional electron in the system, and its formation in either the excited state or the ground state has little effect on the reaction energetics (Figure S3.11). We conducted an extensive search for the different symmetry positions of the extra H atom in the [mpg-CN+H]• system and found that the lowest energy position of Int1 ( $\Delta E = +1.4$  eV) corresponds to the structure where the hydrogen atom is located inside the 'triangular pocket' and attached to the nitrogen atom of the heptazine unit, while depending on the location of the hydrogen atom, the relative energy of the system spreads over 3 eV (Figure S3.7). The radical Int1 then reacts with an oxygen molecule, forming a peroxy radical Int2 ( $\Delta E = -1.3$  eV). An alternative mechanism in which the O<sub>2</sub> molecule captures the hydrogen atom from [mpg-CN+H]• instead and forms the HO<sub>2</sub>• is less thermodynamically feasible (+0.4 eV uphill) and can be excluded (Figure S3.9). The peroxy radical Int2 recovers an H-atom from [mpg-CN+H]• to create a hydroperoxide intermediate Int3 ( $\Delta E = -1.1$  eV), which then loses a water molecule to produce 2b ( $\Delta E = -3.0$  eV).

In the absence of photoexcitation, the transfer of H-atom from 1b to carbon nitride would be the only uphill step. To accurately compute the energy of this step, the transfer was also simulated to another model of polymeric carbon nitride, namely melon-CN.<sup>196</sup> The energy of transfer to the melon model was found to be within 0.3 eV of the mpg-CN model (Table S3.3), which justified the use of the mpg-CN model. The electronic energy



change for the H-atom transfer to mpg-CN was then computed more accurately using the HSE06 hybrid functional. After considering the vibrational frequencies of adsorbates and gas-phase entropies, the Gibbs free energy change of +1.5 eV for this step was determined. This value is significantly smaller than the *endo*-C–H BDFE in  $\beta$ -position to amide nitrogen in 1b of 4.03 eV or 92.9 kcal·mol<sup>-1</sup> in vacuum. In other words, the homolytic C–H bond cleavage, which is intrinsically highly exergonic, becomes more facile when the H-atom is transferred to mpg-CN.

To evaluate the potential of mpg-CN excited state to homolytically cleave various X–H bonds, we investigated the p*K*<sub>a</sub> value of protonated mpg-CN in water, which we found to be 6.60±0.3. The material contains a diverse range of protonation sites, each with different basicity, and thus, the obtained value should be considered as an "average" or "apparent" p*K*<sub>a</sub> value. Although the p*K*<sub>a</sub> of bare heptazinium cation is expected to be close to zero or even negative due to the mutual electron-withdrawing effect of (sp<sup>2</sup>)N atoms, the measured p*K*<sub>a</sub> indicates that protonated mpg-CN acts as a weak acid. This apparent discrepancy could be explained by the presence of adjacent heptazine units that form a "triangular pocket" and stabilize a proton, similar to a proton sponge. Using the obtained p*K*<sub>a</sub> value and an *E*<sub>VB</sub> of +1.45 V vs. NHE,<sup>179</sup> we calculated FBDFE to be 100±0.4 kcal·mol<sup>-1</sup> or 4.32±0.02 eV using equation (3.1). This indicates that upon mpg-CN band gap excitation, it can potentially homolytically cleave X–H bonds with BDFE values less than 100 kcal·mol<sup>-1</sup> (Supplementary Discussion 4).

When carbon nitrides with a more positive valence band potential, like K-PHI with +2.2 V vs. NHE,<sup>122</sup> and higher surface basicity (p*K*<sub>a</sub> of the conjugated acid > 6.6), are excited at their band gap, they can cleave even stronger polar X–H bonds. By substituting the p*K*<sub>a</sub> and *E*<sub>VB</sub> values into equation (3.1), we can deduce FBDFE to be greater than 117.4 kcal·mol<sup>-1</sup>, which is close to the O–H BDFE in water of 123 kcal·mol<sup>-1</sup>.<sup>146</sup> K-PHI, for example, is capable of evolving O<sub>2</sub> from water upon illumination,



facilitated by the removal of photogenerated electrons from the conduction band by a sacrificial electron acceptor.<sup>182</sup> In this study, K-PHI also demonstrates comparable and high activity in the oxidation of 1b (as shown in Table 3.1).

Many photocatalytic reactions facilitated by graphitic carbon nitride involve cleavage of strong C–H, O–H and N–H bonds with BDFE in the range of 80–123 kcal·mol<sup>-1</sup> (Table S3.4).<sup>122, 160, 164, 182, 197, 198</sup> Often, a basic environment is required to promote the cleavage of these bonds.<sup>159, 164</sup> However, even without adding a base, mpg-CN, K-PHI and Na-PHI photocatalyze the cleavage of O–H and N–H bonds in carboxylic acids and carbamates to a certain degree. Ionic g-CN materials have a more basic character than covalent g-CN due to the presence of deprotonated imide functionalities and have a valence band with a potential that is 0.7 V more positive. This combination of properties is responsible for higher yields in oxidation of toluene to dibenzyl disulfide<sup>122</sup> and Minisci coupling<sup>160</sup>. The results summarized in Table S3.4 confirm that g-CN materials can be used as photobases to mediate oxidative ES-PCET. However, the use of an additional base can be beneficial to suppress the proton back-transfer to the intermediate and obtain higher yields.

Equation (3.1) suggests that the cleavage of strong X–H bonds can be achieved by combining a superbases with a strong oxidant in a single reaction. However, this method is limited to FBDFE values of 71–98 kcal·mol<sup>-1</sup> because electron-rich superbases would react with strong oxidants.<sup>199</sup> Carbon nitrides are relatively chemically stable as they lack X–H bonds, except for the NH- and NH<sub>2</sub>-groups. To design and synthesize semiconductor materials for X–H functionalization of organic compounds via excited state PCET, two strategies can be employed: increasing surface basicity by incorporating deprotonated cyanamide moieties<sup>200, 201</sup> and shifting  $E_{VB}$  to more positive values by incorporating electron-accepting moieties.



### 3.4. Conclusion

We have developed an optimized photocatalytic protocol to convert oxazolidinones into their corresponding 2,4-diones using cheap semiconductor mpg-CN photocatalyst and oxygen gas as a terminal oxidant on a millimolar scale. The heterogeneous organophotocatalytic method is exceeding in yield and is more convenient compared to homogeneous photoredox catalysis and regular oxidative systems such as  $\text{RuO}_4/\text{NaIO}_4$ . Several lines of evidence, including the irrelevance of  $\text{O}_2$  pressure to the product yield, the high oxidation potential of oxazolidinones (+1.26...1.98 V vs. SCE), and tr-PL data, exclude SET and EnT pathways. DFT calculations suggest that the initial step involving  $\text{sp}^3$  C–H bond cleavage in oxazolidinone via PCET is energetically uphill. However, mpg-CN as the organophotocatalyst overcomes this energy barrier by converting the irradiation energy into the driving force for PCET.

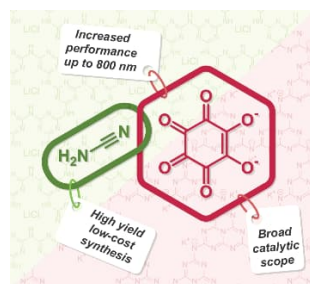


## Chapter 4. Mixed Phase Carbon Nitrides for Multiple Photocatalytic Applications

---

### 4.1. Overview

Two series of novel carbon nitride photocatalysts, Rho-CN (“Rhodizonate-doped Carbon Nitride”) and Rho-CN-TC (Rho-CN treated in potassium thiocyanate melt), are synthesized in a multi-step fashion *via* copolymerization of cyanamide with potassium rhodizonate. The formed ionic carbon nitrides are composed of poly(triazine imide) (PTI/Li<sup>+</sup>Cl<sup>-</sup>) and potassium poly(heptazine imide) (K-PHI) phases and provide a broad absorption range up to 800 nm. The photocatalysts were characterized by several techniques (including DRUV-Vis, PXRD, FT-IR, SEM and electrochemical methods) and studied in a series of photocatalytic reactions, including red light-promoted benzylamine oxidation, dual photoredox/nickel C-N cross coupling and hydrogen peroxide evolution. The optimal ratio of rhodizonate dopant in its mixture with cyanamide was found to be 0.5% mol. The performance of the newly synthesized materials is comparable to the activities of the benchmark catalysts K-PHI and CN-OA-m (defective poly(heptazine imide) doped with oxamide), while not requiring more expensive nitrogen sources for preparation, like 5-aminotetrazole, or multiple oven cycles.



This chapter is an adapted version of the article:

A. Galushchinskiy, C. Pulignani, H. Szalad, E. Reisner, J. Albero, N. V. Tarakina, C. M. Pelicano, Hermenegildo García, O. Savateev, M. Antonietti. Heterostructured PHI-PTI/Li<sup>+</sup>Cl<sup>-</sup> Carbon Nitrides for Multiple Photocatalytic Applications. *Solar RRL* 2023 (under revision)



## 4.2. Introduction

Graphitic carbon nitrides (g-CNs) are a class of materials consisting of  $sp^2$ -hybridized carbon and nitrogen in a stoichiometry similar to  $C_3N_4$ .<sup>121</sup> These materials can be divided into two categories: heptazine-based and triazine-based g-CNs.<sup>202, 203</sup> The most thermodynamically stable form of g-CN is considered to be a material where carbon and nitrogen atoms form heptazine units that are linked together via bridging nitrogen atoms, and the layers of heptazine units are attracted by van der Waals forces. The synthesis of g-CN materials involves calcination of nitrogen-rich precursors like urea, cyanamide, or melamine at temperatures ranging from 550 to 600°C.<sup>204</sup> The onset of light absorption for g-CNs is around 470 nm, corresponding to an optical gap of 2.7 eV, which is on the edge of the visible range of the electromagnetic spectrum.<sup>117</sup> For optimal use in photo(electro)catalysis, it is essential to narrow the optical gap to 2.5-2 eV to increase the amount of light absorbed. Several methods have been developed to achieve this, including substitutional doping of C and N atoms with heteroelements and vacancies,<sup>205</sup> formation of heterojunctions between g-CN and other semiconductors,<sup>17</sup> and formation of triazine-heptazine donor-acceptor structures.<sup>206</sup> Modified carbon nitrides with a narrowed optical gap can be used as photocatalysts for various reactions, such as hydrogen evolution,<sup>207</sup> pollutant degradation,<sup>208</sup> oxidation reactions,<sup>209</sup> and other complex organic transformations<sup>210</sup>.

This chapter describes the synthesis of carbon nitride materials with a triazine-heptazine donor-acceptor structure via co-condensation of potassium rhodizonate and cyanamide in a LiCl:KCl eutectic mixture at 550°C. The resulting materials exhibit a red-shifted absorption edge, which is dependent on the content of potassium rhodizonate in the mixture, with the edge being shifted up to 800 nm with increasing content of potassium rhodizonate.



## 4.3. Results and Discussion

### 4.3.1. Synthetic Approach

The objective of this study was to synthesize carbon nitride materials by co-polymerizing nitrogen-rich precursors with functionalized organic dyes in the conjugated system of heptazine layers to extend visible light absorption beyond 450 nm. However, finding the optimal dye is challenging due to several factors. The dye should be thermally stable, but most organic dyes decompose at temperatures lower than 500 °C, which is the minimum temperature required for the formation of heptazine-based carbon nitrides, like melon.<sup>211</sup> Moreover, the chemical integrity of the dye should be preserved during extended reaction times at elevated temperatures, as the formation of nucleophilic species such as ammonia can disrupt the dye's conjugated system. Additionally, the dye should have reactive functional groups to enable its electronic structure to interact with the rest of the material. Finally, the dye should maintain its absorbance in the 450-800 nm range and be easily synthesized in large quantities.

We selected potassium rhodizonate ( $K_2Rho$ ), the dipotassium salt of 3,4,5,6-tetraoxocyclohexene-1,2-diol, which is used in niche applications related to the analysis of heavy metal content through formation of colored or insoluble complexes (*e.g.*, in lead rapid abrasion test kits).<sup>212</sup>  $K_2Rho$  is a fairly strongly absorbing dye with an absorption maximum in the blue to green-yellow region of visible spectrum ( $\epsilon = 3.3 \cdot 10^4 \text{ L} \cdot \text{mol}^{-1} \cdot \text{cm}^{-1}$  at  $\lambda_{\text{max}} = 483 \text{ nm}$  in aqueous media).<sup>213</sup> This gives the dye its deep, almost black, purplish-red color in bulk, and it is stable at least until 300 °C.<sup>214</sup> Thermogravimetric analysis experiments demonstrate 67% mass retention up until 600 °C (Figure S4.10), and it can easily be prepared by oxidation of inositol, which is a bulk chemical.<sup>215</sup> Its conjugated system is stabilized by equal delocalization of double negative charge between carbonyl groups and provides excellent charge capacity and transfer



properties.<sup>216</sup> However, these functionalities are also susceptible to reaction with nucleophiles while preserving its electronic structure.<sup>217</sup> As a reactive nitrogen-rich compound and a co-polymerization coupling partner for  $K_2Rho$ , we chose cyanamide, which is a known cheap bulk precursor to mesoporous carbon nitrides.<sup>179</sup> Additionally, cyanamide has strongly nucleophilic nitrogen atoms which can react with carbonyl groups of  $K_2Rho$  and, unlike most aliphatic and (hetero)aromatic amines, is weakly acidic with a  $pK_a$  of 10.3,<sup>218</sup> which is crucial as  $K_2Rho$  tends to decompose rapidly in basic media<sup>213</sup>. Finally, the viability of our synthetic strategy is supported by the fact that cyclohexanehexone, a compound structurally-similar to  $K_2Rho$ , was successfully applied in synthesis of  $C_2N$  materials by polycondensation with urea at 500 °C.<sup>219</sup>

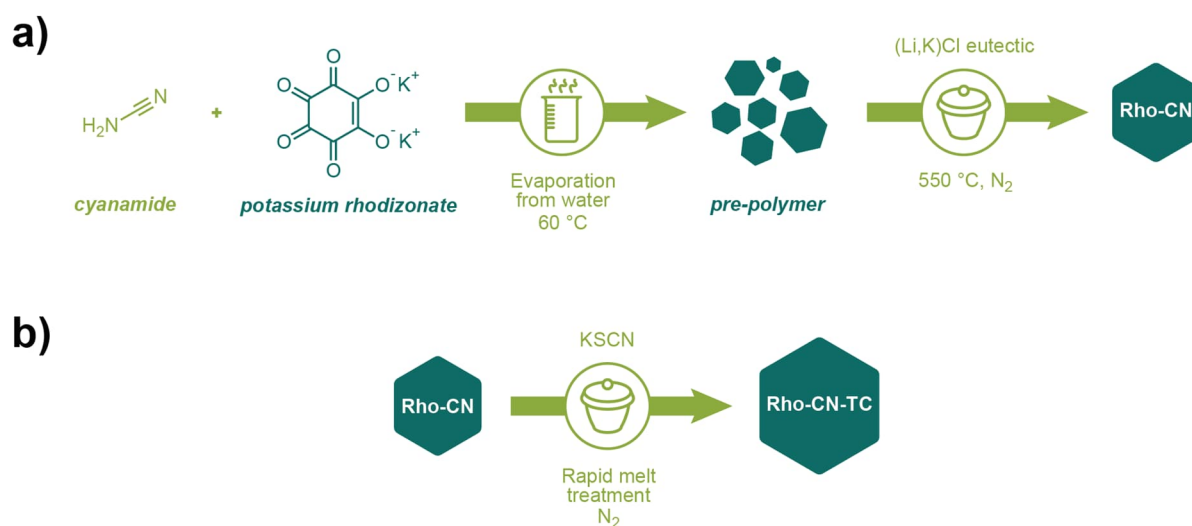


Figure 4.1. Synthesis of photocatalysts. a) Two-step synthesis of Rho-CN. b) Synthesis of Rho-CN-TC catalysts by KSCN melt treatment of Rho-CN.

We employed a two-step method to synthesize Rho-CN materials with varying molar percentages of  $K_2Rho$  in the starting mixture. The first step involved co-evaporating an aqueous solution of cyanamide and  $K_2Rho$  mixture at 60 °C, resulting in a beige to brown-green or dark brown non-homogeneous solid mass, which is suspected to be a solid gel network of cyanamide oligomers linker by rhodizonate units, possibly



containing unreacted starting materials and/or dicyandiamide.<sup>219</sup> The pre-polymer was then mixed with eutectic (K,Li)Cl mixture and annealed at 550 °C under nitrogen to produce Rho-CN-0.25, Rho-CN-0.5, and Rho-CN-1 (“Rho-CN” stands for “Rhodizonate-doped Carbon Nitride”; numbers indicate molar percentage of  $K_2Rho$  in the starting mixture) (Figure 4.1a). The materials were obtained by washing out the salt template from the formed solid, with yields of up to 65% retention of combined organic mass. To increase the content of anionic fractions and introduce cyanimide groups, which can facilitate transfer of photogenerated electrons to the reagents or co-catalyst,<sup>220, 221</sup> the Rho-CN materials were additionally treated in KSCN melt, resulting in three corresponding Rho-CN-TC catalysts (“TC” refers to “ThioCyanate”) (Figure 4.1b).<sup>222</sup> The six catalysts were then characterized and tested in a series of photocatalytic experiments. The appearance of the materials is shown in Figure 4.2.

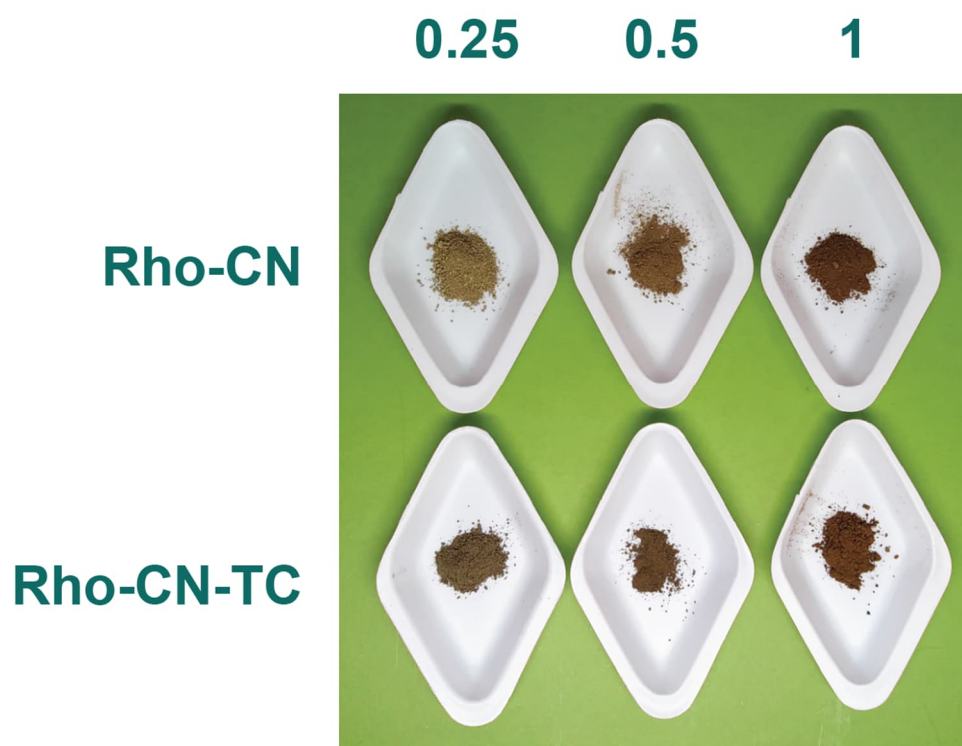


Figure 4.2. Appearance of Rho-CN-X and Rho-CN-TC-X catalysts, where X is the number indicating amount of  $K_2Rho$  in starting cyanamide-rhodizonate mixture (top line, in mol. %).



### 4.3.2. Characterization of Materials

#### *Chemical composition*

**Table 4.1** summarizes the elemental composition of the synthesized materials. The C/N ratio is lower than the theoretical value for perfectly-condensed heptazine-based graphitic carbon nitride with the ideal composition of  $C_3N_4$  (0.64), indicating the presence of nitrogen doping. The increased nitrogen content could be due to the presence of terminal anionic -NCN groups at the surface or potential azo -N=N- bridges between units. Moreover, PTI materials are known to form a hexagonal lattice with cavities formed by absent triazine units occupied by alkaline metal chlorides, primarily lithium chloride, and are referred to as PTI/ $M^+Cl^-$  ( $M = Li$  or  $K$ ).<sup>223, 224</sup> ICP-OES results show that the combined metal content in the catalysts varies between 8.4 and 11.8%, with a lithium to potassium gram atomic ratio of about 3:1. This indicates the presence of a large fraction of anionic imide functions in the materials, which is further increased by KSCN melt treatment. Due to the high concentration of potassium ions in the melt, some of the lithium ions are also replaced and washed off the material.

Table 4.1. Chemical composition of synthesized materials.<sup>[a]</sup>

Sample	N, %	C, %	H, %	S, %	C/N, mass	C/H, mass	K, %	Li, %
Rho-CN-0.25	49.3	28.5	1.6	–	0.58	18.4	5.8	3.4
Rho-CN-0.5	47.4	27.6	2	–	0.58	13.8	5.6	3.4
Rho-CN-1	48.2	28.3	1.8	–	0.59	15.6	4.6	3.8
Rho-CN-TC-0.25	47.8	28.0	1.5	0.4	0.59	18.4	8.8	2.7
Rho-CN-TC-0.5	47.0	27.9	1.7	0.3	0.59	16.7	9.9	1.9
Rho-CN-TC-1	47.9	28.4	1.4	0.3	0.59	20.0	7.6	2.9

[a] – Percentage of N, C and H elements was obtained from combustion analysis. Percentage of K and Li was obtained from inductively coupled plasma optical emission spectrometry (ICP-OES). Values given in mass percentages.



The structural composition of the synthesized catalysts was analyzed using powder X-ray diffraction (PXRD) (Figure 4.3a). The broad diffraction peaks indicated that the synthesized materials were nanocrystalline. The PTI/Li+Cl<sup>-</sup> phase was characterized by signature peaks at 12, 21, 24, 29, and 32 degrees and a series of low-intensity peaks at 40-55 degrees.<sup>102, 224</sup> In the case of Rho-CN-0.5, a peak at 7-8 degrees was observed, indicating the presence of the potassium poly(heptazine imide) (K-PHI) phase.<sup>124, 181, 220</sup> This suggests that the addition of 0.5 mol. % of potassium rhodizonate to the cyanamide induced the formation of a hybrid composite comprising PTI/Li+Cl<sup>-</sup> and K-PHI phases. The Rho-CN series demonstrated a relatively high degree of crystallinity, while the Rho-CN-TC catalysts were close to being amorphous, which was attributed to the decrease in PTI/Li+Cl<sup>-</sup> crystallite size during KSCN melt treatment.

The FT-IR analysis showed that the vibrations of heptazine and triazine ring units are situated in the region of 1650-800 cm<sup>-1</sup>. A peak at 804 cm<sup>-1</sup> was observed, indicating the characteristic peak of heptazine. Another peak was observed at approximately 2175 cm<sup>-1</sup>, corresponding to the vibration of triple C≡N bond of anionic cyanamide K-RNCN.<sup>222</sup> The spectra are provided on Figure 4.3b.

X-ray photoelectron spectroscopy (XPS) was utilized to analyze the chemical composition of the synthesized materials from C, N, O, K and Li bond regions (Figure 4.4a-d). The C<sub>1s</sub> region shows characteristic carbon nitride peaks at 284.5 eV (C=C of adventitious carbon) and 287.9 eV (C=N-C of the ring), along with hydroxylated C-OH carbon at 288.1 eV.<sup>225</sup> However, the ratio between the two fits does not correspond to purely heptazine or triazine imide phase, with the 288 eV peak being dominant for the latter.<sup>226</sup> This suggests the presence of the PHI phase, which is supported by the small atomic content of K<sup>+</sup> ions (1.8%) with characteristic peaks at 292.8 and 295.5 eV.



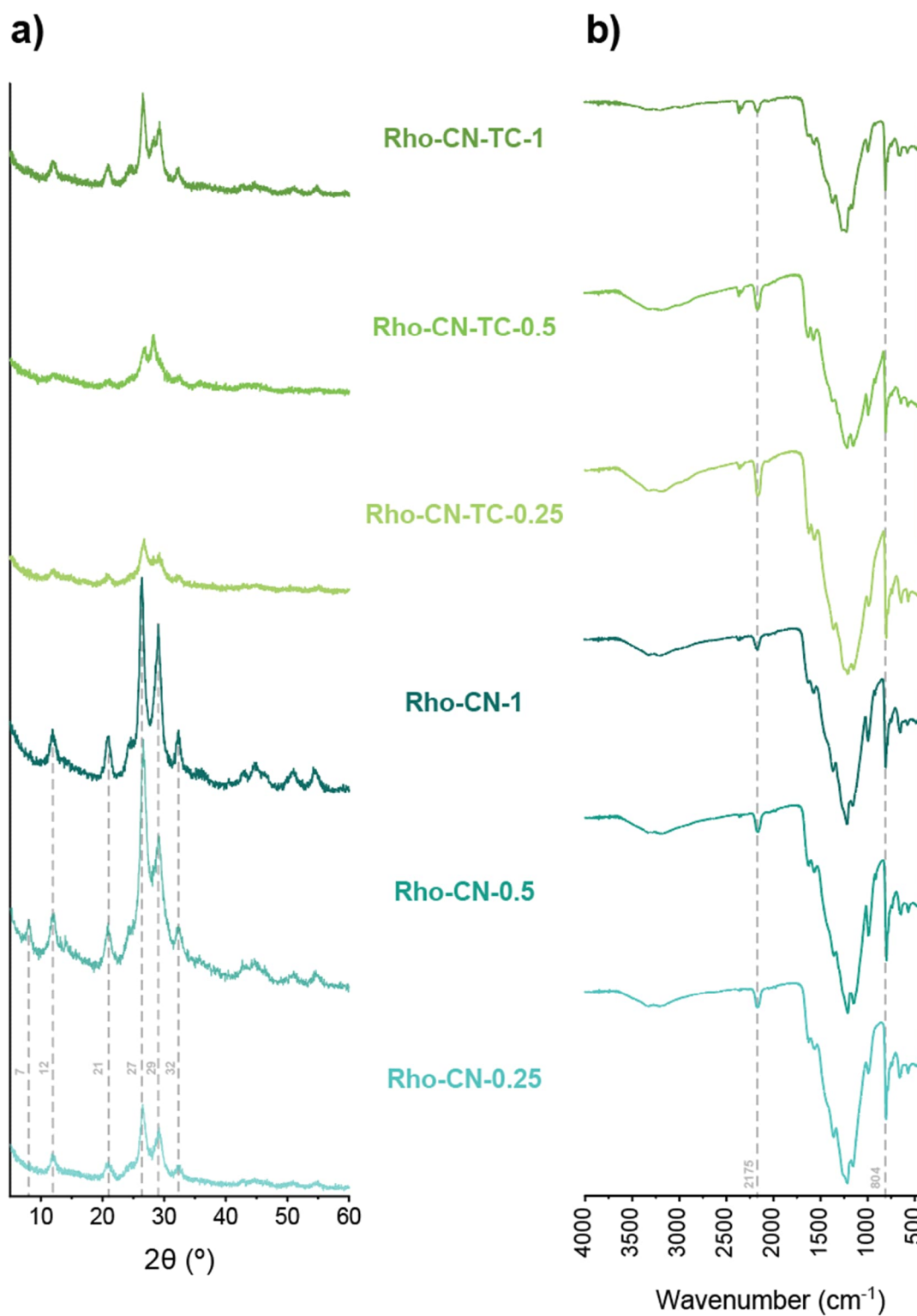


Figure 4.3. Phase and functional groups characterization of the catalysts. a) PXRD patterns of Rho-CN and Rho-CN-TC materials. b) FT-IR spectra of Rho-CN and Rho-CN-TC materials.



The N<sub>1s</sub> region shows typical signals of imide-NH bridges at 399.9 eV and triazine nitrogen at 398.4 eV, with a usual ratio of about 1:3. A weaker peak at 397.5 eV is also present, attributed to deprotonated imide nitrogen characteristic of the PHI phase. The O<sub>1s</sub> region provides three contributions at 530.7 (surface -OH), 531.5 (C-O-C) and 533.0 eV (C=O and adsorbed water). Finally, the Li1s region shows the characteristic 55 eV peak of Li<sup>+</sup> ion.

Proton and carbon magic angle spinning solid state nuclear magnetic resonance (<sup>1</sup>H MAS and <sup>13</sup>C CP-MAS NMR) spectra of Rho-CN-0.5 demonstrate predominance of PTI/Li<sup>+</sup>Cl<sup>-</sup> phase in the material, showing peaks at 5, 8 and 11 ppm at proton and 157, 162 and 167 ppm at carbon spectrum, respectively (Figure 4.4e,f).<sup>227</sup> No characteristic sharp heptazine carbon peaks at 155, 163 and 167 ppm were observed;<sup>228</sup> however, heptazine fraction of the material is supposed to be minor, and its signals may be lost in noise during spectra accumulation due to heavy overlapping with those of PTI/Li<sup>+</sup>Cl<sup>-</sup>.



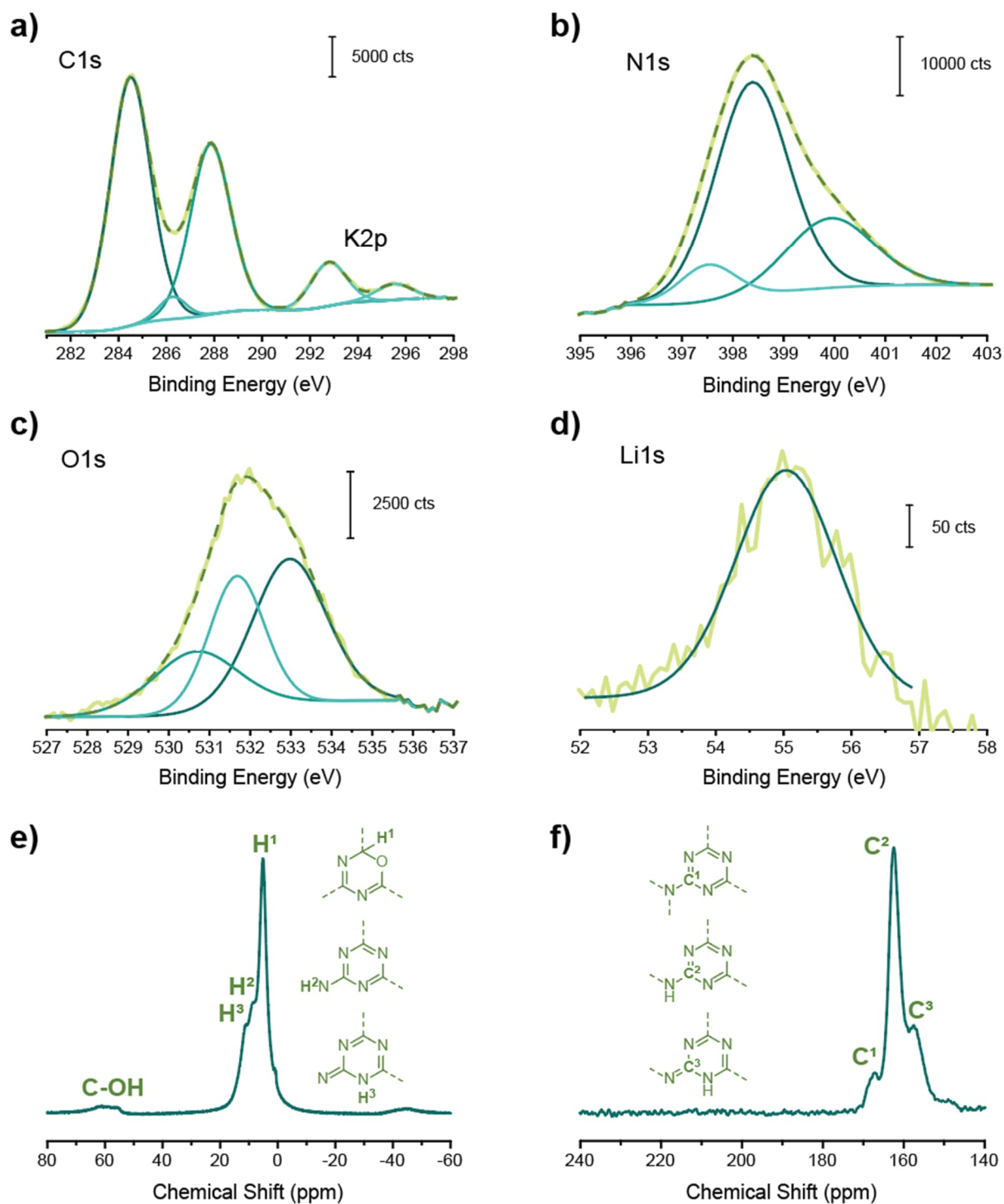


Figure 4.4. Characterization of Rho-CN-0.5 material. a) C<sub>1s</sub> and K<sub>2p</sub> b) N<sub>1s</sub> c) O<sub>1s</sub> and d) Li<sub>1s</sub> XPS spectra; bars indicate Y axis scale in counts. e) <sup>1</sup>H MAS and f) <sup>13</sup>C CP-MAS NMR spectra; chemical structures of heptazine units indicate different types of atoms and their respective signals according to the reference.<sup>227</sup>



### DRUV-Vis and Fluorescence

The electronic spectra of Rho-CN and Rho-CN-TC samples were examined using diffuse reflectance (DR) mode, and the results are shown in [Figure 4.5a](#). The spectra showed several absorption bands, including a primary absorption band at  $\sim 450$  nm, attributed to electron transitions between the valence and conduction band, and an onset of absorption at  $\sim 750$  nm, which is typically assigned to transitions between the non-bonding and antibonding molecular orbitals ( $n-\pi^*$  transitions) based on the theory of molecular orbitals.<sup>229</sup> Increasing the concentration of  $K_2Rho$  in the mixture with cyanamide led to more pronounced  $n-\pi^*$  transitions and increased absorption at wavelengths  $> 450$  nm. The optical bandgap of the materials was determined using modified DRUV-Vis plots (see [Figure S4.2](#)), with Rho-CN-0.25 and Rho-CN-0.5 demonstrating similar bandgap values of 2.58 and 2.56 eV, respectively. These values were slightly lower than the bandgap of K-PHI (2.68 eV) but closer to the bandgap of CN-OA-m (2.32 eV) poly(heptazine imide) catalysts.<sup>221</sup> Treatment with KSCN increased the bandgap of the 0.25% catalyst to 2.73 eV, possibly due to etching of rhodizonate-induced defects in the salt melt, changes in morphology and crystallinity, or sulfur doping ([Table 4.1](#)).<sup>230</sup> In general, the trend observed for both catalyst series was that higher concentrations of  $K_2Rho$  decreased the bandgap by moving the valence band level to more negative values. The bandgap and band positions are discussed further in the electrochemistry section.



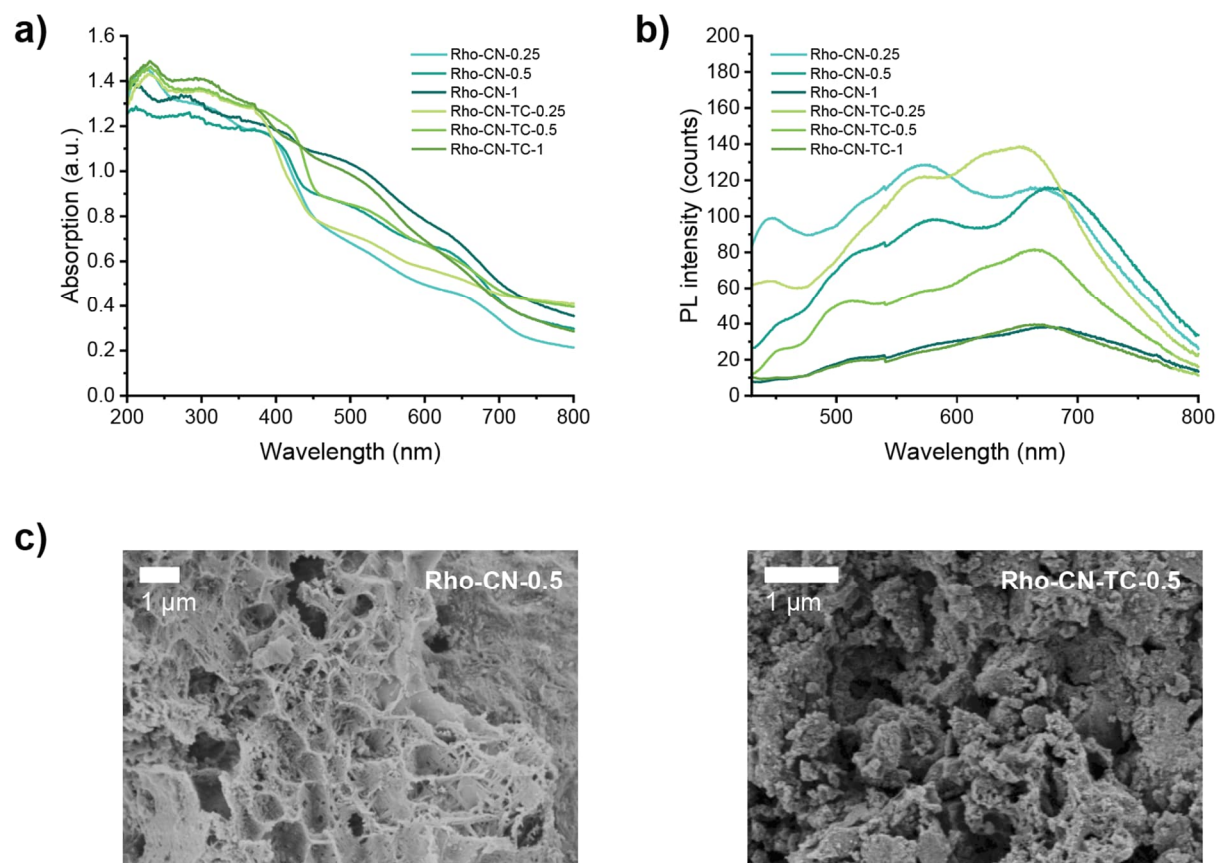


Figure 4.5. Spectroscopic and SEM characterization of Rho-CN and Rho-CN-TC catalysts. a) DRUV-vis absorption spectra of materials. b) Steady-state emission spectra of materials. c) Morphology of materials containing 0.5 mol. %  $K_2Rho$ .

The steady-state fluorescence spectra were obtained by exciting the samples at 410 nm, and the resulting emission spectra were measured in the range of 430-800 nm (Figure 4.5b). Among the synthesized materials, several emission peaks were observed at around 450, 575, and 675 nm. The intensity of these peaks decreased with increasing concentrations of potassium rhodizonate in the reaction mixture. The major emission peak was recorded at 675 nm for samples containing 1 mol.% of  $K_2Rho$ . The overall fluorescence intensity decreased as the concentration of  $K_2Rho$  increased from 0.25 to 1 mol.%, indicating a reduction in the radiative decay of excitons. Time-resolved emission spectroscopy showed that the excitons, which had a lifetime of  $\leq 20$ -60 ps, relaxed through fluorescence. The low quantum yield of fluorescence indicated that the radiative



relaxation of the singlet excited state was not the only pathway for the recovery of the ground state and most likely involved singlet-triplet intersystem crossing.<sup>124, 188</sup> The details are presented in [Table 4.2](#).

Table 4.2. Fluorescence lifetimes for synthesized materials.<sup>[a]</sup>

Sample	Fluorescence lifetime [ps]
Rho-CN-0.25	20.83 ± 0.75
Rho-CN-0.5	26.22 ± 2.25
Rho-CN-1	20.48 ± 1.67
Rho-CN-TC-0.25	59.09 ± 30.25
Rho-CN-TC-0.5	41.78 ± 9.77
Rho-CN-TC-1	29.63 ± 5.83

[a] – Excitation wavelength: 375 nm; emission was detected at 550 nm. The decay curves were fitted using a nonlinear method with a multicomponent decay law.

### *Electron Microscopy*

The morphology of the samples was investigated through SEM and TEM. Representative images of the samples containing 0.5% mol. of potassium rhodizonate are shown in [Figure 4.5c](#). The surface of the 20-70 μm Rho-CN samples displayed macropores and cavities ranging from 0.5-5 μm, as well as rectangular imprints from the salt template crystals which were washed out. Moreover, needle-shaped crystallites and rectangular grid networks on the surface were observed, which may be attributed to the PTI/Li+Cl- phase.<sup>224</sup> The Rho-CN-TC particles had a coarser surface and were generally smaller in size due to etching with KSCN melt. The size of surface crystallites was also reduced, and needle-like structures were absent after treatment, supporting the reduction in crystallinity observed in the powder X-ray diffraction data. It is worth noting that the morphology of the samples was consistent within each class of Rho-CN and Rho-CN-TC.



TEM analysis confirmed the formation of two phases, which are strikingly different in morphology. The sample mostly consists of  $\mu\text{m}$ -sized flakes (Figure 4.6a). High-resolution images obtained from such flakes show numerous nanodomains (about 6 nm) which form a continuous network. Selected area electron diffraction patterns from these flakes and from individual domains in such flakes are indexed in an orthorhombic lattice with unit cell parameters  $a=14.38(14)\text{\AA}$ ,  $b=8.25(15)\text{\AA}$ ,  $c=6.70(2)\text{\AA}$  (Figure 4.6d and 4.6b inset), typical for the PTI structure.<sup>223</sup> A small number of agglomerates that consist of needle-like crystallites belong to the second phase. Inter-planar distances measured on HRTEM images (as for example on Figure 4.6f) are equal to  $d_{100}=10.25\text{\AA}$ , typical for the potassium polyheptazine imide structure.<sup>124</sup> Overall, characterization data suggest that PTI/ $\text{Li}^+\text{Cl}^-$  and PHI phases coexist, while the building units, i.e., triazines and heptazines, are interconnected at the interface between these two phases.



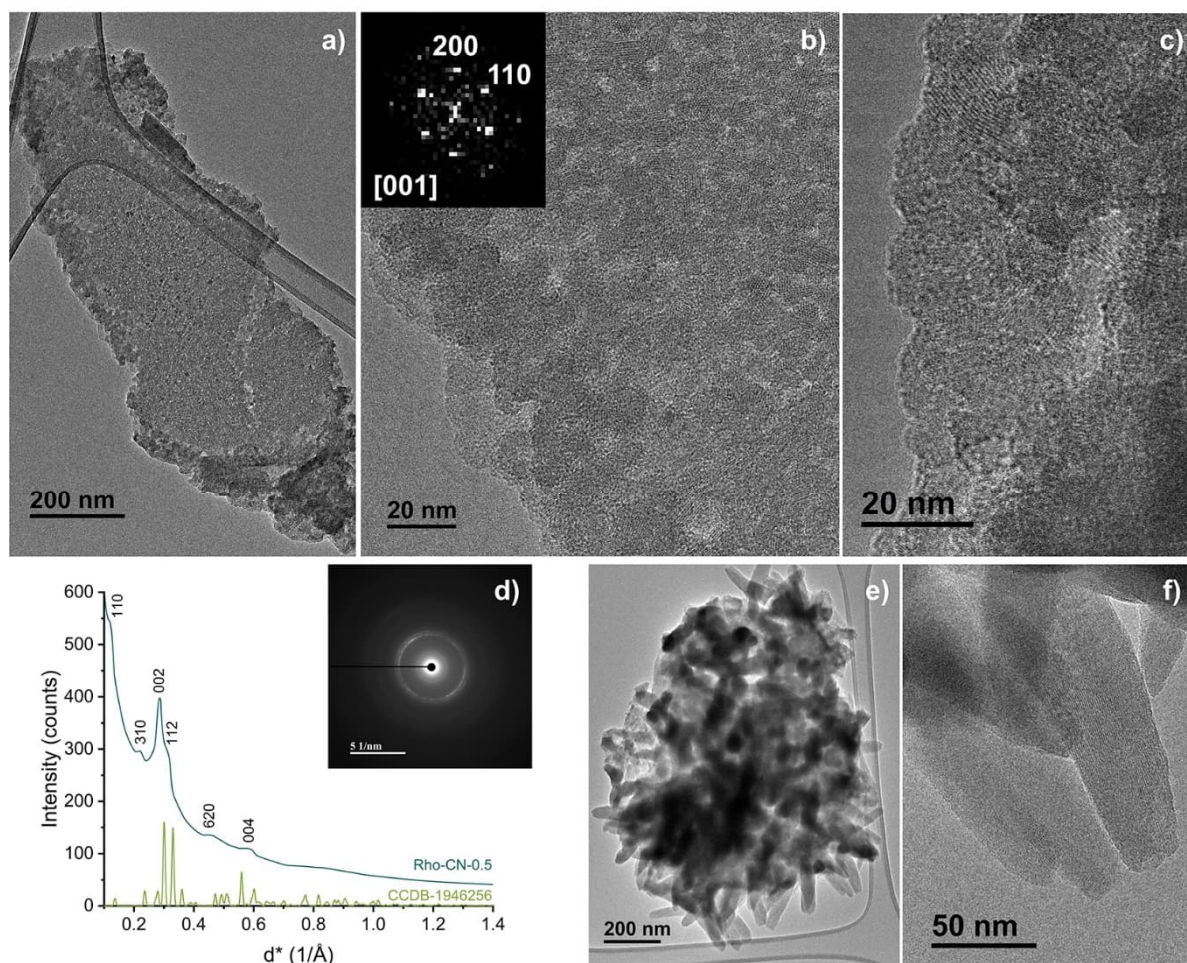


Figure 4.6. a) Low-magnification TEM image, showing typical morphology of the Rho-CN-0.5 sample; b, c) HRTEM images show that flat flakes consist of crystallites of about 6 nm in diameter; inset in b) shows a fast Fourier transform indexed in the orthorhombic unit cell of PTI (CCDB-1946256),<sup>223</sup> d) SAED pattern collected from PTI flakes; Cyan: averaged intensity profile obtained from the SAED pattern shown in inset; Green: theoretical intensity profile obtained using CCDB-1946256 data for the PTI crystal structure. e) Low-magnification TEM image of the second phase in the sample. f) HRTEM image of individual crystals in (e), the distance between lattice planes corresponds to  $d_{100}=10.25\text{\AA}$  of the polyheptazine imide structure.<sup>124</sup>

## Electrochemistry

The electrochemical properties of Rho-CN and Rho-CN-TC photoelectrodes with a conductive Nafion binder were investigated by cyclic voltammetry in aqueous media (0.1 M  $\text{Na}_2\text{SO}_4$ , saturated silver chloride reference electrode). The obtained plots (Figure S4.7) did not yield conclusive data on the values of reduction and oxidation potentials.



The cathodic wave in dark ranges from  $-0.20$  V vs. SHE for Rho-CN-0.5 to  $+0.21$  V vs. SHE for Rho-CN-0.25, while the Rho-CN-TC catalyst shows almost uniform behavior providing a potential around  $-0.10$  V vs. SHE. The electrochemical stability of the samples increases with the concentration of  $K_2Rho$ , as indicated by more stable current values during multiple scans (see [Figure S4.7](#) for CV plots).

The Mott-Schottky analysis ([Figure S4.6](#)) shows that an increase in  $K_2Rho$  concentration in Rho-CN leads to a more positive flatband potential, ranging from  $-0.38$  to  $-0.28$  V vs. SHE. Conversely, for Rho-CN-TC, the trend is reversed with a decrease in flatband potential from  $-0.29$  V for 0.25% to  $-0.51$  V vs. SHE for 1%. By adding the optical bandgap values derived from DRUV-Vis plots to the flatband potentials ([Figure 4.7a](#)), the valence band values were obtained. The materials exhibit slightly higher reductive power than reported PHI-based and NCN-functionalized catalysts,<sup>221</sup> with a narrowed bandgap resulting on cost of oxidation potential. These properties could be useful in designing net-reductive photoredox-processes.

Transient photocurrent response (TPR) and electrochemical impedance spectra (EIS) measurements were conducted in addition to the other experiments. The photocurrent response, in the absence of a sacrificial electron donor, was recorded and ranged from  $150$ - $400$   $nA \cdot cm^{-2}$ , with Rho-CN-0.5 and Rho-CN-TC-1 exhibiting exceptional photocurrents of approximately  $1.2$   $\mu A \cdot cm^{-2}$  during the first scan ([Figure 4.7b](#); data for other samples are shown in [Figure S4.8](#)). This could suggest an optimal concentration of conductive sites created by  $K_2Rho$  dopant. The EIS data for Rho-CN series showed good agreement with the photocurrent values ([Figure 4.7c](#) for Rho-CN-0.5 and Rho-CN-TC-1 samples; plots for other photocatalysts are provided in [Figure S4.9](#)), with samples exhibiting higher conductivity giving higher current. However, there was no such dependency observed in the Rho-CN-TC series, most likely due to the significant structural changes caused by melt treatment, as supported by SEM imaging.



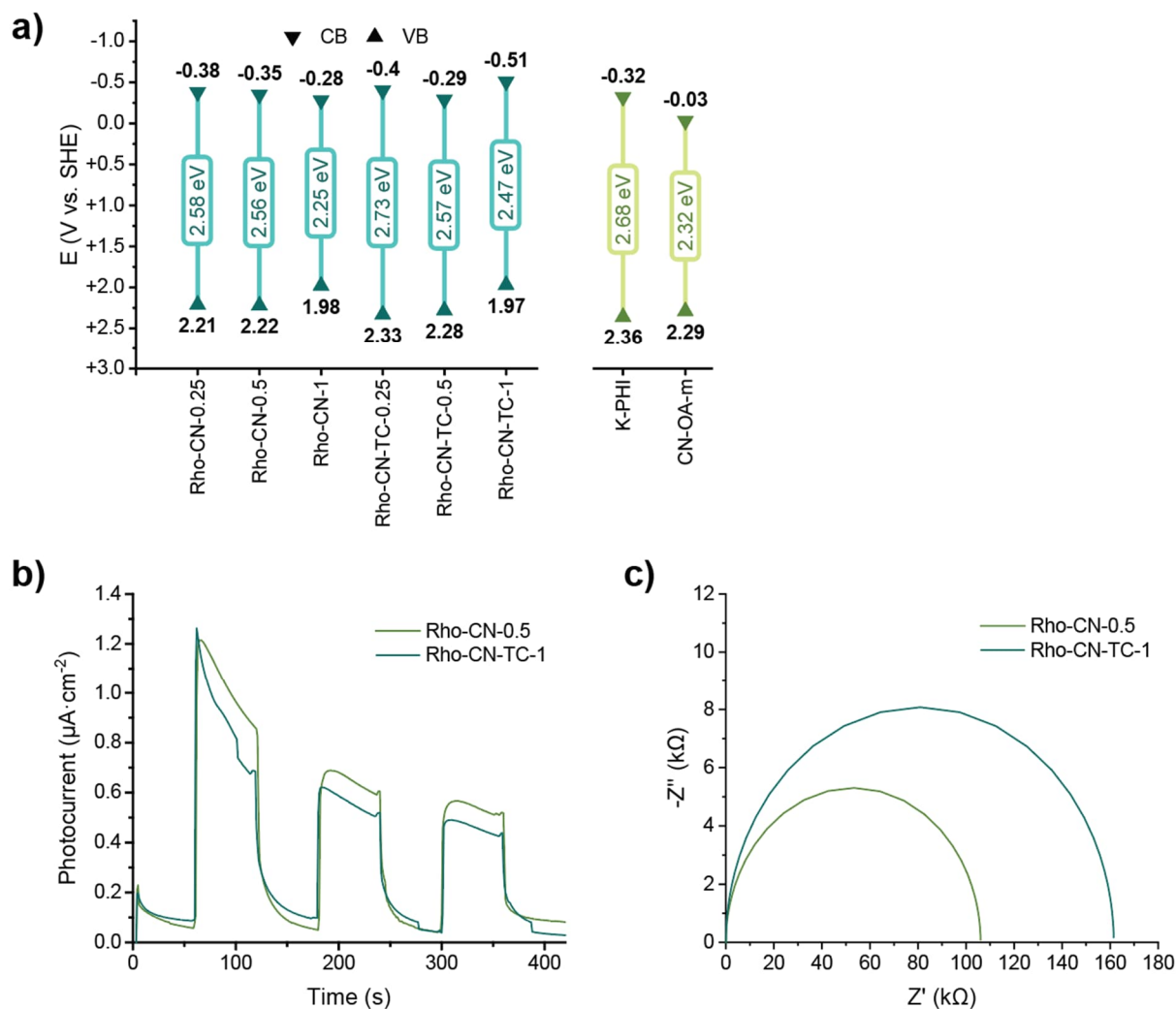


Figure 4.7. Electrochemical properties of photocatalysts. a) Band positions and bandgap values for Rho-CN and Rho-CN-TC materials versus SHE. CB values are the average value from 2 flatband potential measurements, optical bandgaps are derived from DRUV-Vis plots. Comparison values of CB, VB and bandgaps for K-PHI and CN-OA-m benchmark catalysts are sourced from reference.<sup>221</sup> b) Transient photocurrent response of Rho-CN-0.5 and Rho-CN-TC-1 under white LED irradiation with 60 s light and 60 s dark cycles. c) Nyquist plots of potentiostatic EIS spectra of Rho-CN-0.5 and Rho-CN-TC-1.

### 4.3.3. Photocatalytic Performance

#### *Benzylamine Oxidation*

Our investigation of photocatalytic properties of Rho-CN and Rho-CN-TC materials started with evaluating their ability to operate under lower energy irradiation, given



their relatively strong absorbance in the red region of the visible spectrum. As a model reaction, aerobic oxidation of benzylamine to *N*-benzyl-1-phenylmethanimine was chosen; this process is a commonly used benchmark to test the oxidative power of photocatalysts<sup>231-233</sup> since the model substrate has a relatively accessible oxidation potential of +1.04 V vs. SCE (+1.28 V vs. SHE) in acetonitrile.<sup>234</sup> The materials were irradiated under oxygen atmosphere in an acetonitrile solution of benzylamine along with two previously described highly anionic catalysts, K-PHI<sup>180</sup> and CN-OA-m<sup>235</sup>, used as references for comparison. The results of photocatalytic tests are shown in [Figure 4.8a](#). In this reaction, Rho-CN-TC materials provide yields ranging from 65% to quantitative, which is comparable to the 97% obtained for CN-OA-m under the same wavelength. Therefore, Rho-CN-TC catalysts outperform their parent Rho-CN materials (54-77%). In both sets of catalysts, the best results are achieved by the samples prepared from 0.5 mol. % K<sub>2</sub>Rho mixture, indicating the optimal amount of dopant agent. Performance of catalysts in this case may be attributed to several factors, as both direct oxidation of benzylamine by a carbon nitride or energy transfer (EnT) yielding reactive singlet oxygen can occur. However, the reactivity of CNs under longer wavelength irradiation is generally attributed to the predominance of an EnT process,<sup>138, 188</sup> which may indicate better energy transfer and singlet oxygen generation by Rho-CN-TC series catalysts. Given positive Stokes shift, absorption of photons with longer wavelength by Rho-CN-TC would give a less energetic excited state with better spectral overlap with the energy acceptor, in this case O<sub>2</sub>.



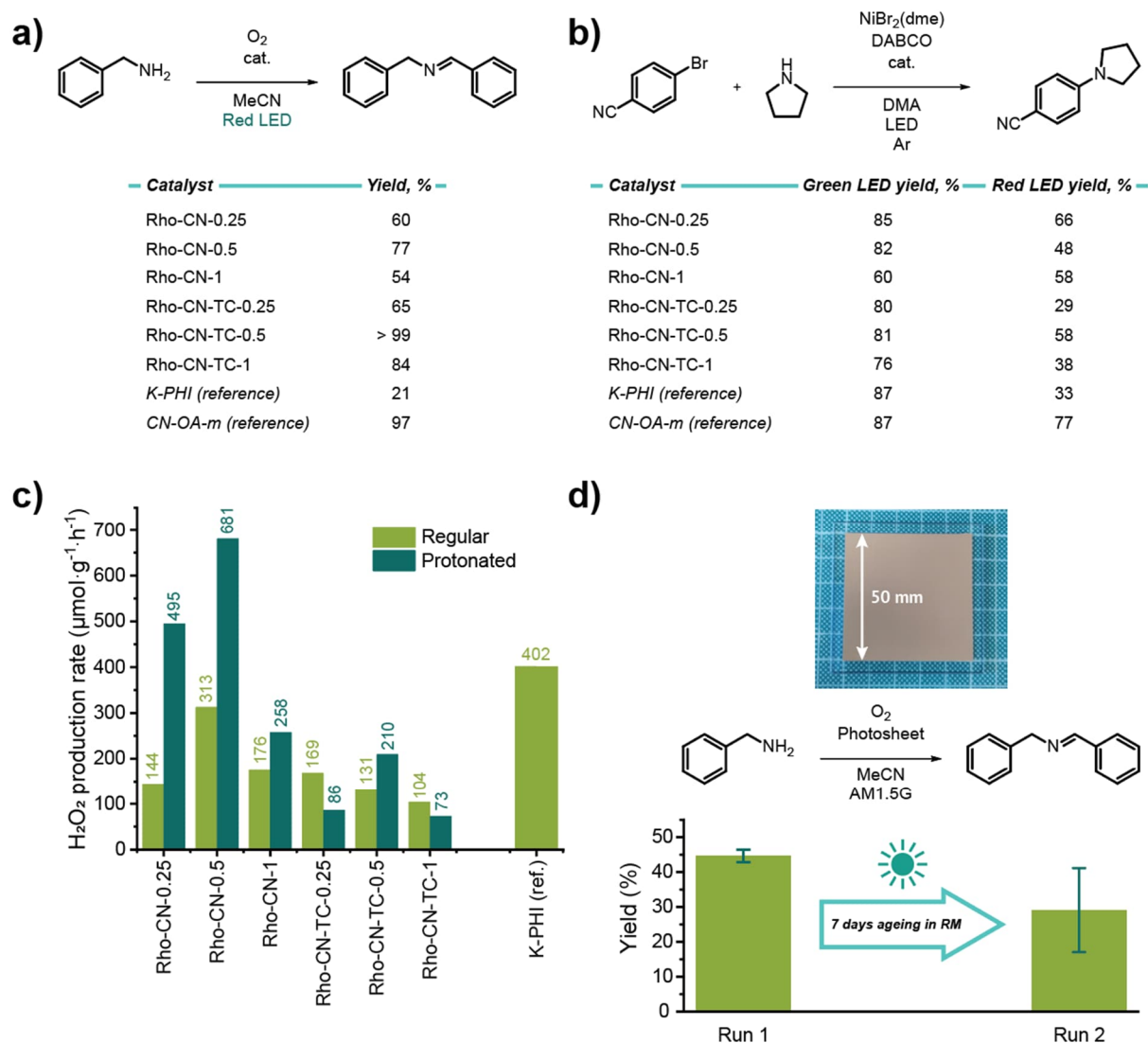


Figure 4.8. Photocatalytic performance of materials. a) Oxidation of benzylamine. Conditions: benzylamine (50  $\mu\text{mol}$ ), photocatalyst (5 mg), acetonitrile (2 mL); oxygen atmosphere introduced by purging the mixture for 60 s, yields are determined by GC-MS. b) Dual photoredox/nickel cross-coupling. Conditions: 4-bromobenzonitrile (200  $\mu\text{mol}$ ), pyrrolidine (1.8 equiv.), DABCO (2.2 equiv.),  $\text{NiBr}_2(\text{dme})$  (5 mol. %), catalyst (12 mg), *N,N*-dimethylacetamide (DMA, 1 mL), argon atmosphere. c) Hydrogen peroxide evolution. Conditions: catalyst (5 mg), water-methanol mixture (2 mL, 4:1 v/v), white LED; oxygen atmosphere introduced by purging the mixture for 60 s. d) Benzylamine oxidation experiment with ca. 25  $\text{cm}^2$  photocatalytic sheet (top) in flow cell prepared from Rho-CN-0.5. Conditions: pre-oxygenated solution of benzylamine in acetonitrile (0.025 M), 1.6667  $\text{mL}\cdot\text{min}^{-1}$  flow rate,  $480\pm 10$  s residence time. Graph (bottom) indicates yields of imine in 2 runs before and after ageing in reaction mixture determined by HPLC (DAD detector at 254 nm). See Supporting Information for detailed description of photocatalytic experiments.



### *Dual Photoredox/Nickel C-N Cross-Coupling*

Palladium-catalyzed C-C and C-heteroatom cross-coupling reactions play an important role in general synthetic and discovery organic chemistry,<sup>236-238</sup> and a vast field of research is dedicated to developing more earth-abundant and cheap alternatives to precious metals. While nickel-based catalysts display generally lower performance to palladium due to a number of kinetics-related issues and poor availability of precatalysts,<sup>239</sup> coupling them with photocatalysts significantly speeds up their redox cycle by promoting the formation of active Ni(I) or Ni(0) species, which allows for compatible performance and the possibility to utilize Ni<sup>2+</sup> precatalysts.<sup>240</sup> There are a number of publications proving carbon nitriles to be photoredox auxiliaries to nickel complexes in C-C, C-N, C-S and C-O coupling reactions.<sup>179, 241, 242</sup> Therefore, we chose C-N cross-coupling between 4-bromobenzonitrile and pyrrolidine as our next model reaction to study the photocatalytic performance of the new materials. Again, K-PHI and CN-OA-m were selected as reference catalysts. The reaction was carried out either under green (530 nm) or red (625 nm)<sup>243</sup> LED irradiation to prevent metal catalyst losses as nickel black which is common under shorter wavelength light.<sup>240</sup> The results are shown in [Figure 4.8b](#). Under green light, the samples demonstrated compatible performance to the reference catalysts, albeit being slightly inferior under irradiation with red light. Similar to benzylamine oxidation, the tendency for 0.5 mol. % K<sub>2</sub>Rho sample to demonstrate higher yields is somewhat preserved. However, Rho-CN-0.5 is the less active catalyst of Rho-CN series under 625 nm despite having higher absorption at this wavelength than Rho-CN-0.25.

### *Hydrogen Peroxide Evolution (HPE)*

Hydrogen peroxide is a valuable and atom-efficient bulk oxidizer; however, the main method of its production relies on sequential cycle of reduction and autooxidation of



anthraquinones catalyzed by palladium.<sup>244</sup> The main drawbacks of this process are the necessity for large amounts of organic 'carrier' and hazardous hydrogen gas used in the reduction step, thus raising demand for cheap, safe and fast method for production. The extensive research on this topic includes electrochemical<sup>245</sup> and photocatalytic<sup>246, 247</sup> processes using cheap bulk chemicals as sacrificial donors. To test the ability of our materials to produce hydrogen, we carried out the reaction in 4:1 v/v mixture of water and methanol, which served as a sacrificial donor of electrons for the catalysts. The H<sub>2</sub>O<sub>2</sub> content was measured after 1 h of irradiation photometrically by formation of complex with titanium(IV) oxysulfate. K-PHI was used as a benchmark catalyst, providing 402  $\mu\text{mol}\cdot\text{g}^{-1}\cdot\text{h}^{-1}$  of hydrogen peroxide. The results are shown in [Figure 4.8c](#). As well as in organic transformation, the trend for 0.5% mol. K<sub>2</sub>Rho samples is observed in HPE reaction with Rho-CN-0.5 providing 313  $\mu\text{mol}\cdot\text{g}^{-1}\cdot\text{h}^{-1}$  of peroxide. Rho-CN-TC series demonstrates marginally worse performance. As it is reported that low pH increases photocatalytic peroxide production,<sup>248, 249</sup> and considering our highly anionic samples should provide plenty of local acidic sites after protonation, catalysts H-Rho-CNs and H-Rho-CN-TCs were prepared by treating the samples with 3 M HCl solution and then tested in the reaction as well. Indeed, despite noticeable discoloration of the catalysts, their activity increased more than twofold up to 681  $\mu\text{mol}\cdot\text{g}^{-1}\cdot\text{h}^{-1}$  in the case of H-Rho-CN-0.5.

### *Flow Photosheet Performance*

Previous experiments demonstrate that, among two series of catalysts, Rho-CN-0.5 possesses an optimal balance between performance and cost efficiency and thus is a more 'universal' catalyst than others. To demonstrate the scalability and recyclability of our catalysts, a 'photosheet' device<sup>250</sup> was assembled by blade-coating 50x50 mm area of a smooth glass panel with ca. 50-55  $\mu\text{m}$  thick layer of Rho-CN-0.5 ([Figure 4.8d](#)). The photosheet was then assembled into a 50x50x10 mm<sup>3</sup> flow cell with a transparent



window and studied for the benzylamine oxidation reaction (0.025 M in acetonitrile solution was used) under irradiation by an AM1.5G solar simulator to emulate outdoor conditions for possible scale-up applications. In 8 min residence time, the catalytic layer was able to provide  $44.7 \pm 1.8\%$  yield. To test the stability and reusability, the photosheet cell was irradiated over the course of 7 days (168 h) filled with oxygenated concentrated benzylamine solution in acetonitrile, and then tested in flow mode again using 0.025 M solution. The yield decreased to  $29.1 \pm 12.0\%$ , indicating a certain degree of catalyst degradation, which is confirmed visually by slight discoloration of the catalyst (see [Figure S4.1c](#) for comparison). The mechanical integrity of the catalytic layer remained unchanged even after multiple runs and cell washings, which demonstrates the potential for fabrication of large working surface devices.

### *Miscellaneous Reactions*

*Hydrogen Evolution:* According to previous results, we chose Rho-CN-0.5 as a model catalyst for hydrogen evolution reaction (HER), as well as its protonated version, H-Rho-CN-0.5. Both materials were used as is, in addition to the samples with pre-deposited nickel phosphide ( $\text{Ni}_2\text{P}$ ) and metallic platinum co-catalysts with ethylene glycol (EG) and triethanolamine (TEOA) being used as sacrificial electron donors in basic aqueous media (self-provided basicity in case of TEOA and KOH in case of EG); finally, in the last pair of samples platinum was photodeposited *in situ*. Reaction was performed under AM1.5G solar simulator. Unfortunately, only traces of hydrogen at the limit of device detection were observed in case of NiP co-catalyst present; some amount was also produced by samples with *in situ* photodeposition of platinum, which clearly comes from the deposition step itself. Both EG and TEOA are shown to be sufficient electron donors for the catalysts based on significant color change from shades of brown to deep green, which was observed previously for electron-proton pair storage of K-PHI carbon nitride.<sup>166</sup> The reason behind the low performance for HER may be due to insufficient



overpotential created by its conductive band, which is  $-0.21$  V vs. SHE (see CV data above), resulting in inability to provide the co-catalyst with enough energy for successful proton reduction to occur. Here, see Supporting Information for experimental details.

*Chromoselectivity:* Previously, our group discovered a reaction of *S*-arylthioacetates oxidation in the presence of aqueous HCl with K-PHI photocatalyst.<sup>80</sup> The selectivity of this reaction depends heavily on the light source used, providing corresponding aryl chlorides under 365 nm UV light, arylsulfonyl chlorides under 465 nm blue light, and diaryl disulfides under longer wavelengths ( $\geq 530$  nm), respectively. Considering the strong absorption  $> 450$  nm, we tested the performance of Rho-CN and Rho-CN-TC catalysts in the oxidation of *S*-acetylthiophenol under irradiation at 530 nm. Thus, under irradiation with green light, Rho-CN-0.5 gave diphenyl disulfide with  $> 95\%$  selectivity, while for K-PHI the selectivity toward this product was 68%. The main side product in both cases was *S*-phenyl benzenesulfonothioate.

Interestingly, upon irradiation of a reaction mixture containing Rho-CN-TC-1 at 465 nm the major product was *S*-phenyl benzenesulfonothioate (49% yield) while diphenyl disulfide was observed as a minor side product (7%). Considering nearly identical potentials of the bands edges for all catalysts of Rho-CN-TC series, this result points to unusual catalytic behavior where multi-step *S*-oxidation is seemingly more kinetically favorable than the single-electron formation of active chlorine species from HCl. This feature may be utilized further in photoredox reaction design to shift the selectivity of known processes towards desired multi-electron processes.

Combination of high-throughput synthesis with statistical analysis is a powerful approach to designing photocatalytically active materials. From the summary shown in [Table 4.3](#), it is clear that there is no single photocatalyst that performs equally well in



all processes. By applying statistical analysis to the whole dataset, we found the CB potential correlates weakly with the yield of cross-coupling product obtained under irradiation with red light (Table S4.3). On the other hand, the VB potential correlates weakly with the yield of cross-coupling product under irradiation with green light. Such results might be explained by the change of the mechanism from electron transfer under green light (driving force for the photoinduced electron transfer is the decisive factor) to energy transfer under red light (better spectral overlap between a sensitizer excited state and energy acceptor).<sup>243</sup> Fluorescence lifetime alone does not show strong correlation with any of the parameters, which is due to low fluorescence quantum efficiency – radiative relaxation of the excited state is not a dominant pathway for the recovery of the ground state. However, a stronger correlation exists between the product of the CB potential and the fluorescence lifetime and the yield of cross-coupling product under red light (Table S4.4). Nevertheless, in all cases, correlation coefficients are significantly lower than  $\pm 1$  suggesting the influence of other properties of the catalysts on their performance. These properties are, for example, the interface between PTI/Li<sup>+</sup>Cl<sup>-</sup> and K-PHI phases, which is difficult to quantify with a single value.

On the other hand, by considering datasets for Rho-CN and Rho-CN-TC separately, stronger correlations between materials properties and their performance in the selected reaction were found (Table S4.5-8). As seen from Table S4.5, yields of net-oxidative benzylamine transformation enabled by Rho-CN photocatalysts correlate with the VB potential and fluorescence lifetime. Similar correlation is noted between hydrogen peroxide production and fluorescence lifetime. Under green light, more negative CB potential values provide greater yields in dual photoredox/nickel C-N cross-coupling, which is likely due to facilitated Ni(II) to Ni(I) reduction.<sup>240</sup> On the other hand, more positive VB potential values correlate with the yields in dual photoredox/nickel C-N cross-coupling, which points at alternative mechanism involving oxidation of Ni(II) to



Ni(III). Overall, by tuning band position and PL lifetime by changing K<sub>2</sub>Rho/cyanamide ratio, desired performance in a selected process can be achieved.

Table 4.3. Summary of properties and photocatalytic activity of the materials

Catalyst	CB vs. SHE [V]	VB vs. SHE [V]	Fluorescence lifetime [ps]	Hydrogen peroxide evolution [ $\mu\text{mol}\cdot\text{g}^{-1}\cdot\text{h}^{-1}$ ] <sup>[a]</sup>	Benzylamine oxidation yield [%]	Cross-coupling yield [%] <sup>[b]</sup>
Rho-CN-0.25	-0.38	2.21	20.83 ± 0.75	144 (495)	60	85 (66)
Rho-CN-0.5	-0.35	2.22	26.22 ± 2.25	313 (681)	77	82 (48)
Rho-CN-1	-0.28	1.98	20.48 ± 1.67	176 (258)	54	60 (58)
Rho-CN-TC-0.25	-0.40	2.33	59.09 ± 30.25	169 (86)	65	80 (29)
Rho-CN-TC-0.5	-0.29	2.28	41.78 ± 9.77	131 (210)	>99	81 (58)
Rho-CN-TC-1	-0.51	1.97	29.63 ± 5.83	104 (73)	84	76 (38)

[a] – Values in parentheses indicate production for protonated catalyst; [b] – Yields are given for green LED, values in parentheses represent red LED yields.

#### 4.4. Conclusion

Using a multi-step approach, we synthesized a novel ionic Rho-CN carbon nitride materials with high absorption throughout the visible range and multi-phase structure based primarily on PTI/Li<sup>+</sup>Cl<sup>-</sup> with unique morphology. Due to the inexpensiveness and availability of reagents, as well as high yields of final materials and their comparable performance (Table S.4.9), Rho-CNs and Rho-CN-TCs were found to be cost-effective and potentially competitive to known PHI-based carbon nitride materials in lab scale and beyond, as demonstrated by the experiment using a Rho-CN-coated 50x50 mm photocatalytic sheet. The optimal fraction of potassium rhodizonate additive was evaluated to be 0.5 mol. %, as indicated by multiple photocatalytic reactions. Additional potassium thiocyanate rapid melt post-treatment of Rho-CN catalysts provided the Rho-



CN-TC series, which possesses even higher light absorption and thus enhanced performance in net-oxidative reactions. However, improvements in dual nickel catalysis were found to be negligible. These sets of experiments demonstrate the versatility and high tunability of cyanamide-rhodizonate platform to yield photocatalysts for desired applications.



## 5. Overall Conclusions and Outlooks

---

Considering a vast number of reports, solar photocatalysis is a highly desirable target for chemical industry as it would allow to greatly reduce the amount of energy to maintain the desired reaction. The amount of funding provided by the government institutions for solar fuels steadily increases annually, and the first pilot setups are slowly emerging. However, the most attractive targets for solar photocatalysis so far are hydrogen and products of carbon dioxide reduction. Considering numerous reactor designs made specifically for organic photocatalysis and growing amount of research projects implementing reactions carried out under real sunlight, there are good chances that we may see the first commercial setups for solar synthesis in the coming years. Therefore, the search for new sustainable heterogeneous catalysts and possible novel reactions that could not be carried out via conventional processes remains significant. (Chapter 1)

The research started with investigating a side reaction from oxidative [3+2] cycloaddition of aldoximes and nitriles mediated by K-PHI. Although conversion of oximes back to their respective aldehydes and ketones has limited synthetic application, it gave important photophysical insights regarding oxygen sensitization, side products formation, limiting factors that direct the reaction into this specific pathway and how chromoselectivity can affect yields and selectivity of transformations. (Chapter 2)

The next project on organic oxygenation is a great example of how oxygen sensitization may not be the limiting factor of the reaction, but instead, the pathway can be directed by the nature of the substrate. It was discovered that mpg-CN can be used to convert 1,3-oxazolidinones, a widely available heterocyclic motif, into far more valuable and obscure 1,3-oxazolidine-2,4-diones, molecules of great interest for medicinal and agricultural chemistry. Due to the high oxidation potentials of starting materials, this transformation is quite difficult to achieve without using harsh oxidants, but the unique feature of



heptazine basicity provides mpg-CN an ability to employ a PCET process, confirmed by TAS and DFT studies, which is a key advantage over the most commonly used molecular photocatalysts. The main limitations of this reaction are the steric factor of the catalyst and functional group intolerance induced by a relatively high energy light source, which leads to somewhat diminished yields and selectivity. (Chapter 3)

Finally, a new series of carbon nitrides was synthesized (Chapter 4). One of the main issues discovered previously was that while the reactions tend to be more selective under longer wavelength irradiation, carbon nitrides typically lack absorbance above 500-550 nm that is sufficiently strong to allow the desired processes proceed efficiently and within reasonable timespans. For instance, deoxygenation reaction of ketoximes proceeded way more cleanly under red light, but it took about 5 times longer to reach decent conversion rates (Chapter 2). In case of oxidation of oxazolidinones, white LED irradiation that is mostly composed of light below 500 nm, lead to oxidation of some functional groups (Chapter 3). To achieve good reactivity under green and red light, a strategy of doping the bulk CN precursor with an organic dye was utilized, producing the Rho-CN family of the catalysts. Despite consisting of mostly PTI with some amount of PHI phase, these catalysts performed on par with well-known PHI-based carbon nitrides, even under red light. In addition to their remarkable performance in several common reactions, including oxidation of amines, C-N dual nickel photoredox cross-coupling, oxidation of *S*-arylthioacetates, and hydrogen peroxide evolution, one of Rho-CN catalysts demonstrated good results as an active coating in a photocatalytic flow cell under simulated sunlight, demonstrating its feasibility for further scale-up in manufacturing of solar fuels.

Overall, it is safe to say that a significant effort was done to expand the scope of carbon nitrides utilization for diverse photocatalytic processes. This type of materials is still strongly associated with hydrogen evolution reaction and degradation of various kind of



pollutants, and a certain shift of researchers' focus towards production of bulk and fine chemicals may be proficient in discovering novel sustainable photocatalytic processes, bringing us even closer to full-fledged solar economy.



## 6. Acknowledgements

---

The work presented in this thesis is a result of collaborative effort of many researchers from different institutions across EU and the world. Author considers it necessary to honor their contribution here.

### *Chapter 1:*

Dr. Pau Farràs, Dr. Roberto González-Gómez, and Kathryn McCarthy from NUI Galway, Galway, Ireland – *providing data on funding and economical aspects of sunlight-driven photocatalysis.*

### *Chapter 3:*

Dr. Yajun Zou from Xi'an Jiaotong University, Xi'an, China – *initial screening and scale-up experiments;*

Prof. Nikolai Tkachenko and Jokotadeola Odutola from Tampere University, Tampere, Finland – *TAS spectroscopy studies;*

Prof. Núria López and Pavle Nikačević from Institut Català d'Investigació Química (ICIQ), Tarragona, Spain – *DFT calculations.*

### *Chapter 4:*

Prof. Erwin Reisner and Carolina Pulignani from the University of Cambridge, Cambridge, UK – *assistance with electrochemical studies, solar simulator setup and flow photosheet cell assembly, hosting during the secondment at UCAM;*

Dr. Josep Albero Sancho and Horațiu Szalad from Universitat Politècnica de València (UPV), Valencia, Spain – *provision and deconvolution of XPS and SNMR data;*

Dr. Nadezda Tarakina (MPIKG) – *TEM studies.*

Dr. Christian Mark Pelicano (MPIKG) – *assistance with TPR and EIS measurements.*



Additionally, author would like to thank the EU Commission for funding from the European Union's Horizon 2020 research and innovation programme under the Marie Skłodowska-Curie grant agreement No. 861151 Solar2Chem, Olaf Niemeyer (NMR facility of MPIKG), electric, glass blowing and mechanical workshop technicians of MPIKG. Lab technicians of Colloids Department, namely Katharina ten Brummelhuis, Jessica Brandt, Heike Runge, Tina Seemann and Ursula Lubahn, are acknowledged for their analytical work and general assistance with purchases, lab safety, maintenance, etc.



## 7. Appendix — Supplementary Information

---

### 7.1. SI for Chapter 1

**Table S1.1** Photochemistry (PC) and photoelectrochemistry (PEC) based projects funded by the European Commission since 2009 is available as the SI for the original paper at the following link free of charge:

[https://pubs.acs.org/doi/suppl/10.1021/acs.energyfuels.2c00178/suppl\\_file/ef2c00178\\_si\\_001.pdf](https://pubs.acs.org/doi/suppl/10.1021/acs.energyfuels.2c00178/suppl_file/ef2c00178_si_001.pdf)



## 7.2. SI for Chapter 2

### 7.2.1. Materials

#### *Chemicals*

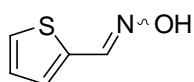
Acetonitrile ( $\geq 99.8\%$ ), ethanol (HPLC grade), toluene (99.8%), acetone (HPLC grade), tetrahydrofuran ( $\geq 99.9\%$ ), methanol (HPLC grade), *N,N*-dimethylformamide ( $\geq 99.8\%$ ), dichloromethane ( $\geq 99.9\%$ ), hexane (98%), ethyl acetate (HPLC grade), hydroxylamine hydrochloride ( $\geq 96\%$ ), *O*-benzyl hydroxylamine hydrochloride ( $\geq 98\%$ ), *O*-methyl hydroxylamine hydrochloride ( $\geq 97\%$ ), aqueous hydroxylamine (50% wt.), hydrogen chloride (37% wt.), sodium hydroxide ( $\geq 97\%$ ), sodium nitrite ( $\geq 98\%$ ), potassium carbonate ( $\geq 99\%$ ), ethyl iodide (98%), borane-dimethylsulfide (2M in THF), Lawesson's reagent (97%), sodium acetate (anhydrous,  $\geq 99\%$ ), 1*H*-pyrrole-2-carbaldehyde (98%), thiophene-2-carbaldehyde (98%), 2,6-dimethoxybenzaldehyde (99%), vanillin (98%), butanal ( $> 98\%$ ), acetophenone (99%), cyclohexanone (99.8%), 4-methylpentan-2-one (98%), 3-methylbutan-2-one (99%), 2,4-dimethylpentan-3-one (99%), 7-hydroxy-2*H*-chromen-2-one (99%), chloroform-*d* (99.8 atom % D), acetonitrile-*d*<sub>3</sub> (99.5 atom % D), dimethylsulfoxide-*d*<sub>6</sub> (99.5 atom % D) were purchased from the vendors and used without additional purification.

#### *Preparation of oximes*

##### *General synthetic procedure for preparation of (hetero)aromatic aldoximes*

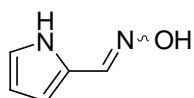
A mixture of corresponding (hetero)aromatic aldehyde (typically 20 mmol), hydroxylamine hydrochloride (1.2 equiv) and potassium carbonate (0.6 equiv) were refluxed in a 1:1 v/v ethanol-water mixture (0.6M) for 20 h. After cooling down in a freezer, the crystallized oxime was filtered off, washed with water and dried at 50 °C in vacuum.

##### *Thiophene-2-carbaldehyde oxime (1a)*



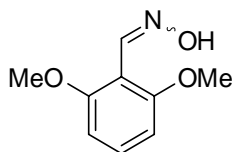
Yield 47%, fine white crystals. This is a known compound<sup>251</sup>. <sup>1</sup>H NMR (400 MHz, DMSO-*d*<sub>6</sub>) δ 11.88 (s, 1H), 7.85 (s, 1H), 7.73 (d, *J* = 5.1 Hz, 1H), 7.47 (dd, *J* = 3.7, 1.0 Hz, 1H), 7.13 (dd, *J* = 5.1, 3.7 Hz, 1H). <sup>13</sup>C NMR (101 MHz, DMSO-*d*<sub>6</sub>) δ 139.87, 131.17, 131.14, 131.11, 126.29.

*1H-pyrrole-2-carbaldehyde oxime (1b)*



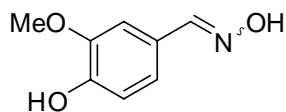
Yield 37%, white powder. This is a known compound<sup>252</sup>. <sup>1</sup>H NMR (400 MHz, DMSO-*d*<sub>6</sub>) δ 11.18 (s, 1H), 11.14 (s, 1H), 7.26 (s, 1H), 6.88 (q, *J* = 2.6 Hz, 1H), 6.55 (dt, *J* = 3.7, 2.2 Hz, 1H), 6.11 (q, *J* = 2.5 Hz, 1H). <sup>13</sup>C NMR (101 MHz, DMSO-*d*<sub>6</sub>) δ 137.26, 123.97, 121.06, 114.02, 108.51.

*2,6-dimethoxybenzaldehyde oxime (1c)*



Yield 89%, white powder. This is a known compound<sup>124</sup>. <sup>1</sup>H NMR (400 MHz, DMSO-*d*<sub>6</sub>) δ 11.07 (s, 1H), 8.17 (s, 1H), 7.30 (t, *J* = 8.4 Hz, 1H), 6.69 (d, *J* = 8.4 Hz, 2H), 3.77 (s, 6H). <sup>13</sup>C NMR (101 MHz, DMSO-*d*<sub>6</sub>) δ 158.25, 142.43, 130.54, 109.33, 104.24, 55.85.

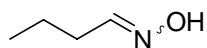
*4-hydroxy-3-methoxybenzaldehyde oxime (1e)*



Yield 76%, light tan crystals. This is a known compound<sup>251</sup>. <sup>1</sup>H NMR (400 MHz, DMSO-*d*<sub>6</sub>) δ 10.85 (s, 1H), 9.36 (s, 1H), 7.99 (s, 1H), 7.16 (d, *J* = 1.8 Hz, 1H), 6.97 (dd, *J* = 8.1, 1.8 Hz, 1H), 6.77 (d, *J* = 8.1 Hz, 1H), 3.77 (s, 3H). <sup>13</sup>C NMR (101 MHz, DMSO-*d*<sub>6</sub>) δ 148.06, 147.99, 147.81, 124.44, 120.50, 115.44, 109.10, 55.45.

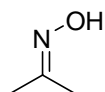
*Synthetic procedures for preparation of ketoximes and aliphatic aldoximes*



*Butyraldehyde oxime (1d)*

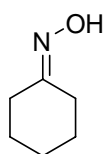
Butanal (420 mg, 5.8 mmol) was dissolved in 4 mL of ethanol, and aqueous hydroxylamine (50% wt, 0.44 mL, 1.15 equiv) was added producing a mild exotherm. The solution was allowed to stand overnight, then diluted with water and extracted with dichloromethane. The extract was dried over sodium sulfate and concentrated in vacuum to give a colorless oil. Yield 250 mg (49%).

This is a known compound<sup>253</sup>. <sup>1</sup>H NMR (400 MHz, CD<sub>3</sub>CN) δ 8.58 (s, 1H), 6.63 (t, *J* = 5.4 Hz, 1H), 2.26 (td, *J* = 7.5, 5.4 Hz, 2H), 1.47 (h, *J* = 7.4 Hz, 2H), 0.93 (t, *J* = 7.4 Hz, 3H). <sup>13</sup>C NMR (101 MHz, CD<sub>3</sub>CN) δ 152.67, 27.38, 20.18, 14.13.

*Acetone oxime (1f)*

A mixture of aqueous hydroxylamine (50% wt, 1.630 g, 24.7 mmol) and acetone (20 mL) was stirred at room temperature overnight. The solvent was evaporated and the product was obtained as colorless volatile crystals. Yield 1.268 g (50%).

This is a known compound<sup>254</sup>. <sup>1</sup>H NMR (400 MHz, CD<sub>3</sub>CN) δ 8.43 – 8.09 (m, 1H), 1.79 (d, *J* = 2.5 Hz, 6H). <sup>13</sup>C NMR (101 MHz, CD<sub>3</sub>CN) δ 155.09, 21.69, 14.55.

*Cyclohexanone oxime (1g)*

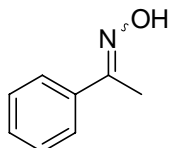
Aqueous hydroxylamine (50% wt, 2.200 g, 33.3 mmol) was diluted with 9 mL of water and heated up to 45 °C. Cyclohexanone (2.500 g, 25.5 mmol) was added and the mixture was stirred at the same temperature for 30 min. The crystals formed were filtered off,



dried on a pump and recrystallized from 3 mL of *n*-hexane. Yield 2.223 g (77%), colorless needles.

This is a known compound<sup>255</sup>. <sup>1</sup>H NMR (400 MHz, CD<sub>3</sub>CN) δ 8.10 – 8.03 (m, 1H), 2.47 – 2.35 (m, 2H), 2.13 (dd, *J* = 7.0, 5.2 Hz, 2H), 1.68 – 1.48 (m, 6H). <sup>13</sup>C NMR (101 MHz, CD<sub>3</sub>CN) δ 160.20, 32.66, 27.83, 26.53, 26.49, 24.70.

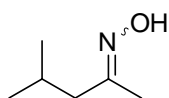
#### Acetophenone oxime (1h)



A mixture of acetophenone (1.200 g, 10 mmol), hydroxylamine hydrochloride (1.10 g, 16 mmol, 1.6 equiv) and anhydrous sodium acetate (1.640 g, 20 mmol, 2 equiv) were refluxed for 2 h in 10 mL of 80% aqueous ethanol. The solvent was evaporated and the residue was washed with water to give colorless crystals. Yield 0.780 g (58%).

This is a known compound<sup>255</sup>. <sup>1</sup>H NMR (400 MHz, DMSO-*d*<sub>6</sub>) δ 11.22 (s, 1H), 7.70 – 7.60 (m, 2H), 7.42 – 7.32 (m, 3H), 2.15 (s, 3H). <sup>13</sup>C NMR (101 MHz, DMSO-*d*<sub>6</sub>) δ 153.35, 137.43, 129.09, 128.84, 126.01, 12.06.

#### 4-methylpentan-2-one oxime (1j)



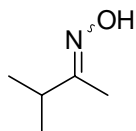
To 5 mL of 4-methylpentan-2-one was added 1.53 mL (1.65 g, 25 mmol) of 40% aqueous hydroxylamine and 2 mL of ethanol. The mixture was vigorously stirred overnight at room temperature, then concentrated under reduced pressure until no distillation was observed at 4 mbar. The crude product was let to stand under 0.05 mbar vacuum for 30 min to remove remaining ketone giving the oxime as a colorless oil. Yield 0.812 g (28%).

<sup>1</sup>H NMR (400 MHz, CD<sub>3</sub>CN) δ 8.46 – 7.97 (m, 1H), 2.20 (d, *J* = 7.5 Hz, 1H), 1.99 (d, *J* = 7.6 Hz, 1H), 1.92 – 1.82 (m, 1H), 1.77 (d, *J* = 5.6 Hz, 3H), 0.88 (dd, *J* = 10.2, 6.6 Hz, 6H). <sup>13</sup>C



NMR (101 MHz, CD<sub>3</sub>CN)  $\delta$  157.79, 157.64, 45.15, 37.62, 26.34, 26.31, 22.83, 22.51, 20.34, 13.16.

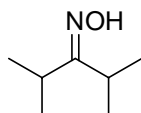
*3-methylbutan-2-one oxime (1k)*



The compound was prepared using the same procedure as for 1j. Colorless oil. Yield 0.758 g (30%).

<sup>1</sup>H NMR (400 MHz, CD<sub>3</sub>CN)  $\delta$  8.21 (s, 1H), 3.36 (hept,  $J$  = 7.0 Hz, 0.5H), 2.44 (hept,  $J$  = 6.9 Hz, 0.5H), 1.72 (d,  $J$  = 12.6 Hz, 3H), 1.01 (dd,  $J$  = 16.6, 7.0 Hz, 6H). <sup>13</sup>C NMR (101 MHz, CD<sub>3</sub>CN)  $\delta$  162.77, 162.29, 34.96, 26.23, 20.00, 18.99, 15.34, 10.71.

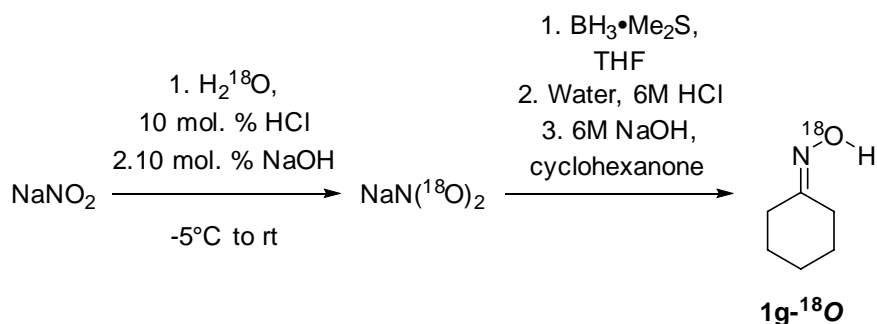
*2,4-dimethylpentan-3-one oxime (1l)*



The compound was prepared using the same procedure as for 1j. Colorless oil. Yield 0.101 g (3%).

<sup>1</sup>H NMR (400 MHz, CD<sub>3</sub>CN)  $\delta$  8.24 (s, 1H), 3.10 (hept,  $J$  = 7.1 Hz, 1H), 2.52 (hept,  $J$  = 6.8 Hz, 1H), 1.07 (dd,  $J$  = 20.6, 7.0 Hz, 12H). <sup>13</sup>C NMR (101 MHz, CD<sub>3</sub>CN)  $\delta$  168.61, 31.17, 27.93, 21.64, 19.02.

*Preparation of cyclohexanone oxime, <sup>18</sup>O-labelled*

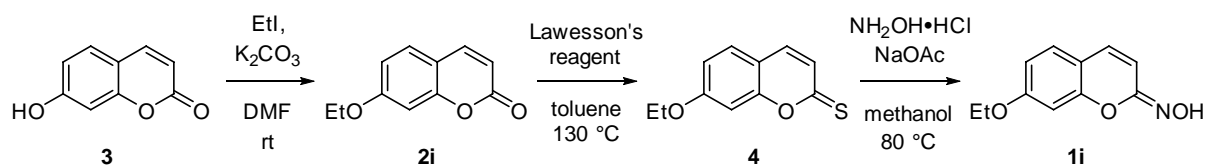


The compound was prepared using adapted procedures for labelled acetophenone oxime.<sup>256</sup>

Step 1. Sodium nitrite (850 mg, 12.3 mmol) was dissolved in water-<sup>18</sup>O (1 g, 97% oxygen-18 content) in a 5 mL screwcap vial with vigorous stirring. The vial was cooled on ethanol-ice bath to -5 °C, purged with nitrogen and 12M HCl (83 µL, 1 mmol, 0.08 equiv) was slowly added dropwise to avoid excessive NO<sub>x</sub> formation. The vial was then sealed tightly and allowed to stir at room temperature for 2 days. After the exchange completion, the mixture was cooled to -5 °C and neutralized with NaOH (40 mg, 1 mmol, 0.08 equiv). The solution was then evaporated to dryness to yield crude <sup>18</sup>O-enriched sodium nitrite (941 mg, 105% yield) which was used directly in the next step without further purification.

Step 2. Sodium nitrite-<sup>18</sup>O (941 mg, crude) was dissolved in 8 mL of THF in a 50 mL round-bottom flask with sonication and thus formed cloudy solution was purged with nitrogen for 10 min and stoppered with a septum. The flask was then cooled in ethanol-ice bath to -5 °C and borane dimethylsulfide complex (2M in THF, 13.8 mL, 28.3 mmol, 2.3 eq) was then slowly syringed through the septum. The reaction mixture was allowed to stir overnight at room temperature, cooled again to -5 °C and then consequently quenched dropwise with water (5.3 mL) and 6M HCl (5.3 mL) with the septum removed. After stirring at room temperature for 15 min, 6M NaOH (5.3 mL) and cyclohexanone (1.24 mL, 12.3 mmol, 1 equiv) were added consequently. The flask was plugged with a greased glass stopper, clipped tightly and stirred on an oil bath at 70 °C for 5 h. The reaction mixture was then partitioned between ethyl acetate (20 mL) and water (20 mL), the organic layer was separated in a funnel and the aqueous layer was extracted with additional ethyl acetate (10 mL). Combined organic phases were washed with 20 mL of brine, dried over magnesium sulfate and evaporated under vacuum to yield a thick colorless oil which was crystallized in 1 mL of *n*-hexane in a freezer overnight. The precipitate formed was filtered off and washed with additional 1 mL of cold *n*-hexane. White granules (420 mg, 30% yield). The product 1g-<sup>18</sup>O was analyzed using GC-MS to determine isotope ratio (64% oxygen-18 content) (see GC-MS data).



Preparation of 7-ethoxy-2*H*-chromen-2-one oxime

The compound was prepared using adapted procedures.<sup>128, 257</sup>

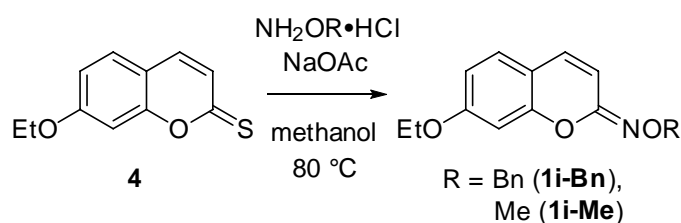
Step 1. A mixture 7-hydroxy-2*H*-chromen-2-one **3** (243 mg, 1.5 mmol), ethyl iodide (181  $\mu$ L, 2.25 mmol, 1.5 equiv) and  $K_2CO_3$  in 3 mL of DMF was stirred at room temperature for 72 h in a stoppered flask. The product was precipitated with 2 mL of brine and extracted with ethylacetate (2x10 mL). Combined organic phases were washed with 5 mL of brine, dried with sodium sulfate and then evaporated to dryness to yield 7-ethoxy-2*H*-chromen-2-one **2i** as a light brown solid (282 mg, 99% yield).  $^1H$  NMR (400 MHz,  $CDCl_3$ )  $\delta$  7.63 (d,  $J$  = 9.4 Hz, 1H), 7.36 (d,  $J$  = 8.5 Hz, 1H), 6.83 (dd,  $J$  = 8.6, 2.4 Hz, 1H), 6.81 – 6.78 (m, 1H), 6.24 (dd,  $J$  = 9.5, 1.0 Hz, 1H), 4.09 (q,  $J$  = 7.0 Hz, 1H), 1.45 (t,  $J$  = 7.0 Hz, 3H).  $^{13}C$  NMR (101 MHz,  $CDCl_3$ )  $\delta$  162.34, 161.47, 156.03, 143.63, 128.86, 113.11, 112.51, 101.38, 77.36, 64.30, 14.70.

Step 2. A mixture of 7-ethoxy-2*H*-chromen-2-one **2i** (0.650 g, 3.4 mmol) and Lawesson's reagent (1.520 g, 3.8 mmol, 1.1 equiv) were suspended in 20 mL of toluene in a 100 mL round-bottom flask. The flask was tightly stoppered and clipped, then placed on an oil bath to stir overnight at 130 °C. After the reaction was completed, the mixture was cooled on an ice bath for 30 min and filtered off. The filtrate was evaporated to dryness, purified via column chromatography (gradient of hexane - ethyl acetate 80:20 to 75:25) and then the compound was additionally recrystallized from 2 mL of toluene to yield 7-ethoxy-2*H*-chromen-2-thione **4** (0.547 g, 78%) as fine yellow needles.  $^1H$  NMR (400 MHz,  $CDCl_3$ )  $\delta$  7.40 (dd,  $J$  = 9.0, 6.0 Hz, 2H), 7.11 (d,  $J$  = 9.2 Hz, 1H), 6.96 (d,  $J$  = 2.4 Hz, 1H), 6.89 (dd,  $J$  = 8.7, 2.4 Hz, 1H), 4.10 (q,  $J$  = 7.0 Hz, 2H), 1.47 (t,  $J$  = 7.0 Hz, 3H).  $^{13}C$  NMR (101 MHz,  $CDCl_3$ )  $\delta$  198.05, 162.84, 158.70, 135.34, 128.80, 126.80, 114.93, 114.38, 100.90, 77.36, 64.51, 14.65.



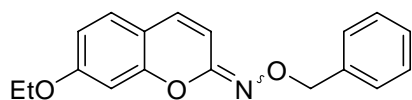
Step 3. A mixture of 7-ethoxy-2*H*-chromen-2-thione **4** (540 mg, 2.6 mmol), hydroxylamine hydrochloride (360 mg, 5.2 mmol, 2 equiv) and anhydrous sodium acetate (435 mg, 5.2 mmol, 2 equiv) was stirred in 30 mL of methanol in a tightly stoppered flask at 80 °C overnight. The reaction mixture was evaporated to dryness, the residue was washed with water, filtered off and dried to yield 7-ethoxy-2*H*-chromen-2-one oxime **1i** (469 mg, 87%) as a pale yellow fine powder which is sufficiently pure by <sup>1</sup>H NMR data for further reactions. <sup>1</sup>H NMR (400 MHz, DMSO-*d*<sub>6</sub>) δ 10.23 (s, 1H), 7.30 – 7.20 (m, 1H), 6.94 (d, *J* = 9.8 Hz, 1H), 6.70 (d, *J* = 1.7 Hz, 1H), 6.68 (d, *J* = 2.4 Hz, 1H), 6.14 (d, *J* = 9.8 Hz, 1H), 4.06 (q, *J* = 7.0 Hz, 2H), 1.32 (t, *J* = 7.0 Hz, 3H). <sup>13</sup>C NMR (101 MHz, DMSO-*d*<sub>6</sub>) δ 160.07, 153.46, 149.00, 128.80, 128.23, 114.40, 113.19, 110.62, 101.24, 63.64, 14.55.

#### Preparation of *O*-alkyl derivatives of 7-ethoxy-2*H*-chromen-2-one oxime



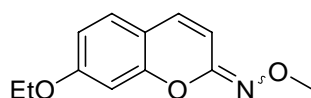
Compounds were prepared similarly to a parent 7-ethoxy-2*H*-chromen-2-one oxime **1i** (section 1.2.4, step 3) from 7-ethoxy-2*H*-chromen-2-thione **4** and corresponding *O*-alkyl hydroxylamine hydrochloride on a 0.73 mmol scale.

#### 7-ethoxy-2*H*-chromen-2-one *O*-benzyl oxime (**1i-Bn**)



Yield 83%, yellow solid. <sup>1</sup>H NMR (400 MHz, CDCl<sub>3</sub>) δ 7.45 (d, *J* = 7.1 Hz, 2H), 7.41 – 7.27 (m, 3H), 7.07 (d, *J* = 8.5 Hz, 1H), 6.80 (d, *J* = 9.8 Hz, 1H), 6.76 (d, *J* = 2.4 Hz, 1H), 6.64 (dd, *J* = 8.5, 2.4 Hz, 1H), 6.11 (d, *J* = 9.7 Hz, 1H), 5.14 (s, 2H), 4.02 (q, *J* = 7.0 Hz, 2H), 1.41 (t, *J* = 7.0 Hz, 3H). <sup>13</sup>C NMR (101 MHz, CDCl<sub>3</sub>) δ 160.80, 153.91, 150.72, 137.94, 130.34, 128.50, 128.33, 127.99, 127.93, 113.27, 111.74, 101.56, 77.36, 76.67, 64.06, 14.80.



*7-ethoxy-2H-chromen-2-one O-methyl oxime (1i-Me)*

Yield 88%, yellow solid.  $^1\text{H}$  NMR (400 MHz,  $\text{CDCl}_3$ )  $\delta$  7.09 (d,  $J = 8.6$  Hz, 1H), 6.84 (d,  $J = 9.7$  Hz, 1H), 6.76 (d,  $J = 2.4$  Hz, 1H), 6.65 (dd,  $J = 8.4, 2.4$  Hz, 1H), 6.14 (d,  $J = 9.9$  Hz, 1H), 4.02 (q,  $J = 7.0$  Hz, 2H), 3.94 (s, 3H), 1.41 (t,  $J = 7.0$  Hz, 3H).  $^{13}\text{C}$  NMR (101 MHz,  $\text{CDCl}_3$ )  $\delta$  160.89, 153.80, 150.48, 130.59, 128.02, 113.27, 113.22, 111.85, 101.46, 77.36, 64.07, 62.86, 14.80.

*Preparation of K-PHI photocatalyst*

Potassium poly(heptazine imide) was prepared according to a described procedure.<sup>124</sup> The catalyst was additionally ball-milled for 5 min after drying. Final K-PHI product is a free-flowing brownish-yellow powder.



## 7.2.2. Light sources

In this work, the following light sources were used: blue LED module with regulated irradiance (declared input electric power 50 W, emission maximum  $\lambda = 461$  nm, measured irradiance  $88 \text{ mW}\cdot\text{cm}^{-2}$ ); red LED module (declared input electric power 50 W, emission maximum  $\lambda = 625$  nm, measured irradiance  $30 \text{ mW}\cdot\text{cm}^{-2}$ ); green LED (declared input electric power 50 W, emission maximum  $\lambda = 525$  nm, measured irradiance  $38 \text{ mW}\cdot\text{cm}^{-2}$ ). Irradiance of the LED modules was measured using PM400 Optical Power and Energy Meter equipped with the integrating sphere S142C and purchased from Thorlabs; emission spectra were recorded with Avantes AvaSpec-ULS2048CL-EVO-RS optic fiber spectrometer (Figure S2.1).

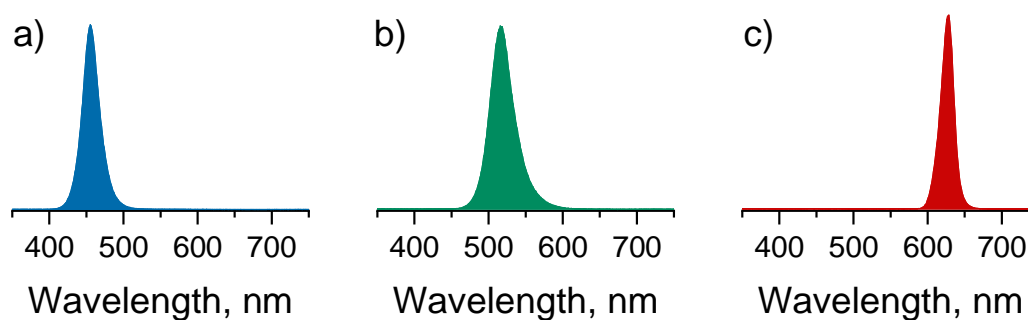


Figure S2.1. Emission spectra of LEDs used in experiments. a) Blue LED b) Green LED c) Red LED

### 7.2.3. Supplementary Methods

#### *NMR*

$^1\text{H}$  and  $^{13}\text{C}$  NMR spectra were recorded on Bruker Ascend 400 MHz (at 400 MHz for Protons and 101 MHz for Carbon-13). Chemical shifts are reported in ppm versus solvent residual peak:  $\text{CDCl}_3$  7.26 ppm ( $^1\text{H}$  NMR), 77.16 ppm ( $^{13}\text{C}$  NMR);  $\text{DMSO-}d_6$  2.50 ppm ( $^1\text{H}$  NMR), 39.52 ppm ( $^{13}\text{C}$  NMR);  $\text{CD}_3\text{CN}$  1.94 ppm ( $^1\text{H}$  NMR), 1.32 ppm, 118.26 ppm ( $^{13}\text{C}$  NMR).

#### *GC-MS*

Agilent 6890 Network GC System coupled with Agilent 5975 Inert Mass Selective detector (electron ionization) were used for reaction mixture composition analysis and to obtain mass spectra of the products.

#### *UV-Vis-NIR measurements*

Absorption spectra were recorded on Shimadzu UV 2600 double-beam spectrometer with interchangeable cuvette and integrating sphere modules for liquid and solid samples, respectively.

#### *Fluorescence measurements*

Monitoring of flow experiments and steady-state fluorescence quenching measurements were done on Jasco FP-8300 fluorescence spectrometer with a xenon lamp light source. The device settings for each experiment are listed in the corresponding sections below.

#### *TCSPC TRES measurements*

Time-resolved fluorescence and phosphorescence experiments were performed on PicoQuant FluoTime 250 fluorescence spectrometer equipped with PicoQuant PDL 820 picosecond diode laser controller; laser source with  $\lambda_{\text{max}} = 375$  nm was used. The device settings for each experiment are listed in the corresponding sections below.



## 7.2.4. Photocatalytic Experiments

### *Photooxidation Experimental Procedures*

Method A (general procedure). In a 5 mL screwcap glass tube with a magnetic stirbar were placed 50  $\mu\text{mol}$  of oxime, 5 mg of K-PHI and 2 mL of acetonitrile. The tube was stoppered with a rubber septum which was pierced with a needle attached to an oxygen-filled balloon. The reaction setup was placed on a magnetic stirrer in front of blue ( $\lambda_{\text{max}} = 461 \text{ nm}$ ) or red ( $\lambda_{\text{max}} = 625 \text{ nm}$ ) LED at 8 cm distance; the irradiance of blue LED was dimmed to match the one of the red LED ( $20 \text{ mW}\cdot\text{cm}^{-2}$  at 8 cm). The reaction mixture was irradiated at room temperature for 24 h with vigorous stirring of 800 rpm and then centrifuged at 13000 rpm for 3 min to separate the catalyst. After decanting, the solvent was removed under vacuum (150 mbar, 45 °C rotary evaporator bath temperature). The residue was mixed with 100  $\mu\text{L}$  of 1,3,5-trimethoxybenzene 0.1M DMSO- $d_6$  solution (10  $\mu\text{mol}$  of internal standard) and transferred to an NMR tube with additional DMSO- $d_6$  rinsing (0.6 mL of solvent is used for washings in total). Conversion and yield were then calculated based on qNMR data.

Method B (for volatile substrates and products). In a 5 mL screwcap glass tube with a magnetic stirbar were placed 50  $\mu\text{mol}$  of oxime, 5 mg of K-PHI and 2 mL of  $\text{CD}_3\text{CN}$ . The tube was stoppered with a rubber septum which was pierced with a needle attached to an oxygen-filled balloon. The reaction setup was placed on a magnetic stirrer in front of blue ( $\lambda_{\text{max}} = 461 \text{ nm}$ ) or red ( $\lambda_{\text{max}} = 625 \text{ nm}$ ) LED at 8 cm distance; the irradiance of blue LED was dimmed to match the one of the red LED ( $20 \text{ mW}\cdot\text{cm}^{-2}$  at 8 cm). The reaction mixture was irradiated at room temperature for 24 h with vigorous stirring of 800 rpm and then centrifuged at 13000 rpm for 3 min to separate the catalyst. The aliquot of 500  $\mu\text{L}$  was transferred to a NMR tube along with 100  $\mu\text{L}$  of 1,3,5-trimethoxybenzene 0.1M  $\text{CD}_3\text{CN}$  solution (10  $\mu\text{mol}$  of internal standard). Conversion and yield were then calculated based on qNMR data with respect to aliquoting factor of 4. This method was used for compounds 1d, 1f, 1g and 1g- $^{18}\text{O}$ .



Method C (control experiment). In a 5 mL screwcap glass tube with a magnetic stirbar were placed 50  $\mu\text{mol}$  of oxime and 2 mL of acetonitrile or  $\text{CD}_3\text{CN}$  depending on starting oxime. The tube was stoppered with a rubber septum which was pierced with a needle attached to an oxygen-filled balloon. The reaction setup was placed on a magnetic stirrer in front of blue ( $\lambda_{\text{max}} = 461 \text{ nm}$ ) LED at 8 cm distance; the irradiance was dimmed to 20  $\text{mW}\cdot\text{cm}^{-2}$  at 8 cm. The reaction mixture was irradiated at room temperature for 24 h with vigorous stirring of 800 rpm and then worked up without centrifugation as described in method A or B with respect to the substrate. Conversion and yield were then calculated based on qNMR data.

Method D (prolonged time experiment). The reaction was carried out with red LED as described in method A or B depending on the substrate, except the reaction time was 120 h.

#### *Quantitative NMR data for oxidation experiments*

Yields and conversions were calculated using the following formulas:

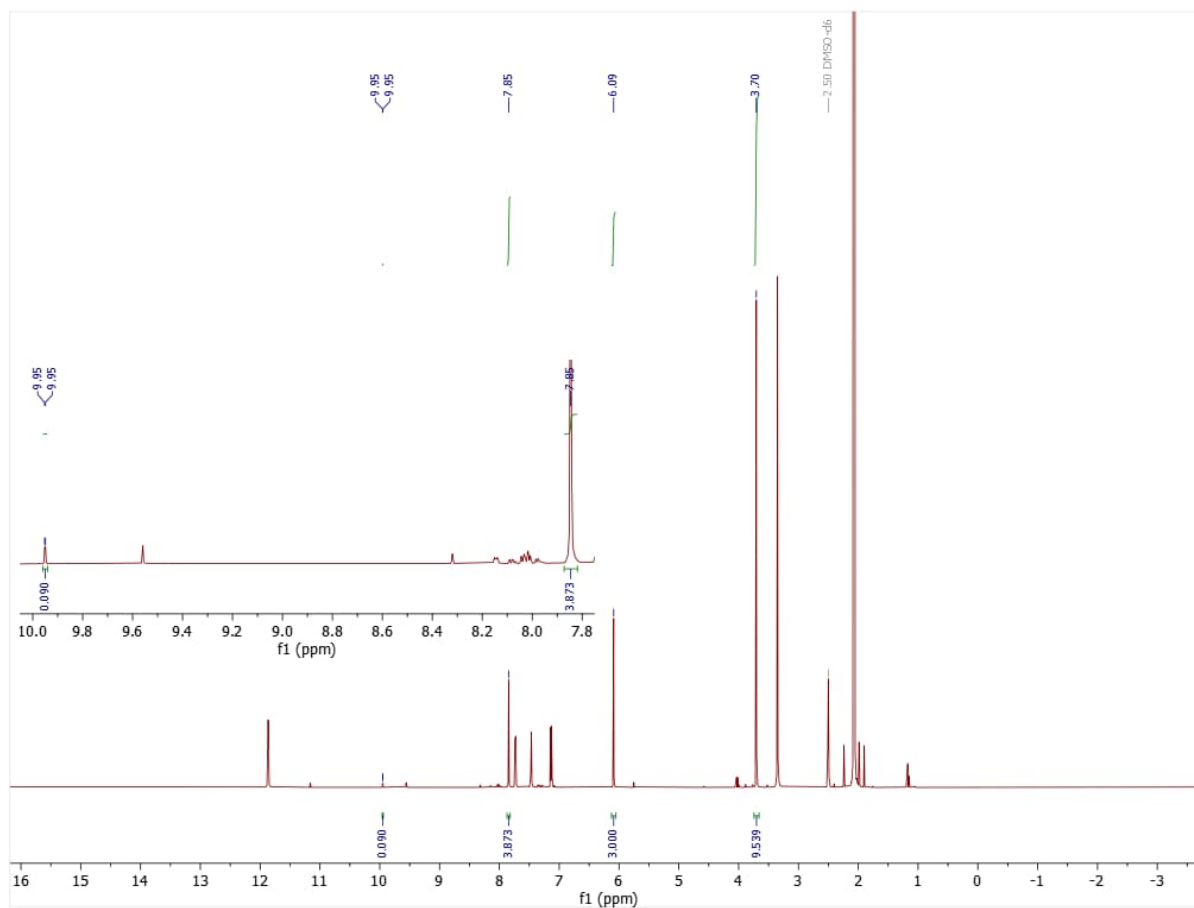
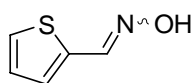
$$Y = \frac{I_{\text{carb}} \cdot N_{\text{St}} \cdot n_{\text{St}}}{I_{\text{St}} \cdot N_{\text{carb}} \cdot n_{\text{Ox}}} \cdot AF \cdot 100\%$$

$$X = \left(1 - \frac{I_{\text{Ox}} \cdot N_{\text{St}} \cdot n_{\text{St}}}{I_{\text{St}} \cdot N_{\text{Ox}} \cdot n_{\text{Ox}}}\right) \cdot AF \cdot 100\%$$

Where  $Y$  is yield,  $X$  is conversion,  $I_{\text{carb}}$  is integral intensity of a carbonyl product signal,  $N_{\text{carb}}$  is number of protons corresponding to a carbonyl product signal,  $I_{\text{St}}$  is integral intensity of internal 1,3,5-trimethoxybenzene standard (aromatic protons, 3.000),  $N_{\text{St}}$  is number of protons corresponding to the 1,3,5-trimethoxybenzene standard signal (aromatic protons, 3),  $n_{\text{Ox}}$  is amount of starting oxime taken into reaction (50  $\mu\text{mol}$ ),  $n_{\text{St}}$  is amount of 1,3,5-trimethoxybenzene standard (10  $\mu\text{mol}$ ),  $I_{\text{Ox}}$  is integral intensity of a starting oxime signal,  $N_{\text{Ox}}$  is number of protons corresponding to a starting oxime signal,  $AF$  is aliquoting factor (1 is for  $\text{DMSO}-d_6$ , 4 is for  $\text{CD}_3\text{CN}$  samples).



## Thiophene-2-carbaldehyde oxime (1a) oxidation, red LED, 24 h

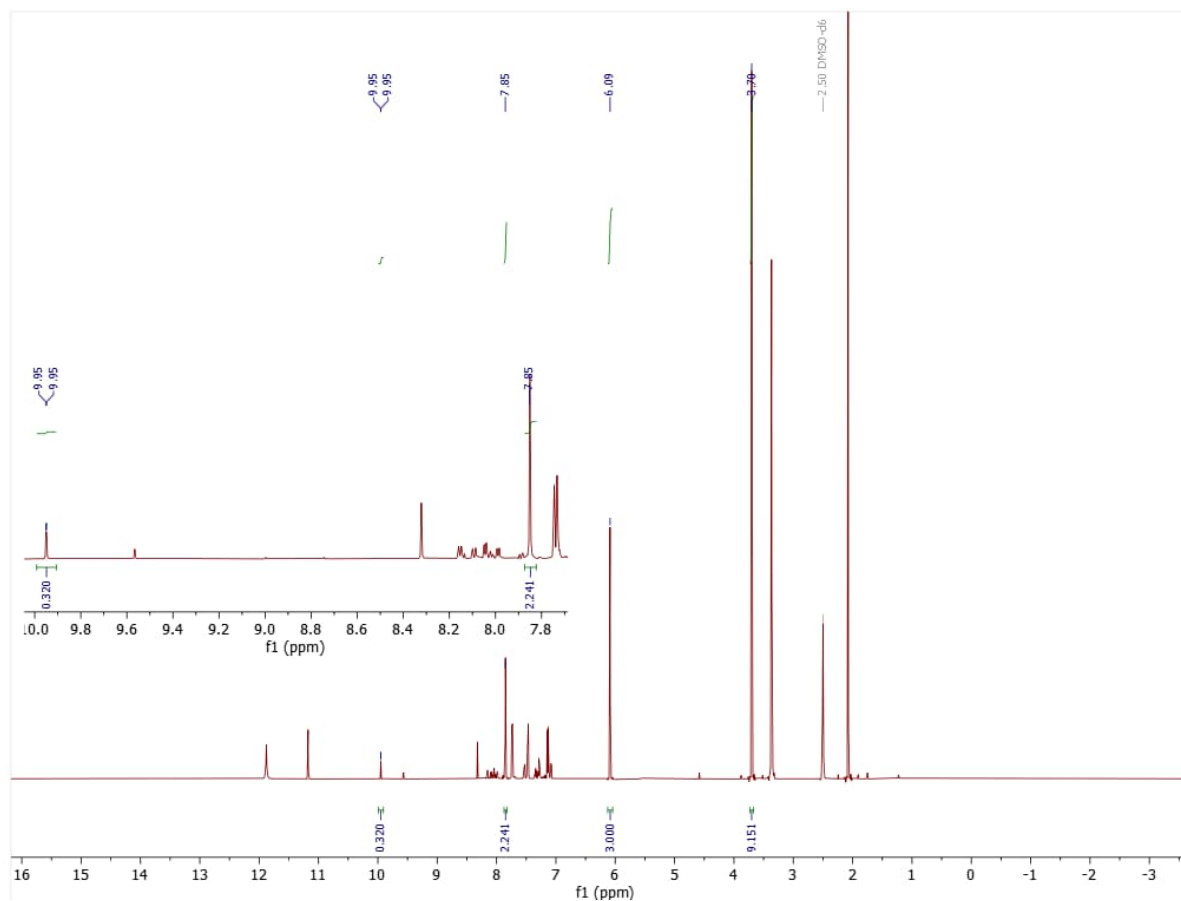
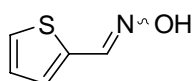


$$Y = \frac{0.090 \cdot 3 \cdot 10}{3.000 \cdot 1 \cdot 50} \cdot 1 \cdot 100\% = 2\%$$

$$X = \left(1 - \frac{3.873 \cdot 3 \cdot 10}{3.000 \cdot 1 \cdot 50}\right) \cdot 1 \cdot 100\% = 23\%$$



## Thiophene-2-carbaldehyde oxime (1a) oxidation, red LED, 120 h

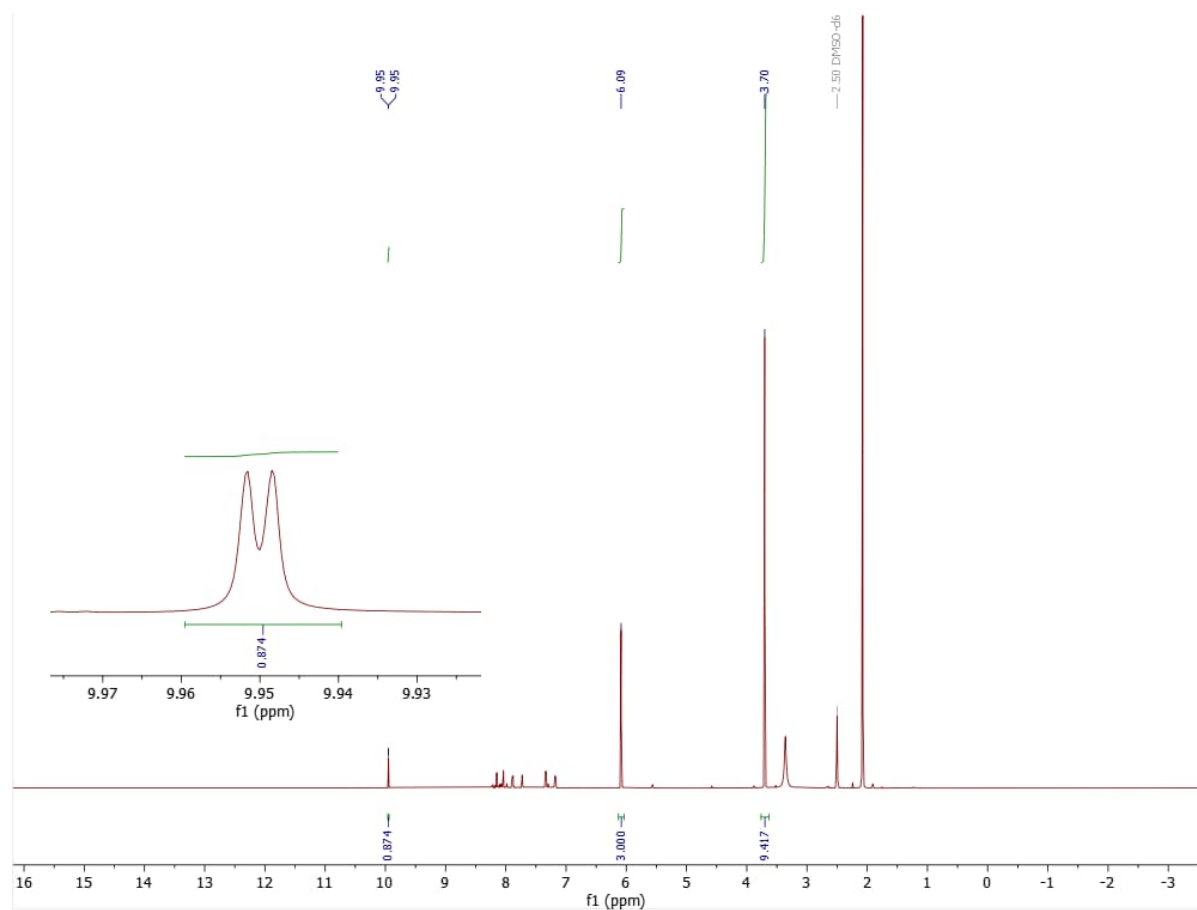
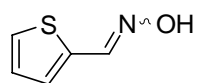


$$Y = \frac{0.320 \cdot 3 \cdot 10}{3.000 \cdot 1 \cdot 50} \cdot 1 \cdot 100\% = 6\%$$

$$X = \left(1 - \frac{2.241 \cdot 3 \cdot 10}{3.000 \cdot 1 \cdot 50}\right) \cdot 1 \cdot 100\% = 55\%$$



## Thiophene-2-carbaldehyde oxime (1a) oxidation, blue LED, 24 h, with K-PHI

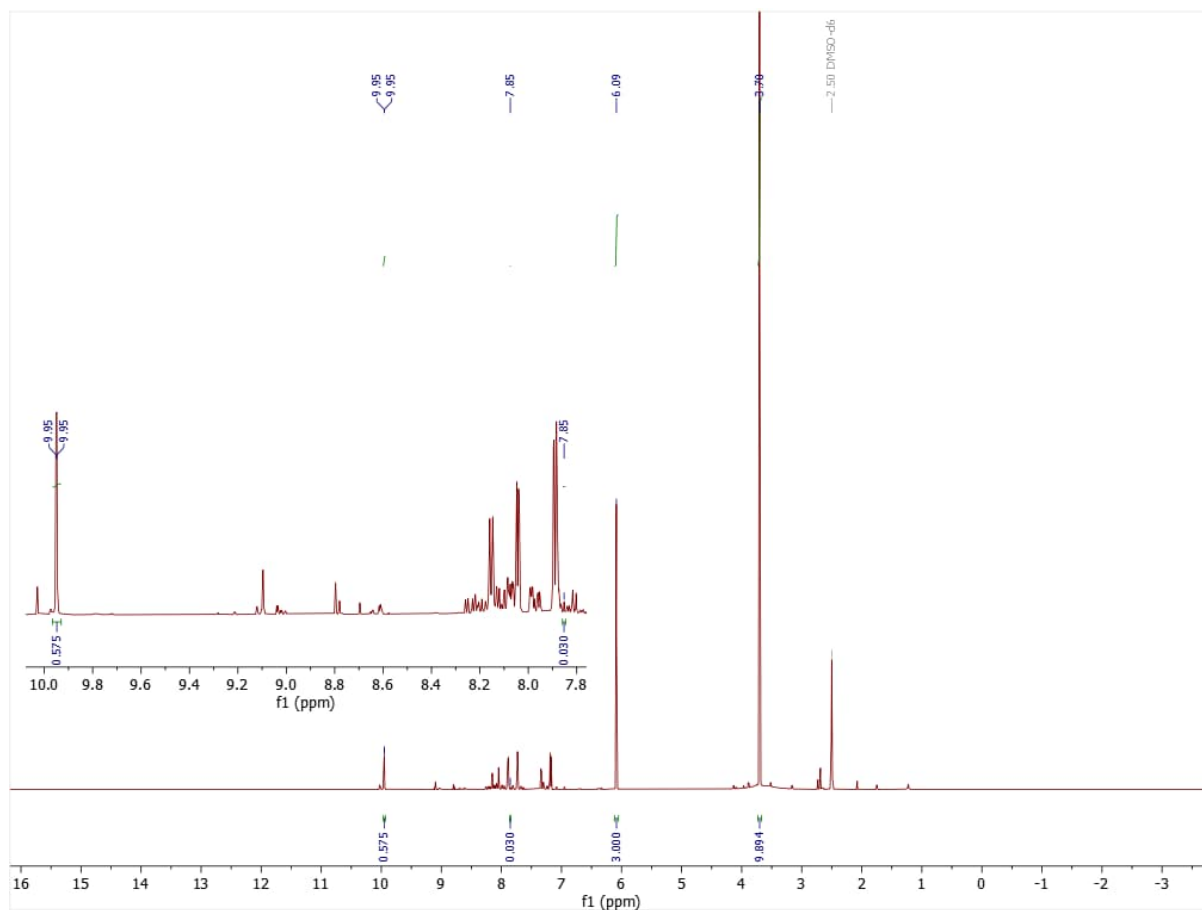
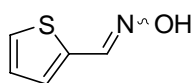


$$Y = \frac{0.874 \cdot 3 \cdot 10}{3.000 \cdot 1 \cdot 50} \cdot 1 \cdot 100\% = 17\%$$

$$X = \left(1 - \frac{0 \cdot 3 \cdot 10}{3.000 \cdot 1 \cdot 50}\right) \cdot 1 \cdot 100\% = 100\%$$



## Thiophene-2-carbaldehyde oxime (1a) oxidation, blue LED, 24 h, without K-PHI

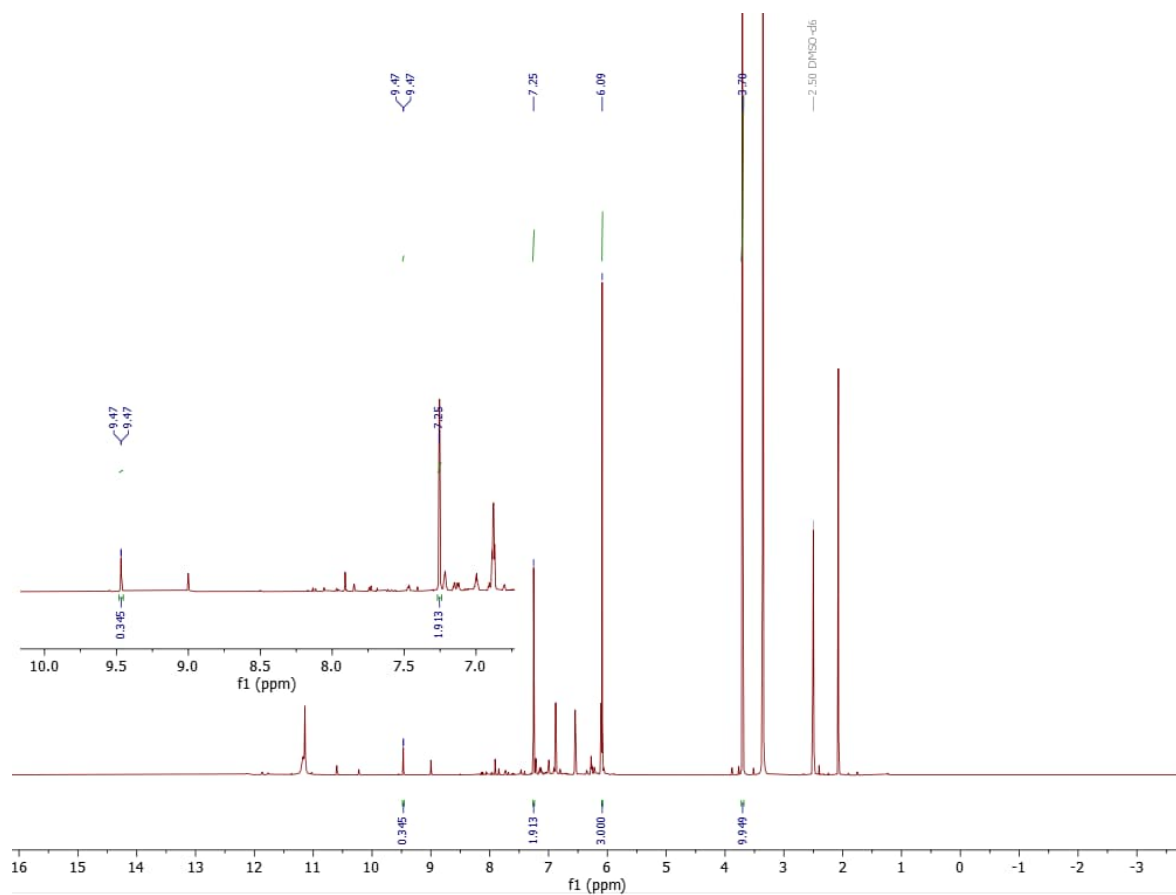
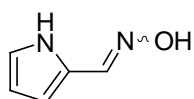


$$Y = \frac{0.575 \cdot 3 \cdot 10}{3.000 \cdot 1 \cdot 50} \cdot 1 \cdot 100\% = 12\%$$

$$X = \left(1 - \frac{0.030 \cdot 3 \cdot 10}{3.000 \cdot 1 \cdot 50}\right) \cdot 1 \cdot 100\% = 99\%$$



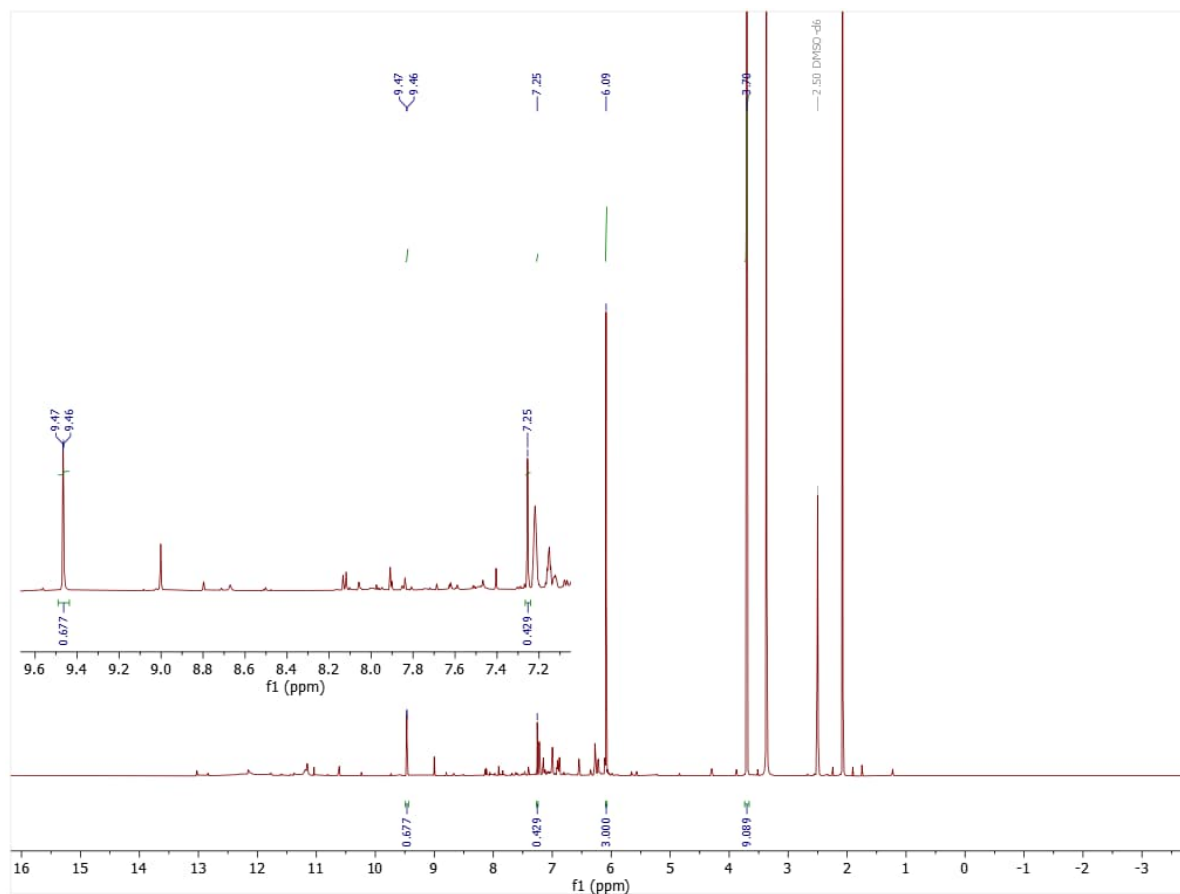
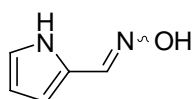
## 1H-pyrrole-2-carbaldehyde oxime (1b) oxidation, red LED, 24 h



$$Y = \frac{0.345 \cdot 3 \cdot 10}{3.000 \cdot 1 \cdot 50} \cdot 1 \cdot 100\% = 7\%$$

$$X = \left(1 - \frac{1.913 \cdot 3 \cdot 10}{3.000 \cdot 1 \cdot 50}\right) \cdot 1 \cdot 100\% = 62\%$$

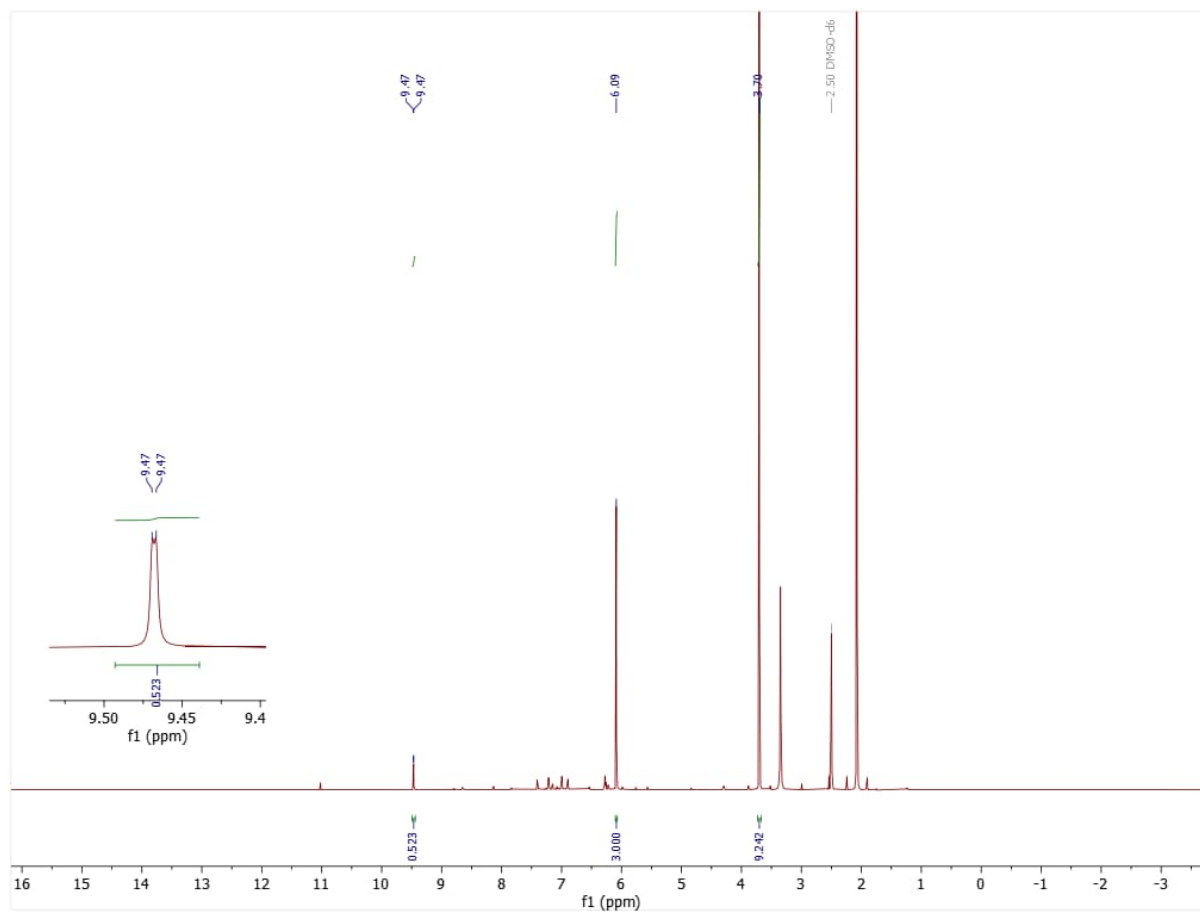
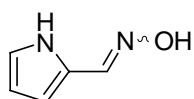


1*H*-pyrrole-2-carbaldehyde oxime (1*b*) oxidation, red LED, 120 h

$$Y = \frac{0.677 \cdot 3 \cdot 10}{3.000 \cdot 1 \cdot 50} \cdot 1 \cdot 100\% = 14\%$$

$$X = \left(1 - \frac{0.429 \cdot 3 \cdot 10}{3.000 \cdot 1 \cdot 50}\right) \cdot 1 \cdot 100\% = 91\%$$



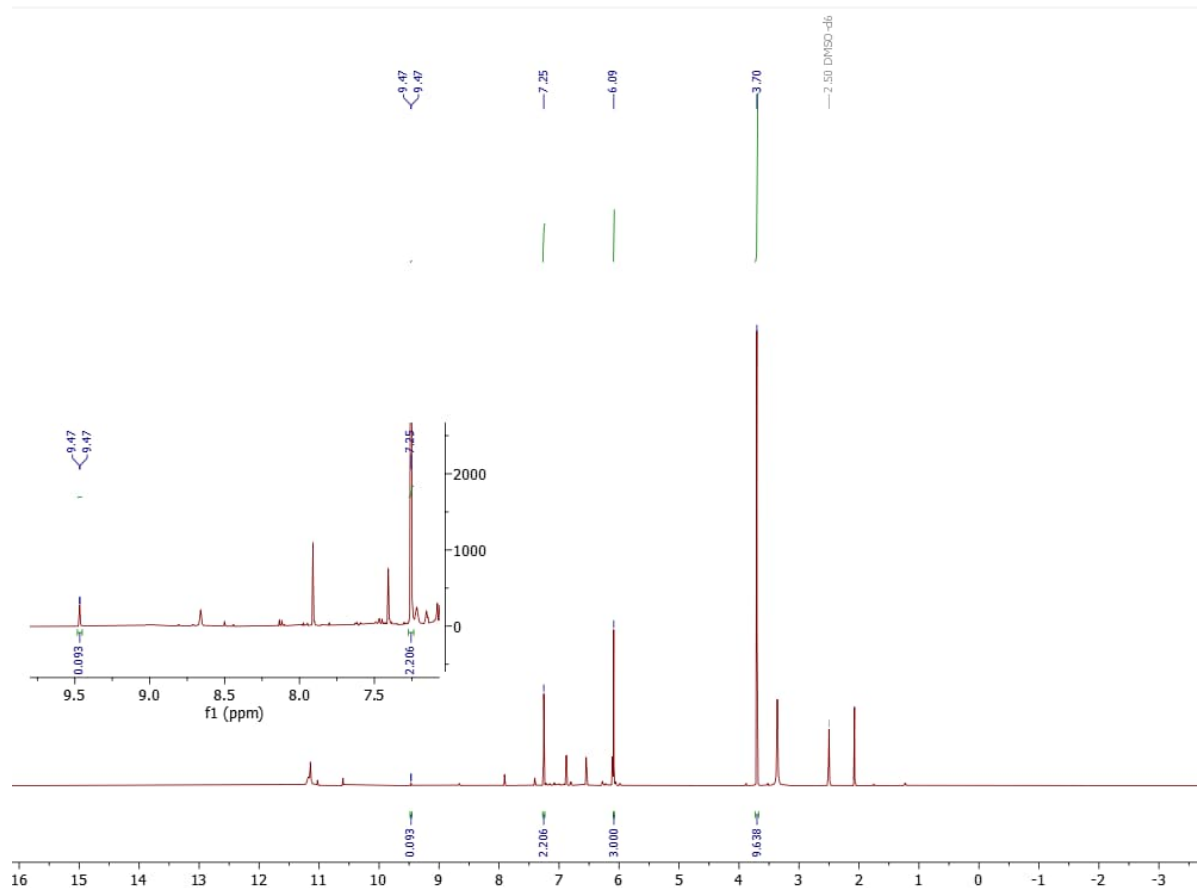
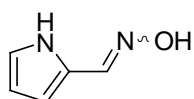
1*H*-pyrrole-2-carbaldehyde oxime (1*b*) oxidation, blue LED, 24 h, with K-PHI

$$Y = \frac{0.523 \cdot 3 \cdot 10}{3.000 \cdot 1 \cdot 50} \cdot 1 \cdot 100\% = 10\%$$

$$X = \left(1 - \frac{0 \cdot 3 \cdot 10}{3.000 \cdot 1 \cdot 50}\right) \cdot 1 \cdot 100\% = 100\%$$



## 1H-pyrrole-2-carbaldehyde oxime (1a) oxidation, blue LED, 24 h, without K-PHI

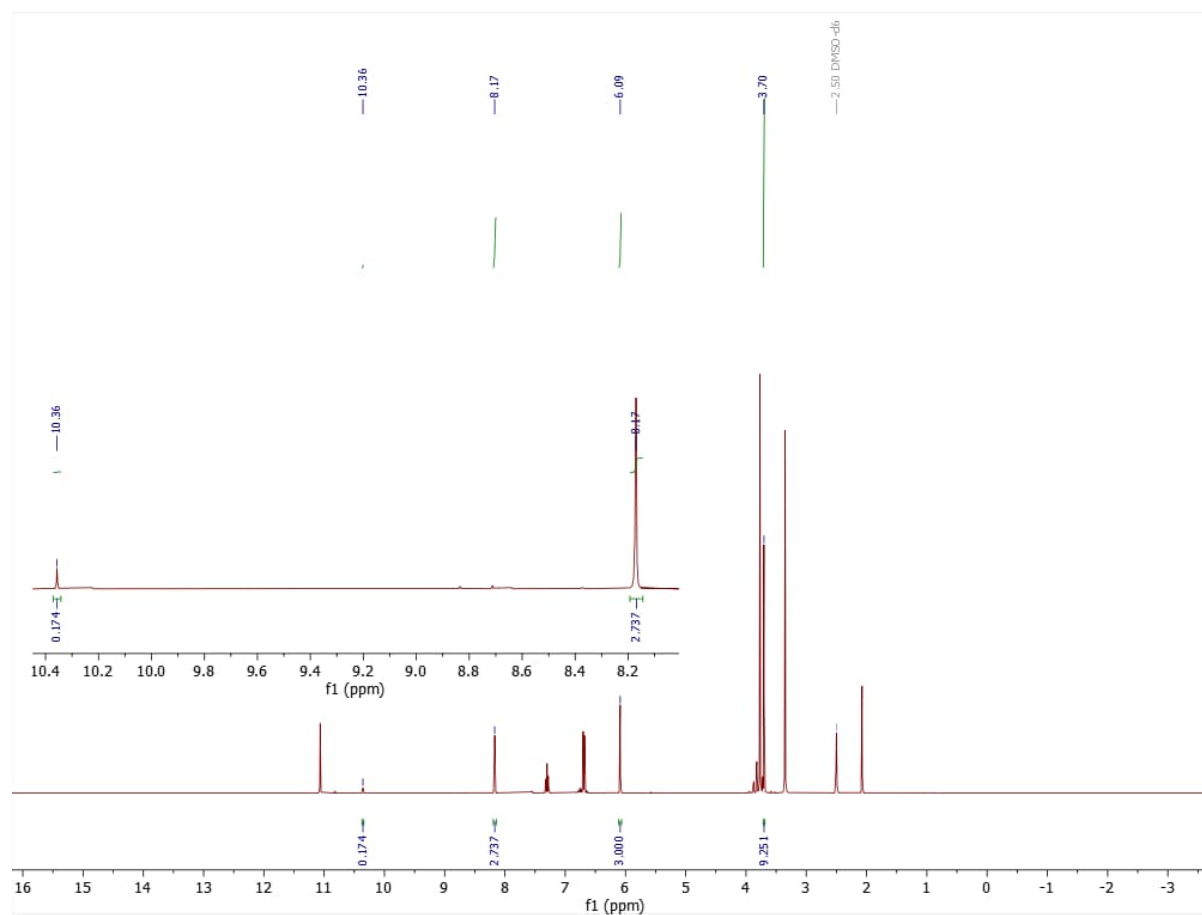
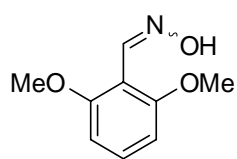


$$Y = \frac{0.093 \cdot 3 \cdot 10}{3.000 \cdot 1 \cdot 50} \cdot 1 \cdot 100\% = 2\%$$

$$X = \left(1 - \frac{2.206 \cdot 3 \cdot 10}{3.000 \cdot 1 \cdot 50}\right) \cdot 1 \cdot 100\% = 56\%$$



## 2,6-dimethoxybenzaldehyde oxime (1c) oxidation, red LED, 24 h

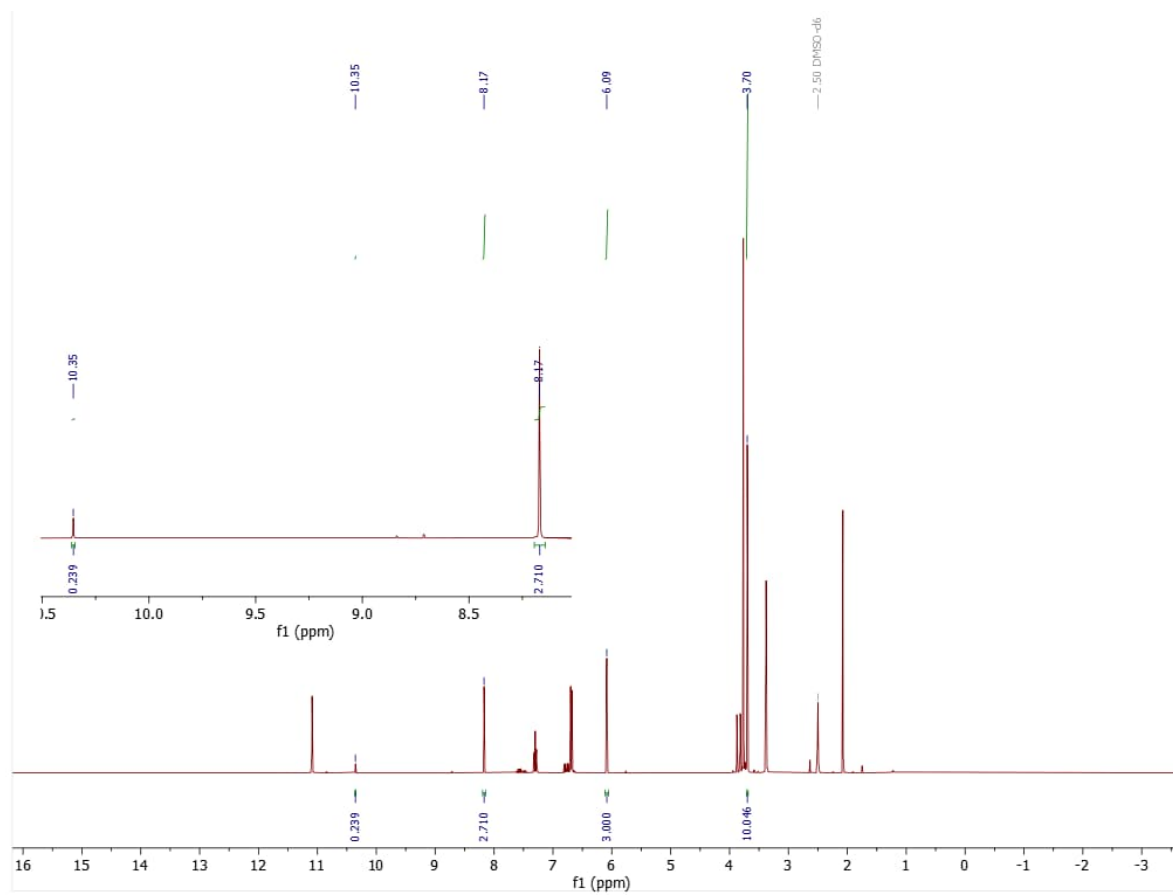
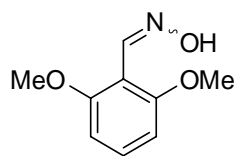


$$Y = \frac{0.174 \cdot 3 \cdot 10}{3.000 \cdot 1 \cdot 50} \cdot 1 \cdot 100\% = 3\%$$

$$X = \left(1 - \frac{2.737 \cdot 3 \cdot 10}{3.000 \cdot 1 \cdot 50}\right) \cdot 1 \cdot 100\% = 45\%$$



## 2,6-dimethoxybenzaldehyde oxime (1c) oxidation, red LED, 120 h

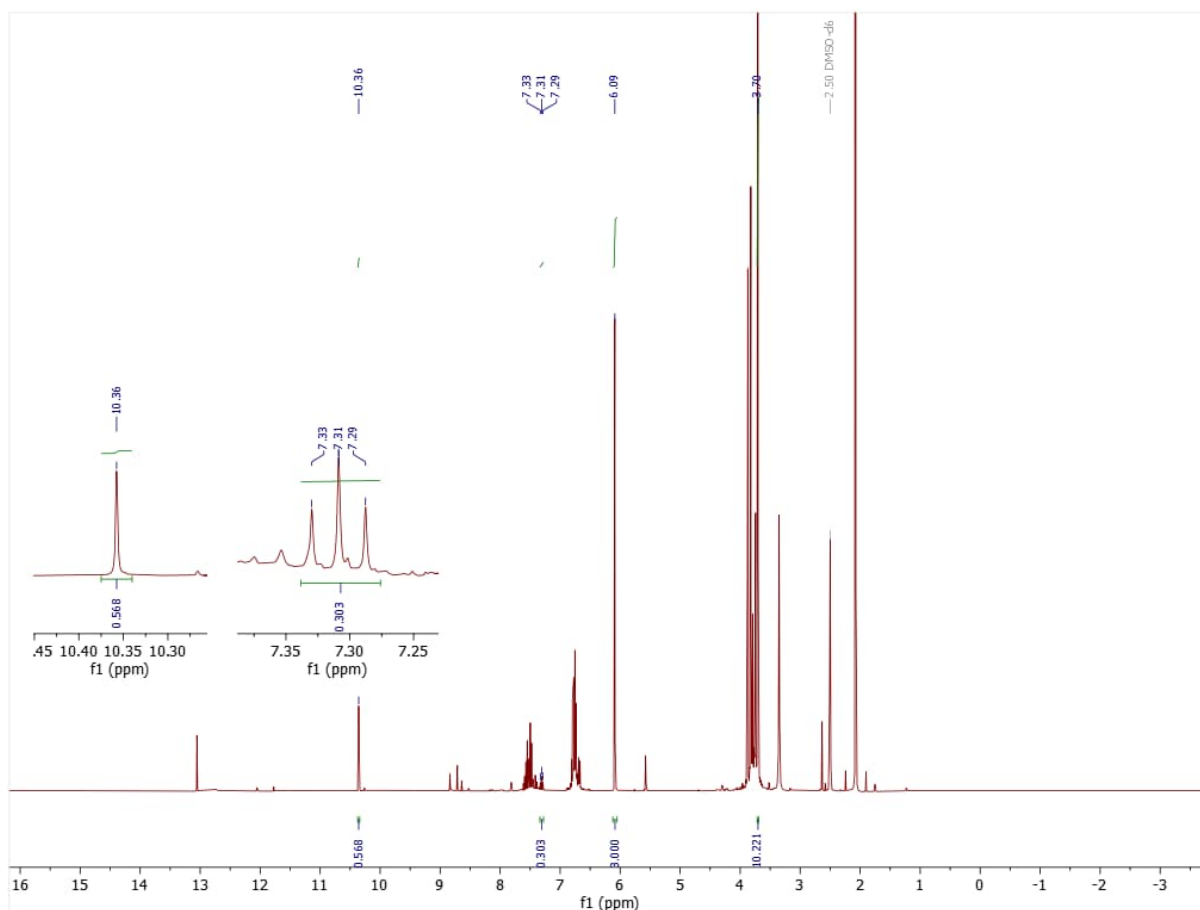
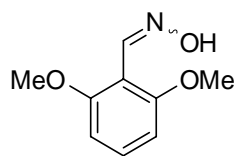


$$Y = \frac{0.239 \cdot 3 \cdot 10}{3.000 \cdot 1 \cdot 50} \cdot 1 \cdot 100\% = 5\%$$

$$X = \left(1 - \frac{2.710 \cdot 3 \cdot 10}{3.000 \cdot 1 \cdot 50}\right) \cdot 1 \cdot 100\% = 46\%$$



## 2,6-dimethoxybenzaldehyde oxime (1c) oxidation, blue LED, 24 h, with K-PHI

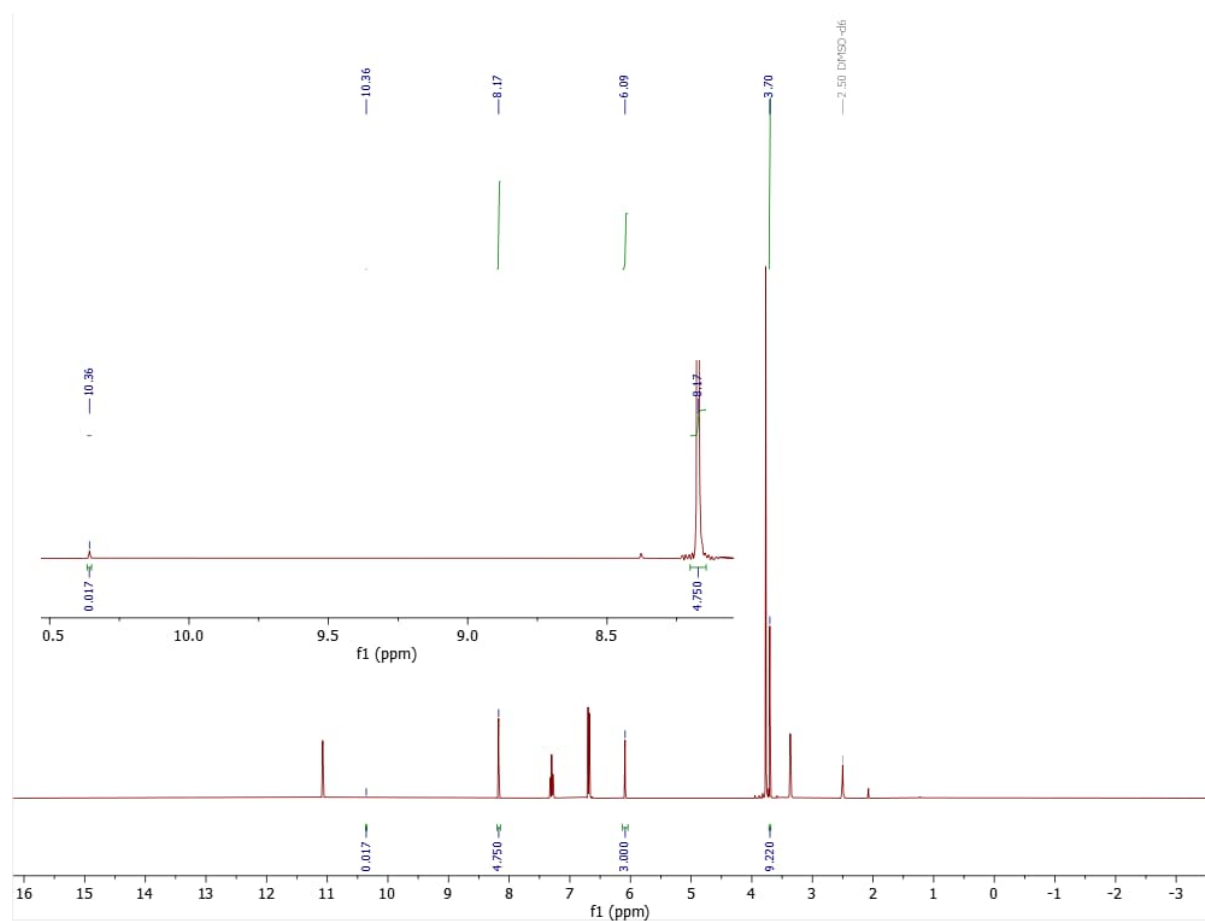
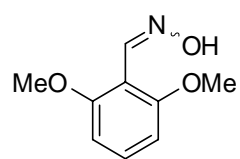


$$Y = \frac{0.568 \cdot 3 \cdot 10}{3.000 \cdot 1 \cdot 50} \cdot 1 \cdot 100\% = 11\%$$

$$X = \left(1 - \frac{0.303 \cdot 3 \cdot 10}{3.000 \cdot 1 \cdot 50}\right) \cdot 1 \cdot 100\% = 94\%$$



## 2,6-dimethoxybenzaldehyde oxime (1c) oxidation, blue LED, 24 h, without K-PHI

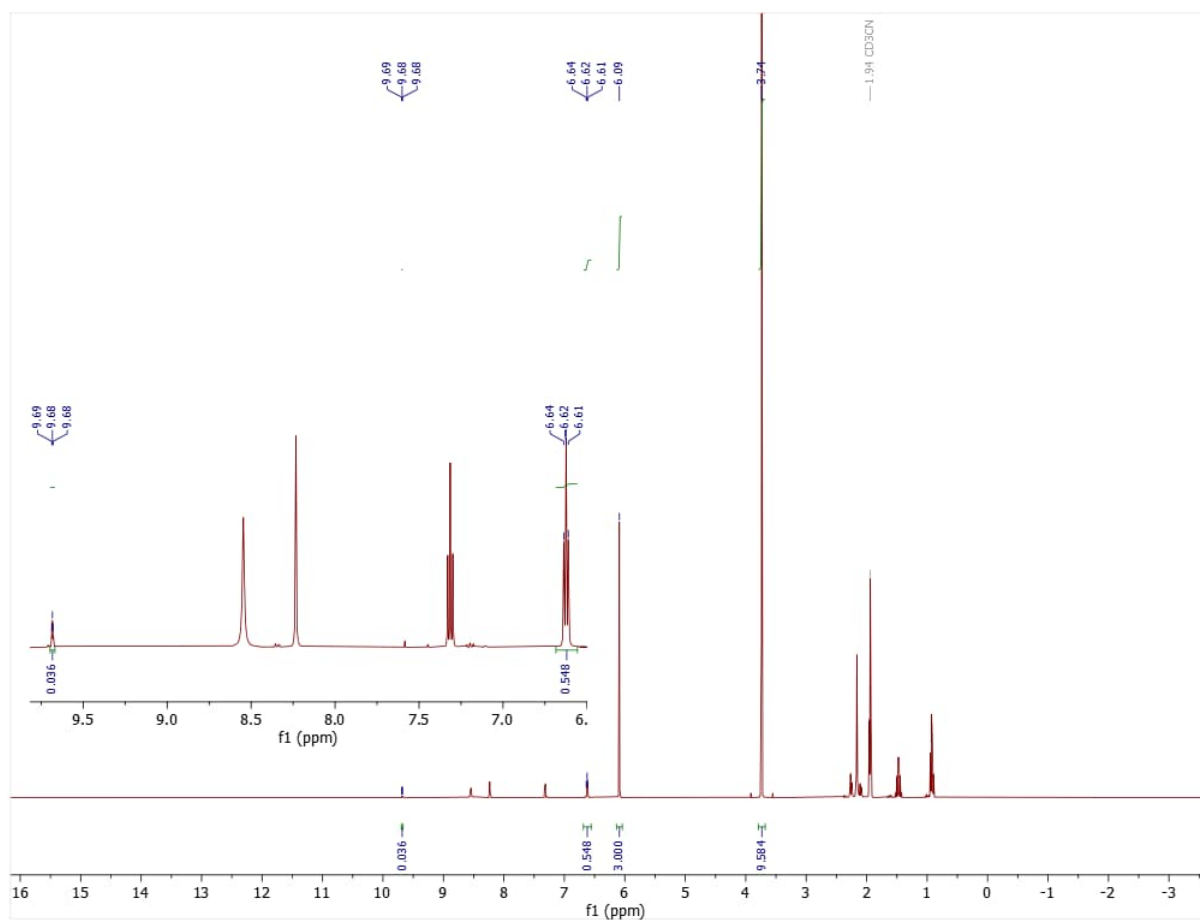
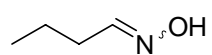


$$Y = \frac{0.017 \cdot 3 \cdot 10}{3.000 \cdot 1 \cdot 50} \cdot 1 \cdot 100\% < 1\%$$

$$X = \left(1 - \frac{4.750 \cdot 3 \cdot 10}{3.000 \cdot 1 \cdot 50}\right) \cdot 1 \cdot 100\% = 5\%$$



## Butanal oxime (1d) oxidation, red LED, 24 h

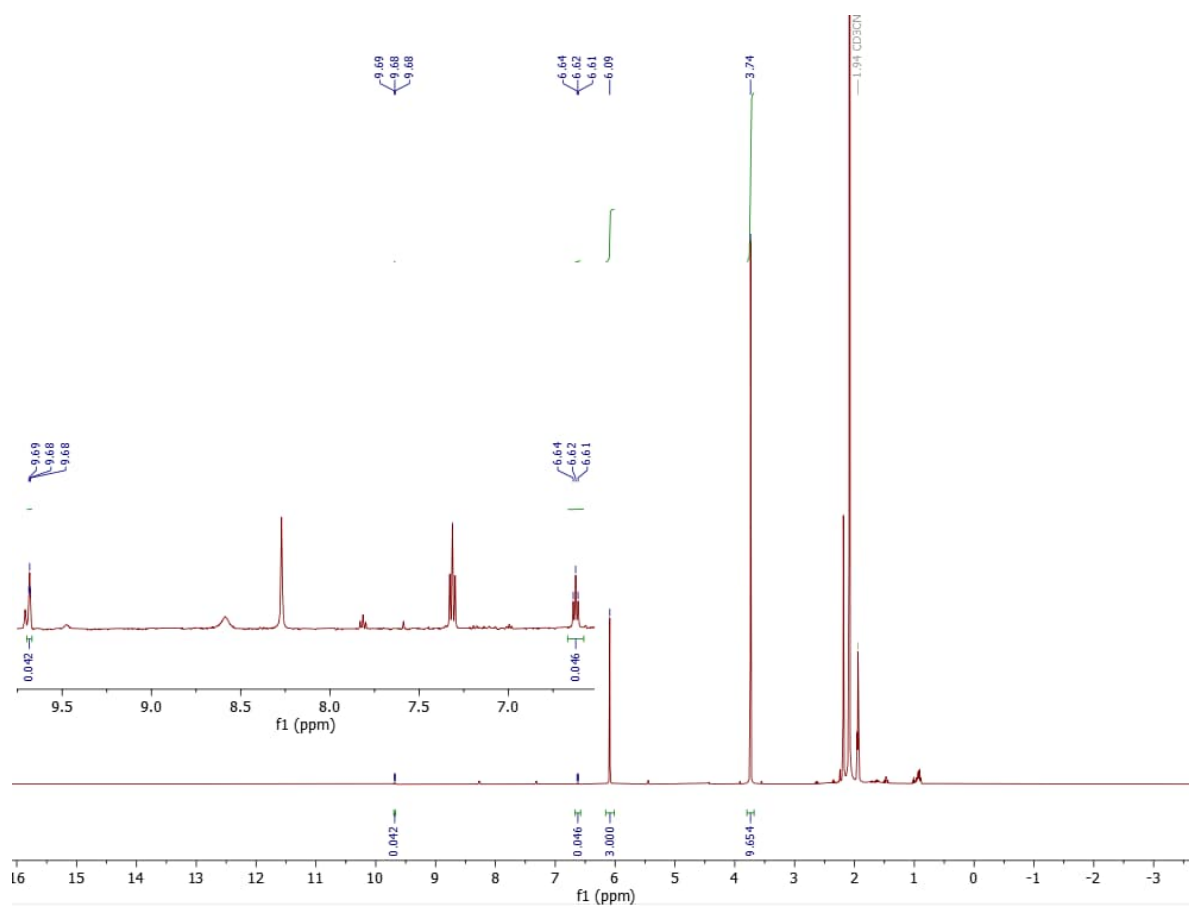
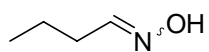


$$Y = \frac{0.036 \cdot 3 \cdot 10}{3.000 \cdot 1 \cdot 50} \cdot 4 \cdot 100\% = 3\%$$

$$X = \left(1 - \frac{0.548 \cdot 3 \cdot 10}{3.000 \cdot 1 \cdot 50}\right) \cdot 4 \cdot 100\% = 56\%$$



## Butanal oxime (1d) oxidation, red LED, 120 h

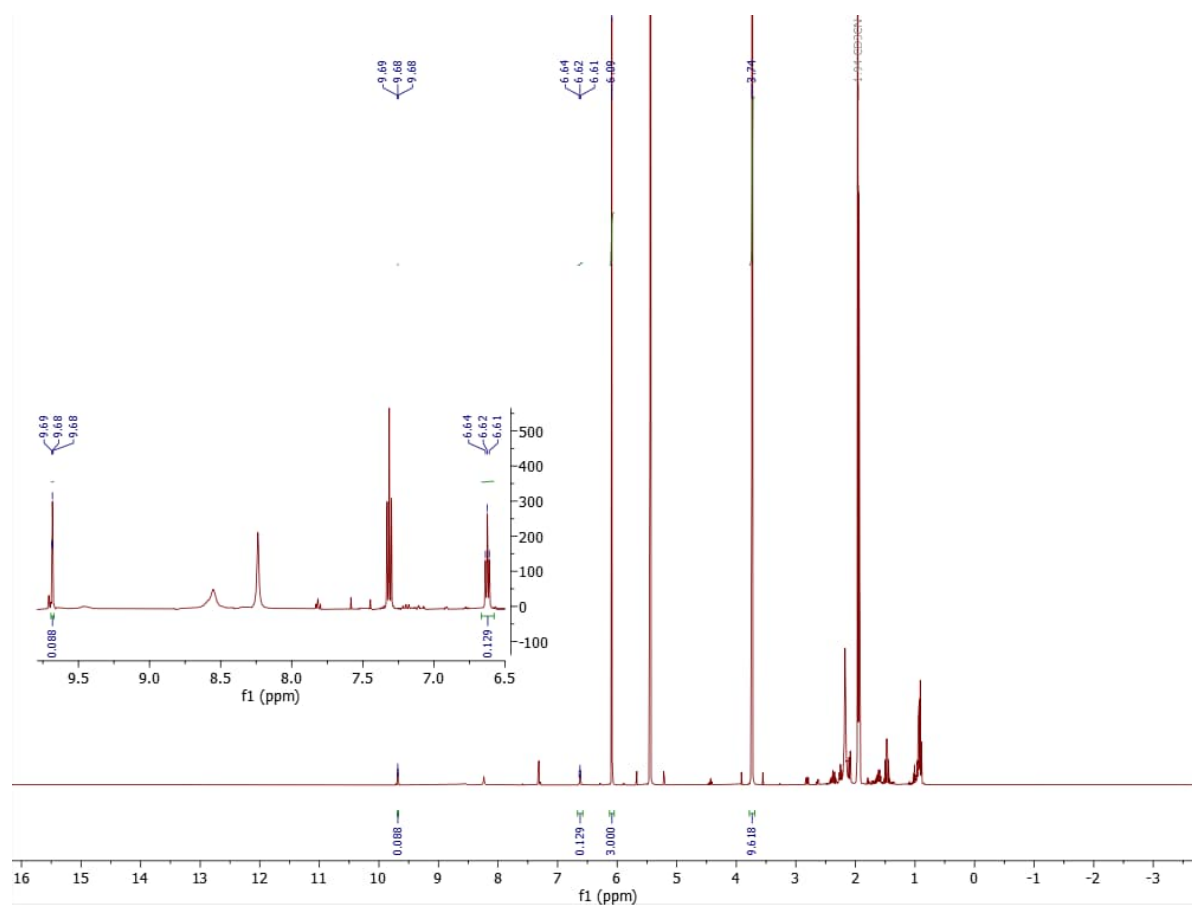
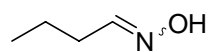


$$Y = \frac{0.042 \cdot 3 \cdot 10}{3.000 \cdot 1 \cdot 50} \cdot 4 \cdot 100\% = 3\%$$

$$X = \left(1 - \frac{0.046 \cdot 3 \cdot 10}{3.000 \cdot 1 \cdot 50}\right) \cdot 4 \cdot 100\% = 96\%$$



## Butanal oxime (1d) oxidation, blue LED, 24 h, with K-PHI

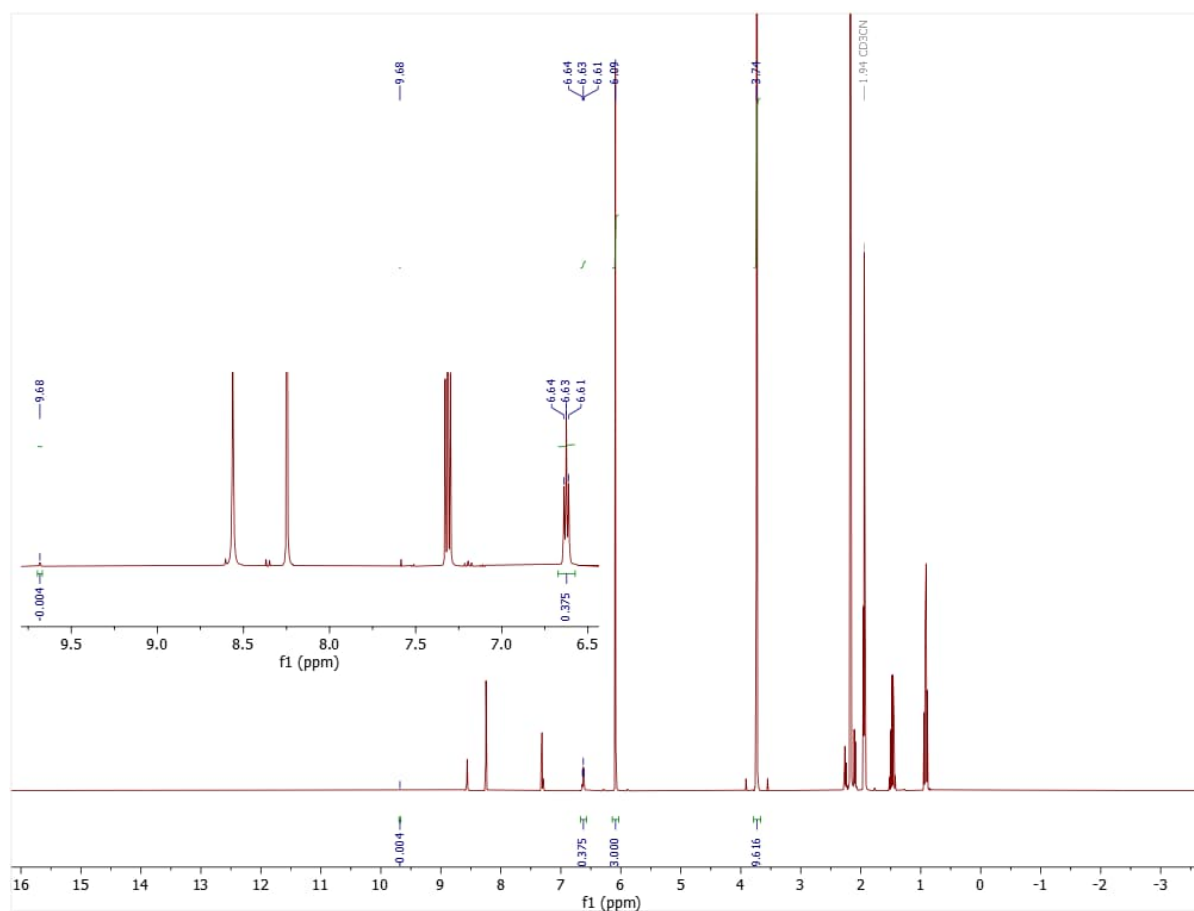
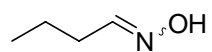


$$Y = \frac{0.088 \cdot 3 \cdot 10}{3.000 \cdot 1 \cdot 50} \cdot 4 \cdot 100\% = 7\%$$

$$X = \left(1 - \frac{0.129 \cdot 3 \cdot 10}{3.000 \cdot 1 \cdot 50}\right) \cdot 4 \cdot 100\% = 90\%$$



## Butanal oxime (1d) oxidation, blue LED, 24 h, without K-PHI

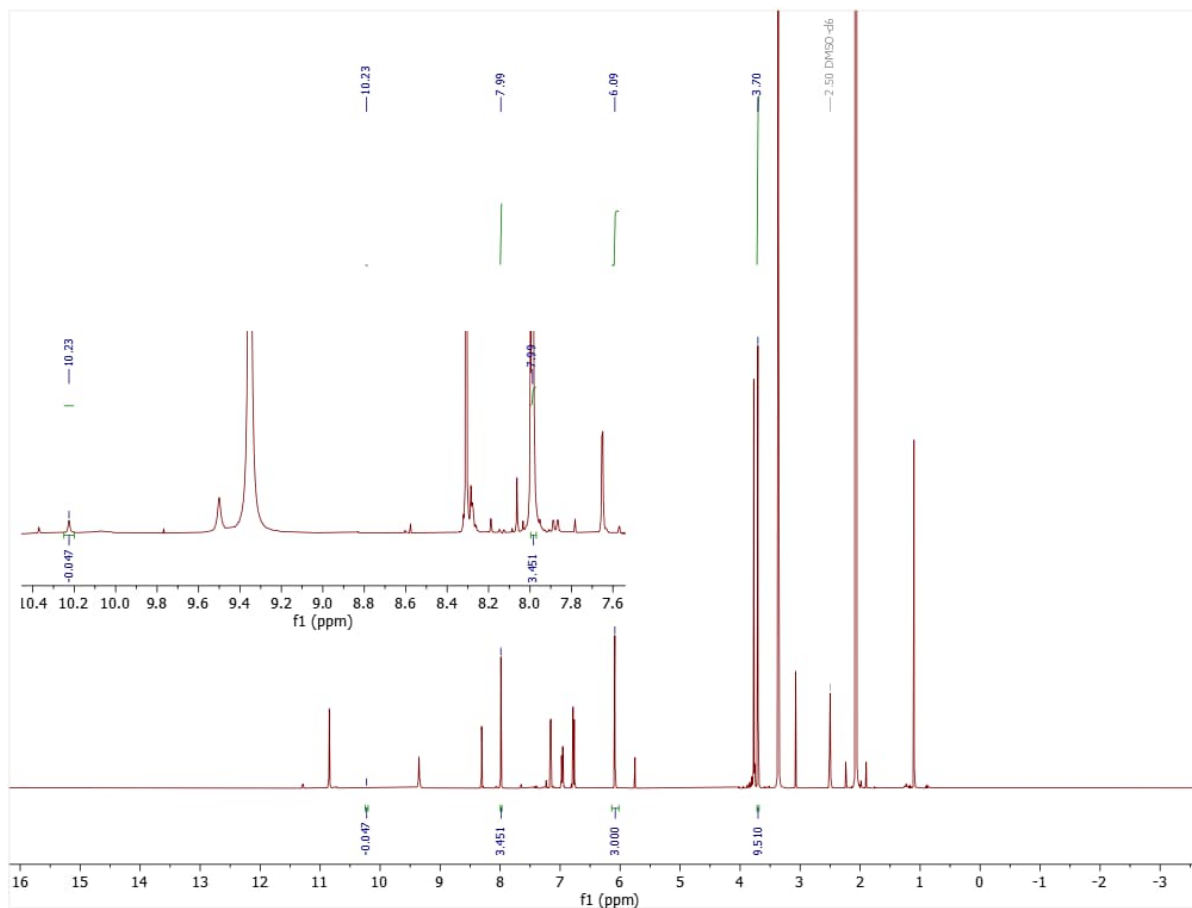
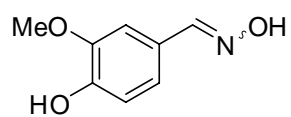


$$Y = \frac{0.004 \cdot 3 \cdot 10}{3.000 \cdot 1 \cdot 50} \cdot 4 \cdot 100\% < 1\%$$

$$X = \left(1 - \frac{0.375 \cdot 3 \cdot 10}{3.000 \cdot 1 \cdot 50}\right) \cdot 4 \cdot 100\% = 70\%$$



## 4-hydroxy-3-methoxybenzaldehyde (1e) oxime oxidation, red LED, 24 h

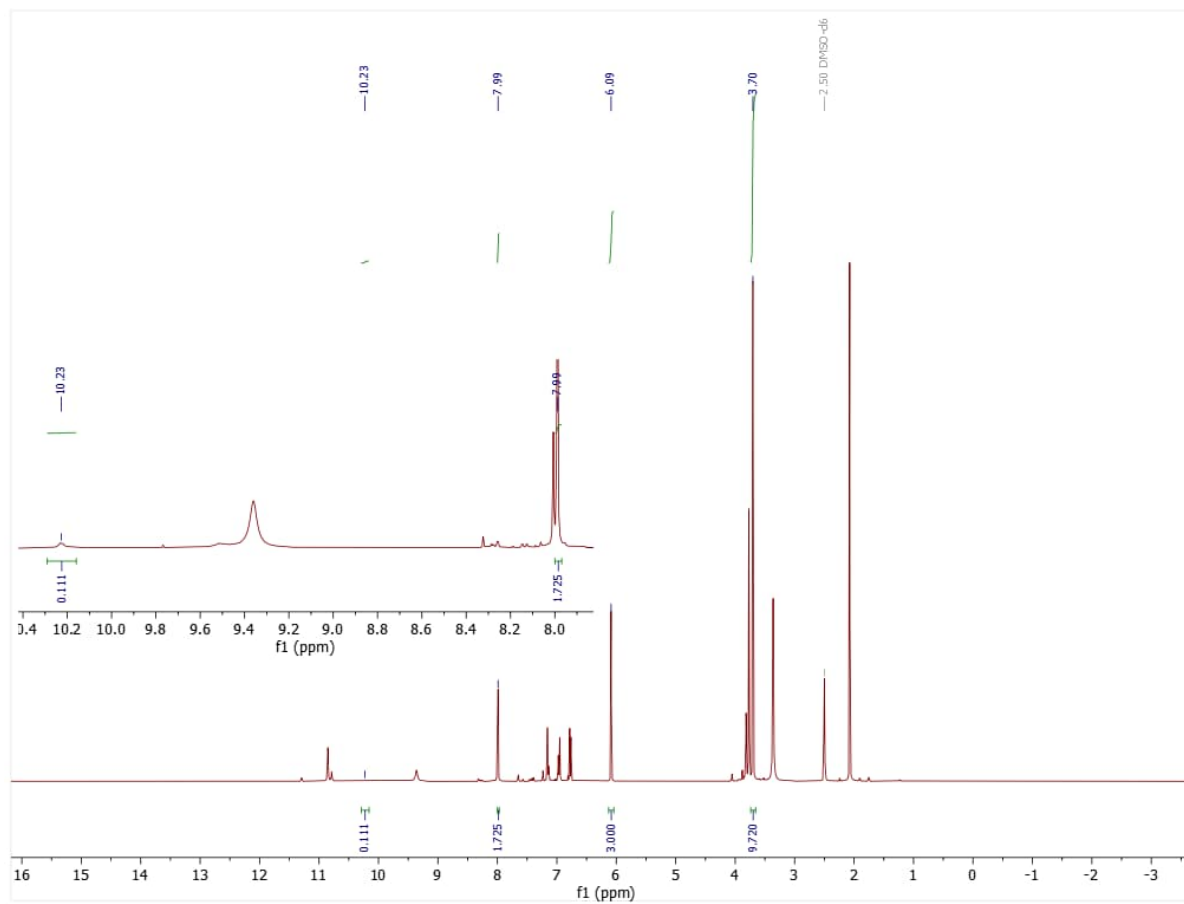
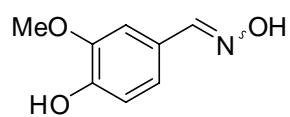


$$Y = \frac{0.047 \cdot 3 \cdot 10}{3.000 \cdot 1 \cdot 50} \cdot 1 \cdot 100\% = 1\%$$

$$X = \left(1 - \frac{3.451 \cdot 3 \cdot 10}{3.000 \cdot 1 \cdot 50}\right) \cdot 1 \cdot 100\% = 31\%$$



## 4-hydroxy-3-methoxybenzaldehyde oxime (1e) oxidation, red LED, 120 h

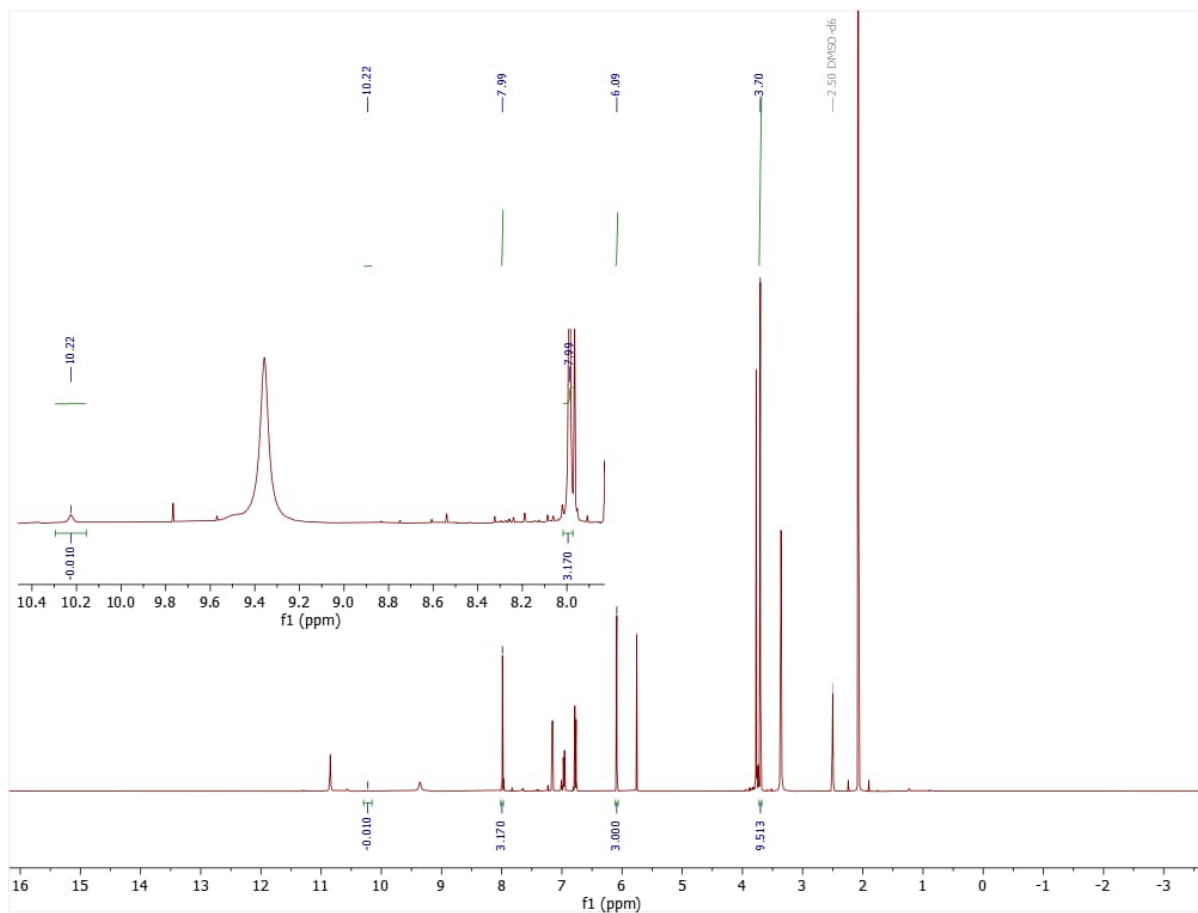
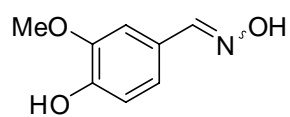


$$Y = \frac{0.111 \cdot 3 \cdot 10}{3.000 \cdot 1 \cdot 50} \cdot 1 \cdot 100\% = 2\%$$

$$X = \left(1 - \frac{1.725 \cdot 3 \cdot 10}{3.000 \cdot 1 \cdot 50}\right) \cdot 1 \cdot 100\% = 65\%$$



## 4-hydroxy-3-methoxybenzaldehyde oxime (1e) oxidation, blue LED, 24 h, with K-PHI

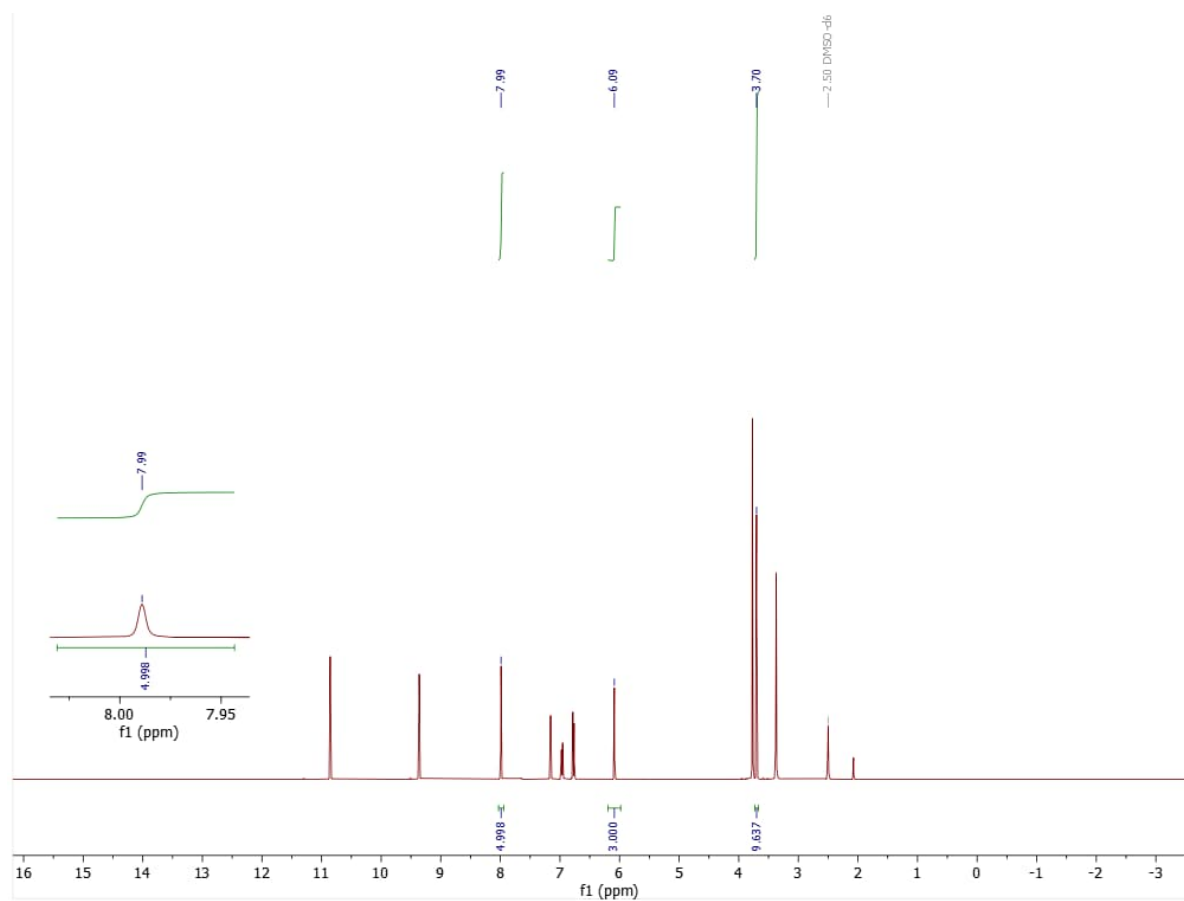
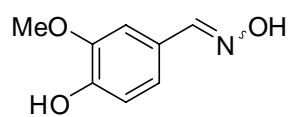


$$Y = \frac{0.010 \cdot 3 \cdot 10}{3.000 \cdot 1 \cdot 50} \cdot 1 \cdot 100\% < 1\%$$

$$X = \left(1 - \frac{3.170 \cdot 3 \cdot 10}{3.000 \cdot 1 \cdot 50}\right) \cdot 1 \cdot 100\% = 37\%$$



## 4-hydroxy-3-methoxybenzaldehyde oxime (1e) oxidation, blue LED, 24 h, without K-PHI

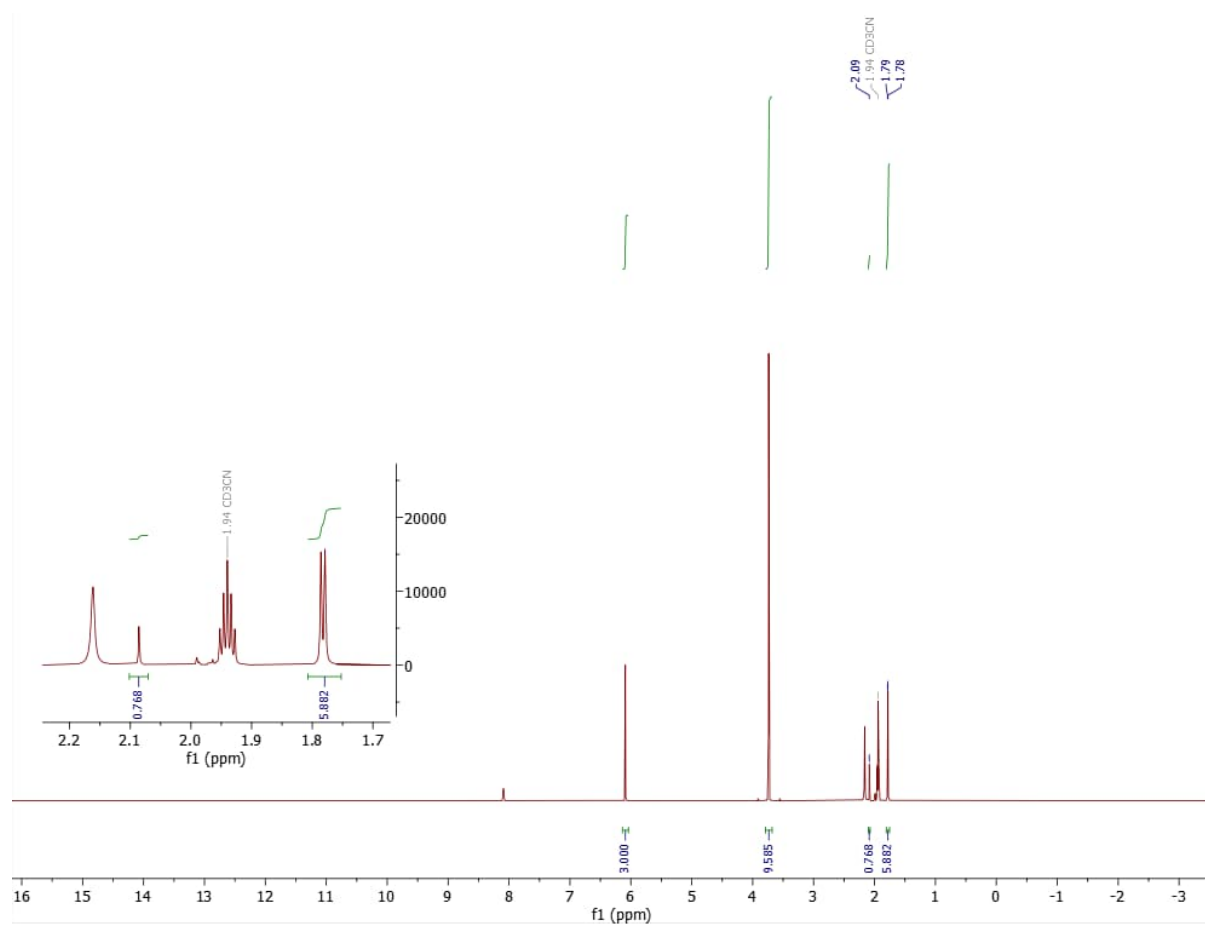
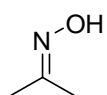


$$Y = \frac{0 \cdot 3 \cdot 10}{3.000 \cdot 1 \cdot 50} \cdot 1 \cdot 100\% = 0\%$$

$$X = \left(1 - \frac{4.998 \cdot 3 \cdot 10}{3.000 \cdot 1 \cdot 50}\right) \cdot 1 \cdot 100\% < 1\%$$



## Acetone oxime (1f) oxidation, red LED, 24 h

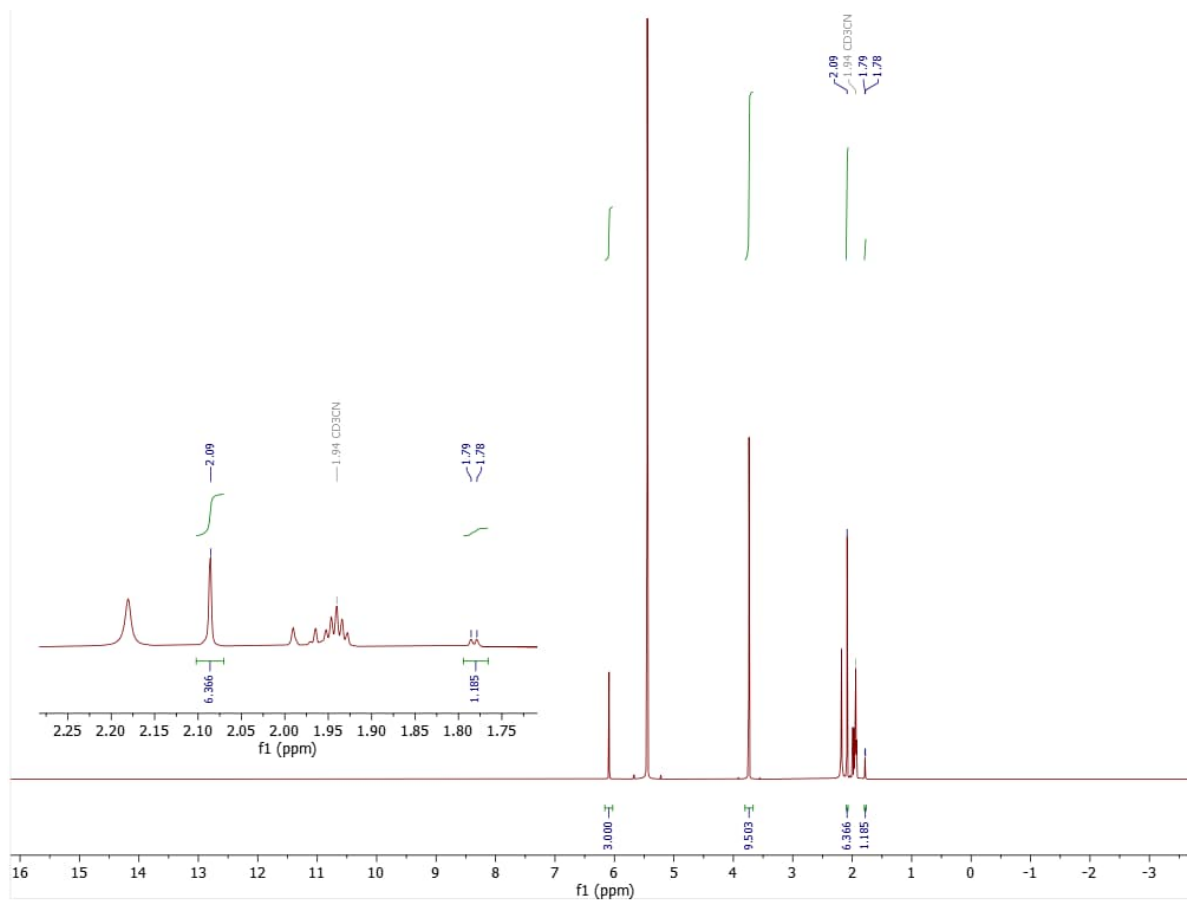
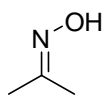


$$Y = \frac{0.768 \cdot 3 \cdot 10}{3.000 \cdot 6 \cdot 50} \cdot 4 \cdot 100\% = 10\%$$

$$X = \left(1 - \frac{5.882 \cdot 3 \cdot 10}{3.000 \cdot 6 \cdot 50}\right) \cdot 4 \cdot 100\% = 22\%$$



## Acetone oxime (1f) oxidation, red LED, 120 h

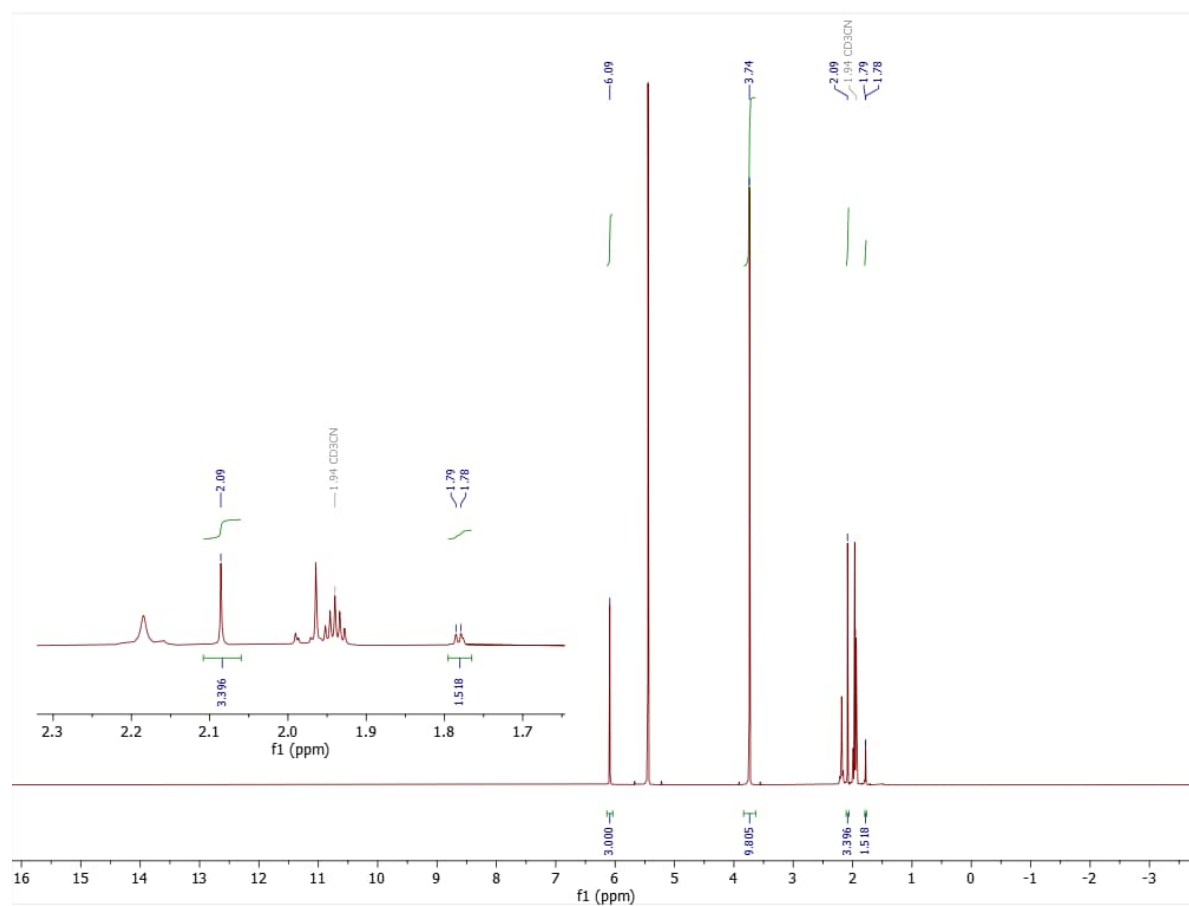
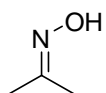


$$Y = \frac{6.366 \cdot 3 \cdot 10}{3.000 \cdot 6 \cdot 50} \cdot 4 \cdot 100\% = 84\%$$

$$X = \left(1 - \frac{1.185 \cdot 3 \cdot 10}{3.000 \cdot 6 \cdot 50}\right) \cdot 4 \cdot 100\% = 85\%$$



## Acetone oxime (1f) oxidation, blue LED, 24 h, with K-PHI

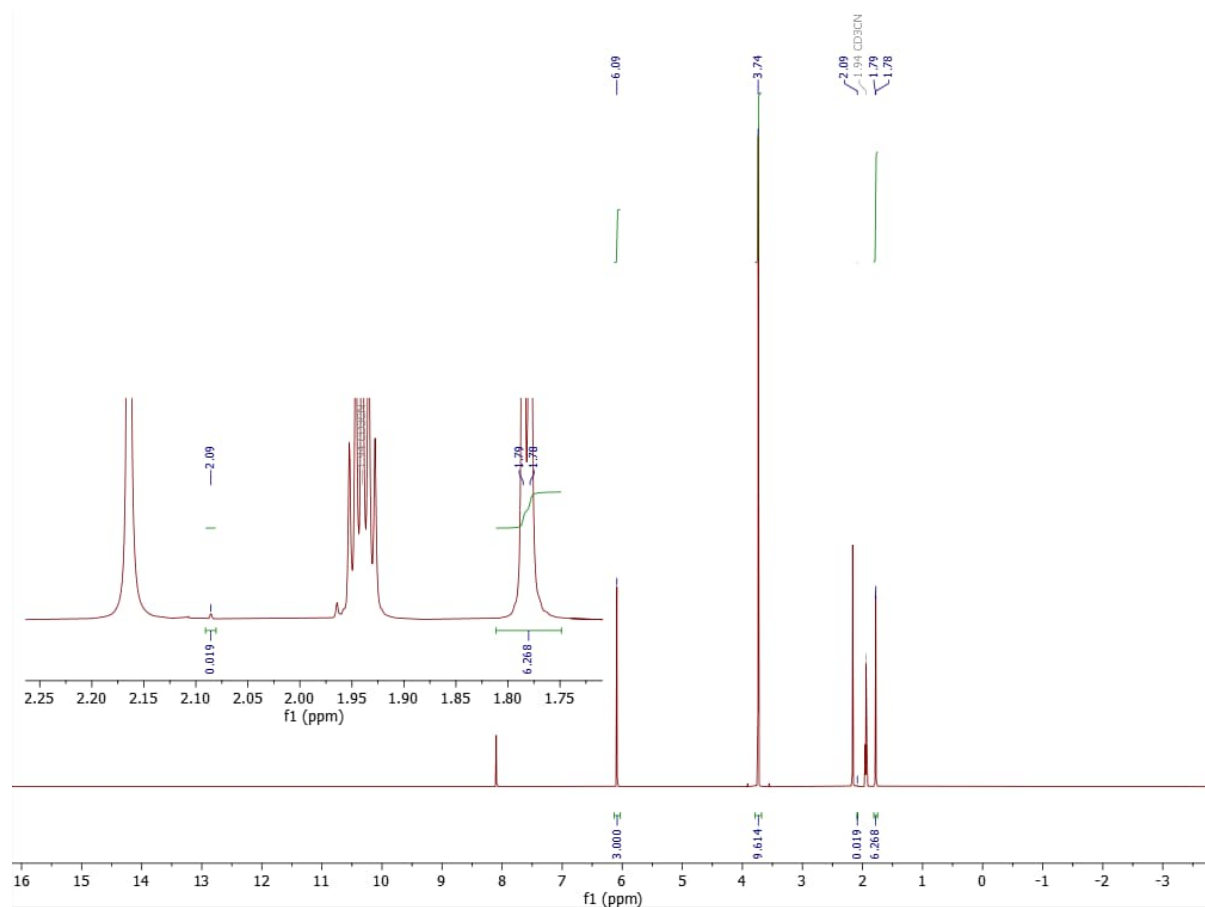
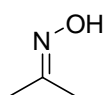


$$Y = \frac{3.396 \cdot 3 \cdot 10}{3.000 \cdot 6 \cdot 50} \cdot 4 \cdot 100\% = 45\%$$

$$X = \left(1 - \frac{1.518 \cdot 3 \cdot 10}{3.000 \cdot 6 \cdot 50}\right) \cdot 4 \cdot 100\% = 80\%$$



## Acetone oxime (1f) oxidation, blue LED, 24 h, without K-PHI

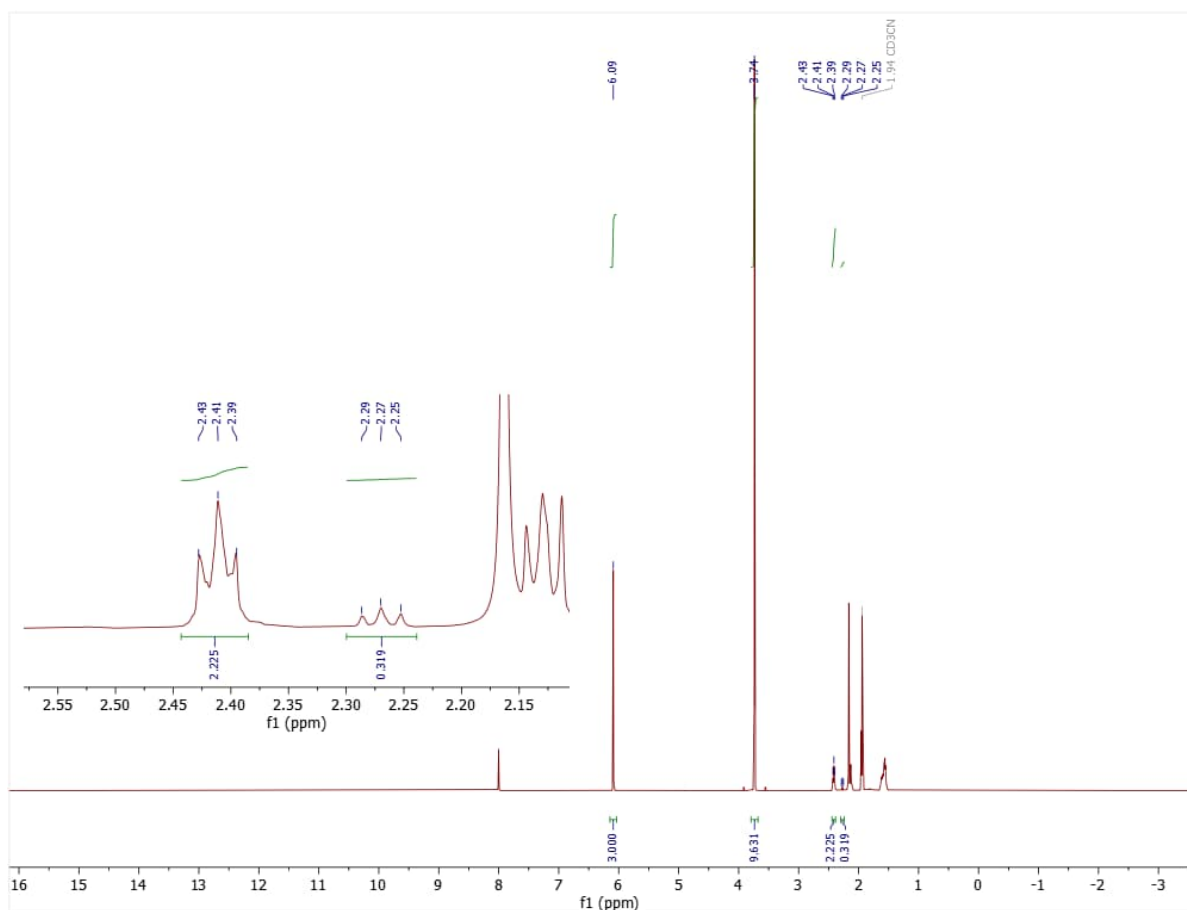
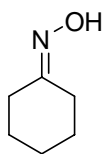


$$Y = \frac{0.019 \cdot 3 \cdot 10}{3.000 \cdot 6 \cdot 50} \cdot 4 \cdot 100\% < 1\%$$

$$X = \left(1 - \frac{6.268 \cdot 3 \cdot 10}{3.000 \cdot 6 \cdot 50}\right) \cdot 4 \cdot 100\% = 16\%$$



## Cyclohexanone oxime (1g) oxidation, red LED, 24 h



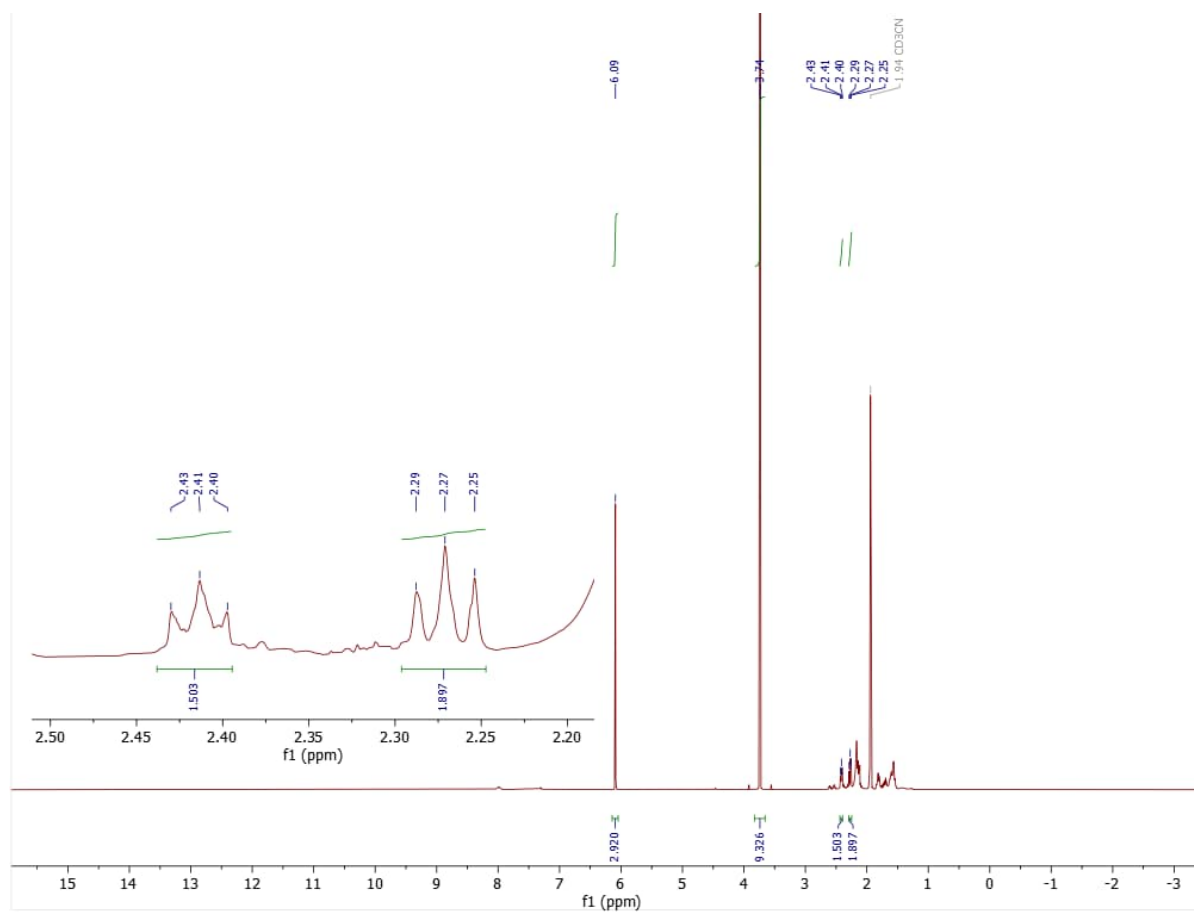
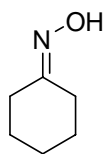
$$Y = \frac{0.319 \cdot 3 \cdot 10}{3.000 \cdot 4 \cdot 50} \cdot 4 \cdot 100\% = 6\%$$

$$X = \left(1 - \frac{2.225 \cdot 3 \cdot 10}{3.000 \cdot 2 \cdot 50}\right) \cdot 4 \cdot 100\% = 11\%$$





## Cyclohexanone oxime (1g) oxidation, blue LED, 24 h, with K-PHI

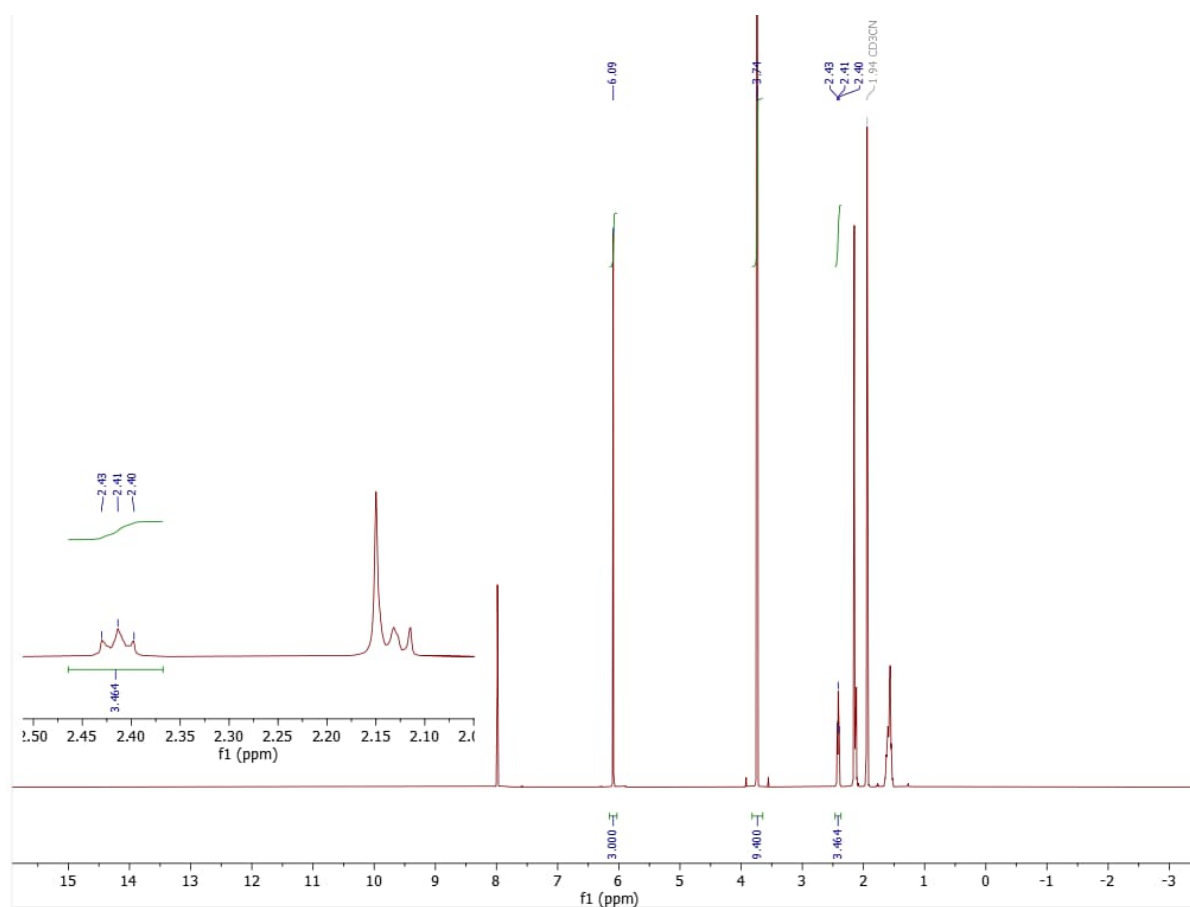
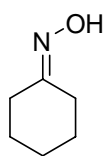


$$Y = \frac{1.897 \cdot 3 \cdot 10}{3.000 \cdot 4 \cdot 50} \cdot 4 \cdot 100\% = 38\%$$

$$X = \left(1 - \frac{1.503 \cdot 3 \cdot 10}{3.000 \cdot 2 \cdot 50}\right) \cdot 4 \cdot 100\% = 40\%$$



## Cyclohexanone oxime (1g) oxidation, blue LED, 24 h, without K-PHI

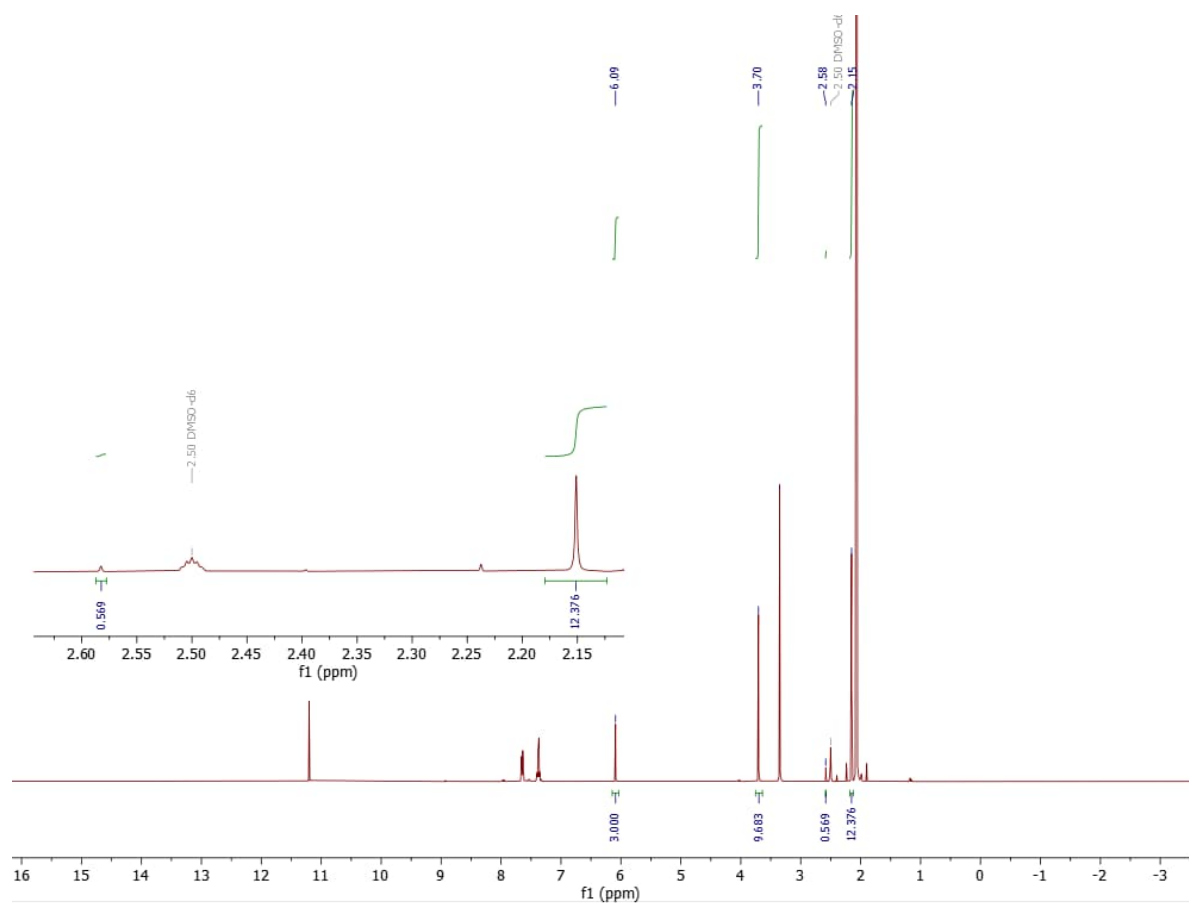
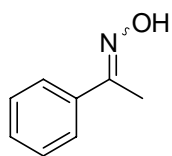


$$Y = \frac{0 \cdot 3 \cdot 10}{3.000 \cdot 4 \cdot 50} \cdot 4 \cdot 100\% = 0\%$$

$$X = \left(1 - \frac{3.464 \cdot 3 \cdot 10}{3.000 \cdot 2 \cdot 50}\right) \cdot 4 \cdot 100\% < 0\%$$



## Acetophenone oxime (1h) oxidation, red LED, 24 h

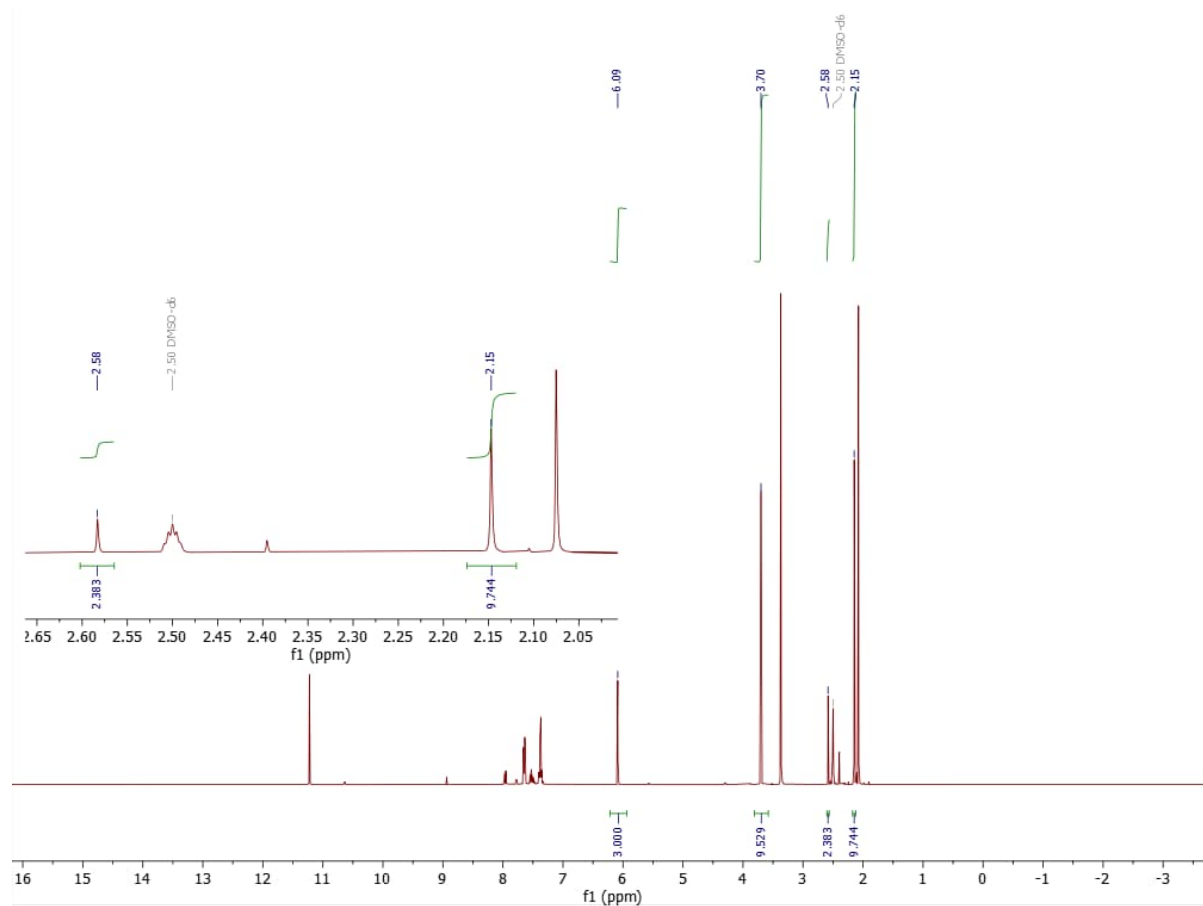
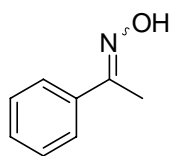


$$Y = \frac{0.569 \cdot 3 \cdot 10}{3.000 \cdot 3 \cdot 50} \cdot 1 \cdot 100\% = 4\%$$

$$X = \left(1 - \frac{12.376 \cdot 3 \cdot 10}{3.000 \cdot 3 \cdot 50}\right) \cdot 1 \cdot 100\% = 17\%$$



## Acetophenone oxime (1h) oxidation, red LED, 120 h

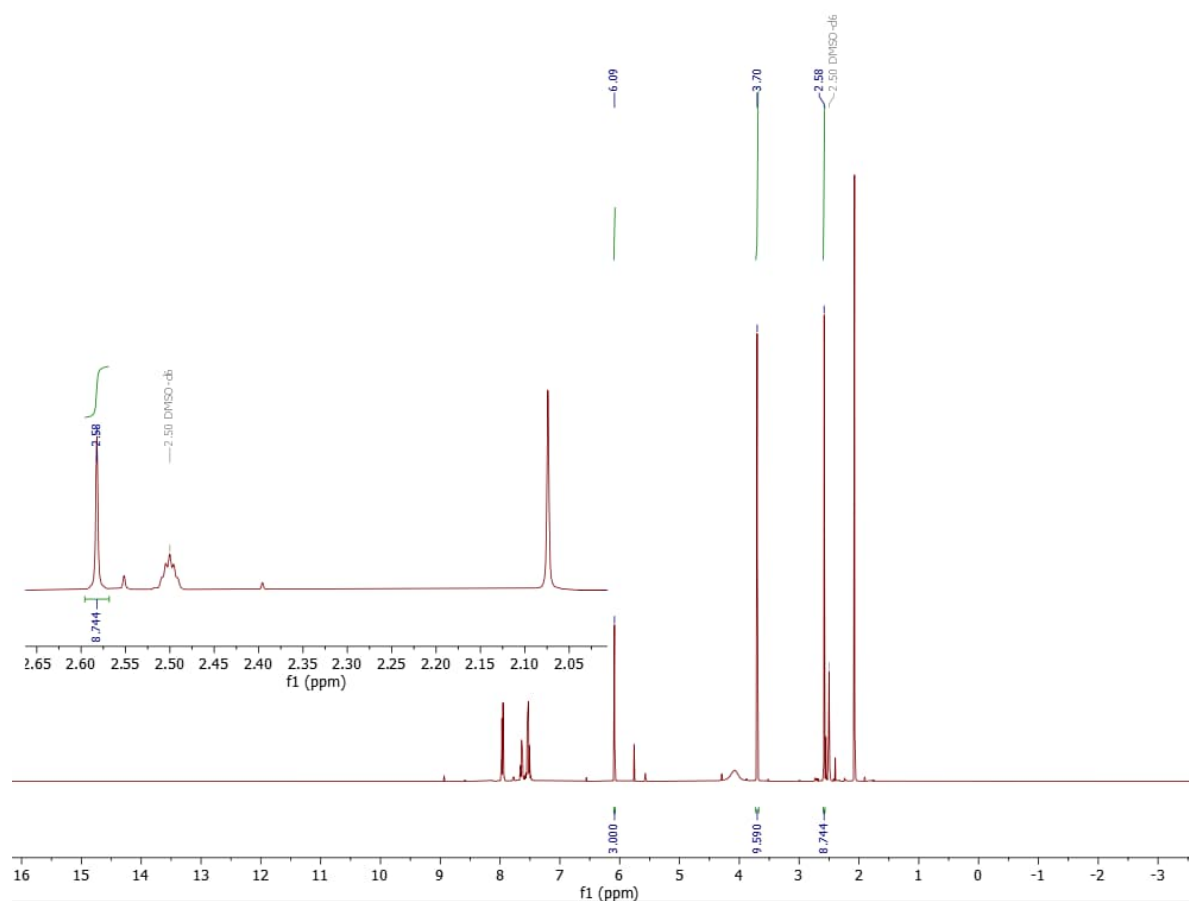
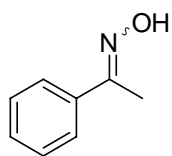


$$Y = \frac{2.383 \cdot 3 \cdot 10}{3.000 \cdot 3 \cdot 50} \cdot 1 \cdot 100\% = 16\%$$

$$X = \left(1 - \frac{9.744 \cdot 3 \cdot 10}{3.000 \cdot 3 \cdot 50}\right) \cdot 1 \cdot 100\% = 35\%$$



## Acetophenone oxime (1h) oxidation, blue LED, 24 h, with K-PHI

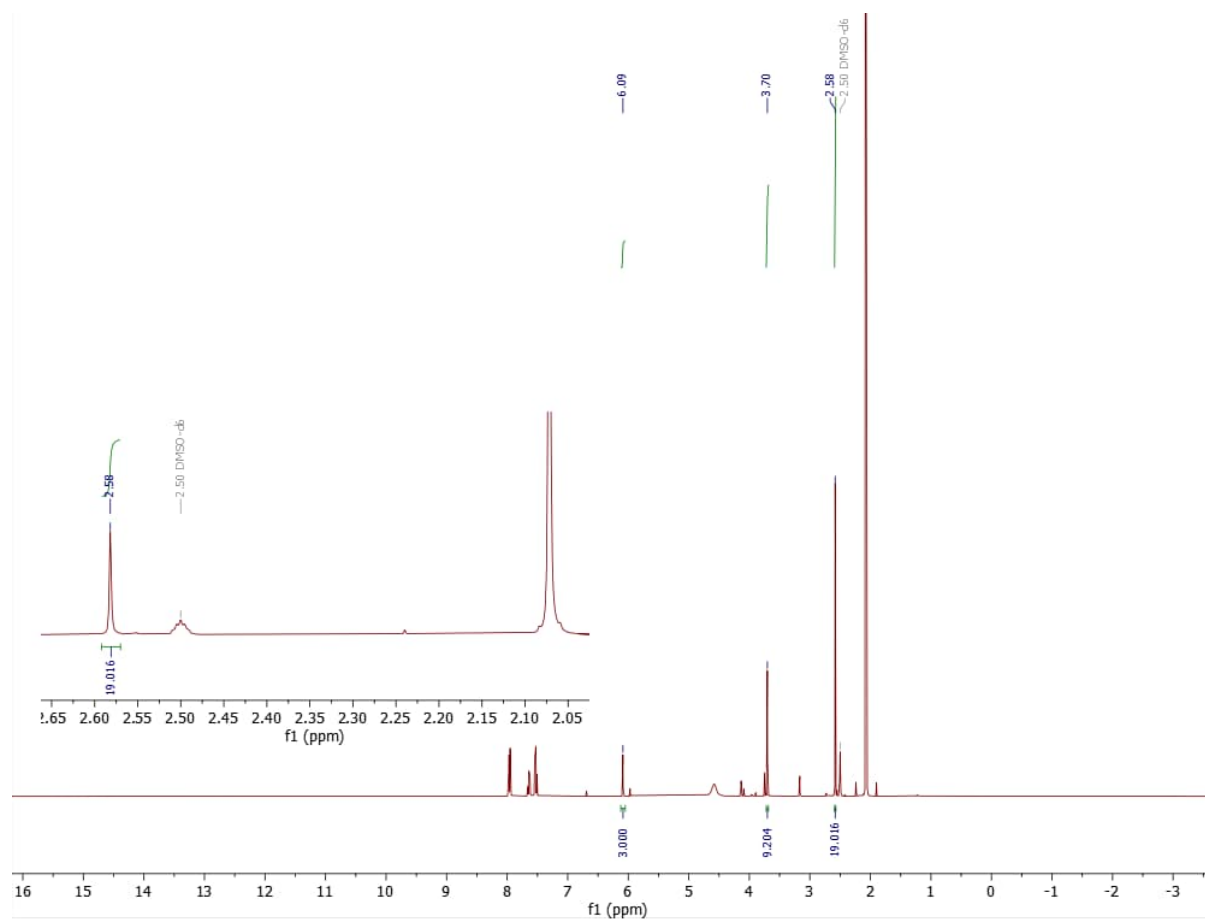
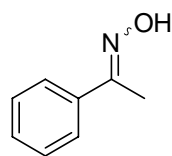


$$Y = \frac{8.744 \cdot 3 \cdot 10}{3.000 \cdot 3 \cdot 50} \cdot 1 \cdot 100\% = 58\%$$

$$X = \left(1 - \frac{0 \cdot 3 \cdot 10}{3.000 \cdot 3 \cdot 50}\right) \cdot 1 \cdot 100\% = 100\%$$



## Acetophenone oxime (1h) oxidation, blue LED, 24 h, without K-PHI

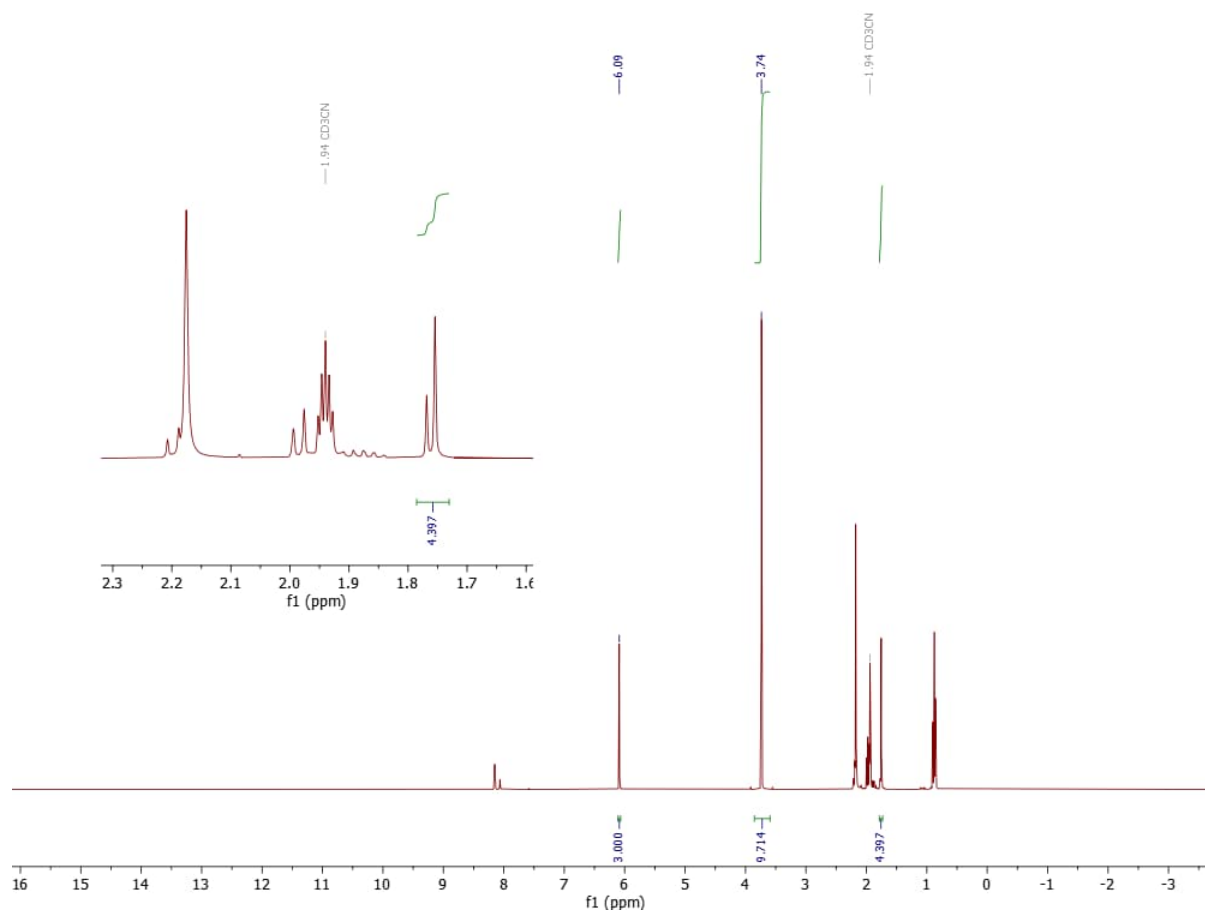
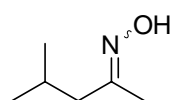


$$Y = \frac{19.016 \cdot 3 \cdot 10}{3.000 \cdot 3 \cdot 50} \cdot 1 \cdot 100\% > 100\%$$

$$X = \left(1 - \frac{0 \cdot 3 \cdot 10}{3.000 \cdot 3 \cdot 50}\right) \cdot 1 \cdot 100\% = 100\%$$



## 4-methylpentan-2-one oxime (1j) oxidation, red LED, 24 h

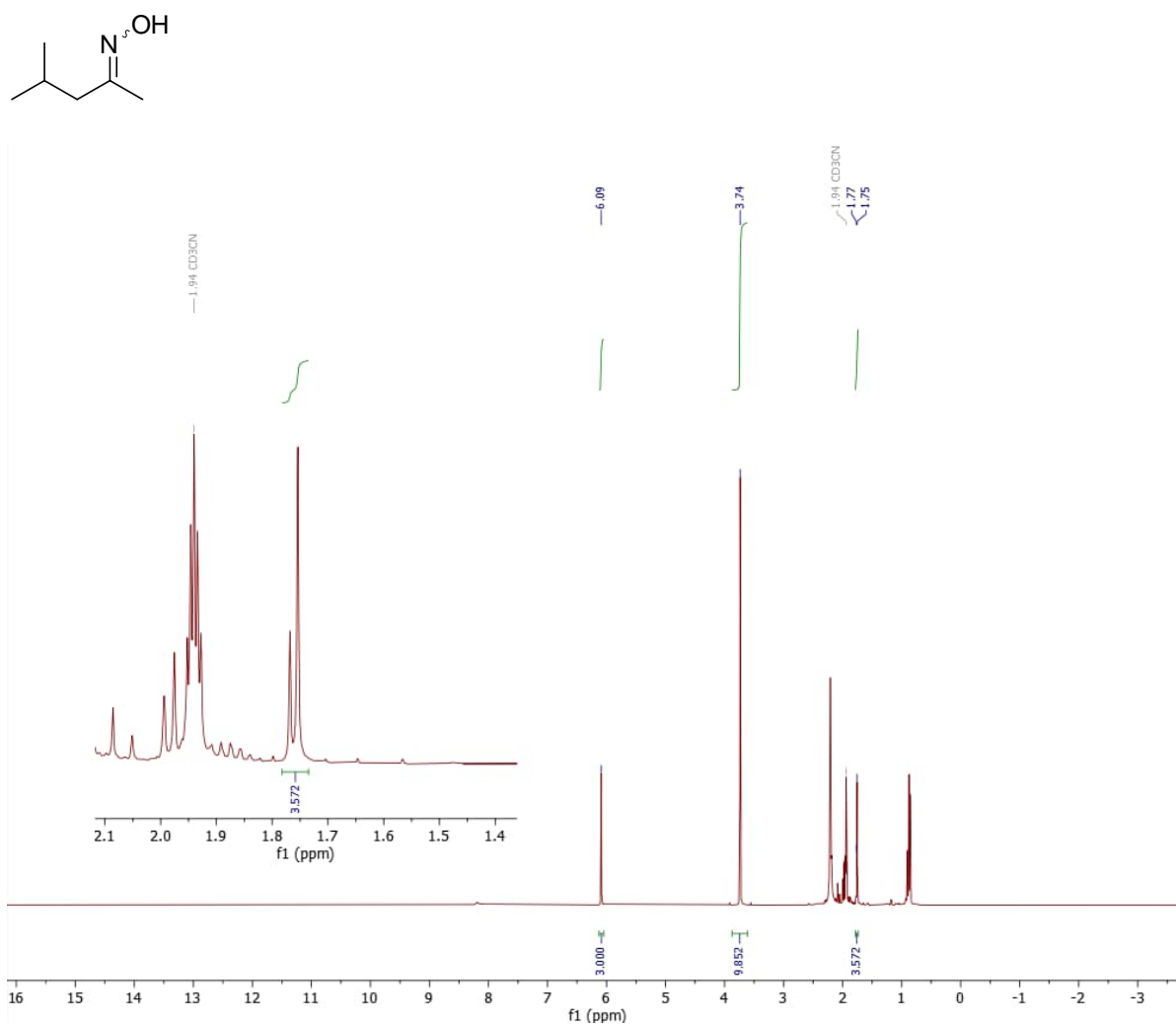


$$Y = \frac{0 \cdot 3 \cdot 10}{3.000 \cdot 2 \cdot 50} \cdot 4 \cdot 100\% = 0\%$$

$$X = \left(1 - \frac{4.397 \cdot 3 \cdot 10}{3.000 \cdot 3 \cdot 50}\right) \cdot 4 \cdot 100\% < 0\%$$



## 4-methylpentan-2-one oxime (1j) oxidation, red LED, 120 h

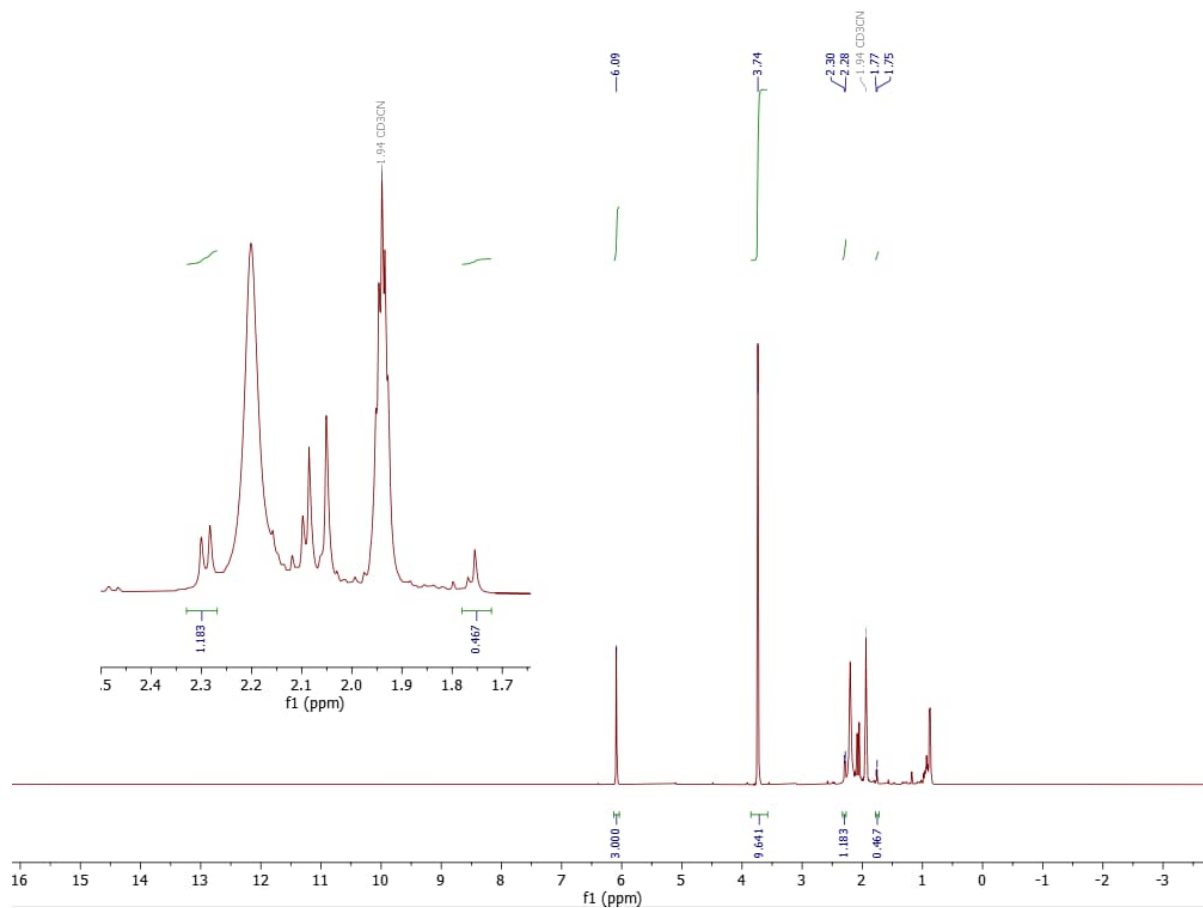
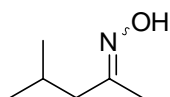


$$Y = \frac{0 \cdot 3 \cdot 10}{3.000 \cdot 2 \cdot 50} \cdot 4 \cdot 100\% = 0\%$$

$$X = \left(1 - \frac{3.572 \cdot 3 \cdot 10}{3.000 \cdot 3 \cdot 50}\right) \cdot 4 \cdot 100\% = 5\%$$



## 4-methylpentan-2-one oxime (1j) oxidation, blue LED, 24 h, with K-PHI

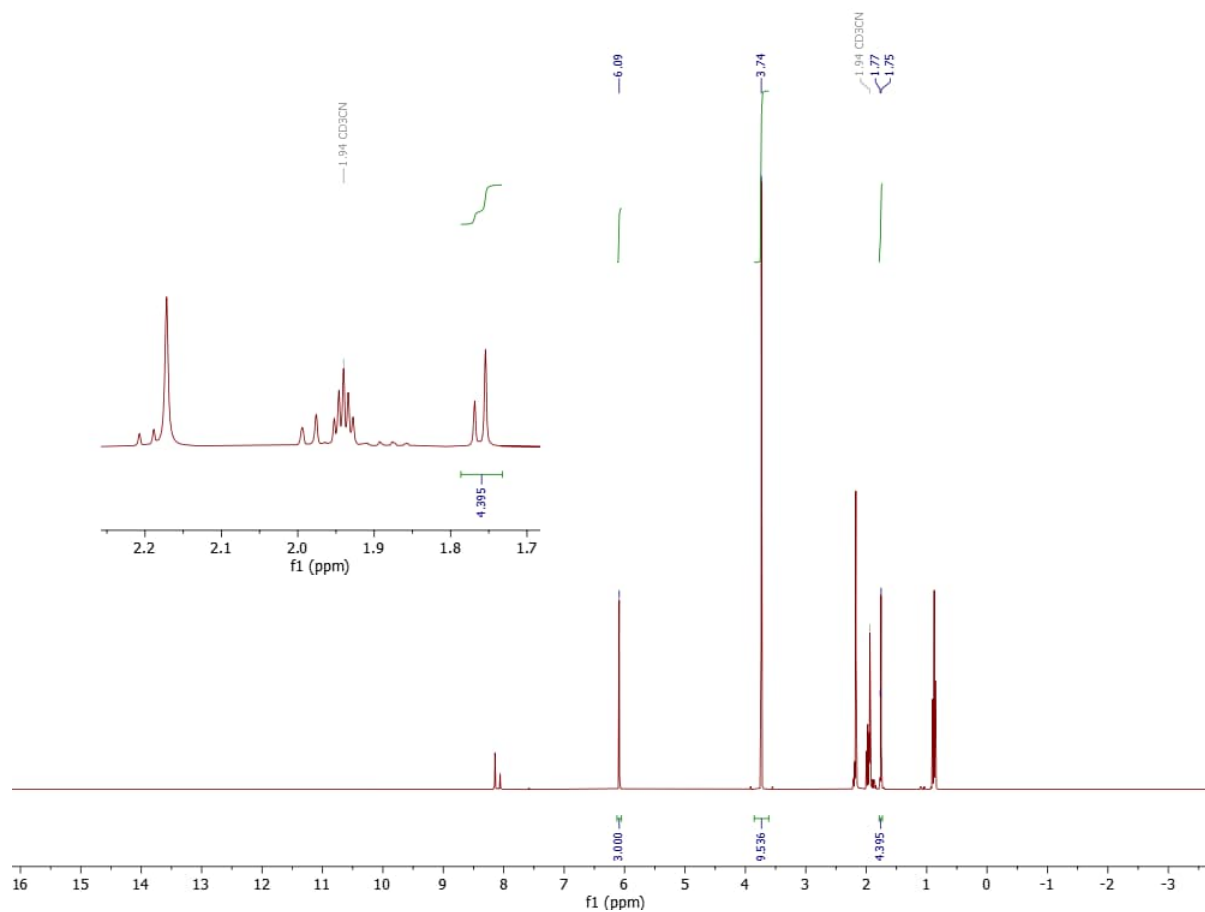
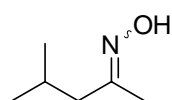


$$Y = \frac{1.183 \cdot 3 \cdot 10}{3.000 \cdot 2 \cdot 50} \cdot 4 \cdot 100\% = 47\%$$

$$X = \left(1 - \frac{0.467 \cdot 3 \cdot 10}{3.000 \cdot 3 \cdot 50}\right) \cdot 4 \cdot 100\% = 88\%$$



## 4-methylpentan-2-one oxime (1j) oxidation, blue LED, 24 h, without K-PHI

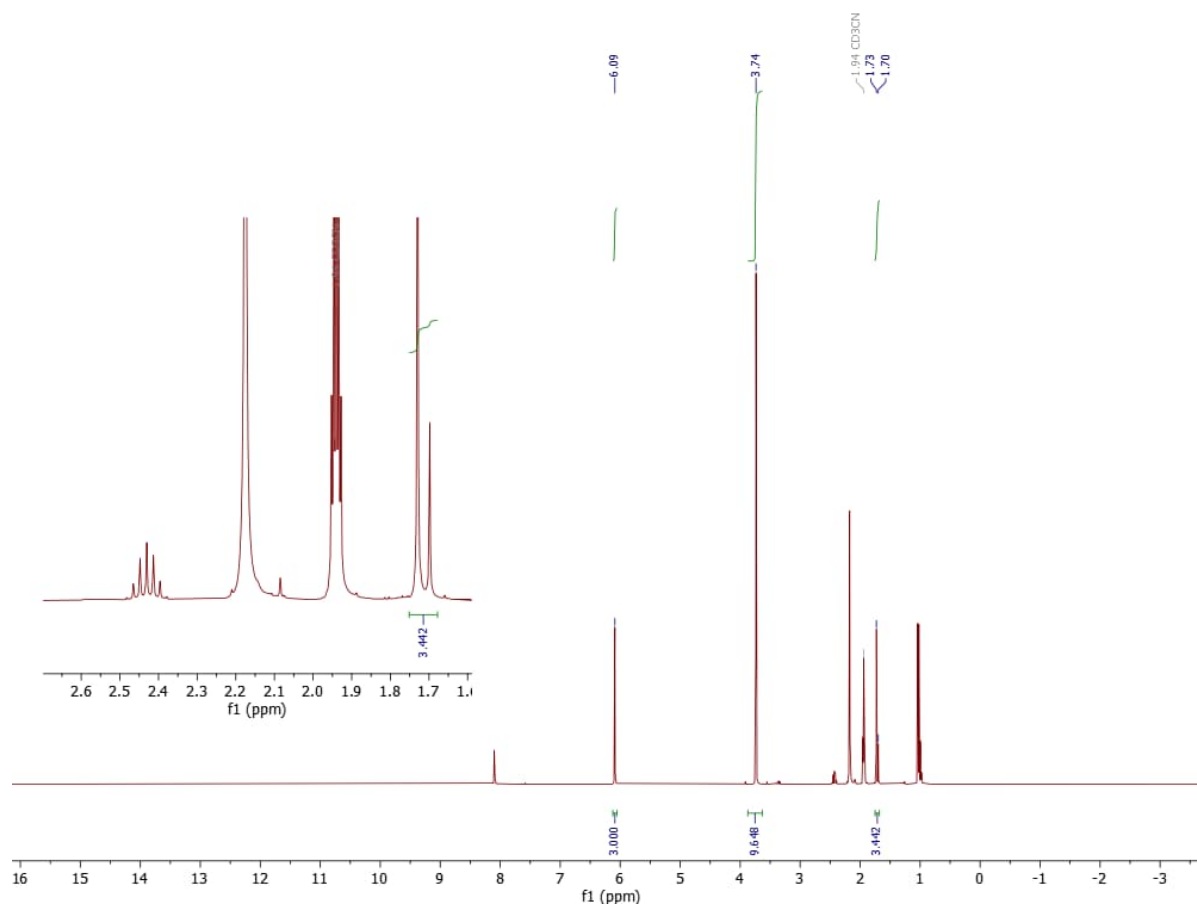
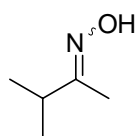


$$Y = \frac{0 \cdot 3 \cdot 10}{3.000 \cdot 2 \cdot 50} \cdot 4 \cdot 100\% = 0\%$$

$$X = \left(1 - \frac{4.395 \cdot 3 \cdot 10}{3.000 \cdot 3 \cdot 50}\right) \cdot 4 \cdot 100\% < 0\%$$



## 3-methylbutan-2-one oxime (1k) oxidation, red LED, 24 h

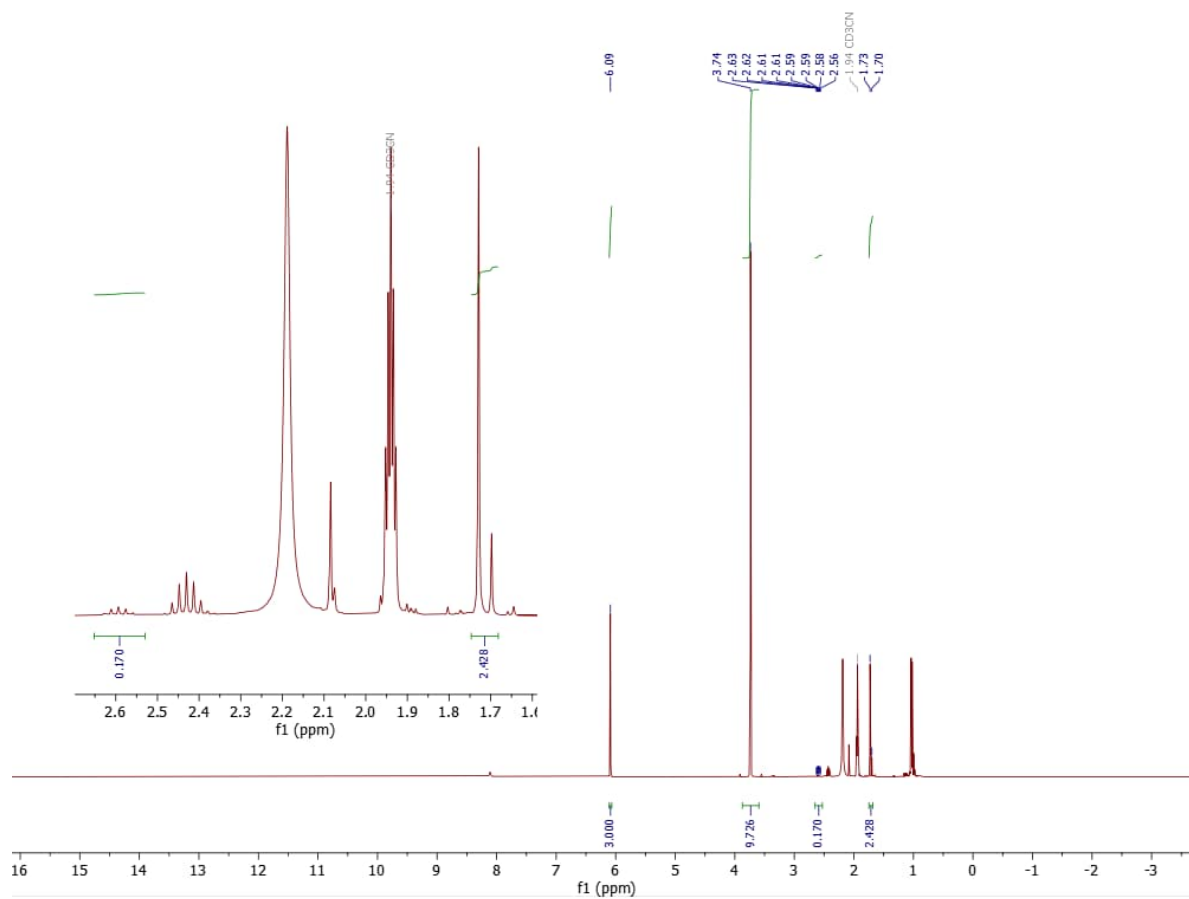
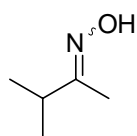


$$Y = \frac{0 \cdot 3 \cdot 10}{3.000 \cdot 1 \cdot 50} \cdot 4 \cdot 100\% = 0\%$$

$$X = \left(1 - \frac{3.442 \cdot 3 \cdot 10}{3.000 \cdot 3 \cdot 50}\right) \cdot 4 \cdot 100\% = 8\%$$



## 3-methylbutan-2-one oxime (1k) oxidation, red LED, 120 h

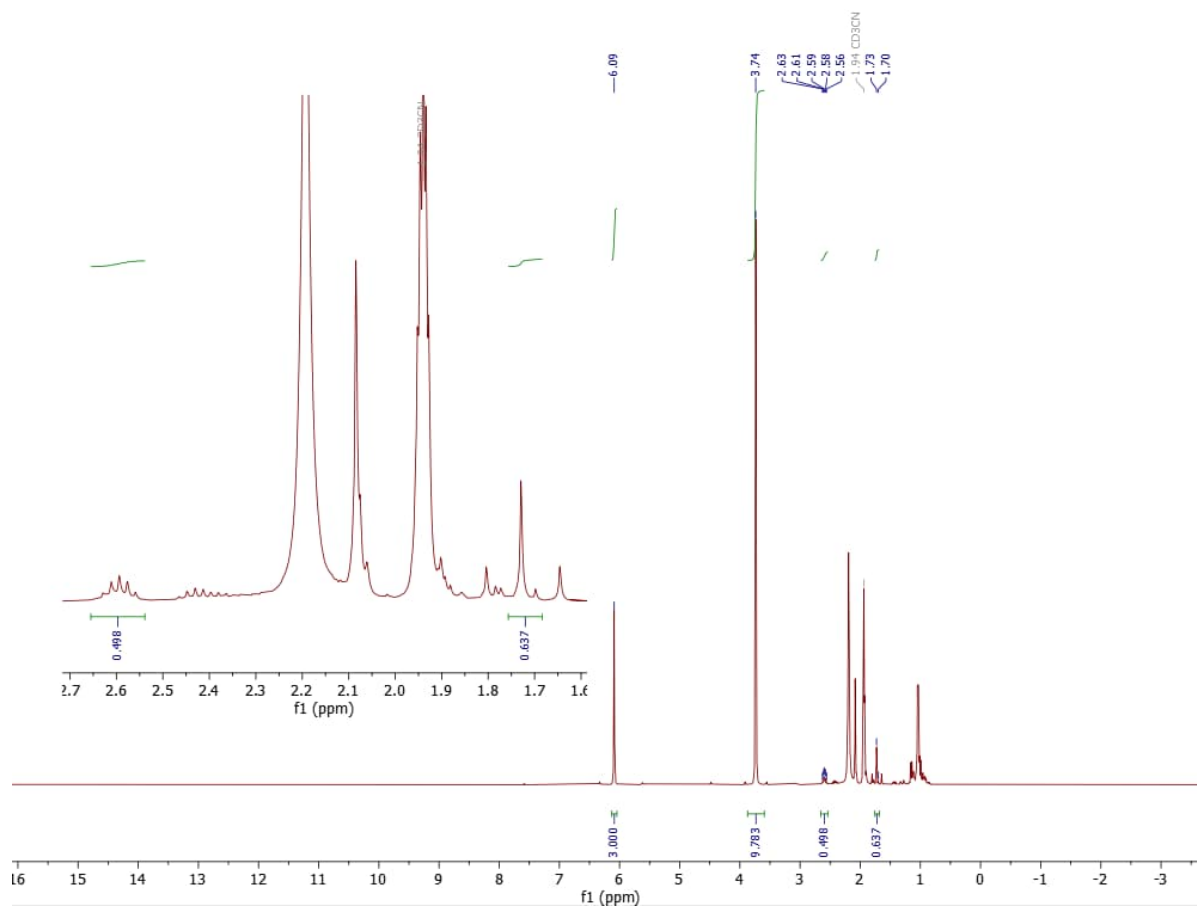
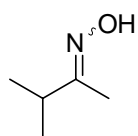


$$Y = \frac{0.170 \cdot 3 \cdot 10}{3.000 \cdot 1 \cdot 50} \cdot 4 \cdot 100\% = 14\%$$

$$X = \left(1 - \frac{2.428 \cdot 3 \cdot 10}{3.000 \cdot 3 \cdot 50}\right) \cdot 4 \cdot 100\% = 35\%$$



## 3-methylbutan-2-one oxime (1k) oxidation, blue LED, 24 h, with K-PHI

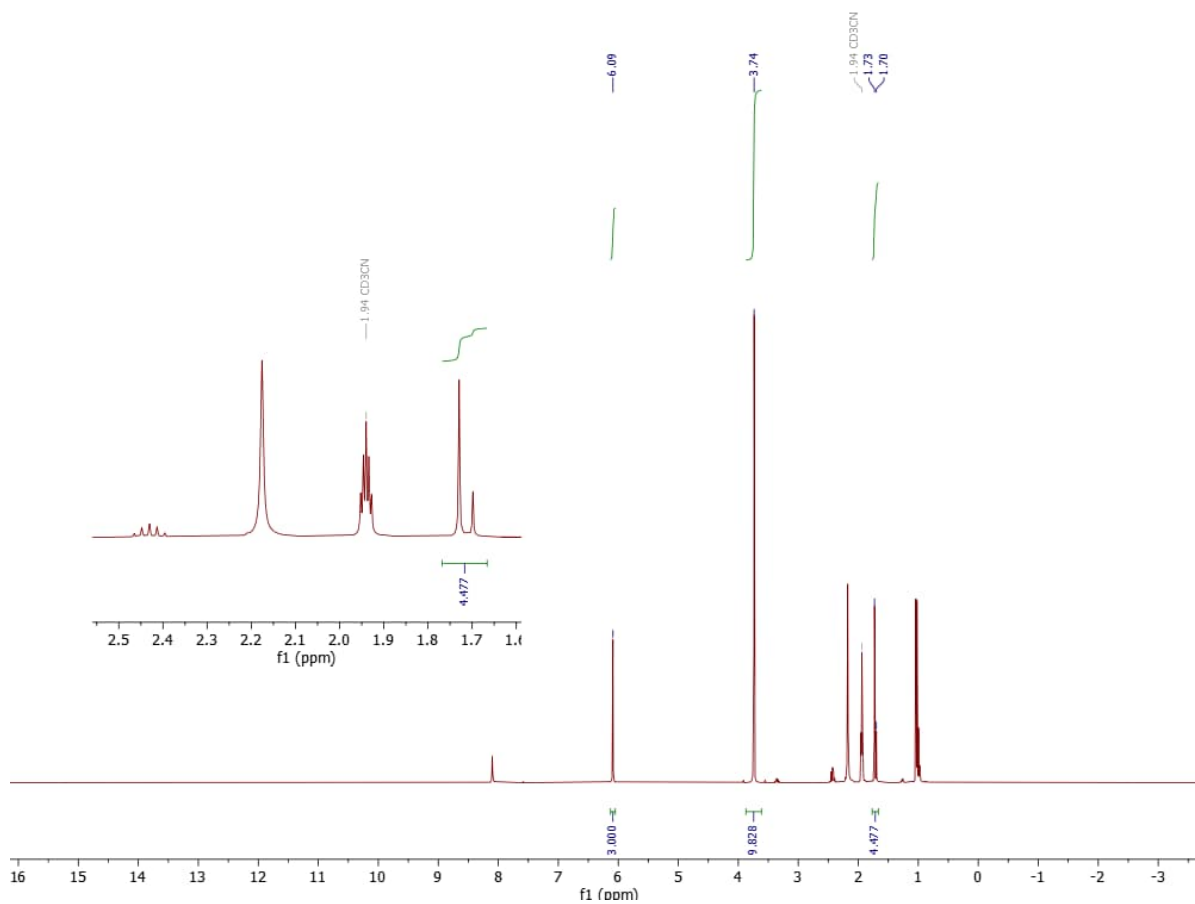
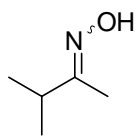


$$Y = \frac{0.498 \cdot 3 \cdot 10}{3.000 \cdot 1 \cdot 50} \cdot 4 \cdot 100\% = 40\%$$

$$X = \left(1 - \frac{0.637 \cdot 3 \cdot 10}{3.000 \cdot 3 \cdot 50}\right) \cdot 4 \cdot 100\% = 83\%$$



## 3-methylbutan-2-one oxime (1k) oxidation, blue LED, 24 h, without K-PHI

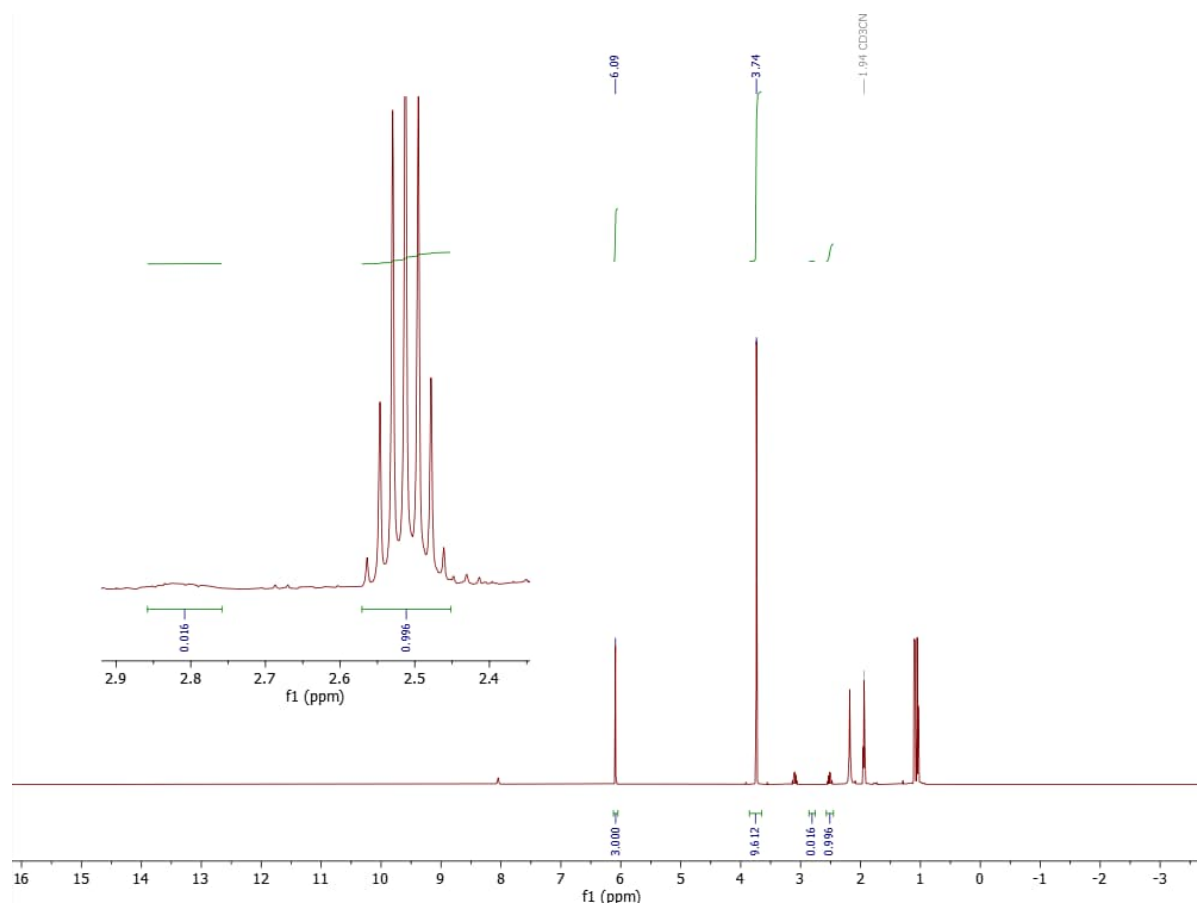
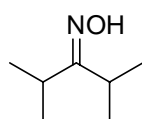


$$Y = \frac{0 \cdot 3 \cdot 10}{3.000 \cdot 1 \cdot 50} \cdot 4 \cdot 100\% = 0\%$$

$$X = \left(1 - \frac{4.477 \cdot 3 \cdot 10}{3.000 \cdot 3 \cdot 50}\right) \cdot 4 \cdot 100\% < 0\%$$



## 2,4-dimethylpentan-3-one oxime (1I) oxidation, red LED, 24 h

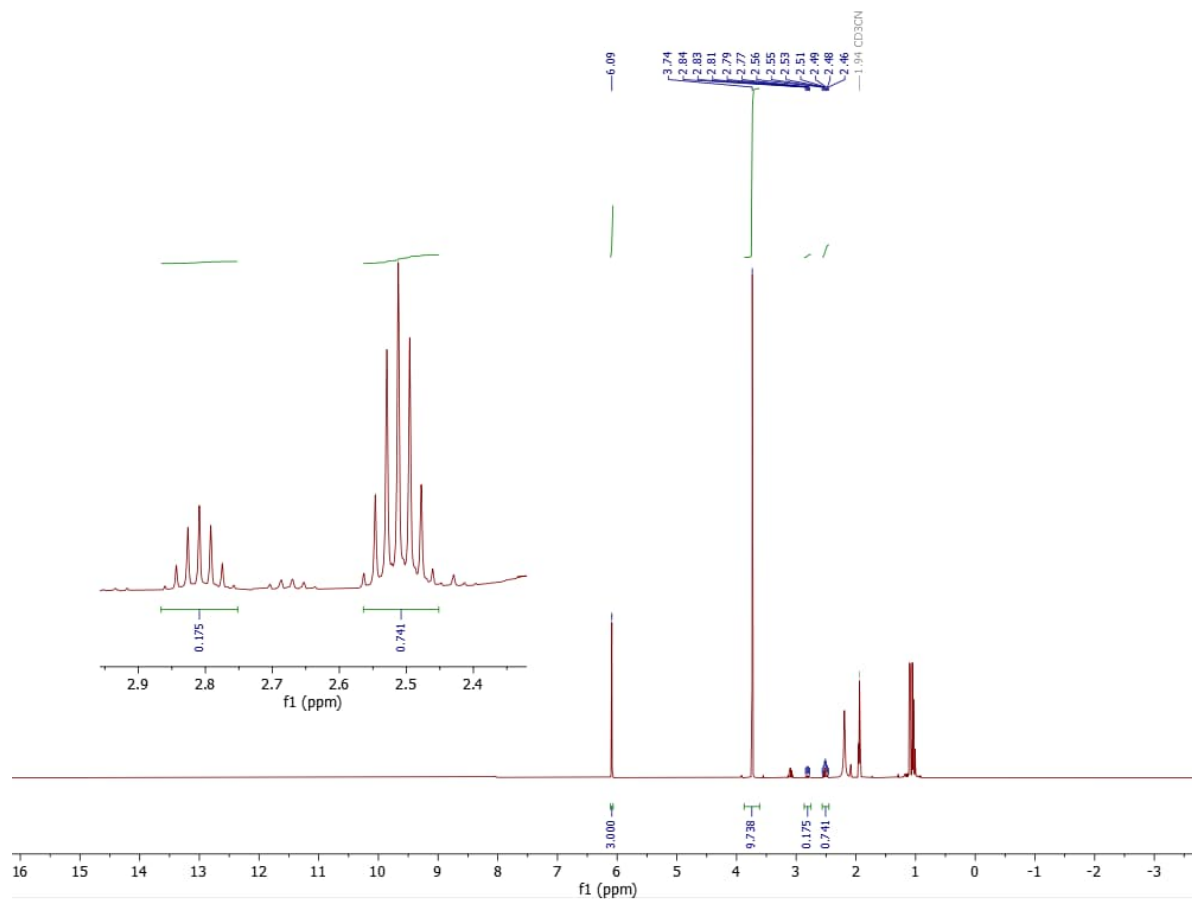
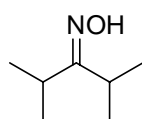


$$Y = \frac{0.016 \cdot 3 \cdot 10}{3.000 \cdot 2 \cdot 50} \cdot 4 \cdot 100\% = 1\%$$

$$X = \left(1 - \frac{0.996 \cdot 3 \cdot 10}{3.000 \cdot 1 \cdot 50}\right) \cdot 4 \cdot 100\% = 20\%$$



## 2,4-dimethylpentan-3-one oxime (1) oxidation, red LED, 120 h

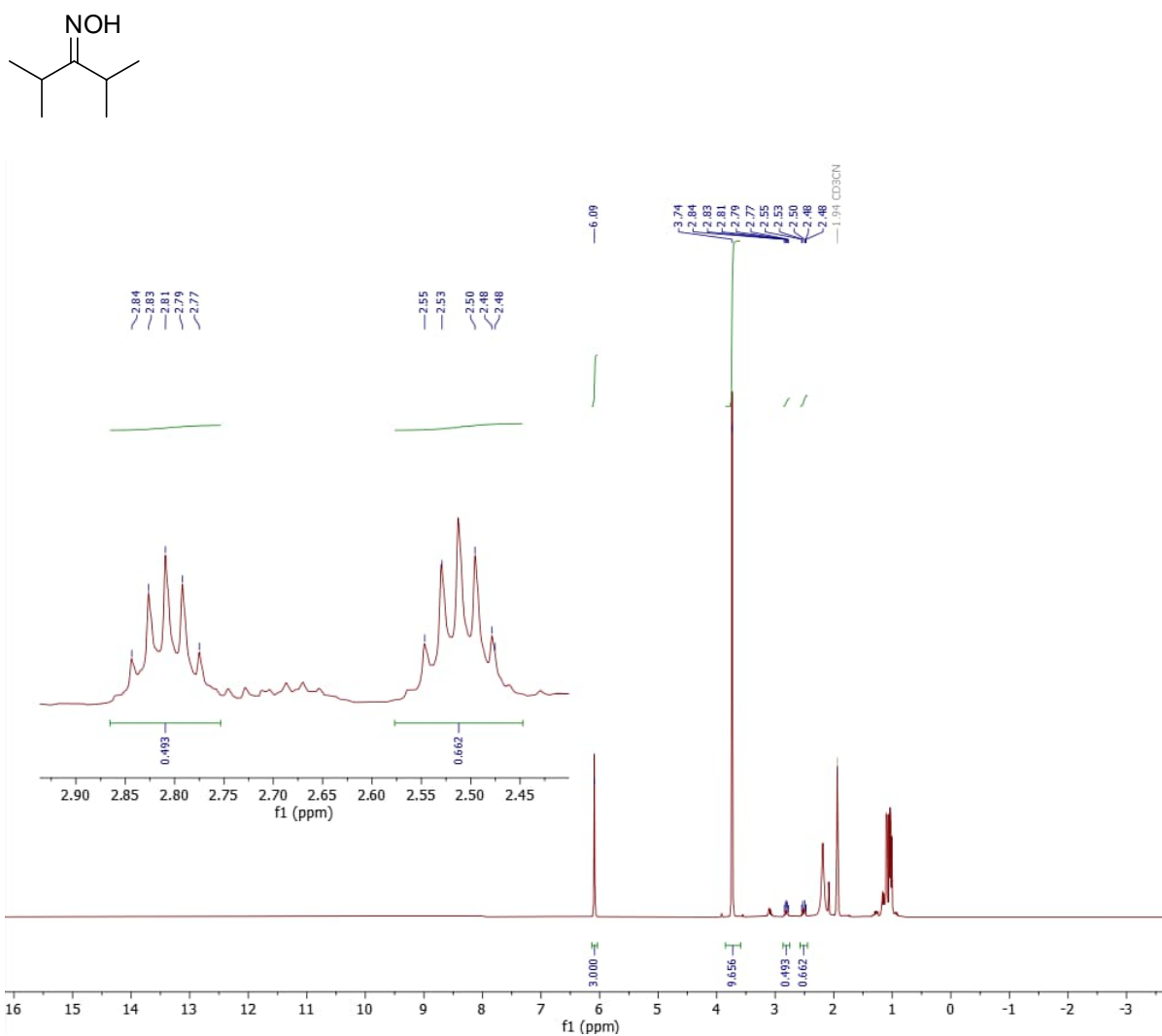


$$Y = \frac{0.175 \cdot 3 \cdot 10}{3.000 \cdot 2 \cdot 50} \cdot 4 \cdot 100\% = 7\%$$

$$X = \left(1 - \frac{0.741 \cdot 3 \cdot 10}{3.000 \cdot 1 \cdot 50}\right) \cdot 4 \cdot 100\% = 41\%$$



## 2,4-dimethylpentan-3-one oxime (1I) oxidation, blue LED, 24 h, with K-PHI

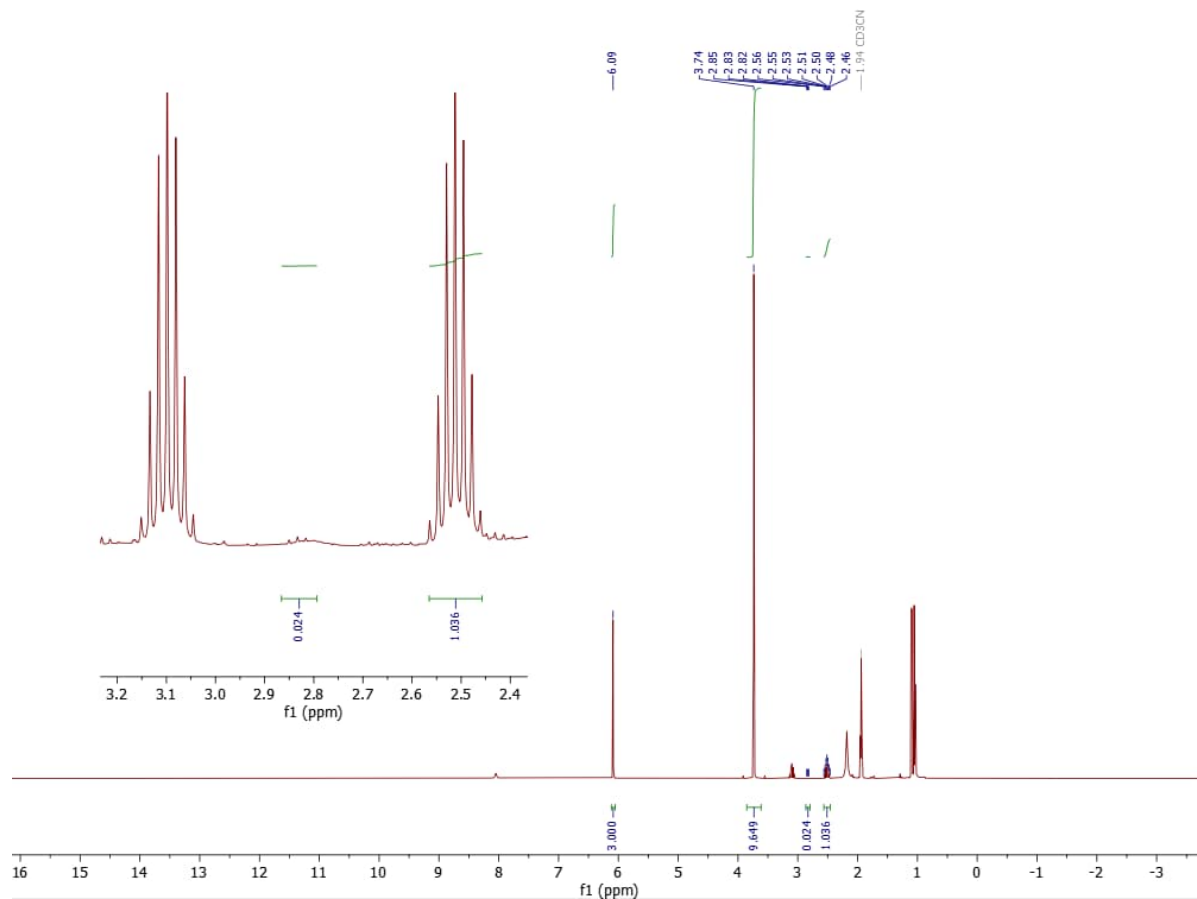
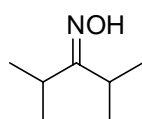


$$Y = \frac{0.493 \cdot 3 \cdot 10}{3.000 \cdot 2 \cdot 50} \cdot 4 \cdot 100\% = 20\%$$

$$X = \left(1 - \frac{0.662 \cdot 3 \cdot 10}{3.000 \cdot 1 \cdot 50}\right) \cdot 4 \cdot 100\% = 47\%$$



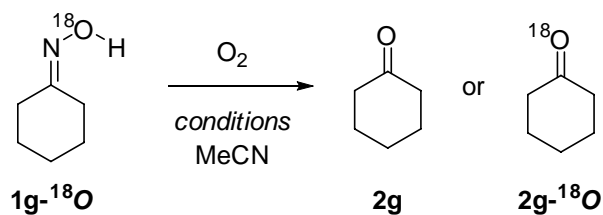
## 2,4-dimethylpentan-3-one oxime (1I) oxidation, blue LED, 24 h, without K-PHI



$$Y = \frac{0.024 \cdot 3 \cdot 10}{3.000 \cdot 2 \cdot 50} \cdot 4 \cdot 100\% = 1\%$$

$$X = \left(1 - \frac{1.036 \cdot 3 \cdot 10}{3.000 \cdot 1 \cdot 50}\right) \cdot 4 \cdot 100\% = 7\%$$

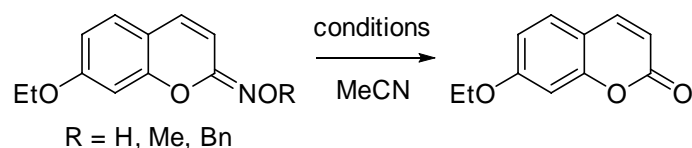


*Isotope Label Oxidation Experiment*

Oxidation of cyclohexanone oxime- $^{18}\text{O}$  was carried out as described in section 4.1 (method B for reactions 1 and 2 or method C for reaction 3) on 50  $\mu\text{mol}$  scale in 2 mL of acetonitrile in three various conditions to determine isotope distribution in the final product:

1. Red LED irradiation, 5 mg K-PHI,
2. Blue LED irradiation, 5 mg K-PHI,
3. Blue LED irradiation.

After workup, 200  $\mu\text{L}$  samples of reaction mixtures were taken directly for GC-MS (10 min run, first 3 min discarded) and 4.71 to 4.79 min part was analyzed (see GC-MS data for details).

*Unsubstituted and O-alkyl 7-ethoxy-2H-chromen-2-one Oxime Oxidation*

The experiments were carried out on 50  $\mu\text{mol}$  scale in 2 mL of acetonitrile as described in section 4.1 (method A or C depending on presence of K-PHI in a mixture) under blue, green or red LED irradiation; qNMR spectra were recorded in  $\text{CDCl}_3$  instead of DMSO using 10  $\mu\text{mol}$  of 1,3,5-trimethoxybenzene as internal standard (see data below).

If reaction was performed under argon atmosphere, the mixture was deoxygenated with 3 freeze-pump-thaw cycles on a Schlenk line.



### Quantitative NMR data

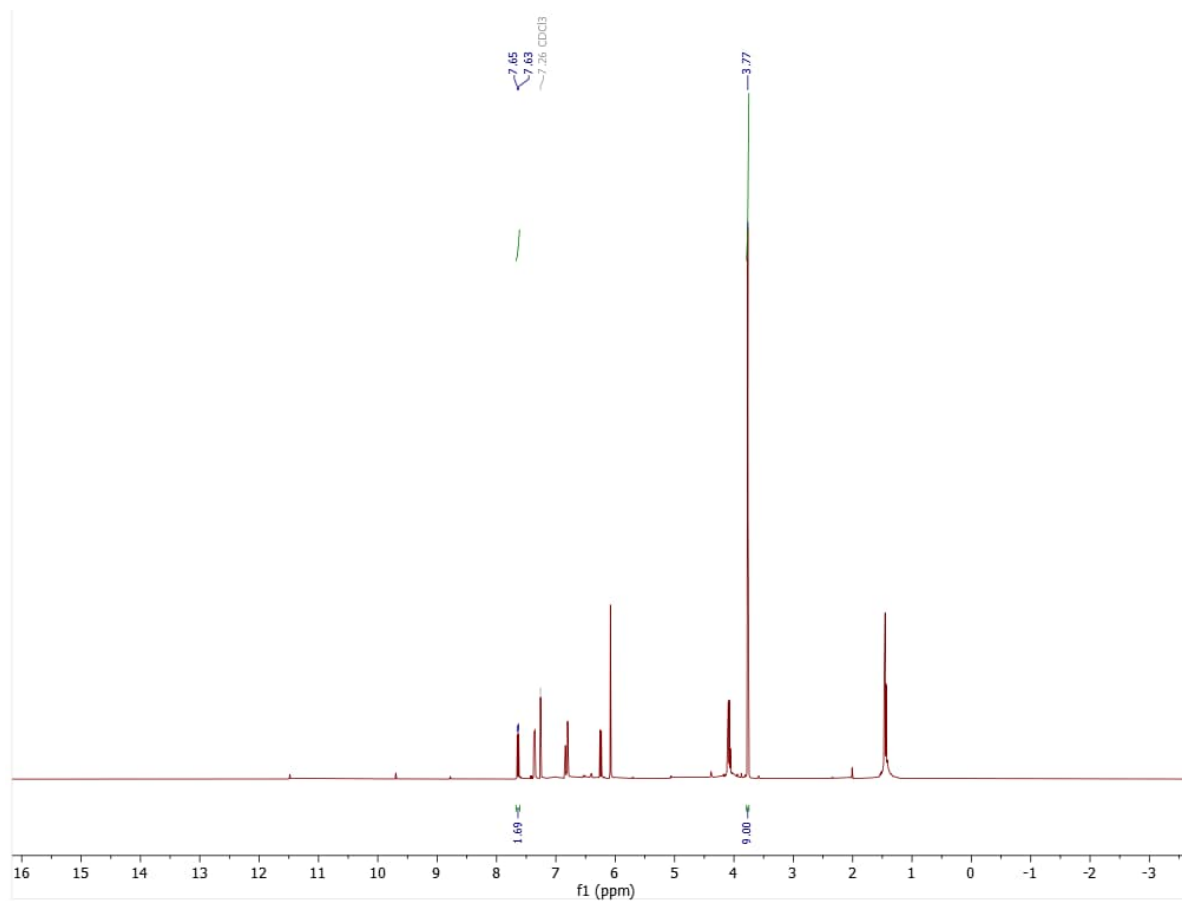
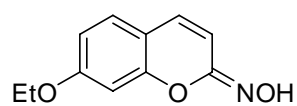
Yields were calculated using the following formulas:

$$Y = \frac{I_{carb} \cdot N_{St} \cdot n_{St}}{I_{St} \cdot N_{carb} \cdot n_{ox}} \cdot 100\%$$

Where  $Y$  is yield,  $I_{carb}$  is integral intensity of a carbonyl product signal,  $N_{carb}$  is number of protons corresponding to a carbonyl product signal,  $I_{St}$  is integral intensity of internal 1,3,5-trimethoxybenzene standard (aliphatic protons, 9.000),  $N_{St}$  is number of protons corresponding to the 1,3,5-trimethoxybenzene standard signal (aliphatic protons, 9),  $n_{ox}$  is amount of starting oxime taken into reaction (50  $\mu$ mol),  $n_{St}$  is amount of 1,3,5-trimethoxybenzene standard (10  $\mu$ mol).



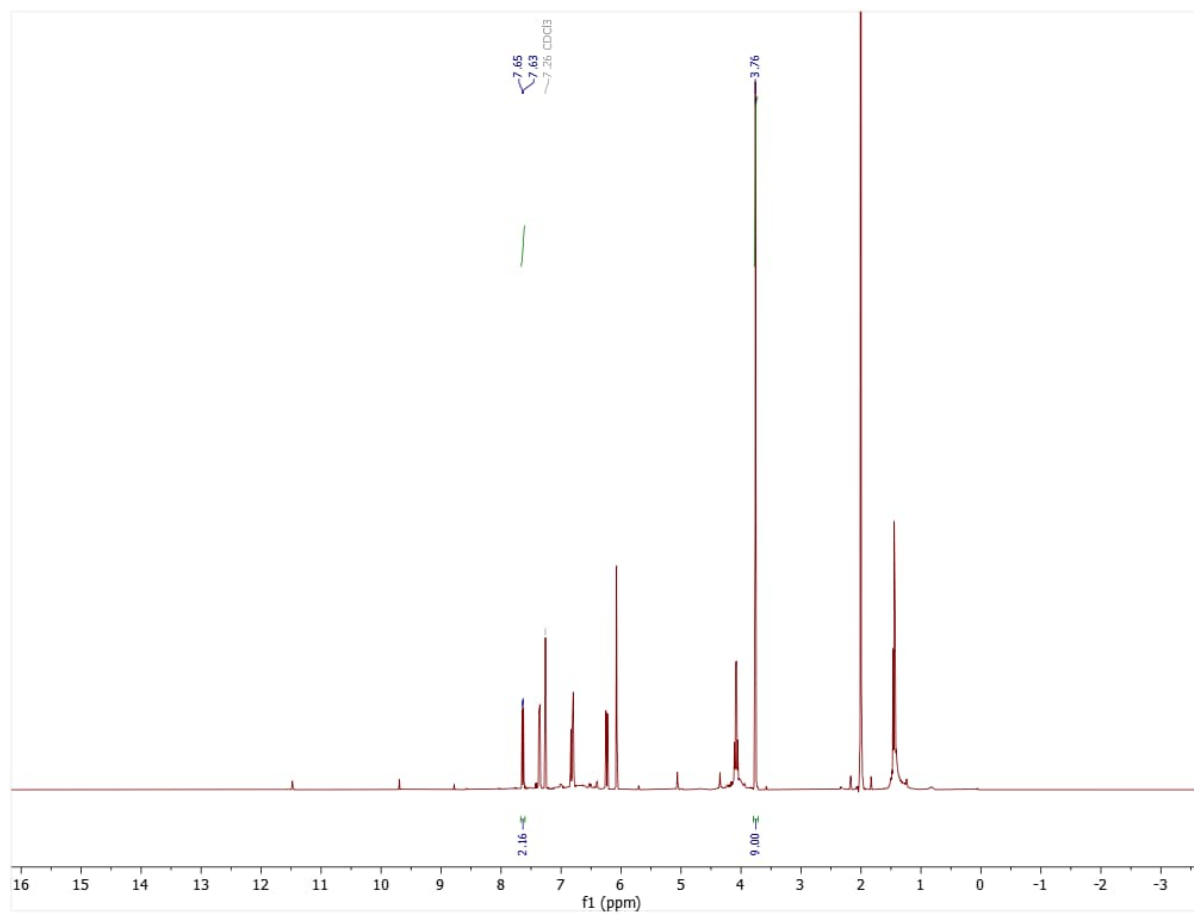
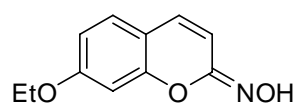
## 7-ethoxy-2H-chromen-2-one oxime (1i), blue LED, standard conditions, entry 1



$$Y = \frac{1.69 \cdot 9 \cdot 10}{9.00 \cdot 1 \cdot 50} \cdot 100\% = 35\%$$



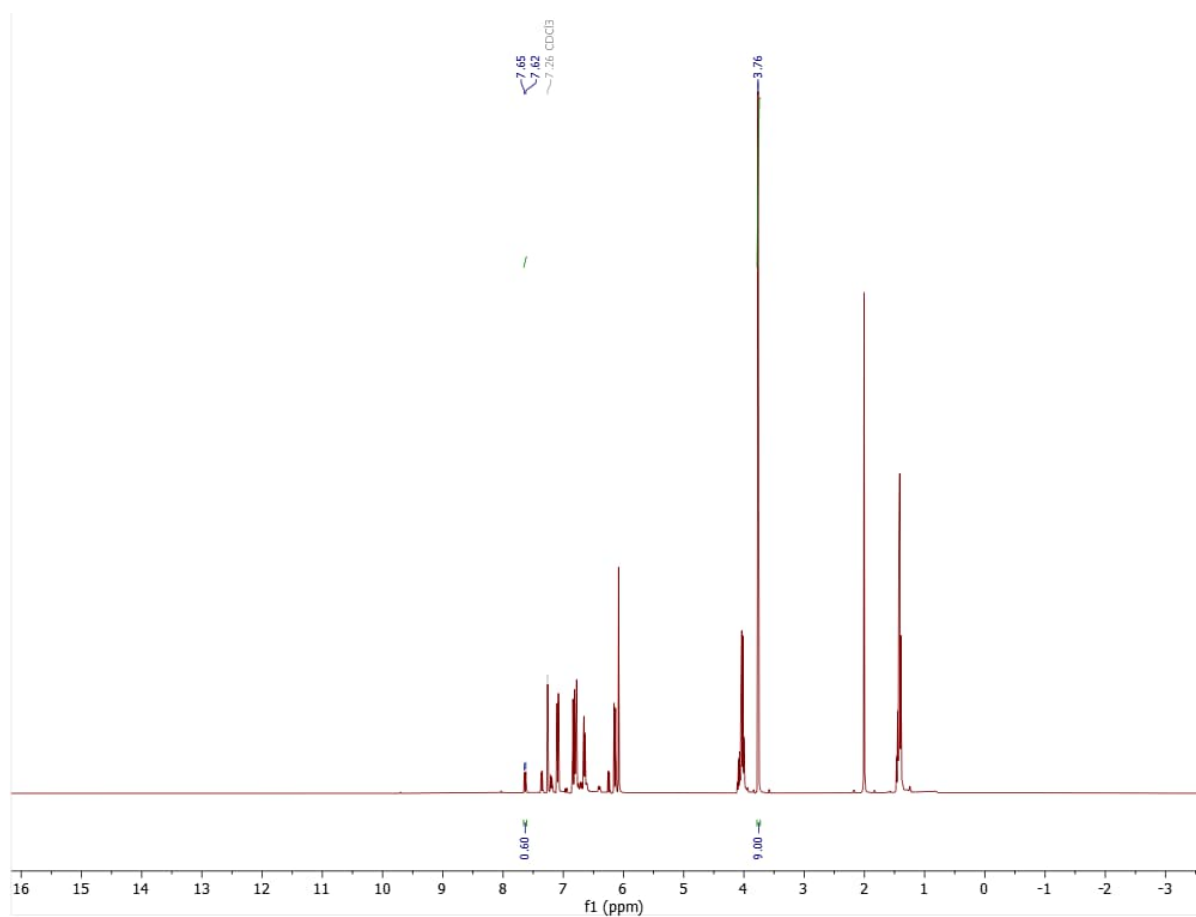
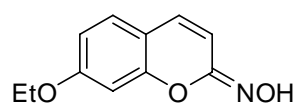
## 7-ethoxy-2H-chromen-2-one oxime (1i), blue LED, standard conditions, entry 2



$$Y = \frac{2.16 \cdot 9 \cdot 10}{9.00 \cdot 1 \cdot 50} \cdot 100\% = 43\%$$



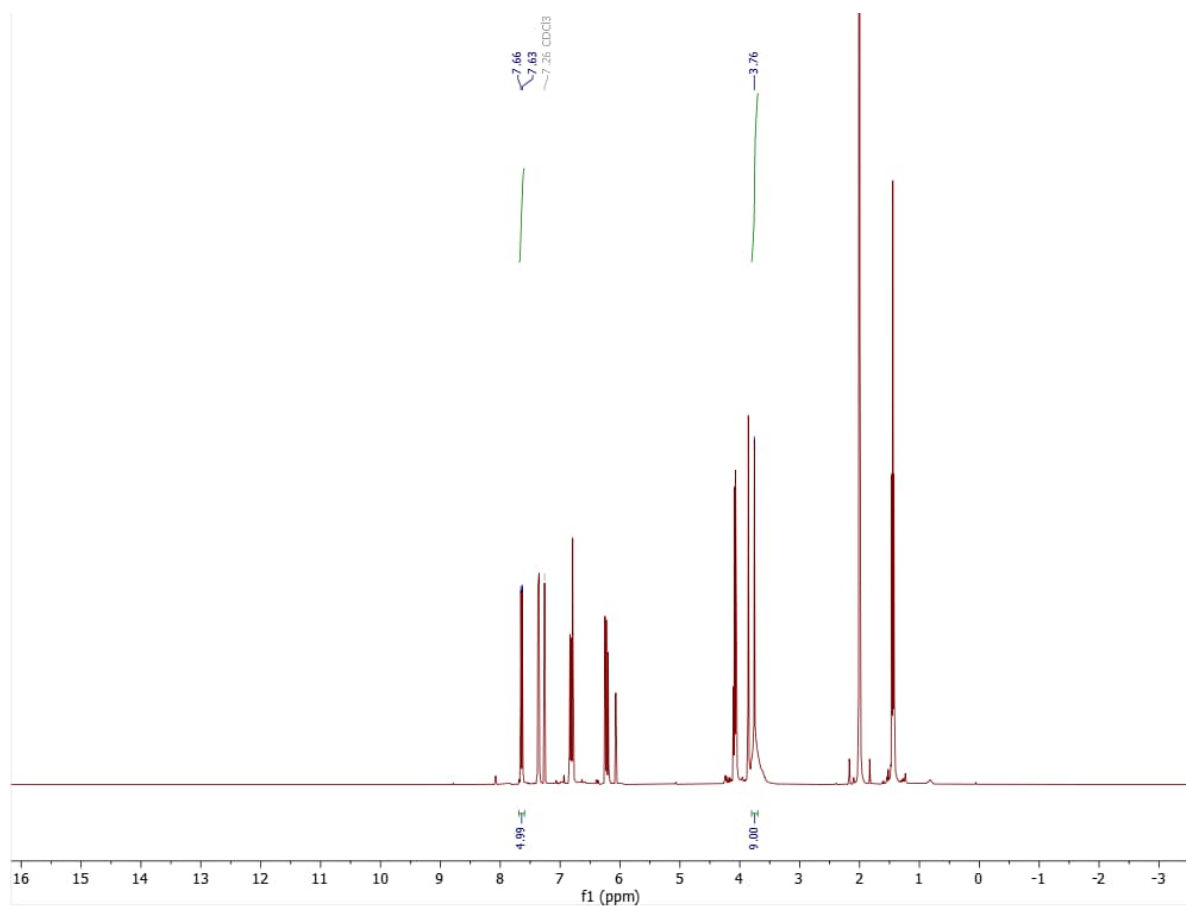
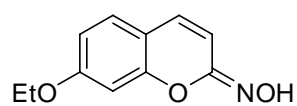
## 7-ethoxy-2H-chromen-2-one oxime (1i), blue LED, under argon



$$Y = \frac{0.60 \cdot 9 \cdot 10}{9.00 \cdot 1 \cdot 50} \cdot 100\% = 12\%$$



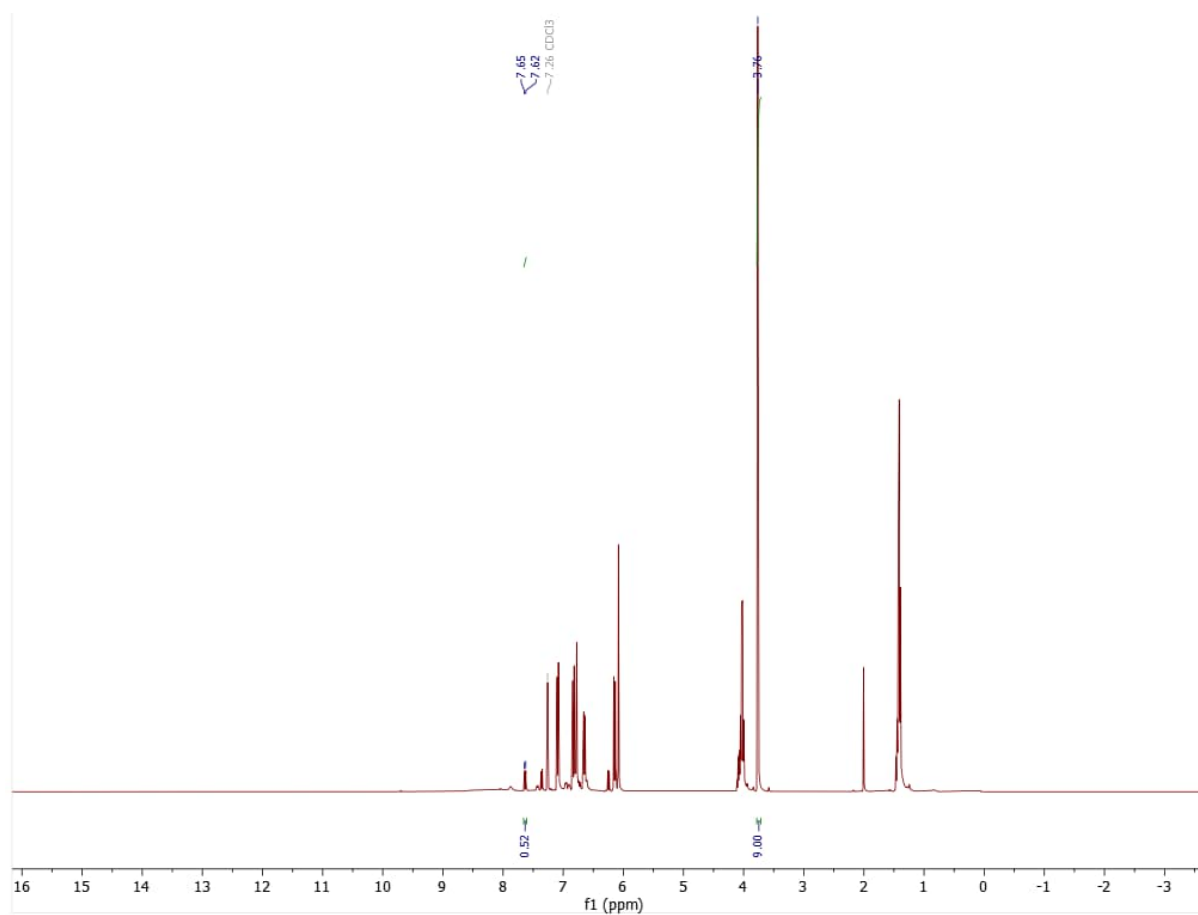
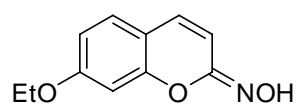
## 7-ethoxy-2H-chromen-2-one oxime (1i), blue LED, no K-PHI



$$Y = \frac{4.99 \cdot 9 \cdot 10}{9.00 \cdot 1 \cdot 50} \cdot 100\% = 99.8\%$$



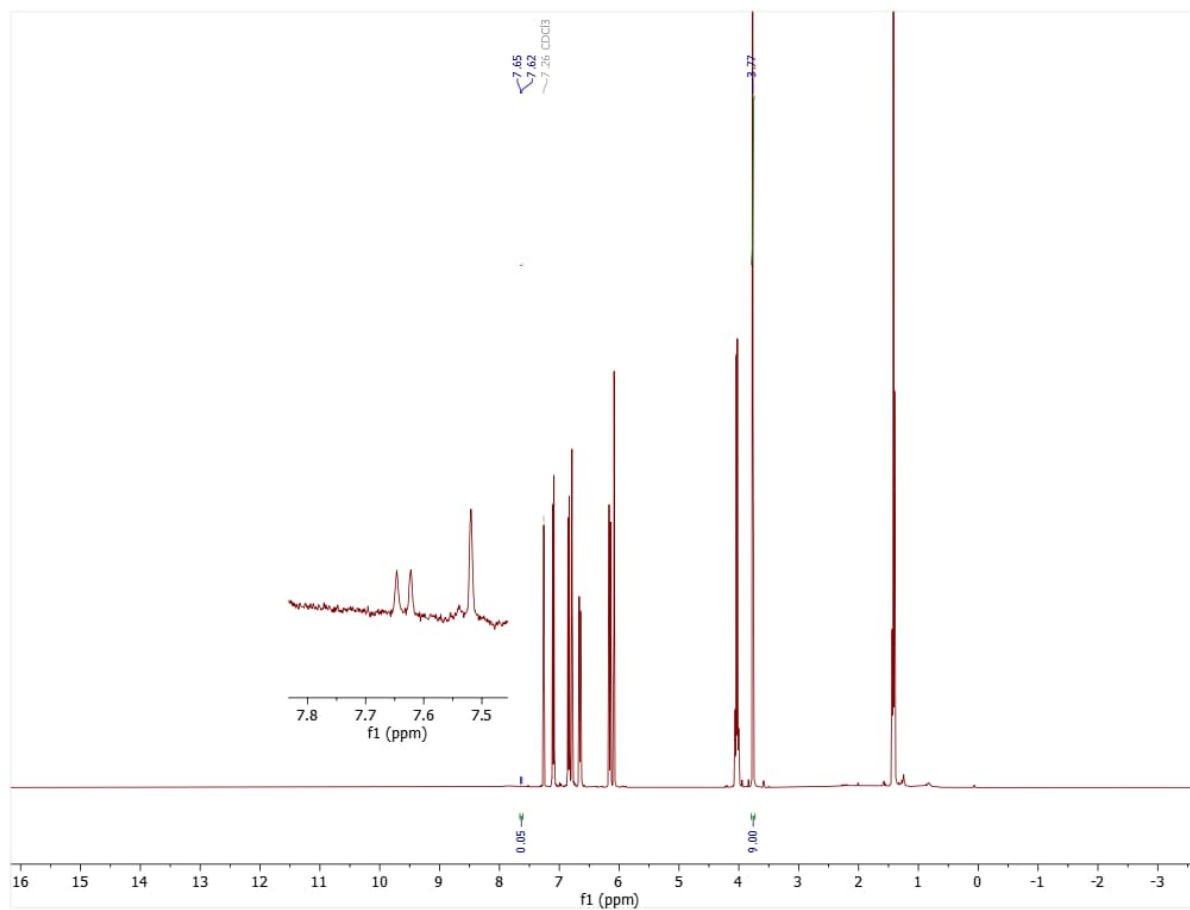
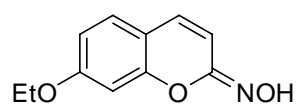
## 7-ethoxy-2H-chromen-2-one oxime (1i), blue LED, under argon, no K-PHI



$$Y = \frac{0.52 \cdot 9 \cdot 10}{9.00 \cdot 1 \cdot 50} \cdot 100\% = 10\%$$



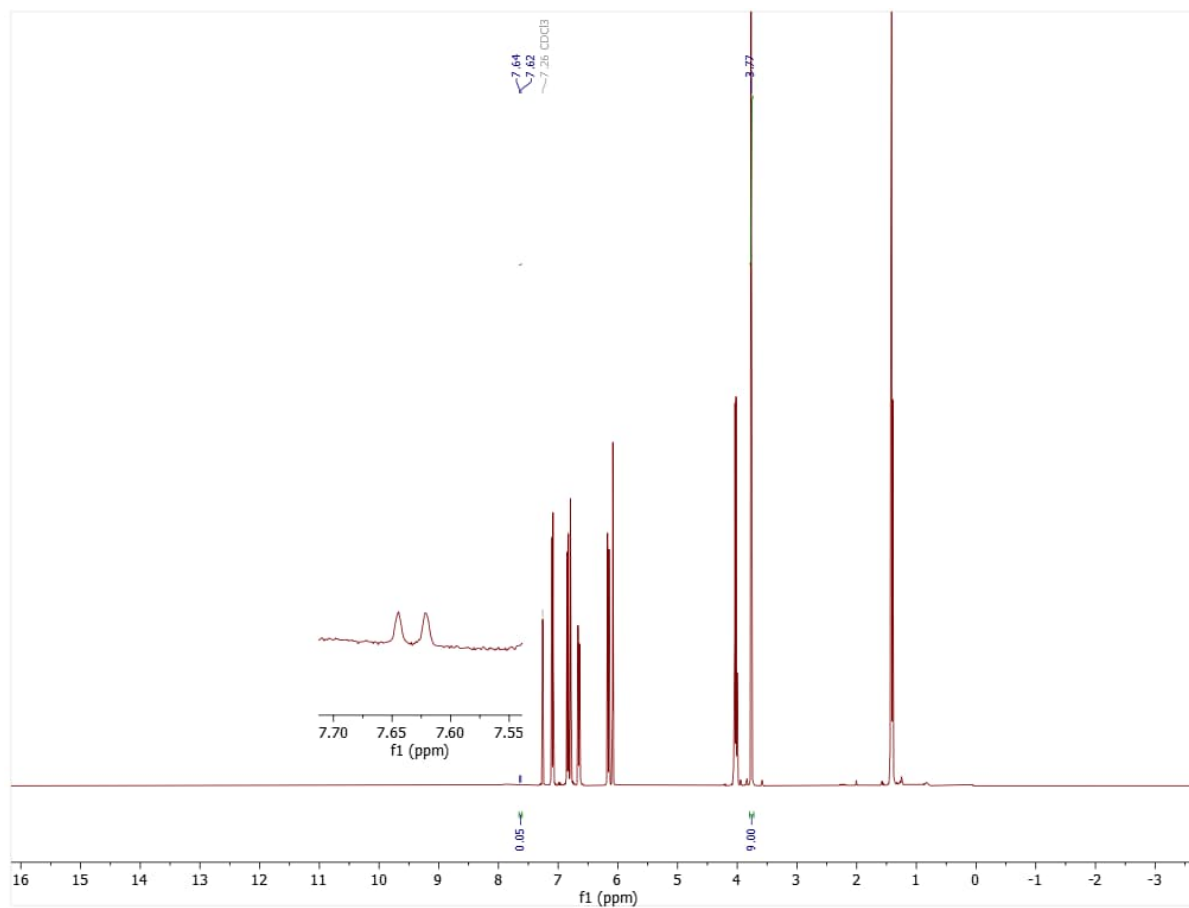
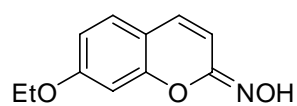
## 7-ethoxy-2H-chromen-2-one oxime (1i), no light, under argon, no K-PHI



$$Y = \frac{0.05 \cdot 9 \cdot 10}{9.00 \cdot 1 \cdot 50} \cdot 100\% = 1\%$$



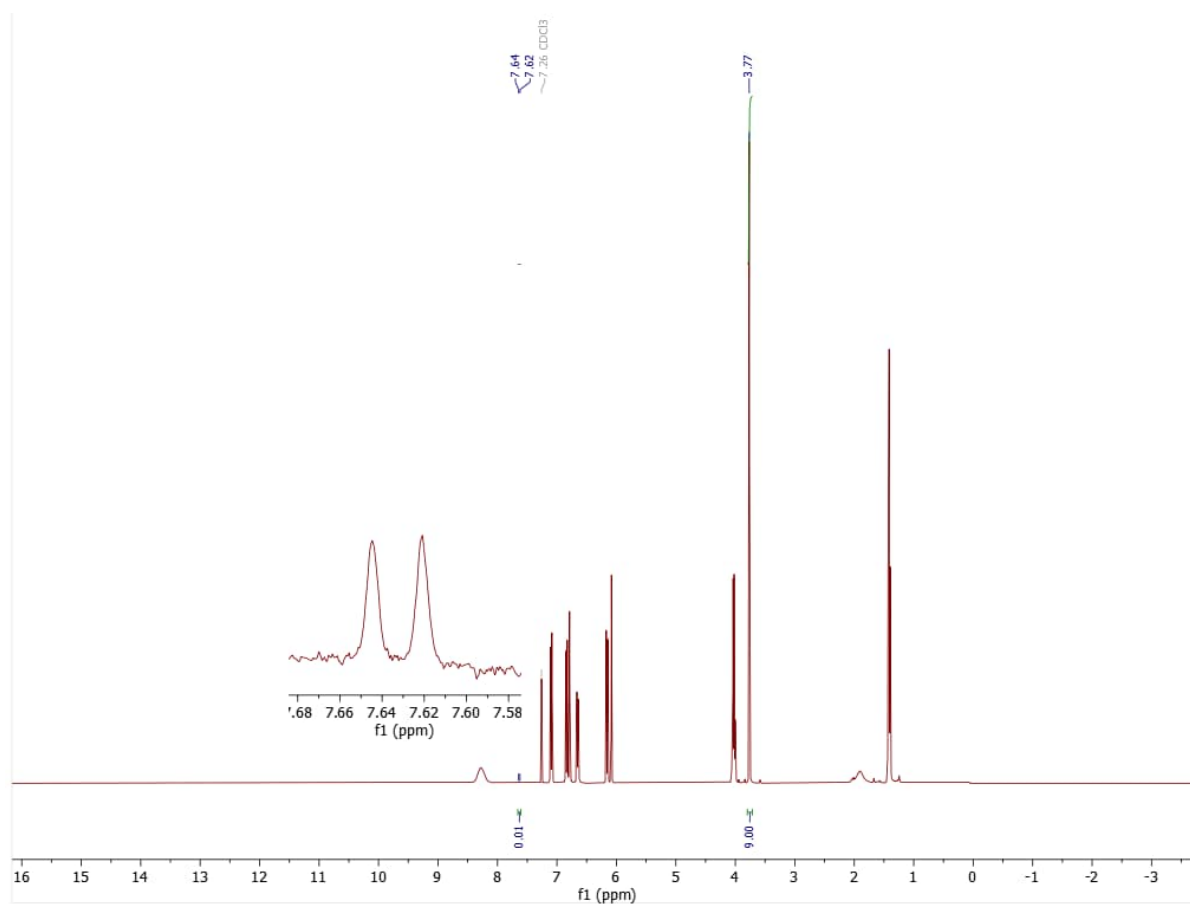
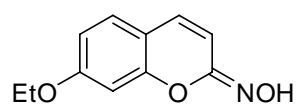
## 7-ethoxy-2H-chromen-2-one oxime (1i), no light, no K-PHI



$$Y = \frac{0.05 \cdot 9 \cdot 10}{9.00 \cdot 1 \cdot 50} \cdot 100\% = 1\%$$



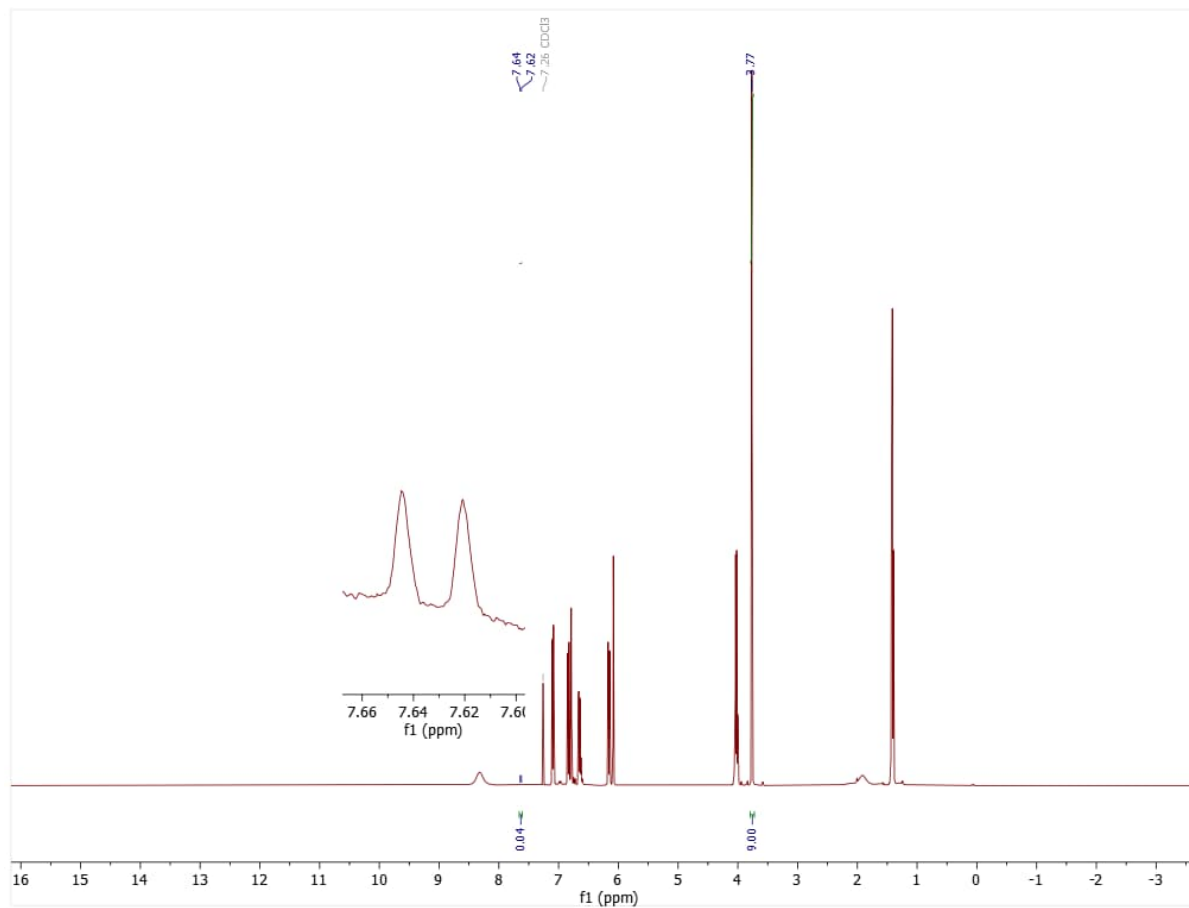
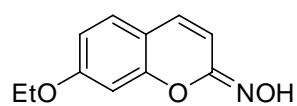
## 7-ethoxy-2H-chromen-2-one oxime (1i), no light



$$Y = \frac{0.01 \cdot 9 \cdot 10}{9.00 \cdot 1 \cdot 50} \cdot 100\% < 1\%$$



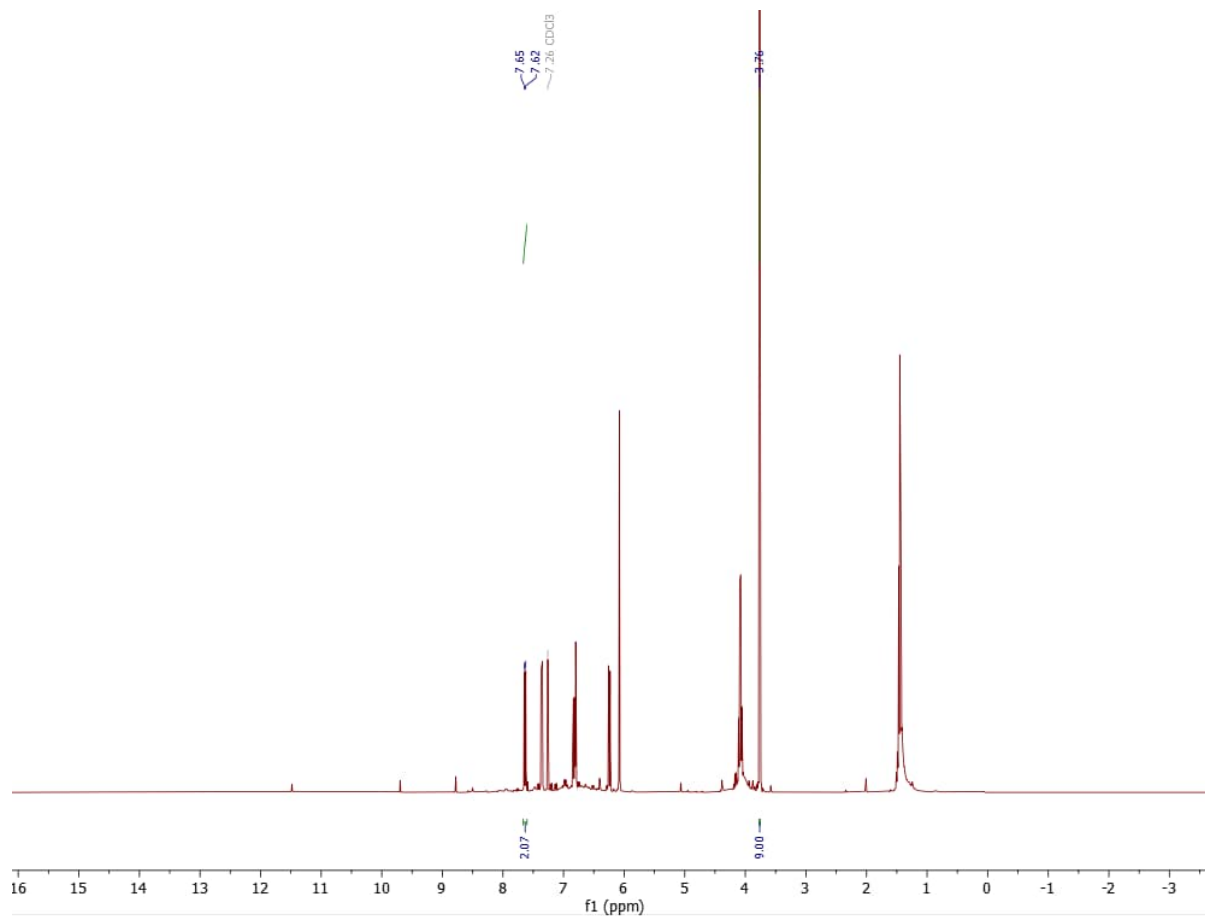
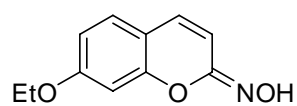
## 7-ethoxy-2H-chromen-2-one oxime (1i), no light, under argon



$$Y = \frac{0.04 \cdot 9 \cdot 10}{9.00 \cdot 1 \cdot 50} \cdot 100\% < 1\%$$



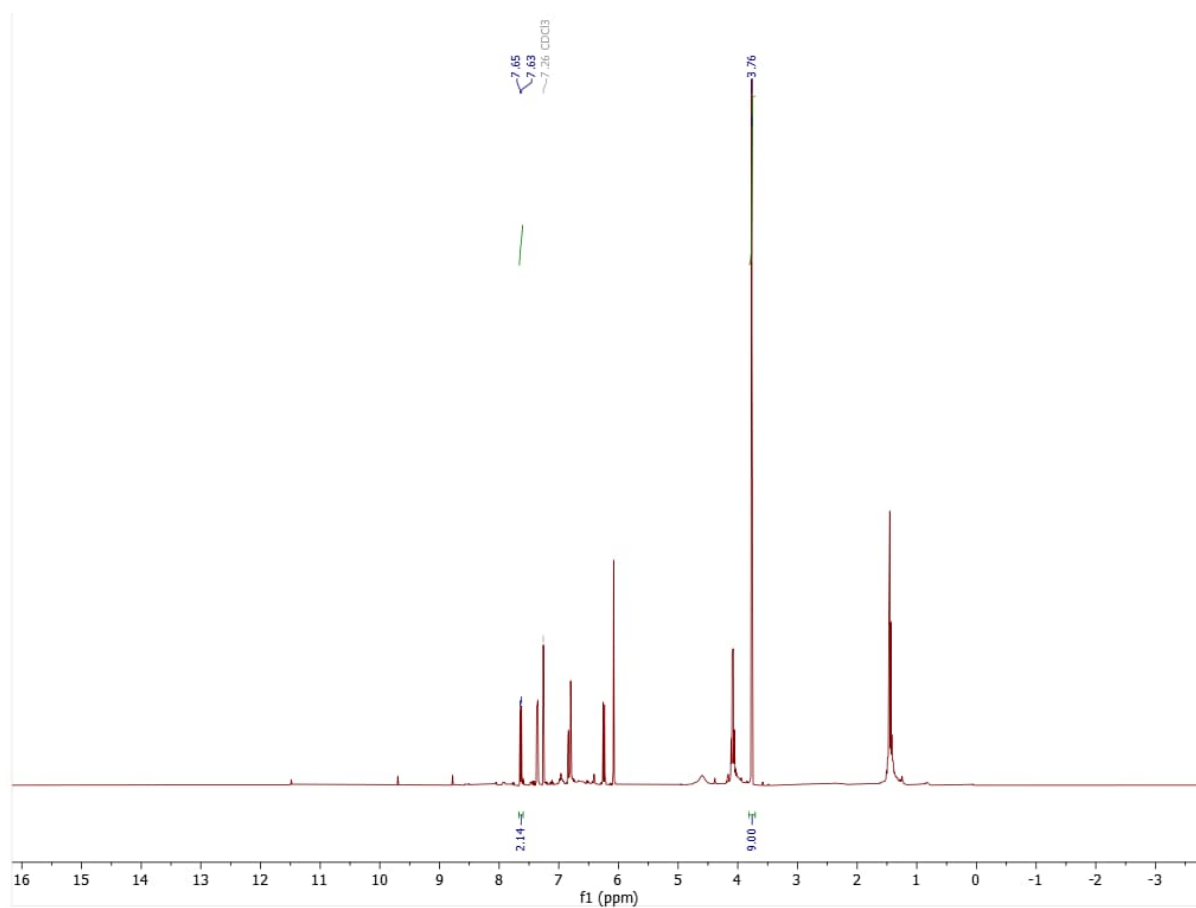
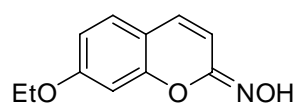
## 7-ethoxy-2H-chromen-2-one oxime (1i), green LED, standard conditions, entry 1



$$Y = \frac{2.07 \cdot 9 \cdot 10}{9.00 \cdot 1 \cdot 50} \cdot 100\% = 41\%$$



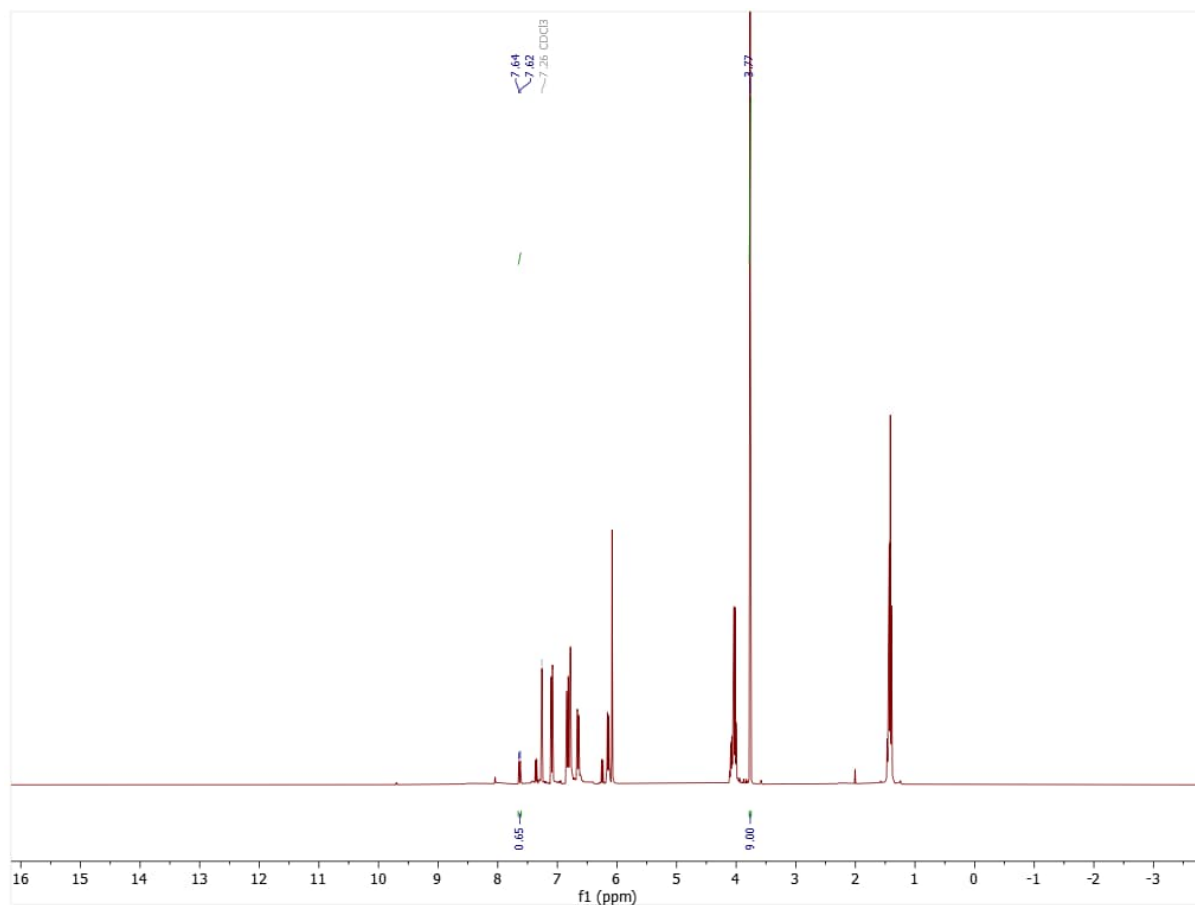
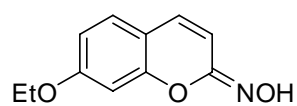
## 7-ethoxy-2H-chromen-2-one oxime (1i), green LED, standard conditions, entry 2



$$Y = \frac{2.14 \cdot 9 \cdot 10}{9.00 \cdot 1 \cdot 50} \cdot 100\% = 43\%$$



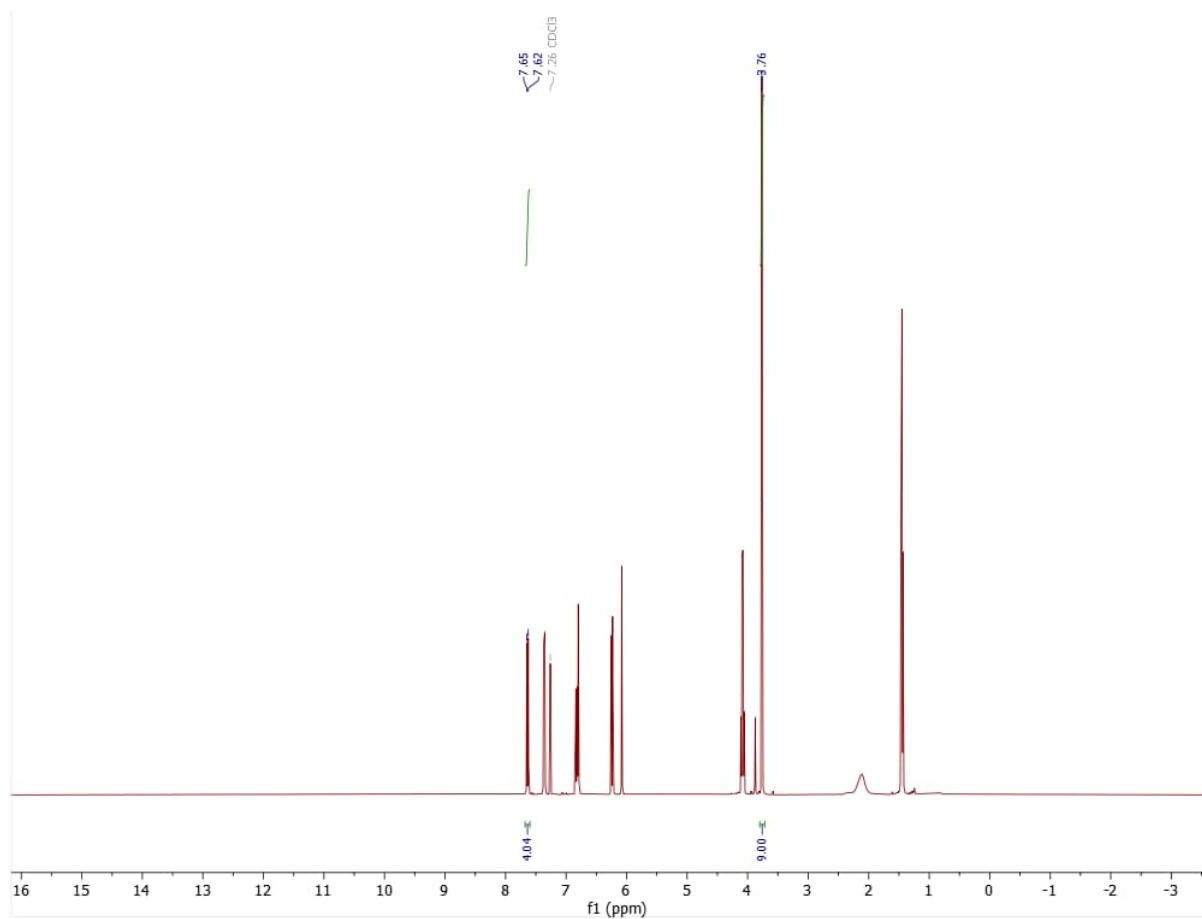
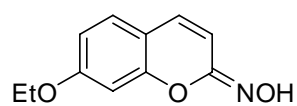
## 7-ethoxy-2H-chromen-2-one oxime (1i), green LED, under argon



$$Y = \frac{0.65 \cdot 9 \cdot 10}{9.00 \cdot 1 \cdot 50} \cdot 100\% = 13\%$$

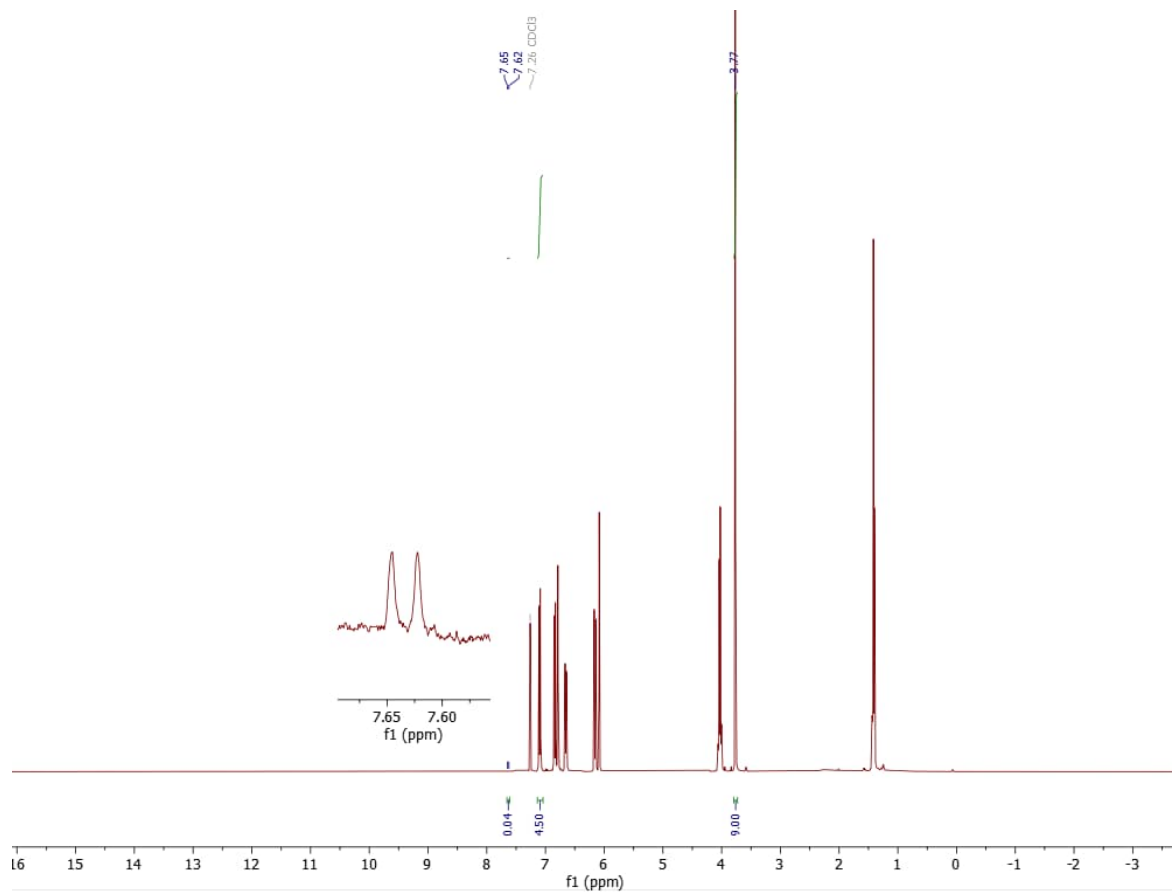
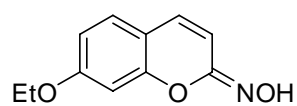


## 7-ethoxy-2H-chromen-2-one oxime (1i), green LED, no K-PHI



$$Y = \frac{4.04 \cdot 9 \cdot 10}{9.00 \cdot 1 \cdot 50} \cdot 100\% = 81\%$$

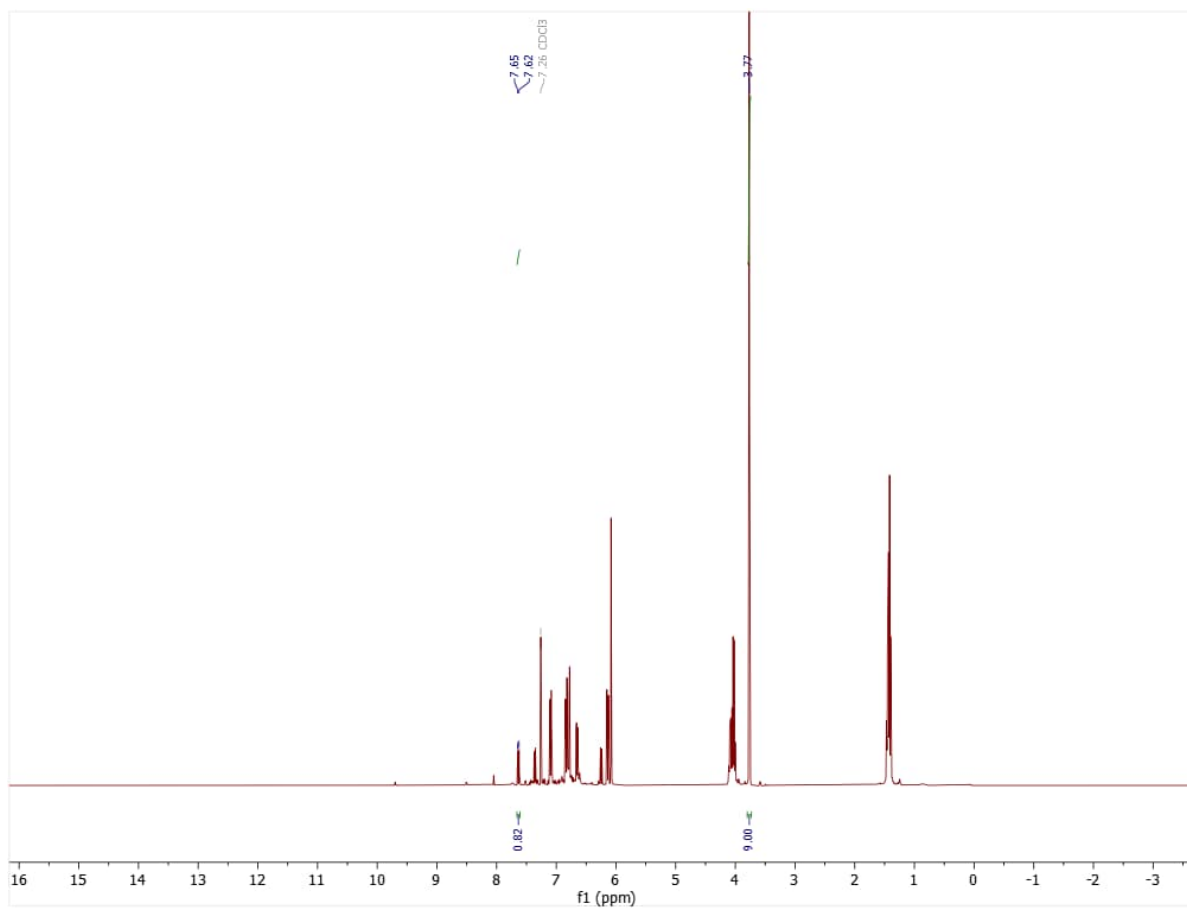
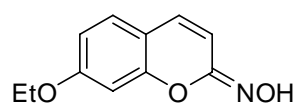


*7-ethoxy-2H-chromen-2-one oxime (1i), green LED, under argon, no K-PHI*

$$Y = \frac{0.04 \cdot 9 \cdot 10}{9.00 \cdot 1 \cdot 50} \cdot 100\% < 1\%$$



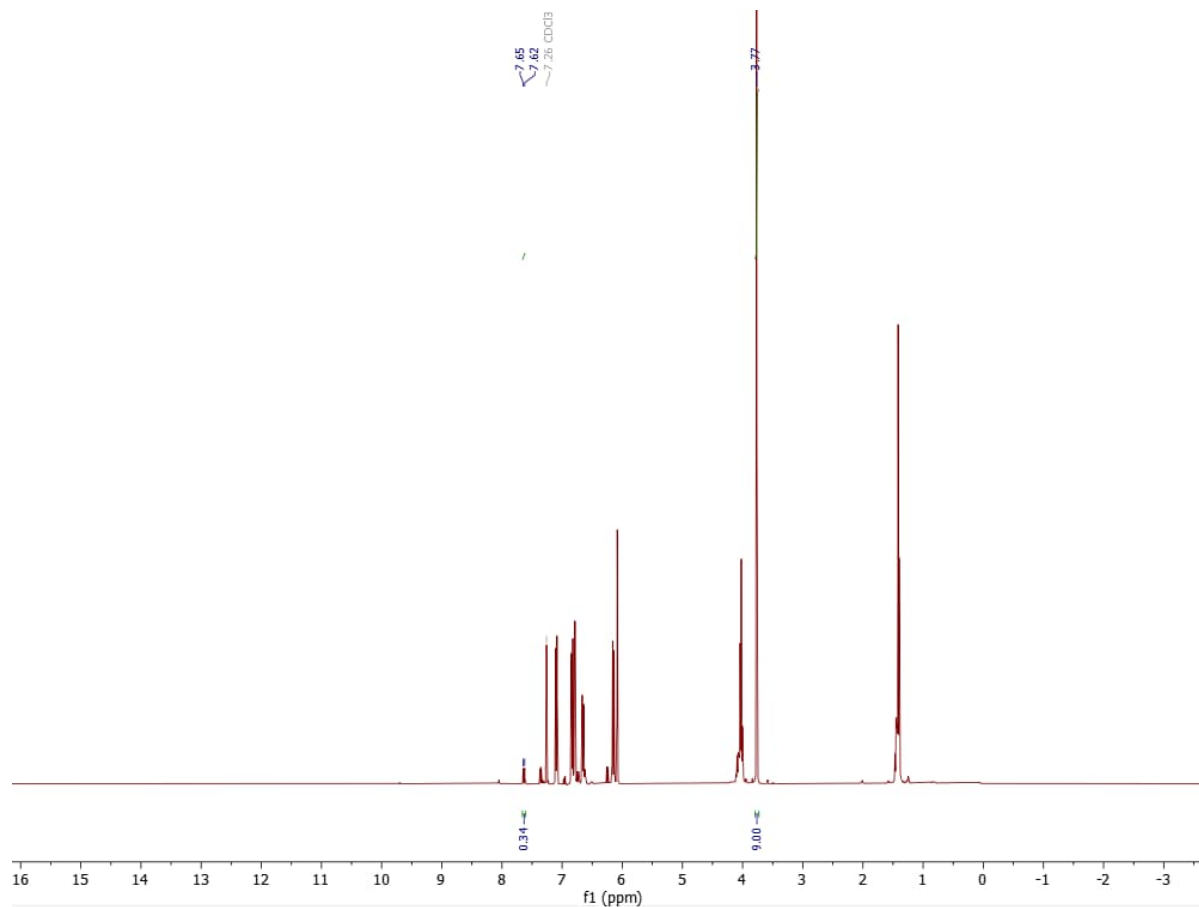
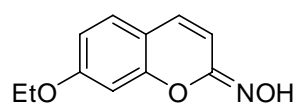
## 7-ethoxy-2H-chromen-2-one oxime (1i), red LED, standard conditions



$$Y = \frac{0.82 \cdot 9 \cdot 10}{9.00 \cdot 1 \cdot 50} \cdot 100\% = 16\%$$



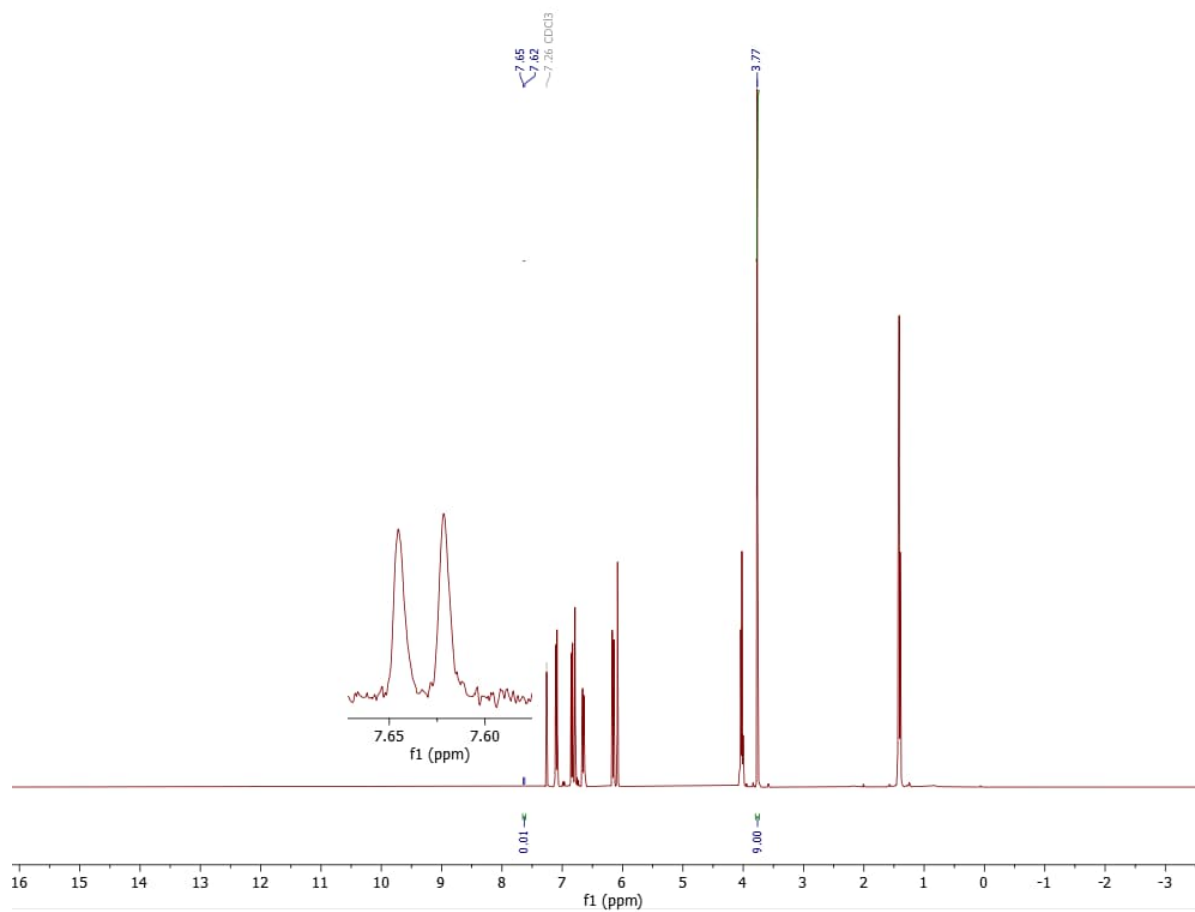
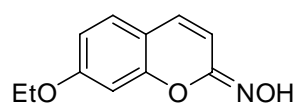
## 7-ethoxy-2H-chromen-2-one oxime (1i), red LED, under argon



$$Y = \frac{0.34 \cdot 9 \cdot 10}{9.00 \cdot 1 \cdot 50} \cdot 100\% = 7\%$$



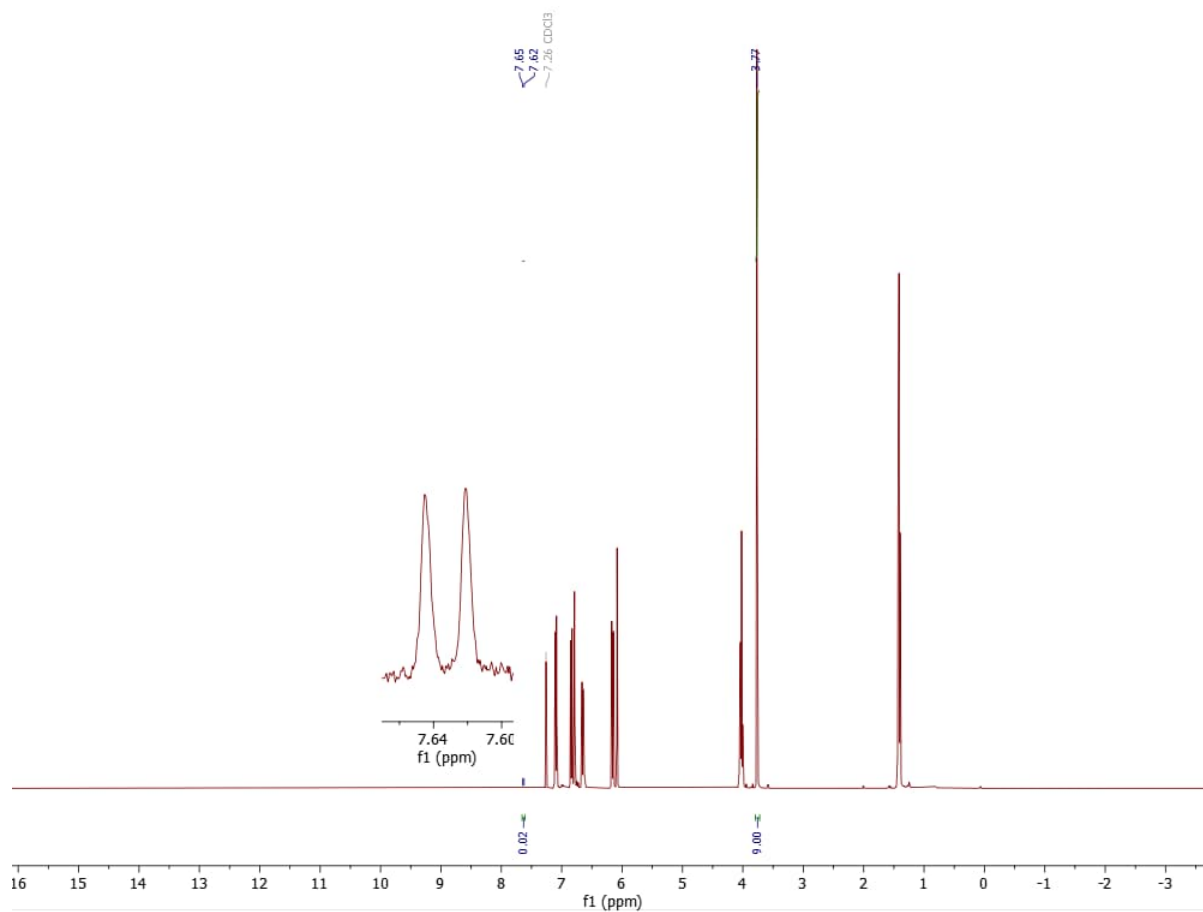
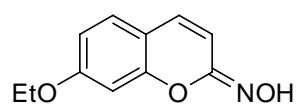
## 7-ethoxy-2H-chromen-2-one oxime (1i), red LED, no K-PHI



$$Y = \frac{0.01 \cdot 9 \cdot 10}{9.00 \cdot 1 \cdot 50} \cdot 100\% < 1\%$$



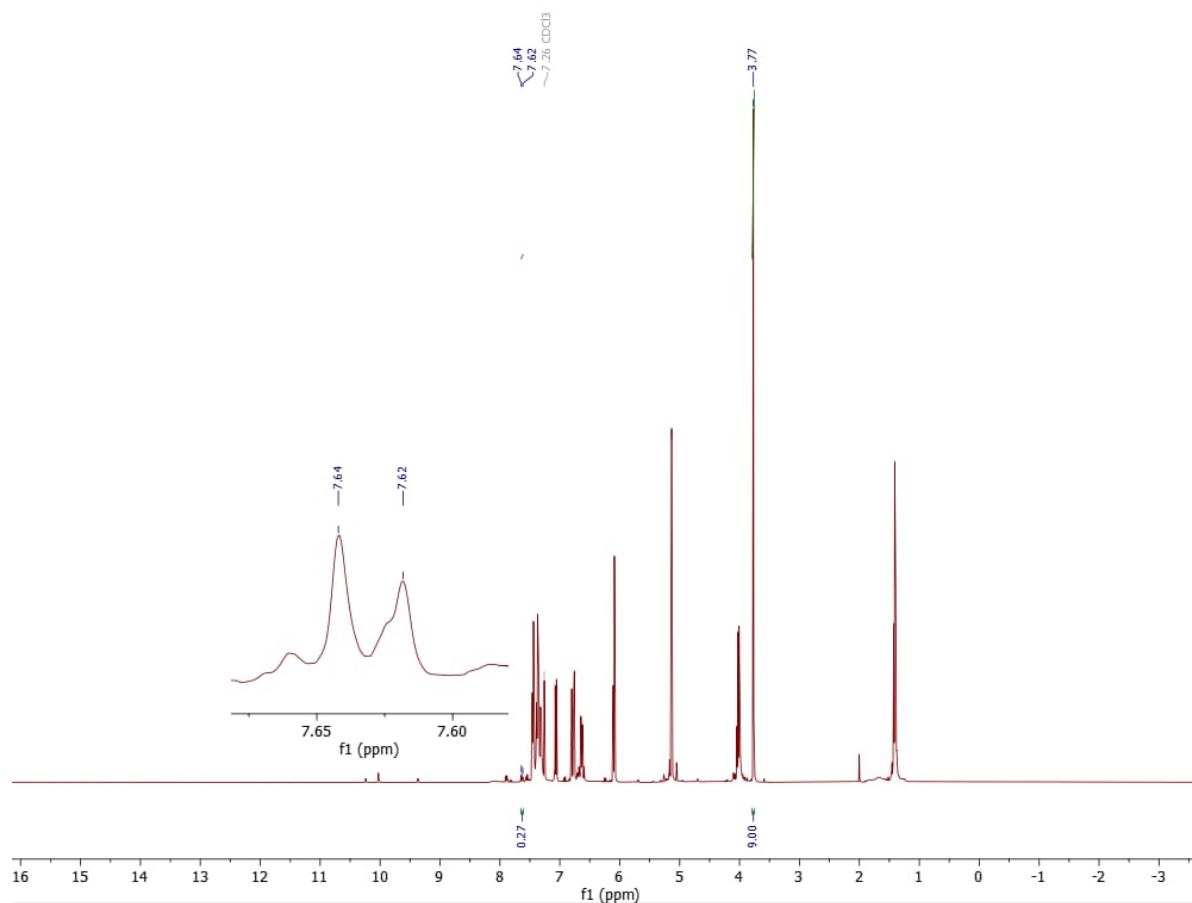
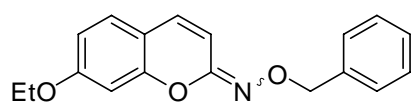
## 7-ethoxy-2H-chromen-2-one oxime (1i), red LED, under argon, no K-PHI



$$Y = \frac{0.02 \cdot 9 \cdot 10}{9.00 \cdot 1 \cdot 50} \cdot 100\% < 1\%$$



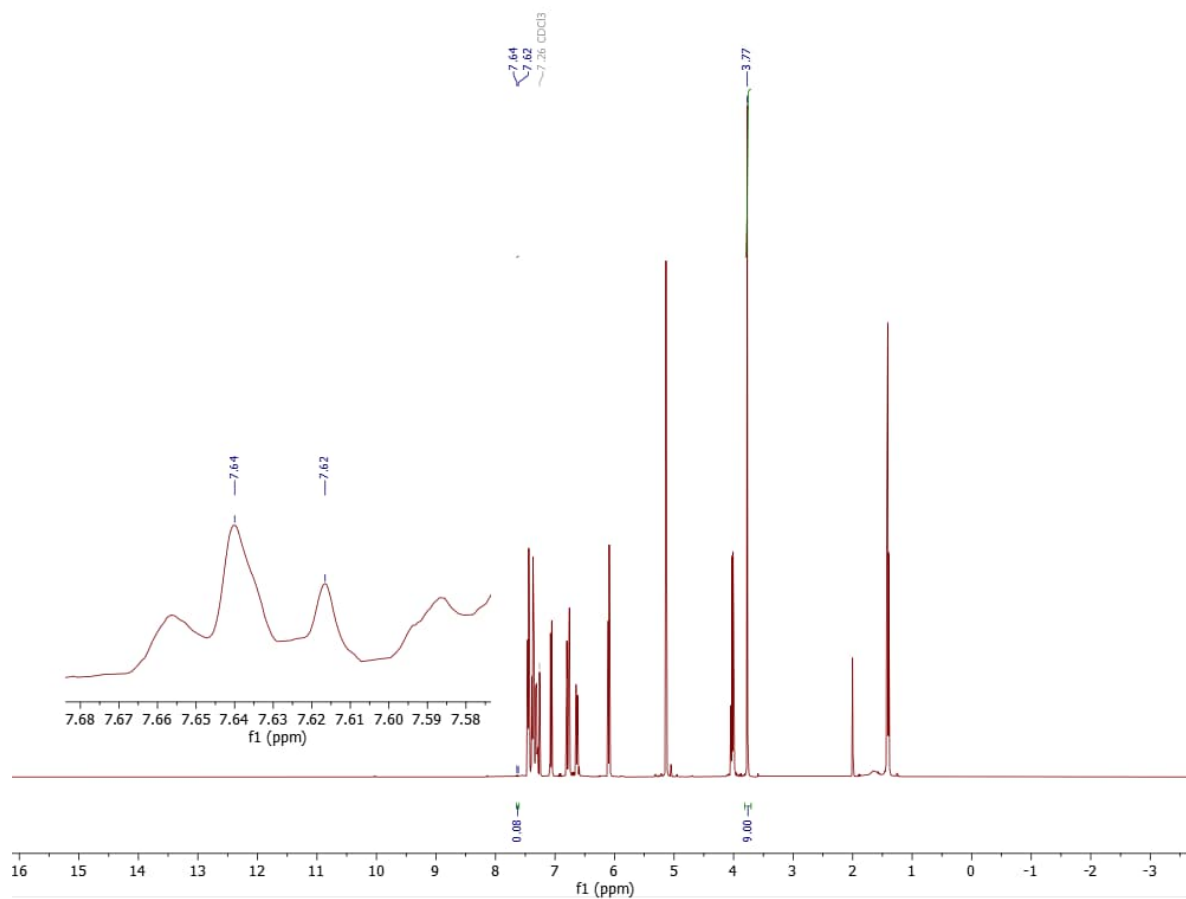
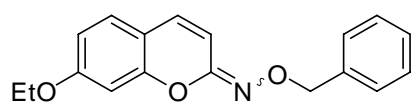
## 7-ethoxy-2H-chromen-2-one O-benzyl oxime (1i-Bn), blue LED, standard



$$Y = \frac{0.27 \cdot 9 \cdot 10}{9.00 \cdot 1 \cdot 50} \cdot 100\% = 5\%$$



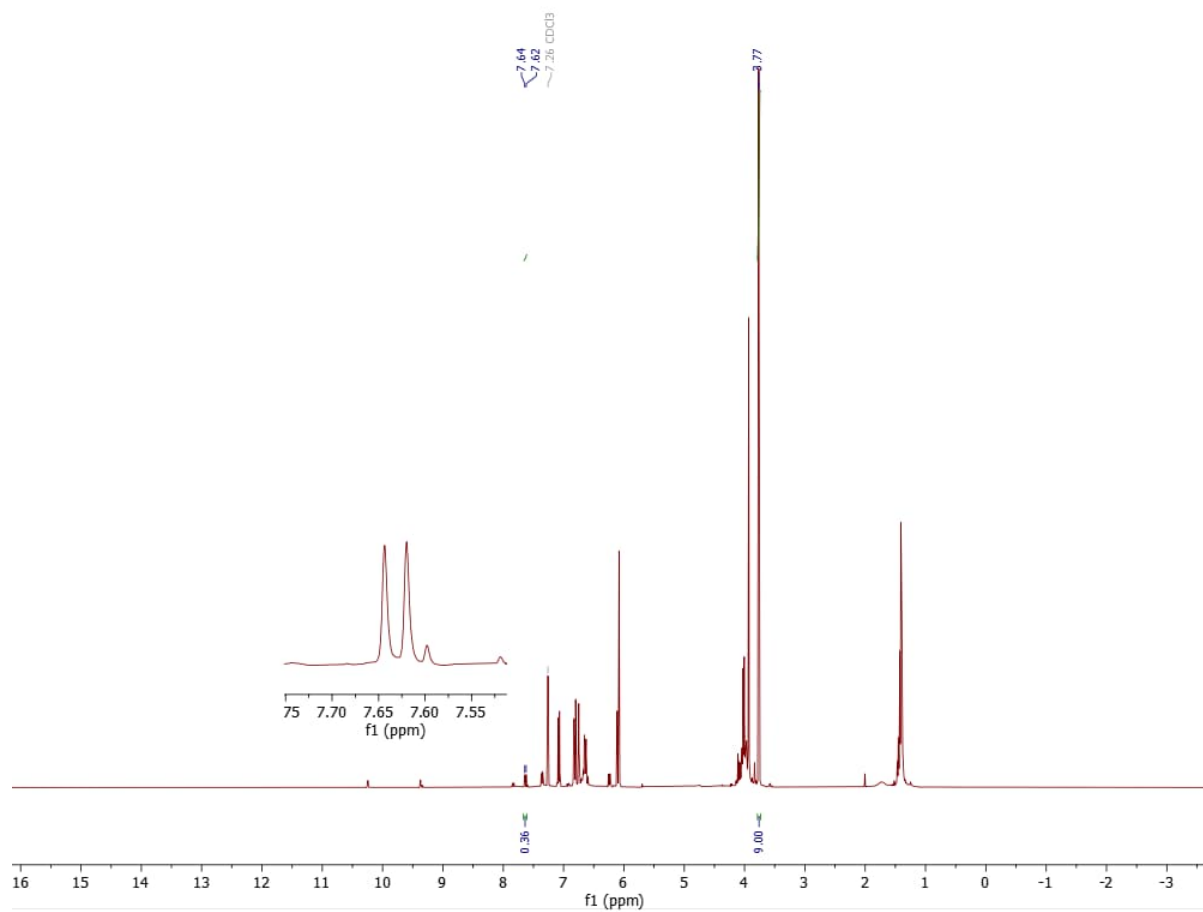
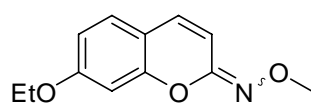
## 7-ethoxy-2H-chromen-2-one O-benzyl oxime (1i-Bn), green LED, standard



$$Y = \frac{0.08 \cdot 9 \cdot 10}{9.00 \cdot 1 \cdot 50} \cdot 100\% = 2\%$$



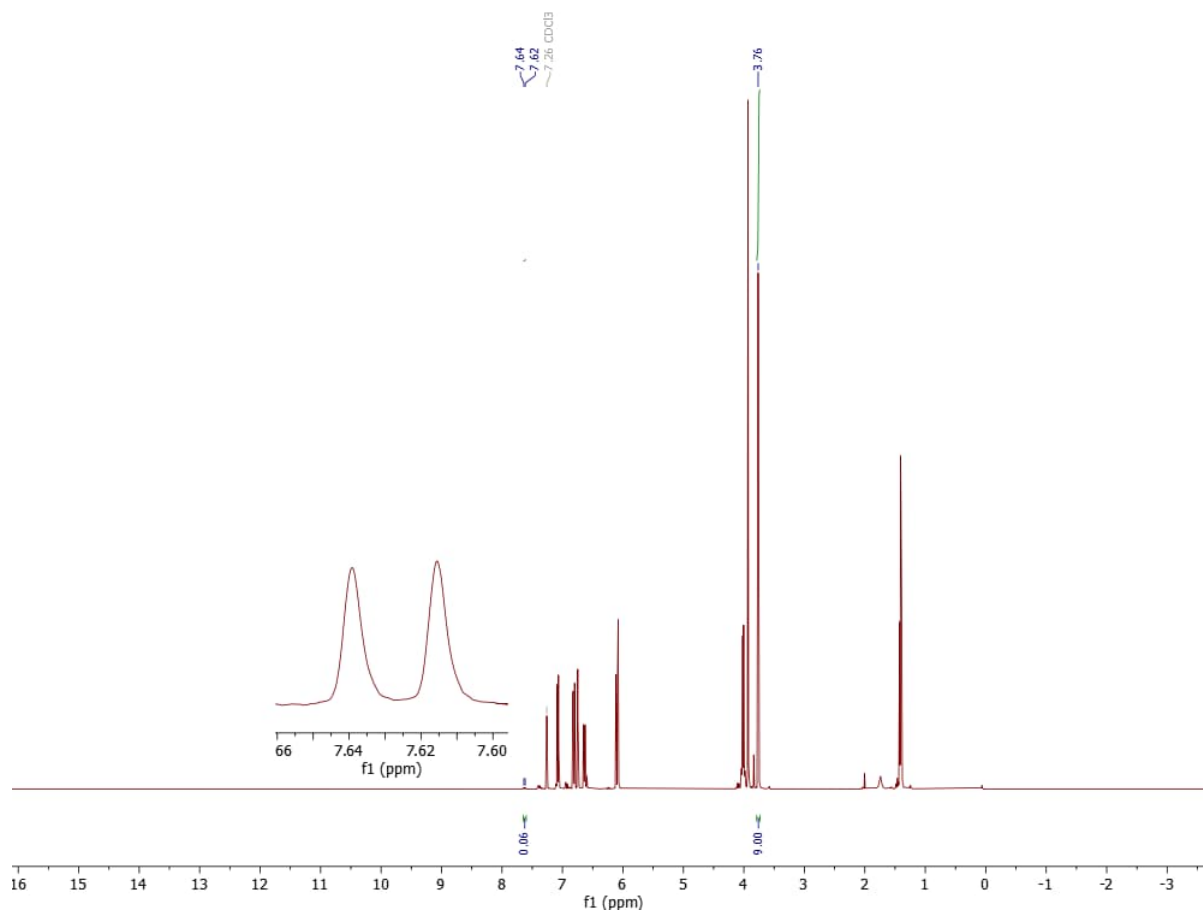
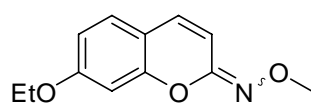
## 7-ethoxy-2H-chromen-2-one O-methyl oxime (1i-Me), blue LED, standard



$$Y = \frac{0.36 \cdot 9 \cdot 10}{9.00 \cdot 1 \cdot 50} \cdot 100\% = 7\%$$



## 7-ethoxy-2H-chromen-2-one O-methyl oxime (1i-Me), green LED, standard



$$Y = \frac{0.06 \cdot 9 \cdot 10}{9.00 \cdot 1 \cdot 50} \cdot 100\% = 1\%$$



## 7.2.5. Absorption and Emission Spectroscopy Experiments

### UV-Vis-NIR

The spectra were recorded in the range from 220 to 1400 nm; K-PHI spectrum was obtained in solid state and  $2.5 \cdot 10^{-4}$  M acetonitrile solutions were used for compounds 1i, 1i-Bn and 1i-Me (Figure S2.2). The small 375-450 nm band in 1i-Me spectrum is supposed to be a yellow-colored decomposition impurity(-ies) that accumulate(s) in the sample upon storage and in solution.

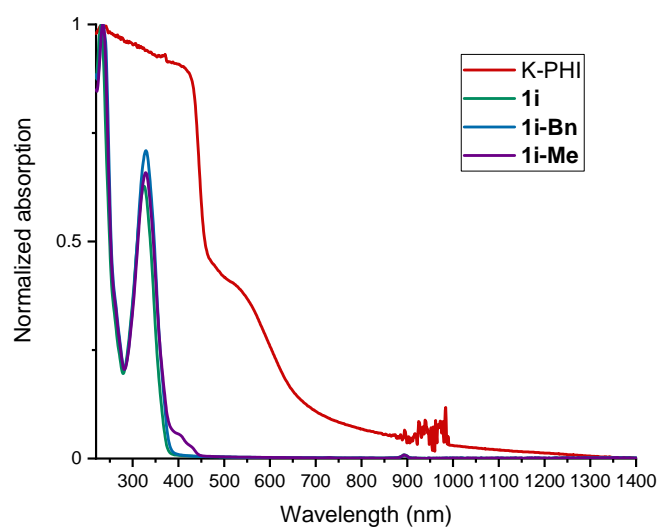


Figure S2.2. UV-Vis-NIR spectra of K-PHI and coumarin oximes.

### Steady-State Emission Quenching Experiment

For this experiment, 4 samples were prepared by mixing 2 mL of acetonitrile, 5 mg of K-PHI and 0, 10, 20 or 50  $\mu$ mol of 7-ethoxy-2*H*-chromen-2-one oxime 1i, respectively (which corresponds to 0, 0.005, 0.010 and 0.025M concentration). The samples were sonicated in vials for 10 min before transferring, then purged with nitrogen for 3 min inside a 1 cm wide 4-sided screwcap quartz cuvette and tightly closed. Each sample was recorded 3 times and the cuvette was vigorously shaken prior to each measurement to redisperse the catalyst.



The device settings for recording emission spectra in these experiments are listed in [Table S2.1](#).

Table S2.1. Jasco FP-8300 settings for SSES (oxime-K-PHI quenching).

Parameter	Value, unit
Ex bandwidth	5 nm
Em bandwidth	5 nm
Response	0.5 s
Sensitivity	High
Measurement range	350-900 nm
Data interval	1 nm
Ex wavelength	375 nm
Auto gain	off
Blank correction	off

The measured spectra are shown on [Figure S2.3](#) (the curves were obtained as 3 measurements' average for each experiment):



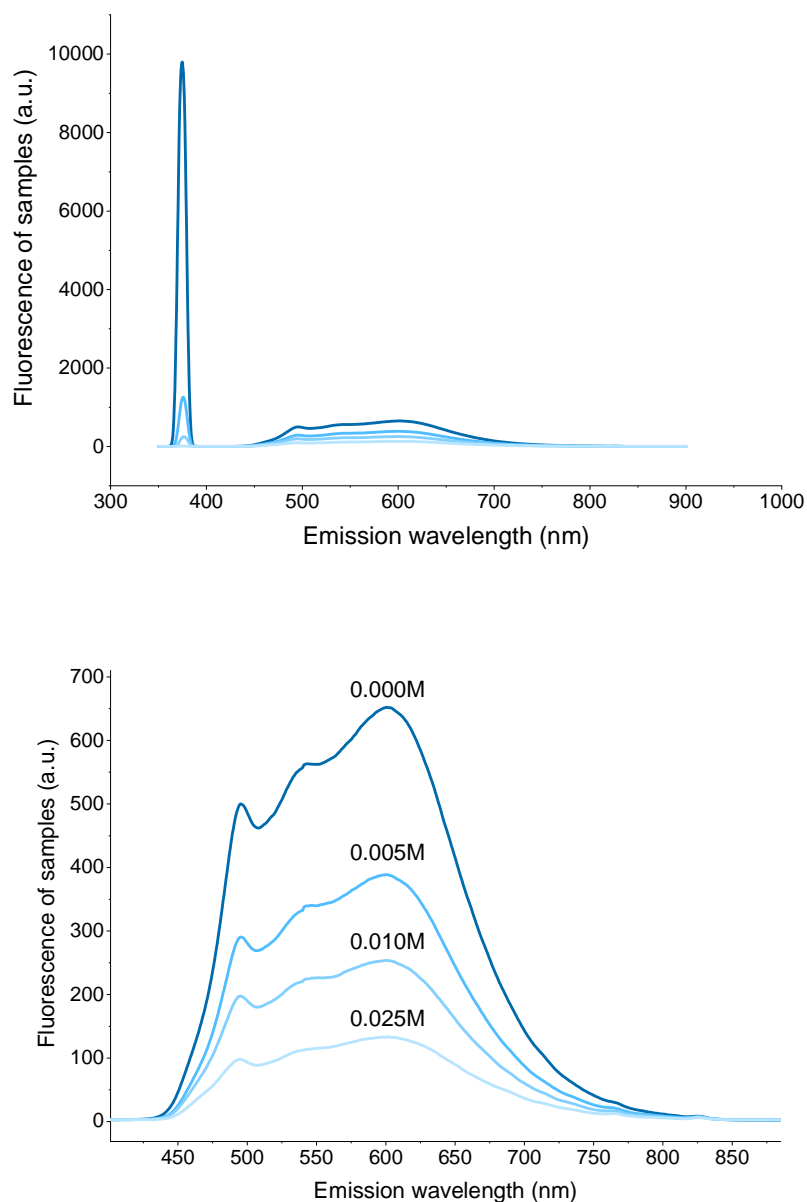


Figure S2.3. Full spectra (top) and main maxima excerpts (bottom) for steady-state quenching experiments; values above the curves show the corresponding oxime concentration.

Absolute emission values at  $\lambda_{\text{max}} = 602 \text{ nm}$  were then used to make a steady-state Stern-Volmer plot according to the equation:

$$\frac{I_0}{I} - 1 = K_{SV} \cdot C_Q,$$



where  $I_0$  is the absolute emission value of the sample without quencher,  $I$  is the absolute emission value of a sample with added quencher,  $K_{SV}$  is the Stern-Volmer constant ( $M^{-1}$ ) and  $C_Q$  is the quencher concentration ( $M$ ). The plot is shown on [Figure S2.4](#).

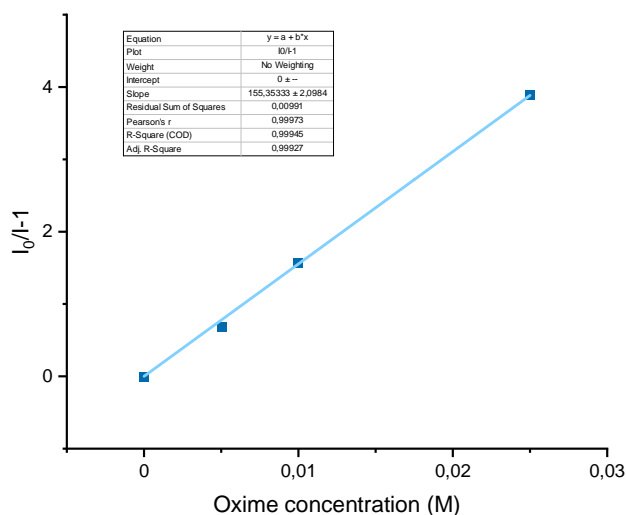


Figure S2.4. Steady-state Stern-Volmer plot

Stern-Volmer constant is thus determined to be  $155.353 \pm 2.098 M^{-1}$ .

### *Time-Resolved Emission Experiments*

#### *Time-resolved emission quenching experiment*

For this experiment, the device was set up as follows ([Table S2.2](#)).



Table S2.2. Device settings for TRES quenching experiment (375 nm laser)

Parameter	Value, unit
Resolution	25 ps
Frequency	20 MHz
Mode	Pulse 10x30 KHz
Polarizer	54.7 °
Emission wavelength	500 nm
Excitation bandwidth	10 nm

The same samples were used as described above; each sample was purged with nitrogen for 3 min prior to experiment and recorded 3 times with vigorous shaking before every measurement. The acquisitions were set to terminate after reaching 10000 counts. The following lifetimes were obtained (Table S2.3).

Table S2.3. Measured fluorescence lifetimes for oxime quenching

Oxime concentration, M	$\tau_1, ns$	$\tau_2, ns$	$\tau_3, ns$	$\bar{\tau}, ns$
0	1.642	1.640	1.665	1.649
0.005	1.706	1.641	1.638	1.662
0.010	1.538	1.499	1.502	1.513
0.025	1.411	1.387	1.338	1.379

The data was used to plot time-resolved Stern-Volmer plot according to the equation:

$$\frac{\tau_0}{\tau} - 1 = K_Q \cdot \tau_0 \cdot C_Q,$$

where  $\tau_0$  is the fluorescence lifetime without quencher,  $\tau$  is a fluorescence lifetime with quencher,  $K_Q$  is quenching rate constant,  $C_Q$  is a quencher concentration. The plot with linear approximation is shown on Figure S2.5:



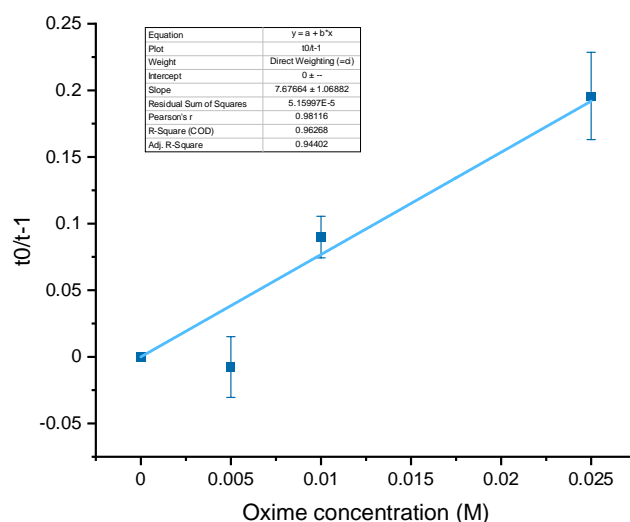


Figure S2.5. Time-resolved Stern-Volmer plot

The quenching rate constant in each case would be calculated as:

$$K_Q = \frac{K_{Slope}}{\tau_0} = \frac{7.677 \pm 1.069}{1.649 \cdot 10^{-9}} = (4.656 \pm 0.648) \cdot 10^9 M^{-1}s^{-1}$$

Note: The inaccuracy in measurements may be attributed to slow degradation of the oxime compound under UV beam: in the set of 3 measurements with added quencher the former usually yield 30-60 ps greater PL lifetimes than the latter, and an acquisition time for decay curves could be sufficient for side photochemical processes to occur (4-8 min).

#### *Singlet-triplet energy gap determination*

For this experiment, the device was set up as follows (Table S2.4).



Table S2.4. Device settings for TRES quenching experiment (375 nm laser)

Parameter	Value, unit (Fluorescence)	Value, unit (Phosphorescence)
Resolution	25 ps	2500 ps
Frequency	40 MHz	1 MHz
Mode	Pulse 10x30 KHz	
Polarizer	54.7 °	
Emission wavelength	425-700 nm with 25 nm gap (12 measurements)	
Excitation bandwidth	10 nm	20 nm

The sample of 5 mg K-PHI in 2 mL of acetonitrile was used (purged with nitrogen for 3 min prior to experiment) and recorded once for both series with vigorous shaking before every 12-measurements set. The acquisitions were set to terminate after reaching 65535 counts.

After recording the decay curves, a count value was taken from every wavelength at specific timestamps:

For fluorescence: 0.1 ns, 1 ns, 2 ns, 5 ns, 10 ns and 20 ns;

For phosphorescence: 50 ns, 100 ns, 200 ns, 500 ns and 950 ns.

These values were used to plot normalized wavelength-versus-counts emission spectra with 25 nm definition for each timestamp of each series (Figures S2.6 and S2.7) and average emission maximum was calculated from these plots for both fluorescence and phosphorescence (Table S2.5).



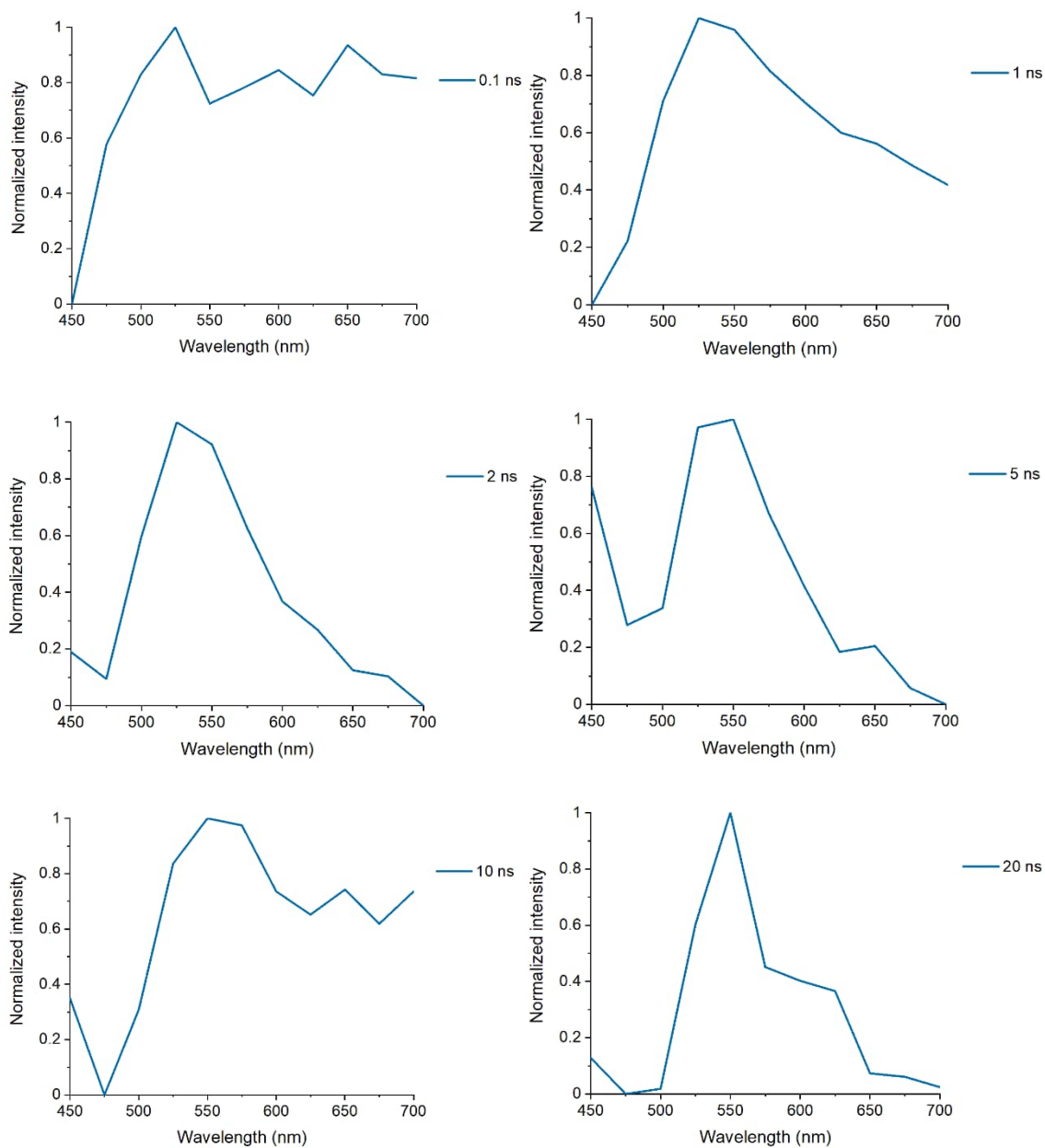


Figure S2.6. Indirect fluorescence spectra at various delay times



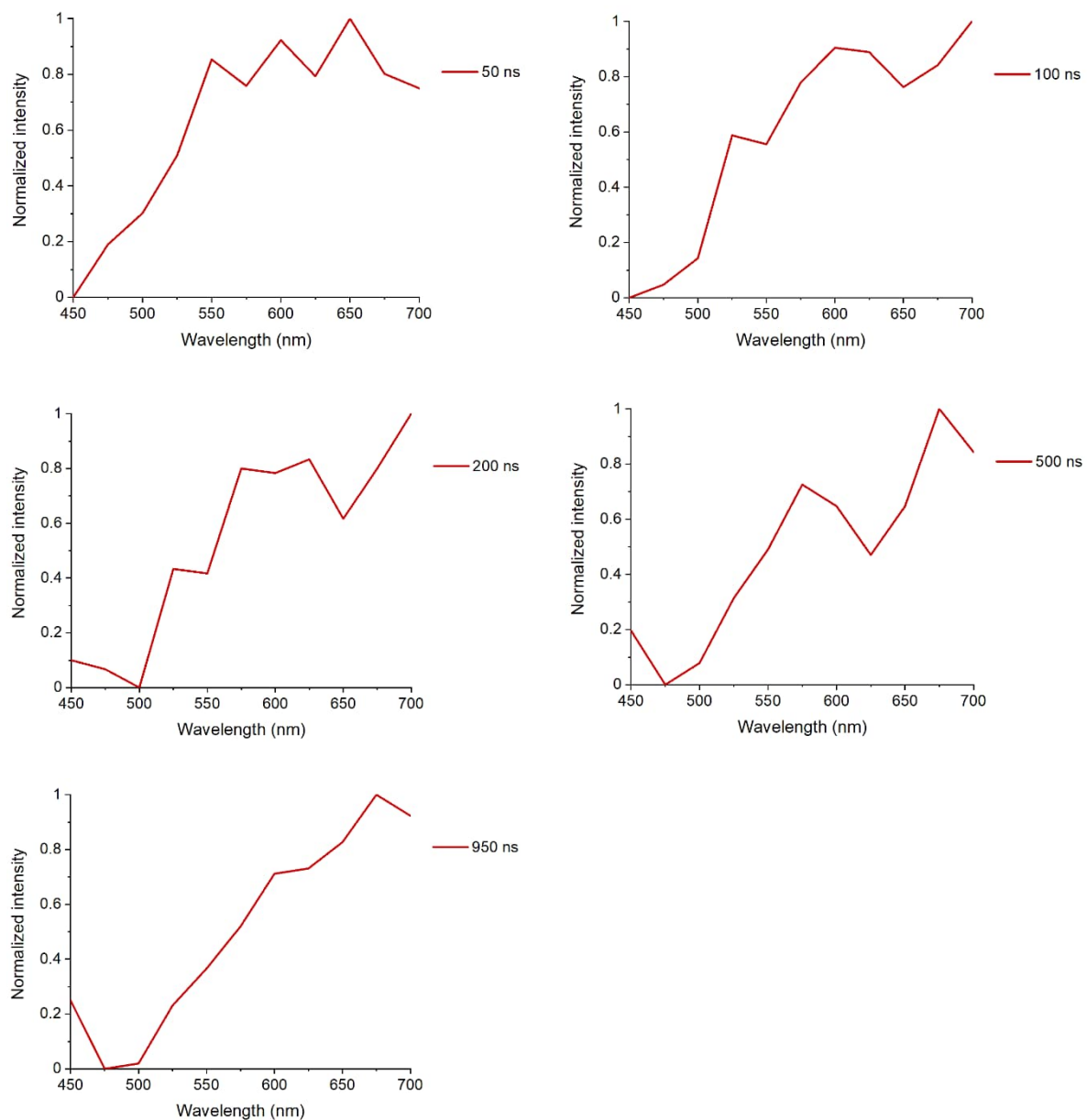


Figure S2.7. Indirect phosphorescence spectra at various delay times



Table S2.5. Emission maxima of K-PHI fluorescence and phosphorescence

Emission type	Series 1	Series 2	Series 3	Series 4	Series 5	Series 6	Average	
	max., nm	max., nm	max., nm	max., nm	max., nm	max., nm	nm	eV
Fluorescence	525	525	525	550	550	550	537.5 ± 13.7	2.31 ± 0.06
Phosphorescence	600	600	625	575	600	-	600.0 ± 17.7	2.07 ± 0.06

With obtained values, the singlet-triplet energy gap is calculated using the equation:

$$\Delta E_{ST} = E_{Fl}^{max} - E_{Ph}^{max} = 0.24 \pm 0.12 \text{ eV}$$

#### Internal Quantum Efficiency Measurements

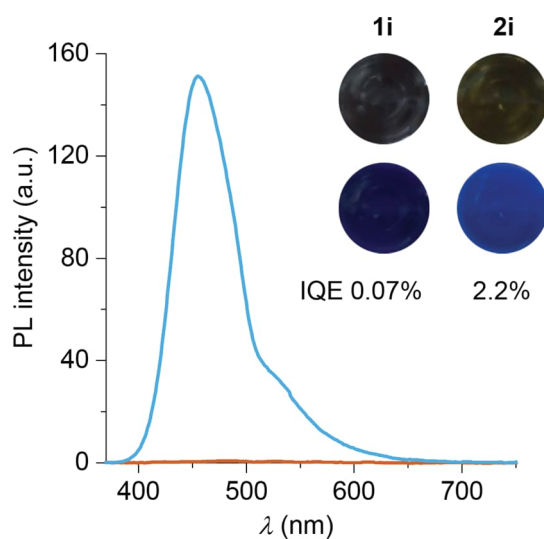
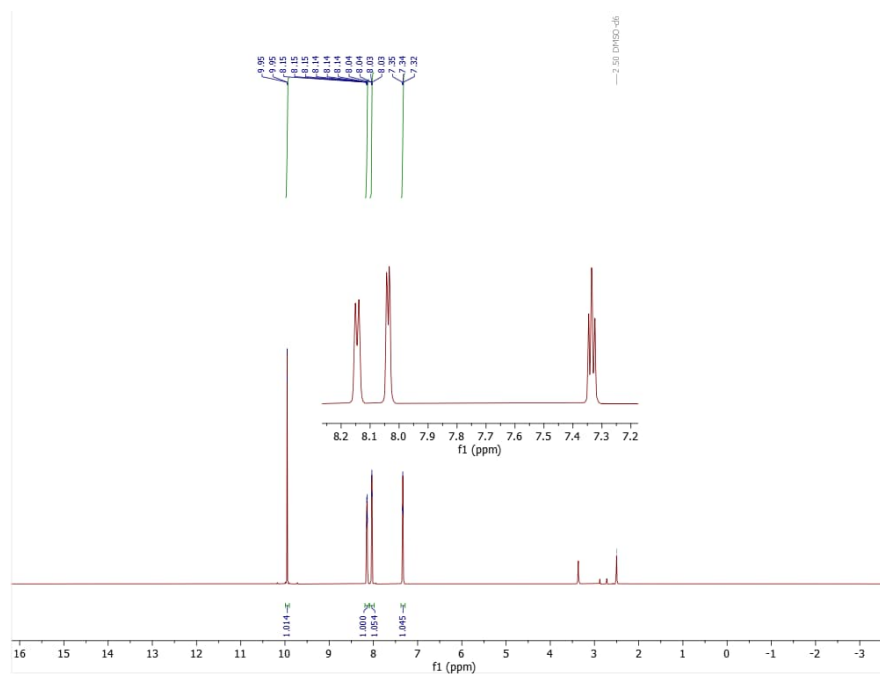
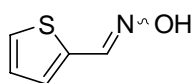
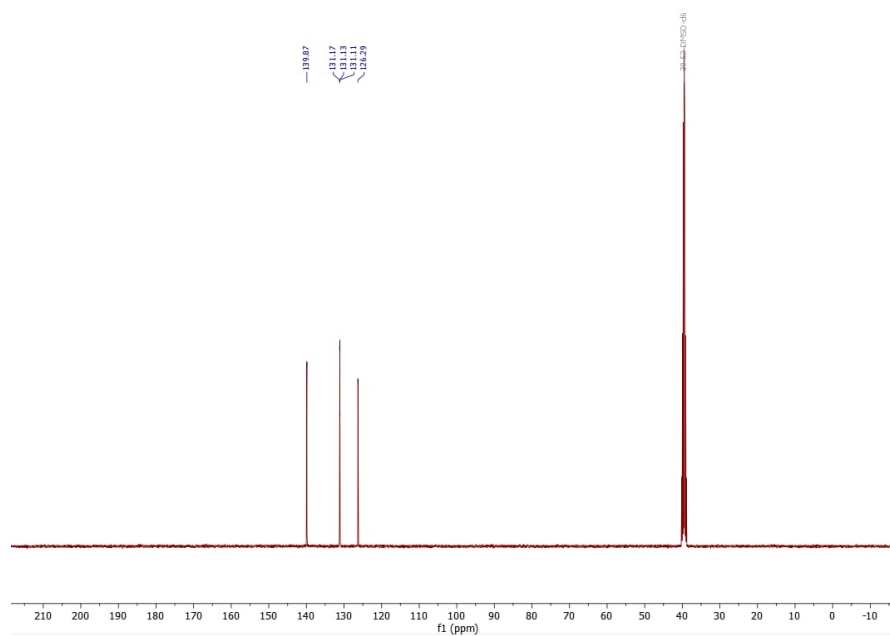
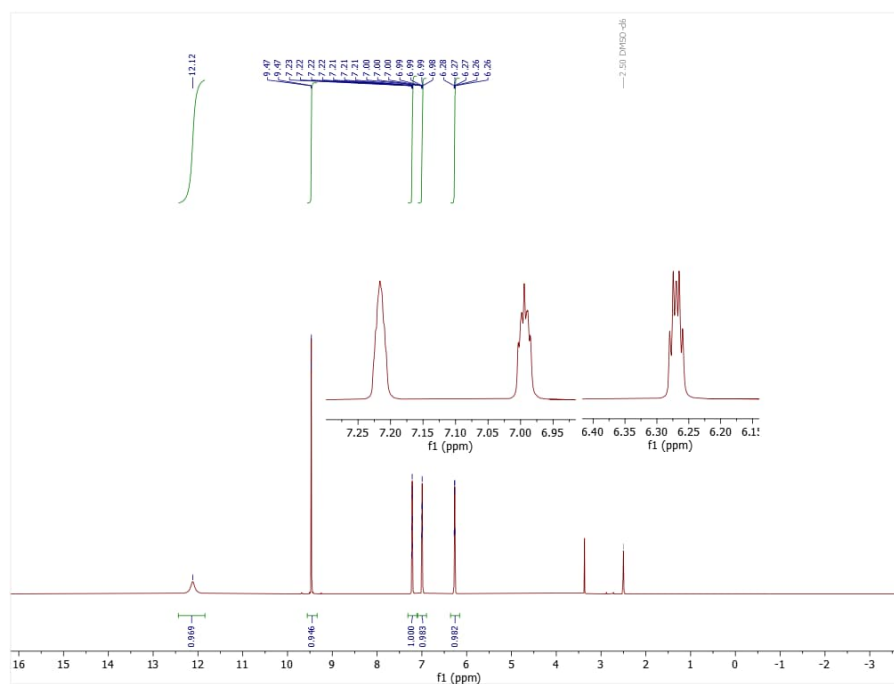
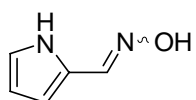
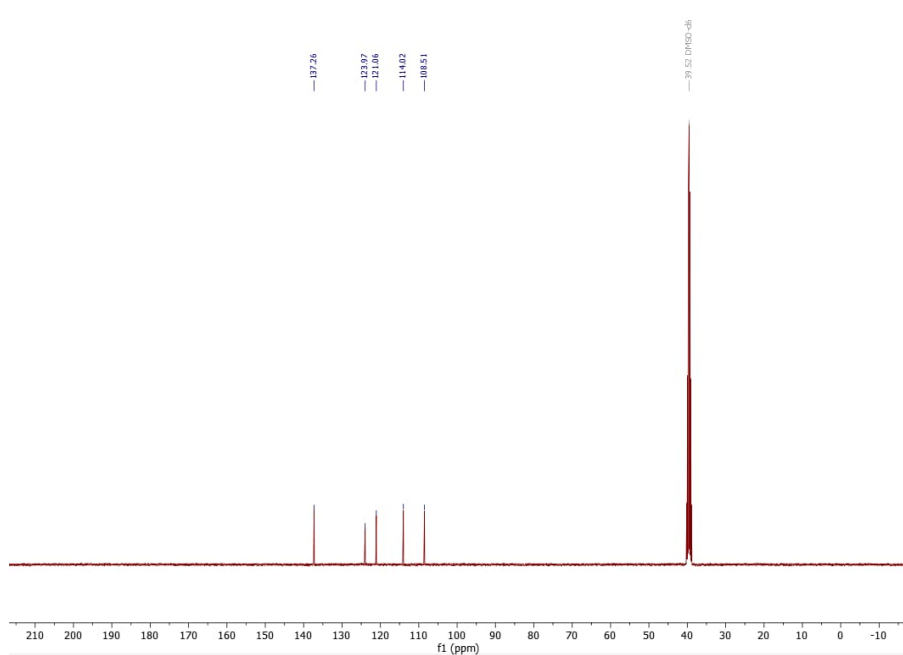


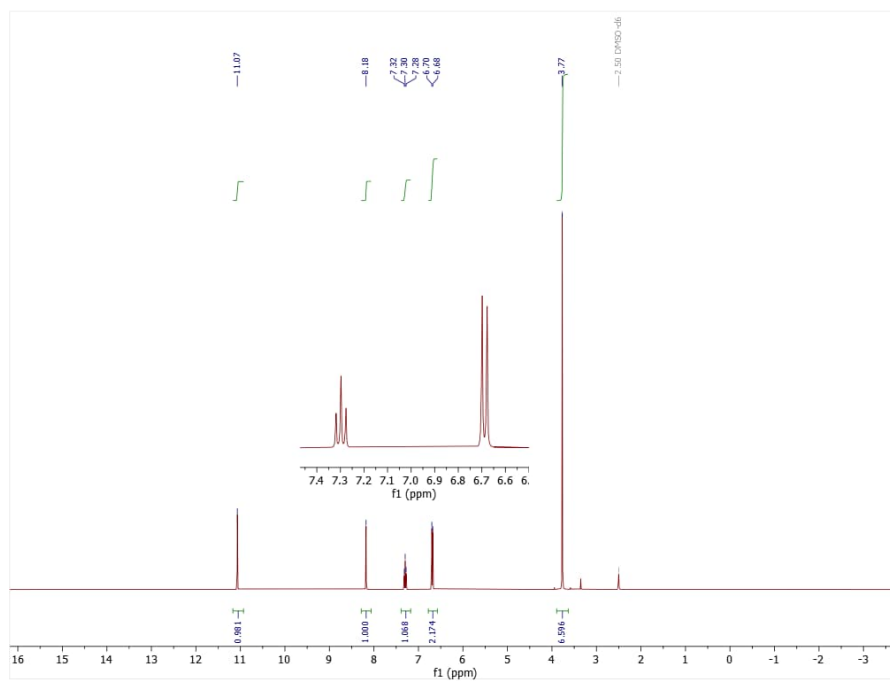
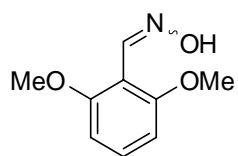
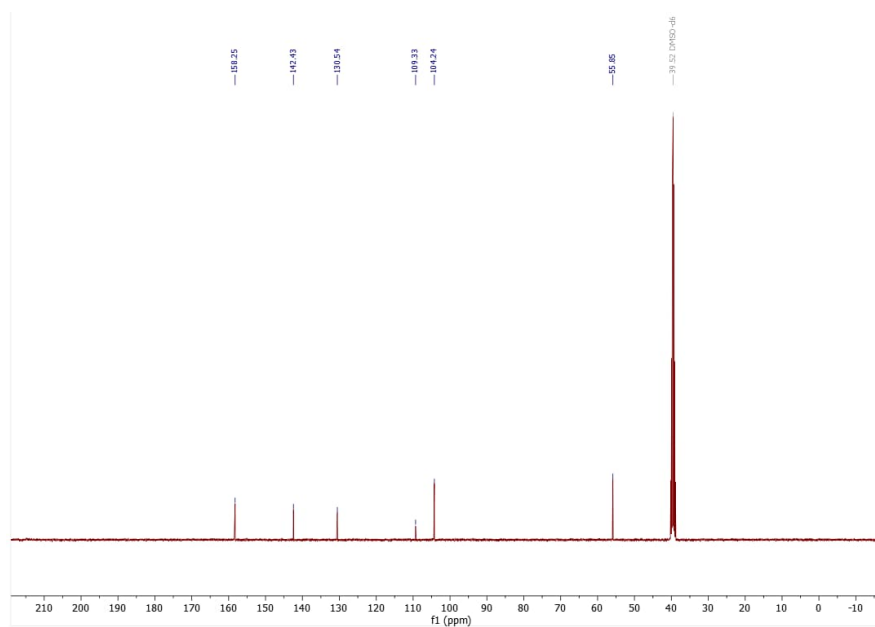
Figure S2.8. IQE values and emission plots for 2i (blue line) and 1i (orange line). Insets show appearance of solution of 2i and 1i in MeCN under ambient light (top) and UV (365 nm, bottom).

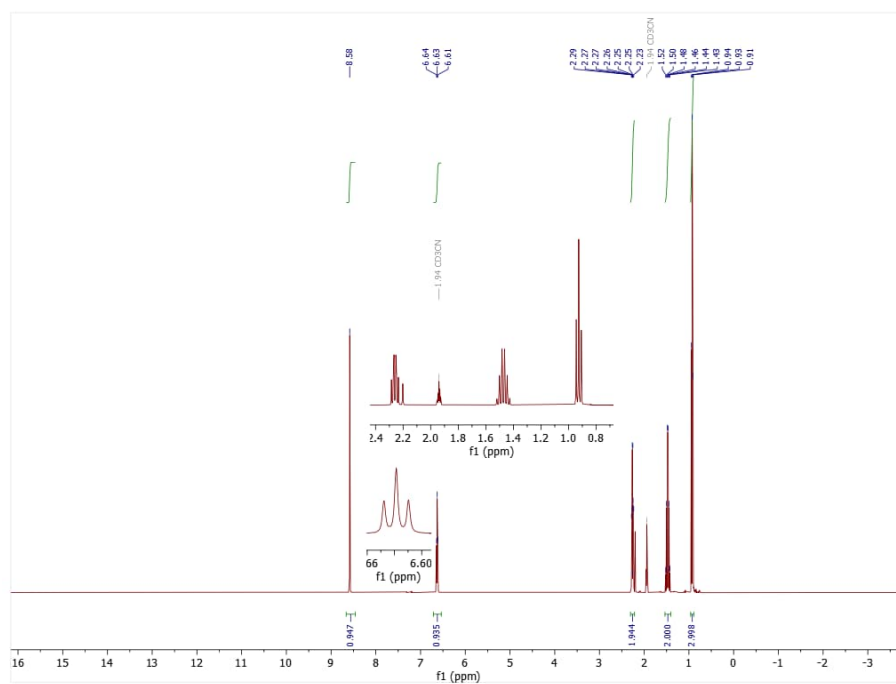
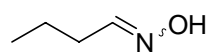
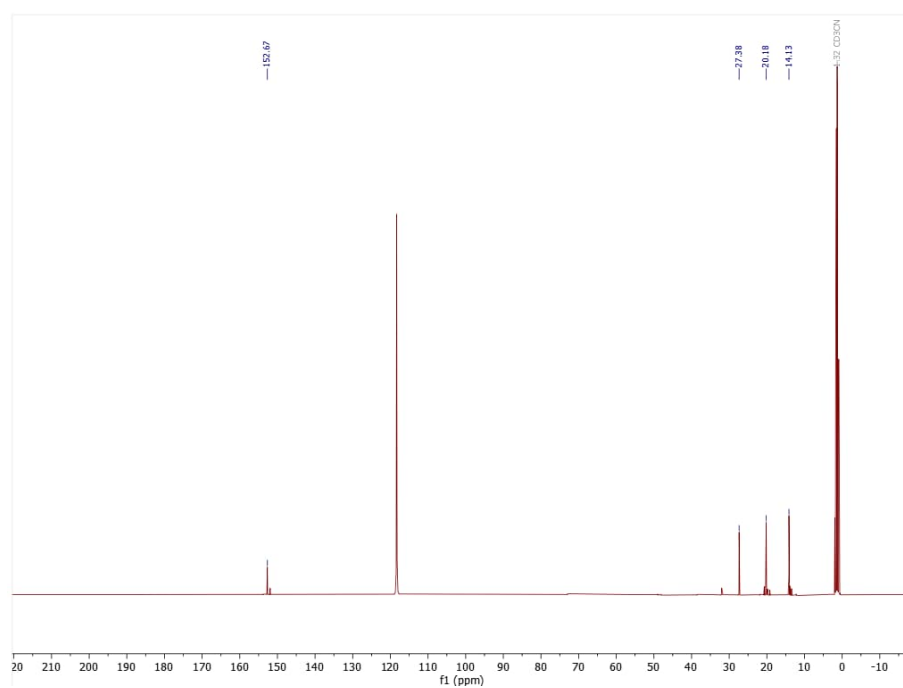


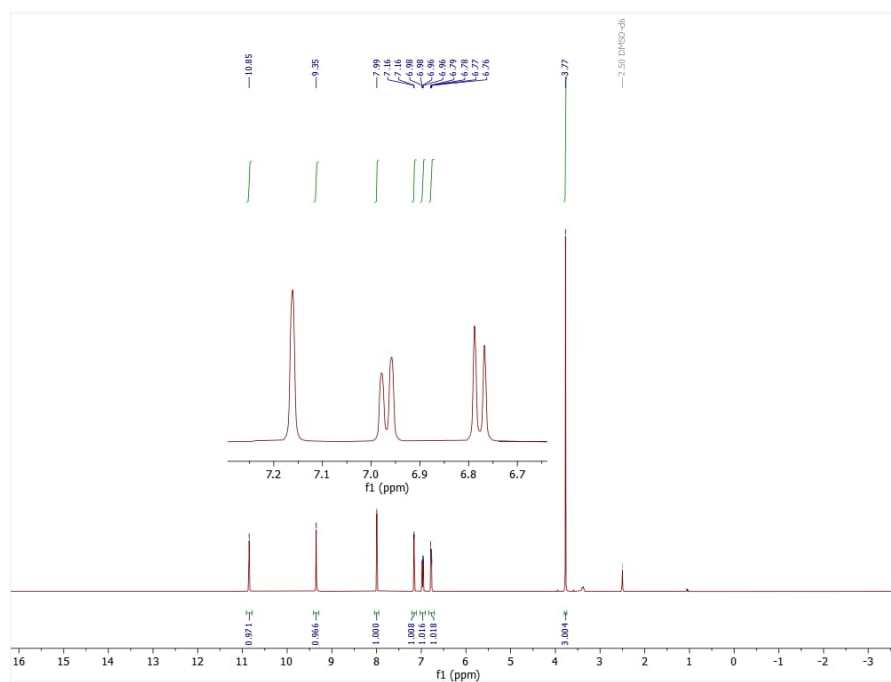
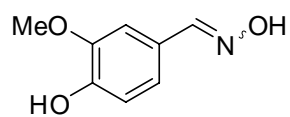
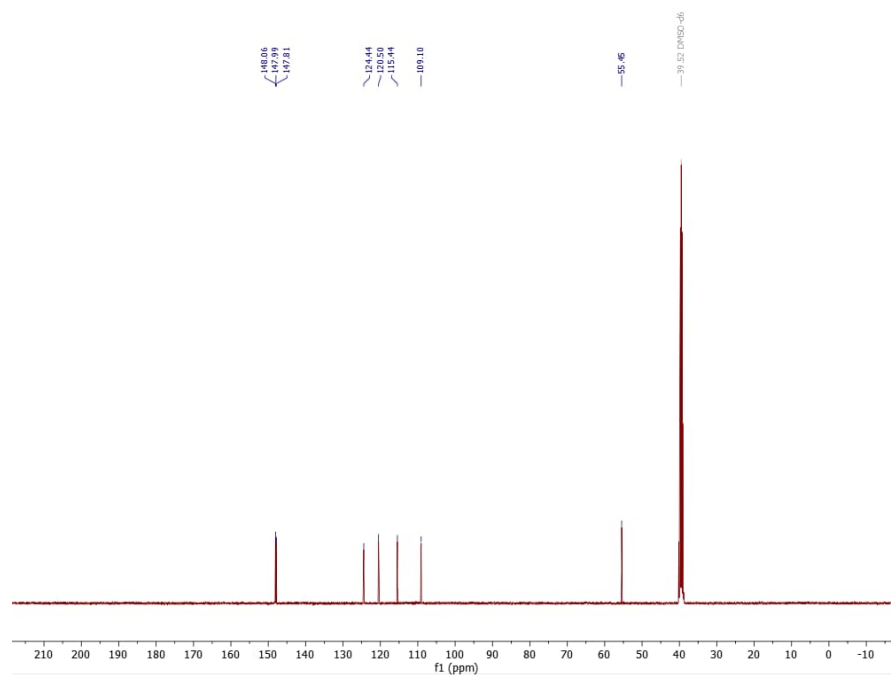
## 7.2.6. NMR Spectra

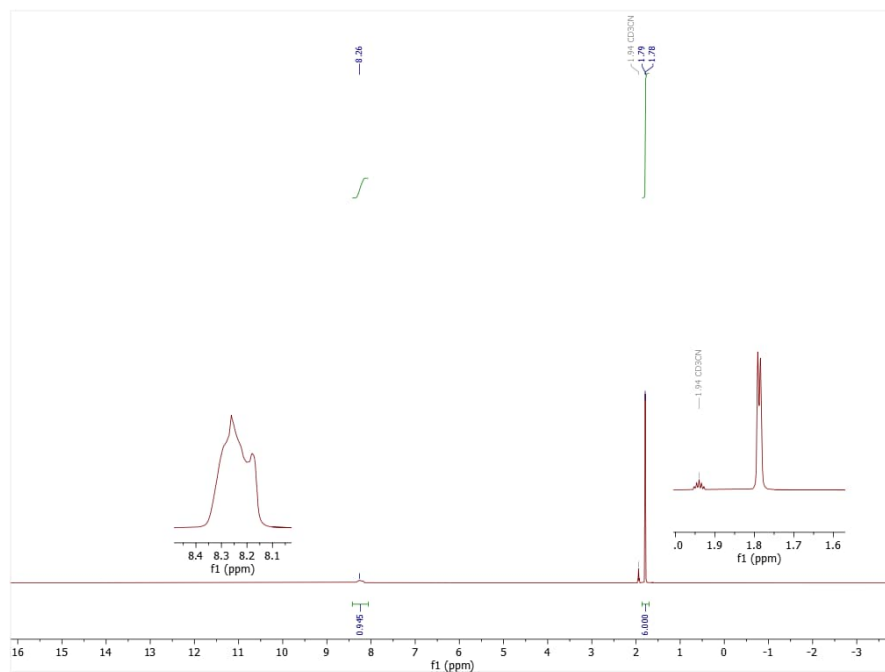
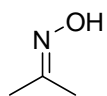
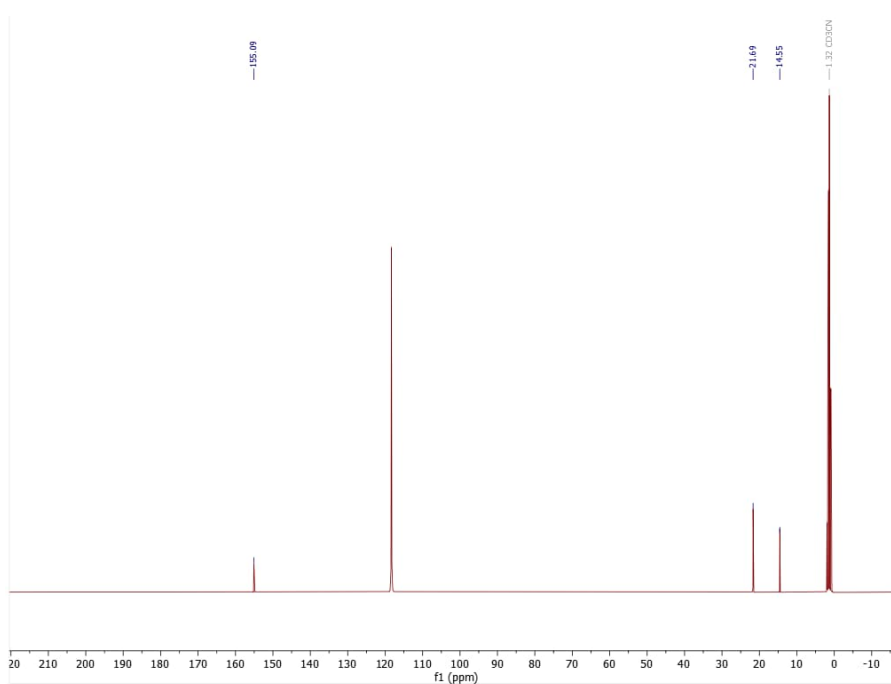
Figure S2.9.  $^1\text{H}$  NMR DMSO- $d_6$  spectrum of 1aFigure S2.10.  $^{13}\text{C}$  NMR DMSO- $d_6$  spectrum of 1a

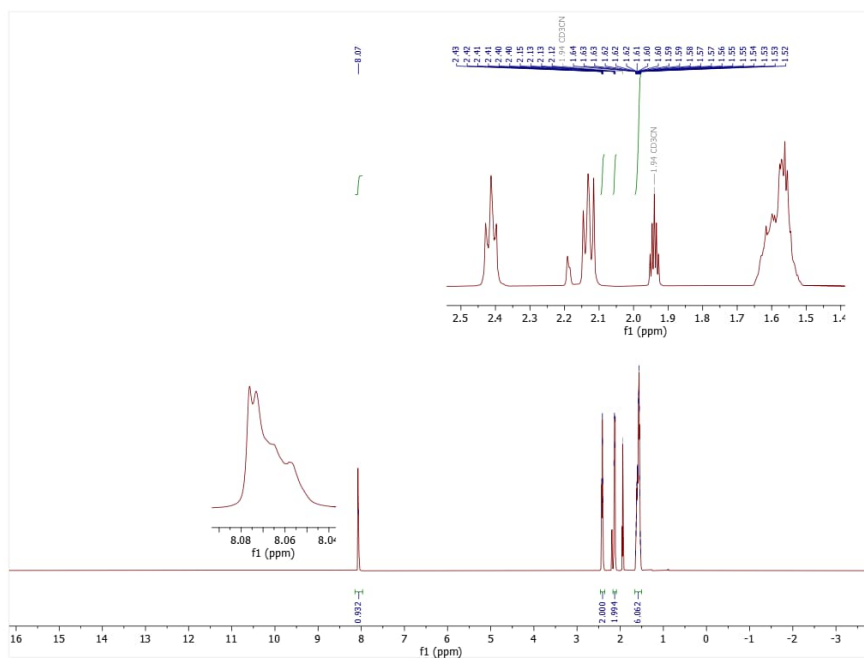
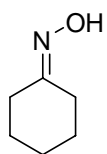
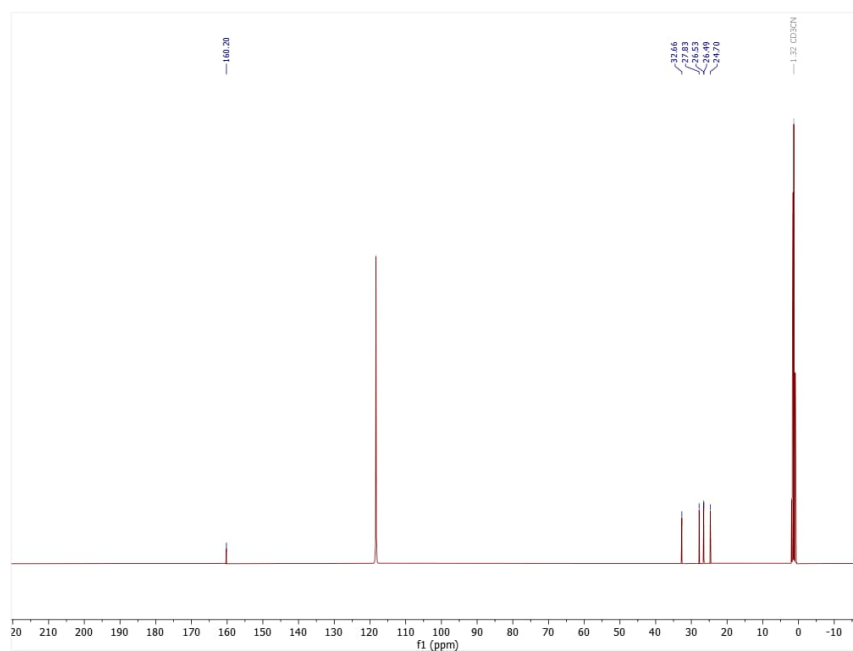
Figure S2.11.  $^1\text{H}$  NMR  $\text{DMSO-}d_6$  spectrum of 1bFigure S2.12.  $^{13}\text{C}$  NMR  $\text{DMSO-}d_6$  spectrum of 1b

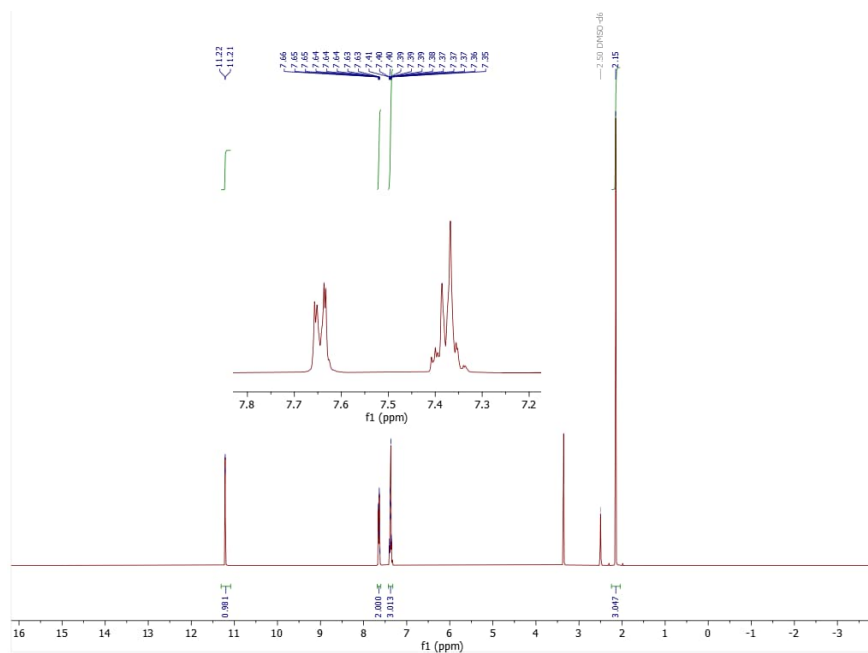
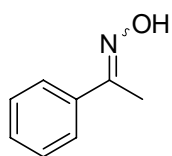
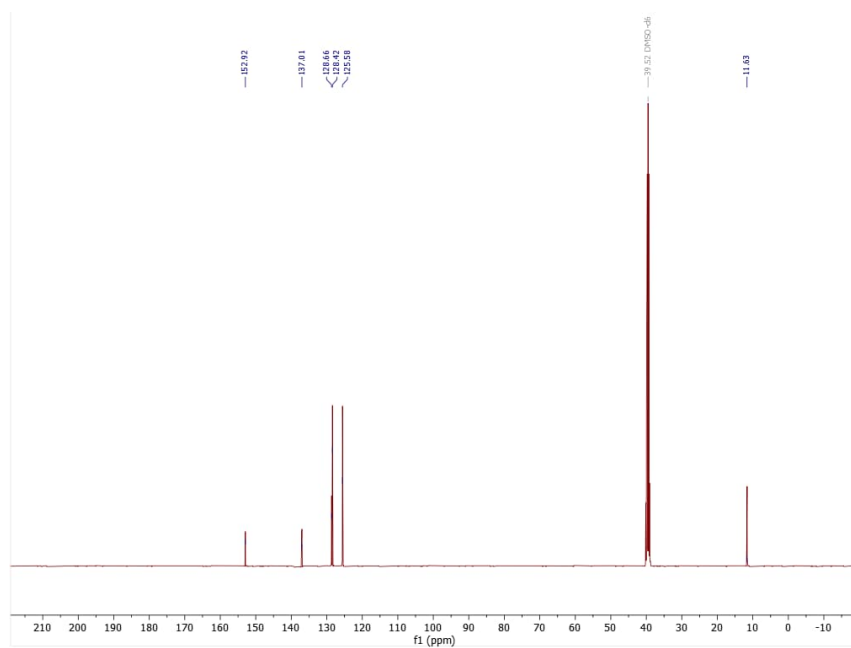
Figure S2.13.  $^1\text{H}$  NMR spectrum of 1cFigure S2.14.  $^{13}\text{C}$  NMR DMSO- $d_6$  spectrum of 1c

Figure S2.15.  $^1\text{H}$  NMR  $\text{CD}_3\text{CN}$  spectrum of 1dFigure S2.16.  $^{13}\text{C}$  NMR  $\text{CD}_3\text{CN}$  spectrum of 1d

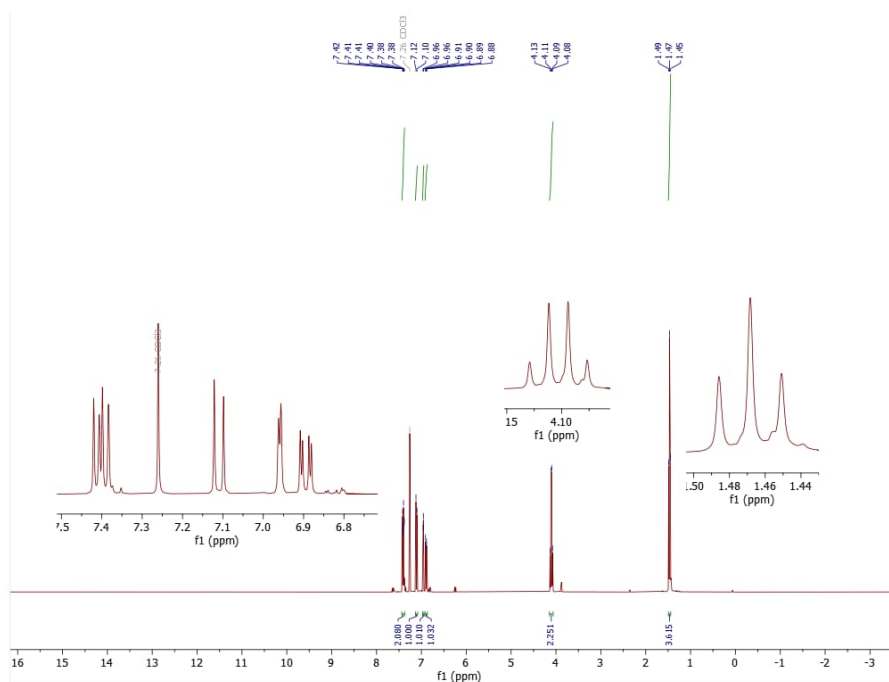
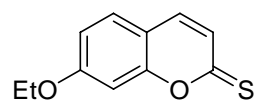
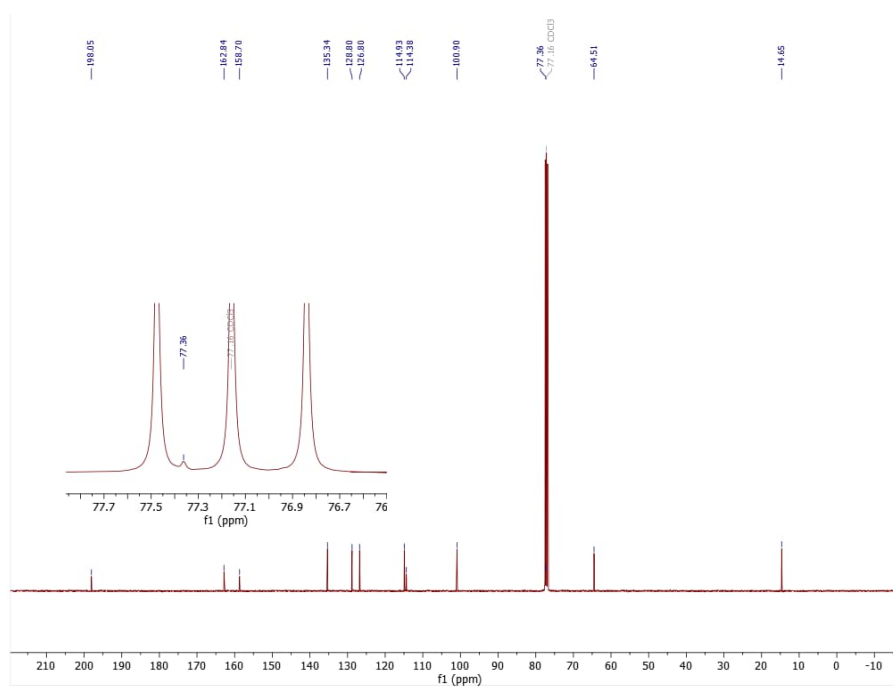
Figure S2.17. <sup>1</sup>H NMR DMSO-*d*<sub>6</sub> spectrum of 1eFigure S2.18. <sup>13</sup>C NMR DMSO-*d*<sub>6</sub> spectrum of 1e

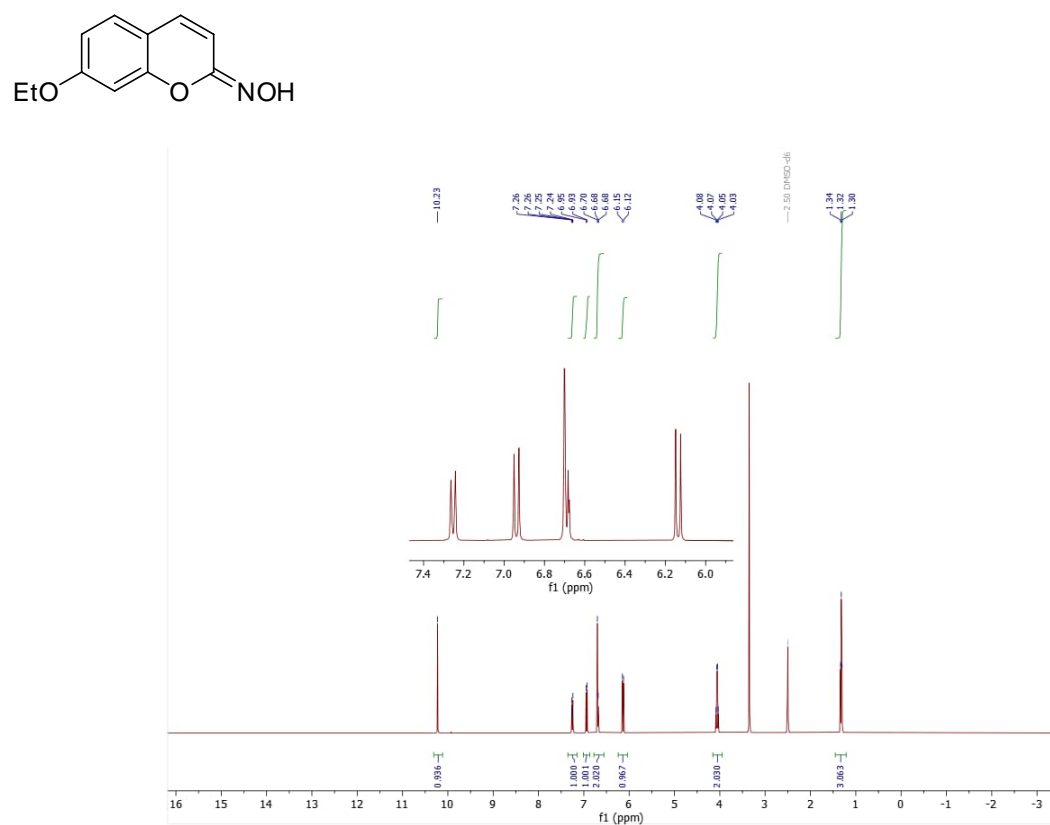
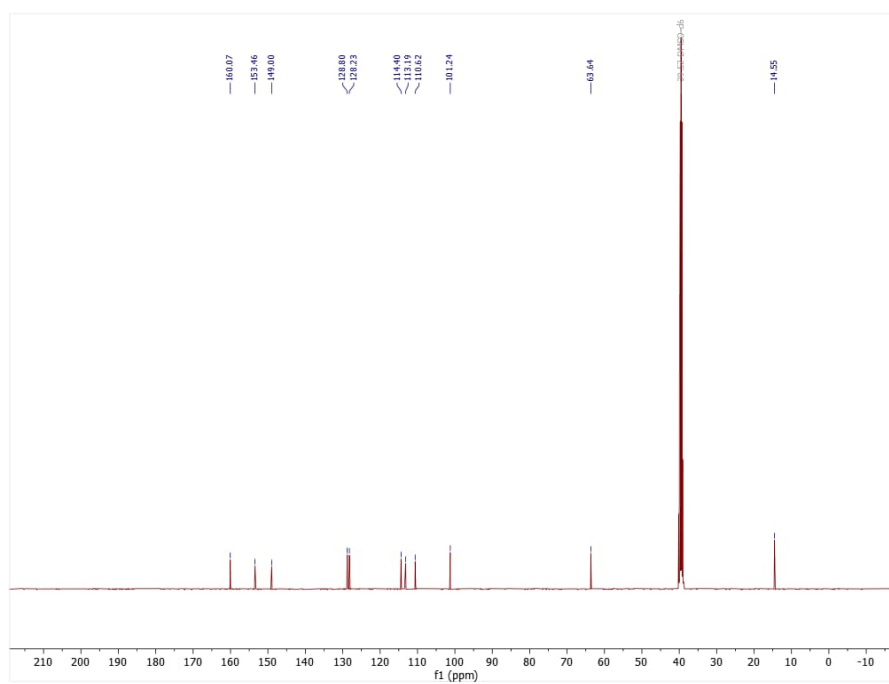
Figure S2.19.  $^1\text{H}$  NMR  $\text{CD}_3\text{CN}$  spectrum of 1fFigure S2.20.  $^{13}\text{C}$  NMR  $\text{CD}_3\text{CN}$  spectrum of 1f

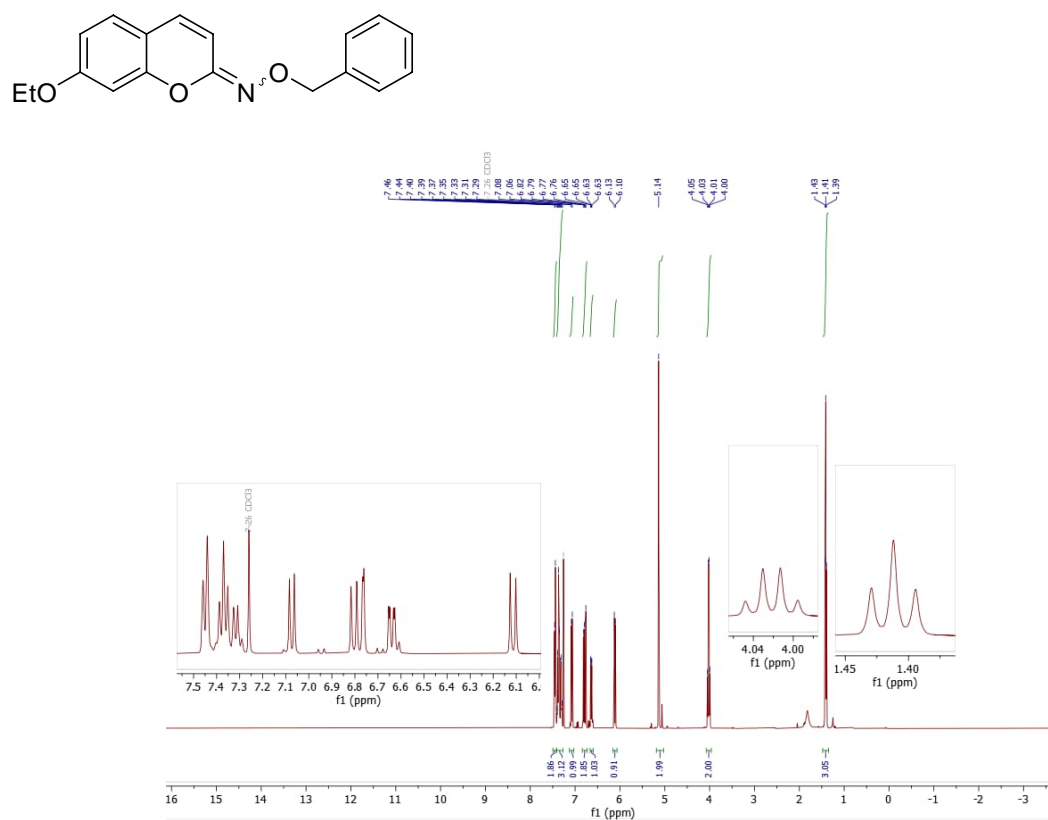
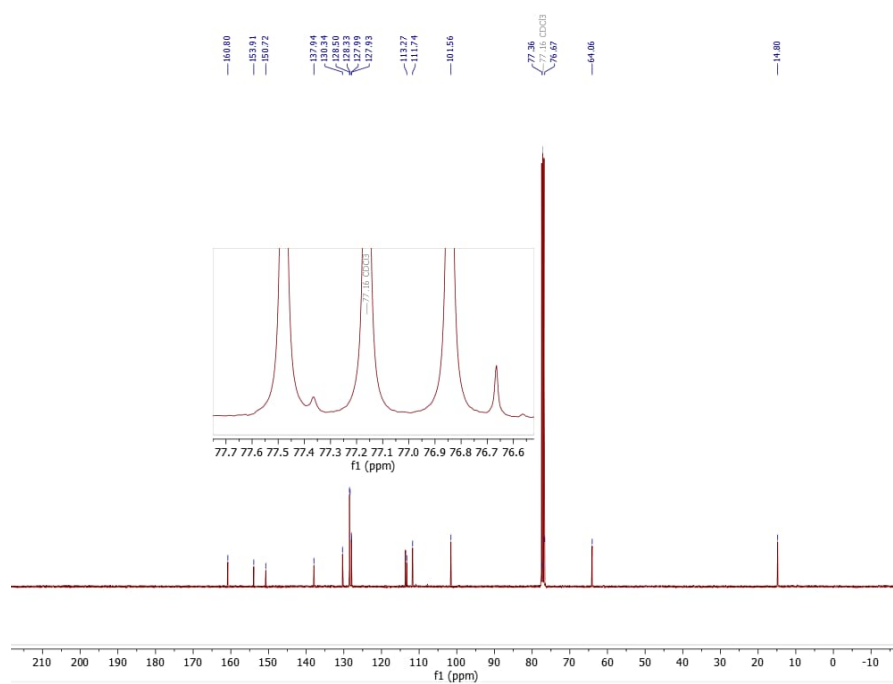
Figure S2.21.  $^1\text{H}$  NMR  $\text{CD}_3\text{CN}$  spectrum of 1gFigure S2.22.  $^{13}\text{C}$  NMR  $\text{CD}_3\text{CN}$  spectrum of 1g

Figure S2.23. <sup>1</sup>H NMR DMSO-d<sub>6</sub> spectrum of 1hFigure S2.24. <sup>13</sup>C NMR DMSO-d<sub>6</sub> spectrum of 1h

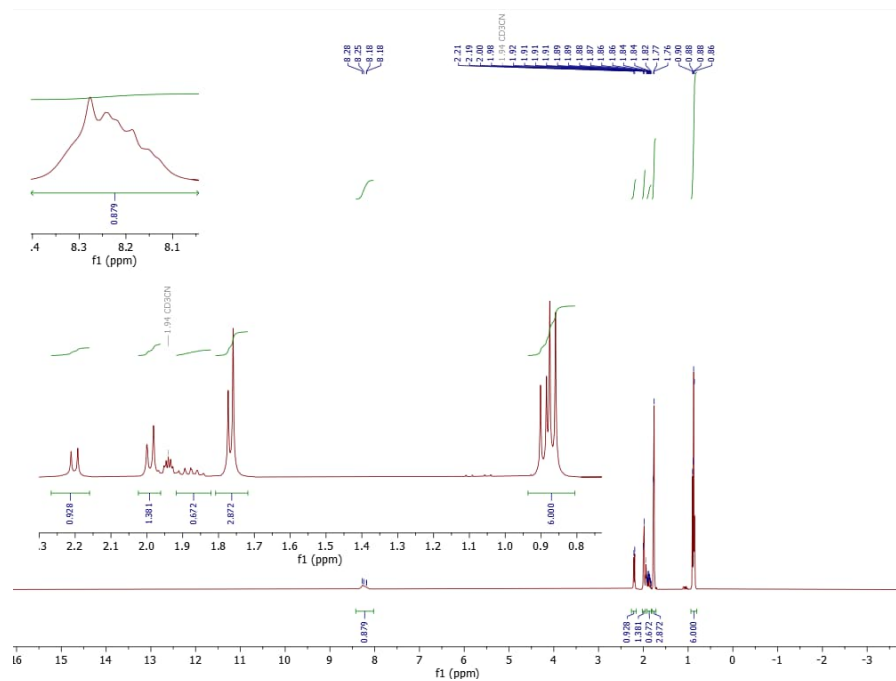
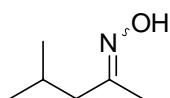
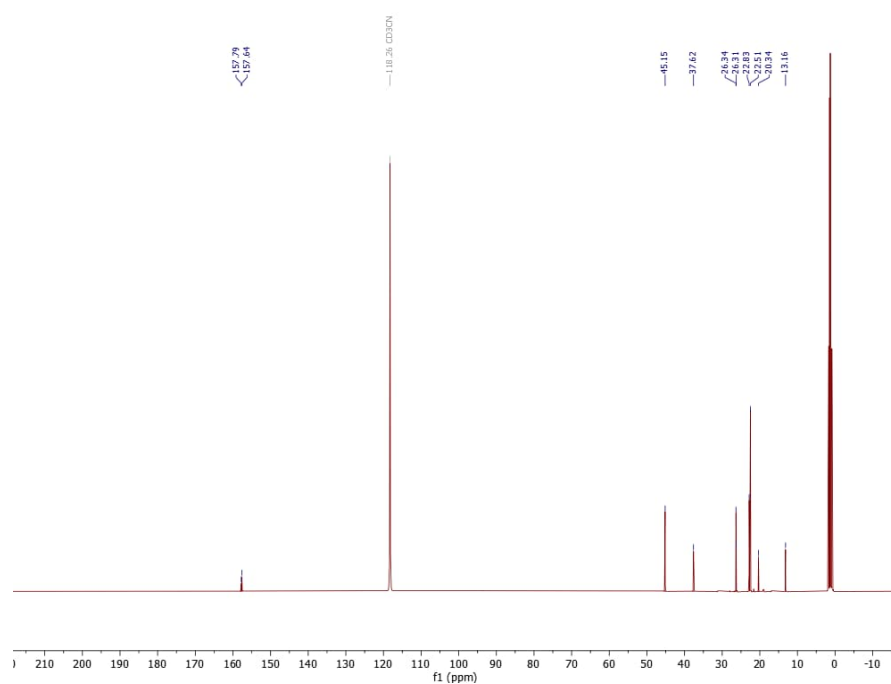


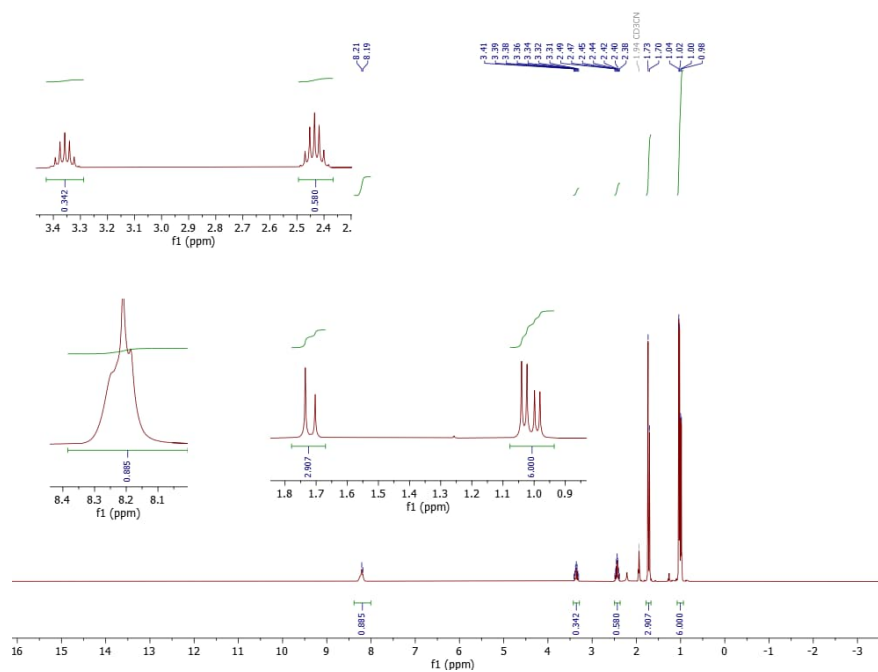
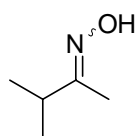
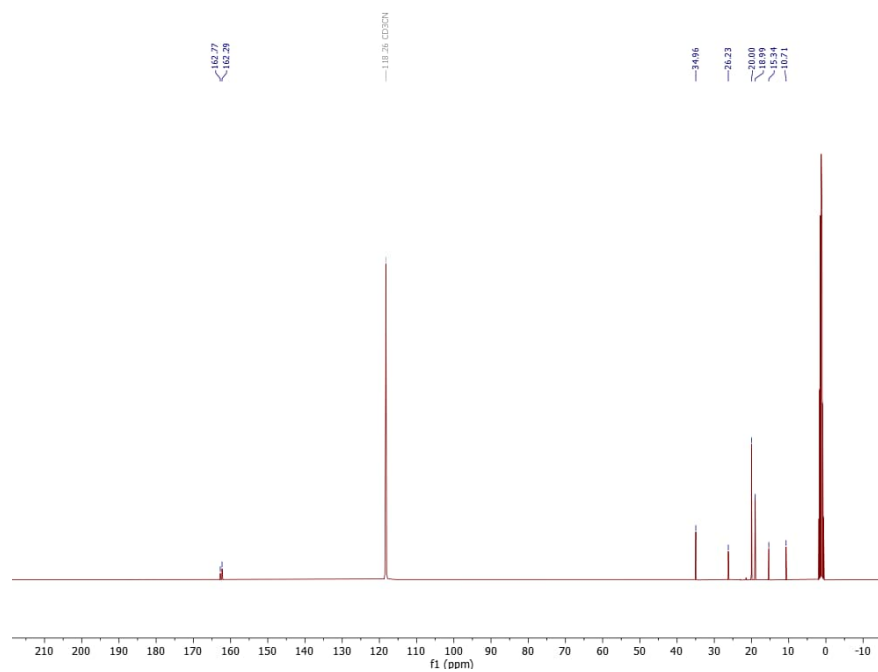
Figure S2.27.  $^1\text{H}$  NMR  $\text{CDCl}_3$  spectrum of 4Figure S2.28.  $^{13}\text{C}$  NMR  $\text{CDCl}_3$  spectrum of 4

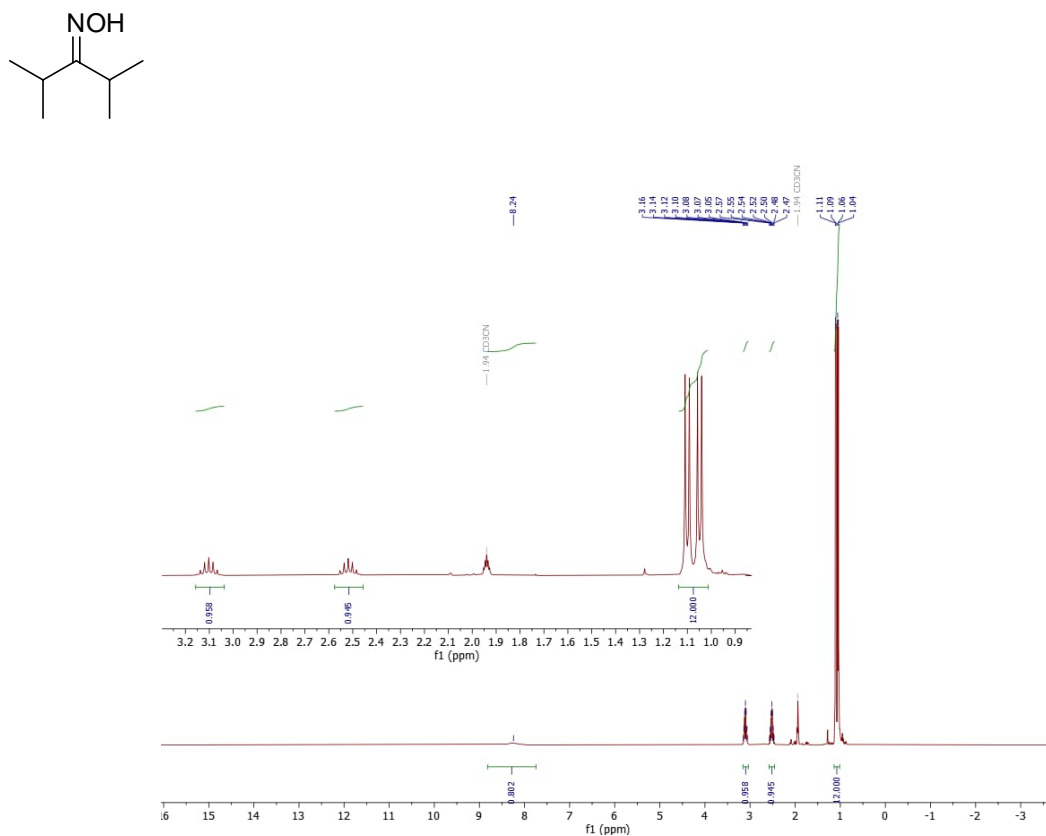
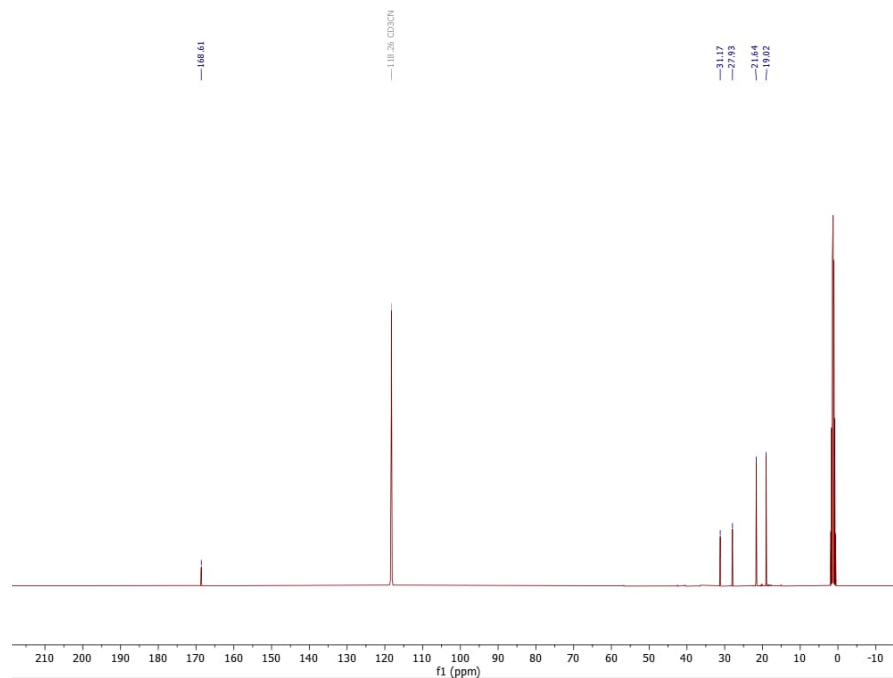
Figure S2.29.  $^1\text{H}$  NMR  $\text{CDCl}_3$  spectrum of 1iFigure S2.30.  $^{13}\text{C}$  NMR  $\text{CDCl}_3$  spectrum of 1i

Figure S2.31. <sup>1</sup>H NMR CDCl<sub>3</sub> spectrum of 1i-BnFigure S2.32. <sup>13</sup>C NMR CDCl<sub>3</sub> spectrum of 1i-Bn

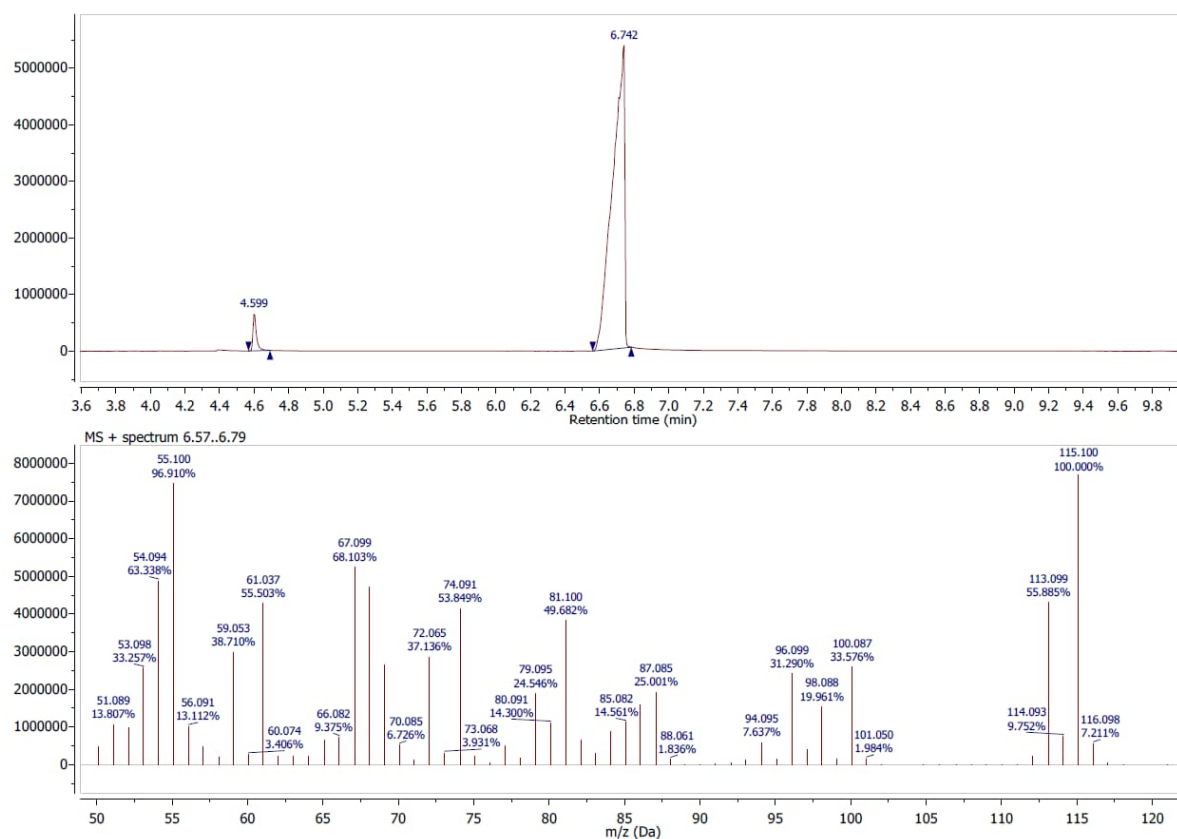


Figure S2.35. <sup>1</sup>H NMR CD<sub>3</sub>CN spectrum of 1jFigure S2.36. <sup>13</sup>C NMR CD<sub>3</sub>CN spectrum of 1j

Figure S2.37.  $^1\text{H}$  NMR  $\text{CD}_3\text{CN}$  spectrum of 1kFigure S2.38.  $^{13}\text{C}$  NMR  $\text{CD}_3\text{CN}$  spectrum of 1k

Figure S2.39.  $^1\text{H}$  NMR  $\text{CD}_3\text{CN}$  spectrum of 11Figure S2.40.  $^{13}\text{C}$  NMR  $\text{CD}_3\text{CN}$  spectrum of 11

## 7.2.7. GC-MS Data



$$m/z_{180} = 115.1$$

$$m/z_{160} = 113.1$$

$$\text{Isotope Purity} = \frac{100}{100 + 55.885} \cdot 100\% = 64\%$$

Figure S2.41. GC-MS chromatogram and mass-spectrum data of cyclohexanone oxime-<sup>18</sup>O

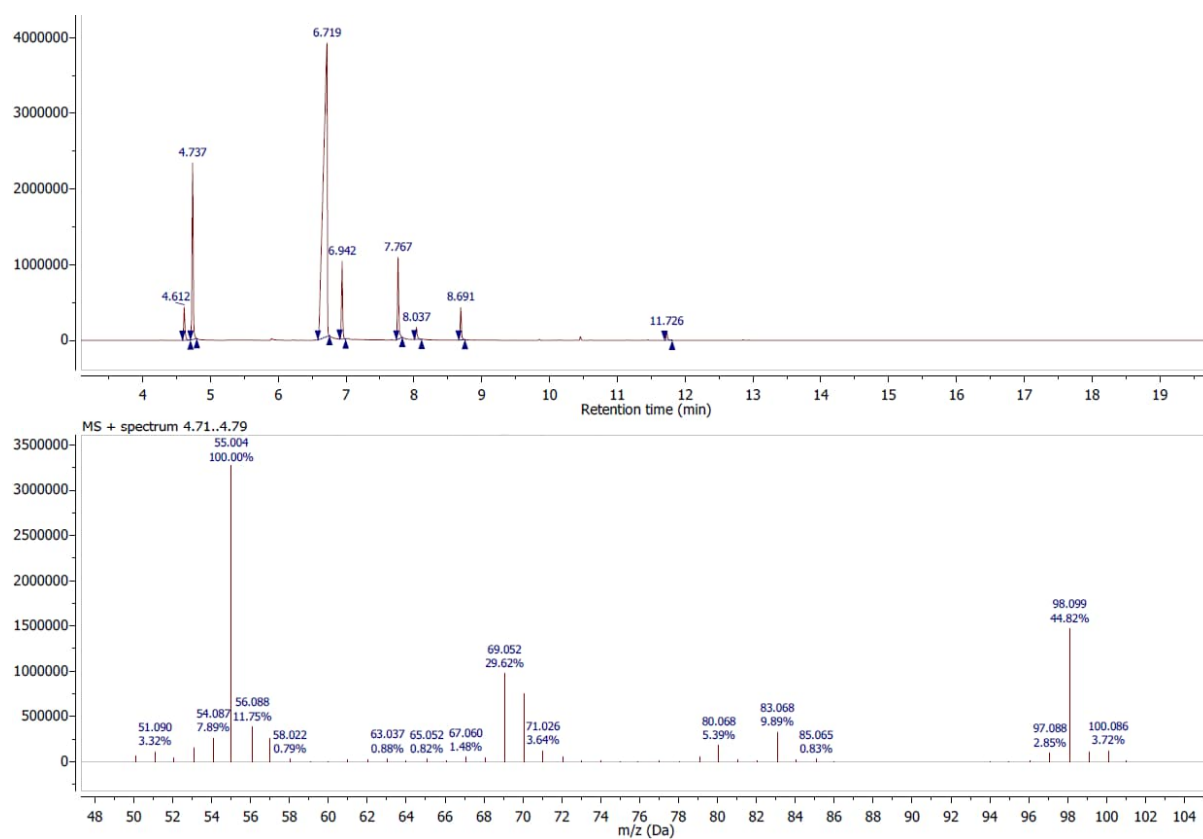


Figure S2.42. Oxidation of cyclohexanone oxime- $^{18}\text{O}$  with K-PHI under blue light (GC-MS of reaction mixture)



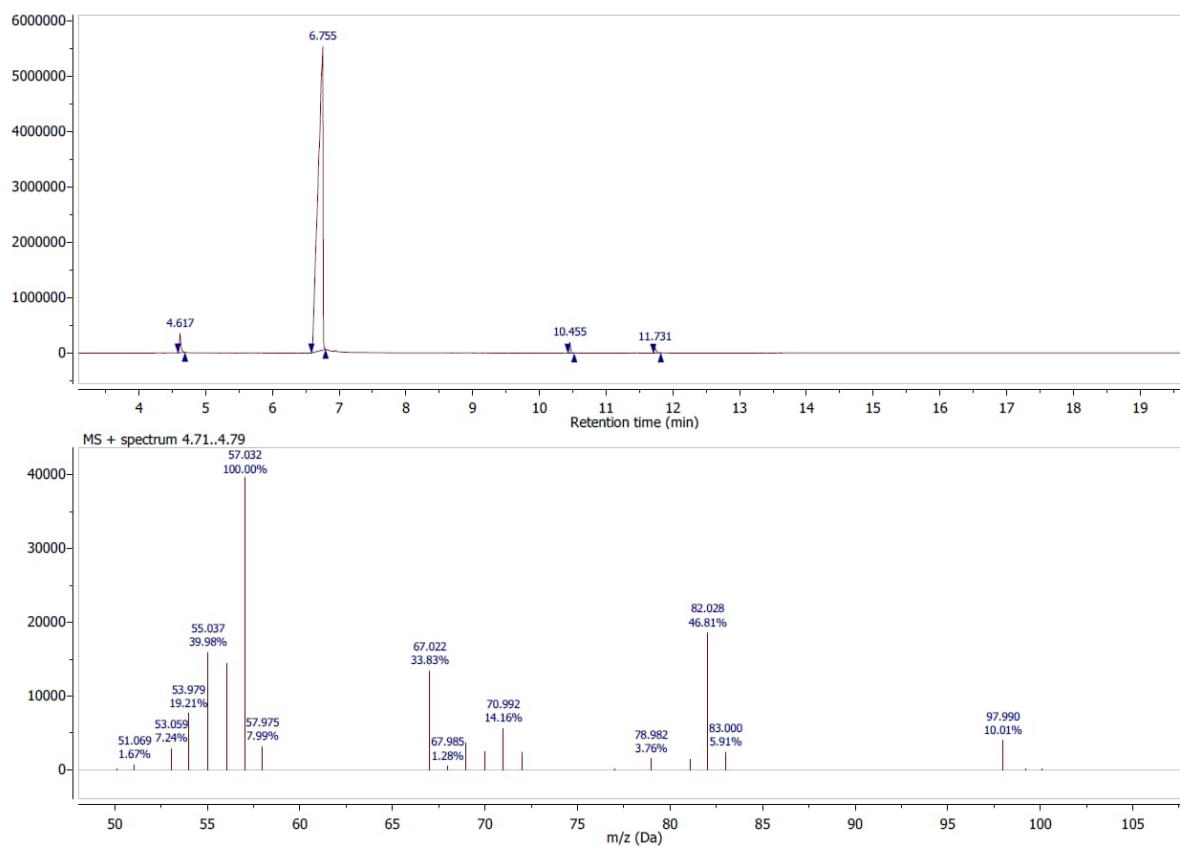


Figure S2.43. Oxidation of cyclohexanone oxime- $^{18}\text{O}$  without K-PHI under blue light (GC-MS of reaction mixture)



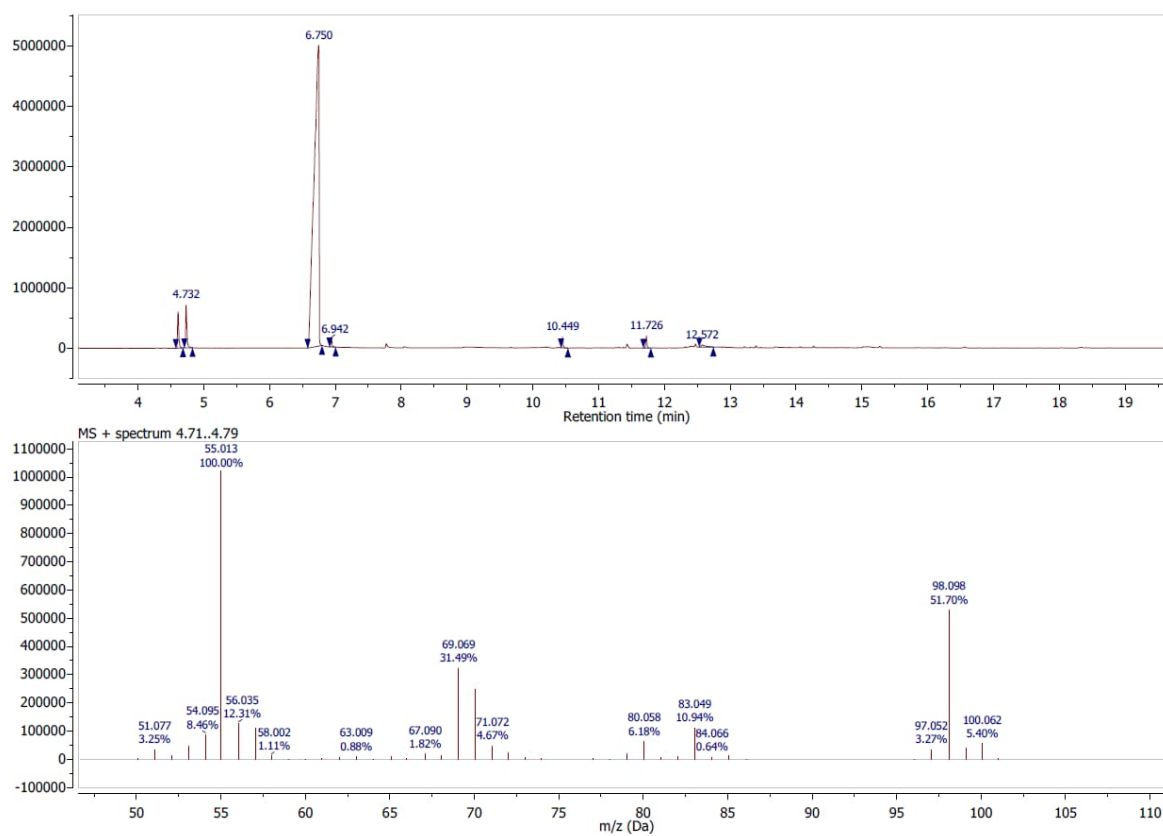


Figure S2.44. Oxidation of cyclohexanone oxime- $^{18}\text{O}$  with K-PHI under red light (GC-MS of reaction mixture)



## 7.2.8. Miscellaneous Data

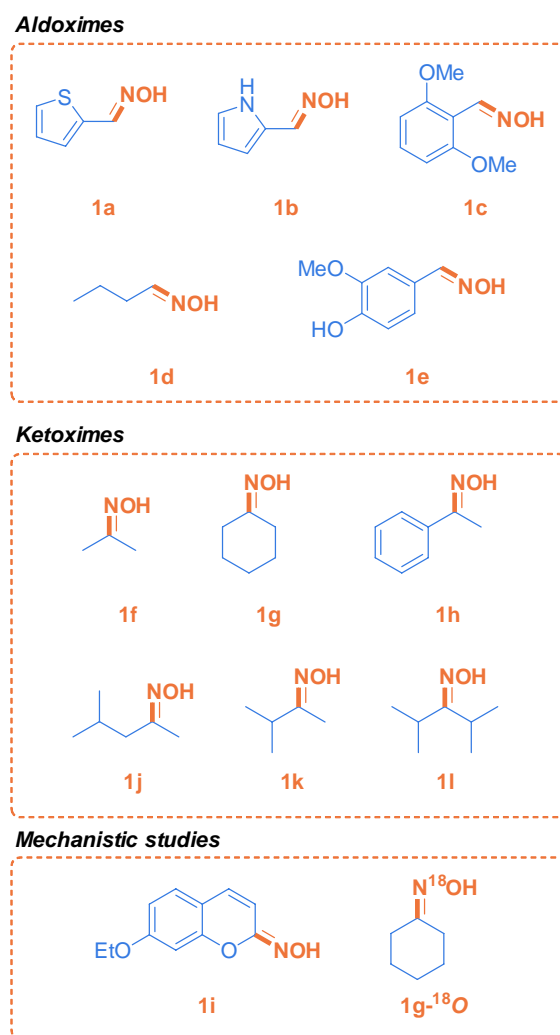
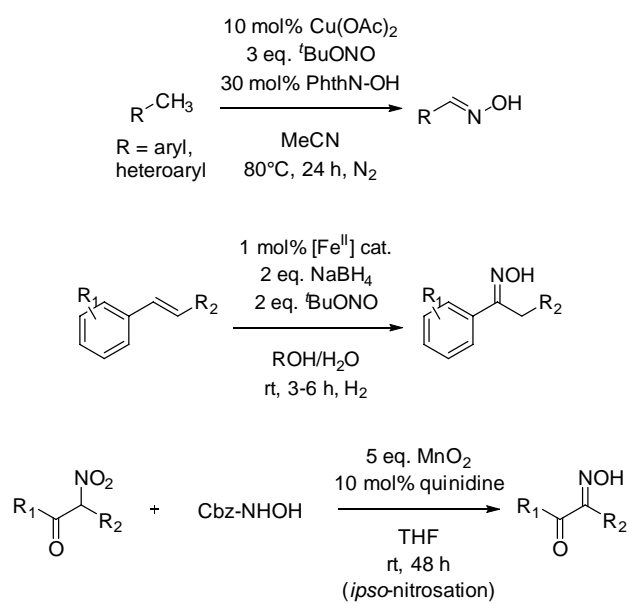


Figure S2.45. Complete reaction scope



Figure S2.46. Selected reaction pathways to obtain oximes from non-carbonyl substrates<sup>126</sup>

## 7.3. SI for Chapter 3

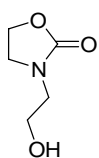
### 7.3.1. Synthetic Procedures

#### *Synthetic Procedures*

Oxazolidinone (1a) was purchased from TCI Chemicals ( $\geq 98\%$ ) and was used as received. All the reagents (purity 97% or greater) and solvents (HPLC grade) used in synthetic procedures and photocatalytic experiments were purchased from chemical supply companies (Sigma-Aldrich (Merck), AlfaAesar, J.T.Baker, VWR or TCI Chemicals) and were used as received.

#### *Preparation of oxazolidinones*

##### *3-(2-Hydroxyethyl)-1,3-oxazolidin-2-one (3)*



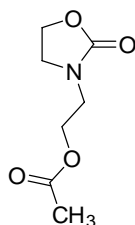
*Method A*, adapted from reference.<sup>258</sup> Sodium metal (46 ~ 60 mg) was dissolved in methanol (4 mL). The solution was added to a mixture of diethanolamine (21 g, 0.2 mol) and methyl carbonate (22.52 g, 0.25 mol). The mixture was stirred at reflux for 4 h and concentrated in vacuum (55 °C, 80 mbar), followed by distillation in high vacuum ( $5.5 \times 10^{-2}$  mbar, 175 ~ 180 °C). The distillation was carried out on a short path setup without excessive heating to prevent polymerization. Yield: 12.56 g, 48% (pale yellow oil). <sup>1</sup>H NMR (400 MHz, CDCl<sub>3</sub>)  $\delta$  4.37 – 4.27 (m, 2H), 3.74 (t,  $J = 5.3$  Hz, 2H), 3.71 – 3.62 (m, 2H), 3.37 – 3.30 (m, 2H). <sup>13</sup>C NMR (101 MHz, CDCl<sub>3</sub>)  $\delta$  159.5, 62.3, 60.4, 46.9, 45.7.

*Method B*. With vigorous stirring, diethanolamine (10.5 g, 0.1 mmol) and ethyl carbonate (12.1 mL, 0.1 mmol) were mixed into a 50 mL round bottom flask equipped with a Dean-Stark trap and a reflux condenser. The mixture was brought to 120 °C and then gradually heated up to 135 °C for approximately 8 h until distillate collection in the trap ceased (ca. 9 mL was collected). The reaction mixture was then dried with stirring under



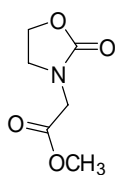
high vacuum ( $5.5 \times 10^{-2}$  mbar) for 2 h. Crude product contains minor impurities of starting materials (less than 10 mol.% in total) and was used without further purification for the synthesis of 1k. Yield of crude compound: 12.4 g, 95% (yellow oil).

### 3-(2-Acetoxy-ethyl)-oxazolidin-2-one (1b)



A solution of acetylchloride (7.38 g, 0.09 mol) in dichloromethane (50 mL) was added dropwise to a stirred solution of 3 (11.79 g, 0.09 mol) and triethylamine (9.54 g, 0.09 mol) in dichloromethane (100 mL) upon cooling on the ice bath. The mixture was stirred overnight and deionized water (200 mL) was added to the mixture. The product was extracted with dichloromethane ( $2 \times 100$  mL). Organic solutions were combined, dried over anhydrous  $\text{Na}_2\text{SO}_4$  and concentrated in vacuum ( $50^\circ\text{C}$ , 30 mbar). Yield: 2.97 g, 19% (white solid).  $^1\text{H}$  NMR (400 MHz,  $\text{CDCl}_3$ )  $\delta$  4.39 – 4.30 (m, 2H), 4.28 – 4.21 (m, 2H), 3.70 – 3.62 (m, 2H), 3.57 – 3.50 (m, 2H), 2.08 (s, 3H).  $^{13}\text{C}$  NMR (101 MHz,  $\text{CDCl}_3$ )  $\delta$  170.9, 158.6, 61.8, 45.9, 45.3, 43.6, 21.0.

### Methyl 2-oxo-3-oxazolidineacetate (1c)

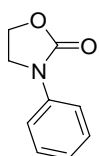


Alkylation procedure was adapted from the reference.<sup>259</sup> Oxazolidinone 1a (1.74 g, 20 mmol) was added to the suspension of NaH (0.84 g, 21 mmol) in DMF (40 mL) cooled on ice bath and under  $\text{N}_2$  flow. The suspension was stirred at room temperature and under  $\text{N}_2$  flow overnight. A solution of methyl 2-bromoacetate (3.21 g, 21 mmol) in DMF (10 mL) was added dropwise to the suspension cooled on water bath. The suspension was stirred at room temperature overnight. Then suspension was quenched with water (200



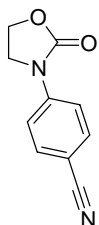
mL), followed by extraction with dichloromethane (50 mL  $\times$  3 times). The organic phases were combined and washed with water (30 mL  $\times$  5 times), dried with Na<sub>2</sub>SO<sub>4</sub> and concentrated in vacuum (50 °C, 30 mbar). The residue was distilled in vacuum and the product was collected as a fraction with boiling point at 116 – 120 °C at  $7.5 \times 10^{-5}$  bar into a receiver cooled with liquid nitrogen. Yield: 1.31 g, 41% (colorless oil). <sup>1</sup>H NMR (400 MHz, CDCl<sub>3</sub>)  $\delta$  4.43 – 4.36 (m, 2H), 4.04 (s, 2H), 3.76 (s, 3H), 3.73 – 3.67 (m, 2H). <sup>13</sup>C NMR (101 MHz, CDCl<sub>3</sub>)  $\delta$  169.0, 158.7, 62.2, 52.5, 45.4, 45.0.

### 3-Phenyl-2-oxazolidinone (1d)



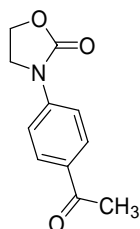
Adapted from reference.<sup>260</sup> Oxazolidinone 1a (1 g, 11.4 mmol), copper iodide (0.065 g, 3 mol%), ( $\pm$ ) *trans*-1,2-diaminocyclohexane (0.129 g, 10 mol%), potassium carbonate (3.14 g, 22.8 mmol) and bromobenzene (1.2 mL, 11.4 mol) were dissolved in 1,4-dioxane (5.7 mL). The mixture was refluxed at 110 °C for 15 h. The reaction mixture was dissolved in ethyl acetate (10 mL) and filtered through silica gel plug, followed by washing with ethyl acetate (10 mL  $\times$  3 times). The solution was concentrated in vacuum (50 °C, 30 mbar). The product was purified by recrystallization in MeCN. Yield: 0.77 g, 41% (dark yellow solid). <sup>1</sup>H NMR (400 MHz, CDCl<sub>3</sub>)  $\delta$  7.54 (d, *J* = 7.7 Hz, 2H), 7.42 – 7.34 (m, 2H), 7.16 – 7.12 (m, 1H), 4.52 – 4.43 (m, 2H), 4.10 – 4.01 (m, 2H). <sup>13</sup>C NMR (101 MHz, CDCl<sub>3</sub>)  $\delta$  155.4, 138.3, 129.2, 124.2, 118.3, 61.4, 45.3.

### 4-(2-Oxo-3-oxazolidinyl)benzonitrile (1e)



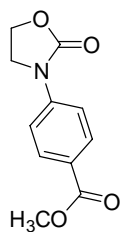
Adapted from reference.<sup>260</sup> Oxazolidinone 1a (1 g, 11.4 mmol), copper iodide (0.065 g, 3 mol%), ( $\pm$ ) *trans*-1,2-diaminocyclohexane (0.129 g, 10 mol%), potassium carbonate (3.14 g, 22.8 mmol) and 4-bromobenzonitrile (2.08 g, 11.4 mol) were dissolved in 1,4-dioxane (5.7 mL). The mixture was refluxed at 110 °C for 15 h. The reaction mixture was dissolved in ethyl acetate (10 mL) and filtered through silica gel plug, followed by washing with ethyl acetate (10 mL  $\times$  3 times). The solution was concentrated in vacuum (50 °C, 30 mbar). The product was purified by re-crystallization in MeCN. Yield: 59 % (white solid). <sup>1</sup>H NMR (400 MHz, CDCl<sub>3</sub>)  $\delta$  7.70 – 7.65 (m, 4H), 4.66 – 4.46 (m, 2H), 4.19 – 4.02 (m, 2H). <sup>13</sup>C NMR (101 MHz, CDCl<sub>3</sub>)  $\delta$  154.7, 142.1, 133.4, 118.8, 118.0, 107.1, 61.5, 44.8.

### 3-(4-acetylphenyl)oxazolidin-2-one (1f)

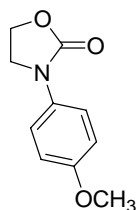


Adapted from reference.<sup>260</sup> Oxazolidinone 1a (1 g, 11.4 mmol), copper iodide (0.065 g, 3 mol%), ( $\pm$ ) *trans*-1,2-diaminocyclohexane (0.129 g, 10 mol%), potassium carbonate (3.14 g, 22.8 mmol) and 4-bromoacetophenone (2.27 g, 11.4 mol) were dissolved in 1,4-dioxane (5.7 mL). The mixture was refluxed at 110 °C for 15 h. The reaction mixture was dissolved in ethyl acetate (10 mL) and filtered through silica gel plug, followed by washing with ethyl acetate (10 mL  $\times$  3 times). The solution was concentrated in vacuum (50 °C, 30 mbar). The product was purified by re-crystallization in MeCN. Yield: 47 % (white solid). <sup>1</sup>H NMR (400 MHz, CDCl<sub>3</sub>)  $\delta$  7.98 (d,  $J$  = 8.9 Hz, 2H), 7.64 (d,  $J$  = 8.9 Hz, 2H), 4.57 – 4.48 (m, 2H), 4.15 – 4.07 (m, 2H), 2.58 (s, 3H). <sup>13</sup>C NMR (101 MHz, CDCl<sub>3</sub>)  $\delta$  197.1, 154.9, 142.4, 132.6, 129.8, 117.3, 61.5, 45.0, 26.6.



*Methyl 4-(2-oxo-3-oxazolidinyl)benzoate (1g)*

Adapted from reference.<sup>260</sup> Oxazolidinone 1a (1 g, 11.4 mmol), copper iodide (0.218 g, 10 mol%), ( $\pm$ ) *trans*-1,2-diaminocyclohexane (0.129 g, 10 mol%), potassium carbonate (3.14 g, 22.8 mmol) and methyl 4-iodobenzoate (2.99 g, 11.4 mol) were dissolved in 1,4-dioxane (5.7 mL). The mixture was refluxed at 110 °C for 15 h. The reaction mixture was dissolved in ethyl acetate (10 mL) and filtered through silica gel plug, followed by washing with ethyl acetate (10 mL  $\times$  3 times). The solution was concentrated in vacuum (50 °C, 30 mbar). Yield: 51% (yellow solid). <sup>1</sup>H NMR (400 MHz, CDCl<sub>3</sub>)  $\delta$  8.06 (d,  $J$  = 8.9 Hz, 2H), 7.64 (d,  $J$  = 9.0 Hz, 2H), 4.57 – 4.49 (m, 2H), 4.16 – 4.07 (m, 2H), 3.91 (s, 3H). <sup>13</sup>C NMR (101 MHz, CDCl<sub>3</sub>)  $\delta$  166.7, 155.0, 142.3, 130.9, 125.5, 117.3, 61.5, 52.3, 45.1.

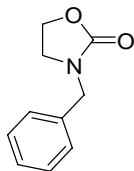
*3-(4-Methoxyphenyl)-2-oxazolidinone (1h)*

Adapted from reference.<sup>260</sup> Oxazolidinone 1a (1 g, 11.4 mmol), copper iodide (0.218 g, 10 mol%), ( $\pm$ ) *trans*-1,2-diaminocyclohexane (0.129 g, 10 mol%), potassium carbonate (3.14 g, 22.8 mmol) and 4-bromoanisole (2.27 g, 11.4 mol) were dissolved in 1,4-dioxane (5.7 mL). The mixture was refluxed at 110 °C for 15 h. The reaction mixture was dissolved in ethyl acetate (10 mL) and filtered through silica gel plug, followed by adding ethyl acetate (10 mL  $\times$  3 times) into the silica gel. The solution was concentrated in vacuum (50 °C, 30 mbar). The product was purified by re-crystallization in MeCN. Yield: 57% (brown solid). <sup>1</sup>H NMR (400 MHz, CDCl<sub>3</sub>)  $\delta$  7.43 (d,  $J$  = 9.2 Hz, 2H), 6.91 (d,  $J$  =



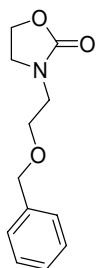
9.2 Hz, 2H), 4.53 – 4.42 (m, 2H), 4.08 – 3.99 (m, 2H), 3.80 (s, 3H).  $^{13}\text{C}$  NMR (101 MHz,  $\text{CDCl}_3$ )  $\delta$  156.5, 155.7, 131.5, 120.4, 114.4, 61.4, 55.7, 45.9.

### 3-Benzylloxazolidin-2-one (1i)



Alkylation procedure was adapted from the reference.<sup>259</sup> Oxazolidinone 1a (1.74 g, 20 mmol) was added to the suspension of NaH (0.84 g, 21 mmol) in DMF (40 mL) cooled on ice bath and under  $\text{N}_2$  flow. The suspension was stirred at room temperature and under  $\text{N}_2$  flow overnight. A solution of benzyl bromide (3.57 g, 21 mmol) in DMF (10 mL) was added dropwise to the suspension cooled on water bath. The suspension was stirred at room temperature overnight. The suspension was quenched with water (200 mL), followed by extraction with dichloromethane (50 mL  $\times$  3 times). The organic phases were combined and washed with water (30 mL  $\times$  5 times), dried with  $\text{Na}_2\text{SO}_4$  and concentrated in vacuum (50  $^\circ\text{C}$ , 30 mbar). The residue was distilled in vacuum and the product was collected as a fraction with boiling point at  $\sim 140$   $^\circ\text{C}$  at  $6.5 \times 10^{-5}$  bar into a receiver cooled with liquid nitrogen. Yield: 2.60 g, 73% (white solid).  $^1\text{H}$  NMR (400 MHz,  $\text{CDCl}_3$ )  $\delta$  7.39 – 7.28 (m, 5H), 4.44 (s, 2H), 4.31 (t,  $J = 7.9$  Hz, 2H), 3.43 (t,  $J = 7.9$  Hz, 2H).  $^{13}\text{C}$  NMR (101 MHz,  $\text{CDCl}_3$ )  $\delta$  158.7, 135.9, 129.0, 128.3, 128.1, 61.9, 48.6, 44.1.

### 3-[2-(Phenylmethoxy)ethyl]-2-oxazolidinone (1j)

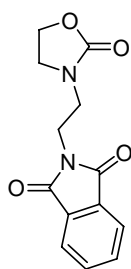


Compound 3 (2.62 g, 20 mmol) was added to the suspension of NaH (0.84 g, 21 mmol) in DMF (40 mL) cooled on ice bath and under  $\text{N}_2$  flow. The suspension was stirred at room



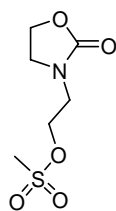
temperature and under N<sub>2</sub> flow overnight. A solution of benzyl bromide (3.57 g, 21 mmol) in DMF (10 mL) was added dropwise to the suspension cooled on water bath. The suspension was stirred at room temperature overnight. The reaction was quenched with water (200 mL), followed by extraction with dichloromethane (50 mL × 3 times). The organic phases were combined and washed with water (30 mL × 5 times), dried with Na<sub>2</sub>SO<sub>4</sub> and concentrated in vacuum (50 °C, 30 mbar). The residue was distilled in vacuum and the product was collected as a fraction with boiling point at ~ 153 °C at 6.9 × 10<sup>-5</sup> bar into a receiver cooled with liquid nitrogen. Yield: 1.55 g, 35% (pale yellow oil). <sup>1</sup>H NMR (400 MHz, CDCl<sub>3</sub>) δ 7.40 – 7.27 (m, 5H), 4.52 (s, 2H), 4.34 – 4.26 (m, 2H), 3.72 – 3.64 (m, 2H), 3.68 – 3.62 (m, 2H), 3.48 (t, *J* = 5.0 Hz, 2H). <sup>13</sup>C NMR (101 MHz, CDCl<sub>3</sub>) δ 158.7, 138.0, 128.6, 128.0, 127.8, 73.2, 68.8, 62.1, 46.1, 44.4.

*2-(2-(2-oxooxazolidin-3-yl)ethyl)isoindoline-1,3-dione (1k)*



*Step 1.* Compound 3 (6.56 g, 0.05 mol) and mesyl chloride (4.65 mL, 0.06 mol) were dissolved in 100 mL of dichloromethane in round bottom flask and cooled with strong stirring on an ethanol-ice bath. To this solution, DIPEA (17.4 mL, 0.1 mol) was added dropwise via pressure-equalized funnel over the course of 10 min. After addition, the solution was stirred for 30 min while on a bath and then for 3 h at room temperature. The reaction mixture was consequently washed with water, saturated sodium bicarbonate and brine and dried over anhydrous sodium sulfate. Dried organic phase was then evaporated to dryness on a rotovap and further dried under high vacuum (5.5 × 10<sup>-2</sup> mbar) for 2 h. Yield of crude 2-(2-(2-oxooxazolidin-3-yl)ethyl) methanesulfonate 4: 6.62 g, 63% (thick yellow oil). The compound was used in the next step without further purification:

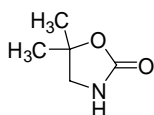




$^1\text{H}$  NMR (400 MHz,  $\text{CDCl}_3$ )  $\delta$  4.43 – 4.34 (m, 4H), 3.75 – 3.69 (m, 2H), 3.64 – 3.60 (m, 2H), 3.06 (s, 3H).

*Step 2.* Compound 4 from the previous step (6.62 g) was dissolved in DMF (75 mL), and potassium phthalimide (6.153 g, 1.05 eq.) was added. The mixture was stirred with reflux condenser at 75 °C for 5 h, then cooled down to room temperature. The suspension was then added dropwise to 250 mL of water vigorously stirred in an Erlenmeyer flask over the course of 30 min and then stirred for additional 30 min. The precipitate was filtered off and discarded, and the filtrate was extracted 3 times with 100 mL ethyl acetate each time. Combined organic extracts were washed with brine, dried over anhydrous sodium sulfate and evaporated to dryness to yield pure product 1k: 3.9 g, 47% (pale yellow solid). Additional crop of product contaminated with phthalimide may be obtained by evaporating the aqueous phase from the extraction to dryness and extracting the residue with hot isopropanol followed by further evaporation.  $^1\text{H}$  NMR (400 MHz,  $\text{CDCl}_3$ )  $\delta$  7.83 (dd,  $J$  = 5.5, 3.0 Hz, 2H), 7.70 (dd,  $J$  = 5.5, 3.0 Hz, 2H), 4.34 – 4.24 (m, 2H), 3.91 – 3.83 (m, 2H), 3.75 – 3.68 (m, 2H), 3.61 – 3.54 (m, 2H).  $^{13}\text{C}$  NMR (101 MHz,  $\text{CDCl}_3$ )  $\delta$  168.42, 158.65, 134.22, 131.95, 123.54, 62.05, 44.24, 43.08, 35.13.

#### 5,5-Dimethyl-2-oxazolidinone (1l)

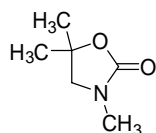


1-Amino-2-methyl-2-propanol (1 g, 11.2 mmol) and dimethylcarbonate (1.26 g, 14 mmol) were mixed, followed by the addition of sodium methoxide solution prepared by dissolving sodium (40 mg, 0.87 mmol) in methanol (2 mL). The mixture was stirred at reflux for 24 h and concentrated in vacuum (50 °C, 30 mbar). Water (5 mL) was added to



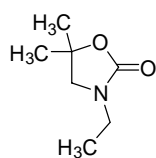
the residue. The suspension was extracted with ethyl acetate (10 mL  $\times$  3 times), dried over Na<sub>2</sub>SO<sub>4</sub> and concentrated in vacuum (50 °C, 30 mbar). Yield: 26% (white solid). <sup>1</sup>H NMR (400 MHz, CDCl<sub>3</sub>)  $\delta$  3.34 (s, 2H), 1.47 (s, 6H). <sup>13</sup>C NMR (101 MHz, CDCl<sub>3</sub>)  $\delta$  159.5, 81.2, 52.8, 27.3.

### 3,5,5-Trimethyl-2-oxazolidinone (1m)



Sodium hydride (0.1 g, 60% dispersion in mineral oil) was washed with hexane (1 mL  $\times$  3 times) and added to tetrahydrofuran (THF) (4 mL). Compound 1m (0.23 g, 2 mmol) was added in portions to the suspension cooled on ice bath. The mixture was stirred under N<sub>2</sub> overnight. Iodomethane (0.3 g, 2 mmol) in 1 mL THF was added to the mixture dropwise in ice bath. The mixture was stirred under N<sub>2</sub> overnight and concentrated in vacuum (50 °C, 30 mbar). Water (20 mL) was added to the residue. The suspension was extracted with dichloromethane (15 mL  $\times$  3 times), dried over Na<sub>2</sub>SO<sub>4</sub> and concentrated in vacuum (50 °C, 30 mbar). Yield: 86% (yellow oil). <sup>1</sup>H NMR (400 MHz, CDCl<sub>3</sub>)  $\delta$  3.28 (s, 2H), 2.88 (s, 3H), 1.45 (s, 6H). <sup>13</sup>C NMR (101 MHz, CDCl<sub>3</sub>)  $\delta$  158.0, 59.2, 31.2, 29.9, 27.6.

### 3-Ethyl-5,5-dimethyl-2-oxazolidinone (1n)

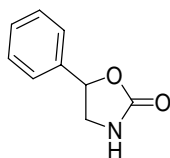


Sodium hydride (0.25 g, 60% dispersion in mineral oil) was washed with hexane (1 mL  $\times$  3 times) and added to tetrahydrofuran (THF) (5 mL). Compound 1m (0.345 g, 3 mmol) was added in portions to the suspension cooled on ice bath. The mixture was stirred under N<sub>2</sub> overnight. Iodoethane (0.47 g, 3 mmol) in 1 mL THF was added to the mixture dropwise in ice bath. The mixture was heated at 90 °C for 80 min in a microwave reactor and concentrated in vacuum (50 °C, 30 mbar). Water (20 mL) was added to the residue. The suspension was extracted with dichloromethane (15 mL  $\times$  3 times), dried over



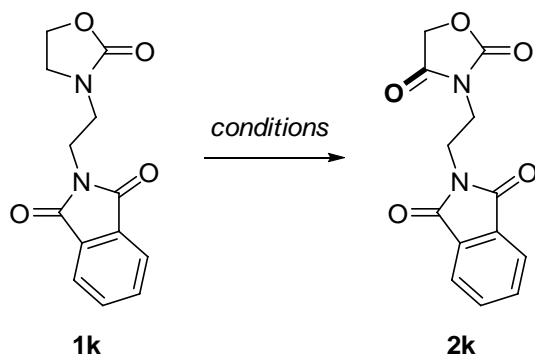
$\text{Na}_2\text{SO}_4$  and concentrated in vacuum (50 °C, 30 mbar). Yield: 45% (colorless oil).  $^1\text{H}$  NMR (400 MHz,  $\text{CDCl}_3$ )  $\delta$  3.34 – 3.29 (m, 2H), 3.27 (s, 2H), 1.44 (s, 6H), 1.15 (t,  $J = 7.3$  Hz, 3H).  $^{13}\text{C}$  NMR (101 MHz,  $\text{CDCl}_3$ )  $\delta$  157.5, 70.7, 56.2, 38.8, 27.5, 12.7.

#### 5-Phenyl-2-oxazolidinone (1o)



2-Amino-1-phenylethanol (1 g, 7 mmol) and dimethylcarbonate (0.787 g, 8.75 mmol) were mixed, followed by the addition of sodium methoxide solution prepared by dissolving sodium (40 mg, 0.87 mmol) in methanol (2 mL). The mixture was stirred at reflux for 24 h and concentrated in vacuum (50 °C, 30 mbar). Water (5 mL) was added to the residue. The suspension was extracted with ethyl acetate (10 mL  $\times$  3 times), dried over  $\text{Na}_2\text{SO}_4$  and concentrated in vacuum (50 °C, 30 mbar). The product was purified by recrystallization in MeCN. Yield: 16% (white solid).  $^1\text{H}$  NMR (400 MHz,  $\text{CDCl}_3$ )  $\delta$  7.46 – 7.35 (m, 5H), 5.66 – 5.62 (m, 1H), 4.01 – 3.97 (m, 1H), 3.57 – 3.53 (m, 1H).  $^{13}\text{C}$  NMR (101 MHz,  $\text{CDCl}_3$ )  $\delta$  159.7, 138.5, 129.1, 129.1, 125.8, 48.4.

#### Conventional oxidation experiments for oxazolidinone 1k



#### Unsuccessful attempts

*Stoichiometric copper(II) acetylacetonate oxidation* (adapted from reference<sup>261</sup>). To a solution of 1k (26 mg, 0.1 mmol) in 1 mL DMSO in a test tube was added powdered



$\text{Cu}(\text{acac})_2$  (26 mg, 0.1 mmol). The suspension was submerged in an oil bath preheated to 135 °C and stirred for 30 min. After cooling to room temperature, the reaction was quenched with water, and the precipitate was analyzed by  $^1\text{H}$  NMR. Product 2k was not detected.

*TEMPO-*t*BuOOH-mediated oxidation.*<sup>262</sup> To a solution of 1k (52 mg, 0.2 mmol) in 1.5 mL acetonitrile was consequently added CuBr (5.7 mg, 20 mol.%), TEMPO (15.6 mg, 0.1 mmol) and 70% aqueous *tert*-butylhydroperoxide (0.274 mL, 2 mmol). The vial was closed and allowed to stir for 8 h at room temperature. The reaction mixture was evaporated using stream of pressurized air and was then analyzed by  $^1\text{H}$  NMR. Product 2k was not detected.

### Successful attempts

*Catalytic ruthenium tetroxide oxidation (1 mmol scale).* In a 25 mL round bottom flask, 1k (260 mg, 1 mmol) was dissolved in 3 mL of ethyl acetate, 2 mL of methyl carbonate and 10 mL of water. Then,  $\text{NaIO}_4$  (1.07 g, 5 mmol) was added to the mixture followed by ruthenium(III) chloride hydrate (17 mg, approx. 7.5 mol.%). The flask was stoppered and vigorously stirred (1200 rpm) overnight at room temperature. The organic layer was then separated in a funnel, dried with anhydrous sodium sulfate and quenched with 5 mL of isopropanol to destroy the tetroxide. The solution was then passed through a plug of silica gel and washed with additional isopropanol, then evaporated to dryness. Yield of crude 2k: 159 mg (58%), tarry greyish mass.

*Catalytic ruthenium tetroxide oxidation (10 mmol scale).* Reaction was carried out in 2-neck 250 mL round bottom flask equipped with overhead Teflon blade stirrer (350 rpm). The procedure and ratios of materials were the same as for 1 mmol scale with a quantity multiplication factor of 10. Yield of crude 2k: 1.15 g (42%), black thick oil.

The product from both runs was combined and purified via flash column chromatography using hexane and ethyl acetate as an eluent (1:1 v/v). Combined yield of pure 2k: 0.8 g (26%), white needles.



## Preparation of Photocatalysts

### *mpg-CN*

The catalyst was prepared according to a previously reported procedure.<sup>179</sup> Cyanamide (3.0 g) and Ludox HS-40 aqueous colloid silica (7.5 g) were mixed in a 10 mL glass vial. The mixture was stirred at room temperature for 30 min until cyanamide has completely dissolved. The resultant solution was stirred at +60 °C for 16 h until water has completely evaporated. Magnetic stir bar was removed and white solid was transferred to the porcelain crucible and heated under N<sub>2</sub> flow in the oven. The temperature was increased from room temperature to 550 °C within 4 h and maintained at 550 °C for 4 h. The crucible was spontaneously cooled to room temperature. The solid from the crucible was briefly grinded in the mortar and transferred to the polypropylene bottle. A solution of (NH<sub>4</sub>)HF<sub>2</sub> (0.24 g·mL<sup>-1</sup>, 50 mL) was added and suspension was stirred at room temperature for 24 h. The solid was filtered, thoroughly washed 3-4 times with water, once with ethanol and dried in vacuum (55 °C, 20 mbar) overnight.

### *K-PHI*

The catalyst was prepared according to a previously reported procedure.<sup>180</sup> A steel ball mill cup was charged with LiCl (2.25 g) and KCl (2.75 g). A steel ball was placed in the cup and the mixture was homogenized using ball milling (20 s<sup>-1</sup>, 2 min). The powder was transferred into a porcelain crucible, covered with a lid, and placed in an oven. The temperature inside the oven was increased from 20 to 580 °C within 4 h under a flow of nitrogen, held at 580 °C for 4 h, and allowed to cool to room temperature. The solid was removed from the crucible and crushed into fine powder using ball milling. The prepared eutectic is a hygroscopic solid that should be used right after preparation. Yield: 4.97 g, 99%. A mixture of 5-aminotetrazole (0.99 g) and LiCl/KCl eutectics (4.97 g) was placed in a steel ball mill cup. The steel ball was inserted and the cup was closed. The mixture of precursors was ground for 5 min at the operational frequency 25 Hz. The resultant flourlike white powder was transferred into a porcelain crucible, covered with a porcelain lid, and placed in an oven. The temperature inside the oven was increased



from 20 to 600 °C within 4 h ( $2.4 \text{ K}\cdot\text{min}^{-1}$ ) under a flow of nitrogen ( $15 \text{ L}\cdot\text{min}^{-1}$ ), after which it was maintained at 600 °C for another 4 h. After that, the oven was allowed to cool slowly to room temperature. The melt from the crucible was transferred into a beaker, and deionized water (50 mL) and a stir bar were added. The suspension was stirred at room temperature for 4 h until it became homogeneous and no agglomerated particles were seen. The solid was separated by centrifugation ( $6500 \text{ min}^{-1}$ , 12 min). The aqueous solution was carefully removed and the residue transferred into a 2 mL safe-lock tube. The solid was washed with water ( $3 \times 1.5 \text{ mL}$ ) using a centrifuge ( $13,500 \text{ min}^{-1}$ , 1 min) and dried under vacuum, giving 256 mg of the dark yellow material.

### *Na-PHI*

The catalyst was prepared according to a previously reported procedure.<sup>181</sup> Melamine (1 g) was thoroughly grinded with NaCl (10 g). Reaction mixture was transferred into a porcelain crucible which was covered with a lid. Crucible was placed in a heating oven and heated under a constant nitrogen flow (15 L/min) to 600 °C with a heating rate of 2.3 °C/min, held at 600 °C for 4 hours, then allowed to cool down. The actual temperature inside the oven chamber could vary by up to 50 °C. The crude product was removed from the crucible, washed with deionized water (1 L), isolated by filtration, then thoroughly washed with deionized water on the filter (1 L) and dried in a vacuum oven at 50 °C for 15 h.



## Light Sources

Unless explicitly specified, in this work, the following light sources were used: blue LED module (emission maximum  $\lambda = 455\text{-}465$  nm, measured optical power  $205\text{ mW cm}^{-2}$ , photon flux  $0.8\text{ }\mu\text{mol cm}^{-2}\text{ s}^{-1}$ ); white LED module 1 (emission maxima  $\lambda = 440, 560$  nm, measured optical power  $106\text{ mW cm}^{-2}$ ); white LED module 2 (emission maxima  $\lambda = 440, 560$  nm, measured optical power  $203\text{ mW cm}^{-2}$ ); green LED module (emission maximum  $\lambda = 525\text{-}535$  nm, measured optical power  $100\text{ mW cm}^{-2}$ , photon flux  $0.4\text{ }\mu\text{mol cm}^{-2}\text{ s}^{-1}$ ); purple LED module (emission maximum  $\lambda = 410$  nm, measured optical power  $103\text{ mW cm}^{-2}$ , photon flux  $0.4\text{ }\mu\text{mol cm}^{-2}\text{ s}^{-1}$ ); red LED module (emission maximum  $\lambda = 620\text{-}625$  nm, measured optical power  $302\text{ mW cm}^{-2}$ , photon flux  $1.6\text{ }\mu\text{mol cm}^{-2}\text{ s}^{-1}$ ), UV LED module 1 (emission maximum  $\lambda = 365$ , measured optical power  $57\text{ mW cm}^{-2}$ , photon flux  $0.2\text{ }\mu\text{mol cm}^{-2}\text{ s}^{-1}$ ), UV LED module 2 (emission maximum  $\lambda = 375$ , measured optical power  $45\text{ mW cm}^{-2}$ , photon flux  $0.1\text{ }\mu\text{mol cm}^{-2}\text{ s}^{-1}$ ). Irradiance of LED modules was measured at 2 cm distance using Thorlabs PM400 Optical Power and Energy Meter equipped with the integrating sphere S142C.



## *Procedures of Photocatalytic Reactions and Mechanistic Studies*

### *Photocatalytic oxidation of oxazolidinone (screening reactions)*

A glass vial (4 mL) was charged with a mixture of substrate (50  $\mu\text{mol}$ ), photocatalyst (5 mg) and acetonitrile (2 mL). Magnetic stir bar was placed in the vial. The vial was purged with  $\text{O}_2$  for 30 s and closed with cap. The reaction mixture was vigorously stirred under light irradiation for 24 h. After the reaction the photocatalyst was filtered, and the mixture was concentrated in vacuum (50  $^\circ\text{C}$ , 30 mbar).  $\text{CDCl}_3$  (0.6 mL) was added to the residue. The yield was quantified using  $^1\text{H}$  NMR with 1,3,5-trimethoxybenzene as internal standard. Blue LED module 1, white LED module 1, green LED module, purple LED module, red LED module and UV LED module 1 were used in screening reactions; during the catalyst screening, the following LED modules were assigned as the optimal ones for the catalysts:

*Blue LED module 1:* mpg-CN, K-PHI, Na-PHI,  $\text{Ir}(\text{ppy})_3$ ,  $\text{Ru}(\text{bpy})_3\text{Cl}_2 \cdot 6\text{H}_2\text{O}$ , riboflavin tetraacetate, Eosin Y,  $\text{WO}_3$ , CdS;

*Green LED module:* Rhodamine B;

*Red LED:* methylene blue;

*UV LED module 1:* benzophenone;

*White LED:* control experiment without photocatalyst.

Results for screening experiments are given in the main text.

### *Photocatalytic oxidation of oxazolidinone (scaled-up reactions)*

A glass reactor (100 mL) ([Figure S3.1](#)) was charged with a mixture of substrate (1.25 mmol), mpg-CN (125 mg) and acetonitrile (50 mL). Magnetic stir bar was placed in the vial. The reactor was purged with  $\text{O}_2$  for 1 min and closed with an internal cold finger condenser connected to cooling circulating water thermostat set at 20  $^\circ\text{C}$ . A balloon filled with  $\text{O}_2$  was connected to the reactor. The reaction mixture was vigorously stirred in the photoreactor with four white LED module 2 (203  $\text{mW cm}^{-2}$ ) that evenly

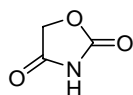


surrounded the reactor. The reaction progress was checked by taking samples for  $^1\text{H}$  NMR every 24 h. After the substrate was completely consumed (24-72 h), the photocatalyst was collected by centrifugation, and the reaction mixture was concentrated in vacuum (50 °C, 30 mbar). Reaction products were isolated and purified by recrystallization, preparative HPLC (JASCO LC-4000 series equipped with Nourion Kromasil 60-10 diol preparative column, gradient 10-50% EA in hexane) or column chromatography using hexane-EA eluent, where applicable. For samples which were challenging to separate, quantitative  $^1\text{H}$  NMR was used with 1,3,5-trimethoxybenzene as an internal standard to calculate the yields.

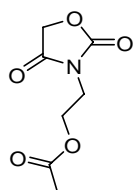


Figure S3.1. Custom reactor for scaled-up photocatalytic reaction with a gas adapter (left) and its internal cold finger condenser (right).

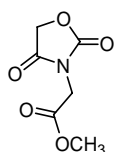


*Oxazolidine-2,4-dione (2a)*

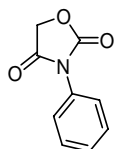
White crystals, yield: 95%.  $^1\text{H}$  NMR (400 MHz,  $\text{CDCl}_3$ )  $\delta$  4.77 (s, 2H).  $^{13}\text{C}$  NMR (101 MHz,  $\text{CDCl}_3$ )  $\delta$  170.58, 154.67, 69.43.

*2-(2,4-dioxooxazolidin-3-yl)ethyl acetate (2b)*

White crystals, yield: 70% after HPLC.  $^1\text{H}$  NMR (400 MHz,  $\text{CDCl}_3$ )  $\delta$  4.72 (s, 2H), 4.34 – 4.27 (m, 2H), 3.87 – 3.80 (m, 2H), 2.05 (s, 3H).  $^{13}\text{C}$  NMR (101 MHz,  $\text{CDCl}_3$ )  $\delta$  171.1, 170.4, 155.7, 68.1, 60.6, 39.6, 20.9.

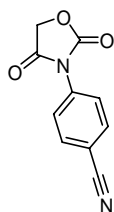
*Methyl 2-(2,4-dioxooxazolidin-3-yl)acetate (2c)*

Colorless oil, yield: 50% after HPLC.  $^1\text{H}$  NMR (400 MHz,  $\text{CDCl}_3$ )  $\delta$  4.82 (s, 2H), 4.31 (s, 2H), 3.80 (s, 3H).  $^{13}\text{C}$  NMR (101 MHz,  $\text{CDCl}_3$ )  $\delta$  169.7, 166.5, 155.1, 68.4, 53.2, 40.5.

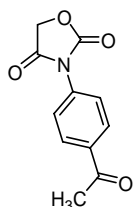
*3-phenyloxazolidine-2,4-dione (2d)*

White solid, yield: 64% after HPLC.  $^1\text{H}$  NMR (400 MHz,  $\text{CDCl}_3$ )  $\delta$  7.55 – 7.39 (m, 5H), 4.87 (s, 2H).  $^{13}\text{C}$  NMR (101 MHz,  $\text{CDCl}_3$ )  $\delta$  169.3, 154.6, 130.7, 129.6, 129.2, 125.7, 67.8.

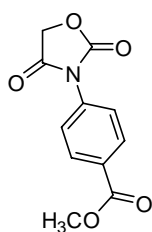


*4-(2,4-dioxooxazolidin-3-yl)benzonitrile (2e)*

White solid, yield: 95%.  $^1\text{H}$  NMR (400 MHz,  $\text{CDCl}_3$ )  $\delta$  7.81 (d,  $J = 8.9$  Hz, 2H), 7.70 (d,  $J = 8.9$  Hz, 2H), 4.92 (s, 2H).  $^{13}\text{C}$  NMR (101 MHz,  $\text{CDCl}_3$ )  $\delta$  168.5, 153.5, 134.7, 133.4, 125.6, 117.9, 112.8, 67.8.

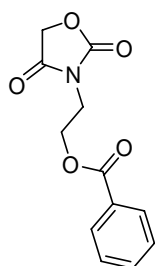
*3-(4-acetylphenyl)oxazolidine-2,4-dione (2f)*

Pale yellow solid, yield: 55% after recrystallization.  $^1\text{H}$  NMR (400 MHz,  $\text{CDCl}_3$ )  $\delta$  8.10 (d,  $J = 8.8$  Hz, 2H), 7.63 (d,  $J = 8.9$  Hz, 2H), 4.91 (s, 2H), 2.64 (s, 3H).  $^{13}\text{C}$  NMR (101 MHz,  $\text{CDCl}_3$ )  $\delta$  196.9, 168.8, 154.0, 137.1, 134.7, 129.5, 125.3, 67.8, 26.9.

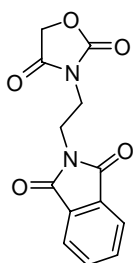
*Methyl 4-(2,4-dioxooxazolidin-3-yl)benzoate (2g)*

Pale beige solid, yield: 59% after recrystallization.  $^1\text{H}$  NMR (400 MHz,  $\text{CDCl}_3$ )  $\delta$  8.18 (d,  $J = 8.9$  Hz, 2H), 7.59 (d,  $J = 8.9$  Hz, 2H), 4.91 (s, 2H), 3.95 (s, 3H).  $^{13}\text{C}$  NMR (101 MHz,  $\text{CDCl}_3$ )  $\delta$  168.8, 166.1, 154.0, 134.6, 130.8, 130.5, 125.1, 67.8, 52.6.

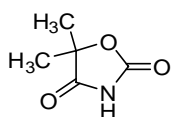


*2-(2,4-dioxooxazolidin-3-yl)ethyl benzoate (2j-a)*

White solid, yield: 33% after HPLC.  $^1\text{H}$  NMR (400 MHz,  $\text{CDCl}_3$ )  $\delta$  8.00 (dd,  $J = 8.4, 1.3$  Hz, 2H), 7.61 – 7.52 (m, 1H), 7.44 (t,  $J = 7.9$  Hz, 2H), 4.73 (s, 2H), 4.58 – 4.46 (m, 2H), 4.06 – 3.95 (m, 2H).

*3-(2-(1,3-dioxoisindolin-2-yl)ethyl)oxazolidine-2,4-dione (2k)*

White needles, yield 55% after flash column chromatography (Hex:EA, gradient 50 to 100% EA).  $^1\text{H}$  NMR (400 MHz,  $\text{CDCl}_3$ )  $\delta$  7.84 (dt,  $J = 6.8, 3.4$  Hz, 2H), 7.73 (dt,  $J = 6.8, 3.4$  Hz, 2H), 4.67 (s, 2H), 4.02 – 3.94 (m, 2H), 3.90 – 3.81 (m, 2H).  $^{13}\text{C}$  NMR (101 MHz,  $\text{CDCl}_3$ )  $\delta$  170.80, 168.57, 155.86, 134.42, 131.82, 123.68, 68.14, 39.57, 35.89.

*5,5-dimethyloxazolidine-2,4-dione (2l, dimethadione)*

White solid, yield: 32% after HPLC.  $^1\text{H}$  NMR (400 MHz,  $\text{CDCl}_3$ )  $\delta$  1.61 (s, 6H).  $^{13}\text{C}$  NMR (101 MHz,  $\text{CDCl}_3$ )  $\delta$  176.6, 153.6, 85.7, 23.6.



### Photocatalytic oxidation under increased oxygen pressure

The reaction was performed at a screening scale conditions (0.025M of substrate, 2.5 mg/mL of catalyst, 2 mL of acetonitrile) using 1b as a substrate in custom-made pressure reactors (Figure S3.2). The reactors were assembled from Ace Glass 8648-17 ~9 mL high pressure screw plug vials by drilling a 2 mm channel through a vial plug and installing a Swagelok SS-OVM2-A-BKB needle valve on top of it in a thread with a custom tightening metal clip to seal gaps between the thread and the plug. A Swagelok SS-400-71-2 thread to ¼" tube connector adapter was installed on the valve to connect to an oxygen line, and the plug thread was wrapped with Teflon tape to additionally seal the connection.



Figure S3.2. Custom reactor for photocatalytic experiments under oxygen pressure.

The reaction was carried out at 1 atm oxygen (no additional pressure, the mixture was purged with oxygen for 1 min), 2, 3 and 4 atm (purging the reaction mixture for 1 min, then purging and pressurizing the reaction chamber). The pressure during the filling was controlled using a manometer built in oxygen line. Each pressure point reaction was performed in a set of 3 experiments. The reaction vessel was irradiated using blue LED module at 2 cm distance for 24 h. After centrifuging off the catalyst, acetonitrile was evaporated, and the yield and conversion values were quantified using  $^1\text{H}$  NMR spectroscopy with 1,3,5-trimethoxybenzene as an internal standard.



### Radical trapping experiment

Reaction mixture in acetonitrile containing 0.025M of 1e, 2.5 mg/mL of catalyst and 0.025M of DMPO was sonicated in a vial for 30 min, then deoxygenized by freeze-pump-thaw technique (3 cycles). A small amount of mixture was syringed out of the vial and transferred to a heat gun dried and argon-purged thin glass capillary under inert atmosphere, then the capillary was sealed and placed inside an EPR tube. The spectra were recorded using Bruker EMXnano EPR spectrometer under 410 nm irradiation provided by optic fiber through the side port of the device; the acquisition was optimal after 15-20 min of irradiation. The resulting spectra are shown on [Figure S3.3](#). Presence of oxygen is exhibited in initial try (lifetime of adduct is approximately 50 min under constant irradiation), while extensive degassing demonstrates absence of stable radicals in the mixture.

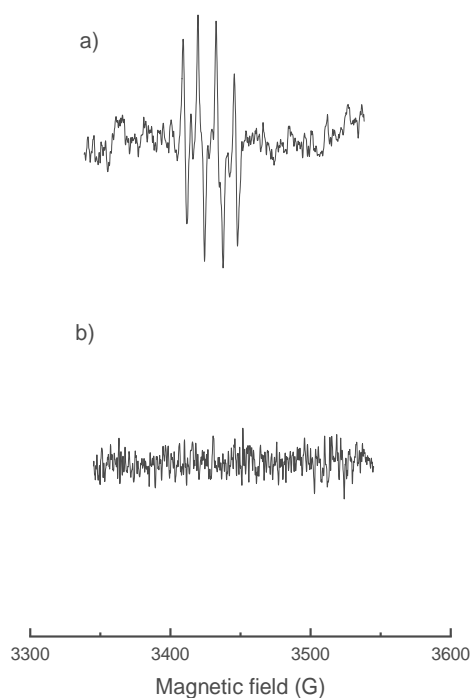


Figure S3.3. EPR spectra of reaction mixture under 15 min *in situ* irradiation in presence of DMPO spin trap: a) in the presence of O<sub>2</sub>. DMPO-OOH adduct signal is present), b) under O<sub>2</sub>-free conditions. The reaction mixture was degassed 5 freeze-pump-thaw cycles.



### Concerted excitation studies

The reaction was performed at a screening scale conditions (0.025M of substrate, 2.5 mg/mL of catalyst, 2 mL of acetonitrile) using 1e as a substrate. The reaction was performed for 3 different experiments, the light intensity was adjusted by varying the distance between a LED and a vial. The yield and conversion values were quantified using  $^1\text{H}$  NMR with 1,3,5-trimethoxybenzene as an internal standard. Conditions and results are listed in [Table S3.1](#).

Table S3.1. Conditions and results of concerted excitation studies.

Entry	Light source(s)	Conversion, %	Yield, %
1	Blue LED (465 nm) at 100 mW·cm <sup>-2</sup>	78.3	40.4
2	Green LED (530 nm) at 100 mW·cm <sup>-2</sup>	30.1	16.5
3	Blue LED (465 nm) at 50 mW·cm <sup>-2</sup> and green LED (530 nm) at 50 mW·cm <sup>-2</sup> ; 100 mW·cm <sup>-2</sup> in total	68.4	29.0



## Apparent quantum yield calculations

### 1. Blue LED

Extinction coefficient of mpg-CN at 465 nm in acetonitrile was calculated using Beer-Lambert law:

$$\varepsilon_{465} = \frac{A_{465}}{c \cdot l} = \frac{0.048}{2.5 \times 0.2} = 0.096 \text{ L} \cdot \text{g}^{-1} \cdot \text{cm}^{-1}, \quad (i)$$

where  $A_{465}$  is absorption value taken from Figure S3.24, 0.048,  $c$  is mpg-CN concentration, 2.5 g·L<sup>-1</sup>,  $l$  is optical path, 0.2 cm.

According to Beer-Lambert law, the transmitted photon flux was calculated:

$$A = \log_{10} \frac{I_0}{I} \rightarrow I = \frac{I_0}{10^{\varepsilon \cdot c \cdot l}} = \frac{0.1}{10^{0.096 \times 2.5 \times 1}} = 0.058 \text{ W} \cdot \text{cm}^{-2}, \quad (ii)$$

where  $l$  is the longest optical path of photoreactor, 1 cm,  $I_0$  is incident light flux reaching reactor's surface from LED, 0.1 W·cm<sup>-2</sup>,  $\varepsilon$  and  $c$  values were taken from equation (i).

Thus, the absorbed light is calculated as:

$$I_{Abs} = I_0 - I = 0.100 - 0.058 = 0.042 \text{ W} \cdot \text{cm}^{-2}. \quad (iii)$$

Using formula (1) from SI, AQY is recalculated:

$$\begin{aligned} AQY_{465 \text{ nm}} &= \frac{n_p \cdot N_A \cdot h \cdot c}{I_{Abs} \cdot t \cdot \lambda \cdot S} \times 100\% \\ &= \frac{2.02 \times 10^{-5} \times 6.022 \times 10^{23} \times 6.626 \times 10^{-34} \times 3 \times 10^8}{0.042 \times 86400 \times 4.65 \times 10^{-7} \times 5.5} \times 100\% \\ &= 0.026\% \end{aligned}$$

LED light intensity is converted to photon flux using the following formula:

$$\begin{aligned} \Phi_{465 \text{ nm}} &= \frac{N_p}{N_A} = \frac{I_0}{N_A \cdot E_{465 \text{ nm}}} = \frac{I_0 \cdot \lambda}{N_A \cdot h \cdot c} = \frac{1 \times 10^{-5} \times 4.65 \times 10^{-7}}{6.022 \times 10^{23} \times 6.626 \times 10^{-34} \times 3 \times 10^8} \\ &= 3.88 \times 10^{-11} \text{ mol} \cdot \text{m}^{-2} \cdot \text{s}^{-1}, \quad (iv) \end{aligned}$$



where  $N_P$  is photon flow,  $\text{m}^{-2} \cdot \text{s}^{-1}$ ,  $N_A$  is Avogadro number,  $6.022 \cdot 10^{23} \text{ mol}^{-1}$ ,  $E_{465 \text{ nm}}$  is energy at 465 nm wavelength,  $I_0$  is incident LED power,  $1 \cdot 10^{-5} \text{ W} \cdot \text{m}^{-2}$ ,  $\lambda$  is wavelength,  $4.65 \cdot 10^{-7} \text{ m}$ ,  $h$  is Planck constant,  $6.626 \cdot 10^{-34} \text{ J} \cdot \text{s}$ ,  $c$  is light speed,  $3 \cdot 10^8 \text{ m} \cdot \text{s}^{-1}$ .

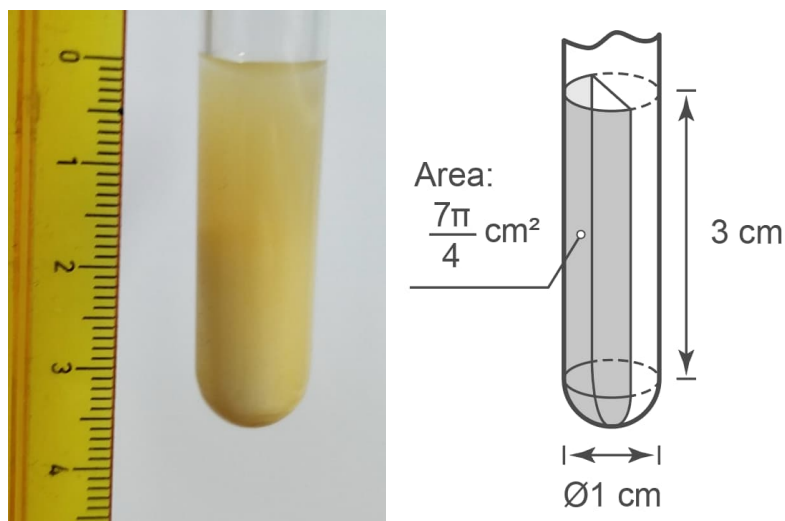


Figure S3.4. Dimensions and irradiated area value of the reaction mixture used for quantum yield calculation.

## 2. UV Led

Extinction coefficient:

$$\varepsilon_{365} = \frac{A_{365}}{c \cdot l} = \frac{0.247}{2.5 \times 0.2} = 0.494 \text{ L} \cdot \text{g}^{-1} \cdot \text{cm}^{-1}$$

Transmitted flux:

$$I = \frac{I_0}{10^{\varepsilon \cdot c \cdot l}} = \frac{0.057}{10^{0.494 \times 2.5 \times 1}} = 0.003 \text{ W} \cdot \text{cm}^{-2}$$

Absorbed flux:

$$I_{Abs} = I_0 - I = 0.057 - 0.003 = 0.054 \text{ W} \cdot \text{cm}^{-2}$$

Quantum yield for mpg-CN:



$$\begin{aligned}
 AQY_{365\text{ nm}} &= \frac{n_p \cdot N_A \cdot h \cdot c}{I_{Abs} \cdot t \cdot \lambda \cdot S} \times 100\% \\
 &= \frac{3.5 \times 10^{-5} \times 6.022 \times 10^{23} \times 6.626 \times 10^{-34} \times 3 \times 10^8}{0.054 \times 86400 \times 3.65 \times 10^{-7} \times 3.8} \times 100\% \\
 &= 0.065\%
 \end{aligned}$$

Photon flux:

$$\begin{aligned}
 \Phi_{365\text{ nm}} &= \frac{N_p}{N_A} = \frac{I_0}{N_A \cdot E_{365\text{ nm}}} = \frac{I_0 \cdot \lambda}{N_A \cdot h \cdot c} = \frac{5.7 \times 10^{-6} \times 3.65 \times 10^{-7}}{6.022 \times 10^{23} \times 6.626 \times 10^{-34} \times 3 \times 10^8} \\
 &= 1.74 \times 10^{-11} \text{ mol} \cdot \text{m}^{-2} \cdot \text{s}^{-1}
 \end{aligned}$$

### NMR Spectroscopy

$^1\text{H}$  and  $^{13}\text{C}$  NMR spectra were recorded on Bruker Ascend 400 MHz (at 400 MHz for Protons and 101 MHz for Carbon-13). Chemical shifts are reported in ppm versus solvent residual peak:  $\text{CDCl}_3$  7.26 ppm ( $^1\text{H}$  NMR), 77.16 ppm ( $^{13}\text{C}$  NMR).

### Cyclic Voltammetry

Measurements were performed in a glass single-compartment electrochemical cell. Glassy carbon (diameter 3 mm) was used as a working electrode (WE), Ag wire in  $\text{AgNO}_3$  (0.01M) with tetrabutylammonium perchlorate (0.1M) in MeCN as a reference electrode (RE), Pt wire as a counter electrode. Each compound was studied in a 50 mM concentration in a 0.1 M tetrabutylammonium perchlorate (TBAP)/MeCN electrolyte solution (10 mL). Before voltammograms were recorded, the solution was purged with Ar, and an Ar flow was kept in the headspace volume of the electrochemical cell during CV measurements. A potential scan rate of  $0.050 \text{ V} \cdot \text{s}^{-1}$  was chosen, and the potential window ranging from +2.5 V to -2.5 V vs. RE (and backwards) was investigated. Cyclic voltammetry was performed under room-temperature conditions ( $\sim 20\text{-}22 \text{ }^\circ\text{C}$ ). Ferrocene (50 mM) was used as an internal reference standard. CV plots vs Fc/Fc<sup>+</sup> couple are shown on [Figure S3.5](#).



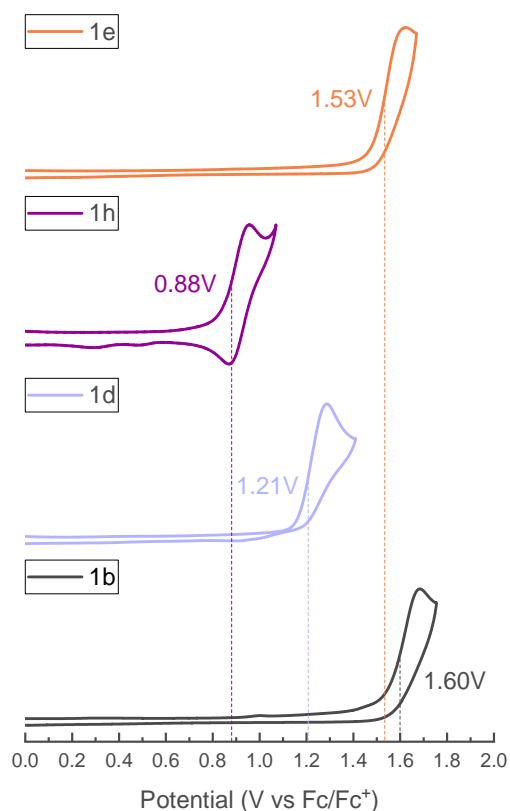


Figure S3.5. Cyclic voltammetry plots for compounds 1b, 1d, 1e and 1h using Fc/Fc<sup>+</sup> as a reference. Values indicate oxidation potentials of the compounds.

Oxidation potential values for Fc/Fc<sup>+</sup> were then translated into SCE scale using the following formula for given cell parameters (solvent and electrolyte)<sup>263</sup>:

$$E_{SCE} = E_{Fc/Fc^+} + 0.380V \quad (2),$$

which gives values of 1.98V for 1b, 1.58V for 1d, 1.91V for 1e and 1.26V for 1h, respectively.



### *Transient Absorption Spectroscopy*

The mpg-CN samples were prepared as dispersions in acetonitrile to characterise their excited state dynamics. First, mpg-CN (5 mg) was prepared in isolation with acetonitrile (2 ml) to determine the excited state dynamics of the catalyst in isolation; then, mpg-CN (5 mg) and oxazolidin-2-one (8 mg, 0.05 mmol) were prepared in acetonitrile (2 ml) to mimic the conditions of the photocatalytic test; finally, oxazolidin-2-one (8 mg, 0.05 mmol) was prepared in 2 ml of acetonitrile as a control to determine if the substrate was excited in these experimental conditions. Before each measurement, the sample dispersions were sonicated for an hour. Measurements were made in a quartz cuvette of path length 2 mm under normal and low oxygen concentrations. Low oxygen concentrations were achieved by degassing with nitrogen during measurements for pump-probe spectroscopy and degassing for 20-30 minutes before measurement for photoluminescence (PL) spectroscopy. An oxygen sensor, 0.3 mM of Palladium (II) meso-tetraphenyl-tetrabenzoporphyrin (PdTPTBP), was added to determine oxygen concentration for PL-spectroscopy measurements.

The steady state absorbance spectra of the PdTPTBP with and without the mpg-CN were measured using a Shimadzu UV-3600 series spectrophotometer. The photoluminescence (PL) spectra were taken with the Edinburgh Instruments FLS1000 with excitation and emission double monochromators. This had a PMT – 900 photomultiplier tube detector and a 450 W xenon arc lamp excitation source for acquisition of the steady state spectra. In addition, a 60 W pulsed xenon flashlamp was used for the acquisition of the time-resolved emission spectra. The PdTPTBP (excitation  $\lambda$ , 623 nm) and the mpg-CN (excitation  $\lambda$ , 355 nm) samples were characterised with slit widths of 1.5 nm (arc lamp for steady state emission) and 3 nm (pulsed lamp for time resolved emission). The mpg-CN tr-PL decays at 540 nm were measured at 1.6  $\mu$ s/channel, an integration time of 210 s and a measurement window of 800  $\mu$ s. While for the PdTPTBP tr-decays at 800 nm were measured at 1.6  $\mu$ s/ channel, a measurement window of 800  $\mu$ s and set to stop at a maximum of 10000 counts per second (cps).



The transient absorption measurements of the samples were made using pump-probe spectroscopy. For the pump-probe spectroscopy, the fundamental laser pulses were generated at 800 nm by the Libra F, Coherent Inc., which was coupled with an optical parametric amplifier (OPA) Topas C, Light Conversion Ltd. These laser pulses were used to produce the pump beam to excite the sample and the probe beam to monitor the spectra. The pump beam wavelength was set at 355 nm and the pump beam power was set at  $500 \pm 30 \mu\text{W}$  (excitation density  $0.1 \text{ mJ}/\text{cm}^2$ ).

For the probe beam, a sapphire crystal was used to produce a continuum of white light in the near-infrared (NIR) and in visible range ( $\geq 500 \text{ nm}$ ). The central detection wavelength in the NIR and visible ranges were 1170 nm, 960 nm, and 600 nm. The probe beam was passed through a delay line for the differential response in time. The transient absorption responses of the probe beam were measured using an ExciPro TA spectrometer (CDP, Inc.). The spectrometer was coupled with an InGaAs diode array to detect NIR wavelengths and a Si charge coupled device (CCD) array to detect visible range wavelengths. For the transient absorption measurements, only the transmittance mode was explored.

The transient absorption used four-exponential global fitting model plus step function (representing a response which was formed but did not decay within the measured time window) as shown as in equation 3:

$$\Delta A(\lambda, t) = A_0(\lambda) + A_1(\lambda)e^{-t/\tau_1} + A_2(\lambda)e^{-t/\tau_2} + A_3(\lambda)e^{-t/\tau_3} + A_4(\lambda)e^{-t/\tau_4} \dots \quad (3)$$

where  $\Delta A(\lambda, t)$  was the transient absorption at a specific wavelength and time;  $A_0(\lambda)$  was the response independent of the delay time;  $A_i(\lambda)$  were the pre-exponential factors or decay associated spectra (DAS); and  $\tau_i$  were the time constants for each decay component.



## Photocatalyst Apparent $pK_a$ and FBDFE Value Determination

### *mpg-CN*

The mpg-CN catalyst (50 mg) was dispersed in 3 mL 37% HCl and vigorously stirred for 3 h at room temperature, then centrifuged out and washed with MiliQ-purified water 3 times to remove acid. The protonated catalyst was then dried in a vacuum oven overnight at 60 °C.

MiliQ-purified water was degassed by purging with argon for 5 h, and the pH was measured to be 6.74 using Fischer Scientific accumet® AE150 pH meter calibrated by 3 standard NIST buffers (pH 4.01, 7.00 and 10.01, Fisher Scientific). Additionally, pH of regular mpg-CN (1 g/L suspension) was measured to be 6.70. Then, a suspension of protonated catalyst was prepared by suspending full amount in 50 mL of degassed MiliQ water with vigorous stirring, and pH was measured to be 5.24. Then, the stirred suspension was titrated with 0.1M KOH solution, and each pH point was recorded 5 s after the addition of titrant solution aliquot. The resulting curve is shown on [Figure S3.6](#).

The  $pK_a$  value of protonated mpg-CN was then determined to be  $6.60 \pm 0.3$  (6.3-6.8) from the titration curve.

Then, formal bond dissociation free energy (FBDFE) value was calculated using following formula:<sup>146</sup>

$$FBDFE = 1.37pKa + 23.06E_{VB} + C_{G,Sol} \quad (4)$$

where  $E_{VB}$  is a valence band potential in mpg-CN vs. NHE couple (+1.45 V),  $C_{G,Sol}$  is  $H^+/H$  standard potential in the solvent (57.6 kcal·mol<sup>-1</sup> for water). Then, the value is calculated to be:

$$FBDFE = 1.37 \times 6.60 + 23.06 \times 1.45 + 57.6 = 100.1 \text{ kcal} \cdot \text{mol}^{-1} = 4.32 \text{ eV}$$

Taking into account uncertainty of  $pK_a$  determination,  $FBDFE = 100 \pm 0.4 \text{ kcal mol}^{-1}$  or  $4.32 \pm 0.02 \text{ eV}$ .



*Poly(heptazine imides)*

*Procedure:* 50 mg of corresponding carbon nitride (Na-PHI or K-PHI) was dispersed in 50 mL of degassed MilliQ water while purging with nitrogen under strong stirring and monitoring pH with a pH meter. Aqueous 0.1 M HCl solution was added in 50  $\mu$ L portions, and pH meter readings were recorded after stabilization in 5-10 s for Na-PHI or 45 s for K-PHI (larger particles and higher density of K-PHI induce significant hysteresis, most likely due to slower ion diffusion). The titration was carried out until reaching pH of 3 in both cases, which takes ca. 2.5 mL of titrant solution. The pKa values of conjugated acid (corresponding H-PHI) were then obtained from titration curves.

Thus, the pKa values are  $7.1 \pm 0.3$  for Na-PHI and  $7.4 \pm 0.3$  for K-PHI.

Using these values, valence band potential values vs. NHE and equation (4), FBDFE for acetonitrile can be calculated:

$$FBDFE_{Na-PHI} = 1.37 \times 7.1 + 23.06 \times 2.54 + 57.6 = 125.9 \text{ kcal} \cdot \text{mol}^{-1} = 5.46 \text{ eV}$$

$$FBDFE_{K-PHI} = 1.37 \times 7.4 + 23.06 \times 2.36 + 57.6 = 122.2 \text{ kcal} \cdot \text{mol}^{-1} = 5.30 \text{ eV}$$

The values are given with standard deviation of  $\pm 0.4 \text{ kcal} \cdot \text{mol}^{-1}$ , or  $\pm 0.02 \text{ eV}$ , considering uncertainty of pKa determination.



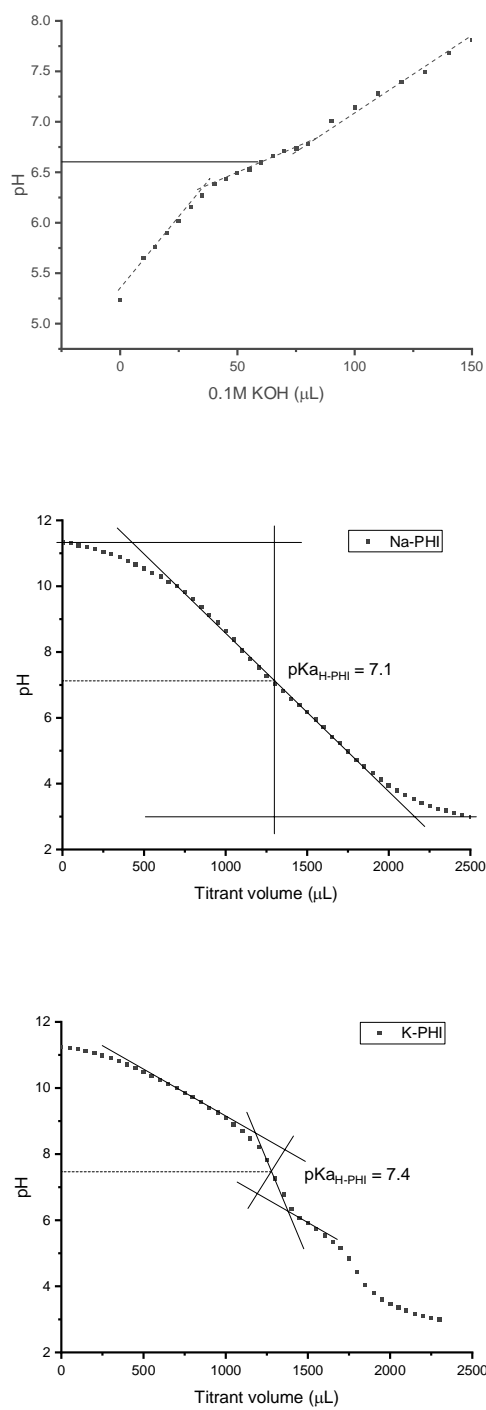


Figure S3.6. Titration curves of protonated mpg-CN (top), Na-PHI (middle) and K-PHI (bottom) with pKa values of conjugated acids extracted from the plots.



## Computational Data

Density Functional Theory (DFT) simulations were performed using the Vienna Ab initio Simulation Package (VASP)<sup>189, 190</sup> and the Perdew–Burke–Ernzerhof (PBE)<sup>191</sup> exchange–correlation functional. Inner electrons were represented by Projected Augmented Wave (PAW)<sup>264</sup> method while the monoelectronic states were represented as plane waves with a kinetic energy cutoff of 450 eV. Spin polarization was included in all simulations. For periodic systems, a Monkhorst–Pack<sup>265</sup> k-point mesh was used in such a way that the number of k-points in each periodic (non-vacuum) direction multiplied with the supercell length in the same direction equaled 28 Å. The electronic convergence threshold was set to  $10^{-6}$  eV, while the total force limit for the ionic convergence was set to 0.01 eV/Å.

The molecular structure of polymeric carbon nitride is known to be complex.<sup>196</sup> A commonly used model structure, mesoporous graphitic carbon nitride (mpg-CN), gives a simulated band gap which matches the experimental data.<sup>266</sup> However, this structure contains highly-condensed heptazine units, making it incompatible with elemental analyses of real samples which show a higher amount of hydrogen present. A different type of structure, melon, shows better agreement with elemental analyses. However, melon structures exhibit significantly higher band gaps than experimentally observed for polymeric carbon nitride.<sup>196, 266</sup> As the photocatalytic properties of this material are of prime importance for this study, we use the highly condensed mpg-CN structure as the main model catalyst for oxazolidinone oxidation reaction and compare the results obtained with the melon-type structures (see below).

Mesoporous graphitic carbon nitride (mpg-CN) was preliminarily modeled as an infinite 2D surface (pristine mpg-CN) with a vacuum layer thickness of 20 Å, perpendicular to the graphene surface. An improved model (terminated surface mpg-CN) was made by cleaving the 2D surface and adding H atoms to the nitrogen atoms left with an incomplete octet by the termination, as well as NH<sub>2</sub> and OH groups to the incomplete octet carbon atoms (Figure S3.7a), consistent with experimental data.<sup>165</sup> The surface termination creates another vacuum layer, which was set to 14 Å. To examine the



influence of the terminal OH groups on the reaction, we also considered models containing only NH<sub>2</sub>, as well as only OH groups (Figure S3.7b and S3.7c). Energy of the rate-determining step with such models was less than 0.02 eV different than with the original model (containing both NH<sub>2</sub> and OH groups), implying that the type of groups at the termination does not significantly influence the oxazolidinone oxidation reaction. The presence of different groups at the termination did not significantly change the electronic density of states (DOS) either (Figure S3.10).

For completeness, we also simulated the PCET involving the s-melon-2D (single-stringed) and melon-2D (triple-stringed) structures (Figure S3.8),<sup>266</sup> containing both NH<sub>2</sub> and OH groups at the termination. The melon models showed energies for the PCET within 0.3 eV of our mpg-CN model (Table S3.2), justifying the use of the mpg-CN model.

All modeled structures were uploaded to the ioChem-BD database,<sup>192, 267</sup> where they are openly accessible.

After finding the most optimal binding site for the H atom on the terminated surface (see Figure S3.7a), the energy change for the first reaction step was calculated using the HSE06 functional,<sup>194</sup> upon which the Gibbs free energy correction at 293 K was added. The correction was calculated using VASPKIT<sup>268</sup> from the data obtained by frozen phonon approach, where the selected atoms relevant for the reaction were displaced in each spatial direction by 0.015 Å, as implemented in VASP.

The effect of implicit MeCN solvent was examined using the VASP-MGCM model.<sup>269</sup> In the pristine mpg-CN, inclusion of the implicit solvent gave a 0.2 eV increase in energy of the hydrogen atom transfer (Table S3.2).



Table S3.2. Electronic potential energy differences for H atom removal from the oxazolidinone 1b (the rate-determining step) with respect to different H atom acceptors. The system shown in bold is the main model used in this work.

H atom acceptor	Implicit solvent <sup>269</sup>	$\Delta E$ (eV)
No acceptor	No	4.03
MeCN	No	2.76
MeCN	Yes	2.90
mpg-CN pristine, 1 layer	No	1.23
mpg-CN pristine, 1 layer	Yes	1.46
mpg-CN pristine, 4 layers	No	1.33
mpg-CN terminated, 1 layer	No	1.36
s-melon-2D	No	1.42
melon-2D	No	1.67



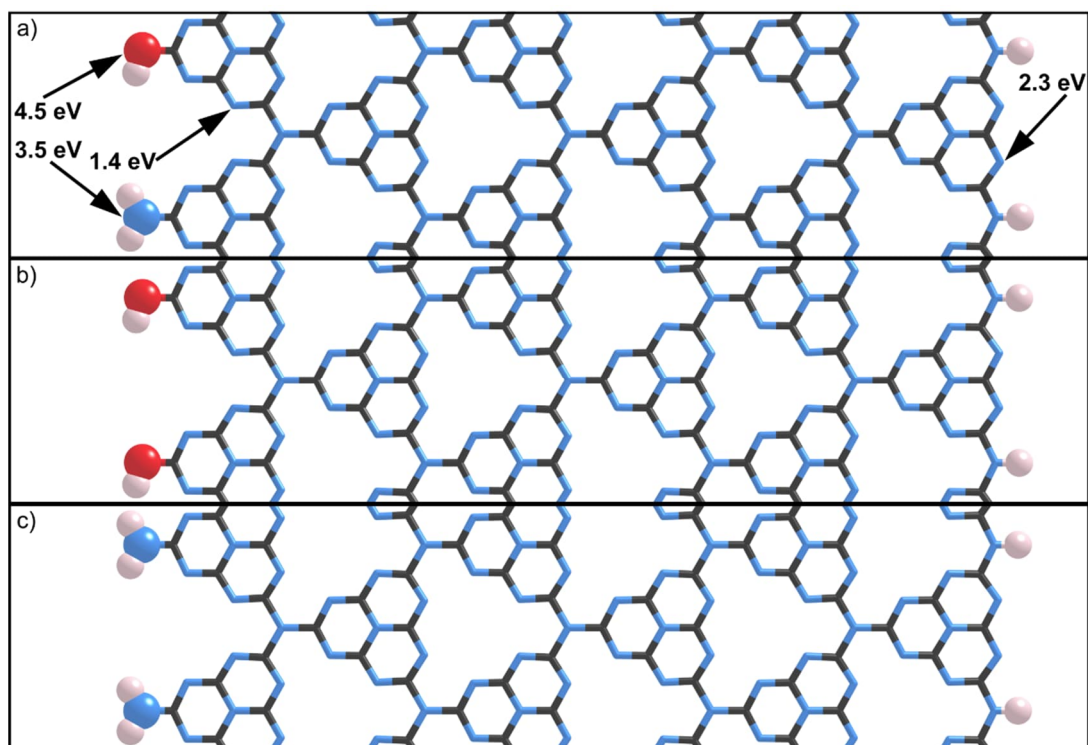


Figure S3.7. Models of terminated surface mpg-CN containing (a) both NH<sub>2</sub> and OH groups; (b) NH<sub>2</sub> groups; (c) OH groups. The arrows point to different potential binding sites for an H atom along with energies of the H atom transfer from oxazolidinone 1b to mpg-CN at the designated position. Visualized with VESTA.<sup>270</sup>



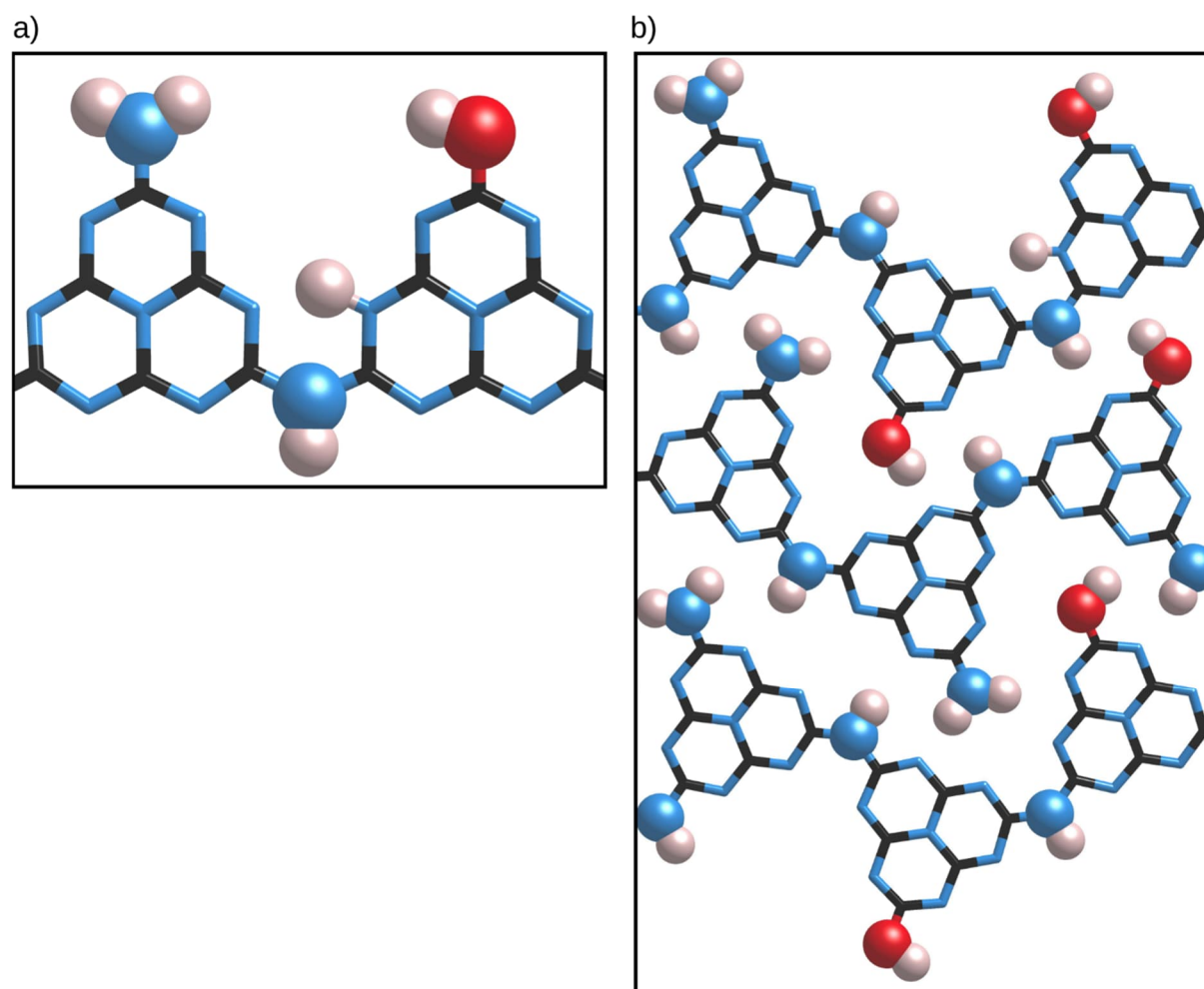


Figure S3.8. s-melon-2D (a) and melon-2D (b) structures of carbon nitride as modeled, after accepting a hydrogen atom from oxazolidinone. Due to significant intramolecular interactions in the melon-2D model, DFT-D3 corrections were added, as implemented in VASP.<sup>271</sup>



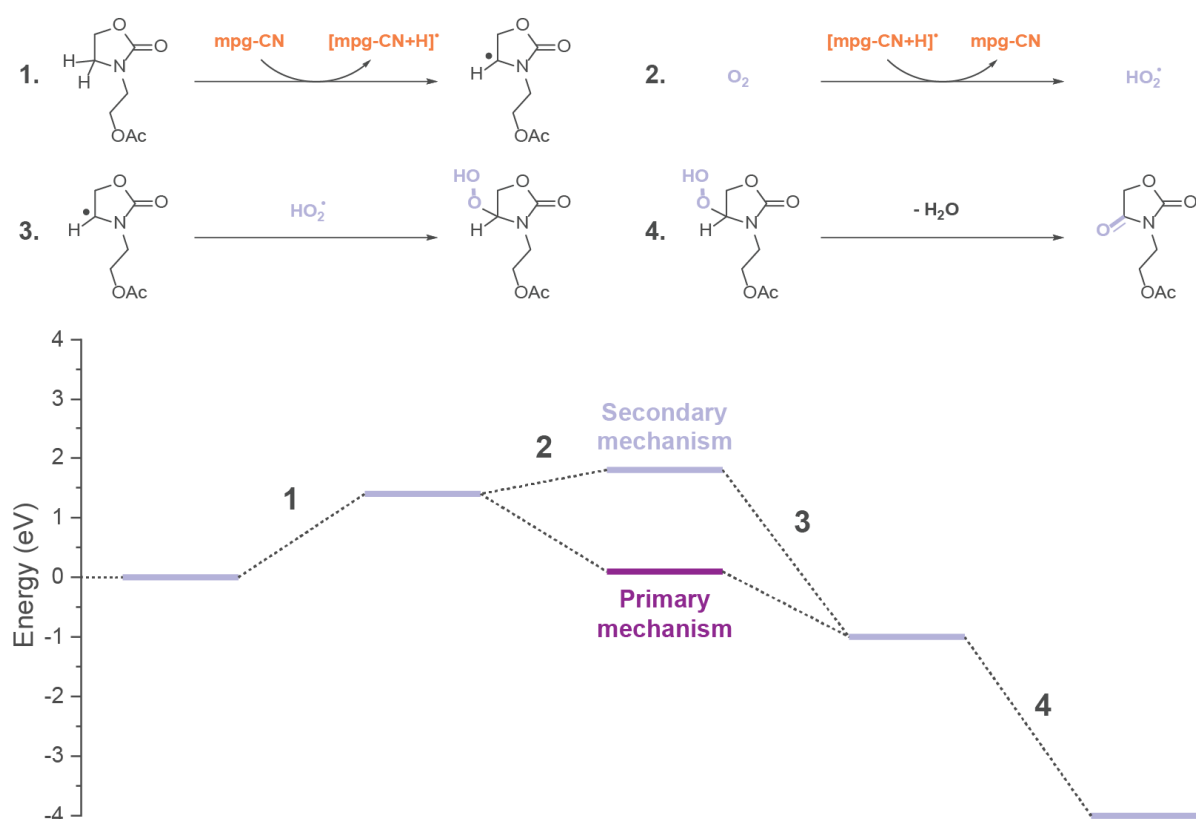


Figure S3.9. An alternative mechanistic pathway for the oxidation of oxazolidinone 1b to oxazolidinedione 2b (top) and the comparison of its energy profile to the primary mechanism (bottom). The alternative mechanism starts the same way as the primary mechanism, by transfer of a H atom from oxazolidinone to mpg-CN. In the second step, the hydrogen atom from [mpg-CN+H]• is captured by an O<sub>2</sub> molecule to form the hydroperoxyl radical, which then reacts with the oxazolidinone radical to form oxazolidinone hydroperoxide. In the final step, which is equivalent in the both mechanistic pathways, a water molecule is eliminated from the hydroperoxide, producing oxazolidinedione 2b.



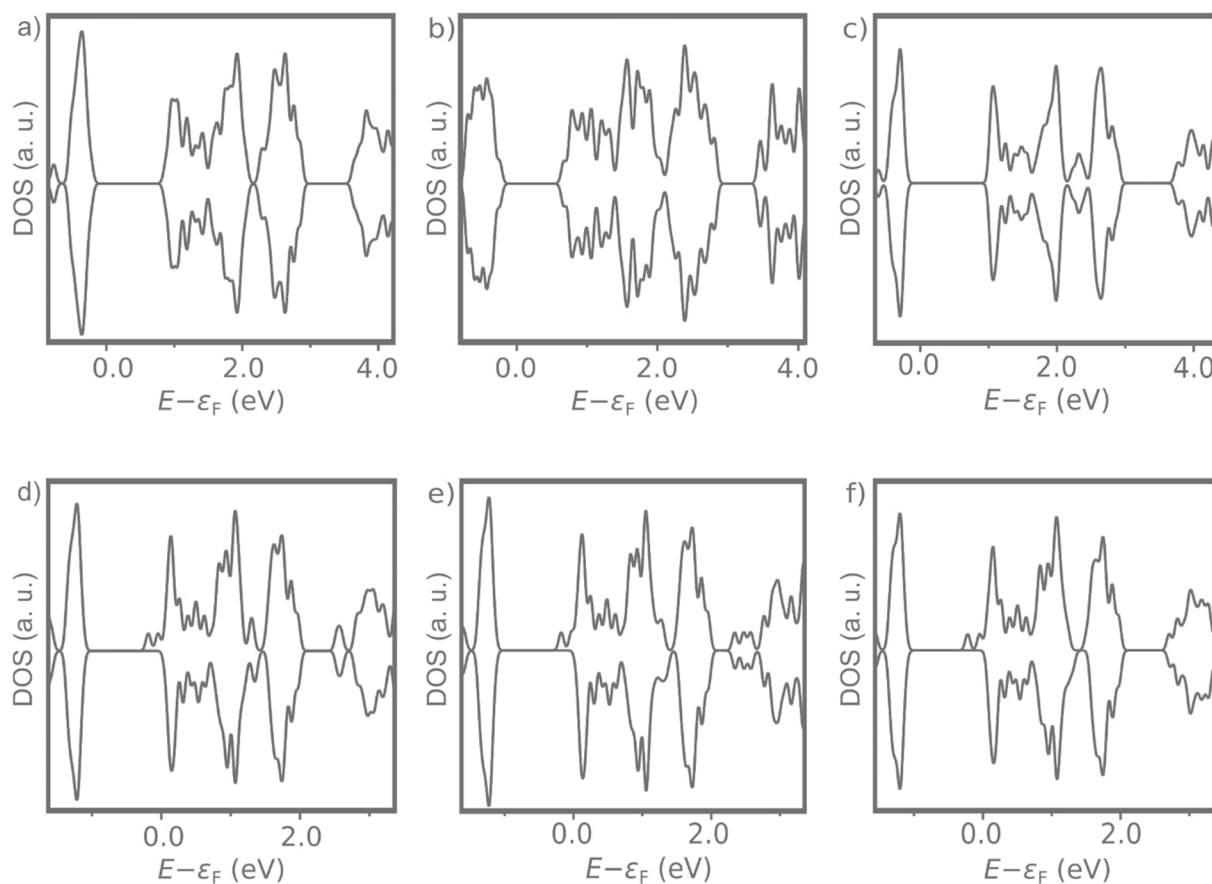


Figure S3.10. DOS plots of terminated mpg-CN containing (a) both  $\text{NH}_2$  and OH groups; (b)  $\text{NH}_2$  groups; (c) OH groups. DOS for these systems after binding an H atom [ $\text{mpg-CN}+\text{H}$ ] $^*$  is shown in (d), (e), and (f), respectively. There is no significant difference in the nature of states between the systems containing different groups at the termination. Binding of the H atom shifts the Fermi level and breaks the symmetry between  $\alpha$  and  $\beta$  states due to an additional electron present in the system.



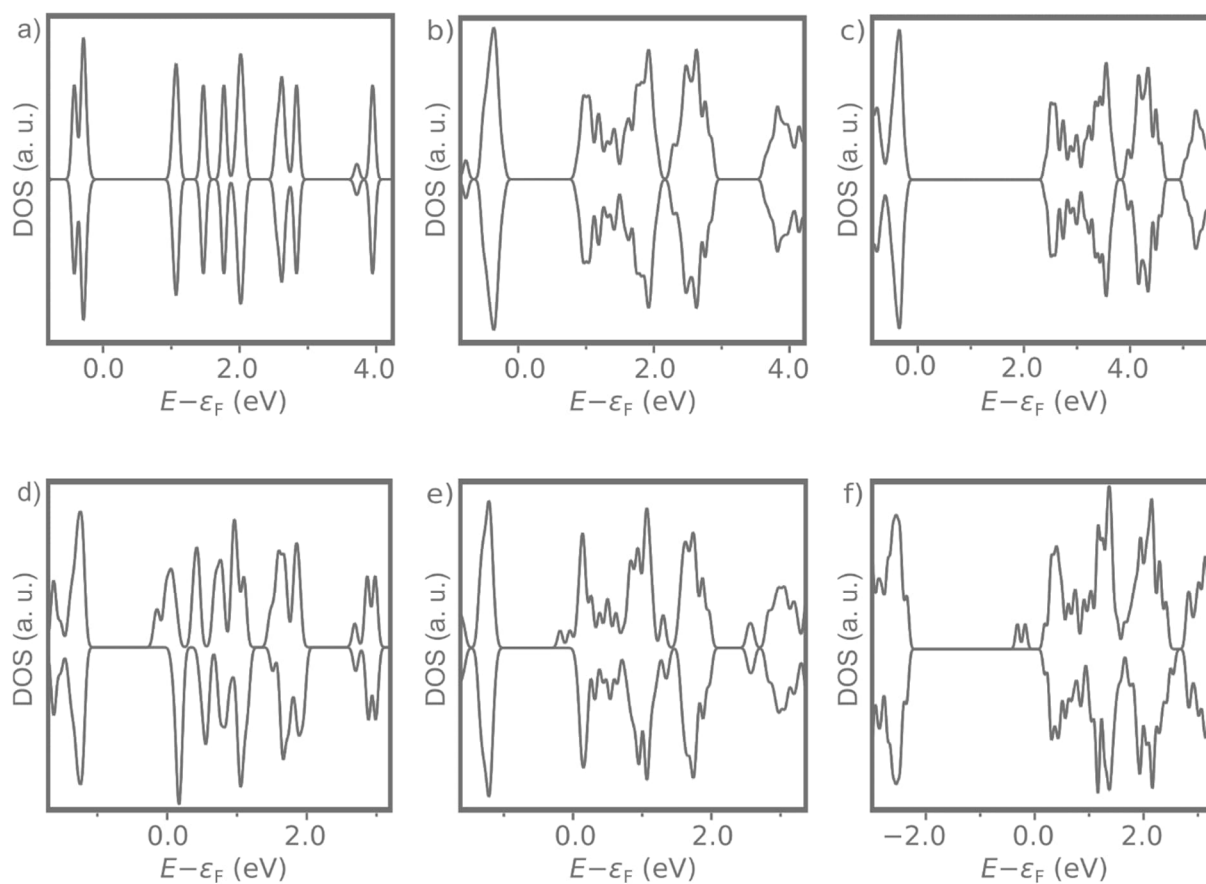


Figure S3.11. DOS for pristine mpg-CN (a), terminated mpg-CN (b), and terminated mpg-CN calculated with the HSE06 hybrid functional (c). DOS for these systems after binding an H atom is shown in (d), (e), and (f), respectively. The terminated surface DOS include more states due to a higher number of atoms in the unit cell, but the termination does not significantly alter the electronic structure. Energy gap obtained with the hybrid functional is larger due to the gap underestimation common with GGA functionals.<sup>272</sup>



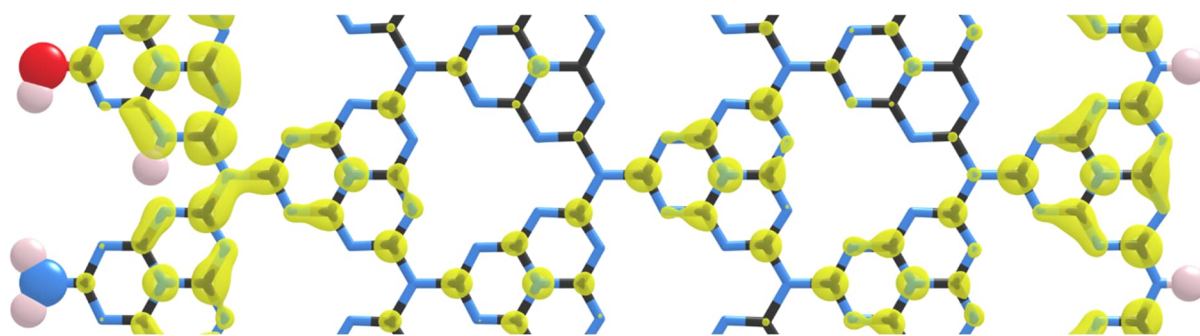


Figure S3.12. Real-space projection of the additional electron in the mpg-CNH system. The isosurface level was set to  $5.2 \cdot 10^{-4} a_0^{-3}$  ( $a_0$ : Bohr radius).

### 7.3.2. Supplementary Notes

#### Supplementary Discussion 1. TAS Results

##### Steady-state absorbance spectroscopy

The steady state spectra of PdTPTBP in the presence and absence of mpg-CN are shown in Figure S3.13. The porphyrin has three bands at 438 nm, 575 nm, and 623 nm according to the spectrum. These bands were still observable after it was mixed with mpg-CN.

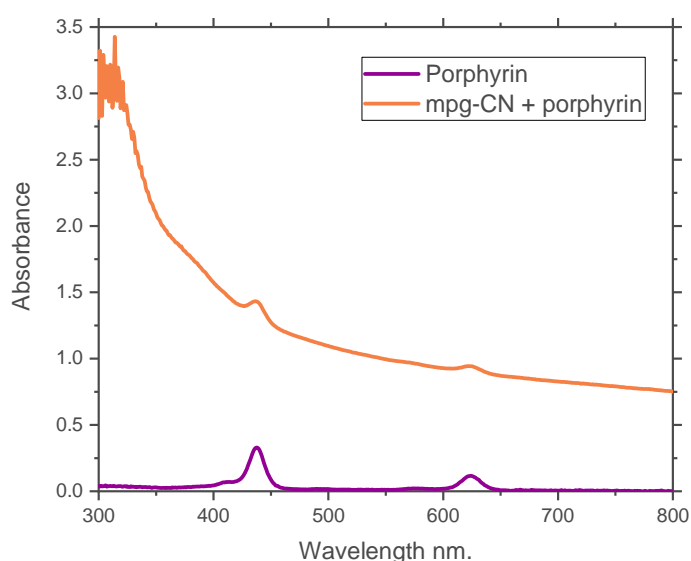


Figure S3.13. Absorbance spectra of PdTPTBP (0.3mM) in the presence and absence of mpg-CN.

##### Time resolved photoluminescence (*tr-PL*) spectroscopy

Investigations of the photoluminescence of mpg-CN in the presence of the oxygen sensor, PdTPTBP were made to determine the oxygen sensitivity of the mpg-CN. The PdTPTBP emission lifetime before and after measurement of the mpg-CN emission was determined to confirm that the sample had been properly degassed. According to the literature,<sup>273</sup> PdTPTBP has an emission lifetime of 286  $\mu$ s at 800 nm but with degassing under the current experimental conditions, it achieved a lifetime of 61  $\mu$ s and was



completely quenched without degassing as shown in Figure S3.14. The mpg-CN decays at 540 nm with and without degassing are shown in Figure S3.15. The decay lifetime of mpg-CN at 540 nm with and without degassing was unchanged. This confirms that the emission of the mpg-CN is not sensitive to oxygen. Therefore, further mpg-CN were made without the oxygen sensor and under normal atmospheric conditions of oxygen.

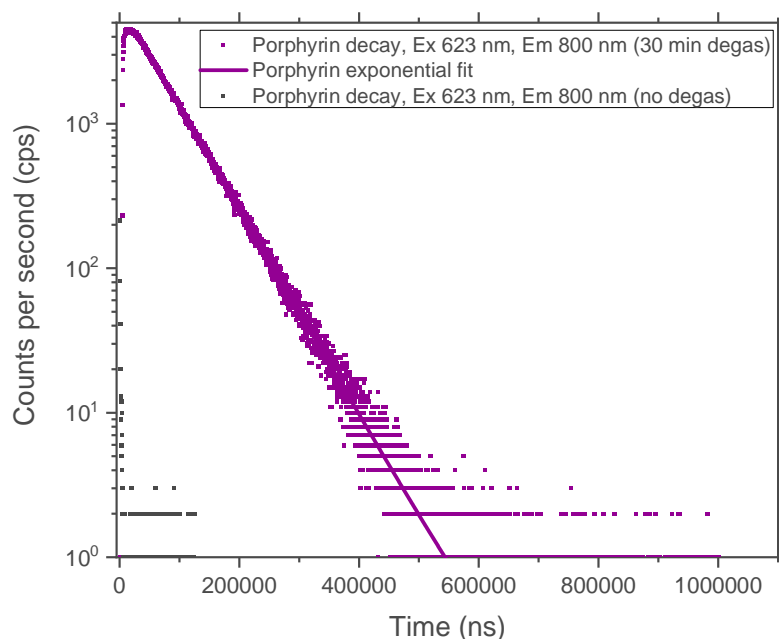


Figure S3.14. PdTPTBP decay at 800 nm, Ex 623 nm in the before (black) and after (purple) degassing with nitrogen.

The tr-PL spectra of the mpg-CN with substrate are shown in Figure S3.15 (plots without substrate are given in the main text, Figure 3.5d). Figure S3.15 shows a fluorescence peak at approx. 472 nm which was measured using the arc xenon lamp. The phosphorescence peak of lower intensity at approx. 540 nm was measured by gating the emission from 40 -100  $\mu$ s with the pulsed xenon lamp. The presence of the substrate does not appear to cause quenching of either the fluorescence or phosphorescence of the mpg-CN.



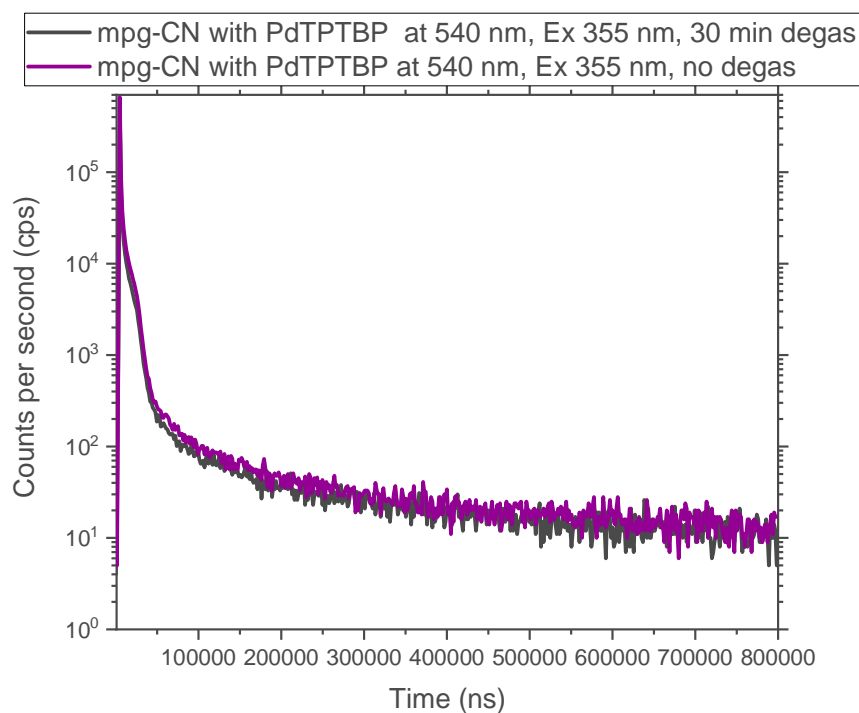


Figure S3.15. mpg-CN and PdTPTBP tr-PL decays at 540 nm before (black) and purple (after) degassing.

The tr-PL decays of the mpg-CN with substrate at 540 nm are shown in [Figure S3.16](#) (plots without substrate are given in the main text, [Figure 3.5c](#)). A triple exponential fitting was used in [Figure S3.17](#), for the measurement of the decays. In the absence of the substrate, the lifetimes ( $\mu\text{s}$ ) and preexponential factors were:

$$\begin{aligned} \Delta I (800 \mu\text{s}, 540 \text{ nm}) \\ = 24.9 + 0.5 * e^{-t/0.5} + 0.08 * e^{-t/6.8} + 5.1 \times 10^{-4} * e^{-t/118.2} \dots \quad (5) \end{aligned}$$

In the presence of substrate, the lifetimes and preexponential factors were:

$$\begin{aligned} \Delta I (800 \mu\text{s}, 540 \text{ nm}) \\ = 22.3 + 0.6 * e^{-t/0.5} + 0.09 * e^{-t/6.7} + 4.9 \times 10^{-4} * e^{-t/120.8} \dots \quad (6) \end{aligned}$$

From the two equations above, we can conclude that the presence of the substrate does not affect the lifetime of the mpg-CN. The substrate does not quench either the singlet



excited state or the triplet excited state on a scale that is sensitive enough to be measured by the instrument.

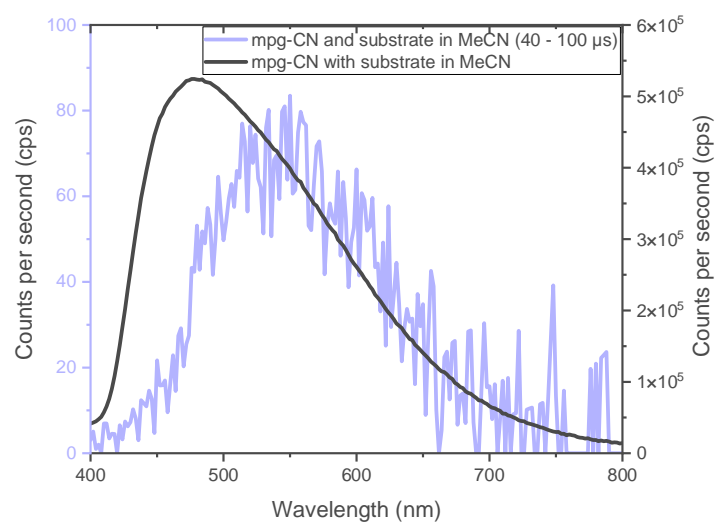


Figure S3.16. tr-PL spectra of mpg-CN with and without substrate.

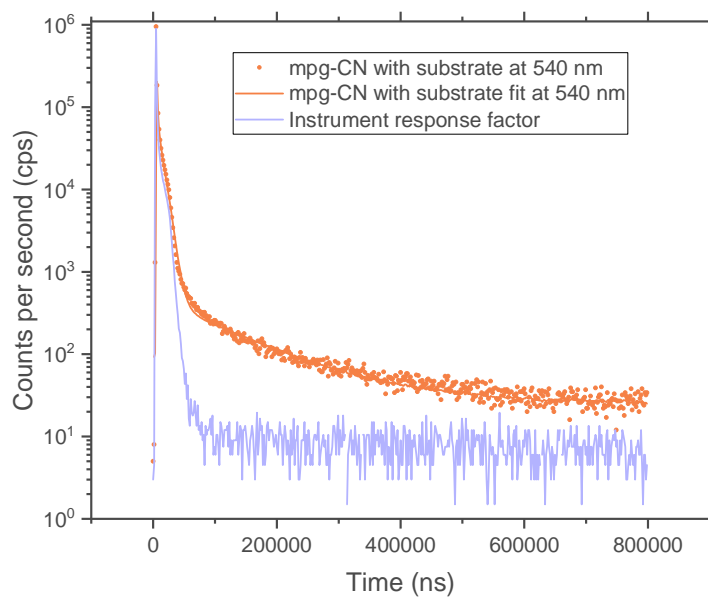


Figure S3.17. tr-PL decay of mpg-CN with substrate.



## Transient Absorption Spectroscopy (TAS)

### Mesoporous graphitic carbon nitride (mpg-CN) in acetonitrile and aerobic conditions

The transient absorption spectra of mpg-CN dispersed in acetonitrile and aerobic conditions at different delay times are shown in [Figure S3.18](#).

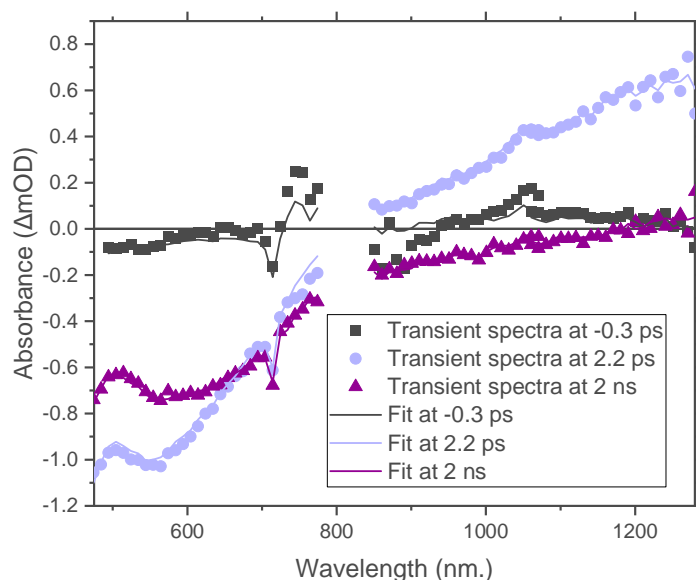


Figure S3.18. Transient absorption spectra of mpg-CN in MeCN and O<sub>2</sub> (Spectra around 800 nm is cut off due to fundamental of the laser).

Just before excitation in [Figure S3.18](#), the negative signal at < 600 nm is due to scattering of the laser beam by the sample. The peak at 710 nm is the fundamental of the second harmonic used to for the excitation (355 nm) left over from the TOPAS C, OPA. A few picoseconds after excitation, there was a strong negative signal between 500 – 750 nm which can be attributed to the ground state bleaching and a positive signal between 850 – 1280 nm which can be attributed to the photogenerated excited state of mpg-CN. The crossing point was around 800 nm. At longer delays of 2 ns, the intensity of the positive signal reduced at a faster rate than the negative signal and the crossing point is red shifted to approx. 1280 nm.



The transient decays of mpg-CN dispersed in acetonitrile and aerobic conditions in the visible (605 nm) and NIR range (960 and 1170 nm) are shown in Figure S3.19. Both the decays in the visible and NIR range did not decay within the 4 ns measurement window. The time constants for the global fitting were: 0.2, 0.7, 18.9 and 477.3 ps. In NIR range, there was a positive signal which decayed and started to become negative within the 4 ns measurement window. In the visible range, there was bleaching which started to decay initially but at approx. 100 ps, the signal intensity started to increase.

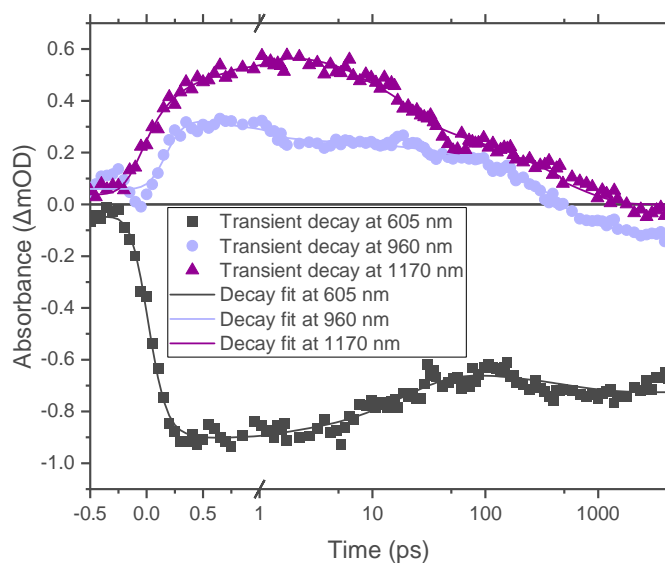


Figure S3.19. Transient decay of mpg-CN in MeCN and O<sub>2</sub> (The first picosecond is in linear scale while the rest has a logarithmic scale).

#### *Mesoporous graphitic carbon nitride (mpg-CN) in acetonitrile and anaerobic conditions*

The transient absorption spectra of mpg-CN dispersed in acetonitrile and anaerobic conditions at different delay times are shown in Figure 3.5f in the main text. There is almost no observable change in the transient spectra at the three delay times (under N<sub>2</sub>) compared to the transient spectra (under O<sub>2</sub>) in Figure S3.19. The only difference being that the crossing point at ns timescales is 1200 nm.



The transient decays of mpg-CN dispersed in acetonitrile under anaerobic conditions in the visible (605 nm) and NIR range (960 and 1170 nm) are shown in [Figure 3.5f](#) in the main text. Both the decays in the visible and NIR range did not decay within the 4 ns measurement window. The time constants for the global fitting were: 0.1, 7.3, 71.2 and 374.9 ps. In NIR range, there was a positive signal which decayed and started to become negative within the 4 ns measurement window. In the visible range, there was bleaching which started to decay initially but at approx. 20 ps, the signal intensity started to increase.

*Mesoporous graphitic carbon nitride (mpg-CN) in acetonitrile and aerobic conditions with oxazolidin-2-one 1b*

The transient absorption spectra of mpg-CN dispersed in acetonitrile and aerobic conditions with the oxazolidin-2-one substrate at different delay times are shown in [Figure S3.20](#). A few picoseconds after excitation, there was a strong negative signal between 500 – 750 nm which can be attributed to the ground state bleaching and a positive signal between 850 – 1280 nm which can be attributed to the photogenerated excited state of mpg-CN. The crossing point somewhere between 750 – 850 nm. At longer delays of 2 ns, the intensity of the positive signal reduced at a faster rate than the negative signal and the crossing point was red shifted to approx. 1280 nm. Overall, there was no difference compared to the absence of substrate in [Figure S3.18](#).



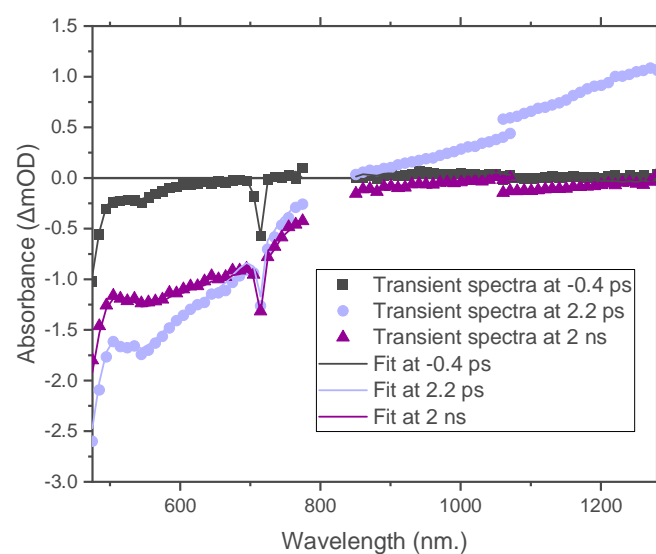


Figure S3.20. Transient absorption spectra of mpg-CN + oxazolidin-2-one in MeCN and O<sub>2</sub> (Spectra around 800 nm is cut off due to fundamental of the laser).

The transient decays of mpg-CN dispersed in acetonitrile and aerobic conditions with oxazolidin-2-one substrate in the visible (605 nm) and NIR range (960 and 1170 nm) are shown in [Figure S3.21](#). The decay in the visible range did not decay within the 4 ns measurement window while the decays in the NIR range decayed to zero and became slightly negative within the 4 ns measurement window. The time constants for the global fitting were: 0.2, 10, 13 and 516 ps. After approx. 100 ps in the visible range, the signal intensity started to increase.



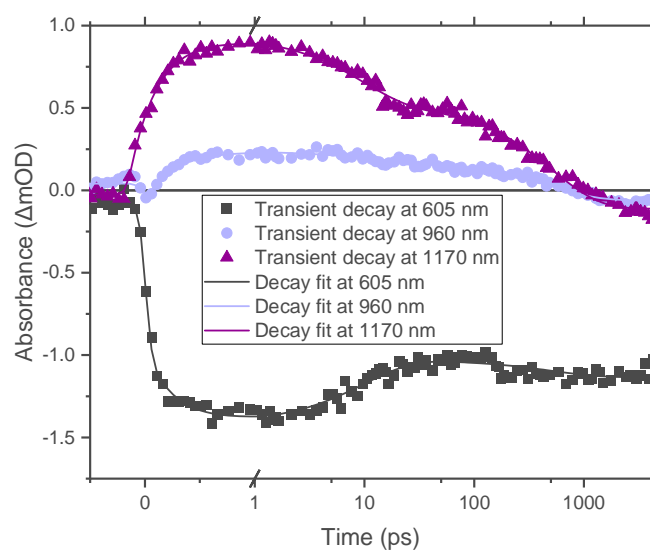


Figure S3.21. Transient decay of mpg-CN + oxazolidin-2-one in MeCN and O<sub>2</sub> (The first picosecond is in linear scale while the rest has a logarithmic scale).

### *Mesoporous graphitic carbon nitride (mpg-CN) in acetonitrile and anaerobic conditions with oxazolidin-2-one 1b*

The transient absorption spectra of mpg-CN dispersed in acetonitrile and anaerobic conditions with the oxazolidin-2-one substrate at different delay times are shown in [Figure S3.22](#). A few picoseconds after excitation in [Figure S3.22](#), there was a strong negative signal between 500 – 750 nm which can be attributed to the ground state bleaching and a positive signal between 750 – 1280 nm which can be attributed to the photogenerated excited state of mpg-CN. The crossing point at approx. 750 nm. At longer delays of 2 ns, the intensity of the positive signal reduced at a faster rate than the negative signal and the crossing point was red shifted to approx. 1100 nm. Overall, there was a slight difference in the crossing point with and without degassing with nitrogen.



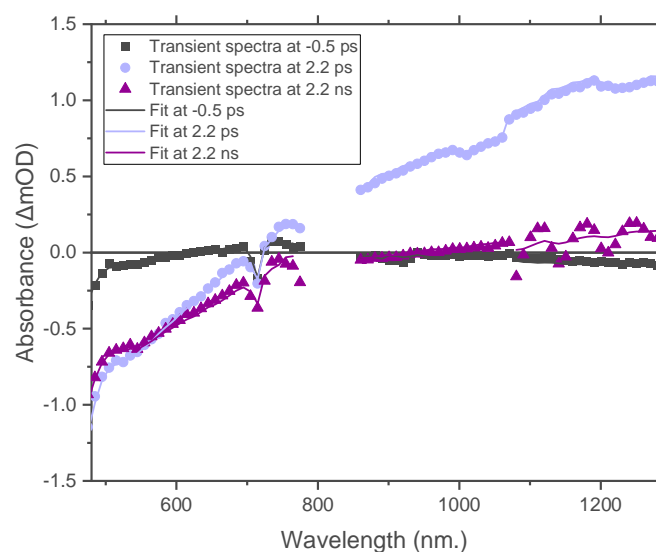


Figure S3.22. Transient absorption spectra of mpg-CN + oxazolidin-2-one in MeCN and N<sub>2</sub> (Spectra around 800 nm is cut off due to fundamental of the laser).

The transient absorption spectra of mpg-CN dispersed in acetonitrile and anaerobic conditions with the oxazolidin-2-one substrate at different delay times are shown in [Figure S3.23](#). The decay in the visible range did not decay within the 4 ns measurement window while the signal in the NIR range decayed to zero and became slightly negative within the 4 ns measurement window. The time constants for the global fitting were: 0.3, 4.6, 54 and 455 ps. After approx. 200 ps in the visible range, the signal intensity started to increase.



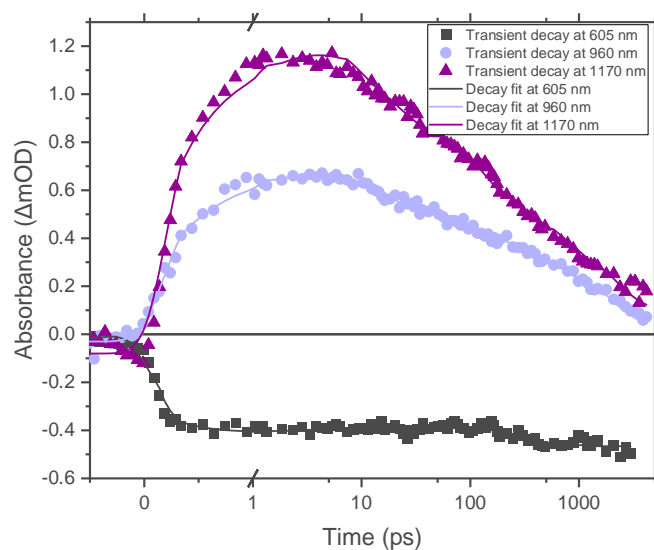


Figure S3.23. Transient decay of mpg-CN + oxazolidin-2-one in MeCN and N<sub>2</sub> (The first picosecond is in linear scale while the rest has a logarithmic scale).

#### *Oxazolidin-2-one 1b in acetonitrile (both aerobic and anaerobic conditions)*

The transient spectra and decay under the same measurement conditions were within noise levels  $\pm 0.05$  mOD and were therefore difficult to decipher for a fit. This confirms that the substrate is at a low enough concentration in the acetonitrile to not interfere with the measurements of the mpg-CN dynamics.

#### *Summary*

The summary of the TAS results of the samples in acetonitrile under aerobic and anaerobic conditions is given in [Table S3.3](#).



Table S3.3. Summary of TAS results.

S/N		mpg-CN alone	mpg-CN + Oxazolidin-2-one
1.	AEROBIC CONDITIONS	Crossing point just after excitation (1 ps)	Approx. 800 nm
2.		Crossing point at the end of measurement window (4 ns)	Approx. 1280 nm
3.		Time constants of decay fit	0.2 ps, 0.7 ps, 18.9 ps and 477.3 ps
4.	ANEROBIC CONDITIONS	Crossing point just after excitation (1 ps)	Approx. 750 nm
5.		Crossing point at the end of measurement window (4 ns)	Approx. 1100 nm
6.		Time constants of decay fit	0.1 ps, 7.3 ps, 71.2 ps and 374.9 ps



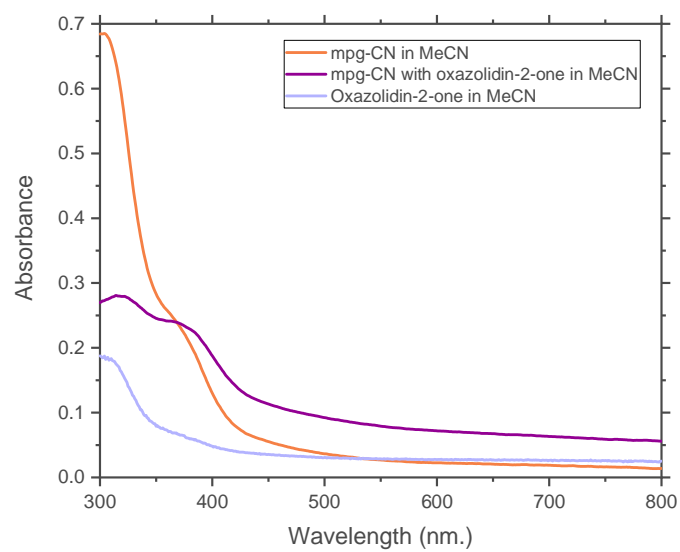


Figure S3.24. Steady state absorbance spectra of all samples in acetonitrile. Path length = 2 mm.



### Supplementary Discussion 2. mpg-CN Recycling, Reuse and Additional Experiments

After the third round, the yield decreased most likely due to partial bleaching of mpg-CN, but also due to loss of the material during recovery from the reaction mixture. A fraction of recovered mpg-CN was 95% of the initial mass after the 1<sup>st</sup> cycle, 86% – after the 2<sup>nd</sup> cycle and 92% – after the 3<sup>rd</sup> cycle.

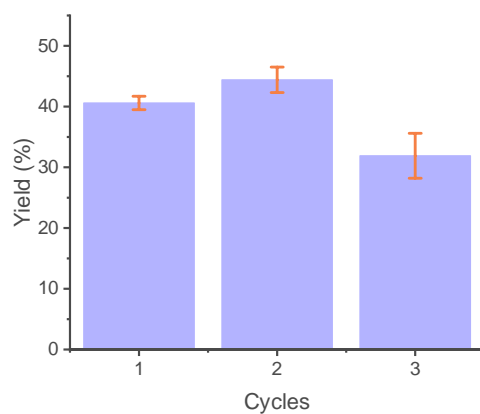


Figure S3.25. Recyclability tests of mpg-CN photocatalyst in oxidation of 1b. Error bars represent average $\pm$ std (n=3).

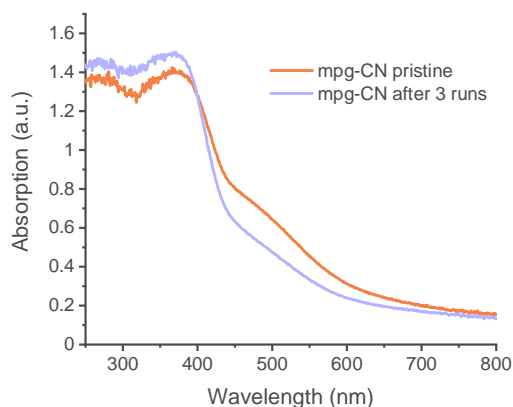


Figure S3.26. DRUV-Vis spectra of pristine mpg-CN and the one after 3 photocatalytic cycles at 465 nm.



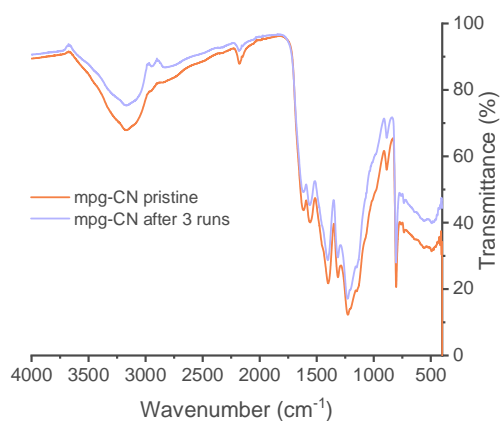


Figure S3.27. FT-IR spectra of pristine mpg-CN and the one after 3 photocatalytic cycles at 465 nm.

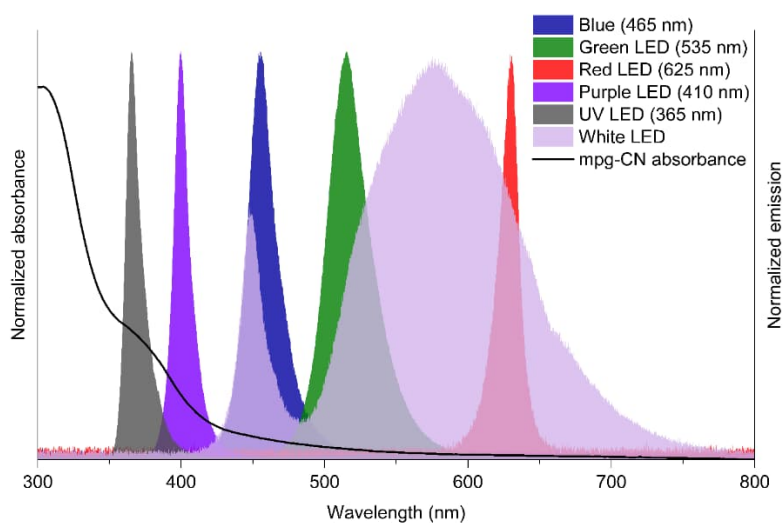


Figure S3.28. Normalized absorbance of mpg-CN dispersion in MeCN and emission of LEDs used in this work.



Table S3.4. Scope of photocatalytic reactions mediated by g-CNs that proceed via X–H bond cleavage.

Entry	Reaction	Reaction scheme	X–H BDFE, kcal mol <sup>-1</sup> [a]	Product yield (ionic g-CN), %	Product yield (covalent g-CN), %
1	Resveratrol dimerization		Phenol O–H 80 <sup>146</sup>	No data	34 (mpg-CN)/86 (mpg-CN) <sup>[b],197</sup>
2	Toluene oxidation		Toluene (sp <sup>3</sup> )C–H 80 <sup>152</sup>	74.5 (K-PHI) <sup>122</sup>	2.4 (mpg-CN) <sup>122</sup>
3	Minisci coupling		THF C–H 84 <sup>152</sup>	80 (NCN-CN <sub>x</sub> ) <sup>160</sup>	30 (Pristine carbon nitride) <sup>160</sup>
4	Cyclization of carbamates		Carbamate N–H 84-104 <sup>274</sup>	3.3 (K-PHI) <sup>[c]</sup>	3.1 (mpg-CN) <sup>[b]</sup>
5	Cyclization of carbamates		Carbamate N–H 84-104 <sup>274</sup>	2.5 (K-PHI) <sup>[c]</sup>	3.1 (mpg-CN) <sup>[b]</sup>
6	Decarboxylation		Carboxylate O–H 104 <sup>275</sup>	38 (K-PHI)	66 (mpg-CN)
7	Decarboxylation		Carboxylate O–H 104 <sup>275</sup>	36 (Na-PHI)	66 (mpg-CN)
8	Oxygen evolution reaction		Water O–H 123 <sup>146</sup>	4.89 <sup>[d],182</sup>	0

[a] – BDFE values were taken from the corresponding reference or calculated using equation:

$$BDFE = BDE - T \times \Delta S$$

where BDE – bond dissociation energy, kcal mol<sup>-1</sup>; T = 298.15K;  $\Delta S = 7.7$  kcal mol<sup>-1</sup>.<sup>275</sup>

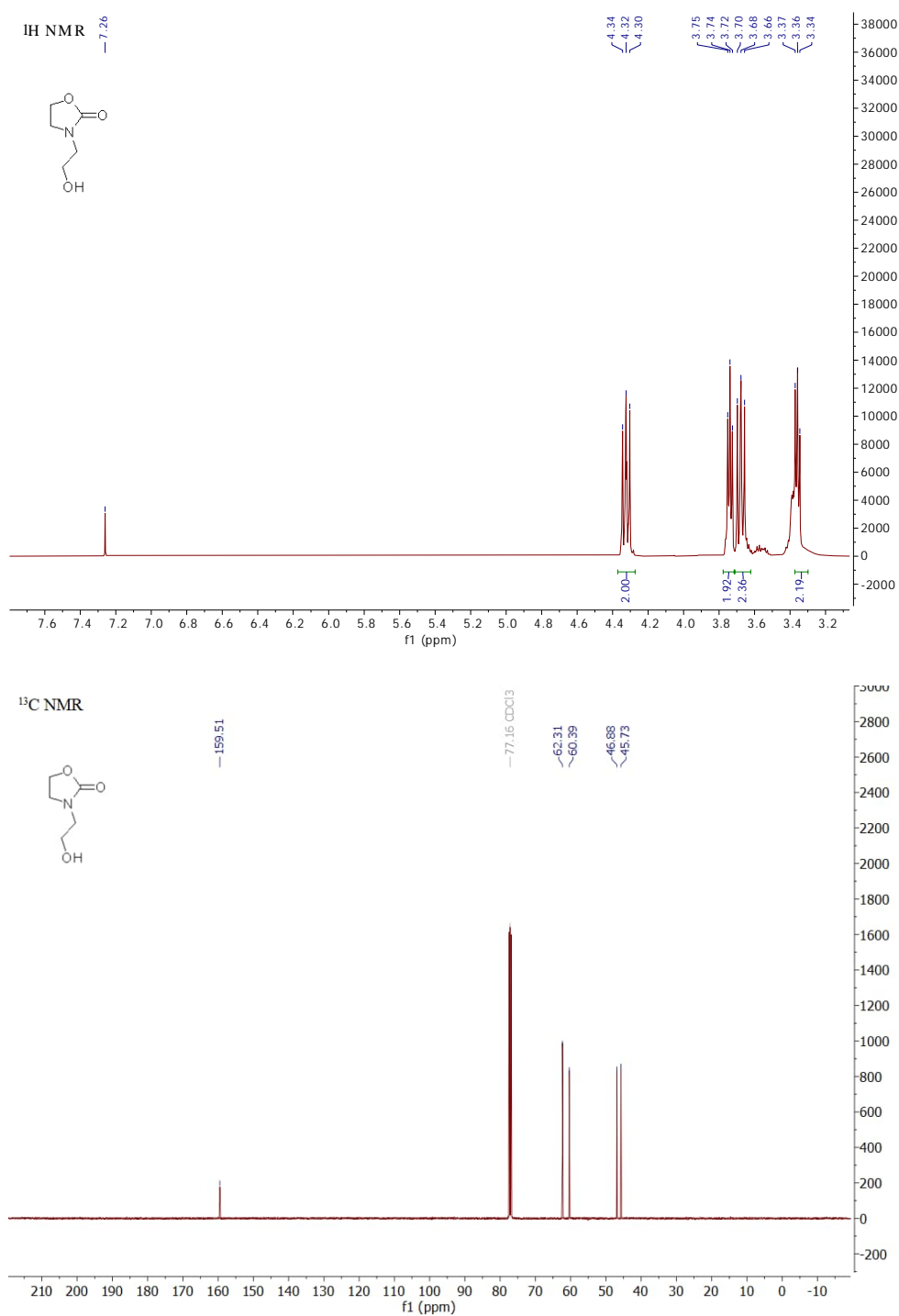
[b] – In the presence of 2,6-lutidine (5 equiv.).

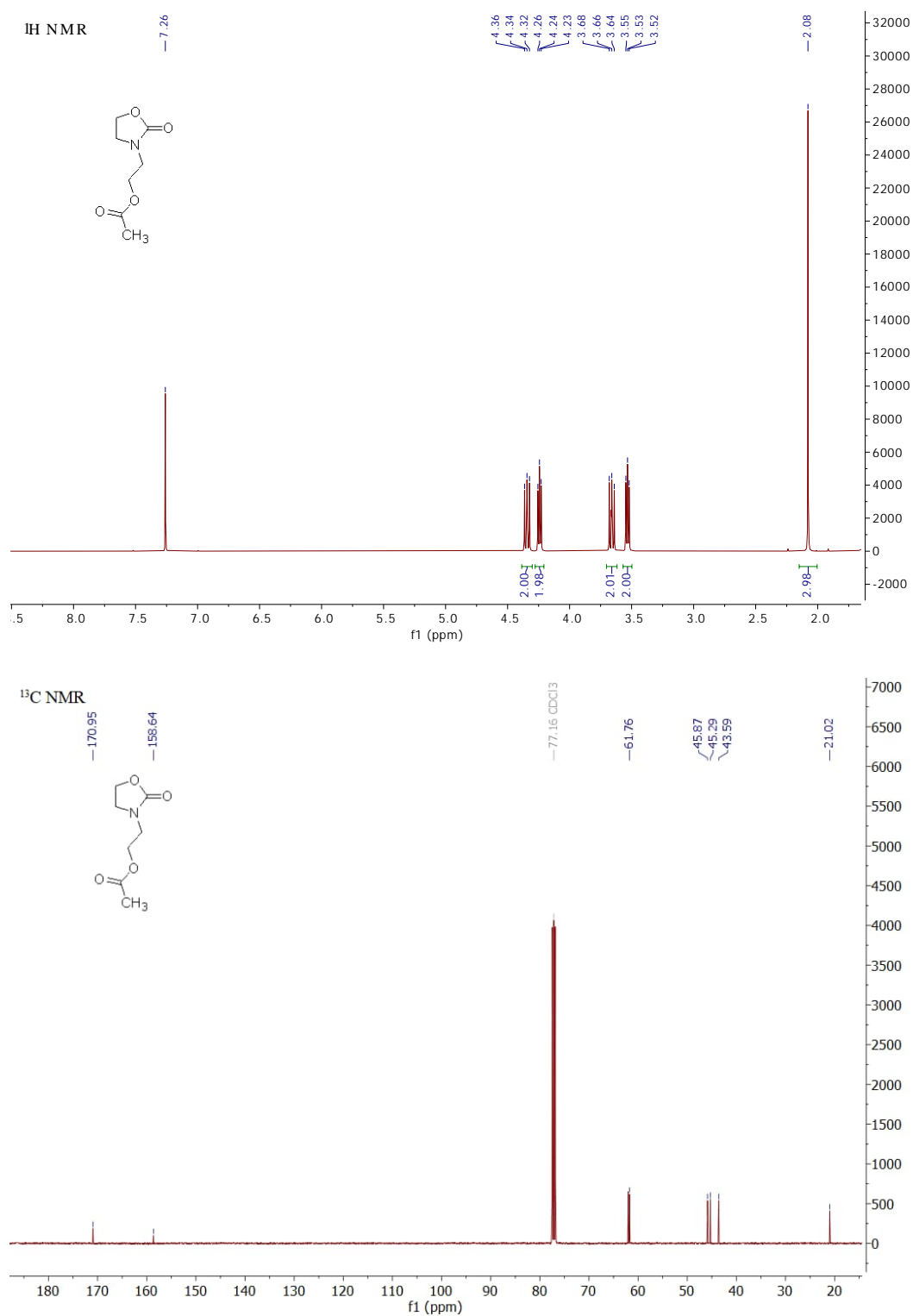
[c] – Compared to the original procedure, reaction was conducted without adding a base.

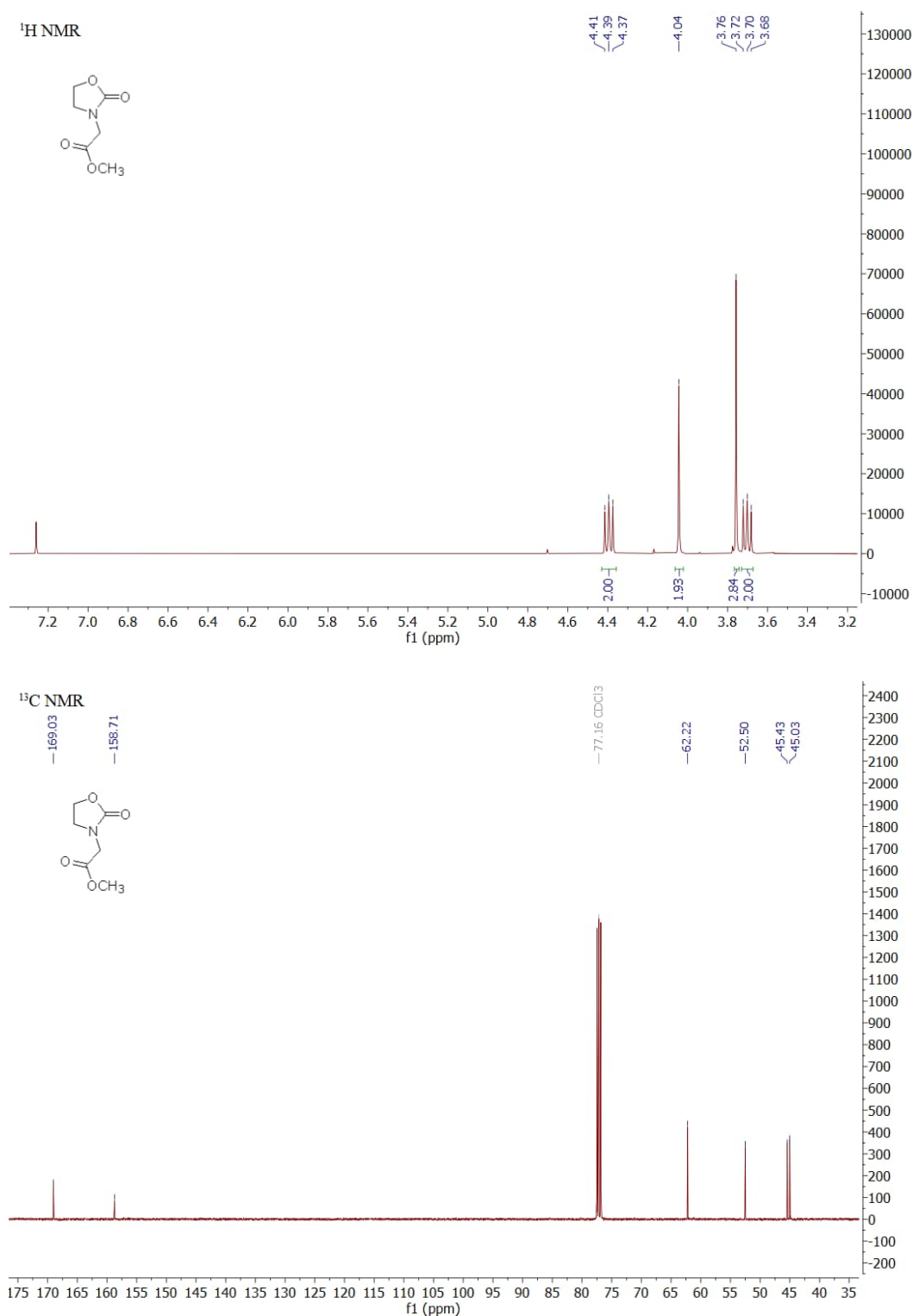
[d] – Initial O<sub>2</sub> evolution rate,  $\mu\text{mol h}^{-1}$ .

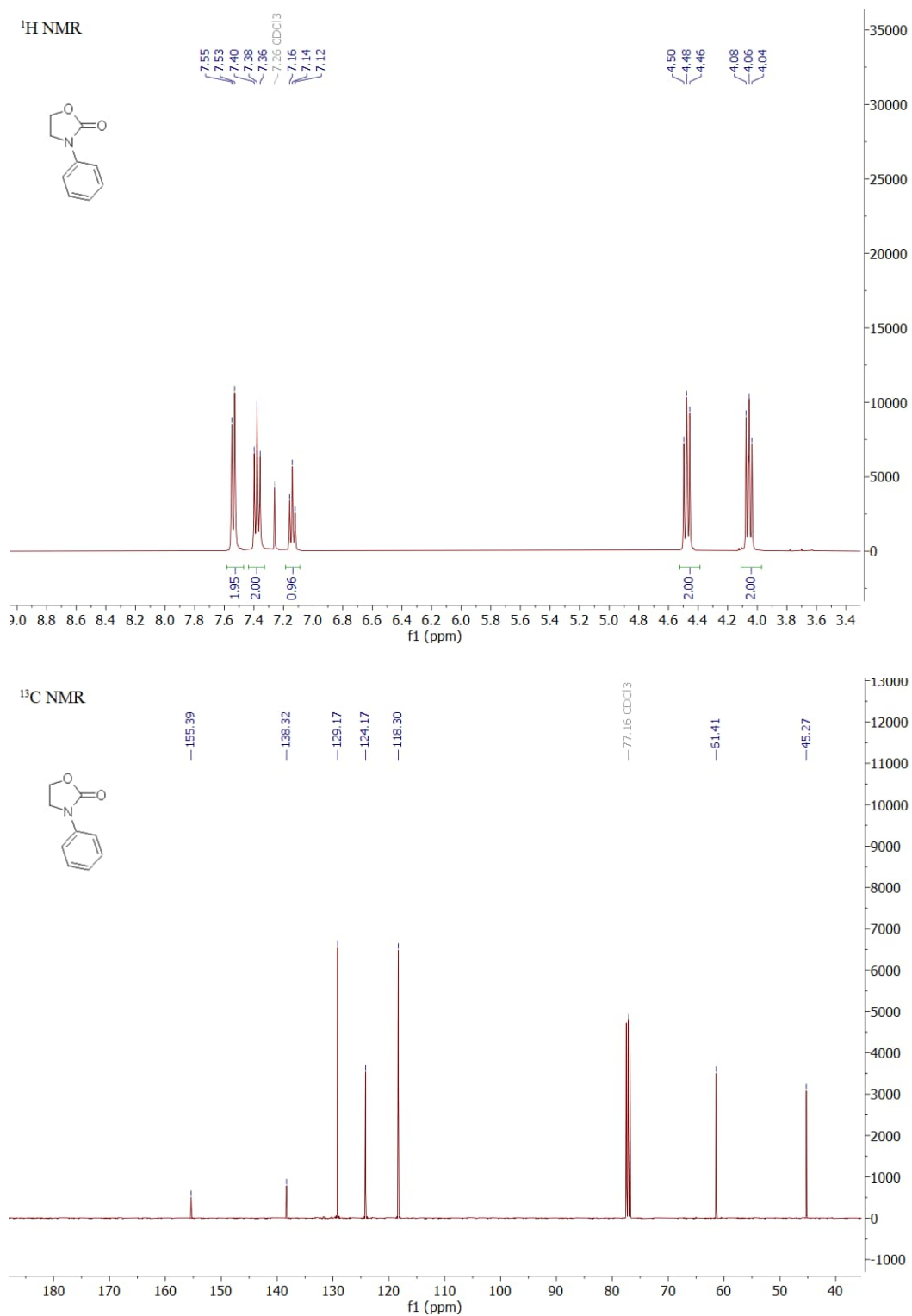


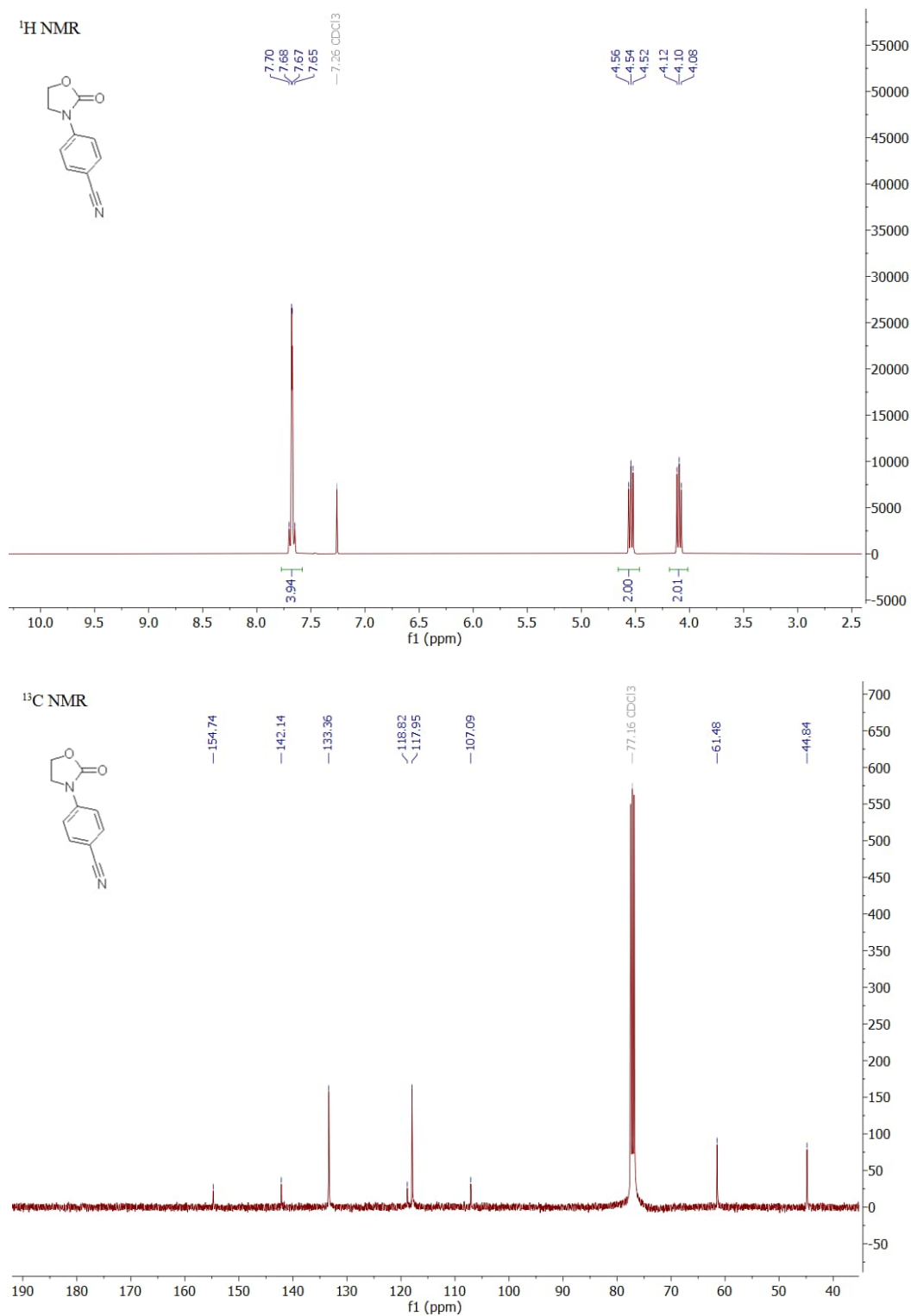
## 7.3.3. Supplementary Figures

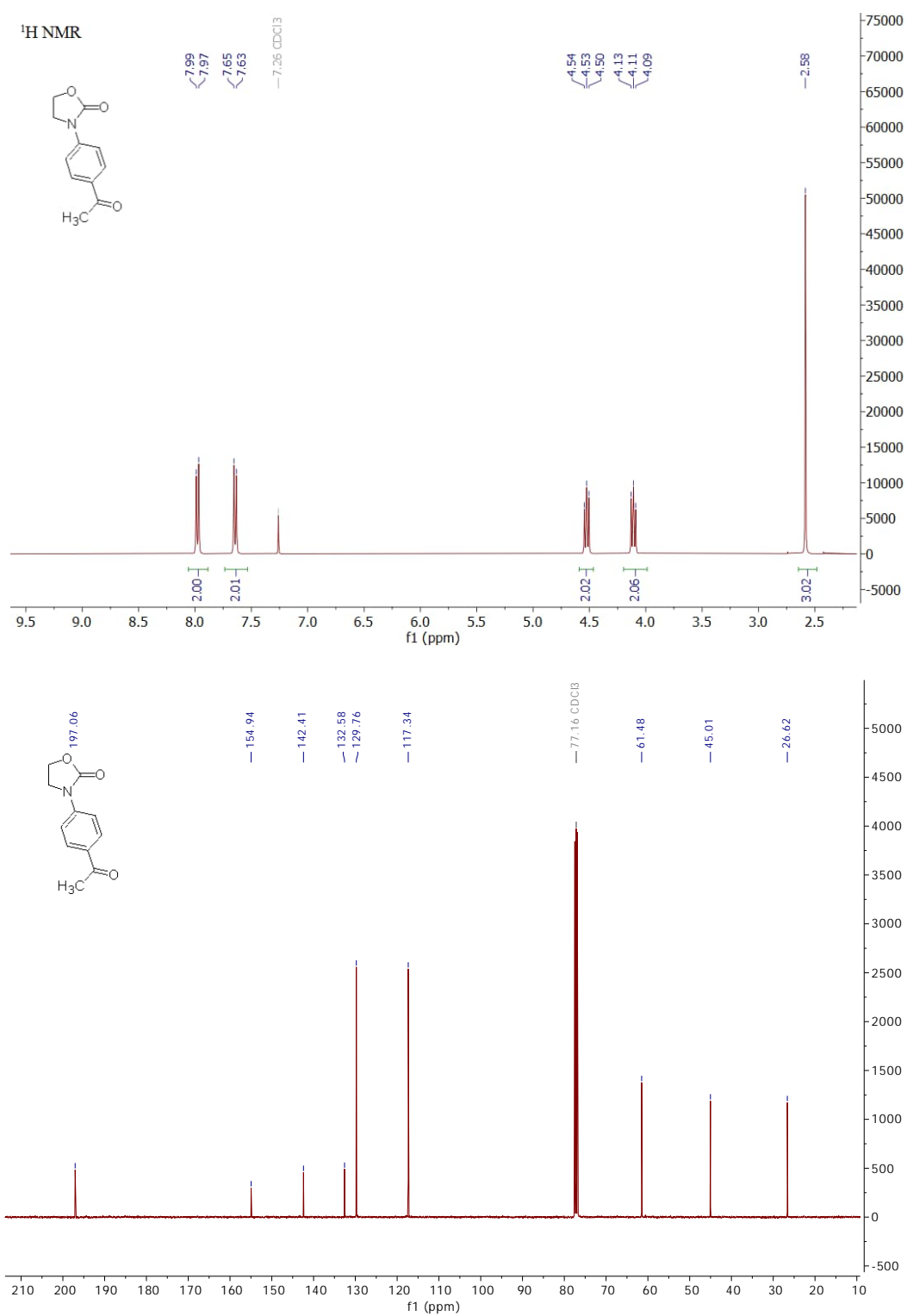
 $^1\text{H}$  and  $^{13}\text{C}$  spectra of oxazolidinonesFigure S3.29.  $^1\text{H}$  (top) and  $^{13}\text{C}$  (bottom) NMR spectra of compound 3 in  $\text{CDCl}_3$ .

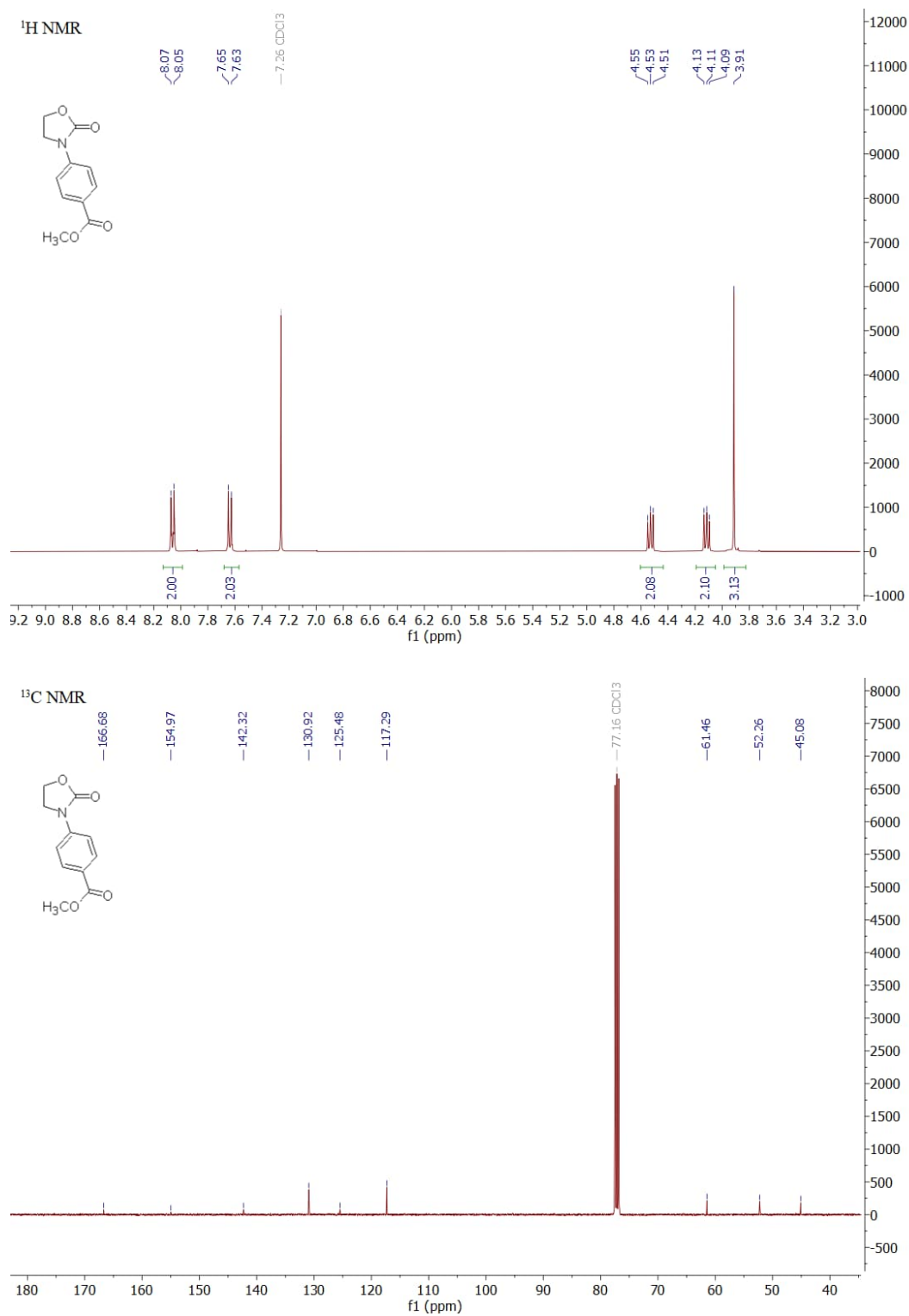
Figure S3.30. <sup>1</sup>H (top) and <sup>13</sup>C (bottom) NMR spectra of compound 1b in CDCl<sub>3</sub>.

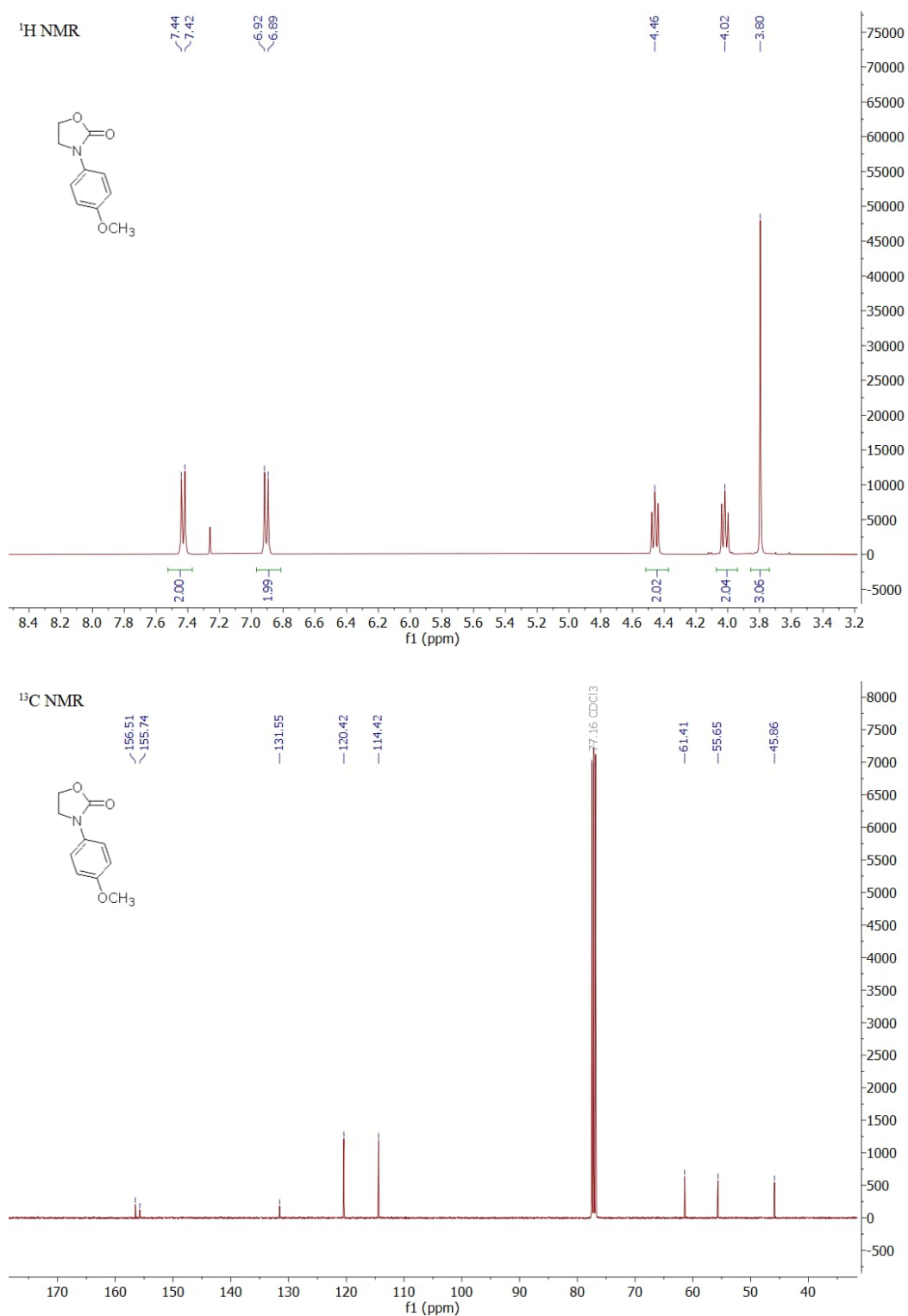
Figure S3.31. <sup>1</sup>H (top) and <sup>13</sup>C (bottom) NMR spectra of compound 1c in CDCl<sub>3</sub>.

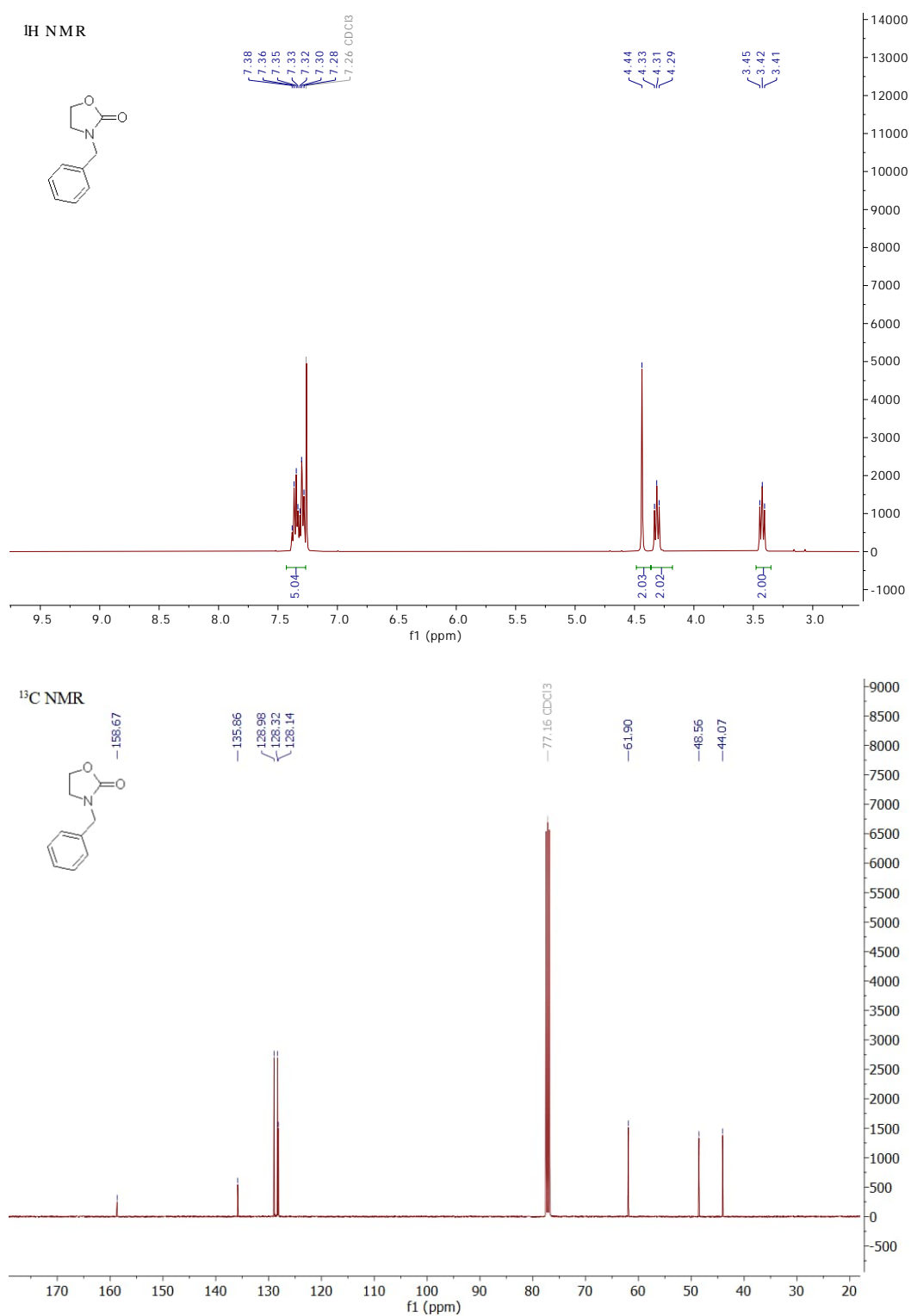
Figure S3.32. <sup>1</sup>H (top) and <sup>13</sup>C (bottom) NMR spectra of compound 1d in CDCl<sub>3</sub>.

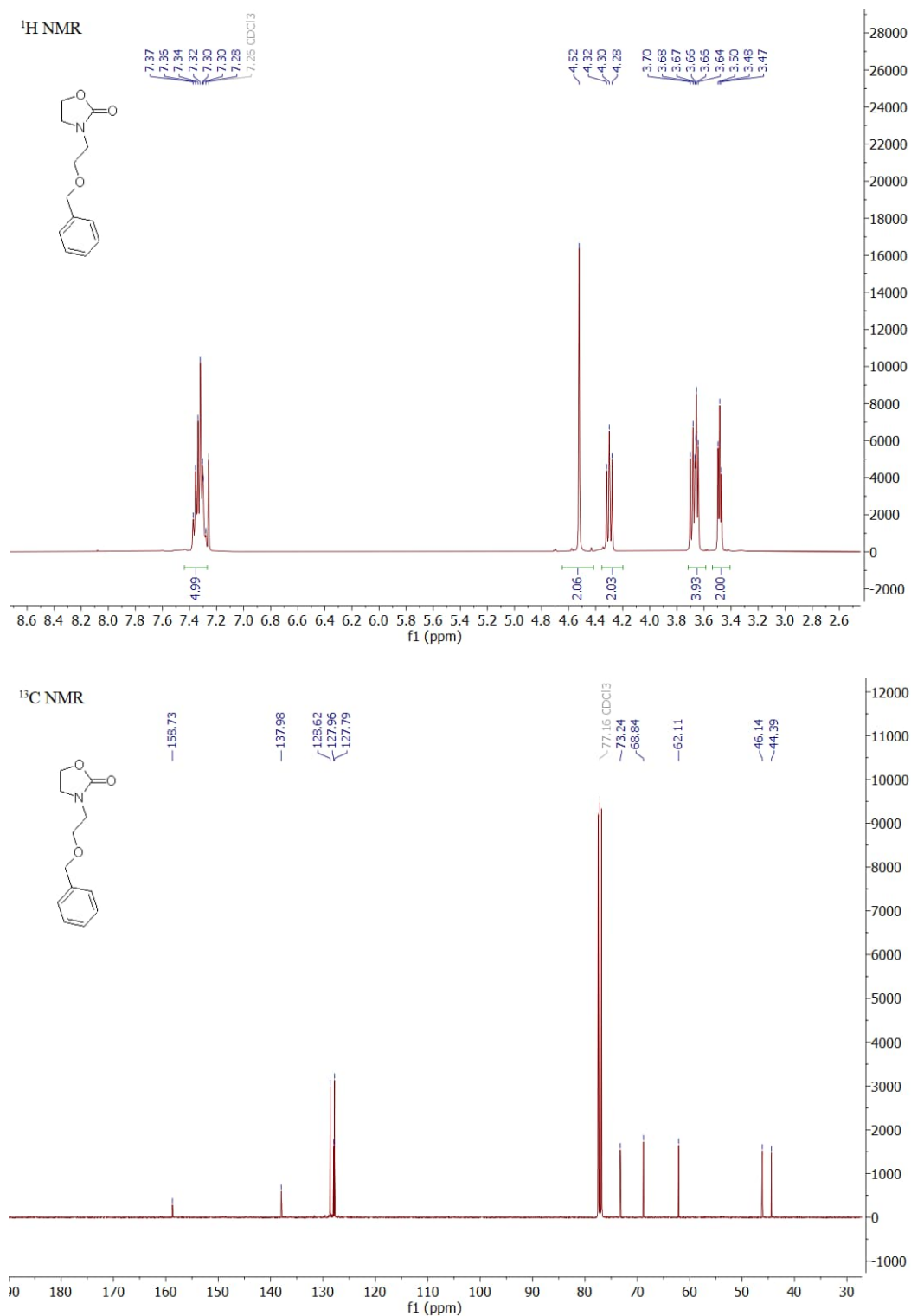
Figure S3.33. <sup>1</sup>H (top) and <sup>13</sup>C (bottom) NMR spectra of compound 1e in CDCl<sub>3</sub>.

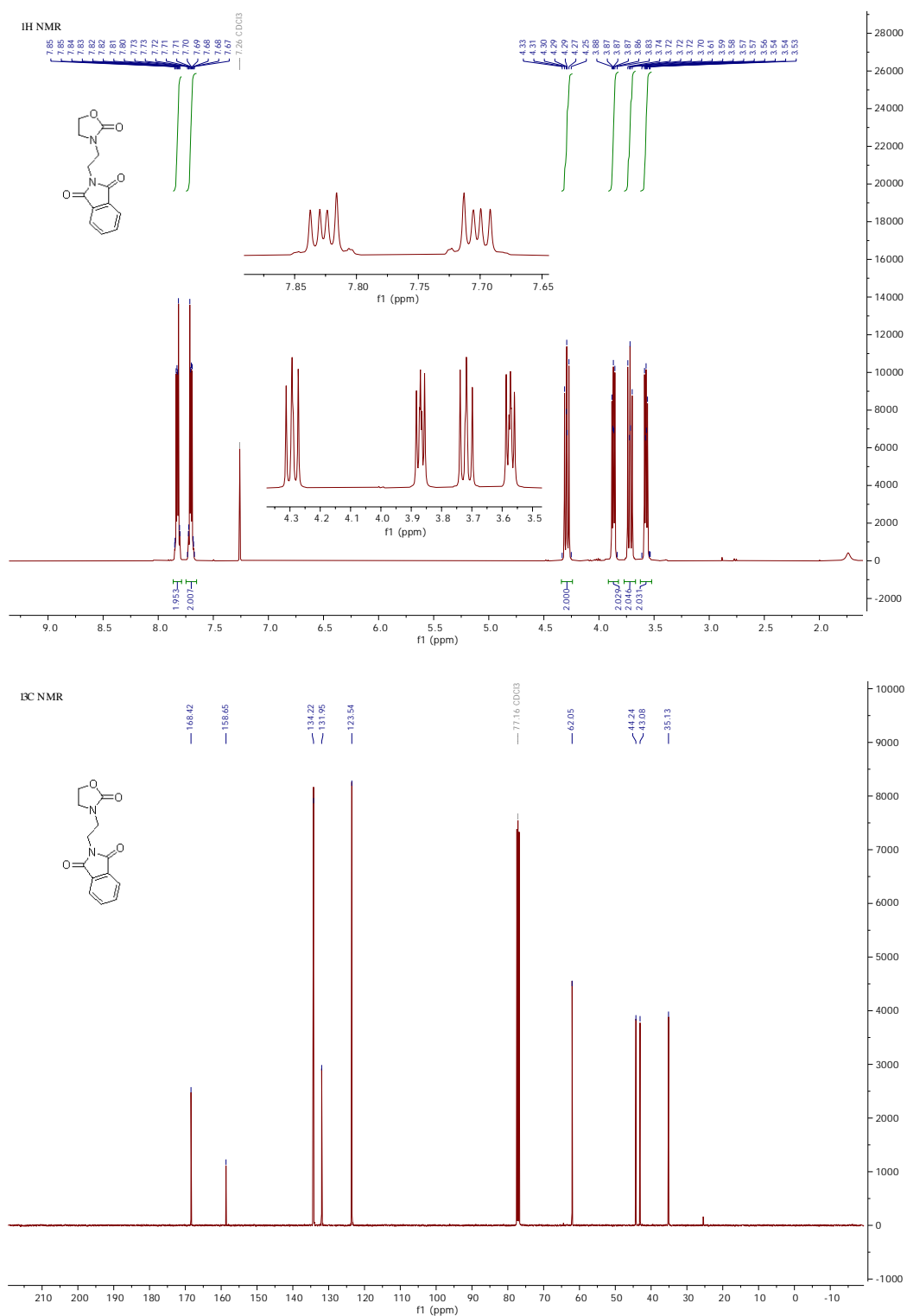
Figure S3.34. <sup>1</sup>H (top) and <sup>13</sup>C (bottom) NMR spectra of compound 1f in CDCl<sub>3</sub>.

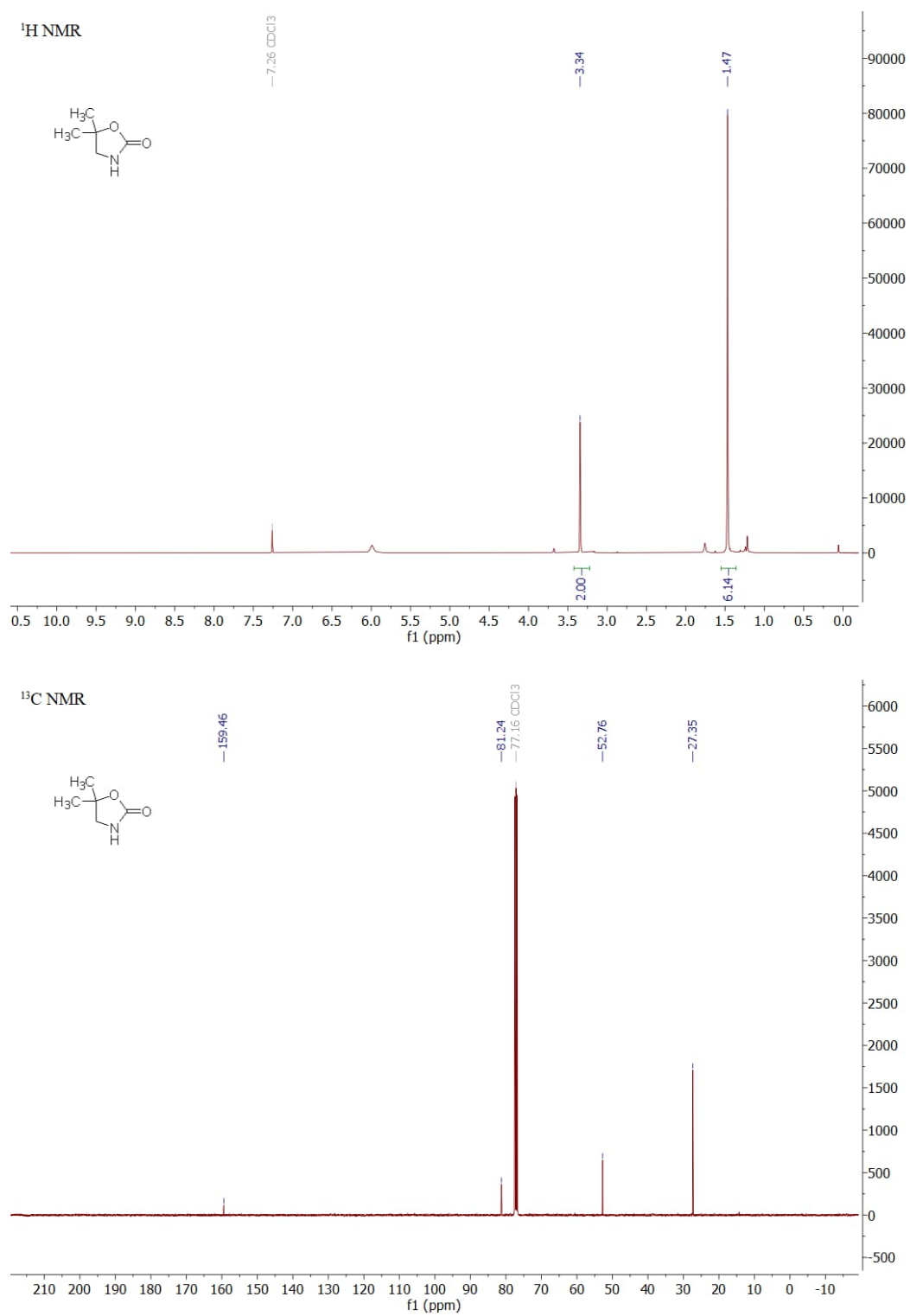
Figure S3.35. <sup>1</sup>H (top) and <sup>13</sup>C (bottom) NMR spectra of compound 1g in CDCl<sub>3</sub>.

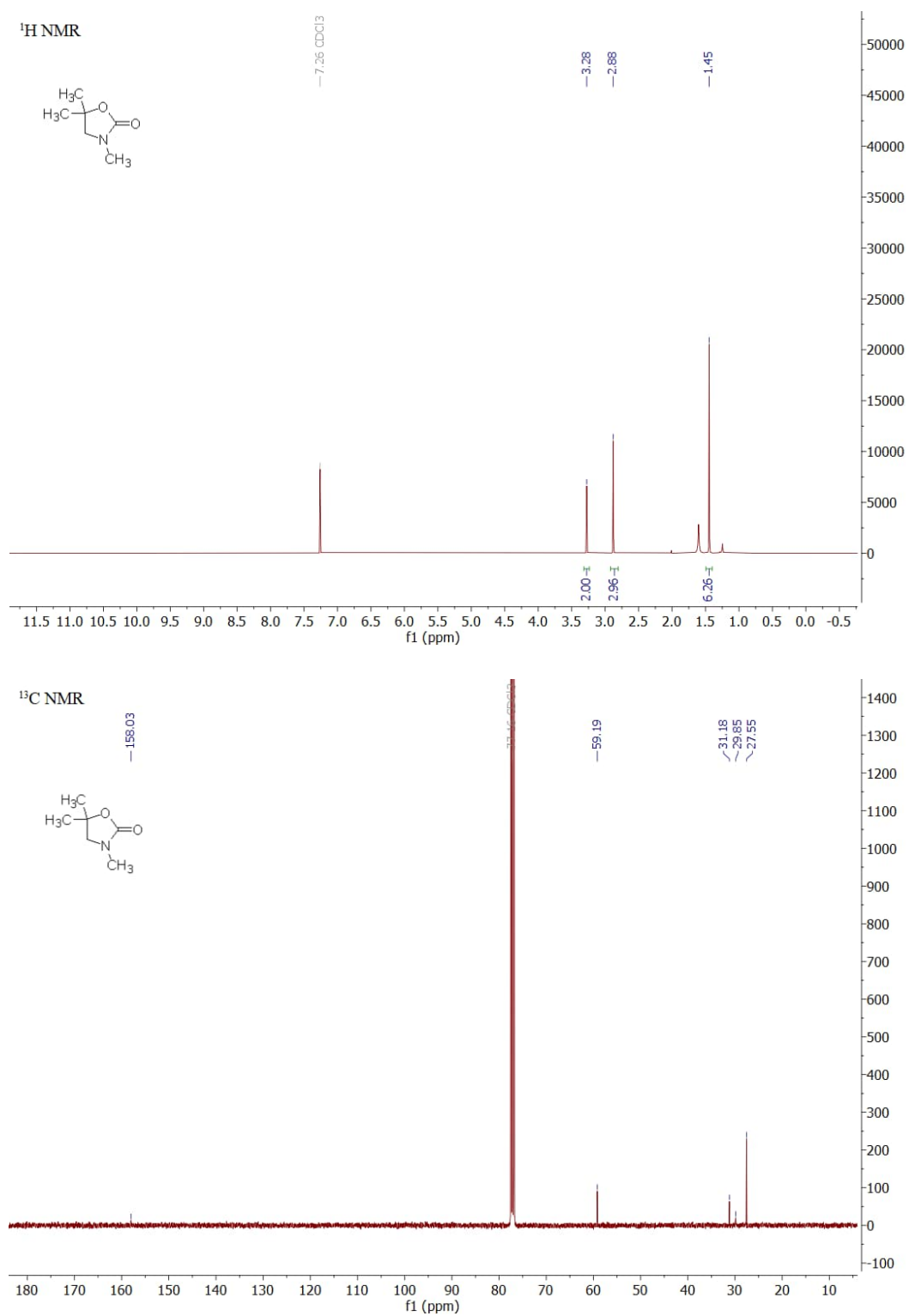
Figure S3.36. <sup>1</sup>H (top) and <sup>13</sup>C (bottom) NMR spectra of compound 1h in CDCl<sub>3</sub>.

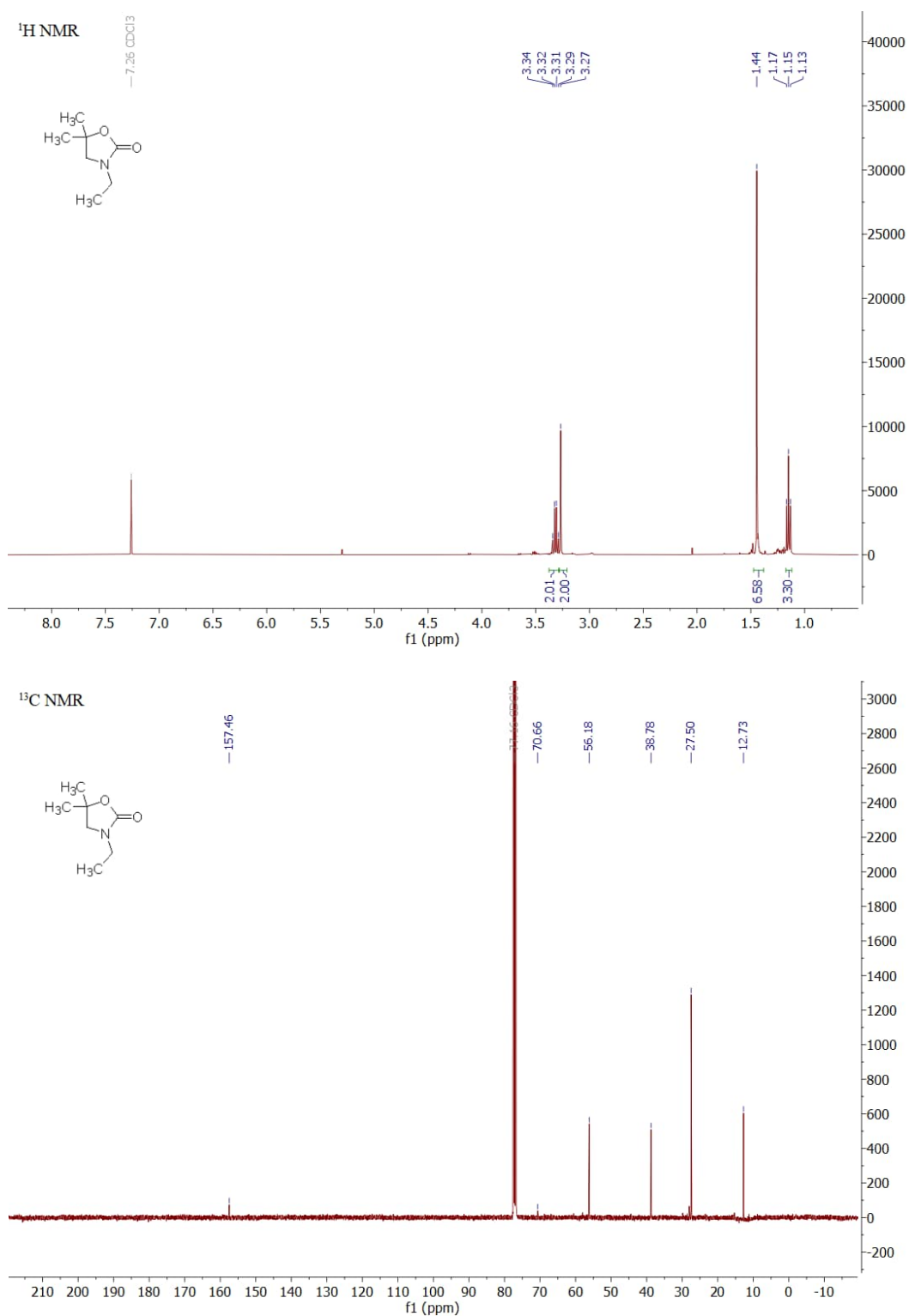
Figure S3.37. <sup>1</sup>H (top) and <sup>13</sup>C (bottom) NMR spectra of compound 1i in CDCl<sub>3</sub>.

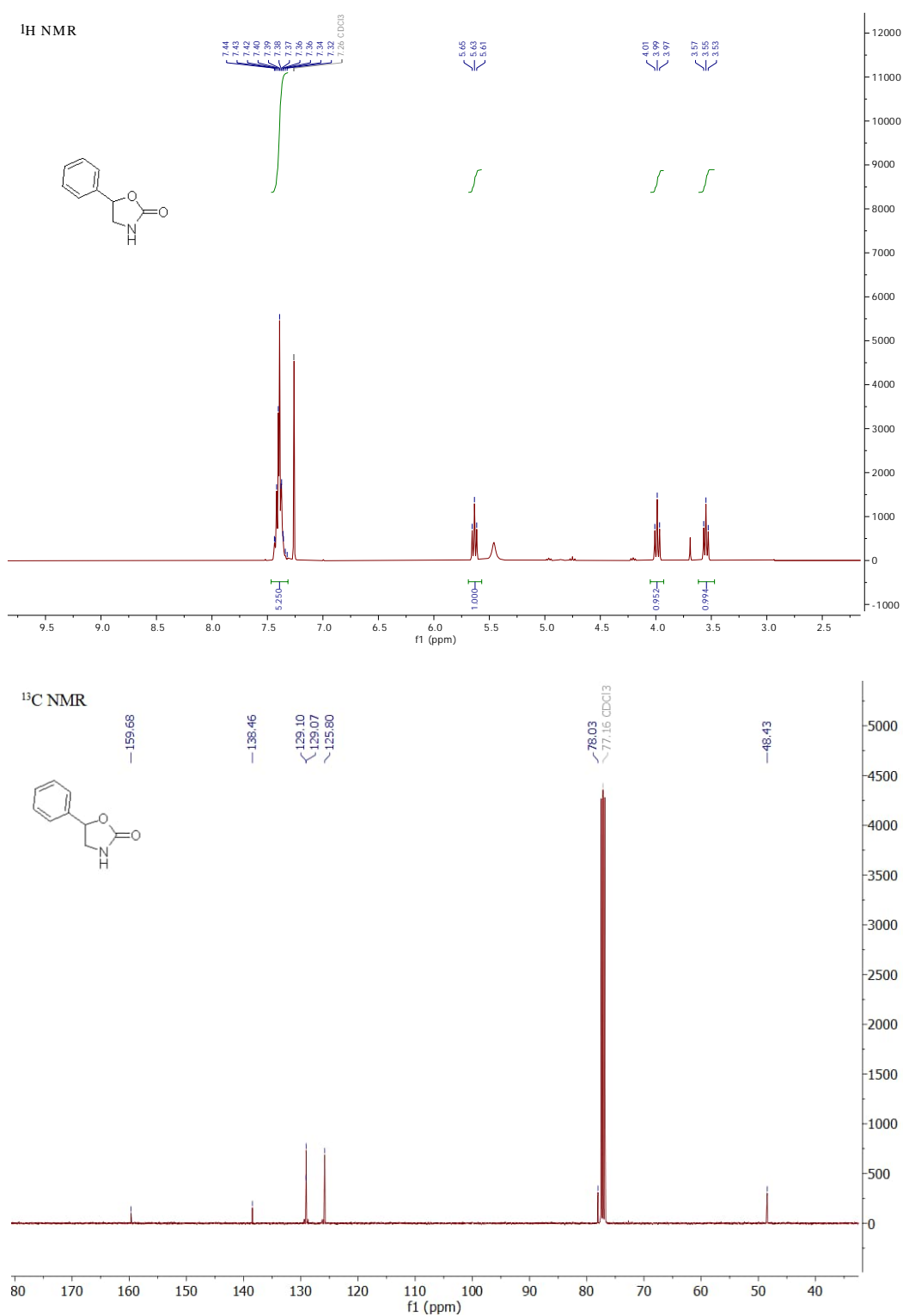
Figure S3.38. <sup>1</sup>H (top) and <sup>13</sup>C (bottom) NMR spectra of compound 1j in CDCl<sub>3</sub>.

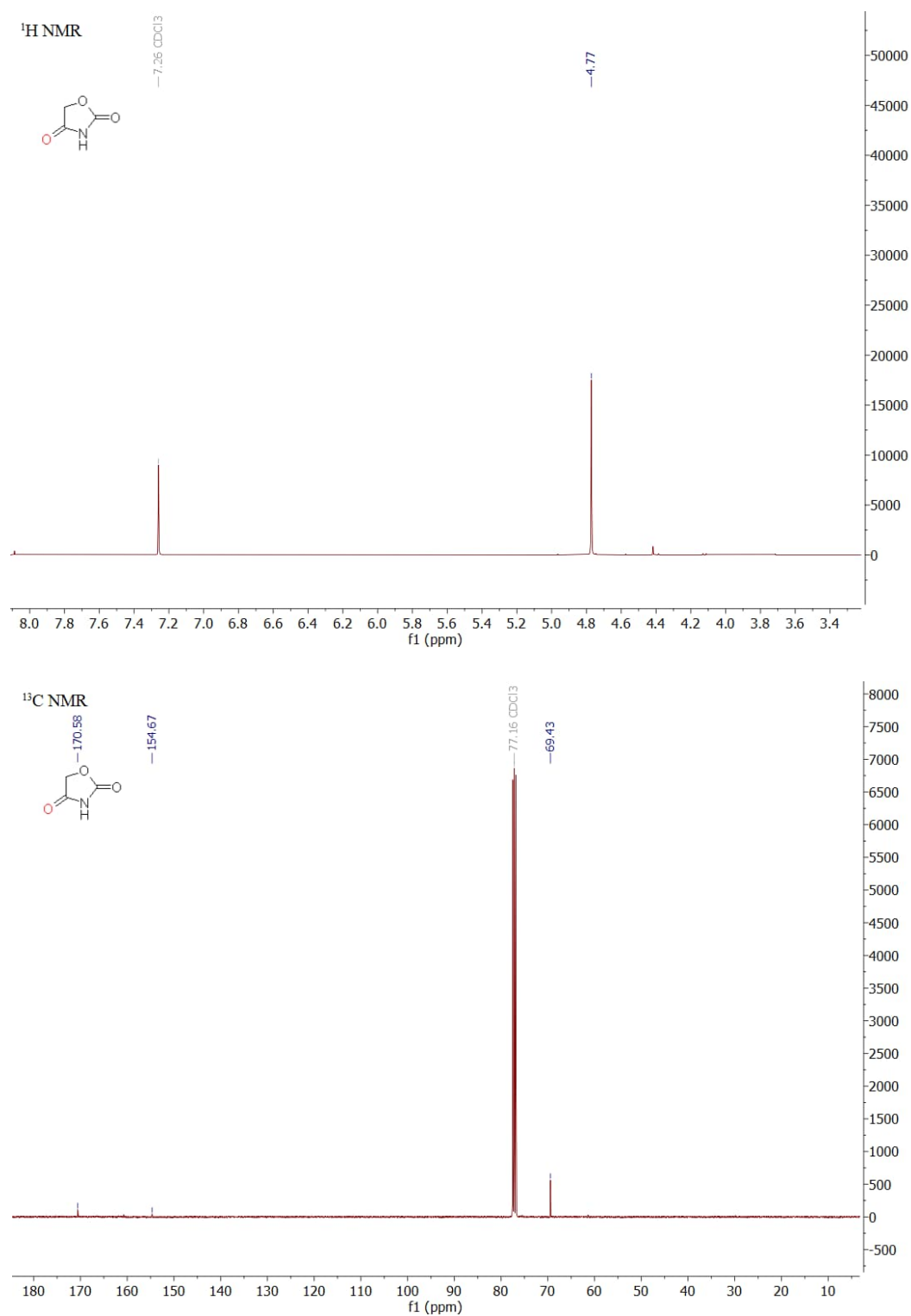
Figure S3.39. <sup>1</sup>H (top) and <sup>13</sup>C (bottom) NMR spectra of compound 1k in CDCl<sub>3</sub>.

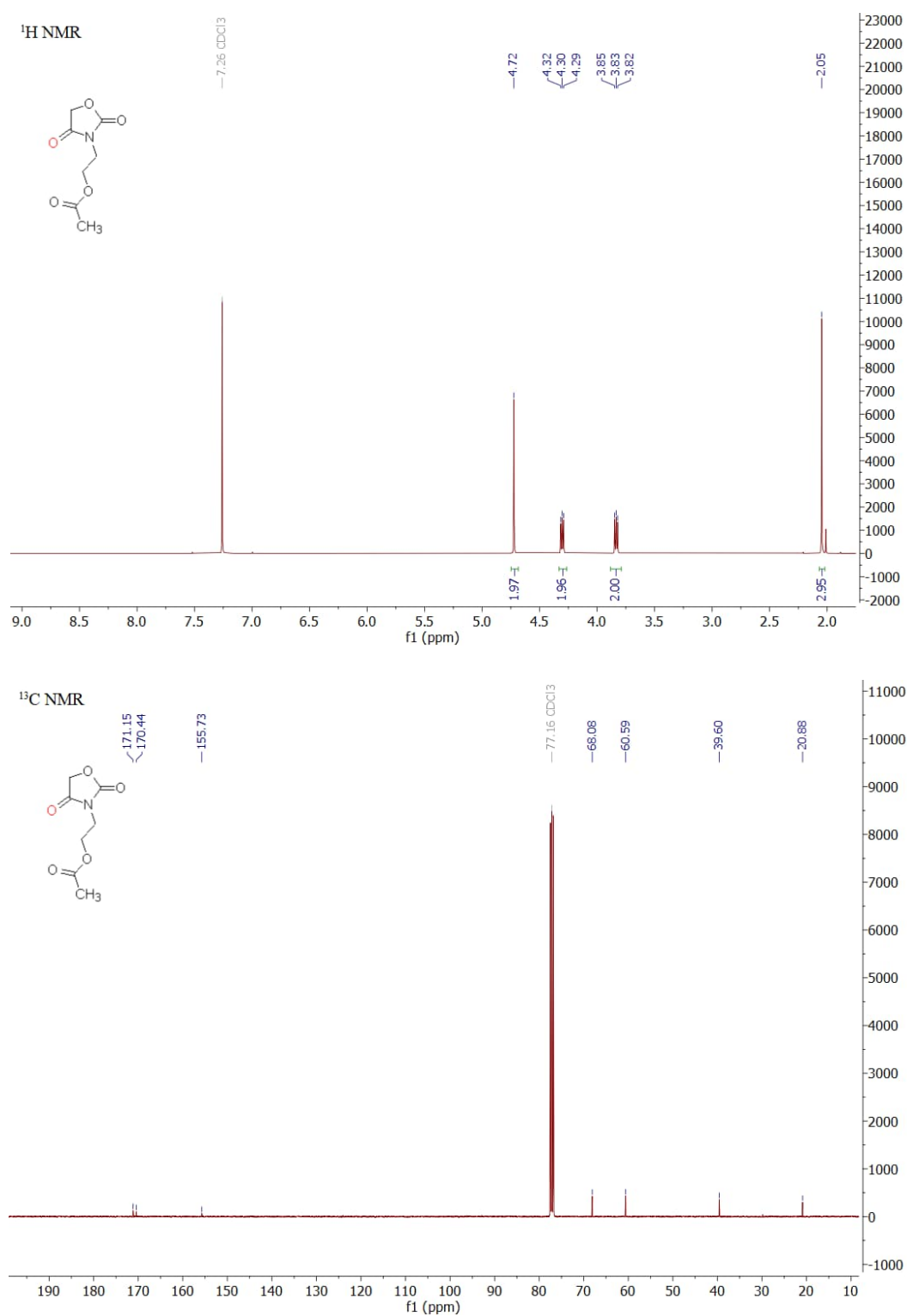
Figure S3.40. <sup>1</sup>H (top) and <sup>13</sup>C (bottom) NMR spectra of compound 11 in CDCl<sub>3</sub>.

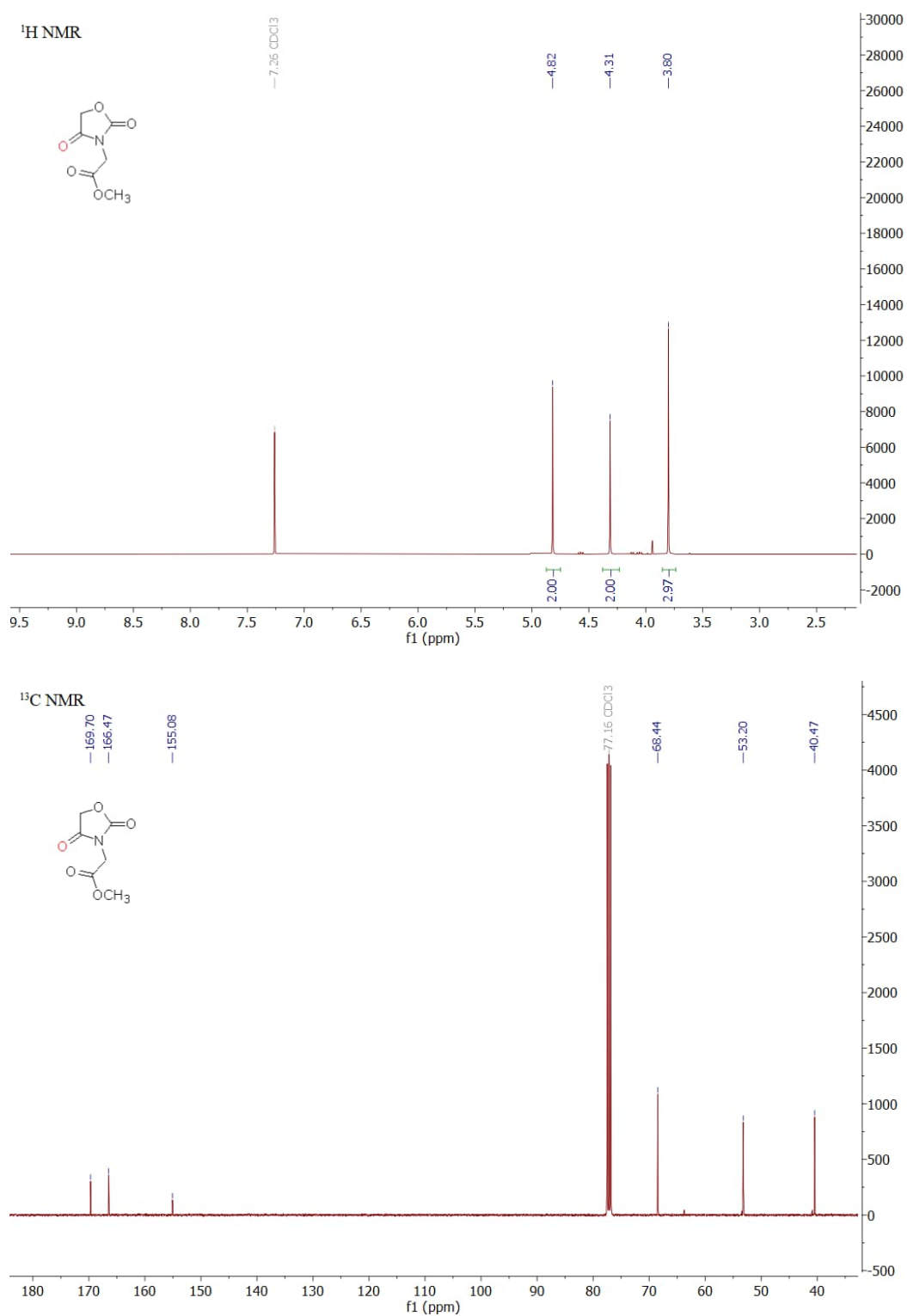
Figure S3.41. <sup>1</sup>H (top) and <sup>13</sup>C (bottom) NMR spectra of compound 1m in CDCl<sub>3</sub>.

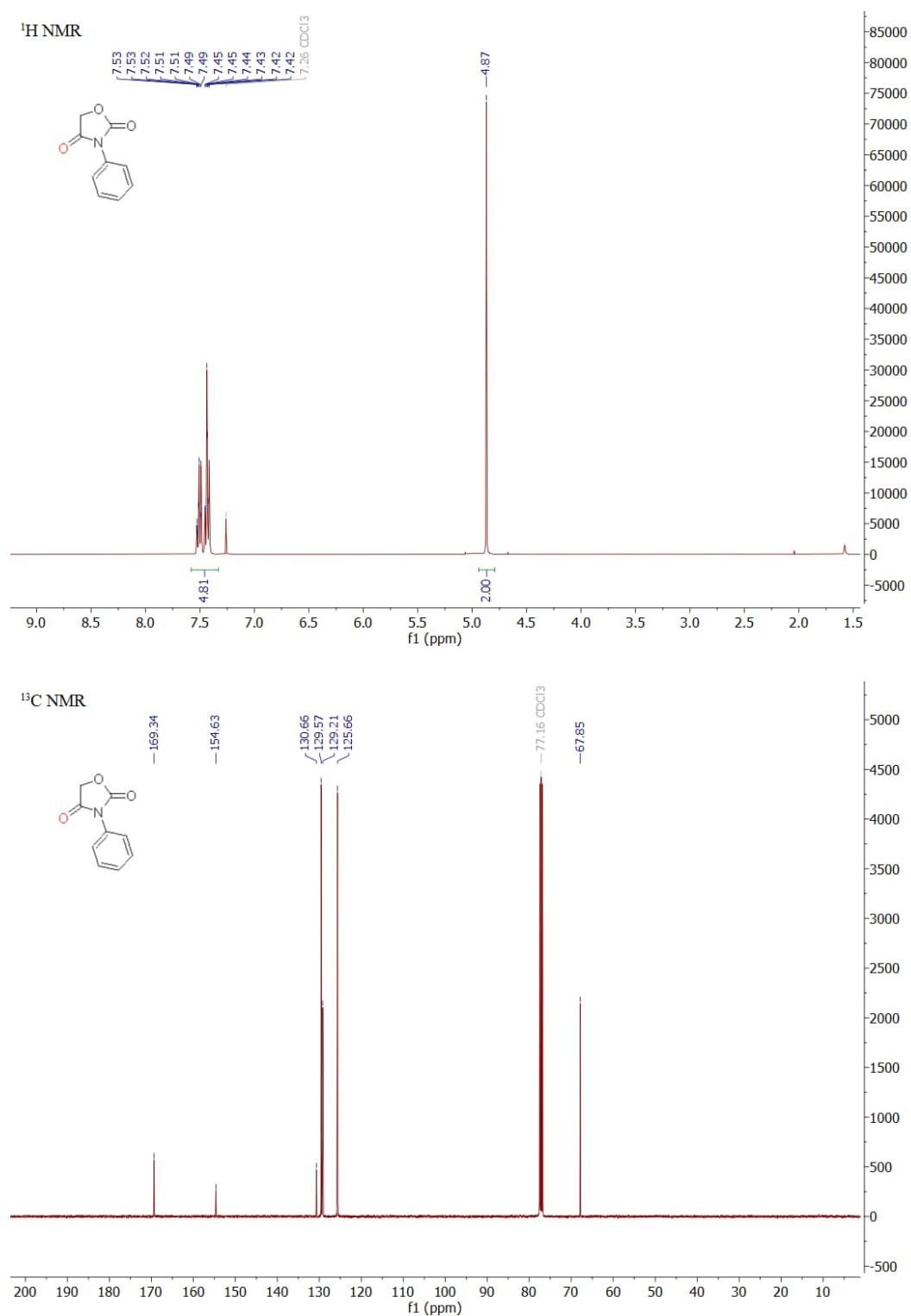
Figure S3.42. <sup>1</sup>H (top) and <sup>13</sup>C (bottom) NMR spectra of compound 1n in CDCl<sub>3</sub>.

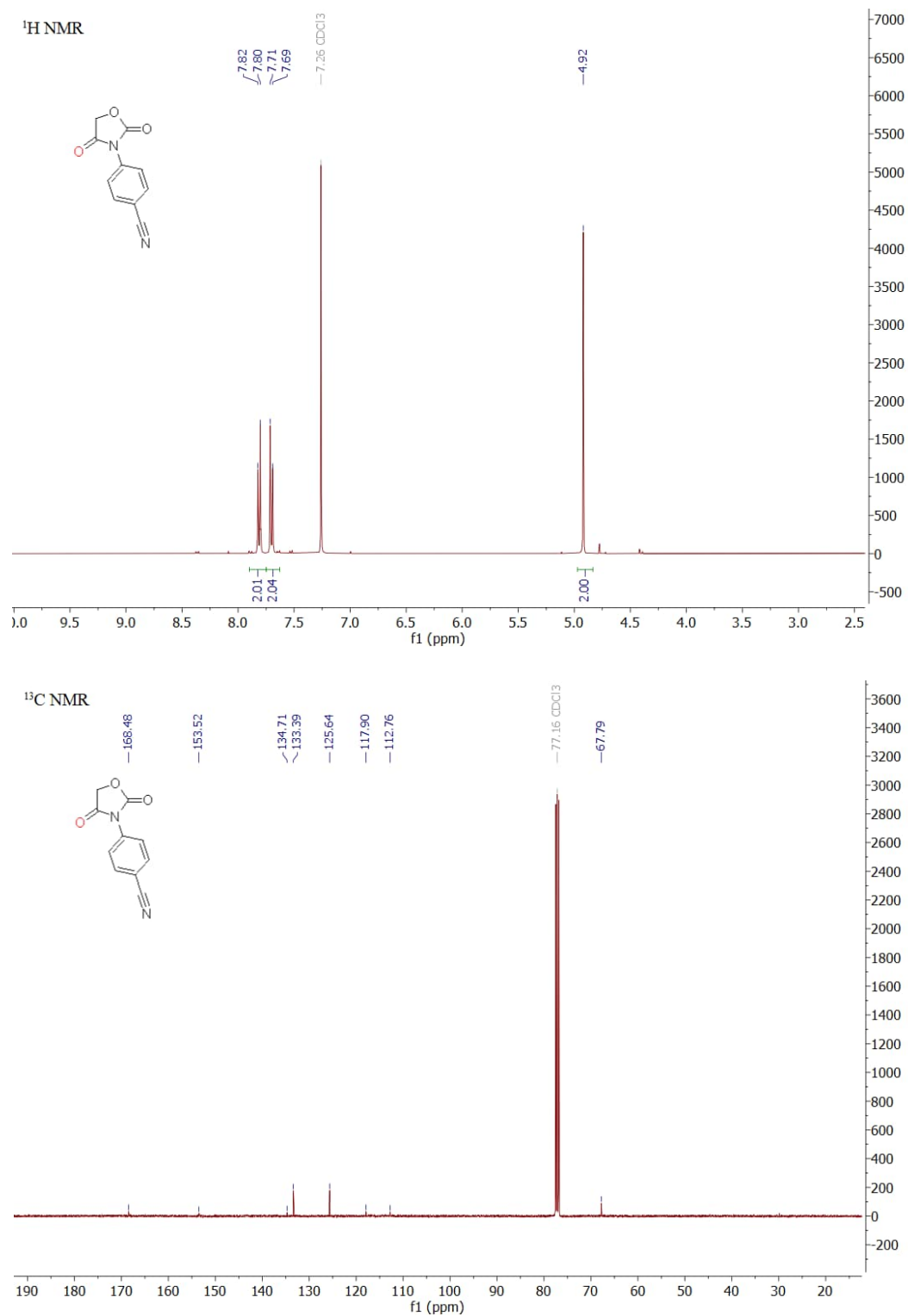
Figure S3.43. <sup>1</sup>H (top) and <sup>13</sup>C (bottom) NMR spectra of compound 1o in CDCl<sub>3</sub>.

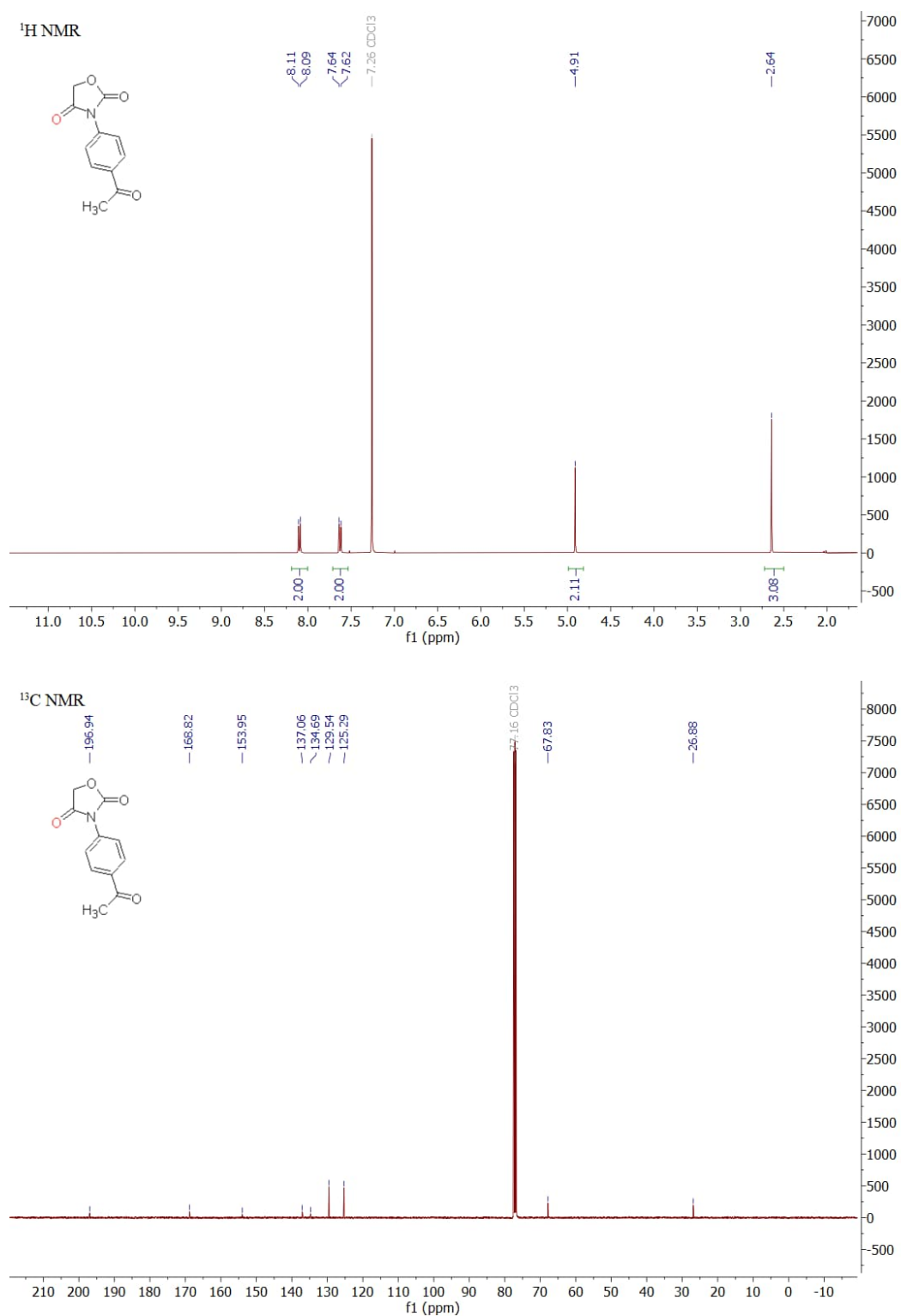
$^1\text{H}$  and  $^{13}\text{C}$  spectra of oxazolidinedionesFigure S3.44.  $^1\text{H}$  (top) and  $^{13}\text{C}$  (bottom) NMR spectra of compound 2a in  $\text{CDCl}_3$ .

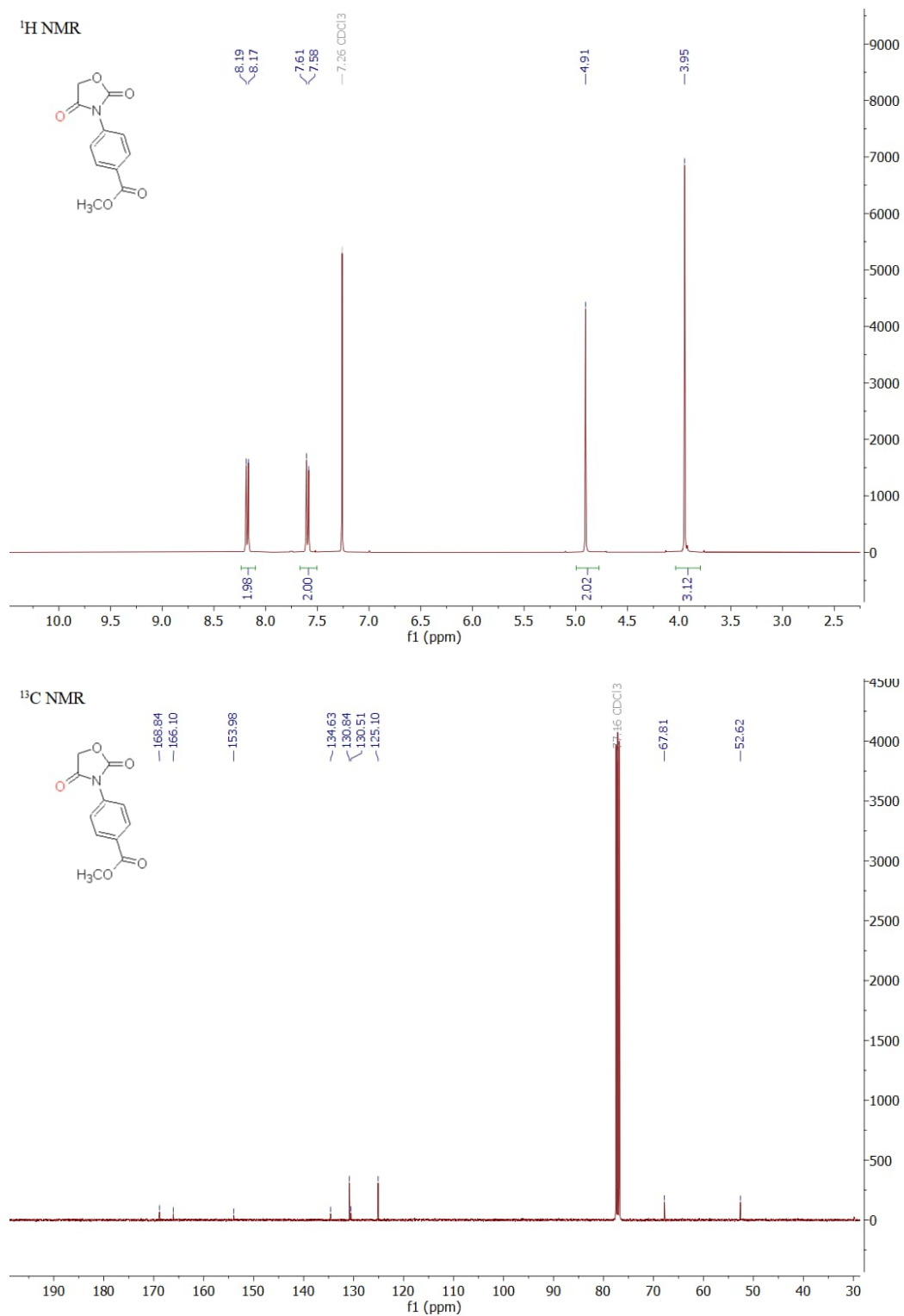
Figure S3.45. <sup>1</sup>H (top) and <sup>13</sup>C (bottom) NMR spectra of compound 2b in CDCl<sub>3</sub>.

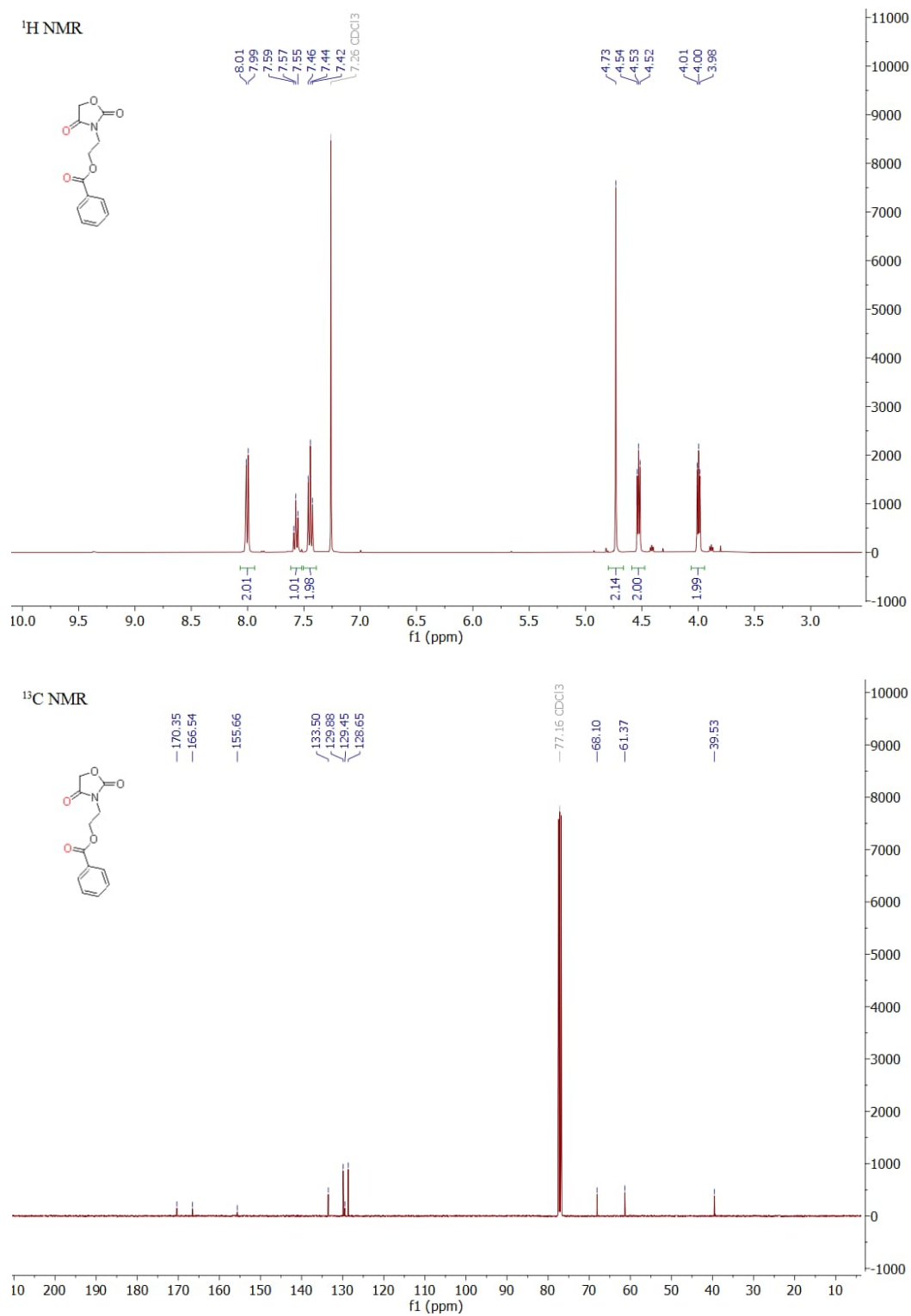
Figure S3.46. <sup>1</sup>H (top) and <sup>13</sup>C (bottom) NMR spectra of compound 2c in CDCl<sub>3</sub>.

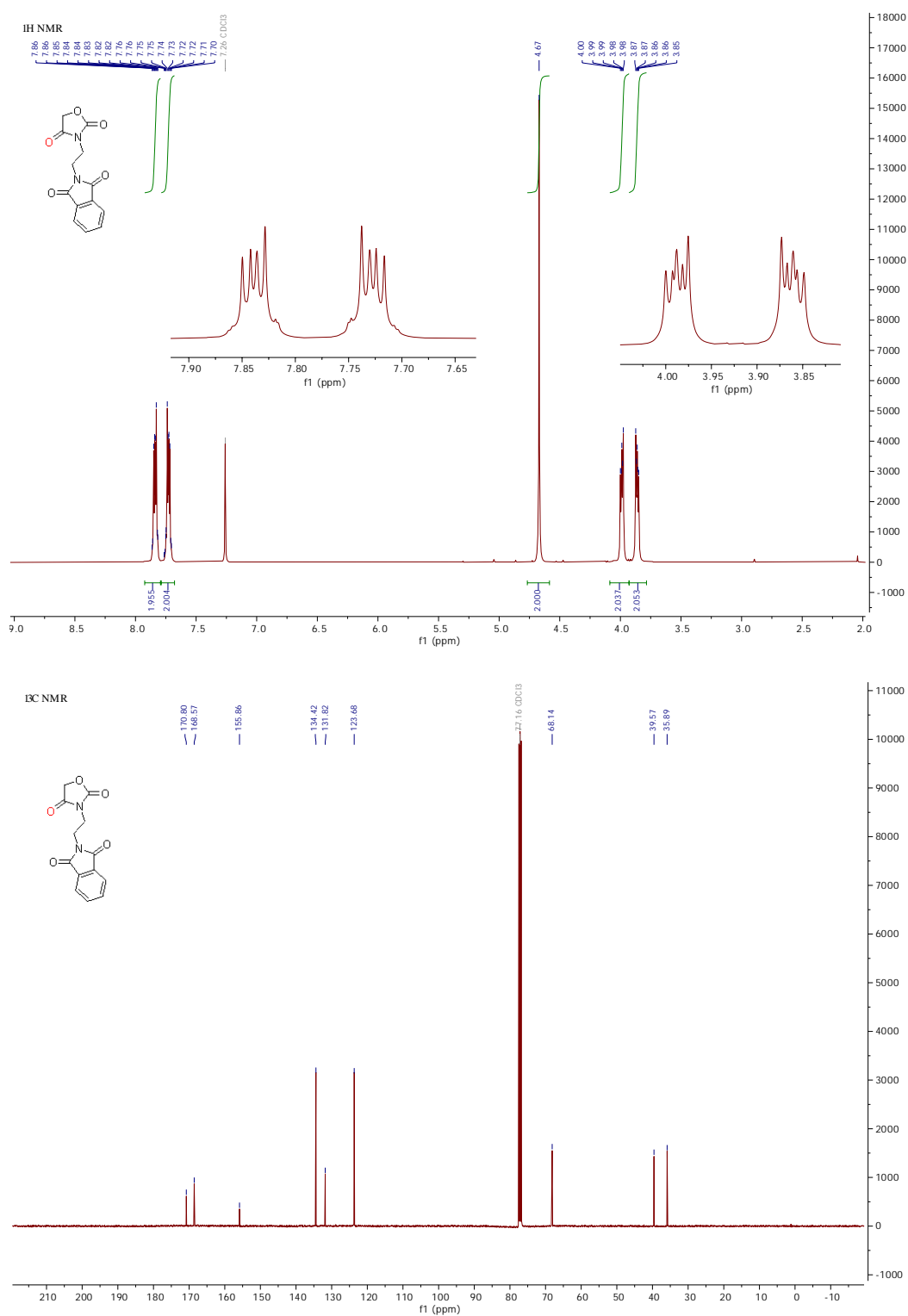
Figure S3.47. <sup>1</sup>H (top) and <sup>13</sup>C (bottom) NMR spectra of compound 2d in CDCl<sub>3</sub>.

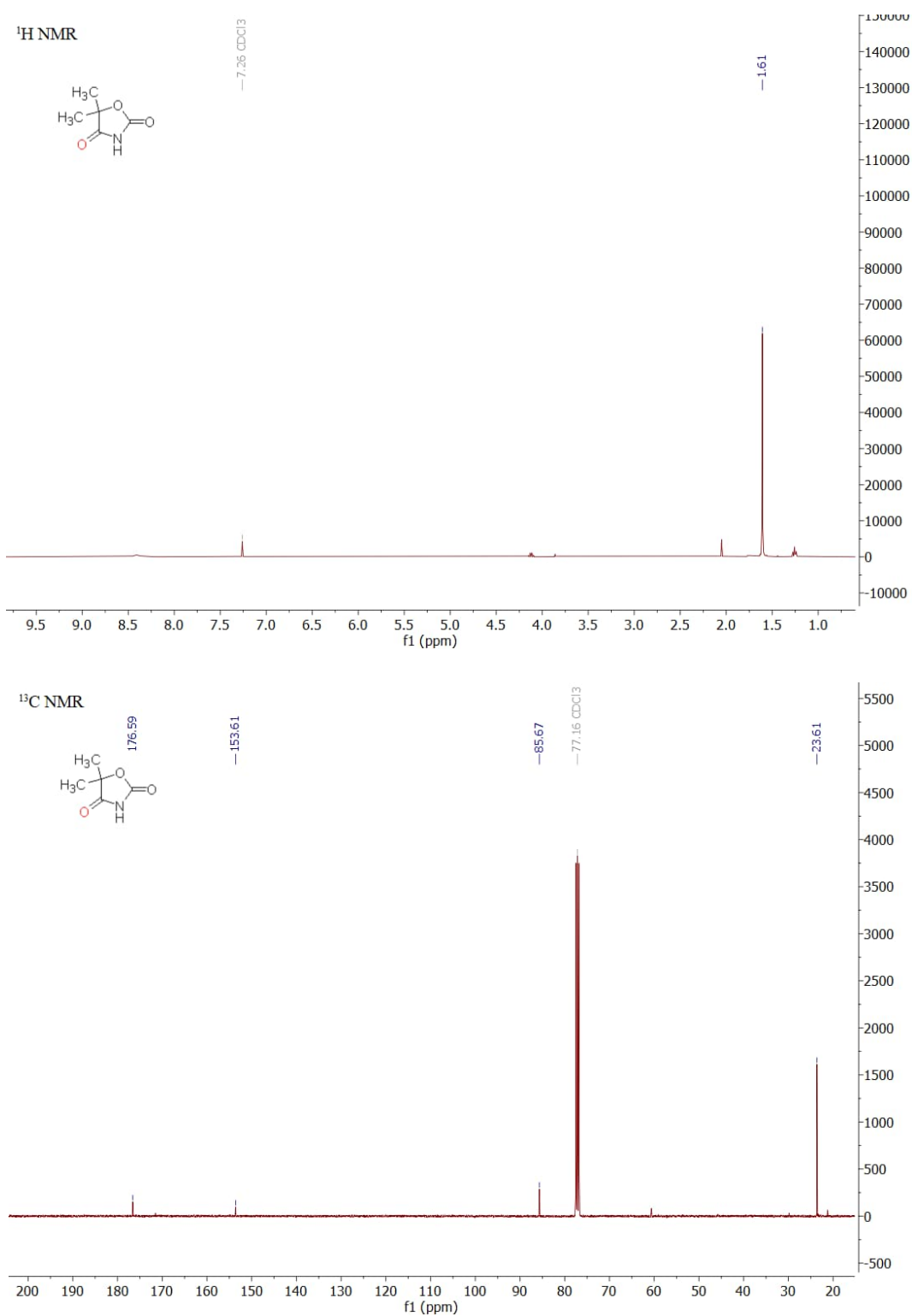
Figure S3.48. <sup>1</sup>H (top) and <sup>13</sup>C (bottom) NMR spectra of compound 2e in CDCl<sub>3</sub>.

Figure S3.49. <sup>1</sup>H (top) and <sup>13</sup>C (bottom) NMR spectra of compound 2f in CDCl<sub>3</sub>.

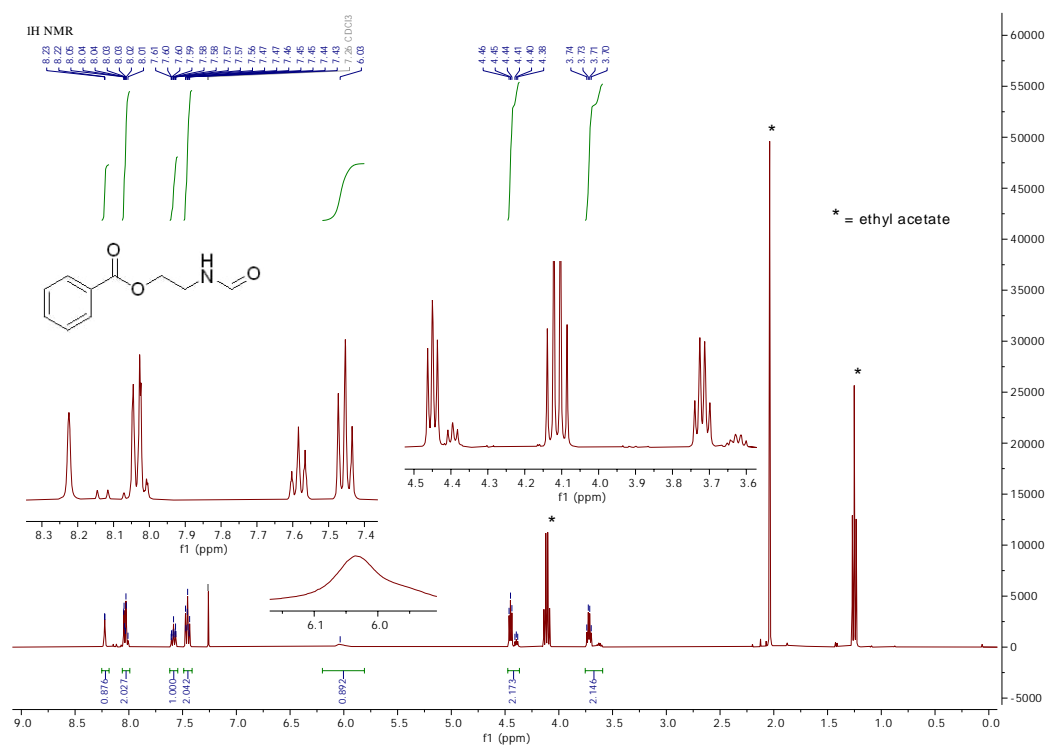
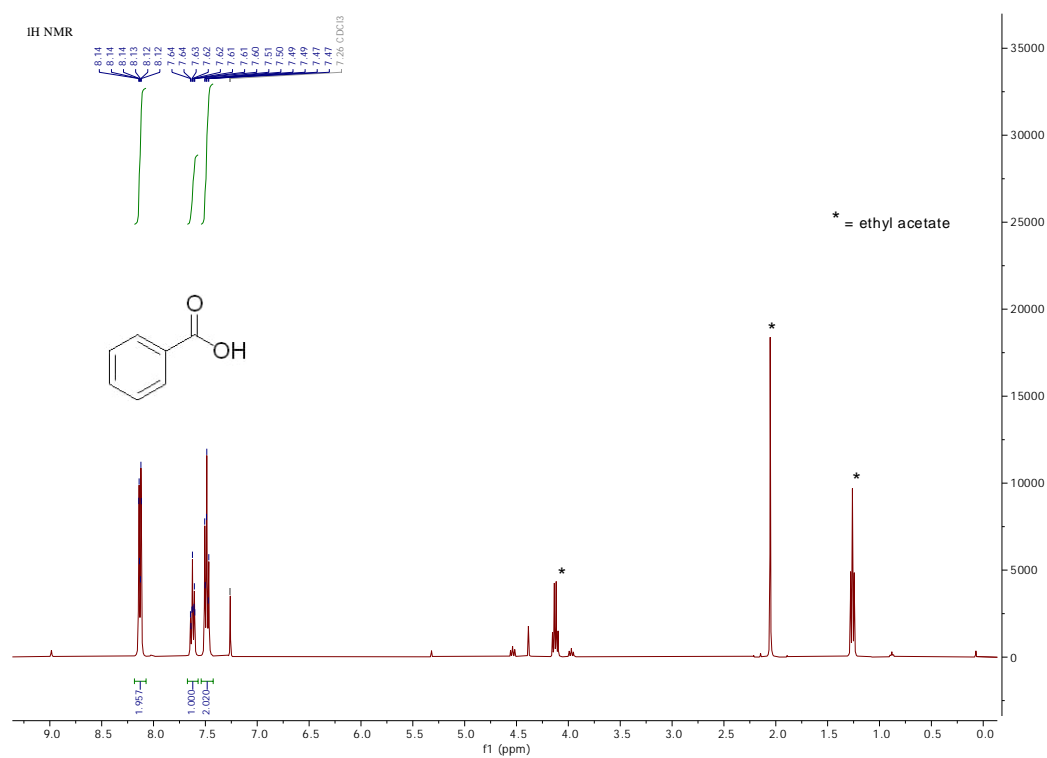
Figure S3.50. <sup>1</sup>H (top) and <sup>13</sup>C (bottom) NMR spectra of compound 2g in CDCl<sub>3</sub>.

Figure S3.51. <sup>1</sup>H (top) and <sup>13</sup>C (bottom) NMR spectra of compound 2j-a in CDCl<sub>3</sub>.

Figure S3.52. <sup>1</sup>H (top) and <sup>13</sup>C (bottom) NMR spectra of compound 2k in CDCl<sub>3</sub>.

Figure S3.53. <sup>1</sup>H (top) and <sup>13</sup>C (bottom) NMR spectra of compound 21 in CDCl<sub>3</sub>.



Figure S3.56. <sup>1</sup>H NMR spectrum of 2j-c side product from HPLC fraction.Figure S3.57. <sup>1</sup>H NMR spectrum of 2j-b side product (benzoic acid) from HPLC fraction.

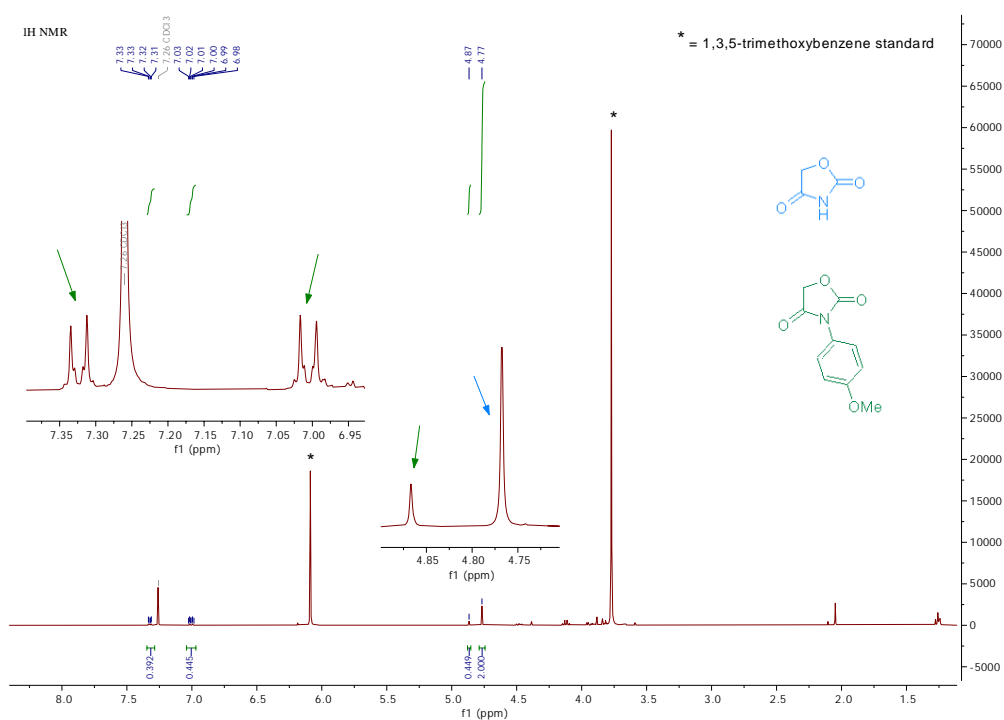


Figure S3.58. <sup>1</sup>H NMR spectrum of oxidation products of 1h. Arrows indicate proton signals of a product of the same color.

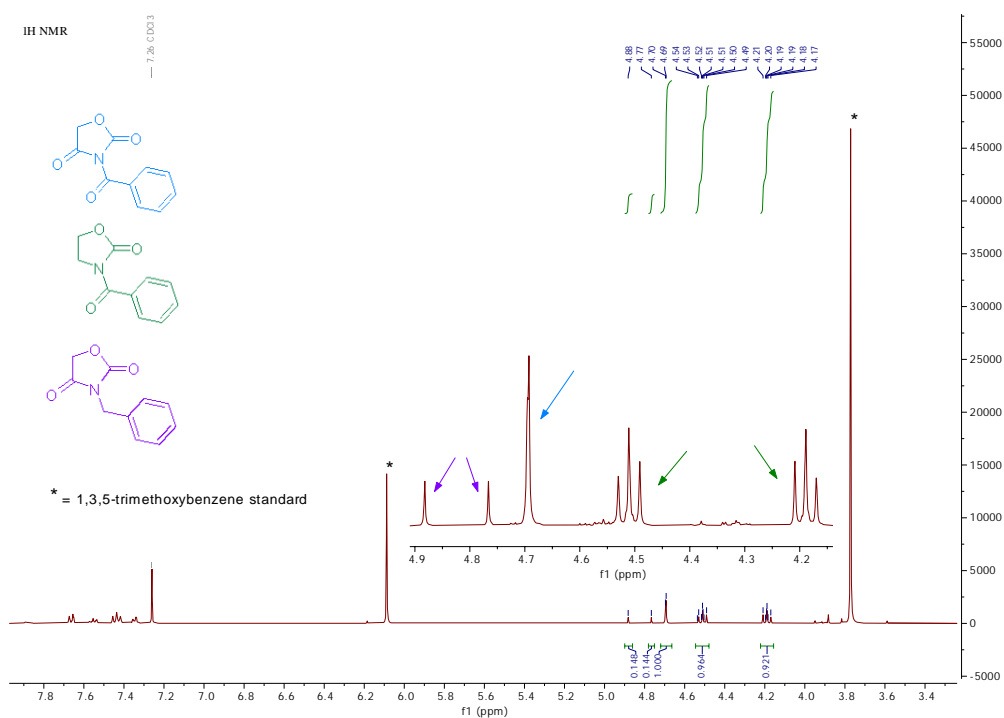
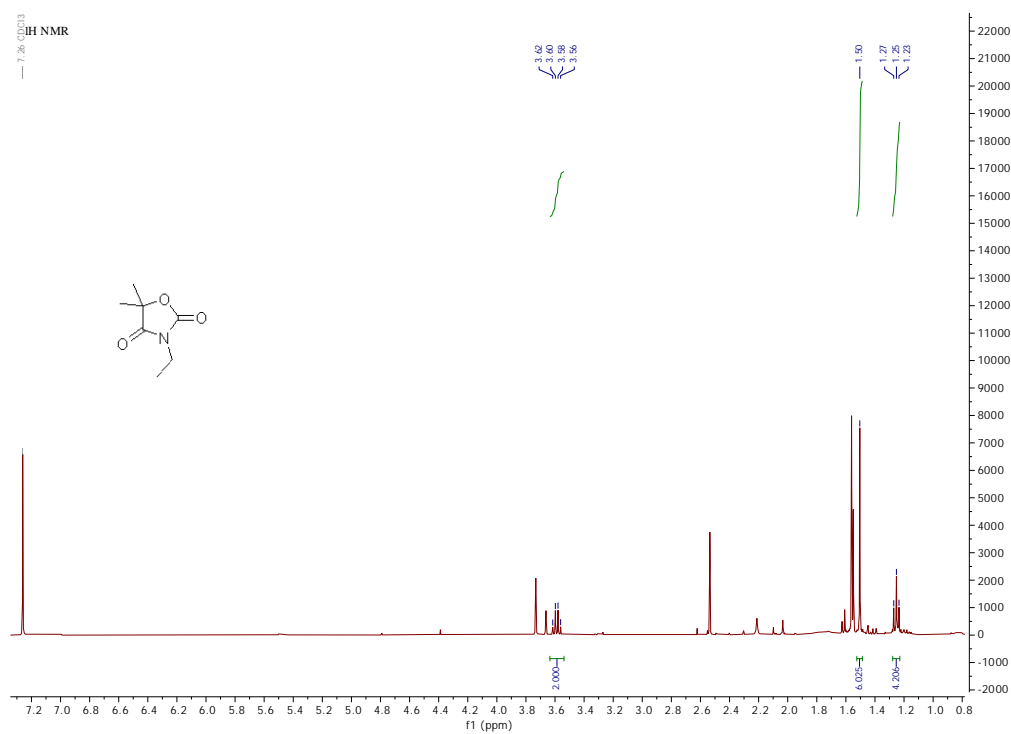
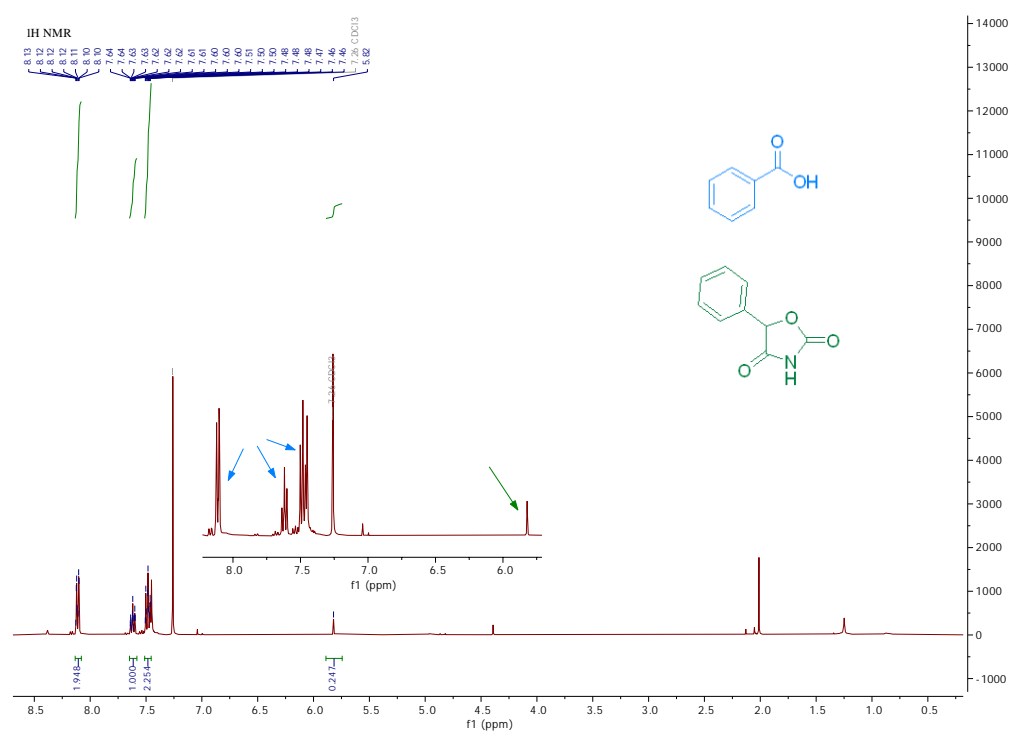


Figure S3.59. <sup>1</sup>H NMR spectrum of oxidation products of 1i. Arrows indicate proton signals of a product of the same color.



Figure S3.60. <sup>1</sup>H NMR spectrum of oxidation products of 1n.Figure S3.61. <sup>1</sup>H NMR spectrum of oxidation products of 1o. Arrows indicate proton signals of a product of the same color.

## 7.4. SI for Chapter 4

### 7.4.1. General Materials and Methods

All chemicals and solvents, except for potassium rhodizonate, were purchased from chemical suppliers (Sigma-Aldrich, Fischer Scientific, Thermo Scientific, etc.) in high purity grade ( $\geq 97\%$  purity for chemicals, HPLC grade and higher for solvents) and were used as received. Potassium rhodizonate was obtained as a technical grade chemical (ca. 85% purity) from Sigma-Aldrich and was used as received.

Agilent 6890 Network GC System coupled with Agilent 5975 Inert Mass Selective detector (electron ionization) were used for reaction mixture composition analysis and to obtain mass spectra of the products. Molecules' identification was done *via* comparison with NIST spectra database.

Elemental analysis was accomplished as combustion analysis using a Vario Micro device. Method allows to identify the elemental ratios of C, N, H, and S atoms in a sample. Inductively coupled plasma-optical emission spectrometry (ICP-OES) was conducted using a Horiba Ultra 2 instrument equipped with photomultiplier tube detector.

Powder X-Ray diffraction patterns were measured on a Bruker D8 Advance diffractometer equipped with a scintillation counter detector with  $\text{CuK}\alpha$  radiation ( $\lambda = 0.15418 \text{ nm}$ ) applying  $2\theta$  step size of  $0.1^\circ$  and counting time of 3 s per step.

Fourier transform infrared (FT-IR) spectra were recorded on Thermo Scientific Nicolet iD5 spectrometer.

For high-resolution transmission electron microscopy (HRTEM) observations, a suspension of the sample in ethanol was sonicated for 10 minutes and then drop-casted to a Au grid with a holey carbon support and dried for 15 minutes. The TEM study was performed using a double Cs corrected JEOL JEM-ARM200F (S)TEM operated at 80kV equipped with a cold-field emission gun. Images were recorded using a Gatan OneView camera operated at low-dose conditions.



MAS NMR data was recorded via a Bruker Avance III HD 400 MHz spectrometer setup.  $^1\text{H}/^{13}\text{C}$  CP MAS spectra were acquired with a 4mm probe spun at a resolution of 10kHz. A  $\pi/2$  pulse length of 2.5  $\mu\text{s}$  was applied with a 2 ms contact time and a 3 s recycle delay.  $^1\text{H}$  MAS NMR spectra were acquired with a 3.2 mm probe spun at 20kHz, a  $\pi/2$  pulse length of 2.5  $\mu\text{s}$  and a 15 s recycle delay.



## 7.4.2. Catalyst Preparation

### *Rho-CN series*

To 3 g of cyanamide and potassium rhodizonate mixture containing 0.25, 0.5 or 1% mol. of potassium rhodizonate in a disposable glass vial with a stir bar was added 5 mL of distilled water, and the mixture was stirred at room temperature for approximately 15 min. Then, the vial was placed to stir at a heating bath pre-heated to 60 °C overnight to remove water and pre-polymerize the reactants. In case of reaction mixture still being a slurry after complete evaporation, the bath temperature may be increased to 65-70 °C. After pre-polymerization is completed, the vial was carefully broken to isolate the solid mass which was then ground in a shaker ball mill (50 s<sup>-1</sup>, 5 min) with 7 g of eutectic LiCl/KCl mixture (3.15 g of LiCl, 3.85 g of KCl). Powdered mix was then put into a crucible and heated in an oven at 550 °C under nitrogen flow for 8 h (4 h slope from room temperature to 550 °C, then holding at 550 °C for 4 h). The resulted solid chunk was then coarsely crushed (by either using a mortar or a shaker ball mill in a short burst of 20-30 s) and shaken with 50 mL of water in a centrifuge tube for 3 h followed by 3 additional washing steps in 50 mL of water each. The slurry was then centrifuged off, water was decanted and the catalyst was dried in a vacuum oven overnight at 60 °C. This catalyst is referred to as Rho-CN-X, where X is the molar percentage value of potassium rhodizonate in a starting cyanamide-rhodizonate mix. The yield varies between 2.1 and 2.3 g of a catalyst (ca. 60-65% based on combined C and N mass).

### *Rho-CN-TC series*

The synthesis was adapted from reported procedure for preparing <sup>NCN</sup>CN<sub>x</sub> carbon nitride from melon.<sup>222</sup> Using mortar and pestle, 0.5 g of corresponding Rho-CN-X catalyst was thoroughly mixed with 1 g of dry KSCN. A mixture was heated in a crucible under nitrogen flow in an oven using following program: reaching 400 °C for ca. 12 min, then holding at this temperature for 4 h, then raised to 500 °C for ca. 4 min, and finally held at 500 °C for 30 min. The resulting mass was washed 3 times with 15 mL of water in a centrifuge tube (1 h for each washing; *care should be taken during the first washing*



step due to possibility of KCN presence in the mixture resulted from thermal decomposition of KSCN!), centrifuged off and dried in a vacuum oven overnight at 60 °C. This catalyst is referred to as Rho-CN-TC-X, where X is the molar percentage value of potassium rhodizonate in a starting cyanamide-rhodizonate mix for corresponding Rho-CN-X precursor. The yield varies between 220 and 280 mg of a catalyst (ca. 44-56% based on combined C and N mass).

#### *Other*

K-PHI<sup>180</sup> and CN-OA-m<sup>235</sup> were synthesized according to literature procedures.



### 7.4.3. Preparation of Photosheets and Photoelectrodes

#### *Photosheets*

The reactor photosheet was fabricated using regular smooth 2 mm thick borosilicate glass pre-cut to the 60x60 mm square panel using adapted literature procedure.<sup>276</sup> Prior to coating, the panel was sonicated for 30 min in EtOH on a sonicating bath, then dried under stream of nitrogen and finally treated with ozone for 10 min. Meanwhile, the paste was prepared by thoroughly grinding Rho-CN-0.5 with ethylene glycol (EG) in a ratio of 100 mg of the catalyst to 115  $\mu\text{L}$  of EG (200 mg of the catalyst would be sufficient to coat 60x60 mm panel; additional amount of extra 5  $\mu\text{L}$  of EG per 100 mg may be necessary in some cases) during the course of ca. 10 min using mortar and pestle. After grinding, the paste should be completely homogenous, contain no coarse particles and spikes, with consistency resembling that of molten chocolate (thick, but very slightly runny). The panel was then fixed on a flat surface by sticking a Scotch® Magic™ Tape (55.8  $\mu\text{m}$  thickness) on the edges leaving 5 mm mask from each side. The paste was then applied to the edge of a sufficiently wide and non-flexible spatula ( $\geq 6$  cm, e.g. thick metal piece, hard plastic panel or broad side of a microscopy slide) and spread several times in different directions over a panel at a minimal possible angle from the panel surface with the ends of the spatula edge always staying on tape mask to achieve uniform coating without voids and trenches. After the coating is done, the panel is treated in an oven at 200 °C for 6 h (heating rate 5 °C·min<sup>-1</sup>) to dry and, after cooling to room temperature, the panel was assembled in a photoreactor flow cell (ca. 25 cm<sup>2</sup> irradiated surface, ca. 25 cm<sup>3</sup> total volume, ca. 13.5 cm<sup>3</sup> working volume in horizontal position) (Figure S4.1).

In the same manner, 5x10 mm test sheets were prepared on pre-cut microscopy slides to evaluate their mechanical stability in solution. The mini-sheets were soaked in deionized water for 72 h with occasional disturbing by rapidly pushing water with a pipette around the slide, then dried naturally in ambient conditions. No detachment of catalytic layer was observed both during and after the soaking.



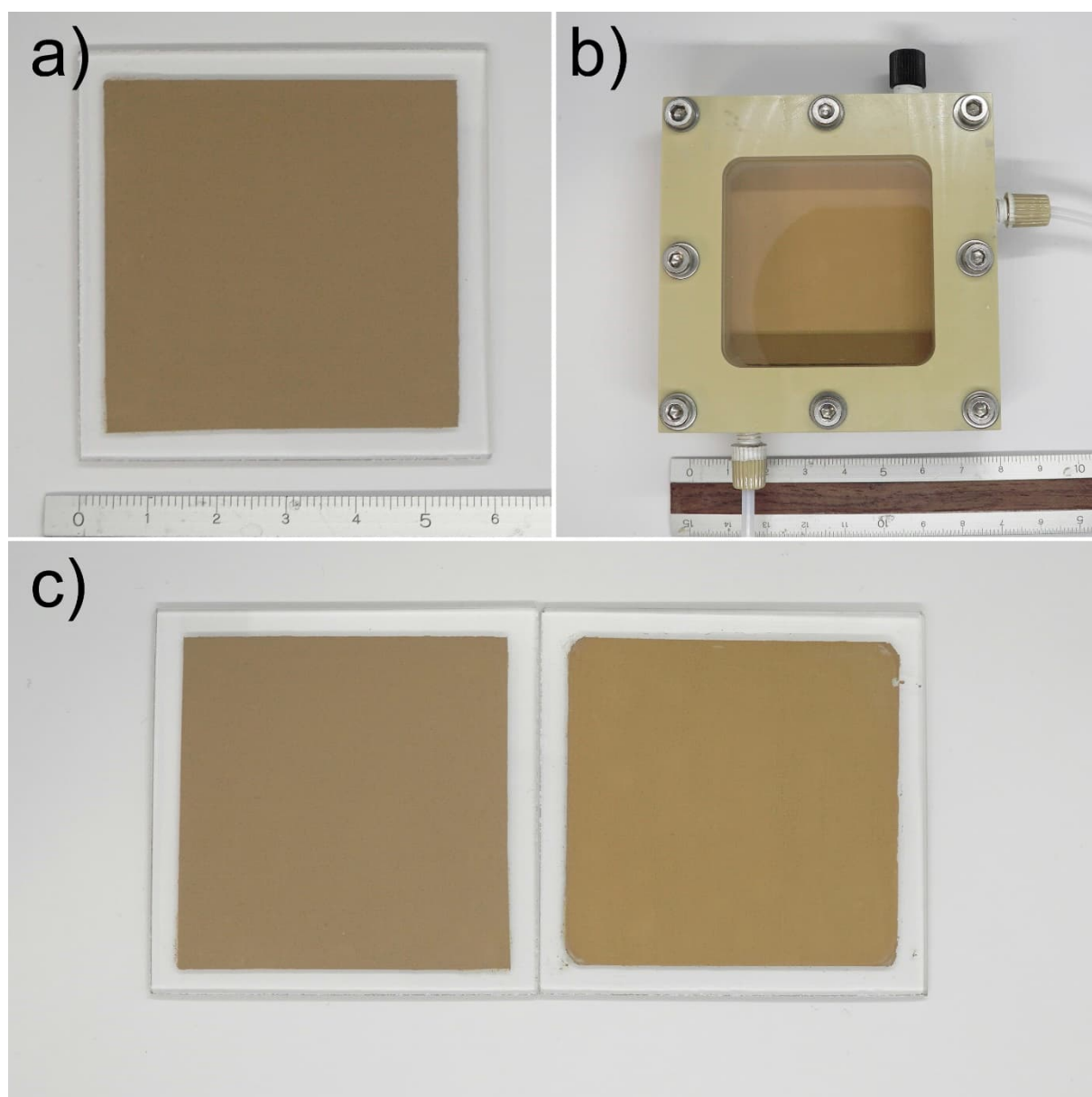


Figure S4.1. Rho-CN-0.5 coated ca. 50x50 mm working area photosheet. a) Pristine photosheet. b) Photosheet assembled into the 50x50x10 mm inner dimensions cell; tubing connectors are located mid-height of the cell, black plug (top) secures the 3<sup>rd</sup> connection. c) Pristine photosheet (left) compared to the one after 168 h ageing while filled with reaction mixture and under irradiation (right).



## Photoelectrodes

FTO coated glass pre-cut in 1x3 cm slides was sequentially sonicated two times in isopropanol and once in ethanol 20 min each time. The slides were then dried in a stream of nitrogen and their conductive side was treated with ozone for 10 min, then a parafilm mask with 0.25 cm<sup>2</sup> circular window was applied to the conductive side of the slide. The suspension, prepared by vigorously stirring 4 mg of catalyst and 10 μL of Nafion solution (20% wt. in water and alcohols) in 0.2 mL of absolute ethanol overnight in a dram vial with occasional 5-10 min sonication, was drop-cast onto the mask window once (10 μL aliquot). After the solvent evaporated, the slides were annealed in a tube furnace over 2 h (150 °C, 5 °C·min<sup>-1</sup> heating rate, argon atm.). After annealing, the T-shape electrode rod (1 cm wide end) was attached to the slide from the non-conductive side end and attached by wrapping a 5 mm wide copper tape around the slide and the rod end. The copper tape connection was then additionally insulated with Teflon tape to prevent circuit shorting.

### 7.4.4. Absorption and Luminescence Characterization

#### UV-Vis Spectroscopy

Optical absorbance spectra of powders were measured on a Shimadzu UV 2600 equipped with an integrating sphere in diffuse reflectance mode using barium sulfate standard to record the baseline. The spectra were recorded in 200 to 800 nm range. Bandgap values were obtaining from Tauc plots (Figure S4.2) from interception of linear approximation of slope with X-axis; the plots were transformed according to formula:

$$X: f(\lambda), [nm] \Rightarrow f\left(\frac{1240}{\lambda}\right), [eV]; \quad Y: f(A) [a. u.] \Rightarrow f(A^2 X^2), [eV^2] \quad (1)$$

The slope approximation was plotted at main transition at ca. 3 eV.



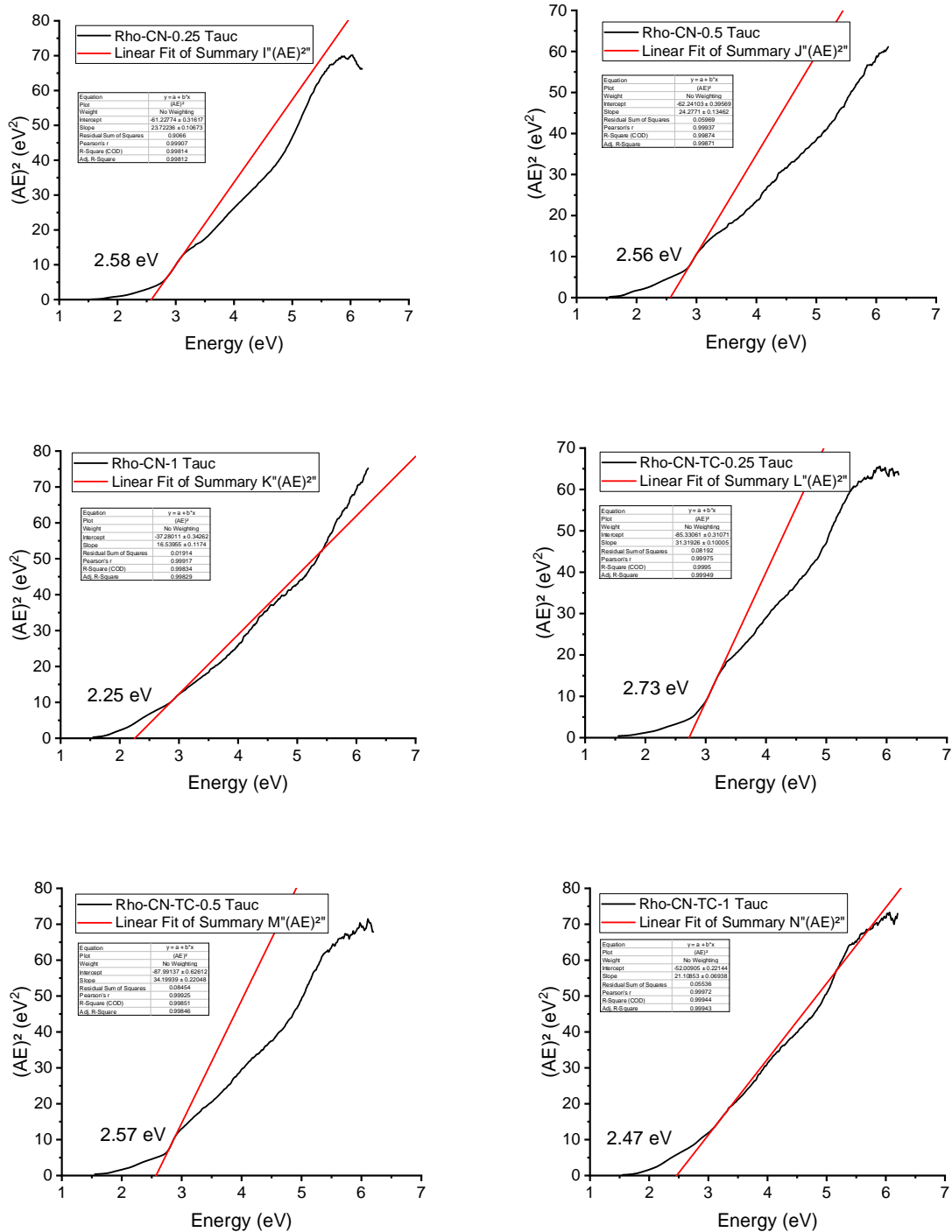


Figure S4.2. Graphical determination of optical bandgap of the catalysts.



### *Steady-State Luminescence*

Steady-state fluorescence spectra were measured on Jasco FP-8300 fluorescence spectrometer in direct mode without integrating sphere. Excitation wavelength was set at 410 nm, and the spectra were recorded in 420 to 800 nm range.

### *Time-Resolved Fluorescence*

TR-PL spectra were recorded on fluorescence lifetime spectrometer (Fluo Time 250, PicoQuant) equipped with PDL 800-D picosecond pulsed diode laser drive. The decay curves were fitted using a nonlinear method with a multicomponent decay law given by  $I(t) = a_1 \exp(-t/\tau_1) + a_2 \exp(-t/\tau_2) + a_1 \exp(-t/\tau_3)$ . The solid-state PL lifetimes were obtained with  $\lambda_{\text{exc}} = 375$  nm and  $\lambda_{\text{em}} = 550$  nm was used for detection. The following settings were used for the spectra acquisition: Laser Frequency 40 MHz, Emission Monochromator Bandwidth 2 nm, Delta (step between  $\lambda_{\text{em}}$ ) 10 nm.



### 7.4.5. SEM Imaging

Scanning electron microscope imaging was performed on SEM Gemini 1550 microscope (Zeiss AG) at 3 kV accelerating voltage.

Morphology of Rho-CN-0.5 and Rho-CN-TC-0.5 samples is shown on [Figure S4.3](#) as representative examples.

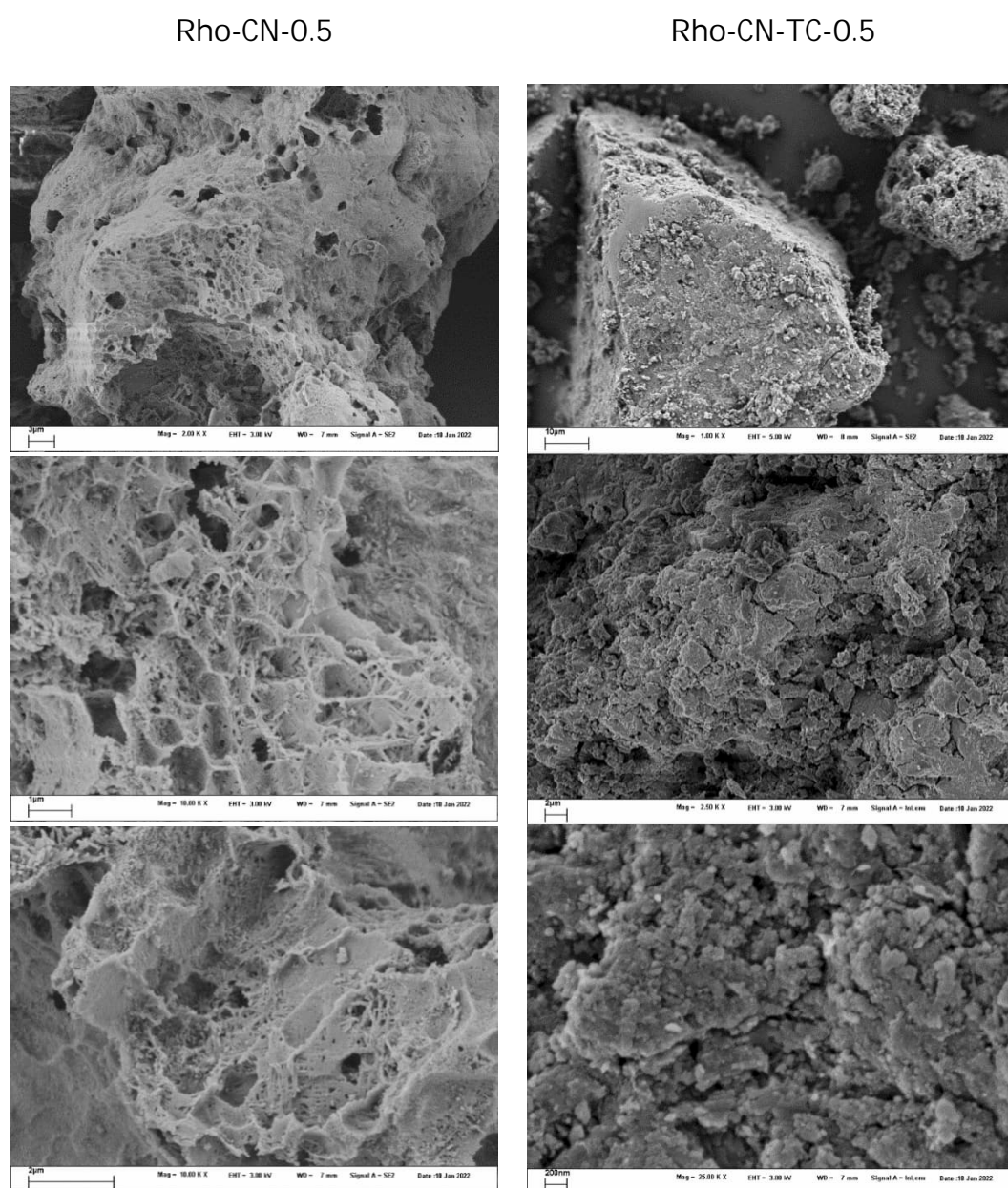


Figure S4.3. SEM images of Rho-CN-0.5 (left) and Rho-CN-TC-0.5 (right) samples.



#### 7.4.6. Photocatalytic Experiments

Batch organic transformations were conducted in custom-made 8x10W LED overhead photoreactors providing blue ( $\lambda_{\text{max}} = 465 \text{ nm}$ ), green ( $\lambda_{\text{max}} = 530 \text{ nm}$ ) or red ( $\lambda_{\text{max}} = 625 \text{ nm}$ ) light irradiation. Reactor appearance and configuration (on example of blue LED setup) is shown on Figure S4.4.

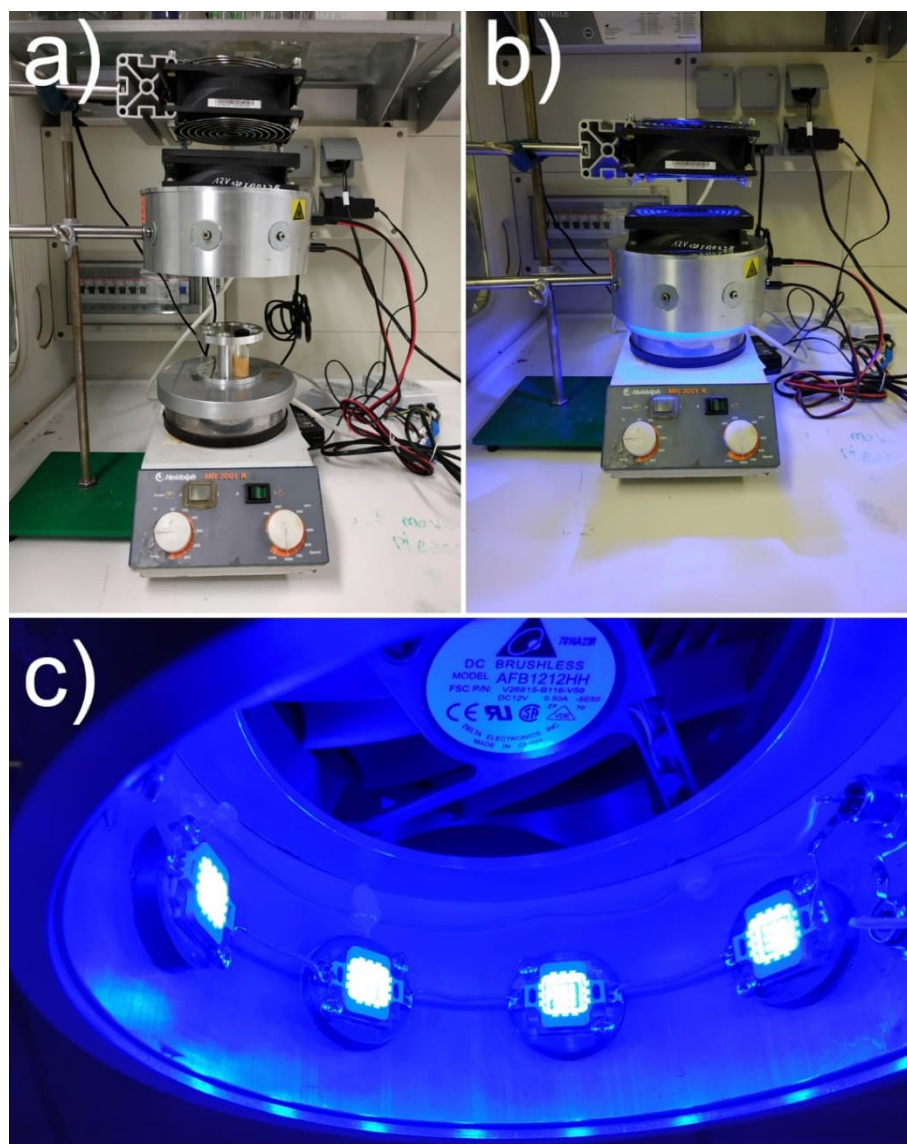


Figure S4.4. LED photoreactor (blue LED configuration shown as representative example). a) Reaction setup with external fan (top) for additional cooling, reactor (middle) with 8 LEDs and internal fan for reaction vials cooling, and 8-position vial holder with a vial set up on a stirplate (bottom). b) Setup assembled and running. c) Inside view of a running reactor.



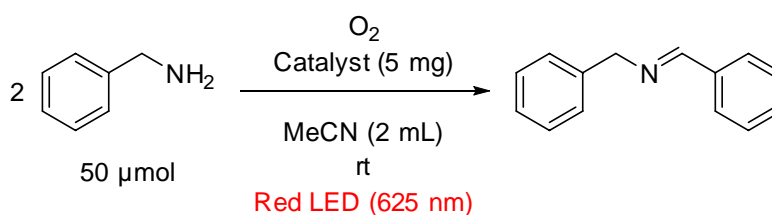
## Hydrogen Peroxide Production

To a mixture of 1.6 mL of water and 0.4 mL of methanol in a screwcap tube with a stir bar was added 5 mg of a carbon nitride catalyst. A reaction mixture was purged with oxygen for 60 s and irradiated for 1 h using white LED (measured optical power 203 mW cm<sup>-2</sup> at 2 cm) under oxygen atmosphere provided by a balloon (via needle pierced through cap septum) with vigorous stirring. After 1 h, the suspension was centrifuged (13000 rpm, 3 min) to remove the catalyst, and a clear supernatant was mixed with 0.5 mL of 2% titanium(IV) oxysulfate solution to form a yellow colored peroxide complex. The solution was transferred to a 1 cm cuvette and then the absorption value of the solution at 410 nm was measured using Shimadzu UV 2600 spectrometer. The absorption value then was converted to a concentration value using photometric calibration curve obtained by mixing 0.5 mL of indicator oxysulfate solution with 2 mL of hydrogen peroxide samples with known concentrations. The productivity value was then obtained by multiplying H<sub>2</sub>O<sub>2</sub> concentration by reaction volume and dividing by a mass of a catalyst.

Protonated version of the catalysts for the tests, H-Rho-CN-X and H-Rho-CN-TC-X, were obtained by stirring 50 mg of the corresponding catalyst in 2 mL of 3M HCl overnight, then centrifuging off from the acid followed by 3 sequential washings with deionized water and drying under vacuum at 60 °C overnight.

## Benzylamine oxidation

### Batch, Red LED



To a glass vial with a stir bar was added 2 mL of acetonitrile, 50  $\mu$ mol of benzylamine (5.5  $\mu$ L, 0.025M) and 5 mg of a catalyst. The vial was gently purged with oxygen for 60 s,



capped and irradiated into 10W red LED photoreactor (625 nm) at room temperature for 48 h. Then, a reaction mixture was centrifuged to remove the catalyst and a supernatant was used directly for GC-MS analysis. The yield was determined by a GC-MS calibration curve with known concentrations of the product with respect to stoichiometry of 2 molecules of benzylamine to 1 molecule of product. The calibration standard of product was prepared according to literature procedure.<sup>277</sup>

#### *Flow Photosheet Cell, Solar Simulator*

For flow experiment, a 0.025 M solution of benzylamine was prepared, typically in 100 mL batches in a round bottom flask, followed by purging with oxygen by double needle technique via septum. About 55 mL of solution was then loaded in a plastic syringe which was then connected to a photosheet flow cell (Figure S4.1) by 1/8" FEP tubing via a Luer adapter. The tubing was purged with the solution up until connection with the cell, and the syringe was placed in a syringe pump. The cell was set up horizontally under vertically configured C2V Optics Sunbrick™ LED solar simulator (set up at AM1.5G 100% intensity) with an outlet 1/8" FEP tubing leading to collection vessel (Figure S4.5). The simulator was then started simultaneously with the syringe pump set up at 1.6667 mL·min<sup>-1</sup> flow rate with a 50 mL limit (30 min total for injection), and residence time was calculated from the start until the moment the solution appears in outlet tube to be 480±10 s using syringe pump timer. Three ca. 1 mL samples were taken immediately after draining to the collection vessel starts, then in the middle (ca. 19 min timestamp) and in the end of injection, respectively, and were analyzed by HPLC Waters Breeze system equipped with refractive index (RID-2414) and diode array UV-vis detectors after being diluted 12.5 times (product concentration at 100% yield normalized to 1 mM). The samples were eluted using isocratic 1:1 acetonitrile-water mixture through analytical C18 column; injection volume 10 µL, DAD detector set at 254 nm, elution time 12 min. Peak at 6.75-8.30 min on absorption chromatogram was integrated.



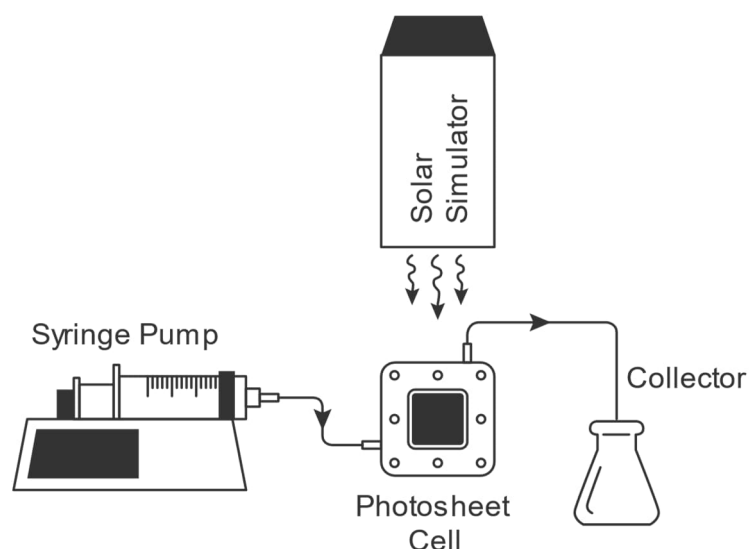
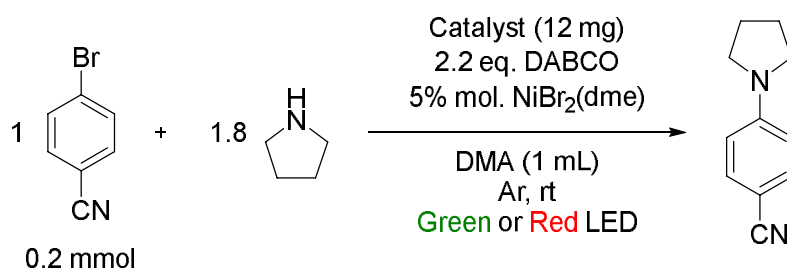


Figure S4.5. Principal scheme of flow setup configuration

After the first run, stability and recyclability test was performed as follows. Oxygenated 0.1 M solution of benzylamine in acetonitrile was prepared as described above, and the cell was filled with the solution and set up under the solar simulator to stand for 7 days (168 h). The solution was replenished every 24 h by purging the cell with fresh 0.1 M benzylamine. After that, the cell was emptied and thoroughly washed with acetonitrile, then dried with a stream of nitrogen. The cell was then used for the second run in the conditions identical to the first run.

#### Dual Nickel Photoredox C-N Cross-Coupling

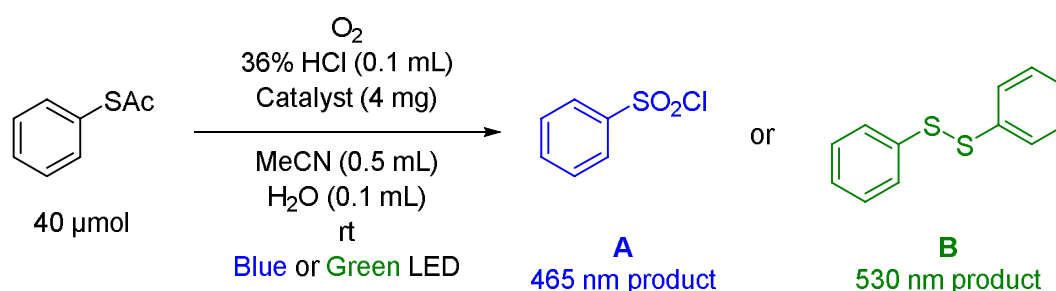


The procedure was previously reported for mpg-CN carbon nitride.<sup>179</sup> To 0.20 mmol of 4-bromobenzonitrile (36.4 mg) in 1 mL *N,N'*-dimethylacetamide (DMA) in a screwcap vial with a stirbar was added 0.36 mmol (29.5  $\mu$ L) of pyrrolidine, 0.44 mmol (49.3 mg) of DABCO and 0.01 mmol (3 mg) of NiBr<sub>2</sub>(dme) complex while purging the solution with



nitrogen. Then, 12 mg of catalyst was added, and the vial was tightly screwed while purging and placed in corresponding 10W LED photoreactor (green, 530 nm, or red, 625 nm, LEDs) and stirred for 24 h. The reaction mixture was then centrifuged off the catalyst and was analyzed by GCMS to quantify the yield. To obtain the GC calibration curve for product, 4-(pyrrolidin-1-yl)benzotrile was isolated in pure form from combined photocatalytic experiments' supernatant liquids by evaporating off the solvent and subjecting the residue to column chromatography (32-63  $\mu\text{m}$  silica, hexane:EA as an eluent in 10:1 to 2:1 gradient).

### Chromoselectivity Tests



The procedure was previously reported for K-PHI carbon nitride.<sup>80</sup> To a screwcap vial with a stirbar, 0.04 mmol of S-phenylthioacetate, acetonitrile (0.5 mL), 36% HCl (0.1 mL), deionized water (0.1 mL) and catalyst (4 mg) were added. The mixture was then purged with oxygen gas for 30 s, the vial was closed and the mixture was irradiated with stirring in corresponding 10W LED reactor (465 or 530 nm). After the reaction was finished, 3 mL of chloroform and 0.3 mL of water were added, and after vigorous shaking the organic layer was separated and dried over sodium sulfate, then used for GCMS quantification without change in concentration. To obtain calibration curves, commercially available benzenesulfonyl chloride and diphenyl disulfide were used; S-phenyl benzenesulfonothioate was prepared and purified according to the reported procedure.<sup>278</sup> Product of 465 nm irradiation, benzenesulfonyl chloride, could not be quantified properly supposedly due to *in situ* hydrolysis during the reaction; besides residual sulfonyl chloride, no other products or leftover starting material were detected



with GCMS after 465 nm irradiation in most cases except for Rho-CN-TC-0.25 and Rho-CN-TC-1. The results are given in Table S4.1.

Table S4.1. Chromoselective oxidation of *S*-phenylthioacetate.

Catalyst	Sulfonyl chloride A yield at 465 nm, %	Disulfide B yield at 530 nm, %
Rho-CN-0.25	4.8	68.7 (13.3) <sup>[b]</sup>
Rho-CN-0.5	3.6	95.7
Rho-CN-1	6.6	73.0 (6.1) <sup>[b]</sup>
Rho-CN-TC-0.25	4.0 (11.0) <sup>[b]</sup>	90.0
Rho-CN-TC-0.5	4.7	76.1 (6.0) <sup>[b]</sup>
Rho-CN-TC-1	0.0 (48.9) <sup>[b]</sup> (6.8) <sup>[c]</sup>	89.0
K-PHI (ref.) <sup>[a]</sup>	0.7	68.3 (14.0) <sup>[b]</sup>

[a] – Reported yields: 90% A (465 nm), 73% B (530 nm).<sup>80</sup>

[b] – Yield of *S*-phenyl benzenesulfonothioate as a side product.

[c] – Yield of diphenyl disulfide as a side product.

### Photocatalytic Hydrogen Evolution

Photocatalytic activity was investigated for Rho-CN-0.5 catalyst. For the experiments, 2 mL of 0.01 M solution of electron donor (either ethylene glycol with additional 1 M KOH or triethylamine) and 4 mg of catalyst in septum stoppered test tubes were used; the solutions were purged for 10 min by double needle technique with nitrogen containing 2% of methane as an internal standard (commercial mixture purchased from BOC Ltd.). In addition to the regular catalyst and H-Rho-CN-0.5 (see hydrogen peroxide production section), versions with pre-deposited cocatalysts (5% wt. NiP and 5% wt. Pt, respectively) were prepared as reported in literature for both regular and protonated catalyst.<sup>279, 280</sup> To the final samples of Rho-CN-0.5 and H-Rho-CN-0.5, 2  $\mu$ L of 8% wt. chloroplatinic acid solution was added for *in situ* platinum deposition. The test tubes



were irradiated with strong stirring under AM1.5G 100% intensity solar simulator at 25 °C, then 100  $\mu$ L gas samples were taken and injected into Shimadzu GC-2010 Plus GCMS device to quantify evolved hydrogen. Only the samples with *in situ* Pt deposition provided reasonable amounts of hydrogen which is naturally generated during deposition step itself; NiP cocatalyst samples gave quantities slightly over detection threshold, the rest failed to provide any.



### 7.4.7. Electrochemical Tests

#### *Impedance Measurements and Mott-Schottky Plots*

Photocatalyst coated FTO glass working electrode (see Section 3 above for preparation details) was assembled into a cell in a 3-neck flask using silver chloride electrode (saturated KCl) as a reference and platinum mesh as a counter electrode, respectively. The cell was filled with 0.1 M Na<sub>2</sub>SO<sub>4</sub> solution in deionized water as electrolyte, and the counter and reference electrodes were immersed in. After purging the solution for 15 min with nitrogen, working electrode was *carefully* immersed into electrolyte to avoid delamination of the active layer from FTO.

The impedance measurements were performed using IviumStat.h potentiostat (Ivium Technologies) with 10 s pre-equilibration in a range of -1.0 to +1.6 V versus reference electrode in a 100 mV step to estimate flatband potential, then region from -0.8 to +0.2 V was additionally scanned 2 times in a 25 mV step fashion to get more accurate data; average value of 2 sets was then used (Figure S4.6). Data for Rho-CN-TC-0.25 was obtained from initial approximate scan only due to mechanical instability of prepared electrodes which leads to ≥90% surface delamination after immersion in most cases. Capacitance values and Mott-Schottky plots were derived from EIS data using ZView software package. The potentials were converted to SHE scale using the following formula:<sup>281</sup>

$$E_{SHE} = E_{SSC(sat)} + 0.22V, \quad (2)$$

where  $E_{SSC(sat)}$  is a potential in saturated Ag/AgCl electrode scale used in the measurements.



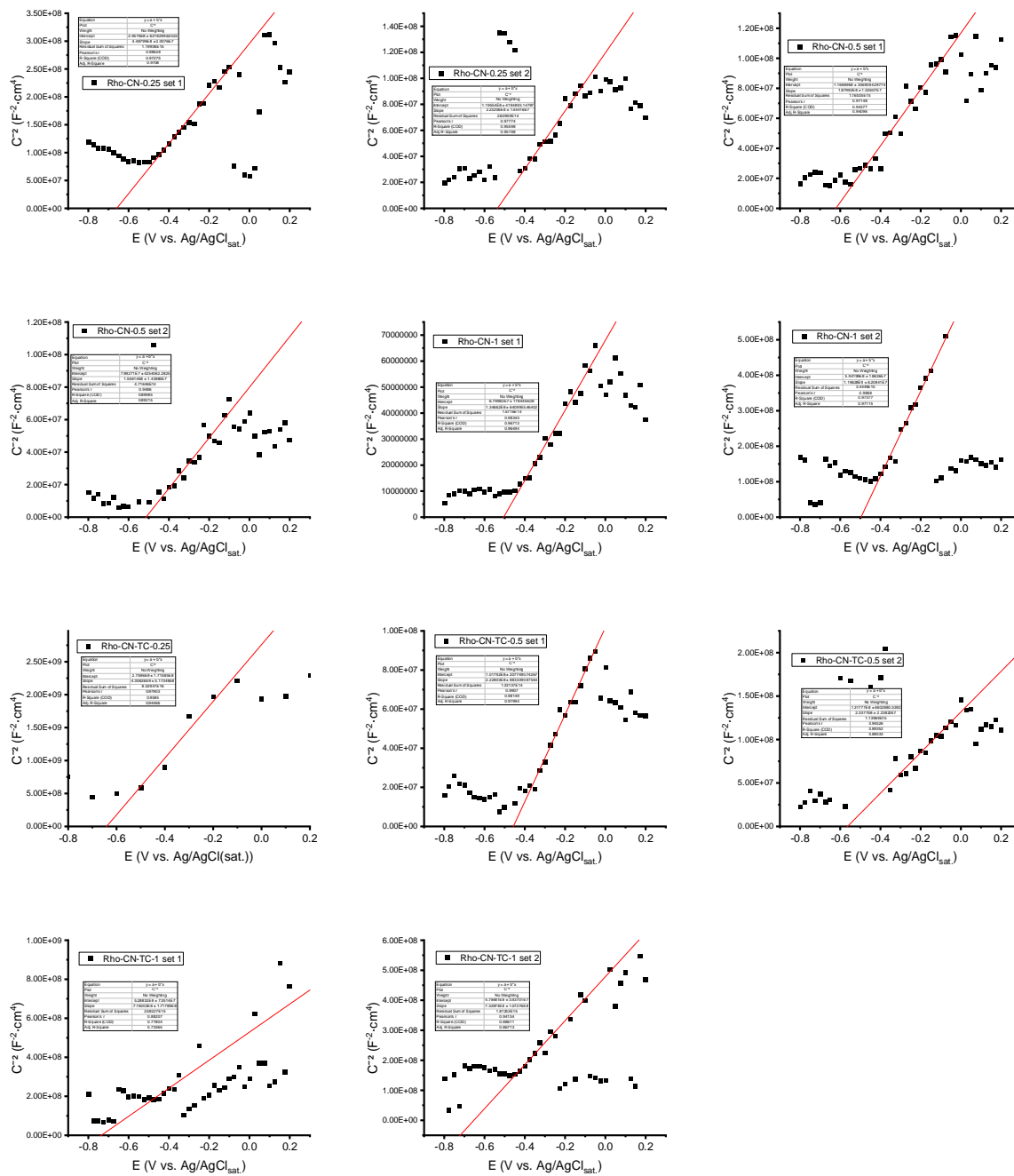


Figure S4.6. Mott-Schottky plots and flatband value determination.



## Cyclic Voltammetry

The cyclic voltammetry measurements were done using the same cell and instrument as impedance experiments (it is advised to do these experiments sequentially on the same sample to avoid mechanical damage of active layer during working electrode swapping). The data was recorded in a range between -1.0 and +1.6 V versus reference electrode with 20 mV·s<sup>-1</sup> scan speed. The initial point of scan is -1.0 V for Rho-CN catalysts and 0.0 V for Rho-CN-TC. A total of 3 cycles for each sample were performed. The reduction peaks (presumably HER) were evaluated at a half-slope point of the 3<sup>rd</sup> scan (Figure S4.7) and was converted to SHE from SSC<sub>sat</sub> using the formula (2) (Table S4.2).

Oxidation potentials could not be clearly determined via CV measurements due to absence of clear peaks on voltammogram (which are overwhelmed by presumably slope of OER processes); in some cases, small peaks prior to main slope appeared on 2<sup>nd</sup> and 3<sup>rd</sup> scans which may be attributed to population of trap states of a material.

Table S4.2. Reduction peaks versus SHE.

Catalyst	E <sub>1/2</sub> , V vs SHE	Catalyst	E <sub>1/2</sub> , V vs SHE
Rho-CN-0.25	+0.21	Rho-CN-TC-0.25	-0.12
Rho-CN-0.5	-0.20	Rho-CN-TC-0.5	-0.09
Rho-CN-1	-0.09	Rho-CN-TC-1	-0.10



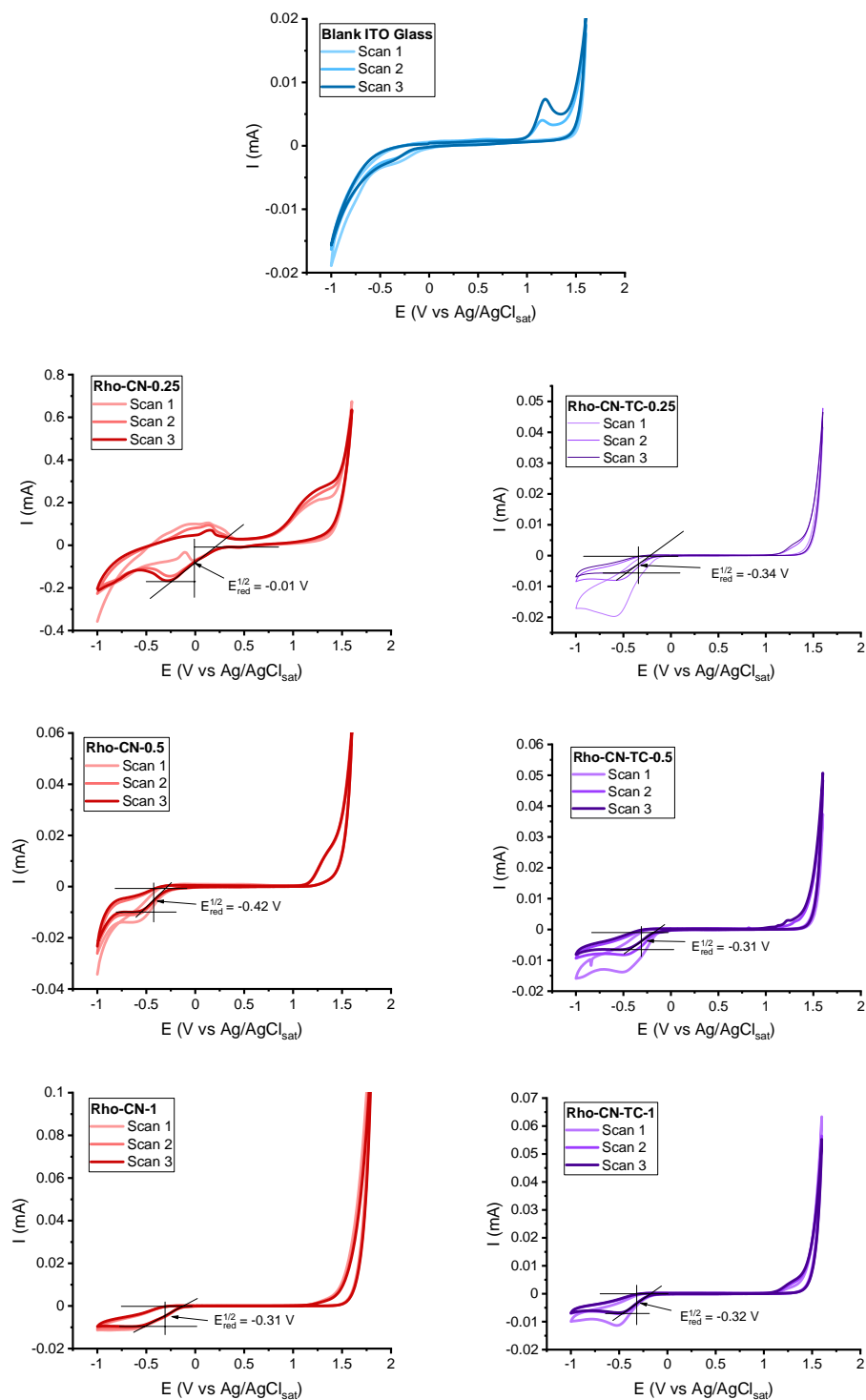


Figure S4.7. Cyclic voltammograms for Rho-CN and Rho-CN catalysts with reduction potential values. The first plot was recorded on blank FTO glass as a background.



### Transient Photocurrent Response

Working electrodes for the measurements were prepared the following way: to 1 mL of MilliQ-purified water, 10 mg of carbon nitride and 40  $\mu\text{L}$  of 5% wt. Nafion solution was added, and the suspension was vigorously stirred overnight. The FTO glass slide cleaned by 3 cycles of 30 min sonication in isopropanol was covered with a duct tape to leave 1.5  $\text{cm}^2$  area on conductive side, and 50  $\mu\text{L}$  of CN suspension was drop-casted and then dried at 60  $^\circ\text{C}$  on a hotplate. After that, the electrode was kept at 120  $^\circ\text{C}$  for 1 h.

The photocurrent was measured at 0.3 V vs.  $E_{\text{ref}}$  under 100  $\text{mW}\cdot\text{cm}^{-2}$  white LED irradiation in 0.2 M aqueous  $\text{Na}_2\text{SO}_4$  with 3.0 M silver chloride reference electrode and platinum counter electrode on Gamry Interface 1010E potentiostat.

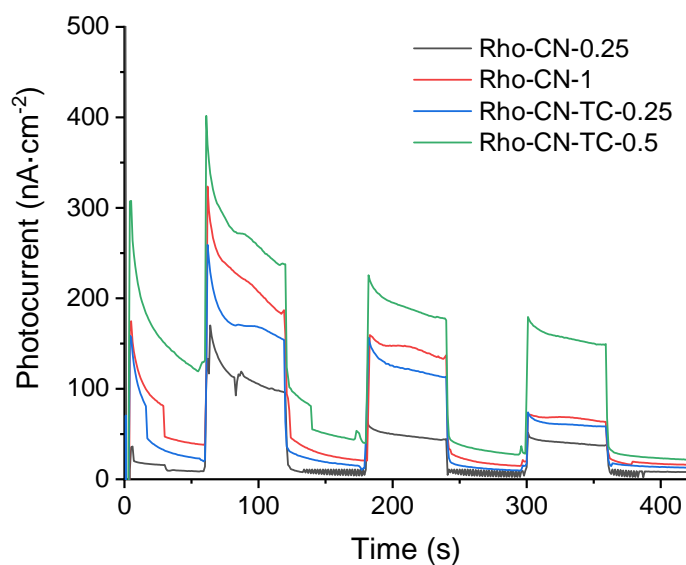


Figure S4.8. Transient photocurrent response for samples Rho-CN-0.25, Rho-CN-1, Rho-CN-TC-0.25, Rho-CN-TC-0.5.



### Electrochemical Impedance Spectroscopy

The measurements were performed with the same electrodes and in the same cell and device as described for transient photocurrent in a frequency range from 10 kHz to 1 Hz. The data was then approximated to a full semicircle using ZView software; the plot for Rho-CN-TC-0.5 could not be processed due to math errors in approximation.

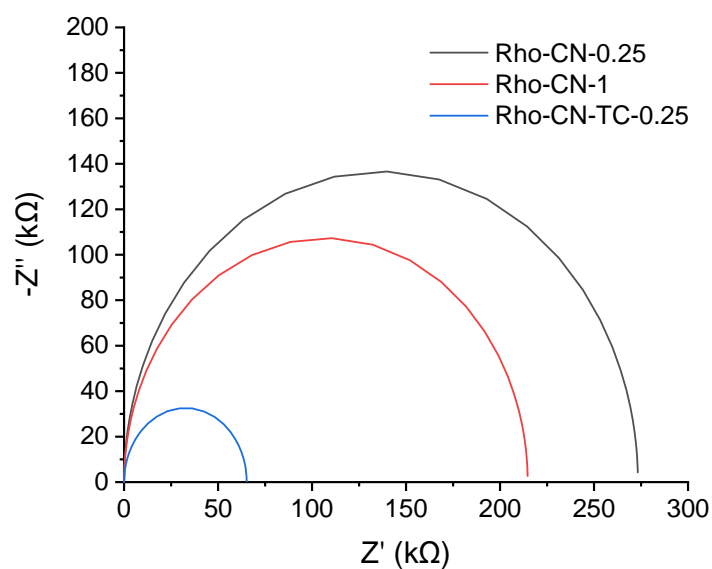


Figure S4.9. EIS plots for samples Rho-CN-0.25, Rho-CN-1, Rho-CN-TC-0.25.



### 7.4.8. Thermogravimetric analysis

The analysis was performed on commercial  $K_2Rho$  sample using NETZSCH TG 209F1 Libra instrument in a PtRh20 85  $\mu$ L open crucible. The results are shown on [Figure S4.10](#).

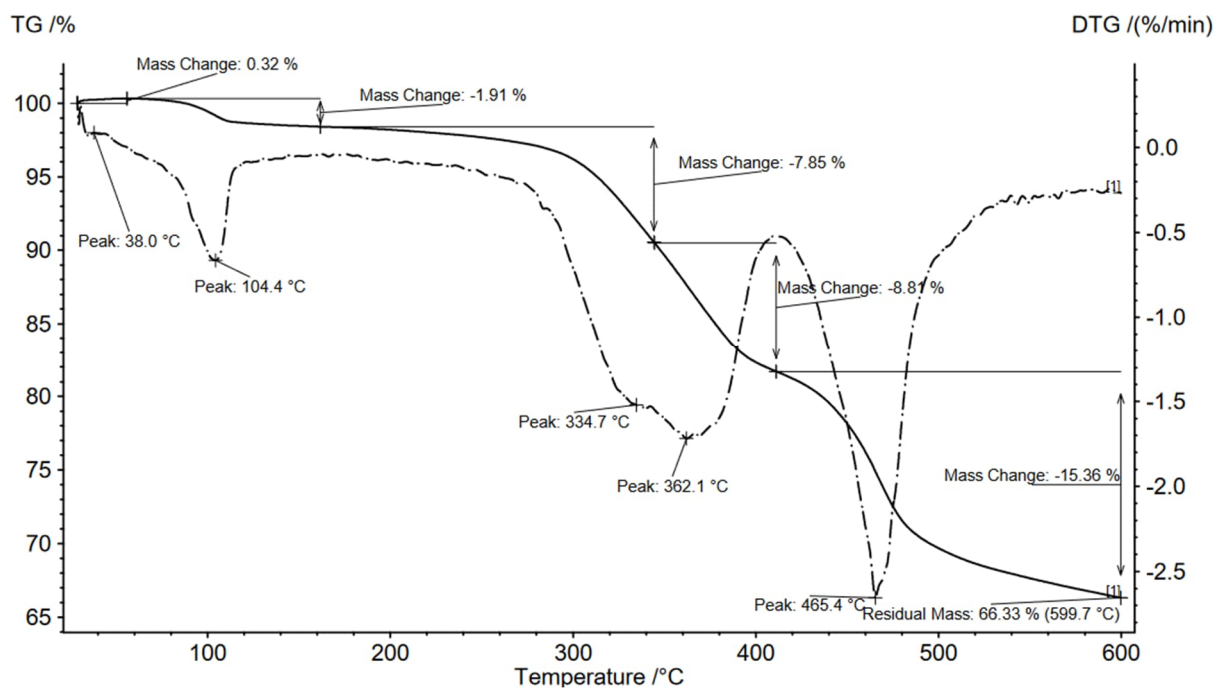


Figure S4.10. TGA plot for potassium rhodizate.



### 7.4.9. X-Ray Photoelectron Spectroscopy

XPS data was recorded by employ of a SPECS spectrometer equipped with a Phoibos 150 MCD-9 detector. The nonmonochromatic X-Ray source (Al and Mg) was operated at 200 W. Before data acquisition, the samples were evacuated at  $10^{-9}$  mbar in the setup antechamber. The work function of the device was calibrated with Ag, Au, and Cu standards. A value of 4.2440 eV was therefore obtained. The measured intensity ratios of the analyzed components were obtained from the area of the corresponding peaks after nonlinear Shirley-type background subtraction and corrected by the transition function of the spectrometer.

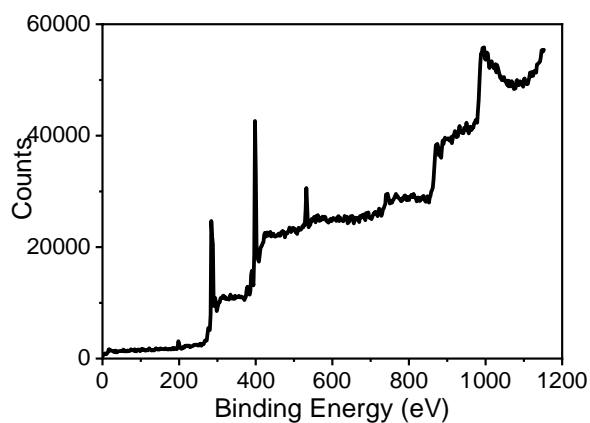


Figure S4.11. Full XPS spectrum of Rho-CN-0.5.

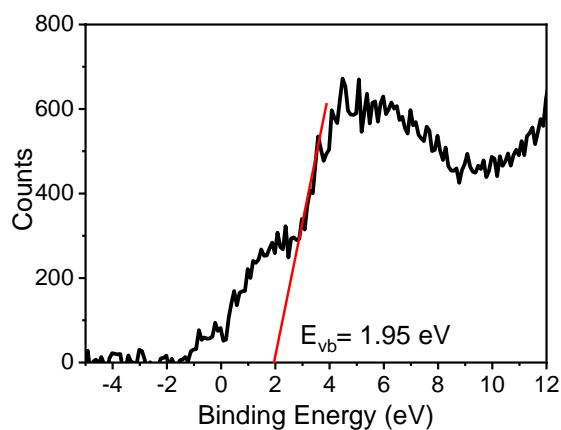


Figure S4.12. XPS valence band determination for Rho-CN-0.5.



## 7.4.10. Correlation Coefficients and Cost Comparison

Table S4.3. Correlation coefficients for full dataset of Rho-CN and Rho-CN-TC materials.

	Hydrogen peroxide evolution (neutral conditions) [ $\mu\text{mol}\cdot\text{g}^{-1}\cdot\text{h}^{-1}$ ]	Hydrogen peroxide evolution (acidic conditions) [ $\mu\text{mol}\cdot\text{g}^{-1}\cdot\text{h}^{-1}$ ] acidic	Benzylamine oxidation yield [%]	Cross- coupling yield (green light), %	Cross- coupling yield (red light), %
CB vs. SHE [V]	0.32	0.32	-0.10	-0.30	0.59
VB vs. SHE [V]	0.24	0.20	0.21	0.72	-0.10
Fluorescence lifetime [ps]	-0.16	-0.56	0.28	0.30	-0.69

Table S4.4. Correlation coefficients for full dataset of Rho-CN and Rho-CN-TC materials.

	Hydrogen peroxide evolution (neutral conditions) [ $\mu\text{mol}\cdot\text{g}^{-1}\cdot\text{h}^{-1}$ ]	Hydrogen peroxide evolution (acidic conditions) [ $\mu\text{mol}\cdot\text{g}^{-1}\cdot\text{h}^{-1}$ ] acidic	Benzylamine oxidation yield [%]	Cross- coupling yield (green light), %	Cross- coupling yield (red light), %
CB potential[V] x Lifetime[ps]	0.24	0.62	-0.19	-0.32	0.87
VB potential[V] x Lifetime[ps]	-0.12	-0.49	0.26	0.34	-0.64



Table S4.5. Correlation coefficients for Rho-CN materials dataset.

	Hydrogen peroxide evolution (neutral conditions) [ $\mu\text{mol}\cdot\text{g}^{-1}\cdot\text{h}^{-1}$ ]	Hydrogen peroxide evolution (acidic conditions) [ $\mu\text{mol}\cdot\text{g}^{-1}\cdot\text{h}^{-1}$ ] acidic	Benzylamine oxidation yield [%]	Cross- coupling yield (green light), %	Cross- coupling yield (red light), %
CB vs. SHE [V]	-0.05	-0.73	-0.46	-0.98	-0.23
VB vs. SHE [V]	0.37	0.91	0.73	0.99	-0.10
Fluorescence lifetime [ps]	0.97	0.86	0.98	0.45	-0.87

Table S4.6. Correlation coefficients for Rho-CN-TC materials dataset.

	Hydrogen peroxide evolution (neutral conditions) [ $\mu\text{mol}\cdot\text{g}^{-1}\cdot\text{h}^{-1}$ ]	Hydrogen peroxide evolution (acidic conditions) [ $\mu\text{mol}\cdot\text{g}^{-1}\cdot\text{h}^{-1}$ ] acidic	Benzylamine oxidation yield [%]	Cross- coupling yield (green light), %	Cross- coupling yield (red light), %
CB vs. SHE [V]	0.41	0.91	0.44	0.94	0.67
VB vs. SHE [V]	0.88	0.46	-0.20	0.95	0.09
Fluorescence lifetime [ps]	1.00	-0.01	-0.64	0.69	-0.40



Table S4.7. Correlation coefficients for Rho-CN materials dataset.

	Hydrogen peroxide evolution (neutral conditions) [ $\mu\text{mol}\cdot\text{g}^{-1}\cdot\text{h}^{-1}$ ]	Hydrogen peroxide evolution (acidic conditions) [ $\mu\text{mol}\cdot\text{g}^{-1}\cdot\text{h}^{-1}$ ] acidic	Benzylamine oxidation yield [%]	Cross- coupling yield (green light), %	Cross- coupling yield (red light), %
CB potential[V] x Lifetime[ps]	-0.66	-1.00	-0.91	-0.89	0.42
VB potential[V] x Lifetime[ps]	0.88	0.96	1.00	0.66	-0.72

Table S4.8. Correlation coefficients for Rho-CN-TC materials dataset.

	Hydrogen peroxide evolution (neutral conditions) [ $\mu\text{mol}\cdot\text{g}^{-1}\cdot\text{h}^{-1}$ ]	Hydrogen peroxide evolution (acidic conditions) [ $\mu\text{mol}\cdot\text{g}^{-1}\cdot\text{h}^{-1}$ ] acidic	Benzylamine oxidation yield [%]	Cross- coupling yield (green light), %	Cross- coupling yield (red light), %
CB potential[V] x Lifetime[ps]	-0.78	0.64	0.98	-0.08	0.88
VB potential[V] x Lifetime[ps]	1.00	0.05	-0.59	0.73	-0.34



Table S4.9. Comparison of Rho-CN and K-PHI

Parameter	Rho-CN-TC	K-PHI
Cost of precursor (name)	0.6 € g <sup>-1</sup> (Cyanamide) <sup>[a]</sup>	0.5 € g <sup>-1</sup> (5-aminotetrazole monohydrate) <sup>[b]</sup>
Material yield	60-65%	~25%

[a] – 250 g package, Merck

[b] – 500 g package, Merck



## 8. Abbreviations

---

AOE	Apparent quantum efficiency
AQY	Apparent quantum yield
BDFE	Bond dissociation free energy
BuOH	Butanol
CB	Conductive band
CCD	Charge coupled device
CN	Carbon nitride
COF	Covalent organic framework
CV	Cyclic voltammetry
DABCO	1,4-diazabicyclo[2.2.2]octane
DAC	Direct air capture
DAD	Diode array detector
DAS	Decay associated spectrum
DFF	Diformylfuran
DFT	Density Functional Theory
DMA, DMAc	<i>N,N</i> -dimethylacetamide
dme	1,2-dimethoxyethane ligand
DMF	<i>N,N</i> -dimethylformamide



DMP	Dess-Martin periodinane
DMPO	5,5-dimethyl-1-pyrroline <i>N</i> -oxide
DMSO	Dimethylsulfoxide
DOS	Density of states
DR	Diffuse reflectance
EA	Ethyl acetate
EC	European Commission
$E_{CB}$	Conductive band potential
EG	Ethylene glycol
EIS	Electrochemical impedance spectroscopy
EnT	Energy transfer
EPR	Electron paramagnetic spectroscopy
EQE	External quantum efficiency
EQY	External quantum yield
EtOH	Ethanol
$E_{VB}$	Valence band potential
FBDfE	Formal bond dissociation free energy
Fc	Ferrocene
FT-IR	Fourier transformed infrared



FTO	Fluorine doped tin oxide
GC-MS	Gas chromatography–mass spectrometry
g-CN	Graphitic carbon nitride
HAT	Hydrogen atom transfer
HER	Hydrogen evolution reaction
HMF	5-hydroxymethylfurfural
HOMO	Highest occupied molecular orbital
HPE	Hydrogen peroxide evolution
HPLC	High-performance liquid chromatography
ICP-OES	Inductively coupled plasma optical emission spectroscopy
IPC	Inclined plate collector
IPEC	Integrated photoelectrochemical (device)
ISC	Intersystem crossing
ITO	Indium tin oxide
K <sub>2</sub> Rho	Potassium rhodizonate
K-PHI	Potassium poly(heptazine imide)
LED	Light emitting diode
LUMO	Lowest unoccupied molecular orbital
MAS	Magic angle spinning



MeCN	Acetonitrile
MeNO <sub>2</sub>	Nitromethane
MeOH	Methanol
MOF	Metal organic framework
mpg-CN	Mesoporous graphitic carbon nitride
Na-PHI	Sodium poly(heptazine imide)
NHE	Normal hydrogen electrode
NHPI	<i>N</i> -hydroxyphthalimide
NIR	Near-infrared light
NMR	Nuclear magnetic resonance
NPhth	<i>N</i> -phtalimidyl
OPA	Optical parametric amplifier
PAW	Projected Augmented Wave
PBE	Perdew-Burke-Ernzerhof
PC	Photocatalytic
PCC	Pyridinium chlorochromate
PCET	Proton-coupled electron transfer
PdTPTBP	Palladium (II) meso-tetraphenyl-tetrabenzoporphyrin
PEC	Photoelectrocatalytic



PL	Photoluminescence
PMP	4-methoxyphenyl
PTI	Poly(triazine imide)
PXRD	Powder X-ray diffraction
qNMR	Quantitative nuclear magnetic resonance
RFTA	Riboflavin tetraacetate
SCE	Standard calomel electrode
SEM	Scanning electron microscopy
SET	Single electron transfer
SHE	Standard hydrogen electrode
STH	Solar-to-hydrogen (conversion)
TAS	Transient absorption spectroscopy
TCSPC	Time-correlated single photon counting
TEM	Transient electron microscopy
TEMPO	2,2,6,6-tetramethylpiperidine- <i>N</i> -oxyl
TEOA	Triethanolamine
TGA	Thermogravimetric analysis
THF	Tetrahydrofuran
TPP	Tetraphenylporphyrin



TPR	Transient photocurrent response
TRES	Time-resolved emission spectroscopy
TRL	Technology readiness level
tr-PL	Time resolved photoluminescence
UV	Ultraviolet (light)
VASP	Vienna Ab initio Simulation Package
VB	Valence band
Vis	Visible (light)
XPS	X-ray photoelectron spectroscopy



## 9. References

---

- [1] Höök, M.; Tang, X. Depletion of fossil fuels and anthropogenic climate change — A review. *Energy Policy* 2013, *52*, 797-809. DOI: 10.1016/j.enpol.2012.10.046.
- [2] Welsby, D.; Price, J.; Pye, S.; Ekins, P. Unextractable fossil fuels in a 1.5 degrees C world. *Nature* 2021, *597* (7875), 230-234. DOI: 10.1038/s41586-021-03821-8.
- [3] Styring, S. Artificial photosynthesis for solar fuels. *Faraday Discuss.* 2012, *155*, 357-376. DOI: 10.1039/c1fd00113b.
- [4] Kalyanasundaram, K.; Graetzel, M. Artificial photosynthesis: biomimetic approaches to solar energy conversion and storage. *Curr. Opin. Biotechnol.* 2010, *21* (3), 298-310. DOI: 10.1016/j.copbio.2010.03.021.
- [5] Zhang, Y. G.; Pagani, M.; Liu, Z.; Bohaty, S. M.; Deconto, R. A 40-million-year history of atmospheric CO<sub>2</sub>. *Philos. Trans. R. Soc. A* 2013, *371* (2001), 20130096. DOI: 10.1098/rsta.2013.0096.
- [6] Balat, M.; Ayar, G. Biomass Energy in the World, Use of Biomass and Potential Trends. *Energy Sources* 2005, *27* (10), 931-940. DOI: 10.1080/00908310490449045.
- [7] Luo, H.; Weeda, E. P.; Alherech, M.; Anson, C. W.; Karlen, S. D.; Cui, Y.; Foster, C. E.; Stahl, S. S. Oxidative Catalytic Fractionation of Lignocellulosic Biomass under Non-alkaline Conditions. *J. Am. Chem. Soc.* 2021, *143* (37), 15462-15470. DOI: 10.1021/jacs.1c08635.
- [8] Lewis, N. S.; Crabtree, G.; Nozik, A. J.; Wasielewski, M. R.; Alivisatos, P.; Kung, H.; Tsao, J.; Chandler, E.; Walukiewicz, W.; Spitler, M.; et al. *Basic Research Needs for Solar Energy Utilization. Report of the Basic Energy Sciences Workshop on Solar Energy Utilization, April 18-21, 2005*; United States: N. p., 2005. DOI: 10.2172/899136.
- [9] NASA. *ModelE AR5 Simulations: Past Climate Change and Future Climate Predictions*. <https://data.giss.nasa.gov/modelE/ar5plots/srlocat.html> (accessed 2021-12-28).
- [10] Tawalbeh, M.; Al-Othman, A.; Kafiah, F.; Abdelsalam, E.; Almomani, F.; Alkasrawi, M. Environmental impacts of solar photovoltaic systems: A critical review of recent progress and future outlook. *Sci. Total Environ.* 2021, *759*, 143528. DOI: 10.1016/j.scitotenv.2020.143528.
- [11] Gueymard, C. A. The SMARTS spectral irradiance model after 25 years: New developments and validation of reference spectra. *Solar Energy* 2019, *187*, 233-253. DOI: 10.1016/j.solener.2019.05.048.
- [12] Enteria, N.; Akbarzadeh, A. *Solar Energy Sciences and Engineering Applications*; CRC Press 2017. DOI: 10.1201/b15507
- [13] Watzke, E.; Kloss, T. Borosilikatglas mit hoher Transmission im UV-Bereich, niedriger Wärmeausdehnung und hoher chemischer Beständigkeit, Verfahren zu seiner Herstellung und seine Verwendung. DE4338128C1, 1995.
- [14] Huo, J.; Lu, D. Characteristics of solar radiation and the impact of clouds at Yangbajing, Tibet. *AIP Conf. Proc.* 2013, *1531*, 564. DOI: 10.1063/1.4804832.
- [15] Pozzo, R. L.; Giombi, J. L.; Baltanás, M. A.; Cassano, A. E. Radiation extinction of slurried TiO<sub>2</sub> as a function of mechanical action and ionic composition of the suspending media: a key factor in the photocatalytic efficiency. *Appl. Catal. B: Environ.* 2002, *38* (1), 61-69. DOI: 10.1016/s0926-3373(02)00027-9.



- [16] Vignolo-Gonzalez, H. A.; Laha, S.; Jimenez-Solano, A.; Oshima, T.; Duppel, V.; Schutzendube, P.; Lotsch, B. V. Toward Standardized Photocatalytic Oxygen Evolution Rates Using RuO<sub>2</sub>@TiO<sub>2</sub> as a Benchmark. *Matter* 2020, 3 (2), 464-486. DOI: 10.1016/j.matt.2020.07.021.
- [17] Jiang, Z.; Qian, K.; Zhu, C.; Sun, H.; Wan, W.; Xie, J.; Li, H.; Wong, P. K.; Yuan, S. Carbon nitride coupled with CdS-TiO<sub>2</sub> nanodots as 2D/0D ternary composite with enhanced photocatalytic H<sub>2</sub> evolution: A novel efficient three-level electron transfer process. *Appl. Catal. B: Environ.* 2017, 210, 194-204. DOI: 10.1016/j.apcatb.2017.03.069.
- [18] Hao, Q.; Song, Y.; Ji, H.; Mo, Z.; She, X.; Deng, J.; Muhmood, T.; Wu, X.; Yuan, S.; Xu, H.; et al. Surface N modified 2D g-C<sub>3</sub>N<sub>4</sub> nanosheets derived from DMF for photocatalytic H<sub>2</sub> evolution. *Appl. Surf. Sci.* 2018, 459, 845-852. DOI: 10.1016/j.apsusc.2018.07.154.
- [19] Zeng, Z.; Quan, X.; Yu, H.; Chen, S.; Zhang, S. Nanoscale lightning rod effect in 3D carbon nitride nanoneedle: Enhanced charge collection and separation for efficient photocatalysis. *J. Catal.* 2019, 375, 361-370. DOI: 10.1016/j.jcat.2019.06.019.
- [20] Dong, W.; Liu, Y.; Zeng, G.; Cai, T.; Shao, L.; Chen, H.; Zeng, W.; Xia, X. Crystal phase engineering Zn<sub>0.8</sub>Cd<sub>0.2</sub>S nanocrystals with twin-induced homojunctions for photocatalytic nitrogen fixation under visible light. *J. Photoch. Photobio. A* 2020, 401. DOI: 10.1016/j.jphotochem.2020.112766.
- [21] Cheng, L.; Yue, X.; Wang, L.; Zhang, D.; Zhang, P.; Fan, J.; Xiang, Q. Dual-Single-Atom Tailoring with Bifunctional Integration for High-Performance CO<sub>2</sub> Photoreduction. *Adv. Mater.* 2021, e2105135. DOI: 10.1002/adma.202105135.
- [22] Meng, S.; Ye, X.; Zhang, J.; Fu, X.; Chen, S. Effective use of photogenerated electrons and holes in a system: Photocatalytic selective oxidation of aromatic alcohols to aldehydes and hydrogen production. *J. Catal.* 2018, 367, 159-170. DOI: 10.1016/j.jcat.2018.09.003.
- [23] Zhao, F.; Feng, Y.; Wang, Y.; Zhang, X.; Liang, X.; Li, Z.; Zhang, F.; Wang, T.; Gong, J.; Feng, W. Two-dimensional gersiloxenes with tunable bandgap for photocatalytic H<sub>2</sub> evolution and CO<sub>2</sub> photoreduction to CO. *Nat. Commun.* 2020, 11 (1), 1443. DOI: 10.1038/s41467-020-15262-4.
- [24] Takata, T.; Jiang, J.; Sakata, Y.; Nakabayashi, M.; Shibata, N.; Nandal, V.; Seki, K.; Hisatomi, T.; Domen, K. Photocatalytic water splitting with a quantum efficiency of almost unity. *Nature* 2020, 581 (7809), 411-414. DOI: 10.1038/s41586-020-2278-9.
- [25] Li, Y.; Ji, M.; Ma, Z.; Meng, L.; He, R.; Peng, S. Hierarchically Porous Polymeric Carbon Nitride as a Volume Photocatalyst for Efficient H<sub>2</sub> Generation under Strong Irradiation. *Solar RRL* 2021, 2100823. DOI: 10.1002/solr.202100823.
- [26] Zhao, G.; Sun, Y.; Zhou, W.; Wang, X.; Chang, K.; Liu, G.; Liu, H.; Kako, T.; Ye, J. Superior Photocatalytic H<sub>2</sub> Production with Cocatalytic Co/Ni Species Anchored on Sulfide Semiconductor. *Adv. Mater.* 2017, 29 (40), 1703258. DOI: 10.1002/adma.201703258.
- [27] *SUNERGY initiative portal*. <https://www.sunergy-initiative.eu/> (accessed 2012-12-28).
- [28] *Innovation Challenge 5: Converting Sunlight into Solar Fuels and Chemicals Roadmap 2020–2050*. <http://mission-innovation.net/wp-content/uploads/2021/03/Converting-Sunlight-into-Solar-Fuels-and-Chemicals-MI-Challenge-5-roadmap-Feb-2021-final.pdf> (accessed 2021-12-28).
- [29] *IEA, Total energy related CO<sub>2</sub> emissions with and without a sustainable recovery, 2005-2023*, IEA, Paris. <https://www.iea.org/data-and-statistics/charts/total-energy-related-co2-emissions-with-and-without-a-sustainable-recovery-2005-2023> (accessed 2021-12-28).
- [30] Benson, E. E.; Kubiak, C. P.; Sathrum, A. J.; Smieja, J. M. Electrocatalytic and homogeneous approaches to conversion of CO<sub>2</sub> to liquid fuels. *Chem. Soc. Rev.* 2009, 38 (1), 89-99. DOI: 10.1039/b804323j.



- [31] Wu, H.-K.; Zhang, F.; Li, J.-Y.; Tang, Z.-R.; Xu, Y.-J. Photo-driven Fischer–Tropsch synthesis. *J. Mater. Chem. A* 2020, *8* (46), 24253-24266. DOI: 10.1039/d0ta09097b.
- [32] Mansoor, R.; Tahir, M. Recent Developments in Natural Gas Flaring Reduction and Reformation to Energy-Efficient Fuels: A Review. *Energ. Fuel*. 2021, *35* (5), 3675-3714. DOI: 10.1021/acs.energyfuels.0c04269.
- [33] Jin, S.; Hao, Z.; Zhang, K.; Yan, Z.; Chen, J. Advances and Challenges for the Electrochemical Reduction of CO<sub>2</sub> to CO: From Fundamentals to Industrialization. *Angew. Chem. Int. Ed. Engl.* 2021, *60* (38), 20627-20648. DOI: 10.1002/anie.202101818.
- [34] Goyal, A.; Marcandalli, G.; Mints, V. A.; Koper, M. T. M. Competition between CO<sub>2</sub> Reduction and Hydrogen Evolution on a Gold Electrode under Well-Defined Mass Transport Conditions. *J. Am. Chem. Soc.* 2020, *142* (9), 4154-4161. DOI: 10.1021/jacs.9b10061.
- [35] Peng, C.; Reid, G.; Wang, H.; Hu, P. Perspective: Photocatalytic reduction of CO<sub>2</sub> to solar fuels over semiconductors. *J. Chem. Phys.* 2017, *147* (3), 030901. DOI: 10.1063/1.4985624.
- [36] Li, K.; An, X.; Park, K. H.; Khraisheh, M.; Tang, J. A critical review of CO<sub>2</sub> photoconversion: Catalysts and reactors. *Catal. Today* 2014, *224*, 3-12. DOI: 10.1016/j.cattod.2013.12.006.
- [37] Wang, W.-N.; Soulis, J.; Yang, Y. J.; Biswas, P. Comparison of CO<sub>2</sub> Photoreduction Systems: A Review. *Aerosol and Air Qual. Res.* 2014, *14* (2), 533-549. DOI: 10.4209/aaqr.2013.09.0283.
- [38] Samanta, S.; Srivastava, R. Catalytic conversion of CO<sub>2</sub> to chemicals and fuels: the collective thermocatalytic/photocatalytic/electrocatalytic approach with graphitic carbon nitride. *Mater. Adv.* 2020, *1* (6), 1506-1545. DOI: 10.1039/d0ma00293c.
- [39] Darkwah, W. K.; Teye, G. K.; Ao, Y. Graphene nanocrystals in CO<sub>2</sub> photoreduction with H<sub>2</sub>O for fuel production. *Nanoscale Adv.* 2020, *2* (3), 991-1006. DOI: 10.1039/c9na00756c.
- [40] Li, D.; Kassymova, M.; Cai, X.; Zang, S.-Q.; Jiang, H.-L. Photocatalytic CO<sub>2</sub> reduction over metal-organic framework-based materials. *Coordin. Chem. Rev.* 2020, *412*, 213262. DOI: 10.1016/j.ccr.2020.213262.
- [41] Tahir, M.; Ali Khan, A.; Tasleem, S.; Mansoor, R.; Fan, W. K. Titanium Carbide (Ti<sub>3</sub>C<sub>2</sub>) MXene as a Promising Co-catalyst for Photocatalytic CO<sub>2</sub> Conversion to Energy-Efficient Fuels: A Review. *Energ. Fuel*. 2021, *35* (13), 10374-10404. DOI: 10.1021/acs.energyfuels.1c00958.
- [42] Lilliestam, J.; Ollier, L.; Labordena, M.; Pfenninger, S.; Thonig, R. The near- to mid-term outlook for concentrating solar power: mostly cloudy, chance of sun. *Energ. Source Part B* 2020, *16* (1), 23-41. DOI: 10.1080/15567249.2020.1773580.
- [43] Schappi, R.; Rutz, D.; Dahler, F.; Muroyama, A.; Haueter, P.; Lilliestam, J.; Patt, A.; Furler, P.; Steinfeld, A. Drop-in fuels from sunlight and air. *Nature* 2021, 63-68. DOI: 10.1038/s41586-021-04174-y.
- [44] Dähler, F.; Wild, M.; Schappi, R.; Haueter, P.; Cooper, T.; Good, P.; Larrea, C.; Schmitz, M.; Furler, P.; Steinfeld, A. Optical design and experimental characterization of a solar concentrating dish system for fuel production via thermochemical redox cycles. *Sol. Energy* 2018, *170*, 568-575. DOI: 10.1016/j.solener.2018.05.085.
- [45] Vázquez, F. V.; Koponen, J.; Ruuskanen, V.; Bajamundi, C.; Kosonen, A.; Simell, P.; Ahola, J.; Frilund, C.; Elfving, J.; Reinikainen, M.; et al. Power-to-X technology using renewable electricity and carbon dioxide from ambient air: SOLETAIR proof-of-concept and improved process concept. *J. CO<sub>2</sub> Util.* 2018, *28*, 235-246. DOI: 10.1016/j.jcou.2018.09.026.



- [46] Fan, W. K.; Tahir, M. Recent developments in photothermal reactors with understanding on the role of light/heat for CO<sub>2</sub> hydrogenation to fuels: A review. *Chem. Eng. J.* 2022, *427*, 131617. DOI: 10.1016/j.cej.2021.131617.
- [47] Joint Center for Artificial Photosynthesis (JCAP). <https://solarfuelshub.org/> (accessed 2021-12-28).
- [48] Liquid Sunlight Alliance (LiSA). <https://www.liquidsunlightalliance.org/> (accessed 2021-12-28).
- [49] Hossain, M. N.; Prslja, P.; Flox, C.; Muthuswamy, N.; Sainio, J.; Kannan, A. M.; Suominen, M.; Lopez, N.; Kallio, T. Temperature dependent product distribution of electrochemical CO<sub>2</sub> reduction on CoTPP/MWCNT composite. *Appl. Catal. B: Environ.* 2022, *304*, 120863. DOI: 10.1016/j.apcatb.2021.120863.
- [50] Variar, A. G.; M.S, R.; Ail, V. U.; S, S. P.; K, S.; Tahir, M. Influence of various operational parameters in enhancing photocatalytic reduction efficiency of carbon dioxide in a photoreactor: A review. *J. Ind. Eng. Chem.* 2021, *99*, 19-47. DOI: 10.1016/j.jiec.2021.04.017.
- [51] Wijffels, R. H.; Barbosa, M. J. An outlook on microalgal biofuels. *Science* 2010, *329* (5993), 796-799. DOI: 10.1126/science.1189003.
- [52] Zhang, Z.; Wang, Y.; Cui, G.; Lu, H.; Abanades, S. Remarkable CO<sub>2</sub> photoreduction activity using TiO<sub>2</sub> nanotube arrays under favorable photothermal conditions driven by concentrated solar light. *Appl. Phys. Lett.* 2021, *119* (12), 123906. DOI: 10.1063/5.0057896.
- [53] Kavil, Y. N.; Shaban, Y. A.; Al Farawati, R. K.; Orif, M. I.; Zobidi, M.; Khan, S. U. M. Efficient Photocatalytic Reduction of CO<sub>2</sub> Present in Seawater into Methanol over Cu/C-Co-Doped TiO<sub>2</sub> Nanocatalyst Under UV and Natural Sunlight. *Water Air Soil Poll.* 2018, *229* (7), 236. DOI: 10.1007/s11270-018-3881-3.
- [54] Gondal, M. A.; Lais, A.; Dastageer, M. A.; Yang, D.; Shen, K.; Chang, X. Photocatalytic conversion of CO<sub>2</sub> into methanol using graphitic carbon nitride under solar, UV laser and broadband radiations. *Int. J. Energ. Res.* 2017, *41* (14), 2162-2172. DOI: 10.1002/er.3777.
- [55] Lan, G.; Li, Z.; Veroneau, S. S.; Zhu, Y. Y.; Xu, Z.; Wang, C.; Lin, W. Photosensitizing Metal-Organic Layers for Efficient Sunlight-Driven Carbon Dioxide Reduction. *J. Am. Chem. Soc.* 2018, *140* (39), 12369-12373. DOI: 10.1021/jacs.8b08357.
- [56] Huang, N. Y.; He, H.; Liu, S.; Zhu, H. L.; Li, Y. J.; Xu, J.; Huang, J. R.; Wang, X.; Liao, P. Q.; Chen, X. M. Electrostatic Attraction-Driven Assembly of a Metal-Organic Framework with a Photosensitizer Boosts Photocatalytic CO<sub>2</sub> Reduction to CO. *J. Am. Chem. Soc.* 2021, *143* (42), 17424-17430. DOI: 10.1021/jacs.1c05839.
- [57] Roy, A.; Chhetri, M.; Prasad, S.; Waghmare, U. V.; Rao, C. N. R. Unique Features of the Photocatalytic Reduction of H<sub>2</sub>O and CO<sub>2</sub> by New Catalysts Based on the Analogues of CdS, Cd<sub>4</sub>P<sub>2</sub>X<sub>3</sub> (X = Cl, Br, I). *ACS Appl. Mater. Inter.* 2018, *10* (3), 2526-2536. DOI: 10.1021/acsami.7b15992.
- [58] Bellardita, M.; Loddo, V.; Palmisano, L. Formation of High Added Value Chemicals by Photocatalytic Treatment of Biomass. *Mini-Rev. Org. Chem.* 2020, *17* (7), 884-901. DOI: 10.2174/1570193x17666200131112856.
- [59] Xiang, Z.; Han, W.; Deng, J.; Zhu, W.; Zhang, Y.; Wang, H. Photocatalytic Conversion of Lignin into Chemicals and Fuels. *ChemSusChem* 2020, *13* (17), 4199-4213. DOI: 10.1002/cssc.202000601.
- [60] Granone, L. I.; Sieland, F.; Zheng, N.; Dillert, R.; Bahnemann, D. W. Photocatalytic conversion of biomass into valuable products: a meaningful approach? *Green Chem.* 2018, *20* (6), 1169-1192. DOI: 10.1039/c7gc03522e.



- [61] Chen, H.; Wan, K.; Zheng, F.; Zhang, Z.; Zhang, H.; Zhang, Y.; Long, D. Recent Advances in Photocatalytic Transformation of Carbohydrates Into Valuable Platform Chemicals. *Front. Chem. Eng.* 2021, 3, 615309. DOI: 10.3389/fceng.2021.615309.
- [62] Speltini, A.; Sturini, M.; Dondi, D.; Annovazzi, E.; Maraschi, F.; Caratto, V.; Profumo, A.; Buttafava, A. Sunlight-promoted photocatalytic hydrogen gas evolution from water-suspended cellulose: a systematic study. *Photochem. Photobiol. Sci.* 2014, 13 (10), 1410-1419. DOI: 10.1039/c4pp00128a.
- [63] Ilkaeva, M.; Krivtsov, I.; García-López, E. I.; Marci, G.; Khainakova, O.; García, J. R.; Palmisano, L.; Díaz, E.; Ordóñez, S. Selective photocatalytic oxidation of 5-hydroxymethylfurfural to 2,5-furandicarboxaldehyde by polymeric carbon nitride-hydrogen peroxide adduct. *J. Catal.* 2018, 359, 212-222. DOI: 10.1016/j.jcat.2018.01.012.
- [64] García-López, E. I.; Pomilla, F. R.; Bloise, E.; Lü, X.-f.; Mele, G.; Palmisano, L.; Marci, G. C<sub>3</sub>N<sub>4</sub> Impregnated with Porphyrins as Heterogeneous Photocatalysts for the Selective Oxidation of 5-Hydroxymethyl-2-Furfural Under Solar Irradiation. *Top. Catal.* 2020, 64 (13-16), 758-771. DOI: 10.1007/s11244-020-01293-0.
- [65] Kausar, S.; Ali Altaf, A.; Hamayun, M.; Danish, M.; Zubair, M.; Naz, S.; Muhammad, S.; Zaheer, M.; Ullah, S.; Badshah, A. Soft template-based bismuth doped zinc oxide nanocomposites for photocatalytic depolymerization of lignin. *Inorg. Chim. Acta* 2020, 502, 119390. DOI: 10.1016/j.ica.2019.119390.
- [66] Lam, E.; Reisner, E. A TiO<sub>2</sub>-Co(terpyridine)<sub>2</sub> Photocatalyst for the Selective Oxidation of Cellulose to Formate Coupled to the Reduction of CO<sub>2</sub> to Syngas. *Angew. Chem. Int. Ed. Engl.* 2021, 60 (43), 23306-23312. DOI: 10.1002/anie.202108492.
- [67] Spasiano, D.; Marotta, R.; Malato, S.; Fernandez-Ibañez, P.; Di Somma, I. Solar photocatalysis: Materials, reactors, some commercial, and pre-industrialized applications. A comprehensive approach. *Appl. Catal. B: Environ.* 2015, 170-171, 90-123. DOI: 10.1016/j.apcatb.2014.12.050.
- [68] Detz, R. J.; Reek, J. N. H.; van der Zwaan, B. C. C. The future of solar fuels: when could they become competitive? *Energ. Environ. Sci.* 2018, 11 (7), 1653-1669. DOI: 10.1039/c8ee00111a.
- [69] Yang, C.; Li, R.; Zhang, K. A. I.; Lin, W.; Landfester, K.; Wang, X. Heterogeneous photoredox flow chemistry for the scalable organosynthesis of fine chemicals. *Nat. Commun.* 2020, 11 (1), 1239. DOI: 10.1038/s41467-020-14983-w.
- [70] Reed, N. L.; Yoon, T. P. Oxidase reactions in photoredox catalysis. *Chem. Soc. Rev.* 2021, 50 (5), 2954-2967. DOI: 10.1039/d0cs00797h.
- [71] Corey, E. J.; Suggs, J. W. Pyridinium chlorochromate. An efficient reagent for oxidation of primary and secondary alcohols to carbonyl compounds. *Tetrahedron Lett.* 1975, 16 (31), 2647-2650. DOI: 10.1016/s0040-4039(00)75204-x.
- [72] Meyer, S. D.; Schreiber, S. L. Acceleration of the Dess-Martin Oxidation by Water. *J. Org. Chem.* 2002, 59 (24), 7549-7552. DOI: 10.1021/jo00103a067.
- [73] Ohsugi, S.-i.; Nishide, K.; Oono, K.; Okuyama, K.; Fudesaka, M.; Kodama, S.; Node, M. New odorless method for the Corey–Kim and Swern oxidations utilizing dodecyl methyl sulfide (Dod-S-Me). *Tetrahedron* 2003, 59 (42), 8393-8398. DOI: 10.1016/j.tet.2003.08.055.
- [74] Abedi, S.; Morsali, A. Ordered Mesoporous Metal–Organic Frameworks Incorporated with Amorphous TiO<sub>2</sub> As Photocatalyst for Selective Aerobic Oxidation in Sunlight Irradiation. *ACS Catal.* 2014, 4 (5), 1398-1403. DOI: 10.1021/cs500123d.
- [75] Tu, Y. Artemisinin - A Gift from Traditional Chinese Medicine to the World (Nobel Lecture). *Angew. Chem. Int. Ed. Engl.* 2016, 55 (35), 10210-10226. DOI: 10.1002/anie.201601967.



- [76] Turconi, J.; Griolet, F.; Guevel, R.; Odon, G.; Villa, R.; Geatti, A.; Hvala, M.; Rossen, K.; Göller, R.; Burgard, A. Semisynthetic Artemisinin, the Chemical Path to Industrial Production. *Org. Process Res. Dev.* 2014, *18* (3), 417-422. DOI: 10.1021/op4003196.
- [77] Cambie, D.; Dobbelaar, J.; Riente, P.; Vanderspikken, J.; Shen, C.; Seeberger, P. H.; Gilmore, K.; Debije, M. G.; Noel, T. Energy-Efficient Solar Photochemistry with Luminescent Solar Concentrator Based Photomicroreactors. *Angew. Chem. Int. Ed. Engl.* 2019, *58* (40), 14374-14378. DOI: 10.1002/anie.201908553.
- [78] Liu, Y.; Wang, B.; Qiao, X.; Tung, C.-H.; Wang, Y. Iodine/Visible Light Photocatalysis for Activation of Alkynes for Electrophilic Cyclization Reactions. *ACS Catal.* 2017, *7* (6), 4093-4099. DOI: 10.1021/acscatal.7b00799.
- [79] Su, Y.; Zhang, L.; Jiao, N. Utilization of natural sunlight and air in the aerobic oxidation of benzyl halides. *Org. Lett.* 2011, *13* (9), 2168-2171. DOI: 10.1021/ol2002013.
- [80] Markushyna, Y.; Schusslbauer, C. M.; Ullrich, T.; Guldi, D. M.; Antonietti, M.; Savateev, A. Chromoselective Synthesis of Sulfonyl Chlorides and Sulfonamides with Potassium Poly(heptazine imide) Photocatalyst. *Angew. Chem. Int. Ed. Engl.* 2021, *60* (37), 20543-20550. DOI: 10.1002/anie.202106183.
- [81] Yuan, J.; Xia, Q.; Zhu, W.; Wu, C.; Wang, B.; Liu, B.; Yang, X.; Xu, Y.; Xu, H. Sunlight-Driven Synthesis of 1,2,4-Thiadiazoles via Oxidative Construction of a Nitrogen-Sulfur Bond Catalyzed by a Reusable Covalent Organic Framework. *ChemPhotoChem* 2020, *4* (6), 445-450. DOI: 10.1002/cptc.201900263.
- [82] Niu, T.; Chen, S.; Hong, M.; Zhang, T.; Chen, J.; Dong, X.; Ni, B. Heterogeneous carbon nitride photocatalyst for C-C bond oxidative cleavage of vicinal diols in aerobic micellar medium. *Green Chem.* 2020, *22* (15), 5042-5049. DOI: 10.1039/d0gc01727b.
- [83] Du, Y.; Pearson, R. M.; Lim, C. H.; Sartor, S. M.; Ryan, M. D.; Yang, H.; Damrauer, N. H.; Miyake, G. M. Strongly Reducing, Visible-Light Organic Photoredox Catalysts as Sustainable Alternatives to Precious Metals. *Chem. Eur. J.* 2017, *23* (46), 10962-10968. DOI: 10.1002/chem.201702926.
- [84] Zhang, S.; Tang, Z.; Bao, W.; Li, J.; Guo, B.; Huang, S.; Zhang, Y.; Rao, Y. Perylenequinonoid-catalyzed photoredox activation for the direct arylation of (het)arenes with sunlight. *Org. Biomol. Chem.* 2019, *17* (17), 4364-4369. DOI: 10.1039/c9ob00659a.
- [85] Koohgard, M.; Karimitabar, H.; Hosseini-Sarvari, M. Visible-light-mediated semi-heterogeneous black TiO<sub>2</sub>/nickel dual catalytic C(sp<sup>2</sup>)-P bond formation toward aryl phosphonates. *Dalton Trans.* 2020, *49* (47), 17147-17151. DOI: 10.1039/d0dt03507f.
- [86] Zhang, W.; Pan, Y.-L.; Yang, C.; Li, X.; Wang, B. Ring-opening C(sp<sup>3</sup>)-C coupling of cyclobutanone oxime esters for the preparation of cyanoalkyl containing heterocycles enabled by photocatalysis. *Org. Chem. Front.* 2019, *6* (15), 2765-2770. DOI: 10.1039/c9qo00625g.
- [87] Akita, M.; Koike, T. Sunlight-driven trifluoromethylation of olefinic substrates by photoredox catalysis: A green organic process. *CR Chim.* 2015, *18* (7), 742-751. DOI: 10.1016/j.crci.2015.01.013.
- [88] Filippini, G.; Longobardo, F.; Forster, L.; Criado, A.; Di Carmine, G.; Nasi, L.; D'Agostino, C.; Melchionna, M.; Fornasiero, P.; Prato, M. Light-driven, heterogeneous organocatalysts for C-C bond formation toward valuable perfluoroalkylated intermediates. *Sci. Adv.* 2020, *6* (46), eabc9923. DOI: 10.1126/sciadv.abc9923.
- [89] Capaldo, L.; Fagnoni, M.; Ravelli, D. Vinylpyridines as Building Blocks for the Photocatalyzed Synthesis of Alkylpyridines. *Chem. Eur. J.* 2017, *23* (27), 6527-6530. DOI: 10.1002/chem.201701346.



- [90] Ma, Q.; Song, J.; Zhang, X.; Jiang, Y.; Ji, L.; Liao, S. Metal-free atom transfer radical polymerization with ppm catalyst loading under sunlight. *Nat. Commun.* 2021, *12* (1), 429. DOI: 10.1038/s41467-020-20645-8.
- [91] Buysch, H.-J. Carbonic Esters. In *Ullmann's Encyclopedia of Industrial Chemistry*, 2000.
- [92] Kumar, A.; Samanta, S.; Srivastava, R. Graphitic Carbon Nitride Modified with Zr-Thiamine Complex for Efficient Photocatalytic CO<sub>2</sub> Insertion to Epoxide: Comparison with Traditional Thermal Catalysis. *ACS Appl. Nano Mater.* 2021, *4* (7), 6805-6820. DOI: 10.1021/acsanm.1c00887.
- [93] Fujishima, A.; Honda, K. Electrochemical photolysis of water at a semiconductor electrode. *Nature* 1972, *238* (5358), 37-38. DOI: 10.1038/238037a0.
- [94] Khyustova, A.; Sirotkin, N.; Kusova, T.; Kraev, A.; Titov, V.; Agafonov, A. Doped TiO<sub>2</sub>: the effect of doping elements on photocatalytic activity. *Mater. Adv.* 2020, *1* (5), 1193-1201. DOI: 10.1039/d0ma00171f.
- [95] Xiao, Q.; Zhang, J.; Xiao, C.; Si, Z.; Tan, X. Solar photocatalytic degradation of methylene blue in carbon-doped TiO<sub>2</sub> nanoparticles suspension. *Sol. Energy* 2008, *82* (8), 706-713. DOI: 10.1016/j.solener.2008.02.006.
- [96] Wang, W.; Xu, D.; Cheng, B.; Yu, J.; Jiang, C. Hybrid carbon@TiO<sub>2</sub> hollow spheres with enhanced photocatalytic CO<sub>2</sub> reduction activity. *J. Mater. Chem. A* 2017, *5* (10), 5020-5029. DOI: 10.1039/c6ta11121a.
- [97] Ma, Z.; Sa, R.; Li, Q.; Wu, K. Interfacial electronic structure and charge transfer of hybrid graphene quantum dot and graphitic carbon nitride nanocomposites: insights into high efficiency for photocatalytic solar water splitting. *Phys. Chem. Chem. Phys.* 2016, *18* (2), 1050-1058. DOI: 10.1039/c5cp05847c.
- [98] Velo-Gala, I.; López-Peñalver, J. J.; Sánchez-Polo, M.; Rivera-Utrilla, J. Role of activated carbon surface chemistry in its photocatalytic activity and the generation of oxidant radicals under UV or solar radiation. *Appl. Catal. B: Environ.* 2017, *207*, 412-423. DOI: 10.1016/j.apcatb.2017.02.028.
- [99] Rosso, C.; Filippini, G.; Criado, A.; Melchionna, M.; Fornasiero, P.; Prato, M. Metal-Free Photocatalysis: Two-Dimensional Nanomaterial Connection toward Advanced Organic Synthesis. *ACS Nano* 2021, *15* (3), 3621-3630. DOI: 10.1021/acsnano.1c00627.
- [100] Nicks, J.; Sasitharan, K.; Prasad, R. R. R.; Ashworth, D. J.; Foster, J. A. Metal–Organic Framework Nanosheets: Programmable 2D Materials for Catalysis, Sensing, Electronics, and Separation Applications. *Adv. Funct. Mater.* 2021, *31* (42), 2103723. DOI: 10.1002/adfm.202103723.
- [101] Wang, S.; Sun, Q.; Chen, W.; Tang, Y.; Aguila, B.; Pan, Y.; Zheng, A.; Yang, Z.; Wojtas, L.; Ma, S.; et al. Programming Covalent Organic Frameworks for Photocatalysis: Investigation of Chemical and Structural Variations. *Matter* 2020, *2* (2), 416-427. DOI: 10.1016/j.matt.2019.10.026.
- [102] Mazzanti, S.; Savateev, A. Emerging Concepts in Carbon Nitride Organic Photocatalysis. *ChemPlusChem* 2020, *85* (11), 2499-2517. DOI: 10.1002/cplu.202000606.
- [103] Oelgemoller, M. Solar Photochemical Synthesis: From the Beginnings of Organic Photochemistry to the Solar Manufacturing of Commodity Chemicals. *Chem. Rev.* 2016, *116* (17), 9664-9682. DOI: 10.1021/acs.chemrev.5b00720.
- [104] Cambie, D.; Noel, T. Solar Photochemistry in Flow. *Top. Curr. Chem. (Z)* 2018, *376* (6), 45. DOI: 10.1007/s41061-018-0223-2.



- [105] Tembhurne, S.; Nandjou, F.; Haussener, S. A thermally synergistic photo-electrochemical hydrogen generator operating under concentrated solar irradiation. *Nat. Energy* 2019, 4 (5), 399-407. DOI: 10.1038/s41560-019-0373-7.
- [106] Nishiyama, H.; Yamada, T.; Nakabayashi, M.; Maehara, Y.; Yamaguchi, M.; Kuromiya, Y.; Nagatsuma, Y.; Tokudome, H.; Akiyama, S.; Watanabe, T.; et al. Photocatalytic solar hydrogen production from water on a 100-m<sup>2</sup> scale. *Nature* 2021, 598 (7880), 304-307. DOI: 10.1038/s41586-021-03907-3.
- [107] Heinemann, C.; Xing, X.; Warzecha, K. D.; Ritterskamp, P.; Görner, H.; Demuth, M. An asymmetric induction principle and biomimetics with photons via electron transfer. *Pure Appl. Chem.* 1998, 70 (11), 2167-2176. DOI: 10.1351/pac199870112167.
- [108] Wau, J. S.; Robertson, M. J.; Oelgemoller, M. Solar Photooxygenations for the Manufacturing of Fine Chemicals - Technologies and Applications. *Molecules* 2021, 26 (6), 1685. DOI: 10.3390/molecules26061685.
- [109] Noël, T. *Photochemical Processes in Continuous-Flow Reactors*; World Scientific Publishing Europe Ltd., 2017. DOI: 10.1142/q0065.
- [110] McAtee, R. C.; McClain, E. J.; Stephenson, C. R. J. Illuminating Photoredox Catalysis. *Trends Chem.* 2019, 1 (1), 111-125. DOI: 10.1016/j.trechm.2019.01.008.
- [111] Zhang, Z.; Qiu, C.; Xu, Y.; Han, Q.; Tang, J.; Loh, K. P.; Su, C. Semiconductor photocatalysis to engineering deuterated *N*-alkyl pharmaceuticals enabled by synergistic activation of water and alkanols. *Nat. Commun.* 2020, 11 (1), 4722. DOI: 10.1038/s41467-020-18458-w.
- [112] Bellotti, P.; Koy, M.; Gutheil, C.; Heuvel, S.; Glorius, F. Three-component three-bond forming cascade via palladium photoredox catalysis. *Chem. Sci.* 2021, 12 (5), 1810-1817. DOI: 10.1039/d0sc05551d.
- [113] Welin, E. R.; Le, C.; Arias-Rotondo, D. M.; McCusker, J. K.; MacMillan, D. W. Photosensitized, energy transfer-mediated organometallic catalysis through electronically excited nickel(II). *Science* 2017, 355 (6323), 380-385. DOI: 10.1126/science.aal2490.
- [114] Yi, X.; Hu, X. Intermolecular oxidative amination of unactivated alkenes by dual photoredox and copper catalysis. *Chem. Sci.* 2021, 12 (5), 1901-1906. DOI: 10.1039/d0sc05952h.
- [115] Romero, N. A.; Nicewicz, D. A. Organic Photoredox Catalysis. *Chem. Rev.* 2016, 116 (17), 10075-10166. DOI: 10.1021/acs.chemrev.6b00057.
- [116] Ong, W. J.; Tan, L. L.; Ng, Y. H.; Yong, S. T.; Chai, S. P. Graphitic Carbon Nitride (g-C<sub>3</sub>N<sub>4</sub>)-Based Photocatalysts for Artificial Photosynthesis and Environmental Remediation: Are We a Step Closer To Achieving Sustainability? *Chem. Rev.* 2016, 116 (12), 7159-7329. DOI: 10.1021/acs.chemrev.6b00075.
- [117] Wang, X.; Maeda, K.; Thomas, A.; Takanabe, K.; Xin, G.; Carlsson, J. M.; Domen, K.; Antonietti, M. A metal-free polymeric photocatalyst for hydrogen production from water under visible light. *Nat. Mater.* 2009, 8 (1), 76-80. DOI: 10.1038/nmat2317.
- [118] Dai, Y.; Li, C.; Shen, Y.; Lim, T.; Xu, J.; Li, Y.; Niemantsverdriet, H.; Besenbacher, F.; Lock, N.; Su, R. Light-tuned selective photosynthesis of azo- and azoxy-aromatics using graphitic C<sub>3</sub>N<sub>4</sub>. *Nat. Commun.* 2018, 9 (1), 60. DOI: 10.1038/s41467-017-02527-8.
- [119] Chen, J.; Cen, J.; Xu, X.; Li, X. The application of heterogeneous visible light photocatalysts in organic synthesis. *Catal. Sci. Technol.* 2016, 6 (2), 349-362. DOI: 10.1039/c5cy01289a.
- [120] Yang, C.; Wang, B.; Zhang, L.; Yin, L.; Wang, X. Synthesis of Layered Carbonitrides from Biotic Molecules for Photoredox Transformations. *Angew. Chem. Int. Ed. Engl.* 2017, 56 (23), 6627-6631. DOI: 10.1002/anie.201702213.



- [121] Savateev, A.; Ghosh, I.; Konig, B.; Antonietti, M. Photoredox Catalytic Organic Transformations using Heterogeneous Carbon Nitrides. *Angew. Chem. Int. Ed. Engl.* 2018, *57* (49), 15936-15947. DOI: 10.1002/anie.201802472.
- [122] Savateev, A.; Kurpil, B.; Mishchenko, A.; Zhang, G.; Antonietti, M. A "waiting" carbon nitride radical anion: a charge storage material and key intermediate in direct C-H thiolation of methylenes using elemental sulfur as the "S"-source. *Chem. Sci.* 2018, *9* (14), 3584-3591. DOI: 10.1039/c8sc00745d.
- [123] Zhou, Q. Q.; Zou, Y. Q.; Lu, L. Q.; Xiao, W. J. Visible-Light-Induced Organic Photochemical Reactions through Energy-Transfer Pathways. *Angew. Chem. Int. Ed. Engl.* 2019, *58* (6), 1586-1604. DOI: 10.1002/anie.201803102.
- [124] Savateev, A.; Tarakina, N. V.; Strauss, V.; Hussain, T.; Ten Brummelhuis, K.; Sanchez Vadillo, J. M.; Markushyna, Y.; Mazzanti, S.; Tyutyunnik, A. P.; Walczak, R.; et al. Potassium Poly(Heptazine Imide): Transition Metal-Free Solid-State Triplet Sensitizer in Cascade Energy Transfer and [3+2]-cycloadditions. *Angew. Chem. Int. Ed. Engl.* 2020, *59* (35), 15061-15068. DOI: 10.1002/anie.202004747.
- [125] Wuts, P. G. M. *Greene's Protective Groups in Organic Synthesis*; Wiley, 2014. DOI: 10.1002/9781118905074.
- [126] Bolotin, D. S.; Bokach, N. A.; Demakova, M. Y.; Kukushkin, V. Y. Metal-Involving Synthesis and Reactions of Oximes. *Chem. Rev.* 2017, *117* (21), 13039-13122. DOI: 10.1021/acs.chemrev.7b00264.
- [127] Tagawa, Y. Nitrosation of Active Methyl and Methylene Groups on *N*-Heteroaromatics. *Mini-Rev. Org. Chem.* 2011, *8* (2), 186-196. DOI: 10.2174/157019311795177709.
- [128] Lee, S. K.; Choi, M. G.; Chang, S.-K. Signaling of chloramine: a fluorescent probe for trichloroisocyanuric acid based on deoxygenation of a coumarin oxime. *Tetrahedron Lett.* 2014, *55* (51), 7047-7050. DOI: 10.1016/j.tetlet.2014.10.132.
- [129] Sanchez-Arroyo, A. J.; Pardo, Z. D.; Moreno-Jimenez, F.; Herrera, A.; Martin, N.; Garcia-Fresnadillo, D. Photochemical Oxidation of Thioketones by Singlet Molecular Oxygen Revisited: Insights into Photoproducts, Kinetics, and Reaction Mechanism. *J. Org. Chem.* 2015, *80* (21), 10575-10584. DOI: 10.1021/acs.joc.5b01710.
- [130] Padwa, A. Photochemistry of the carbon-nitrogen double bond. *Chem. Rev.* 2002, *77* (1), 37-68. DOI: 10.1021/cr60305a004.
- [131] Becker, M. R.; Richardson, A. D.; Schindler, C. S. Functionalized azetidines via visible light-enabled aza Paterno-Buchi reactions. *Nat. Commun.* 2019, *10* (1), 5095. DOI: 10.1038/s41467-019-13072-x.
- [132] Jiang, Y. X.; Chen, L.; Ran, C. K.; Song, L.; Zhang, W.; Liao, L. L.; Yu, D. G. Visible-Light Photoredox-Catalyzed Ring-Opening Carboxylation of Cyclic Oxime Esters with CO<sub>2</sub>. *ChemSusChem* 2020, *13* (23), 6312-6317. DOI: 10.1002/cssc.202002032.
- [133] Chen, J.; Wang, P. Z.; Lu, B.; Liang, D.; Yu, X. Y.; Xiao, W. J.; Chen, J. R. Enantioselective Radical Ring-Opening Cyanation of Oxime Esters by Dual Photoredox and Copper Catalysis. *Org. Lett.* 2019, *21* (23), 9763-9768. DOI: 10.1021/acs.orglett.9b03970.
- [134] Nancoz, C.; Rumble, C.; Rosspointner, A.; Vauthey, E. Bimolecular photoinduced electron transfer in non-polar solvents beyond the diffusion limit. *J. Chem. Phys.* 2020, *152* (24), 244501. DOI: 10.1063/5.0012363.
- [135] Chang, R. *Physical Chemistry for the Biosciences*; 2005.



- [136] Brunschwig, B.; Sutin, N. Reactions of the excited states of substituted polypyridinechromium(III) complexes with oxygen, iron(II) ions, ruthenium(II) and -(III), and osmium(II) and -(III) complexes. *J. Am. Chem. Soc.* 2002, *100* (24), 7568-7577. DOI: 10.1021/ja00492a023.
- [137] Demas, J. N.; Harris, E. W.; McBride, R. P. Energy transfer from luminescent transition metal complexes to oxygen. *J. Am. Chem. Soc.* 2002, *99* (11), 3547-3551. DOI: 10.1021/ja00453a001.
- [138] Wang, H.; Jiang, S.; Chen, S.; Li, D.; Zhang, X.; Shao, W.; Sun, X.; Xie, J.; Zhao, Z.; Zhang, Q.; et al. Enhanced Singlet Oxygen Generation in Oxidized Graphitic Carbon Nitride for Organic Synthesis. *Adv. Mater.* 2016, *28* (32), 6940-6945. DOI: 10.1002/adma.201601413.
- [139] Wu, W.; Han, C.; Zhang, Q.; Zhang, Q.; Li, Z.; Gosztola, D. J.; Wiederrecht, G. P.; Wu, M. Functionalizing carbon nitride with heavy atom-free spin converters for enhanced  $^{1}O_2$  generation. *J. Catal.* 2018, *361*, 222-229. DOI: 10.1016/j.jcat.2018.03.006.
- [140] Xu, S.; Yuan, Y.; Cai, X.; Zhang, C. J.; Hu, F.; Liang, J.; Zhang, G.; Zhang, D.; Liu, B. Tuning the singlet-triplet energy gap: a unique approach to efficient photosensitizers with aggregation-induced emission (AIE) characteristics. *Chem. Sci.* 2015, *6* (10), 5824-5830. DOI: 10.1039/c5sc01733e.
- [141] Shao, W.; Yang, C.; Li, F.; Wu, J.; Wang, N.; Ding, Q.; Gao, J.; Ling, D. Molecular Design of Conjugated Small Molecule Nanoparticles for Synergistically Enhanced PTT/PDT. *Nano-Micro Lett.* 2020, *12* (1). DOI: 10.1007/s40820-020-00474-6.
- [142] Zhang, C.; Zhao, Y.; Li, D.; Liu, J.; Han, H.; He, D.; Tian, X.; Li, S.; Wu, J.; Tian, Y. Aggregation-induced emission (AIE)-active molecules bearing singlet oxygen generation activities: the tunable singlet-triplet energy gap matters. *Chem. Commun. (Camb.)* 2019, *55* (10), 1450-1453. DOI: 10.1039/c8cc09230c.
- [143] Wang, L.; Li, T.; Feng, P.; Song, Y. Theoretical tuning of the singlet-triplet energy gap to achieve efficient long-wavelength thermally activated delayed fluorescence emitters: the impact of substituents. *Phys. Chem. Chem. Phys.* 2017, *19* (32), 21639-21647. DOI: 10.1039/c7cp02615c.
- [144] Prier, C. K.; Rankic, D. A.; MacMillan, D. W. C. Visible Light Photoredox Catalysis with Transition Metal Complexes: Applications in Organic Synthesis. *Chemical Reviews* 2013, *113* (7), 5322-5363. DOI: 10.1021/cr300503r.
- [145] Kisch, H. Semiconductor Photocatalysis—Mechanistic and Synthetic Aspects. *Angew. Chem. Int. Ed. Engl.* 2013, *52* (3), 812-847. DOI: 10.1002/anie.201201200.
- [146] Warren, J. J.; Tronic, T. A.; Mayer, J. M. Thermochemistry of proton-coupled electron transfer reagents and its implications. *Chem. Rev.* 2010, *110* (12), 6961-7001. DOI: 10.1021/cr100085k.
- [147] Gentry, E. C.; Knowles, R. R. Synthetic Applications of Proton-Coupled Electron Transfer. *Accounts Chem. Res.* 2016, *49* (8), 1546-1556. DOI: 10.1021/acs.accounts.6b00272.
- [148] Costentin, C.; Robert, M.; Savéant, J.-M. Concerted Proton–Electron Transfers: Electrochemical and Related Approaches. *Accounts Chem. Res.* 2010, *43* (7), 1019-1029. DOI: 10.1021/ar9002812.
- [149] Tyburski, R.; Liu, T.; Glover, S. D.; Hammarstrom, L. Proton-Coupled Electron Transfer Guidelines, Fair and Square. *J. Am. Chem. Soc.* 2021, *143* (2), 560-576. DOI: 10.1021/jacs.0c09106.
- [150] Bonin, J.; Robert, M. Photoinduced Proton-Coupled Electron Transfers in Biorelevant Phenolic Systems. *Photochem. Photobiol.* 2011, *87* (6), 1190-1203. DOI: 10.1111/j.1751-1097.2011.00996.x.
- [151] Capaldo, L.; Ravelli, D. Hydrogen Atom Transfer (HAT): A Versatile Strategy for Substrate Activation in Photocatalyzed Organic Synthesis. *Eur. J. Org. Chem.* 2017, *2017* (15), 2056-2071. DOI: 10.1002/ejoc.201601485.



- [152] Capaldo, L.; Ravelli, D.; Fagnoni, M. Direct Photocatalyzed Hydrogen Atom Transfer (HAT) for Aliphatic C–H Bonds Elaboration. *Chem. Rev.* 2022, 122 (2), 1875-1924. DOI: 10.1021/acs.chemrev.1c00263.
- [153] Murray, P. R. D.; Cox, J. H.; Chiappini, N. D.; Roos, C. B.; McLoughlin, E. A.; Hejna, B. G.; Nguyen, S. T.; Ripberger, H. H.; Ganley, J. M.; Tsui, E.; et al. Photochemical and Electrochemical Applications of Proton-Coupled Electron Transfer in Organic Synthesis. *Chem. Rev.* 2022, 122 (2), 2017-2291. DOI: 10.1021/acs.chemrev.1c00374.
- [154] Tsui, E.; Metrano, A. J.; Tsuchiya, Y.; Knowles, R. R. Catalytic Hydroetherification of Unactivated Alkenes Enabled by Proton-Coupled Electron Transfer. *Angew. Chem. Int. Ed. Engl.* 2020, 59 (29), 11845-11849. DOI: 10.1002/anie.202003959.
- [155] Roos, C. B.; Demaerel, J.; Graff, D. E.; Knowles, R. R. Enantioselective Hydroamination of Alkenes with Sulfonamides Enabled by Proton-Coupled Electron Transfer. *J. Am. Chem. Soc.* 2020, 142 (13), 5974-5979. DOI: 10.1021/jacs.0c01332.
- [156] Fan, X.-Z.; Rong, J.-W.; Wu, H.-L.; Zhou, Q.; Deng, H.-P.; Tan, J. D.; Xue, C.-W.; Wu, L.-Z.; Tao, H.-R.; Wu, J. Eosin Y as a Direct Hydrogen-Atom Transfer Photocatalyst for the Functionalization of C–H Bonds. *Angew. Chem. Int. Ed. Engl.* 2018, 57 (28), 8514-8518. DOI: 10.1002/anie.201803220.
- [157] Chen, C.; Shi, T.; Chang, W.; Zhao, J. Essential Roles of Proton Transfer in Photocatalytic Redox Reactions. *ChemCatChem* 2015, 7 (5), 724-731. DOI: 10.1002/cctc.201402880.
- [158] Laudadio, G.; Deng, Y.; Wal, K. v. d.; Ravelli, D.; Nuño, M.; Fagnoni, M.; Guthrie, D.; Sun, Y.; Noël, T. C(sp<sup>3</sup>)-H functionalizations of light hydrocarbons using decatungstate photocatalysis in flow. *Science* 2020, 369 (6499), 92-96. DOI: 10.1126/science.abb4688.
- [159] Yang, Q.; Pan, G.; Wei, J.; Wang, W.; Tang, Y.; Cai, Y. Remarkable Activity of Potassium-Modified Carbon Nitride for Heterogeneous Photocatalytic Decarboxylative Alkyl/Acyl Radical Addition and Reductive Dimerization of para-Quinone Methides. *ACS Sustain. Chem. Eng.* 2021, 9 (5), 2367-2377. DOI: 10.1021/acssuschemeng.0c08771.
- [160] Vijeta, A.; Reisner, E. Carbon nitride as a heterogeneous visible-light photocatalyst for the Minisci reaction and coupling to H<sub>2</sub> production. *Chem. Commun.* 2019, 55 (93), 14007-14010, 10.1039/C9CC07348E. DOI: 10.1039/C9CC07348E.
- [161] Rabe, E. J.; Corp, K. L.; Huang, X.; Ehrmaier, J.; Flores, R. G.; Estes, S. L.; Sobolewski, A. L.; Domcke, W.; Schlenker, C. W. Barrierless Heptazine-Driven Excited State Proton-Coupled Electron Transfer: Implications for Controlling Photochemistry of Carbon Nitrides and Aza-Arenes. *J. Phys. Chem. C* 2019, 123 (49), 29580-29588. DOI: 10.1021/acs.jpcc.9b08842.
- [162] Corp, K. L.; Rabe, E. J.; Huang, X.; Ehrmaier, J.; Kaiser, M. E.; Sobolewski, A. L.; Domcke, W.; Schlenker, C. W. Control of Excited-State Proton-Coupled Electron Transfer by Ultrafast Pump-Push-Probe Spectroscopy in Heptazine-Phenol Complexes: Implications for Photochemical Water Oxidation. *J. Phys. Chem. C* 2020, 124 (17), 9151-9160. DOI: 10.1021/acs.jpcc.0c00415.
- [163] Hwang, D.; Schlenker, C. W. Photochemistry of carbon nitrides and heptazine derivatives. *Chem. Commun.* 2021, 57 (74), 9330-9353. DOI: 10.1039/d1cc02745j.
- [164] Rieth, A. J.; Qin, Y.; Martindale, B. C. M.; Nocera, D. G. Long-Lived Triplet Excited State in a Heterogeneous Modified Carbon Nitride Photocatalyst. *J. Am. Chem. Soc.* 2021, 143 (12), 4646-4652. DOI: 10.1021/jacs.0c12958.
- [165] Das, S.; Murugesan, K.; Villegas Rodríguez, G. J.; Kaur, J.; Barham, J. P.; Savateev, A.; Antonietti, M.; König, B. Photocatalytic (Het)arylation of C(sp<sup>3</sup>)-H Bonds with Carbon Nitride. *ACS Catal.* 2021, 11 (3), 1593-1603. DOI: 10.1021/acscatal.0c05694.



- [166] Markushyna, Y.; Lamagni, P.; Teutloff, C.; Catalano, J.; Lock, N.; Zhang, G.; Antonietti, M.; Savateev, A. Green radicals of potassium poly(heptazine imide) using light and benzylamine. *J. Mater. Chem. A* 2019, 7 (43), 24771-24775, 10.1039/C9TA09500D. DOI: 10.1039/C9TA09500D.
- [167] Mazzanti, S.; Schritt, C.; Brummelhuis, K.; Antonietti, M.; Savateev, A. Multisite PCET with photocharged carbon nitride in dark. *Exploration* 2021, 1 (3). DOI: 10.1002/exp.20210063.
- [168] Zhou, H.; Mu, S.; Ren, B.-H.; Zhang, R.; Lu, X.-B. Organocatalyzed carboxylative cyclization of propargylic amides with atmospheric CO<sub>2</sub> towards oxazolidine-2,4-diones. *Green Chem.* 2019, 21 (5), 991-994. DOI: 10.1039/c8gc03929a.
- [169] Nair, V. A.; Mustafa, S. M.; Mohler, M. L.; Dalton, J. T.; Miller, D. D. Synthesis of oxazolidinedione derived bicalutamide analogs. *Tetrahedron Lett.* 2006, 47 (23), 3953-3955. DOI: 10.1016/j.tetlet.2006.03.146.
- [170] Cox, J. M.; Chu, H. D.; Yang, C.; Shen, H. C.; Wu, Z.; Balsells, J.; Crespo, A.; Brown, P.; Zamlynyy, B.; Wiltsie, J.; et al. Mineralocorticoid receptor antagonists: identification of heterocyclic amide replacements in the oxazolidinedione series. *Bioorg. Med. Chem. Lett.* 2014, 24 (7), 1681-1684. DOI: 10.1016/j.bmcl.2014.02.057.
- [171] Yeh, V.; Iyengar, R. Oxazoles. In *Comprehensive Heterocyclic Chemistry III*, 2008; pp 487-543.
- [172] Cao, Y.; Suzuki, K.; Tajima, T.; Fuchigami, T. Electrolytic partial fluorination of organic compounds. Part 78: Regioselective anodic fluorination of 2-oxazolidinones. *Tetrahedron* 2005, 61 (28), 6854-6859. DOI: 10.1016/j.tet.2005.04.057.
- [173] Gramain, J.-C.; Remuson, R. Photo-oxidation of oxazolidones and hydantoin in the presence of benzophenone. *J. Chem. Soc.* 1982. DOI: 10.1039/p19820002341.
- [174] Huang, W.; Wang, M.; Yue, H. Conversion of *N*-Acyl Amino Acids into Imides via Oxidative Decarboxylation Induced by Ag<sup>+</sup>/Cu<sup>2+</sup>/S<sub>2</sub>O<sub>8</sub><sup>2-</sup> in Water. *Synthesis* 2008, 2008 (9), 1342-1344. DOI: 10.1055/s-2008-1072563.
- [175] Biswas, S.; Khanna, H. S.; Nizami, Q. A.; Caldwell, D. R.; Cavanaugh, K. T.; Howell, A. R.; Raman, S.; Suib, S. L.; Nandi, P. Heterogeneous Catalytic Oxidation of Amides to Imides by Manganese Oxides. *Sci. Rep.* 2018, 8 (1), 13649. DOI: 10.1038/s41598-018-31729-3.
- [176] Sperry, J. The Oxidation of Amides to Imides: A Powerful Synthetic Transformation. *Synthesis* 2011, 2011 (22), 3569-3580. DOI: 10.1055/s-0030-1260237.
- [177] Nicolaou, K. C.; Mathison, C. J. Synthesis of imides, *N*-acyl vinylogous carbamates and ureas, and nitriles by oxidation of amides and amines with Dess-Martin periodinane. *Angew. Chem. Int. Ed. Engl.* 2005, 44 (37), 5992-5997. DOI: 10.1002/anie.200501853.
- [178] Lu, W.; Mei, C.; Hu, Y. Visible-Light-Driven Oxidation of *N*-Alkylamides to Imides Using Oxone/H<sub>2</sub>O and Catalytic KBr. *Synthesis* 2018, 50 (15), 2999-3005. DOI: 10.1055/s-0036-1591575.
- [179] Ghosh, I.; Khamrai, J.; Savateev, A.; Shlapakov, N.; Antonietti, M.; König, B. Organic semiconductor photocatalyst can bifunctionalize arenes and heteroarenes. *Science* 2019, 365 (6451), 360-366. DOI: 10.1126/science.aaw3254.
- [180] Savateev, A.; Dontsova, D.; Kurpil, B.; Antonietti, M. Highly crystalline poly(heptazine imides) by mechanochemical synthesis for photooxidation of various organic substrates using an intriguing electron acceptor – Elemental sulfur. *J. Catal.* 2017, 350, 203-211. DOI: 10.1016/j.jcat.2017.02.029.
- [181] Chen, Z.; Savateev, A.; Pronkin, S.; Papaefthimiou, V.; Wolff, C.; Willinger, M. G.; Willinger, E.; Neher, D.; Antonietti, M.; Dontsova, D. "The Easier the Better" Preparation of Efficient Photocatalysts—



- Metastable Poly(heptazine imide) Salts. *Adv. Mater.* 2017, 29 (32), 1700555. DOI: 10.1002/adma.201700555.
- [182] Savateev, A.; Pronkin, S.; Epping, J. D.; Willinger, M. G.; Wolff, C.; Neher, D.; Antonietti, M.; Dontsova, D. Potassium Poly(heptazine imides) from Aminotetrazoles: Shifting Band Gaps of Carbon Nitride-like Materials for More Efficient Solar Hydrogen and Oxygen Evolution. *ChemCatChem* 2017, 9 (1), 167-174. DOI: 10.1002/cctc.201601165.
- [183] Sender, M.; Ziegenbalg, D. Light Sources for Photochemical Processes – Estimation of Technological Potentials. *Chem.-Ing.-Tech.* 2017, 89 (9), 1159-1173. DOI: 10.1002/cite.201600191.
- [184] Martín, V. S.; Palazón, J. M.; Rodríguez, C. M.; Nevill, C. R.; Hutchinson, D. K. Ruthenium(VIII) Oxide. In *Encyclopedia of Reagents for Organic Synthesis*, 2013.
- [185] Zhang, Y.; Ye, C.; Li, S.; Ding, A.; Gu, G.; Guo, H. Eosin Y-catalyzed photooxidation of triarylphosphines under visible light irradiation and aerobic conditions. *RSC Advances* 2017, 7 (22), 13240-13243. DOI: 10.1039/c6ra25469a.
- [186] Gramain, J.-C.; Remuson, R.; Troin, Y. A new photo-oxidation: the transformation of lactams into imides. *J. Chem. Soc. Chem. Comm.* 1976, (6). DOI: 10.1039/c39760000194.
- [187] Gramain, J.-C.; Remuson, R.; Troin, Y. Une nouvelle réaction de photooxydation: transformation de lactames et d'amides en imides et hydroperoxydes. *Tetrahedron* 1979, 35 (6), 759-765. DOI: 10.1016/0040-4020(79)80092-7.
- [188] Galushchinskiy, A.; ten Brummelhuis, K.; Antonietti, M.; Savateev, A. Insights Into the Mechanism of Energy Transfer with Poly(Heptazine Imide)s in a Deoxygenation Reaction. *ChemPhotoChem* 2021, 5 (11), 1020-1025. DOI: 10.1002/cptc.202100088.
- [189] Kresse, G.; Furthmüller, J. Efficient iterative schemes for ab initio total-energy calculations using a plane-wave basis set. *Phys. Rev. B* 1996, 54 (16), 11169-11186. DOI: 10.1103/physrevb.54.11169.
- [190] Kresse, G.; Joubert, D. From ultrasoft pseudopotentials to the projector augmented-wave method. *Phys. Rev. B* 1999, 59 (3), 1758-1775. DOI: 10.1103/PhysRevB.59.1758.
- [191] Perdew, J. P.; Burke, K.; Ernzerhof, M. Generalized Gradient Approximation Made Simple. *Phys. Rev. Lett.* 1996, 77 (18), 3865-3868. DOI: 10.1103/PhysRevLett.77.3865.
- [192] Nikačević, P. DOI: 10.19061/iochem-bd-1-249. Access link for reviewers: <https://iochem-bd.iciq.es/browse/review-collection/100/40299/3d42cf404391d9635add44a1>. DOI: 10.19061/iochem-bd-1-234.
- [193] Actis, A.; Melchionna, M.; Filippini, G.; Fornasiero, P.; Prato, M.; Salvadori, E.; Chiesa, M. Morphology and Light-Dependent Spatial Distribution of Spin Defects in Carbon Nitride. *Angew. Chem. Int. Ed. Engl.* 2022, 61 (43), e202210640. DOI: 10.1002/anie.202210640.
- [194] Heyd, J.; Scuseria, G. E.; Ernzerhof, M. Hybrid functionals based on a screened Coulomb potential. *J. Chem. Phys.* 2003, 118 (18), 8207-8215. DOI: 10.1063/1.1564060.
- [195] Heyd, J.; Scuseria, G. E.; Ernzerhof, M. Erratum: "Hybrid functionals based on a screened Coulomb potential" [J. Chem. Phys. 118, 8207 (2003)]. *J. Chem. Phys.* 2006, 124 (21). DOI: 10.1063/1.2204597.
- [196] Lau, V. W.-h.; Lotsch, B. V. A Tour-Guide through Carbon Nitride-Land: Structure- and Dimensionality-Dependent Properties for Photo(Electro)Chemical Energy Conversion and Storage. *Adv. Energy Mater.* 2022, 12 (4), 2101078. DOI: 10.1002/aenm.202101078.
- [197] Song, T.; Zhou, B.; Peng, G.-W.; Zhang, Q.-B.; Wu, L.-Z.; Liu, Q.; Wang, Y. Aerobic Oxidative Coupling of Resveratrol and its Analogues by Visible Light Using Mesoporous Graphitic Carbon Nitride (mpg-



- C3N4) as a Bioinspired Catalyst. *Chem. Eur. J.* 2014, 20 (3), 678-682. DOI: 10.1002/chem.201303587.
- [198] Cai, Y.; Tang, Y.; Fan, L.; Lefebvre, Q.; Hou, H.; Rueping, M. Heterogeneous Visible-Light Photoredox Catalysis with Graphitic Carbon Nitride for  $\alpha$ -Aminoalkyl Radical Additions, Allylations, and Heteroarylations. *ACS Catal.* 2018, 8 (10), 9471-9476. DOI: 10.1021/acscatal.8b02937.
- [199] Waidmann, C. R.; Miller, A. J. M.; Ng, C.-W. A.; Scheuermann, M. L.; Porter, T. R.; Tronic, T. A.; Mayer, J. M. Using combinations of oxidants and bases as PCET reactants: thermochemical and practical considerations. *Energ. Environ. Sci.* 2012, 5 (7), 7771-7780, 10.1039/C2EE03300C. DOI: 10.1039/C2EE03300C.
- [200] Kröger, J.; Podjaski, F.; Savasci, G.; Moudrakovski, I.; Jiménez-Solano, A.; Terban, M. W.; Bette, S.; Duppel, V.; Joos, M.; Senocrate, A.; et al. Conductivity Mechanism in Ionic 2D Carbon Nitrides: From Hydrated Ion Motion to Enhanced Photocatalysis. *Adv. Mater.* 2022, 34 (7), 2107061. DOI: 10.1002/adma.202107061.
- [201] Teixeira, I. F.; Tarakina, N. V.; Silva, I. F.; López-Salas, N.; Savateev, A.; Antonietti, M. Overcoming Electron Transfer Efficiency Bottlenecks for Hydrogen Production in Highly Crystalline Carbon Nitride-Based Materials. *Adv. Sustainable Syst.* 2022, 6 (3), 2100429. DOI: 10.1002/adsu.202100429.
- [202] Savateev, A.; Antonietti, M. Ionic Carbon Nitrides in Solar Hydrogen Production and Organic Synthesis: Exciting Chemistry and Economic Advantages. *ChemCatChem* 2019, 11 (24), 6166-6176. DOI: 10.1002/cctc.201901076.
- [203] Miller, T. S.; Jorge, A. B.; Suter, T. M.; Sella, A.; Cora, F.; McMillan, P. F. Carbon nitrides: synthesis and characterization of a new class of functional materials. *Phys. Chem. Chem. Phys.* 2017, 19 (24), 15613-15638. DOI: 10.1039/c7cp02711g.
- [204] Thomas, A.; Fischer, A.; Goettmann, F.; Antonietti, M.; Müller, J.-O.; Schlögl, R.; Carlsson, J. M. Graphitic carbon nitride materials: variation of structure and morphology and their use as metal-free catalysts. *J. Mater. Chem.* 2008, 18 (41), 4893-4908. DOI: 10.1039/b800274f.
- [205] Cao, S.; Low, J.; Yu, J.; Jaroniec, M. Polymeric photocatalysts based on graphitic carbon nitride. *Adv. Mater.* 2015, 27 (13), 2150-2176. DOI: 10.1002/adma.201500033.
- [206] Zhang, G.; Lin, L.; Li, G.; Zhang, Y.; Savateev, A.; Zafeiratos, S.; Wang, X.; Antonietti, M. Ionothermal Synthesis of Triazine-Heptazine-Based Copolymers with Apparent Quantum Yields of 60% at 420 nm for Solar Hydrogen Production from "Sea Water". *Angew. Chem. Int. Ed. Engl.* 2018, 57 (30), 9372-9376. DOI: 10.1002/anie.201804702.
- [207] Liu, D.; Li, C.; Zhao, C.; Zhao, Q.; Niu, T.; Pan, L.; Xu, P.; Zhang, F.; Wu, W.; Ni, T. Facile synthesis of three-dimensional hollow porous carbon doped polymeric carbon nitride with highly efficient photocatalytic performance. *Chem. Eng. J.* 2022, 438. DOI: 10.1016/j.cej.2022.135623.
- [208] Ni, T.; Zhang, H.; Yang, Z.; Zhou, L.; Pan, L.; Li, C.; Yang, Z.; Liu, D. Enhanced adsorption and catalytic degradation of antibiotics by porous OD/3D Co<sub>3</sub>O<sub>4</sub>/g-C<sub>3</sub>N<sub>4</sub> activated peroxydisulfate: An experimental and mechanistic study. *J. Colloid Interf. Sci.* 2022, 625, 466-478. DOI: 10.1016/j.jcis.2022.06.057.
- [209] Liu, D.; Li, C.; Ni, T.; Gao, R.; Ge, J.; Zhang, F.; Wu, W.; Li, J.; Zhao, Q. 3D interconnected porous g-C<sub>3</sub>N<sub>4</sub> hybridized with Fe<sub>2</sub>O<sub>3</sub> quantum dots for enhanced photo-Fenton performance. *Appl. Surf. Sci.* 2021, 555. DOI: 10.1016/j.apsusc.2021.149677.
- [210] Markushyna, Y.; Smith, C. A.; Savateev, A. Organic Photocatalysis: Carbon Nitride Semiconductors vs. Molecular Catalysts. *Eur. J. Org. Chem.* 2019, 2020 (10), 1294-1309. DOI: 10.1002/ejoc.201901112.



- [211] Botari, T.; Huhn, W. P.; Lau, V. W.-h.; Lotsch, B. V.; Blum, V. Thermodynamic Equilibria in Carbon Nitride Photocatalyst Materials and Conditions for the Existence of Graphitic Carbon Nitride g-C<sub>3</sub>N<sub>4</sub>. *Chem. Mater.* 2017, *29* (10), 4445-4453. DOI: 10.1021/acs.chemmater.7b00965.
- [212] Beale, A. M.; Craigmill, A. L.; Wetzlich, S. A rapid lead test: public outreach and testing to detect leachable lead in ceramic ware. *Arch. Environ. Contam. Toxicol.* 1991, *20* (3), 423-426. DOI: 10.1007/BF01064414.
- [213] Iraci, G.; Back, M. H. The photochemistry of the rhodizonate dianion in aqueous solution. *Can. J. Chem.* 1988, *66* (5), 1293-1294. DOI: 10.1139/v88-209.
- [214] Potassium rhodizonate, technical, 85%, CAS RN: 13021-40-4; 392340; Aldrich, Sigma Aldrich: Taufkirchen, Germany. April 4, 2022. <https://www.sigmaaldrich.com/DE/en/sds/aldrich/392340> (accessed 2022-11-06).
- [215] Preisler, P. W.; Berger, L. Preparation of Tetrahydroxyquinone and Rhodizonic Acid Salts from the Product of the Oxidation of Inositol with Nitric Acid. *JACS* 2002, *64* (1), 67-69. DOI: 10.1021/ja01253a016.
- [216] Lee, M.; Hong, J.; Lopez, J.; Sun, Y.; Feng, D.; Lim, K.; Chueh, W. C.; Toney, M. F.; Cui, Y.; Bao, Z. High-performance sodium-organic battery by realizing four-sodium storage in disodium rhodizonate. *Nat. Energy* 2017, *2* (11), 861-868. DOI: 10.1038/s41560-017-0014-y.
- [217] Eistert, B.; Fink, H.; Werner, H.-K. Phenazin-Derivate aus Rhodizonsäure. *Liebigs Ann. Chem.* 1962, *657* (1), 131-141. DOI: 10.1002/jlac.19626570118.
- [218] GÜthner, T.; Mertschenk, B. Cyanamides. In *Ullmann's Encyclopedia of Industrial Chemistry*, 2006.
- [219] Fechler, N.; Zussblatt, N. P.; Rothe, R.; Schlogl, R.; Willinger, M. G.; Chmelka, B. F.; Antonietti, M. Eutectic Syntheses of Graphitic Carbon with High Pyrazinic Nitrogen Content. *Adv. Mater.* 2016, *28* (6), 1287-1294. DOI: 10.1002/adma.201501503.
- [220] Schlomberg, H.; Kroger, J.; Savasci, G.; Terban, M. W.; Bette, S.; Moudrakovski, I.; Duppel, V.; Podjaski, F.; Siegel, R.; Senker, J.; et al. Structural Insights into Poly(Heptazine Imides): A Light-Storing Carbon Nitride Material for Dark Photocatalysis. *Chem. Mater.* 2019, *31* (18), 7478-7486. DOI: 10.1021/acs.chemmater.9b02199.
- [221] Teixeira, I. F.; Tarakina, N. V.; Silva, I. F.; Atta Diab, G. A.; Salas, N. L.; Savateev, A.; Antonietti, M. Improving hydrogen production for carbon-nitride-based materials: crystallinity, cyanamide groups and alkali metals in solution working synergistically. *J. Mater. Chem. A* 2022, *10* (35), 18156-18161. DOI: 10.1039/d2ta05571f.
- [222] Lau, V. W.; Moudrakovski, I.; Botari, T.; Weinberger, S.; Mesch, M. B.; Duppel, V.; Senker, J.; Blum, V.; Lotsch, B. V. Rational design of carbon nitride photocatalysts by identification of cyanamide defects as catalytically relevant sites. *Nat. Commun.* 2016, *7*, 12165. DOI: 10.1038/ncomms12165.
- [223] Liao, C. Z.; Lau, V. W.; Su, M.; Ma, S.; Liu, C.; Chang, C. K.; Sheu, H. S.; Zhang, J.; Shih, K. Unraveling the Structure of the Poly(triazine imide)/LiCl Photocatalyst: Cooperation of Facile Syntheses and a Low-Temperature Synchrotron Approach. *Inorg. Chem.* 2019, *58* (23), 15880-15888. DOI: 10.1021/acs.inorgchem.9b02287.
- [224] Wirnhier, E.; Dobliger, M.; Gunzelmann, D.; Senker, J.; Lotsch, B. V.; Schnick, W. Poly(triazine imide) with intercalation of lithium and chloride ions [(C<sub>3</sub>N<sub>3</sub>)<sub>2</sub>(NH<sub>x</sub>)Li<sub>(1-x)</sub>]<sub>3</sub>LiCl]: a crystalline 2D carbon nitride network. *Chem. Eur. J.* 2011, *17* (11), 3213-3221. DOI: 10.1002/chem.201002462.



- [225] Dontsova, D.; Pronkin, S.; Wehle, M.; Chen, Z.; Fettkenhauer, C.; Clavel, G.; Antonietti, M. Triazoles: A New Class of Precursors for the Synthesis of Negatively Charged Carbon Nitride Derivatives. *Chem. Mater.* 2015, *27* (15), 5170-5179. DOI: 10.1021/acs.chemmater.5b00812.
- [226] Burmeister, D.; Tran, H. A.; Muller, J.; Guerrini, M.; Cocchi, C.; Plaickner, J.; Kochovski, Z.; List-Kratochvil, E. J. W.; Bojdys, M. J. Optimized Synthesis of Solution-Processable Crystalline Poly(Triazine Imide) with Minimized Defects for OLED Application. *Angew. Chem. Int. Ed. Engl.* 2022, *61* (3), e202111749. DOI: 10.1002/anie.202111749.
- [227] Mesch, M. B.; Barwinkel, K.; Krysiak, Y.; Martineau, C.; Taulelle, F.; Neder, R. B.; Kolb, U.; Senker, J. Solving the Hydrogen and Lithium Substructure of Poly(triazine imide)/LiCl Using NMR Crystallography. *Chem. Eur. J.* 2016, *22* (47), 16878-16890. DOI: 10.1002/chem.201603726.
- [228] Jin, Z.; Jiang, X.; Zhang, Q.; Huang, S.; Zhang, L.; Huang, L.; He, T.; Zhang, H.; Ohno, T.; Ruan, S.; et al. Infrared response in photocatalytic polymeric carbon nitride for water splitting via an upconversion mechanism. *Commun. Mater.* 2020, *1* (1), 104252. DOI: 10.1038/s43246-020-00093-Z.
- [229] Zhang, G.; Savateev, A.; Zhao, Y.; Li, L.; Antonietti, M. Advancing the  $n \rightarrow \pi^*$  electron transition of carbon nitride nanotubes for H<sub>2</sub> photosynthesis. *J. Mater. Chem. A* 2017, *5* (25), 12723-12728. DOI: 10.1039/c7ta03777e.
- [230] Lv, H.; Huang, Y.; Koodali, R. T.; Liu, G.; Zeng, Y.; Meng, Q.; Yuan, M. Synthesis of Sulfur-Doped 2D Graphitic Carbon Nitride Nanosheets for Efficient Photocatalytic Degradation of Phenol and Hydrogen Evolution. *ACS Appl. Mater. Interfaces* 2020, *12* (11), 12656-12667. DOI: 10.1021/acsami.9b19057.
- [231] Chandra, M.; Guharoy, U.; Pradhan, D. Boosting the Photocatalytic H<sub>2</sub> Evolution and Benzylamine Oxidation using 2D/1D g-C<sub>3</sub>N<sub>4</sub>/TiO<sub>2</sub> Nanoheterojunction. *ACS Appl. Mater. Interfaces* 2022, *14* (19), 22122-22137. DOI: 10.1021/acsami.2c03230.
- [232] Wei, S.; Zhong, H.; Wang, H.; Song, Y.; Jia, C.; Anpo, M.; Wu, L. Oxygen vacancy enhanced visible light photocatalytic selective oxidation of benzylamine over ultrathin Pd/BiOCl nanosheets. *Appl. Catal. B-Environ.* 2022, *305*, 121032. DOI: 10.1016/j.apcatb.2021.121032.
- [233] Su, Z.; Zhang, B.; Cheng, X.; Xu, M.; Chen, G.; Sha, Y.; Wang, Y.; Hu, J.; Duan, R.; Zhang, J. SnS<sub>2</sub>/polypyrrole for high-efficiency photocatalytic oxidation of benzylamine. *Dalton Trans.* 2022, *51* (36), 13601-13605. DOI: 10.1039/d2dt01899c.
- [234] Ung, S. P. M.; Perepichka, I.; Li, C. J. Visible-Light Mediated Photooxidative Phosphorylation of Benzylamines: A Novel and Mild Pathway Towards  $\alpha$ -Aminophosphorus Compounds. *Helv. Chim. Acta* 2021, *105* (1), e202100190. DOI: 10.1002/hlca.202100190.
- [235] Zhang, G.; Li, G.; Lan, Z. A.; Lin, L.; Savateev, A.; Heil, T.; Zafeiratos, S.; Wang, X.; Antonietti, M. Optimizing Optical Absorption, Exciton Dissociation, and Charge Transfer of a Polymeric Carbon Nitride with Ultrahigh Solar Hydrogen Production Activity. *Angew. Chem. Int. Ed. Engl.* 2017, *56* (43), 13445-13449. DOI: 10.1002/anie.201706870.
- [236] Biffis, A.; Centomo, P.; Del Zotto, A.; Zecca, M. Pd Metal Catalysts for Cross-Couplings and Related Reactions in the 21st Century: A Critical Review. *Chem. Rev.* 2018, *118* (4), 2249-2295. DOI: 10.1021/acs.chemrev.7b00443.
- [237] Ruiz-Castillo, P.; Buchwald, S. L. Applications of Palladium-Catalyzed C-N Cross-Coupling Reactions. *Chem. Rev.* 2016, *116* (19), 12564-12649. DOI: 10.1021/acs.chemrev.6b00512.
- [238] Johansson Seechurn, C. C.; Kitching, M. O.; Colacot, T. J.; Snieckus, V. Palladium-catalyzed cross-coupling: a historical contextual perspective to the 2010 Nobel Prize. *Angew. Chem. Int. Ed. Engl.* 2012, *51* (21), 5062-5085. DOI: 10.1002/anie.201107017.



- [239] Cooper, A. K.; Burton, P. M.; Nelson, D. J. Nickel versus Palladium in Cross-Coupling Catalysis: On the Role of Substrate Coordination to Zerovalent Metal Complexes. *Synthesis* 2019, 52 (04), 565-573. DOI: 10.1055/s-0039-1690045.
- [240] Gisbertz, S.; Reischauer, S.; Pieber, B. Overcoming limitations in dual photoredox/nickel-catalysed C–N cross-couplings due to catalyst deactivation. *Nat. Catal.* 2020, 3 (8), 611-620. DOI: 10.1038/s41929-020-0473-6.
- [241] Cavedon, C.; Madani, A.; Seeberger, P. H.; Pieber, B. Semiheterogeneous Dual Nickel/Photocatalytic (Thio)etherification Using Carbon Nitrides. *Org. Lett.* 2019, 21 (13), 5331-5334. DOI: 10.1021/acs.orglett.9b01957.
- [242] Pieber, B.; Malik, J. A.; Cavedon, C.; Gisbertz, S.; Savateev, A.; Cruz, D.; Heil, T.; Zhang, G.; Seeberger, P. H. Semi-heterogeneous Dual Nickel/Photocatalysis using Carbon Nitrides: Esterification of Carboxylic Acids with Aryl Halides. *Angew. Chem. Int. Ed. Engl.* 2019, 58 (28), 9575-9580. DOI: 10.1002/anie.201902785.
- [243] Zou, Y.; Abednatanzi, S.; Gohari Derakhshandeh, P.; Mazzanti, S.; Schusslbauer, C. M.; Cruz, D.; Van Der Voort, P.; Shi, J. W.; Antonietti, M.; Guldi, D. M.; et al. Red edge effect and chromoselective photocatalysis with amorphous covalent triazine-based frameworks. *Nat. Commun.* 2022, 13 (1), 2171. DOI: 10.1038/s41467-022-29781-9.
- [244] Campos-Martin, J. M.; Blanco-Brieva, G.; Fierro, J. L. Hydrogen peroxide synthesis: an outlook beyond the anthraquinone process. *Angew. Chem. Int. Ed. Engl.* 2006, 45 (42), 6962-6984. DOI: 10.1002/anie.200503779.
- [245] Shi, X.; Siahrostami, S.; Li, G. L.; Zhang, Y.; Chakthranont, P.; Studt, F.; Jaramillo, T. F.; Zheng, X.; Nørskov, J. K. Understanding activity trends in electrochemical water oxidation to form hydrogen peroxide. *Nat. Commun.* 2017, 8 (1), 701. DOI: 10.1038/s41467-017-00585-6.
- [246] Liu, J.; Zou, Y.; Jin, B.; Zhang, K.; Park, J. H. Hydrogen Peroxide Production from Solar Water Oxidation. *ACS Energy Lett.* 2019, 4 (12), 3018-3027. DOI: 10.1021/acscenergylett.9b02199.
- [247] Hou, H.; Zeng, X.; Zhang, X. Production of Hydrogen Peroxide by Photocatalytic Processes. *Angew. Chem. Int. Ed. Engl.* 2020, 59 (40), 17356-17376. DOI: 10.1002/anie.201911609.
- [248] Teranishi, M.; Naya, S.-i.; Tada, H. Temperature- and pH-Dependence of Hydrogen Peroxide Formation from Molecular Oxygen by Gold Nanoparticle-Loaded Titanium(IV) Oxide Photocatalyst. *J. Phys. Chem. C* 2016, 120 (2), 1083-1088. DOI: 10.1021/acs.jpcc.5b10626.
- [249] Gryszel, M.; Sytnyk, M.; Jakesova, M.; Romanazzi, G.; Gabrielsson, R.; Heiss, W.; Glowacki, E. D. General Observation of Photocatalytic Oxygen Reduction to Hydrogen Peroxide by Organic Semiconductor Thin Films and Colloidal Crystals. *ACS Appl. Mater. Interfaces* 2018, 10 (16), 13253-13257. DOI: 10.1021/acsami.8b01295.
- [250] Uekert, T.; Bajada, M. A.; Schubert, T.; Pichler, C. M.; Reisner, E. Scalable Photocatalyst Panels for Photoreforming of Plastic, Biomass and Mixed Waste in Flow. *ChemSusChem* 2021, 14 (19), 4190-4197. DOI: 10.1002/cssc.202002580.
- [251] Wang, E.-C.; Huang, K.-S.; Chen, H.-M.; Wu, C.-C.; Lin, G.-J. An Efficient Method for the Preparation of Nitriles via the Dehydration of Aldoximes with Phthalic Anhydride. *J. Chin. Chem. Soc.-Taip.* 2004, 51 (3), 619-627. DOI: 10.1002/jccs.200400093.
- [252] Anderson, H. J. Pyrrole Chemistry: II. 2-Pyrrolicarbonitrile, 1-Methyl-2-Pyrrolicarbonitrile, and Their Nitration Products. *Can. J. Chem.* 1959, 37 (12), 2053-2058. DOI: 10.1139/v59-298.
- [253] Pedras, M. S.; Minic, Z.; Thongbam, P. D.; Bhaskar, V.; Montaut, S. Indolyl-3-acetaldoxime dehydratase from the phytopathogenic fungus *Sclerotinia sclerotiorum*: purification,



- characterization, and substrate specificity. *Phytochemistry* 2010, 71 (17-18), 1952-1962. DOI: 10.1016/j.phytochem.2010.10.002.
- [254] Pohjakallio, A.; Pihko, P. M. Enantioselective synthesis of 2-isoxazolines by a one-flask conjugate addition/oxime-transfer process. *Chem. Eur. J.* 2009, 15 (16), 3960-3964. DOI: 10.1002/chem.200802684.
- [255] Augustine, J. K.; Kumar, R.; Bombrun, A.; Mandal, A. B. An efficient catalytic method for the Beckmann rearrangement of ketoximes to amides and aldoximes to nitriles mediated by propylphosphonic anhydride (T3P®). *Tetrahedron Lett.* 2011, 52 (10), 1074-1077. DOI: 10.1016/j.tetlet.2010.12.090.
- [256] Pusterla, I.; Bode, J. W. The mechanism of the alpha-ketoacid-hydroxylamine amide-forming ligation. *Angew. Chem. Int. Ed. Engl.* 2012, 51 (2), 513-516. DOI: 10.1002/anie.201107198.
- [257] Jafarpour, F.; Darvishmolla, M. Peroxy mediated Csp(2)-Csp(3) dehydrogenative coupling: regioselective functionalization of coumarins and coumarin-3-carboxylic acids. *Org. Biomol. Chem.* 2018, 16 (18), 3396-3401. DOI: 10.1039/c7ob02771k.
- [258] Vani, P. V. S. N.; Chida, A. S.; Srinivasan, R.; Chandrasekharam, M.; Singh, A. K. Synthesis of *N*-Vinyl-2-Oxazolidone: A Commercially Important Intermediate. *Synthetic Commun.* 2006, 31 (13), 2043-2046. DOI: 10.1081/scc-100104422.
- [259] Poindexter, G. S.; Owens, D. A.; Dolan, P. L.; Woo, E. The use of 2-oxazolidinones as latent aziridine equivalents. 2. Aminoethylation of aromatic amines, phenols, and thiophenols. *J. Org. Chem.* 2002, 57 (23), 6257-6265. DOI: 10.1021/jo00049a037.
- [260] Chang, Z.; Huang, J.; Wang, S.; Chen, G.; Zhao, H.; Wang, R.; Zhao, D. Copper catalyzed late-stage C(sp<sup>3</sup>)-H functionalization of nitrogen heterocycles. *Nat. Commun.* 2021, 12 (1), 4342. DOI: 10.1038/s41467-021-24671-y.
- [261] Oliver-Meseguer, J.; Liu, L.; Garcia-Garcia, S.; Canos-Gimenez, C.; Dominguez, I.; Gavara, R.; Domenech-Carbo, A.; Concepcion, P.; Leyva-Perez, A.; Corma, A. Stabilized naked sub-nanometric Cu clusters within a polymeric film catalyze C-N, C-C, C-O, C-S, and C-P bond-forming reactions. *J. Am. Chem. Soc.* 2015, 137 (11), 3894-3900. DOI: 10.1021/jacs.5b00222.
- [262] Yu, H.; Chen, Y.; Zhang, Y. TBHP/TEMPO-Mediated Oxidative Synthesis of Imides from Amides. *Chinese J. Chem.* 2015, 33 (5), 531-534. DOI: 10.1002/cjoc.201500190.
- [263] Pavlishchuk, V. V.; Addison, A. W. Conversion constants for redox potentials measured versus different reference electrodes in acetonitrile solutions at 25°C. *Inorg. Chim. Acta* 2000, 298 (1), 97-102. DOI: 10.1016/s0020-1693(99)00407-7.
- [264] Blochl, P. E. Projector augmented-wave method. *Phys. Rev. B* 1994, 50 (24), 17953-17979. DOI: 10.1103/physrevb.50.17953.
- [265] Monkhorst, H. J.; Pack, J. D. Special points for Brillouin-zone integrations. *Phys. Rev. B* 1976, 13 (12), 5188-5192. DOI: 10.1103/PhysRevB.13.5188.
- [266] Im, C.; Kirchhoff, B.; Krivtsov, I.; Mitoraj, D.; Beranek, R.; Jacob, T. Structure and optical properties of polymeric carbon nitrides from atomistic simulations. *Arxiv* 2023.
- [267] Alvarez-Moreno, M.; de Graaf, C.; Lopez, N.; Maseras, F.; Poblet, J. M.; Bo, C. Managing the computational chemistry big data problem: the ioChem-BD platform. *J. Chem. Inf. Model.* 2015, 55 (1), 95-103. DOI: 10.1021/ci500593j.



- [268] Wang, V.; Xu, N.; Liu, J.-C.; Tang, G.; Geng, W.-T. VASPKIT: A user-friendly interface facilitating high-throughput computing and analysis using VASP code. *Comput. Phys. Commun.* 2021, 267. DOI: 10.1016/j.cpc.2021.108033.
- [269] Garcia-Rates, M.; Lopez, N. Multigrid-Based Methodology for Implicit Solvation Models in Periodic DFT. *J. Chem. Theory Comput.* 2016, 12 (3), 1331-1341. DOI: 10.1021/acs.jctc.5b00949.
- [270] Momma, K.; Izumi, F. VESTA: a three-dimensional visualization system for electronic and structural analysis. *J. Appl. Crystallogr.* 2008, 41 (3), 653-658. DOI: 10.1107/s0021889808012016.
- [271] Grimme, S.; Antony, J.; Ehrlich, S.; Krieg, H. A consistent and accurate ab initio parametrization of density functional dispersion correction (DFT-D) for the 94 elements H-Pu. *The Journal of Chemical Physics* 2010, 132 (15), 154104. DOI: 10.1063/1.3382344.
- [272] Bagayoko, D. Understanding density functional theory (DFT) and completing it in practice. *AIP Adv.* 2014, 4 (12). DOI: 10.1063/1.4903408.
- [273] Borisov, S. M.; Nuss, G.; Haas, W.; Saf, R.; Schmuck, M.; Klimant, I. New NIR-emitting complexes of platinum(II) and palladium(II) with fluorinated benzoporphyrins. *J. Photoch. Photobio. A* 2009, 201 (2-3), 128-135. DOI: 10.1016/j.jphotochem.2008.10.003.
- [274] Kaur, R. P.; Singh, H. Effect of cyclization on bond dissociation enthalpies, acidities and proton affinities of carbamate molecules: A theoretical study. *Results Chem.* 2019, 1, 100003. DOI: 10.1016/j.rechem.2019.100003.
- [275] Blanksby, S. J.; Ellison, G. B. Bond Dissociation Energies of Organic Molecules. *Accounts Chem. Res.* 2003, 36 (4), 255-263. DOI: 10.1021/ar020230d.
- [276] Peng, G.; Xing, L.; Barrio, J.; Volokh, M.; Shalom, M. A General Synthesis of Porous Carbon Nitride Films with Tunable Surface Area and Photophysical Properties. *Angew. Chem. Int. Ed. Engl.* 2018, 57 (5), 1186-1192. DOI: 10.1002/anie.201711669.
- [277] Stevens, C. V.; Moonen, K. One-Pot Synthesis of N-Chloroacetyl 1-Aminoalkyl Phosphonates - Precursors of 4-Phosphono- $\beta$ -Lactams. *Synthesis* 2005, 2005 (20), 3603-3612. DOI: 10.1055/s-2005-918440.
- [278] Mampuy, P.; Zhu, Y.; Vlaar, T.; Ruijter, E.; Orru, R. V.; Maes, B. U. Sustainable three-component synthesis of isothioureas from isocyanides, thiosulfonates, and amines. *Angew. Chem. Int. Ed. Engl.* 2014, 53 (47), 12849-12854. DOI: 10.1002/anie.201406717.
- [279] Pichler, C. M.; Uekert, T.; Reisner, E. Photoreforming of biomass in metal salt hydrate solutions. *Chem. Commun. (Camb.)* 2020, 56 (43), 5743-5746. DOI: 10.1039/d0cc01686a.
- [280] Indra, A.; Acharjya, A.; Menezes, P. W.; Merschjann, C.; Hollmann, D.; Schwarze, M.; Aktas, M.; Friedrich, A.; Lochbrunner, S.; Thomas, A.; et al. Boosting Visible-Light-Driven Photocatalytic Hydrogen Evolution with an Integrated Nickel Phosphide-Carbon Nitride System. *Angew. Chem. Int. Ed. Engl.* 2017, 56 (6), 1653-1657. DOI: 10.1002/anie.201611605.
- [281] McCafferty, E. *Introduction to Corrosion Science*; Springer New York, NY, 2010. DOI: 10.1007/978-1-4419-0455-3.



## Afterword

---

I asked the earth to open up the sky  
To get inside and live with me for life  
I stand before the sun  
Rise up and see the shape of things to come  
Coil, "Heaven's Blade". *Ape of Naples*, 2005

Abandoning prospective corporate position, crossing the Baltic Sea the most convenient way (via Istanbul), and resettling from Peterhof to its spiritual Prussian twin Potsdam. All because that particular PhD project looked 'sufficiently weird' to you.

And it was damn worth it. No regrets.

Despite a very dystopian start with gloomy October sky, quarantine enclosure and food bags left at the doorstep, things turned out really great eventually. I'm glad I became a member of the awesome Max Planck community, made new friends and hanged out at BBQ parties. And yeah, did a bit of science in between.

First and foremost, thanks to my insanely supportive parents, an enormous part of my success lies on your shoulders. Huge thanks to Markus and Sasha for accepting me and, more importantly, tolerating me all this time into the walls of MPIKG. Shoutout to amazing Solar2Chem/Sorry4Chem Gang for some really quality time together on our semi-annual events and cool collaborations (and to Pau for all the funding!). Extra special thanks go to the present and former members and associates of Innovative Heterogeneous Photocatalysis group, namely Stefano, Zhenia, Gaofeng, Yajun, Lu, Ingrid, Christian, Vitaliy, Gabriel, Sonia, Ivo, Andrea, Giuseppe and Vitor, for your help and support, as well as to the rest of Colloids Department. And thanks to The Great COVID Circus for making my quest of getting to Germany and my adaptation here a bit extra spicy.

That small institute on the hills of Golm changed my life quite a bit, and I will always remember it wherever I go.

